Experimental Assessment and Computational Modeling of Adhesive, Self Piercing Rivets (SPR), and Hybrid (Adhesive-SPR) Joints: Enhancing Joint Performance for Aluminum Sheet Material

by

Ahmed Hanafy Ibrahim

A thesis

presented to the University of Waterloo

in fulfillment of the

thesis requirement for the degree of

Doctor of Philosophy

in

Mechanical and Mechatronics Engineering

Waterloo, Ontario, Canada, 2023

Examining Committee Membership

The following members served on the Examining Committee for this thesis. The decision of the Examining Committee is by majority vote.

External Examiner	Franck Lauro Professor, Laboratoire d'Automatique, de Mécanique et d'Informatique Industrielles et Humaines Université Polytechnique Hauts-de-France
Supervisor	Duane S. Cronin Professor, Department of Mechanical and Mechatronics Engineering Canada Research Chair in Trauma Biomechanics and Injury Prevention Director, Impact Mechanics and Material Characterization Group University of Waterloo
Internal Examiner	Adrian Gerlich Professor, Department of Mechanical and Mechatronics Engineering Director, Centre for Advanced Material Joining University of Waterloo
Internal Examiner	Hamid Jahed Professor, Department of Mechanical and Mechatronics Engineering University Research Chair in Cold Spray Technology Director, Fatigue and Stress Analysis Laboratory University of Waterloo
Internal-External Examiner	Boxin Zhao Professor, Department of Chemical Engineering Director, Surface Science and Bio-nanomaterials Laboratory Group University of Waterloo

Author's Declaration

I hereby declare that I am the sole author of this thesis. This is a true copy of the thesis, including any required final revisions, as accepted by my examiners.

I understand that my thesis may be made electronically available to the public.

Abstract

The implementation of aluminum alloys in future vehicle construction (*e.g.,* body-in-white) can reduce weight by 30-45%, improving the fuel economy of internal combustion vehicles and increasing the battery range of electric and hybrid variants. Critical to enabling the adoption of aluminum alloys and multi-material structures in the automotive industry are robust joining methods that play a crucial role in structural performance; crashworthiness; durability; and noise, vibration and harshness. Structural adhesives and self-piercing rivets (SPRs) have demonstrated aluminum and multi-material joining capability with promising mechanical performance, relative to traditional and emerging joining technologies. Hybrid joining, augmenting adhesives with SPRs, has been explored to address the limitations of individual joining methods and to enable further weight reduction opportunities. However, the limited mechanical response data on hybrid joints and lack of validated computational models often lead to expensive and time-consuming experimental testing and over-design of the joint.

In the first phase of this research, experimental studies were undertaken to assess the mechanical response of adhesive, SPR and hybrid joints made with aluminum sheet material at specimen (coupon) and component (vehicle-scale structure) levels. First, seven aluminum surface preparation methods were investigated, and the method that achieved cohesive failure within the adhesive layer and maximized single-lap shear joint (SLJ) strength was adopted throughout the study. Next, the specimen-level experiments investigated the influence of loading mode, joint-level morphology, aluminum sheet thickness, and alloy type on joint strength, stiffness and energy absorption. Shear (SLJ) and tension (H-specimens) test specimens were created with adhesive, SPR, and hybrid joints using two aluminum alloys (AA6061-T6 and AA5052-H32) with three sheet metal thicknesses (1, 2 and 3 mm), commonly used in the automotive industry. All test specimens were fabricated in symmetrical configurations (the same alloy type and equal sheet thickness) for a total of 108 specimens (36 specimens per joining method), with three repeats for each test condition. The morphology of the adhesive, SPR and hybrid joints was quantified to ensure joint consistency and link the effect of joint attributes (*e.g.*, bond line thickness and SPR mechanical interlock) to the mechanical response. Hybrid joining process variations were assessed to enhance joint strength and stiffness of hybrid joints made with thick sheet material, and the process with improved joint-level morphology was evaluated in subsequent specimen and component level tests. Lastly, vehicle-scale structural components were created from two hat sections made with 3 mm thick AA6061-T6 alloy and joined together to create a tube. The Caiman tubes were joined using adhesive, SPR, and hybrid joining, and then tested under Mode I loading with three repeats for each joining method.

SLJ and H-specimens with adhesive joining exhibited higher strength (up to 360%) and stiffness (up to 422%) compared to SPR joints, while SPR joints demonstrated higher energy absorption (up to 352%) co-depending on the loading mode, aluminum sheet thickness, and alloy type. Hybrid joints with 1 and 2 mm thick sheets enhanced the performance of the individual joining methods, demonstrating strength and stiffness comparable to or higher than the individual joints, and energy absorption substantially higher (up to 336% higher than adhesive and up to 53.5% higher than SPR). Hybrid joints made with 3 mm sheets exhibited reduced strength and stiffness relative to adhesive joints; however, a statistically significant performance improvement was realized using the hybrid joining process variation proposed in this study for thick sheet material. Importantly, hybrid joining substantially increased the peak load and energy of the Caiman components relative to adhesive joining (244% and 1461%, respectively), highlighting the importance of hybrid joining relative to adhesive for bonded structures under Mode I loading.

In the second phase of this research, finite element (FE) models of the specimen configurations (SLJ and H-specimen), and joining methods were created using a cohesive zone model (CZM) with material-level properties for adhesives, constraint and CZM models with parameters calibrated in this work for SPR rivets, and an integrated CZM-CZM and CZM-Constraint models for hybrid joints. The specimen-specific FE models were verified and validated using the experimental data for each sheet thickness (22 models in total). Next, FE models of the Caiman test were developed to validate the joining models at a component level (5 models in total), using the experimental load-displacement response and optical measurements of failure progression and joint separation. Lastly, FE investigations were conducted to assess the influence of key joint attributes, relevant to automotive, on the mechanical response of the joints. The FE models of the adhesive, SPR and hybrid joints were able to predict joint response for varying test specimen geometry, adherend thickness, and modes of loading. The hybrid CZM-CZM model demonstrated a high level of accuracy and excellent computational efficiency, predicting the Caiman test peak load within 9.5%, and with reduced simulation runtime compared to the CZM-Constraint model.

The results of this research study highlighted important parameters in terms of automotive structure design trade-offs (*e.g.,* joining method, joint morphology, sheet thickness and alloy type), while statistical analysis provided evidence that hybrid joining can enhance the strength, stiffness and energy absorption relative to adhesive or SPR joining. The demonstrated multi-scale approach to develop, verify and validate joining models allowed for predicting the mechanical response of the individual and hybrid joints under different modes of loading. The results of this research study provide an experimental and computational basis for research and design of structural-scale joining methods for lightweight vehicles.

Acknowledgments

First and foremost, I would like to praise Allah, the most merciful, for his countless blessings which cannot be enumerated.

My most profound appreciation goes to my supervisor Professor Duane Cronin for his remarkable coaching and excellent guidance. Thank you for believing in me and for continuously giving me opportunities to learn and challenge myself. You have been very generous with your valuable time and knowledge, and I am eternally indebted to you for everything you have taught me over the last five years.

I would sincerely like to thank my thesis committee: Professor Hamid Jahed, Professor Adrian Gerlich, and Professor Boxin Zhao for their insightful comments and questions which incented me to enhance and polish my research. I am truly grateful to Professor Franck Lauro for agreeing to serve as an external examiner for my Ph.D. defence. I would also like to thank Professor Michael Worswick for the use of his test equipment during a critical time of this research, and for his remarkable teaching skills which helped me in my coursework and research. Additionally, without the support of our research associates, Brock Watson, Jose Imbert-Boyd and Amir, lab technicians Tom Gawel, Eckhard Budziarek, the team at the Engineering Machine Shop, and our administrative staff Denise Porter, and Laurie Wilfong, this work would not have been possible. I want to thank Abdelbaset Midawi and Cameron Tolton for assisting me with the setup for the Caiman and material characterization tests and sharing with me the experience they gained from their research on resistance spot welding. I would like to express my gratitude to all members of the Impact Mechanics and Material Characterization (IMMC) group, and my fellow adhesive group members (Brock Watson, Devon Hartlen, Chi-Hsiang Liao, Luis Trimino, Brian Liu, Yu Zeng, and Ramin Dehghani), who made the workspace motivating, collaborative and productive.

I am particularly grateful to Brock Watson, Devon Hartlen, Mike Bustamante, Aleksander Rycman, Chi-Hsiang Liao, Dilaver Singh and Donata Gierczycka for all the meaningful technical discussions and enjoyable group outings.

I would like to gratefully acknowledge the financial support provided for my research by the Ontario Advanced Manufacturing Consortium (AMC), 3M Canada, and the Department of Mechanical and Mechatronics Engineering at the University of Waterloo. The computational resources provided by the Digital Research Alliance of Canada were crucial to the completion of this research within the Ph.D. program timeframe.

Alhamdulillah, I cannot express what the unconditional love and support of my mother, my father and my sisters have meant to me. To my wife and my children, thank you for being with me every step of the journey. I am indebted to you and could not have completed the journey without your love and support. I owe you everything.

Dedication

To my father for his sacrifices and selflessness.
To my mother for her precious love, care and dedication.
To my wife for always loving, inspiring and supporting me.
To my children for filling my life with light and my heart with joy.
To my sisters who never stopped believing in me.

Table of Contents

List of Figures

List of Tables

List of Abbreviations

CZM	Cohesive Zone Model
Adherend	Base material / Parent metal
BiW	Body-in-White
RSW	Resistance spot welding
DCB	Double cantilever beam
DIC	Digital image correlation
DSLR	Digital single-lens reflex
ENF	End notch flexural
FE	Finite element
LEFM	Linear elastic fracture mechanics
LVDT	Linear variable differential transformer
RDCB	Rigid double cantilever beam
BSS	Bonded shear specimen
SD	Standard deviation
SE	Standard error
SLJ	Single lap shear joint
TDCB	Tapered double cantilever beam
EV	Electric Vehicle
FDS	Flow drilling screw
RIVTAC™	High-speed impact riveting technology
FEW	Friction Element Welding
SPR	Self-piercing rivet / Self-piercing riveting
ASTM	American Society for Testing and Materials
H-specimen	H-shaped specimen comprising two joined U-sections
OEM	Original equipment manufacturer
RT	Room temperature
SEM	Scanning electron microscopy
NSDL	Near-surface deformed layer
CT	Cross tension
UHSS	Ultra-high-strength steel
IRSA	Impact-resistant structural adhesive
LED	Light emitting diode
CAA	Chromic acid anodizing
PAA	Phosphoric acid anodization
BSAA	Boric sulfuric acid anodizing
UTS	Ultimate tensile strength
YS	Yield strength
YM	Young’s Modulus
JC	Johnson Cook
SD	Solvent degreased
SDSG	Solvent degreased followed by sol-gel treatment
SDGB	Solvent degreased followed by grit blasting
SDA	Solvent degreased followed by abrading

SDASG	Solvent degreased followed by abrading and sol-gel treatment
SDSEP	Solvent degreased followed by self-etching primer
Sol-gel	Solution-gelation process in which metal alkoxide solution transforms into a polymerized gel through hydrolysis and condensation reactions
XPS	X-ray photoelectron spectroscopy

Nomenclature

a	Length of the adhesive bond area
w	Width of the adhesive bond area
F	Load applied and measured by load cell
$E_{adherend}$	Young's Modulus of base metal
E_I, E_{II}	Stiffness (elastic moduli) of traction-separation response in Mode I and II
G_{Ic}, G_{IIc}	Critical energy release rate (fracture toughness) of adhesive in Mode I and II
T_I, T_{II}	Traction of cohesive zone model in Mode I and II
T_{Imax}, T_{IImax}	Peak traction of cohesive zone model in Mode I and II
δ_I, δ_{II}	Separation of cohesive zone model in Mode I and II
$\delta_I^0, \delta_{II}^0$	Separation at damage initiation of cohesive zone model in Mode I and II
$\delta_I^f, \delta_{II}^f$	Separation at failure of cohesive zone model in Mode I and II
fg	Ratio of area under plastic region to total area (G_c) in a traction-separation response
R_a	Mean arithmetic surface roughness
R_q	Surface roughness measurement based on root mean square roughness
R_z	Difference between the tallest peak and deepest value in the surface profile
γ_{SV}	Free surface energy coefficient for solid-vapour interface
γ_{SL}	Free surface energy coefficient for solid-liquid interface
γ_{LV}	Free surface energy coefficient for liquid-vapour interface
R^2	Coefficient of determination
T_g	Glass transition temperature
r_{Iy}	Plastic deformation zone of a sharp crack
x	SPR rivet flaring
f_n^{max}, f_t^{max}	Peak load of the SPR constraint model under normal and tangential loading
$\delta_t^{fail}, \delta_t^{fail}$	Separation at failure of SPR constraint model under normal and tangential loading
γ^d, γ^p	Dispersive and polar components of the surface energy

Chapter 1: Introduction

The automotive industry is rapidly adopting disruptive technologies and lightweight materials to achieve a significant reduction in vehicle weight, improve fuel economy, and increase the range of electric vehicle batteries (Czerwinski, 2021; Henriksson and Johansen, 2016; Luk *et al.*, 2018). Automotive engineers have achieved advances in vehicle aerodynamics and powertrain efficiency. However, the implementation of lightweight, high-performance materials, such as aluminum, ultra-high-strength steel and carbon fibre-reinforced polymer composites in a vehicle body-in-white (BiW) and closures (*e.g.*, hood, fenders, outer doors, trunk lid) remains a promising opportunity for making a significant vehicle weight reduction (Pagerit *et al.*, 2006). Aluminum has proven to be an ideal material for lightweight applications because it reduces structure weight by up to 50% without compromising structural safety (Hirsch, 2014), and according to the Centre of Automotive Research, aluminum utilization in a mid-size sedan is expected to overcome third-generation steel by 2035 (Figure 1). The European Union Super-Light-Car project developed a multi-material car structure incorporating aluminum and advanced joining technologies that resulted in a 34% weight reduction without compromising vehicle safety performance (achieved a 5-star rating in the Euro NCAP test) (Hirsch, 2014). In 2015, the Ford Motor Company began producing full aluminum body F-150 trucks, with an overall weight reduction of 317 kg (700 lbs).

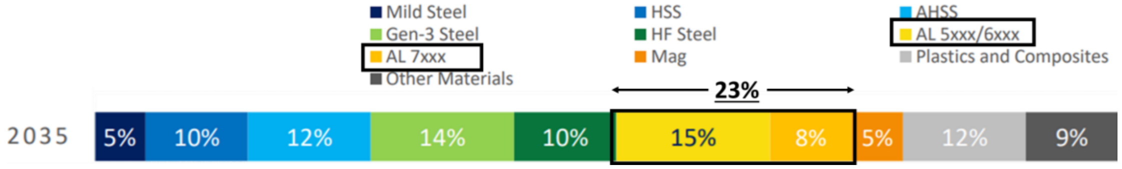

Figure 1: Predicted average vehicle structure (BiW and Closures) material utilization percentage by curb weight of a mid-size sedan in 2035. Adapted from (Modi and Vadhavkar, 2019)

Critical to enabling the implementation of aluminum and future multi-material systems in vehicle structures are the joining methods that play an immense role in structural performance; crashworthiness; durability; and noise, vibration and harshness. Yet, traditional joining methods, such as RSW, have limitations when joining aluminum alloys. The higher electrical conductivity of aluminum requires RSW equipment capable of providing higher current and weld forces, leading to limited electrode life due to tip erosion and particle deposition. Therefore, modern, more efficient aluminum joining technologies that can be implemented in a mass-production environment have gained remarkable attention. Numerous researchers have investigated the mechanical performance of self-piercing rivets (SPR), adhesive bonding, MIG welding, and laser welding, to understand the mechanical behaviour of joining technologies with multi-material joining capability (Koganti and Weishaar, 2009). Adhesives and SPR have demonstrated promising mechanical performance and the potential to enable future materials and multi-material systems needed for vehicle weight reduction (Meschut *et al.*, 2014b), thus, it was no surprise that both joining technologies are forecasted to rapidly increase in use relative to traditional joining techniques such as RSW (Figure 2). Both technologies have attracted major automotive original equipment manufacturers (OEMs) (Fu and Mallick, 2003; Haque, 2018; Huang *et al.*, 2017); however, barriers remain with respect to the implementation of individual joining methods. Therefore, researchers investigated combining joining methods, also known as hybrid joining, focusing on augmenting adhesive bonding with another joining technology, such as SPR riveting (Di Franco *et al.*, 2013), friction stir spot welding (Adibeig *et al.*, 2020), clinching (Lei *et al.*, 2018), bolting (Romanov *et al.*, 2021), and mixed adhesives (Zaeri and Saeidi Googarchin, 2019). Combining the advantages of adhesives and SPR joining (henceforth referred to as hybrid joining) could address the limitations of individual joining methods, improve the mechanical response, and enable further lightweight opportunities (Di Franco *et al.*, 2012; Hahn *et al.*, 2014; Meschut *et al.*, 2014a). Thus, the current study is focused on understanding and assessing the mechanical behaviour of hybrid joints relative to individual joints to enhance the joint performance of aluminum sheet material. This study also addresses the development of computationally efficient FE models to predict the response of hybrid joints with a high level of accuracy to support the implementation of hybrid joining in aluminum and multi-material systems.

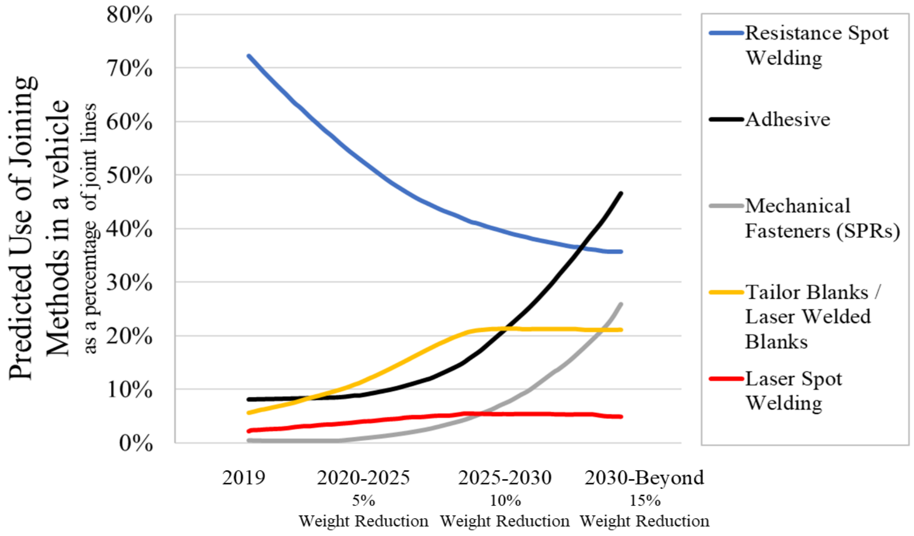

Figure 2: Forecasted utilization of joining technologies in the automotive industry. Adapted from Modi and Vadhavkar (2019)

1.1 Motivation for Research

The primary motivation for the current research was driven by the need to join lightweight sheet materials, such as aluminum sheet metal, to enable lighter, more efficient structures (*e.g.*, BiW) in future vehicles. To utilize aluminum alloys and multi-material systems in vehicle construction, the mechanical behaviour of compatible joining technologies needs to be understood, characterized and computationally modelled. High-tenacity structural adhesive joining has notable advantages, such as broad material joining capability; uniform stress distribution; improved structural stiffness and enhanced vibration absorption; and joint sealing (Kinloch, 2003; Wu *et al.*, 2018). Also, SPR can join a range of multi-materials or multiple sheets of mixed materials, is environmentally friendly (no fumes, sparks, or noise), and does not require predrilling or surface preparation (Li *et al.*, 2017). However, adhesives and SPR joining technologies have limitations that arise during vehicle production and service life, making the use of individual joining methods significantly challenging, especially for high-volume production and non-luxury class vehicles. The challenges associated with adhesives include rigorous surface preparation requirements; component fixturing and positioning; curing time and delayed joint strength development; and more importantly limited joint strength under peel/tension loading (dos Reis *et al.*, 2019; Ritter, 1999; Ufferman *et al.*, 2018). Also, SPR joining has critical limitations, such as (a) lack of protection against galvanic corrosion when joining dissimilar materials; (b) discrete load distribution, causing stress concentration and non-uniform structural deformations; and (c) generally lower structural stiffness compared to adhesive joints. Meschut *et al.* (2014b) stated that exploiting the lightweight potential of future materials mandates combining SPR and adhesive joining. In their investigation of different joining methods for automotive applications, including clinching, self-piercing rivets, high-impact riveting, resistance element welding (RSW) and friction element welding (FEW), the peak load of SLJ joined using the previous joining method barely achieved 8 kN. However, when the joints were augmented with adhesives, the peak load for each joint was more than doubled, demonstrating the superior strength of hybrid joints under shear loading.

Research on hybrid joining made with adhesive and SPR has been limited, and there is a lack of data on the mechanical behaviour of these joints under different loading conditions (Di

Franco *et al.*, 2013). Also, in the limited published studies on the mechanical response of hybrid joint SLJ the results were inconsistent: strength improvement (Di Franco *et al.*, 2013) versus strength reduction (Meschut *et al.*, 2014b) compared to adhesive-only joints. Previous case studies reported that hybrid joining could induce SPR rivet or base material fracture (Hahn and Wibbeke, 2005), and adhesive squeeze-out (Hahn *et al.*, 2014). However, no single study has investigated the adhesive, SPR and hybrid joints under different loading modes to understand and quantify the mechanical response of hybrid joints relative to the individual joining methods. Additionally, two key joint design attributes that have been reported to substantially influence the behaviour of individual joining methods are sheet metal thickness and material yield strength (*i.e.,* alloy type). Yet, these factors have not been systematically investigated in hybrid joints.

Computational modeling of joining methods used has been essential for the design and assessment of automotive structures (Lanzerath and Pasligh, 2014; Pasligh *et al.*, 2017; Yao *et al.*, 2017). Cohesive zone modelling (CZM) has been used to computationally model adhesive joints and predict their mechanical response up to failure (Campilho *et al.*, 2012; Ibrahim *et al.*, 2023; Watson *et al.*, 2019). Traditionally, adopting CZM required multiple characterization tests under each mode of loading (Mode I, Mode II and mixed modes), and complex analysis techniques to account for adherend deformation, which presented challenges for measuring the CZM parameters. Thus, many researchers have calibrated or optimized the CZM parameters to match the adhesive joint mechanical response in relevant coupon-level tests, such as single lap shear or H-shaped specimens (Ezzine *et al.*, 2018; Weiland *et al.*, 2019). Similarly, researchers have taken a trial and error or optimization approaches to calibrate the model input parameters of SPR rivets based on experimental load-displacement response only, neglecting the local joint kinematics. The calibration of adhesive CZM and SPR models generally leads to case-specific computational models that can not predict tests with complex modes of loading or be extended to larger-scale models of joined structures (*e.g.*, automotive structure components). Therefore, there is a need to assess a systematic, multi-scale approach to develop and validate a hybrid joint model and then assess the model prediction accuracy and computational efficiency at a large scale.

The lack of hybrid joining mechanical behaviour data and computational models require newer vehicles to undergo prohibitively expensive and time-consuming experimental testing and joint over-designing, resulting in conservative weight reduction and slow vehicle body development (Kleinbaum *et al.*, 2019; Sun *et al.*, 2018). As a result, lightweight vehicles with improved fuel economy and reduced emission or increased electrical battery range will not be available for consumers at affordable prices or within a realistic timeframe. Ultimately, the outcomes of this research will facilitate the implementation of hybrid joining in the automotive industry, which is mandated to enable weight reduction opportunities and support the design and development of future vehicles.

1.2 Objectives and Scope of Research

To implement hybrid joining, extensive experimental testing is needed to understand, assess, and improve the mechanical behaviour of hybrid joints relative to individual joints. In addition, a high-fidelity computational model of hybrid joining, capable of predicting joint damage and failure, is a key requirement to enable the development, assessment and optimization of future vehicle structures and BiW, while reducing the costly and time-consuming experimental testing. The goals of this research are:

- to understand, characterize and enhance the mechanical behaviour (strength, stiffness, and energy absorption) of hybrid joints applied to aluminum sheet metal

- to develop finite element models for hybrid joining, compatible with large-scale modes (*e.g.,* models of full vehicles) and capable of predicting joint damage and failure with a high level of accuracy.

The multi-scale approach followed in this work addresses adhesive characterization at a material level, understands and assesses the joining methods and key influencing parameters at the specimen level, and then investigates the joint behaviour at the component level using a structural scale test. The approach focuses on tackling the research objectives systematically to achieve research goals, such that it addresses the individual joining methods (adhesive-only and SPR-only) to establish a baseline for hybrid joints and relate the hybrid joining behaviour to the intrinsic responses and joint morphologies of individual joints. A graphical representation of the multi-scale approach followed in this work shows the experimental and computational work completed at specimen and component levels (Figure 3).

The work presented was applied to aluminum alloys due to their proven application in lightweight vehicle structures and BiW, and because of their essential role in exploiting lightweight multi-material systems. Nevertheless, the research methods could be extended to future materials and joining technologies.

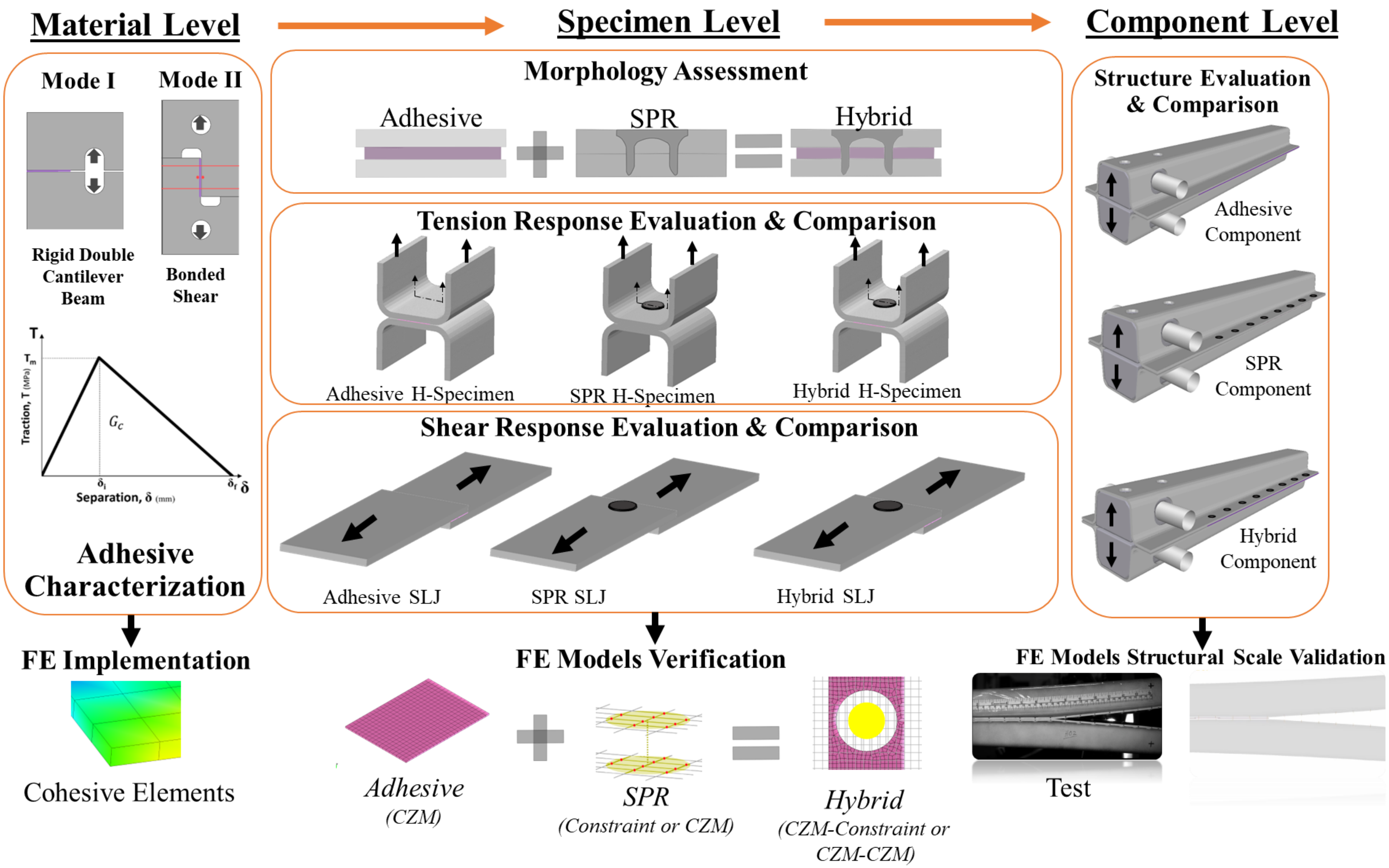

Figure 3: A graphical representation showing the multi-scale approach followed in this research.

The objectives of this study are:

O1) Identify surface treatment methods for aluminum bonding that achieve a cohesive failure behaviour and maximize joint strength

Seven contemporary surface treatments including, mechanical and chemical methods (solvent degreasing, grit-blasting, abrading, self-etching primer, sol-gel, abrading and sol-gel, and regreasing using a forming lubricant) were assessed using adhesively bonded aluminum SLJ tests according to ASTM D1002-10 (2019). The SLJ peak load and failure mechanism were investigated for all surface treatments. The treatments that achieved cohesive failure and maximized joint strength relative to the manufacturer data were identified and further assessed for wetting behaviour. Also, the mean arithmetic surface roughness (R_a) of the treated adherends was measured to understand the influence of surface roughness on the SLJ joint strength. Finally, the effect of surface wettability on the SLJ joint strength was assessed to explain how surface treatments improved the interfacial strength.

Achieving this objective was critical to avoid reduced adhesive joint strength due to interfacial failure, which would lead to a flawed comparison between the adhesive, SPR and hybrid joints throughout the study.

O2) Measure the cross-sectional attributes of adhesive-only, SPR-only and hybrid joints to assess joint quality, and investigate the relationship between joint morphology and the mechanical response of the joints

The physical attributes (*i.e.,* adhesive bond line thickness, SPR head height, SPR mechanical interlock, and SPR bottom thickness) of adhesive-only, SPR-only and hybrid joints were measured from cross-sectioned joints using the opto-digital microscope. Bond line thickness was measured from the SLJ and H-specimens. Twelve sets (Thirty-six specimens, considering three repeats) were sectioned, using a precision cutter, to reveal the morphology of SPR rivet and hybrid joints made with two aluminum alloys (AA6061 and AA5052) having three symmetrical stacks of 1, 2 and 3 mm thick sheets each. The physical attributes measurements were used to (a) ensure that the SPR and hybrid joints met the quality guidelines available in the literature, (b) understand how the presence of adhesive affected the formation of SPR joint, and (c) investigate the relationship between the morphology and the mechanical response of the joints at specimen level (proposed in O3).

O3) Assess the mechanical response (strength, stiffness and energy absorption) of adhesive-only, SPR-only and hybrid joints under shear and tension loading configurations

H-shaped and SLJ test specimens, joined using adhesive-only, SPR-only and hybrid joining, were tested to measure the strength, stiffness and energy absorption of the joints under tension and shear loading. Two aluminum alloys (AA6061 and AA5052) with varying sheet thickness (1, 2 and 3 mm) were used to prepare thirty-six sets of test specimens (hundred and eight test specimens, considering three repeats). The results compared the mechanical behaviour of the individual and hybrid joints under the same test conditions, which allowed quantifying the benefits of hybrid joints. In addition, statistical analysis was performed to investigate the interaction between the joining methods, aluminum alloy yield strength and sheet metal thickness, highlighting the influence of adherend deformation on the mechanical behaviour of each joining method. Importantly, the experimental results supported the development of the adhesive-only, SPR-only and hybrid joining FE model and served in the model development, calibration and validation process. Also, this objective potentially addressed the lack of data in the literature on the response of hybrid joints.

O4) Investigate three hybrid joining process variations to improve the mechanical performance of hybrid joints

It was reported that hybrid joining could degrade joint strength relative to adhesive-only or SPR-only joints. Therefore, three process variations (using a shim at the SPR rivet location, applying the SPR process after adhesive curing, and applying the SPR process at the end of the adhesive curing process at curing temperature) were investigated to enhance the mechanical response of hybrid joints. The physical attributes of joints created using the process variations were measured and compared to joints created using the traditional hybrid joining process. The process variation showing enhanced joint morphology was implemented and investigated using SLJ test specimens to verify and quantify the improvement in the mechanical performance, relative to the experimental results data of the traditional hybrid joining (O3).

O5) Develop, verify and validate adhesive, SPR and hybrid joining models

The mechanical behaviour of hybrid joining is complex due to combining the intrinsic responses of adhesive bonding and SPR joining. Thus, a systematic approach with multi-level verification and validation was required to develop a hybrid joining FE model with a high level of accuracy. For this purpose, FE models of adhesive-only and SPR-only were developed, verified, and validated to ensure that the individual joints have sufficient fidelity at specimen and component levels. The validated FE models were integrated to develop a hybrid joining model without requiring calibration or correction factors. The hybrid joining model was validated under shear and tension loadings using the specimen level test data (O3). Finally, the hybrid joining FE model was implemented and validated at the component level using the Caiman test data.

1.3 Organization of Thesis

This thesis is organized into seven chapters, including the introduction chapter (Figure 4). Chapter two provides the state-of-art and background information on the characterization, testing and mechanical behaviour of adhesive, SPR and hybrid joints, and the current approaches available to model these joining methods at specimen and component levels. In addition, the existing quantitative techniques/tests used to assess the morphology and mechanical response of the adhesive, SPR and hybrid joints are discussed. In the same chapter, the gaps that need to be addressed to understand the mechanical behaviour of hybrid joints are highlighted. Also, the limitations of the widely accepted FE modeling approaches of individual joining methods are reviewed in terms of accuracy and compatibility with large-scale models. Finally, the limited attempts to develop a hybrid adhesive-SPR model are explained.

Chapter three introduces the methodologies used in test specimen manufacturing, preparation and experimental testing. First, the aluminum sheet metal material characterization and surface treatment assessment are described. Then, the details of the joint morphology assessment and measurements of SPR joint physical attributes are illustrated. After that, the preparation, test and analysis techniques used for the adhesive, SPR and hybrid joined H-shaped and SLJ specimens are explained. Finally, the details of the component-level Caiman testing, preparation and analysis are laid out.

Chapter four presents and discusses all the experimental results. First, the aluminum sheet metal characterization is undertaken. After that, the aluminum surface treatment is identified, and recommendations for surface preparation are presented. The physical attributes of the joints are compared to the quality guidelines available in the literature and the influence of hybrid joining on the adhesive and SPR joint morphology is discussed. The mechanical response of adhesive, SPR and hybrid joining is assessed at the specimen level under shear and tension loading, and the effect of sheet material thickness and aluminum alloy type is highlighted using statistical analysis. Additionally, hybrid joining process variations are assessed and the SLJ test results are compared with traditional hybrid joints. Finally, the mechanical response of adhesive, SPR and hybrid joints is discussed and compared at the component level using the Caiman test. Further investigations on the influence of the hybrid joining process variation and SPR rivet spacing on the component-level mechanical response are presented.

Chapter five introduces the methodologies used for developing the computational models for adhesive, SPR and hybrid joints. This chapter explains the development and validation of the adhesive CZM models, and then illustrates the methods used to calibrate the parameters required to model the SPR rivet using two different approaches (constraint and CZM). It also describes the procedure for integrating the adhesive and SPR FE models while accounting for the hybrid joining effect on joint morphology and adhesive degradation. Within the section pertaining to each joining method, the development of the SLJ and H-specimens models made with AA6061-T6 alloy is explained. After that, the computational methods used to develop the Caiman models, including the joining methods, are described. The results of the FE models are presented in chapter six, along with a comparison of the pertinent experimental test data from chapter four in a systematic approach to verify and validate the FE models of the individual and hybrid joints.

The conclusions of this thesis and recommended future work are presented in chapter seven.

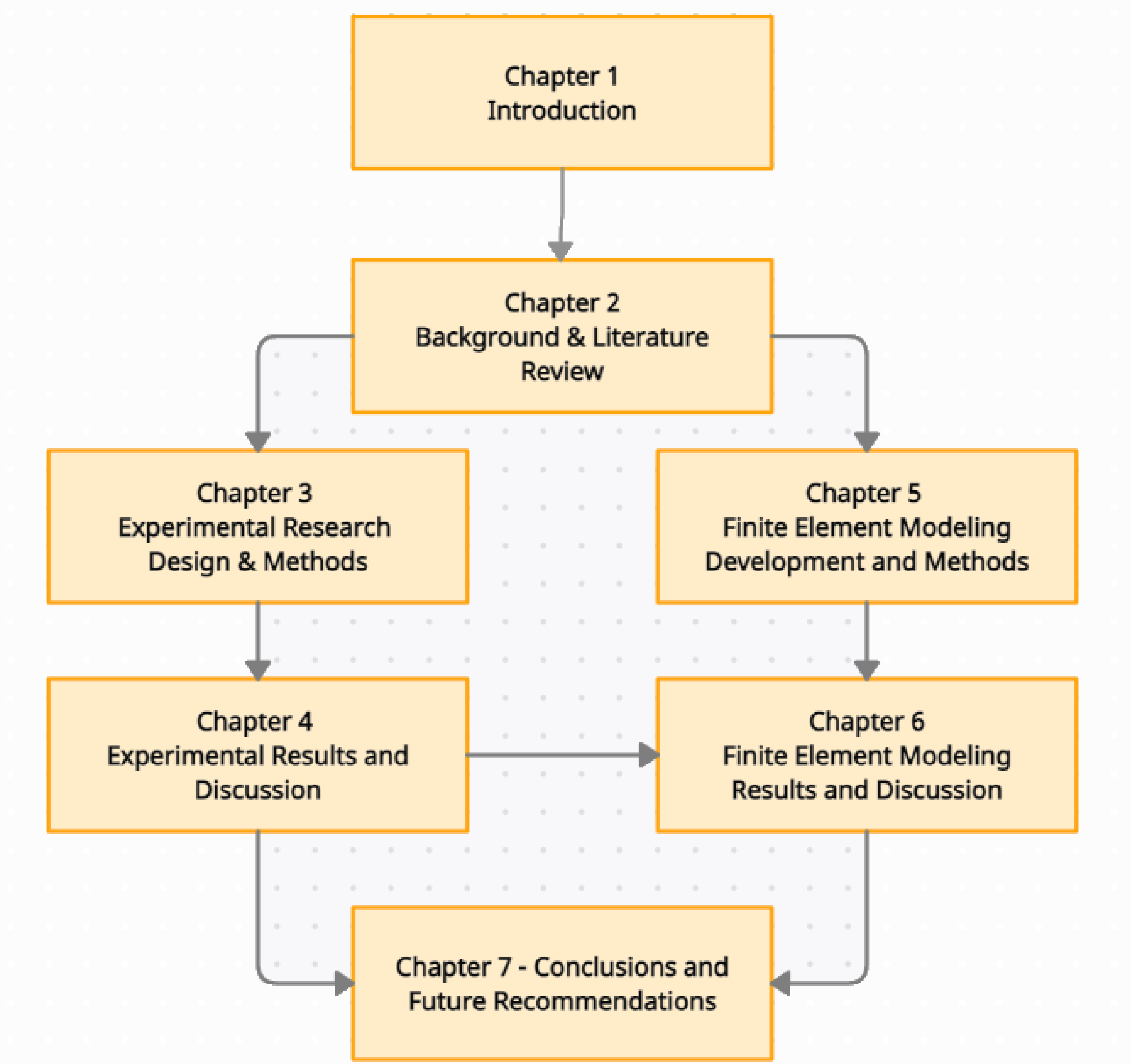

Figure 4: Diagram illustrating the thesis organization.

1.4 Publications and Contributions

Some of the work presented in this thesis has been published in refereed journals. The first article, Ibrahim and Cronin (2022), outlines the experimental testing and characterization of the adhesive, SPR and hybrid joints under tension loading using H-specimens. The second article, Ibrahim *et al.* (2023), presents a methodology for modeling adhesively bonded joints under various modes of loading using material-level adhesive characterization data. In addition to these refereed articles, the work completed in this program was extended to address the reliability aspects of adhesive joints and an article that assesses a novel fatigue life prediction approach for adhesive joints was submitted to the Journal of Adhesion (June 2023). The fatigue life prediction approach enables estimating the fatigue life of adhesive joints regardless of joint configuration or the mode of loading, using linear elastic fracture mechanics. Also, a refereed conference proceeding that compares the mechanical response of adhesive and SPR joints under tension loading was presented and published at the 2021 SEM Annual Conference and Exposition (Ibrahim and Cronin, 2021). Additionally, various aspects of the work presented in this thesis were presented at refereed conferences and industrial settings, such as the 2020 Arcelor Mittal Annual Innovation Seminar, the 2021 Adhesive Bonding Conference (AB2021), 2022 3M Global Annual Meeting (Pangea Chapter) and 2023 Adhesive Bonding Conference (AB2023). Although some of the work presented in this thesis contributed to three refereed journal articles and four conference participations, two additional refereed journal articles are expected to be submitted for review before the end of 2023.

Chapter 2: Background and Literature Review

2.1 Aluminum Sheet Metal

Automotive manufacturers have adopted aluminum alloys in passenger vehicles for decades to produce: a) lighter vehicle structures (*e.g.,* BiW) and b) more efficient powertrains (*e.g.*, engine blocks and transmission components) (Gould, 2012). The recent development of sheet metal forming and joining technologies have enabled the implementation of rolled aluminum alloys to produce hollow vehicle body components with a significant weight reduction of nearly 30-40% (Tisza and Czinege, 2018). With vehicle BiW representing nearly 30% of total vehicle weight, it has been an attractive target for aluminum sheet metal implementation to achieve significant vehicle weight reduction. However, material and manufacturing costs, forming limitations, and joining capabilities have been major barriers challenging the implementation of aluminum alloys in a high-volume production environment (Tisza and Czinege, 2018).

Many studies have demonstrated that introducing aluminum alloys in the vehicle body components can aid in the improvement of vehicle safety, driver handling experience, pedestrian protection, and vehicle recycling (European Aluminum Association (EAA), 2012; Tisza and Czinege, 2018). In particular, heat-treatable aluminum alloys such as 6xxx aluminum alloys (Al-Mg-Si series) have a strong potential for vehicle structural applications owing to their demonstrated formability, corrosion resistance and strength relative to other aluminum alloys. This series of alloys exhibits a significant increase in yield and ultimate strength when subjected to artificial age hardening (*i.e.*, heat treatment), which can be undertaken during the cycle used to cure the applied paint during vehicle production, known as the paint bake cycle (Prillhofer *et al.*, 2014). The 7xxx series alloys are also heat-treatable and generally offer higher strength compared to 6xxx alloys; however, SPR joining may not apply to this series due to its relatively limited formability at room temperature (Jäckel *et al.*, 2017). Although the 6xxx series aluminum alloys have identical primary alloying elements, the alloys used in transportation applications have been tuned to enhance formability and accelerate artificial age hardening. For example, North American automotive OEMs have adopted the AA6111 alloy in T4 temper, while European counterparts have used AA6016-T4 (Hirsch, 2014; McMurray *et al.*, 2010). During the paint bake cycle, automotive aluminum alloys (usually in T4 temper) are subjected to a thermal treatment of 180^{o} C for 20-30 minutes, which increases alloy strength by precipitation hardening and tempers the alloys to T6 (T6 temper has nearly 60% higher yield strength compared to T4 temper) (Prillhofer *et al.*, 2014). Aluminum AA6061 is another alloy that has been widely used in structural components in automotive, aerospace, and marine production (Nguyen *et al.*, 2011; Staley and Lege, 1993). This alloy has advantages over other 6xxx series alloys, such as i) commercial availability; ii) cost-efficiency; and iii) availability of a broad range of sheet thicknesses and various heat treatments. Importantly, it has a chemical composition and mechanical properties that are relatively similar to automotive alloys (Table 1 and Table 2).

Table 1: Typical chemical composition for AA6111-T6 and AA6061-T6 sheet alloys (The Aluminium Association, 2015)

Alloy	**Si wt.%**	Fe wt.%	Cu wt.%	Mn wt.%	**Mg wt.%**	Cr wt.%	Zn wt.%	Ti wt.%	Other wt.%
AA6061	0.4 – 0.8	0.7	0.15 - 0.4	0.15	0.8 - 1.2	0.04 - 0.35	0.25	0.15	0.15
AA6016	0.9 - 1.5	0.5	0.25	0.2	0.2 - 0.6	0.1	0.2	0.15	0.15
AA6111	0.6 – 1.1	0.4	0.5 - 0.9	0.1 – 0.45	0.5 - 1.0	0.1	0.15	0.1	0.15

Numerous researchers used the AA6061 and AA5052 alloys to study advanced joining technologies owing to their availability and wide use in industries. The effect of laser welding parameters, surface cleaning, filler wire addition, and backing strip on the quality of laser welded joints using a range of AA5052 sheet metal thicknesses (El-Batahgy and Kutsuna, 2009). The quasi-static strength and fatigue life of single-lap shear specimens joined using SPR were investigated with different sheet thicknesses of aluminum AA5052 (Zhao *et al.*, 2015). Multi-material test samples made with high-strength steel and aluminum (AA5052) were used to assess the static strength and fatigue life of clinched, SPR and RSW joints using SLJ and CT specimens (Mori *et al.*, 2012). In this work, the AA6061-T6 alloy offered mechanical properties relatively similar to the properties of automotive alloys in service (*e.g.*, AA6111-T6). In addition, aluminum AA5052-H32 alloy offered distinct yield strength (42% lower), allowing for the influence of adherend yield strength on the mechanical behaviour of individual and hybrid joints to be assessed (O3) (Table 2).

Table 2: Typical mechanical properties of AA6111-T6, AA6061-T6 and AA6061-T6 sheet alloys (Campbell, 2008; Wong, 1984)

Aluminum Alloy	Yield Strength, MPa	Ultimate Tensile Strength, MPa
AA6111-T6	310	350
AA-6016-T6	285	310
AA6061-T6	275-289	310-314
AA5052-H32	167	231

2.2 Structural Adhesives

Adhesives are essential components of many industries such as automotive, aerospace, oil and gas and other major industries. They are primarily composed of natural and/or synthetic polymers, with synthetic polymers more common in industrial applications. In general, adhesives can be classified in several ways based on chemistry, form (two-parts, single part, paste, film, etc.), function, cure type (room temperature (RT), ultra-violet (UV) cure, pressure-sensitive, etc.), or specific properties (strength, toughness, heat resistance, electrical conductivity, etc.). With the continuous development of adhesives, it is common to find modern adhesives being described with a combination of classifications, *i.e.*, toughened high-strength two-part RT-cure epoxy adhesive. When classified based on chemistry, the main classifications are thermosets, thermoplastics, and elastomers. Thermosetting adhesives, such as epoxy, acrylic, polyester, polyimides, and phenolics, exhibit irreversible cross-linking due to the formation of strong covalent intermolecular bonds. Cross-linking is usually initiated using heat and results in a significant increase in the adhesive strength, modulus of elasticity and relative brittleness. On the other hand, thermoplastics, which melt and soften when heated, do not exhibit the formation of new cross-links, making these materials weak due to relying on the secondary bonds of the long polymer chains alternating with monomer units.

A structural adhesive is a material that bonds together structural elements to produce a permanent bond that transmits structural stresses and provides structural integrity according to design requirements (Dillard, 2010). Structural adhesives are generally manufactured using thermosetting epoxy or acrylic bases, or a thermoplastic with a urethane base. In general, modern epoxy adhesives have been improved to provide better mechanical, thermal and chemical properties (Barbosa *et al.*, 2016), making them suitable for structural applications in several industries. In addition, epoxy adhesives can achieve excellent adhesion, which is often referred to as the molecular forces of attraction between the adhesive and substrates to be joined, resulting in a strong metal-to-metal bond and allowing dissimilar material joining (Kinloch, 1984; Schmidt and Bell, 1986). However, structural epoxy adhesives often experience relatively low ductility and fracture toughness (Barbosa *et al.*, 2016). Therefore, newer generations of these adhesives are enhanced using toughening agents to provide improved impact absorption and enhanced resistance to crack growth.

2.2.1 Toughened Epoxy Structural Adhesives

Many researchers have described improvements achieved in the fracture toughness of epoxy adhesives. Earlier studies focused on epoxide systems toughened with carboxyl terminated copolymers of butadiene-acrylonitrile (CTBN) rubber particles to quantify the toughening benefits and understand the toughening mechanisms. Bucknall and Yoshii (1978) investigated the effect of toughening diglycidyl ether of Bisphenol A (DGEBA) epoxy adhesive using CTBN rubber particles and reported a linear increase of the fracture resistance with rubber phase volume. Pearson and Yee (1986) observed fracture surfaces of toughened and un-toughened epoxy using Scanning Electron Microscopy (SEM) and reported that the toughening mechanisms of epoxy systems toughened with rubber particles are (i) cavitation and fracturing of the rubber particles, and (ii) dilation and plastic deformation of the surrounding matrix. Bagheri and Pearson (1996) concluded that epoxy-toughened adhesives exhibit shear yielding (shear bands) at the crack tip due to the inclusion of rubber particles. They have also reported that introducing microvoids, using plastic hollow spheres, adds another toughening mechanism called microcracking. Recent work investigated epoxy-based adhesives toughened with dual toughening agents, rubber particles in addition to one or more agents such as aluminum (Hu *et al.*, 2013), clay (Szymańska *et al.*, 2018) and cork (Barbosa *et al.*, 2016), to enhance the fracture toughness of modern epoxy adhesives and add tailored features such as impact resistance. Barbosa *et al.* (2016) summarized the toughening mechanisms presented in the literature. Depending on the toughening agents and epoxy matrix, the primary toughening mechanisms are crazing, shear bands combined with crazing, rubber stretching and tearing, and cavitation (voids formation) (Figure 5a-d).

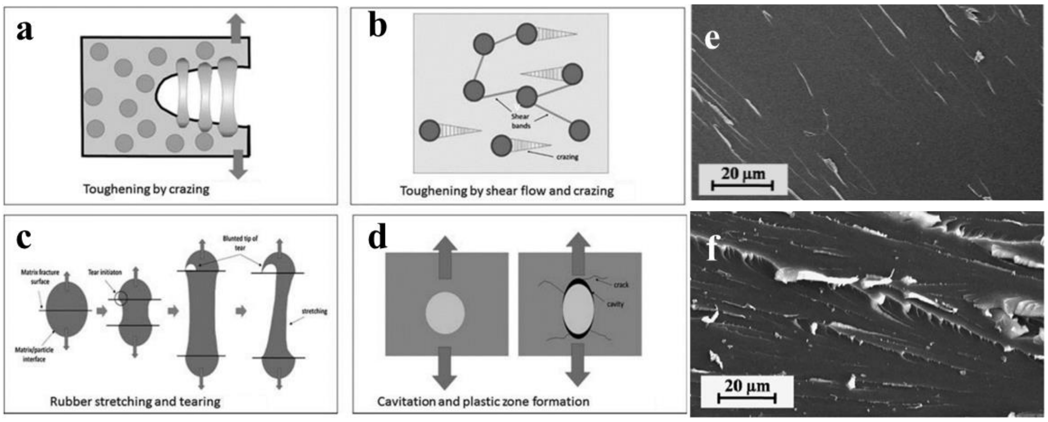

Figure 5: Toughening mechanisms in epoxy adhesives (a-d) with SEM images of the fracture surfaces of neat (e) and toughened (e) epoxy adhesive. Adapted from Barbosa *et al.*, (2016) and Tang *et al.* (2013)

Toughening agents influence not only the fracture toughness but also the mechanical properties of epoxy adhesive. The stress, strain, Young's modulus, and impact resistance of toughened epoxy adhesive could be substantially different from untoughened adhesives. Tang *et al.* (2013) demonstrated that the adhesive response was brittle and essentially elastic to ultimate failure (0.0259 mm/mm) with a relatively high Young's modulus (3.18 GPa) when no toughening agent was present. As rubber particles increased in the epoxy system, the strain to failure increased, the tensile strength at failure decreased, the modulus of elasticity decreased, and the impact strength increased. At a rubber fraction of 9.2% by weight, the strain to failure increased to 0.0556 mm/mm, and the modulus of elasticity decreased to 2.56 GPa. Although the peak stress decreased from 71.4 MPa (0.0 wt%) to 65.3 MPa (9.2 wt%), the impact strength, measured using the Charpy impact test, increased to 29.35KJ/m^2 (an increase of 49.3% compared to neat epoxy) highlighting a substantial increase in the ability of the material to absorb energy before failure. The toughness (area under the stress-strain curve) of the toughened epoxy system was about 50% larger compared to neat epoxy. The scanning electron microscope (SEM) images showed that the fracture surface of neat epoxy was flat and smooth with no indication of plastic deformation (Figure 5e); however, the fracture surface of toughened epoxy was rough and showed river-like lines with hackles and ribbons (Figure 5f).

Adhesives used in the transportation industry are generally exposed to environmental factors that could alter the original adhesive properties, and Banea and Da Silva (2010) highlighted that the temperature effect on adhesives is an important factor to consider in the automotive design phase. In their work, they tested two different automotive adhesives in the bulk form under tensile loading, a thermoplastic urethane-based flexible adhesive, and a structural thermosetting toughened epoxy adhesive. When the toughened epoxy adhesive exhibited elevated temperature, a large decrease in strength at failure and modulus of elasticity were measured (Figure 6a and Figure 6b); however, an increase in strain to failure was observed (Figure 6c). On the contrary, at a temperature below room temperature (RT), the same adhesive became more brittle resulting in more apparent tensile strength, and a lower strain to failure.

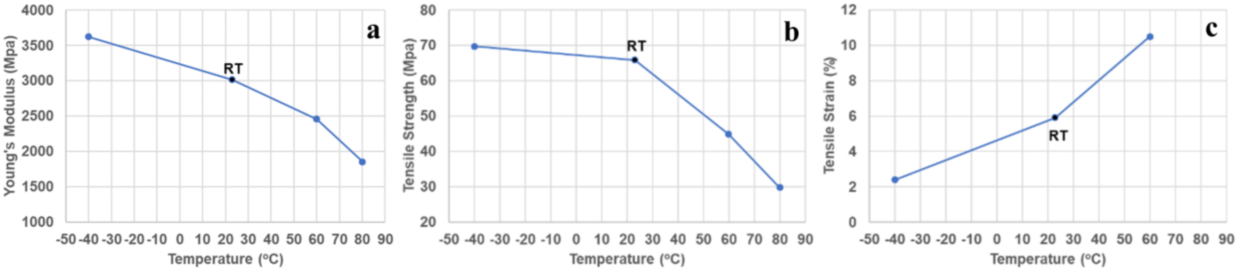

Figure 6: The effect of temperature on Young's modulus (a), tensile strength (b) and tensile strain (c) of toughened epoxy adhesive. Adapted from (Banea and Da Silva, 2010)

One important property of adhesives, and polymers in general, is the glass transition temperature (T_g), which is often measured using differential scanning calorimetry (DSC), thermo-mechanical analysis (TMA), or dynamic mechanical analysis (DMA). Bascom and Cottington

(1976), who investigated the effect of temperature on the fracture behaviour of toughened epoxy adhesives, showed that when the adhesive temperature is elevated closer to T_g, the toughness of epoxy adhesives increases due to rubber-like behaviour. According to Carbas *et al.* (2014), at a temperature below T_g, polymer molecules cannot move away from each other because they are confined with a very limited group or branch movement freedom. At temperatures above T_g, molecules can shift or slide away from each other giving polymer chains mobility freedom and the material state changes from a glassy state to a rubber-like state. The variation of molecular mobility of adhesive materials brings unavoidable changes in their mechanical properties, therefore, it is very important to consider the effect of T_g in automotive design. In the same study, the authors observed that T_g was dependent on the curing temperature, reporting that T_g increased as the curing temperature increased until it reached a maximum value, $T_{g,\infty}$, then dropped. Also, it was demonstrated that elevating the curing temperature of adhesives, below $T_{g,\infty}$, resulted in improved adhesive mechanical properties, *i.e.*, higher modulus of elasticity and higher strength, due to the increase of cross-linking and reduction of free volume (*i.e.*, density increased). However, curing epoxy adhesives at a temperature above the $T_{g,\infty}$ value caused performance degradation and decreased the strength and stiffness of cured adhesives due to thermal degradation or oxidative cross-linking (Figure 7).

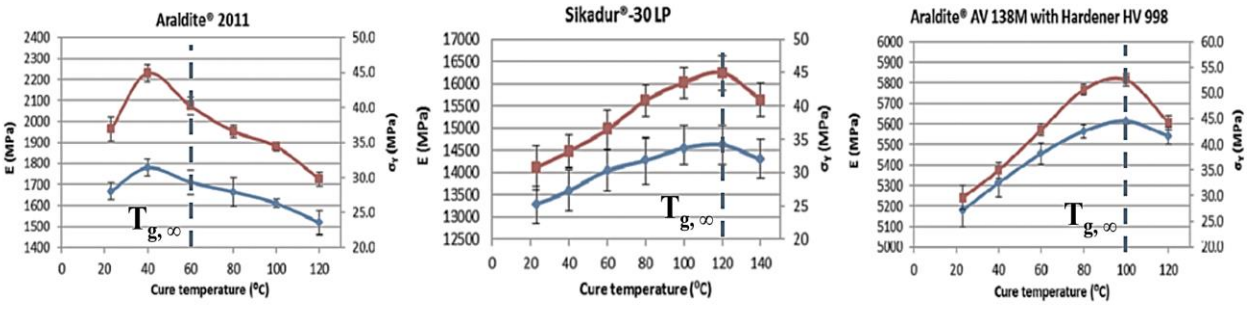

Figure 7: The effect of curing temperature on the mechanical properties (*i.e.*, Young's modulus and tensile strength) of three widely used epoxy adhesives. Adapted from Carbas *et al.* (2014)

Modern epoxy-based structural adhesive toughened with dual agents (*e.g.,* rubber and aluminum particles), being the most common in transportation applications, is the primary focus of this work. The adhesive considered in this study was identified with a curing temperature and T_g substantially higher than the service and testing temperature in order to isolate the influence of these key parameters on this study.

2.2.2 Surface Preparation of Aluminum for Adhesive Application

The use of aluminum alloys and adhesive joining in aircraft structural components has motivated many researchers to study the effect of various surface treatments on aluminum oxide morphology, surface energy and wettability, and surface roughness of aluminum, and further assess the mechanical performance and failure modes of the adhesively bonded aluminum joints (Leena *et al.*, 2016; Saleema *et al.*, 2012; Saleema and Gallant, 2013). The goal of aluminum surface treatment is to ensure the formation of intrinsic adhesion at the aluminum/adhesive interface to maximize adhesive joint strength and achieve cohesive failure (failure within the adhesive layer) (Figure 8). A weak interfacial strength could lead to a failure at the aluminum/adhesive interface, resulting in reduced adhesive joint strength and premature joint separation (Figure 8). Thus, it was important to identify efficient and applicable surface treatments that could be used to prepare adhesively bonded aluminum joints and achieve a cohesive failure within the adhesive layer consistently. In this section, the adhesion theories that are most relevant to aluminum/epoxy adhesion are summarised, and the background information related to the effects of aluminum oxide, wettability and surface roughness on adhesive joint strength are discussed.

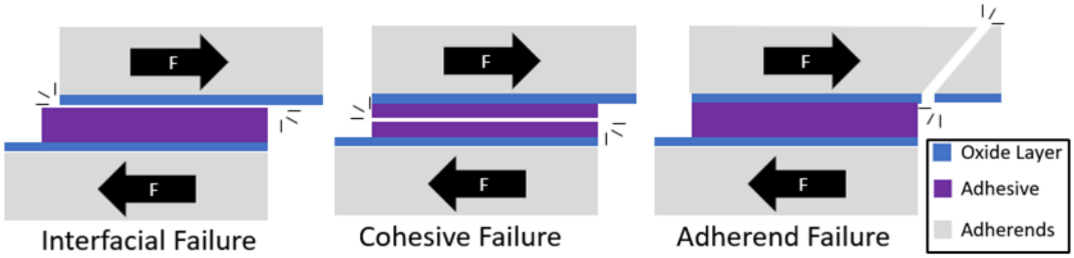

Figure 8: Failure modes of adhesively bonded aluminum joints.

There is an industrial and academic need to develop an understanding of the adhesion mechanisms and how those mechanisms contribute to the bonded joint performance (Abrahami *et al.*, 2017). According to the mechanical theory, surface porosity and roughness directly influence the degree of adhesion. As the adhesive flows into the base metal surface irregularities and cavities, it creates a mechanical interlock. In contrast, the adsorption theory describes the adhesion by the forces formed due to the adsorption of the macro-molecules of the mobile phase (epoxy) onto the base metal and explains the adsorption forces by:

- the Van der Waals interaction (weak physical bonding but contributes to the overall adhesion);
- chemical bonds (covalent, ionic or metallic bonds which are not common between dissimilar materials but can be encouraged using pre-treatments);
- and acid-base interaction.

Interestingly, each theory on its own could not provide a comprehensive explanation for adhesion, but the combination of the mechanical interlock, along with atomic and molecular interactions, was reported to be critical for the formation of strong interfacial bonds (Abrahami *et al.*, 2017).

Surface treatments were often assessed by the change in wettability, which is characterized using the apparent contact angle (*i.e.*, the angle between the liquid/air interface and solid surface). The contact angle is measured qualitatively using the optical imaging of a droplet deposited into a solid surface of engineering materials. When the deposited droplet reaches equilibrium, the interface molecular forces are balanced, and the equilibrium energy state is given by the Young relation (Adams *et al.*, 1988):

$$\gamma_{SV} = \gamma_{SL} + \gamma_{LV} \,.\cos\theta \qquad \text{Equation 1}$$

Where θ is the contact angle for the solid flat substrate (Figure 9a), and γ represent the free surface energy coefficients for solid-vapour (SV), solid-liquid (SL) and liquid-vapour (LV) interfaces. When the SV surface energy is high, adhesives and liquids, in general, tend to easily spread on that solid surface achieving a contact angle below 90^{o}. Although the Young relation assumes a smooth and homogeneous solid surface, most engineering materials and surface preparation techniques have some degree of surface roughness (Kubiak *et al.*, 2011). Immense scientific efforts have explored the influence of surface roughness on contact angle measurement and wettability characteristics (Choi *et al.*, 2009; Cox, 1983; Kubiak *et al.*, 2011; Wenzel, 1936). According to (Kubiak et al, 2011a), values obtained using contact angle optical measurement may differ from the equilibrium value, at which the internal liquid force, gravity forces and capillary forces are in balance due to surface non-uniformity, and surface roughness. Therefore, the measured contact angle of engineering materials might not correspond to the equilibrium energy state given by Equation 1. The model proposed by Wenzel (1936) for contact angle characterization of rough surfaces has been used in the literature to address this limitation (Alfano *et al.*, 2012). (Figure 9b)

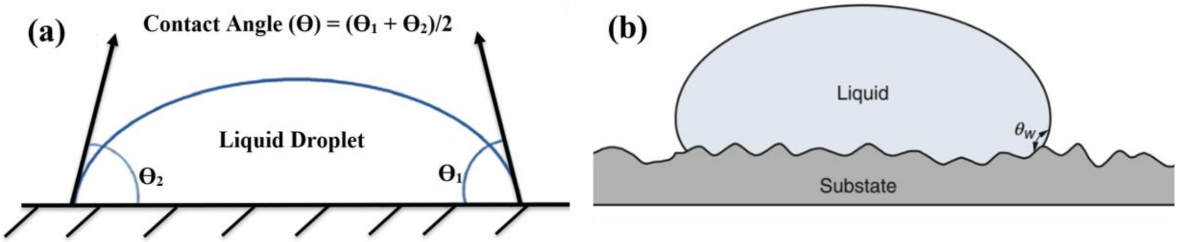

Figure 9: Contact angle illustration for a flat surface following (a) Young's equation and (b) Wenzel's model.

When aluminum is exposed to the oxygen in the air, it forms surface oxides which vary in thickness and structure, depending on the environmental conditions. The oxide layers that form on aluminum have a significant impact on the adhesively bonded joint strength and failure modes. The 2 – 60 nm thick oxide layer, which is instantly formed on aluminum, creates weak adhesion characteristics (Cavezza *et al.*, 2020). The oxide layer formed is composed of thin amorphous oxide (Al_2O_3) adjacent to the metal, and on top of that, there is a layer of hydrated (AlOOH) and hydroxylated ($Al(OH)_3$) oxides. When using sheet material, an important factor that can affect the oxide layer and adhesion characteristics is the influence of the rolling process (hot or cold), which creates what is known as the near-surface deformed layer (NSDL). The rolling process causes deformation near the sheet material surface which can initiate cracks in the oxide layers, and transform the cracked oxides into other surface areas. The thickness of the NSDL was reported to vary between 1.5 to 8 um. In addition to achieving an intrinsic adhesion at the aluminum/adhesive interface, the adhesive must spread over the bonding area and displace air and contaminants without including air pockets or porosity to enhance the physical adsorption and molecular interaction, leading to a strong and reliable adhesive bond (Alfano *et al.*, 2012).

Mechanical surface treatments, such as abrading, sanding, or grit blasting, are widely used in the literature and industry. Hariss and Beevers (1999) reported that mechanical removal of the oxide layer using grit blasting not only improved joint strength but also enhanced the surface chemistry of aluminum for adhesive bonding. However, they highlighted that peaks and asperities resulting from grit-blasting could reduce the wettability of the treated surface, and reported that the presence of grit media residue made this effect more pronounced. Boutar *et al.* (2016) investigated the effect of surface roughness and wettability on the strength of aluminum single-lap shear joints using mechanical testing, fracture surface examination, and surface roughness measurements using a differential inductance feeler. The surface roughness profilometry parameters R_a (arithmetic average height), R_q (root mean square roughness), and R_z (ten-point height) were compared for non-abraded and abraded aluminum alloy adherends yielding R_a values ranging from 0.3 um (non-abraded) to 3 um (using p50 abrasion). The results indicated that a surface roughness (R_a) of 0.6 +/- 0.19 um was the optimum surface roughness for providing maximum wettability (contact angle of 62.01^o) and maximum joint shear strength using standard SLJ specimens (ASTM D1002).

Chemical treatments, such as chromic acid anodizing (CAA), have been widely used in aircraft production to improve adhesive joint strength and durability by introducing changes in surface roughness, chemistry and porosity. Venables *et al.* (1979) used a scanning transmission electron microscope to examine the surface morphology of the oxide layers formed on aluminum using three of the most widely used chemical surface treatment techniques in the aircraft industry to prepare aluminum structures for adhesive bonding. In their study, aluminum (AA2024-T3) surfaces were prepared using the CAA process, phosphoric acid anodization (PAA) process, which was developed by Boeing as a safer, chromate-free alternative to CAA, and the widely used Forest Product Laboratory (FPL) etching process. The oxide surface developed after the CAA treatment was characterized by a highly porous dense oxide layer with a thickness of 15,000 nm (Figure

10a). In contrast, the PAA oxide surface developed a thinner oxide layer (4000 nm) composed of hexagonal cells and protrusions (whiskers) (Figure 10b), and the FPL process developed the thinnest oxide layer (400 nm) with protrusions (Figure 10c). They suggested that while the morphology of the PAA might indicate better adhesion due to the mechanical interlocking capabilities of the developed oxide layer, the CAA surface treatment would provide better corrosion protection and long-term joint durability. Later, Boeing patented boric sulfuric acid anodizing (BSAA), which provided better corrosion resistance relative to PAA, but a relatively lower adhesion performance and durability due to the lower porosity of the formed oxide (Zhang *et al.*, 2008).

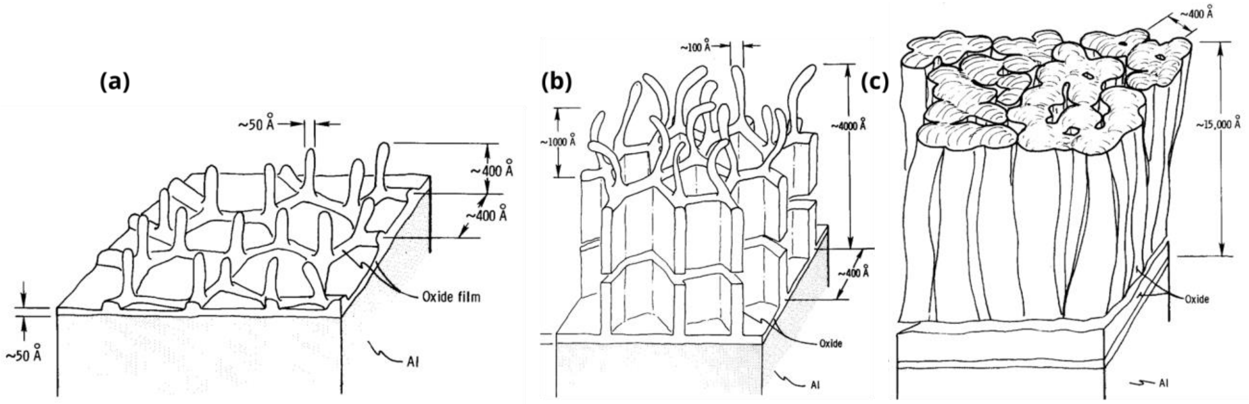

Figure 10: Oxide structures formed on aluminum surface treated using FPL (a), PAA (b) and CAA (c) processes. Reproduced with permission from Venables *et al.*, (1979)

Although anodizing and etching treatments have achieved superior aluminum bonding, the major drawbacks of these approaches are that they are relatively costly and not easily applicable in a laboratory environment due to their health and safety risks. Therefore, there was a need for other chemical treatments that could be applied in a laboratory environment and have the potential to be scaled for high-volume production. Crook *et al.* (1998) presented a two-step surface treatment that included rinsing the aluminum adherends with diluted sodium metasilicate solution followed by a diluted aqueous epoxy-silane solution. They reported that the two processes were synergetic and offered a significant increase in joint strength and higher tolerance to surface contamination and humidity. Treated test specimens, made from aluminum (AA7075), showed a significant increase in fracture toughness. Additionally, Saleema *et al.* (2012) proposed a sodium hydroxide (NaOH) chemical treatment to remove the weak native aluminum oxide layer and increase the surface roughness of AA6061 adherends. An increase in surface roughness was reported (*i.e.*, R_a increased from 0.3 to 0.94 um), and the subsequent single-lap shear joint strength and adhesive failure mode were comparable to the PAA and CAA treatment results reported in work carried out by (Piwowarczyk and Korzeniowski, 2018). Another interesting surface treatment is the use of sol-gel (*i.e.*, a solution-gelation process in which metal alkoxide solution transforms into a polymerized gel through hydrolysis and condensation reactions) technology. The use of sol-gel has been emerging as a surface preparation method for metals and composites in aircraft applications. Fink *et al.* (2010) used a commercially available sol-gel kit (AC130, 3M; USA) having a zirconium compound, glacial acetic acid, a silane compound, a surfactant, and water. The authors reported that the Institute of Composite Structures and Adaptive Systems of the German Aerospace Center DLR experienced high reliability and performance of structures treated using sol-gel, and that industrial implementation was carried out on some Boeing 787 parts. Nevertheless, this work did not consider comparing sol-gel to an industry-standard surface treatment (*e.g.*, CAA), making it difficult to quantify the associated joint strength improvement relative to other standard treatments.

Eco-friendly surface treatments offer lower health and safety risks and less dependency on the skills and finesse of the user (Alfano *et al.*, 2012). Alfano *et al.* (2012) examined the effect of laser irradiation on the surface topology of aluminum (AA6082-T6) treated using a range of laser spacing (50-150 um), laser power (40-100 W) and scan speed (500 - 1000 mm/s). Laser irradiation promoted the formation of a thermal oxide layer (Figure 11a-f) and improved the surface morphology and joint peel strength relative to grit-blasting (Figure 11b). Wu *et al.* (2016) investigated of the effect laser ablation treatment on the response of adhesive-bonded aluminum joints using quasi-static testing of single-lap shear samples, surface topography (SEM images and surface roughness using a 3D optical profilometer), and surface chemistry analysis (XPS). The authors reported that higher laser ablation energy fluence levels (>19.01 J/cm^2) improved joint strength by 25% and increased the extent of cohesive failure. Although the surface roughness arithmetic mean value (R_a) was about 7.5 um, the joint exhibited the highest strength, which was contradictory to the findings by Boutar *et al.* (2016) who found that the optimum strength corresponded to R_a value of 0.6 um. The author explained that the change in surface chemistry and the development of a more uniform and thicker aluminum oxide layer resulted in a joint improvement. In a study funded by General Motors Global Research (Zheng *et al.*, 2015), Atmospheric plasma was used to treat the aluminum adherends of single-lap shear specimens made of two aluminum alloys used in the automotive industry with sheet thicknesses of 1.0 mm and 0.9 mm. The results suggested that it was necessary to select an adhesive with an adhesion strength higher than the joint strength to achieve a cohesive failure. Also, their contact angle measurement showed that the contact angle measurements using distilled water were 60% lower after plasma treatment indicating improved wettability (Table 3). Saleema and Gallant (2013) used plasma treatment to improve the bonding strength of aluminum (AA6061-T6) alloy; however, in extreme humidity and temperature conditions, the joints failed at only 4 MPa compared to 24 MPa in room conditions. Adding a mechanical abrading treatment before plasma treatment was recommended to improve joint durability.

Table 3: The contact angle measurements for two automotive aluminum alloys before and after plasma treatment. (Zheng *et al.*, 2015)

Adherend Material	**As-Received Contact Angle (degrees)**		**Plasma Treated Contact Angle (degrees)**	
	Distilled Water	Diiodomethane	Distilled Water	Diiodomethane
Automotive Aluminum Alloy (A)	94.3	56.7	47.2	53.9
Automotive Aluminum Alloy (B)	93.4	54.8	37.6	53.6

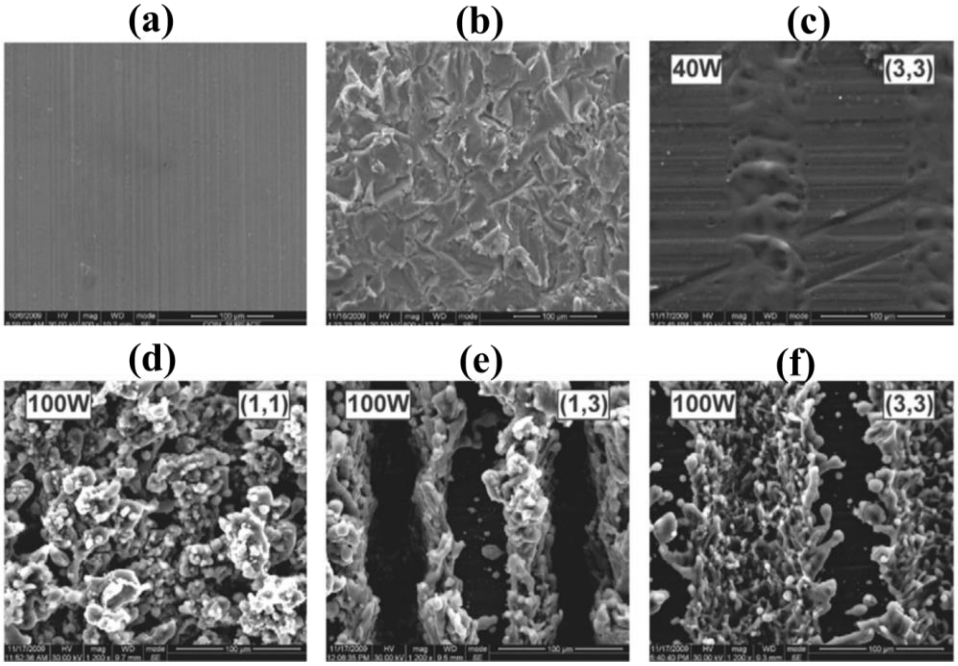

Figure 11: SEM surface images for (a) as-produced surface; (b) grit-blasted surface; and (c-f) laser-treated surfaces using a range of laser power (40-100 W), laser spacing (50 – 150 um), and scanning speed (500 – 1000 mm/s). Reproduced with permission from Alfano *et al.* (2012)

Ultimately, preparing aluminum to achieve proper adhesion and cohesive failure is a key requirement for bonded joints. A surface treatment may work for one adhesive but not for the others. Therefore, a study that compares a broad range of surface treatments (*e.g.*, grit-blasting, abrading, sanding, and sol-gel) is needed to identify surface treatment methods that achieve cohesive failure and maximize joint strength for the particular adhesive used in this work. Also, investigating the surface roughness and wettability behaviour for the best-performing surface treatment may help better understand how these surface treatments improved the SLJ joint strength.

2.2.3 Specimen-Level Mechanical Response of Adhesively Bonded Joints

Single-lap shear (SLJ) test specimens (Figure 12a), such as the ASTM Standards D1002 and D3165 (both specimens have identical dimensions), and ISO 4587:2003, have been used to evaluate the mechanical response (*i.e.,* strength, stiffness and energy absorption) of adhesively bonded joints using metallic and non-metallic adherends (Watson *et al.*, 2019). The popularity of this test specimen in the transportation industry could be explained as follows: i) the test specimens are simple to prepare, bond and test (da Silva *et al.*, 2018; Watson *et al.*, 2019); ii) there is well-established literature demonstrating successful usage of the SLJ test specimen to investigate adhesively bonded joints for transportation applications (Banea *et al.*, 2018; Watson *et al.*, 2019); and, iii) the mechanical behaviour, stress distribution and failure of the SLJ joints could be predicted using readily available analytical models (Harris and Adams, 1984) or FE models (Watson *et al.*, 2019). Adhesively bonded SLJ joints exhibit edge effects, and complex stress distribution within the bonding area, including both tension and shear stresses along the overlap length (Reis *et al.*, 2011; Watson *et al.*, 2019). According to da Silva *et al.* (2018), the complex mixture of shear and tension stress distribution along the overlap region makes SLJ test specimens very useful for validation tests. Thus, the SLJ test specimen has been a simple and economical specimen for the assessment, comparison, evaluation and quality control of factors and variables affecting the mechanical performance parameters of adhesively bonded joints. For example, SLJ specimens have been used to assess the effect of factors such as overlap length, yield strength, stiffness, and thickness of adherends on joint strength (Reis *et al.*, 2011; Watson *et al.*, 2019). Karachalios *et al.* (2013a) investigated the effect of the overlap length on the adhesively bonded SLJ specimens made of ductile steel prepared according to ASTM D-1002, using varying overlap length ranging from 12.5 mm to 60 mm (free length was kept constant at 63.5 mm). The experimental results showed an increase in joint strength with overlap length for four different adhesives, demonstrating an almost linear relation when the data were fitted with linear regression trend lines (minimum R^2 value of 0.9605). The authors reported that for a relatively short overlap the whole length of the overlap was involved in transferring the load causing global yielding in the bonded area. In contrast, when the overlap was long, the bonding area exhibited localized shear strain regions, because some regions in the middle of the overlap/bonded area were still elastic. They also revealed that there is an interaction between the adhesive brittleness and the effect of localized shear strain regions of bonded joints with long overlap. For brittle adhesives, the failure due to the localized shear strain near the ends of the overlap was more pronounced. According to (Karachalios *et al.*, 2013b), shorter overlap (10-20 mm) resulted in more bending than the longer ones, while the joint strength was dominated by the mechanical properties of the adherends in longer overlaps. Watson *et al.* (2019) reported a failure strength for 1.65 mm-thick aluminum (AA5182) SLJ joints of 22.09 MPa (7.125 kN) at a displacement of ~2.2 mm. Also, Leena *et al.* (2016) reported a maximum of 19 MPa (6.129kN) for a similar thickness but a different aluminum alloy. Although, the failure strength of adhesive joints is adhesive-specific, and depends on surface preparation and adherends characteristics, those failure strength values are close to the values reported in the technical data sheet of the adhesives used in automotive applications (3M, 2016).

Adhesively bonded joints are sensitive to the mode of loading and generally exhibit lower strength in tension (*i.e.*, Mode I). Ufferman *et al.* (2018) used cross tension (CT) test specimens to evaluate the mechanical performance of adhesively bonded aluminum joints (Figure 12b). They compared the joint strength and energy absorption of adhesively bonded CT and SLJ specimens, showing that Mode I joints exhibited 83% lower strength (1.77 kN vs. 10.64 kN), and 85% lower energy absorption (11.1 J vs. 74.6 J) compared to Mode II joints (SLJ specimens). The displacement value at failure (~6.7 mm) and post-failure images of CT specimens demonstrated that substantial adherend bending took place, which could reduce joint strength or impose a pronounced effect of adherend material properties on the overall joint response. Ciardiello *et al.* (2020) investigated adhesively bonded H-shaped specimens made of boron steel under a variety of loading orientations and concluded that the joints under tension loading had 50% lower joint strength compared to shear loading. Weiland *et al.* (2019) used an H-shaped specimen (Figure 12c), comprising two double U-sections and also known as LWF-KS-II, due to its increased stiffness and limited bending of adherends. The results showed that bonded joints under Mode I loading failed at a displacement of 1.5 mm and exhibited a peak force of 12 kN. The shear-loaded joints failed at a displacement of 4.08 mm and exhibited a peak force of 33.05kN (almost three times the peak force under Mode I). Although the H-specimen joint strength in this study was nearly seven times higher than the CT joint strength reported by Ufferman *et al.* (2018), the displacement to failure was 77% lower (1.5 mm versus 6.7 mm). This comparison indicated that H-shaped specimens provide limited adherend bending compared to CT specimens. Importantly, the literature has little work done on adhesively bonded aluminum joints under Mode I loading; however, vehicle components exhibit different loading orientations during service life (Ciardiello *et al.*, 2020). Therefore, it is crucial to evaluate the mechanical performance of adhesively bonded joints under Mode I loading.

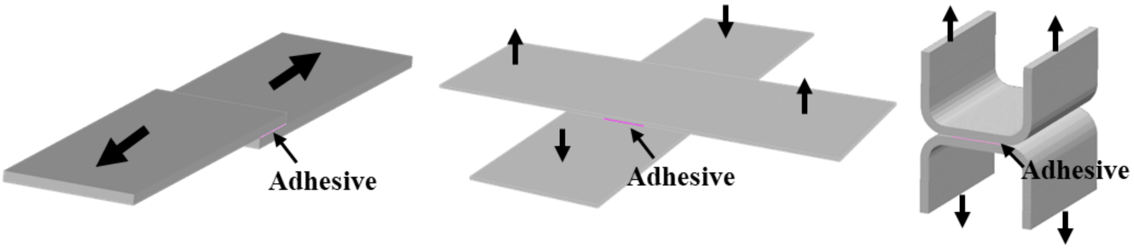

(a) Adhesively Bonded SLJ Specimen

(b) Adhesively Bonded Cross Tension Specimen

(C) Adhesively Bonded H-Specimen

Figure 12: Adhesively joined single-lap shear (SLJ) specimen (a), cross tension (CT) specimen (b), and (c) H-specimen (arrows indicate loading direction, adhesive layer in purple).

Previous studies on the effect of sheet metal thickness and aluminum alloy type (*i.e.*, yield strength) on the mechanical response of adhesive joints have been carried out but did not generally focus on aluminum-aluminum joining. da Silva *et al.* (2008) assessed the influence of adherend properties (yield strength and thickness), adhesive properties (thickness and toughness), joint overlap, and surface treatment on the SLJ joint strength using the Taguchi method. Among the assessed parameters, adherend yield strength and adherend thickness showed the most significant contribution to joint strength. Also, da Silva *et al.* (2009) highlighted the importance of considering the sheet thickness (*i.e.*, adherend thickness) when evaluating the mechanical performance of bonded joints. In their work, they explained that the influence of sheet thickness on SLJ joint strength changed according to the adherend material yield strength. When the adherends had a low yield strength, increasing the thickness reduced the plastic deformation within the adherends. On the contrary, when the adherend yield strength was higher, the bending moment increased with increasing sheet thickness, which led to a reduction in joint strength. Reis *et al.* (2011) prepared SLJ test specimens using three adherend materials with a significant difference in stiffness and yield strength (*i.e.*, composite, steel and aluminum (6082-T6)). The authors reported that the highest shear strength was obtained for the joint made of the material having maximum stiffness. Also, an interaction between the overlap length and adherend material was reported, meaning that the effect of overlap length on the SLJ joint varied according to the material. However, the effect of the adherend yield strength could not be isolated experimentally because the effect of material stiffness could not be neglected. Recently, Watson *et al.* (2019) compared the SLJ joint strength for specimens made of ultra-high-strength steel (UHSS) (Usibor ®, yield strength (YS) = 1500 MPa, Young's modulus (YM)= 200 GPa), aluminum (AA5182, YS = ~135 MPa, YM= 70 GPa), and magnesium (ZEK-100, YS = ~145 MPa, YM= 45 GPa). The authors reported that UHSS joints exhibited a significantly higher strength compared to the aluminum and magnesium joints. Although the thickness of magnesium and aluminum adherends was identical, and the stiffness of magnesium samples was lower (36%), the SLJ joints exhibited the same joint strength. This observation confirmed that the effect of yield strength on SLJ joint strength could be more pronounced compared to the effect of stiffness.

2.2.4 Finite Element Modeling of Adhesively Bonded Joints

Finite element modeling is commonly used in the automotive industry for structural investigation and crash simulations. Several FE approaches, such as continuum mechanics, linear elastic fracture mechanics and the extended finite element method (XFEM), are available for modeling adhesive bonding and simulating the damage and failure of adhesive joints. In the continuum mechanics approach, the adhesive material is modelled using three-dimensional elements with a material model having visco-elastic or visco-elastoplastic formulation. The stress-strain constitutive relationship of the adhesive is usually augmented with a failure criterion based on maximum stress, strain or strain energy. Many researchers adopted this approach (Adams *et al.*, 1997; Trimiño and Cronin, 2016); however, recent studies have identified that stress singularities at joint corners, mesh size dependency, and the high computational time made this approach prohibitive in large models required in industrial applications, such as full vehicle models (da Silva and Campilho, 2012). For example, a prohibitively fine mesh size (<0.1 mm) was required to converge the stress distribution of an SLJ model at the boundaries of the adhesive (Gonçalves *et al.*, 2002). The extended finite element method approach can be useful when the crack path is not known as the crack propagation follows the maximum principal stresses/strains at the crack tip. However, in adhesive joints, it was shown that this could lead to damage progression within the adherends, resulting in a non-physical response (Campilho *et al.*, 2011). Similar to the continuum approach, XFEM may not be computationally efficient when implemented in large models.

The cohesive zone method (CZM) is a fracture mechanics-based approach with initially linear elastic behaviour followed by the initiation and progression of damage. The CZM approach was originally presented to model the crack growth in concrete. The elastic behaviour is described by an elastic constitutive matrix that shows how the nominal traction (stress between the bonded interfaces) relates to the nominal strain across the cohesive element (separation). At each integration point, the force components are divided by the original area to get the nominal stresses; then, the separations (*i.e.*, relative displacements of the top and bottom faces of the cohesive element) are calculated from the nodal coordinates and divided by the original thickness to get the nominal strains. The CZM approach has been attractive for modelling adhesives as it can capture the adhesive damage initiation, progression and failure (Lanzerath and Pasligh, 2014; Park and Paulino, 2011) while providing a middle ground of computational efficiency and accuracy. Also, it is readily available in commercial FE packages (*e.g.*, LS-DYNA, LSTC, Livermore Software Technology; and Abaqus, Simulia, Dassault Systems), which makes it simple to use. The CZM elements can predict the behaviour of adhesive joints using a relatively coarse mesh and a single element through the thickness, providing the required computational efficiency and suitability for large FE models. CZM requires prior knowledge of the potential crack zone (Karachalios *et al.*, 2013b), and in the case of adhesive joining, the crack zone is known beforehand. When damage initiates in CZM elements, the softening behaviour and loss of stiffness can make it hard for the FE simulation to converge. Some of these problems with convergence can be solved by using viscous regularization of the constitutive equations. This makes the tangent stiffness matrix of a material that is softening positive for small enough time steps.

For adhesive modeling, cohesive elements are placed between the continuum elements representing the adherends to simulate the cohesive behaviour under different loading conditions (*i.e.*, Mode I, II, and mixed mode). The CZM requires a traction-separation relationship to describe the constitutive behaviour of the cohesive zone elements. There are several traction-separation relationships, and the shape of the traction-separation curve plays a crucial role in the joint response and convergence of the FE model. In a bilinear traction-separation relationship, as the cohesive element separates, traction linearly increases to reach a maximum value then decreases linearly to zero resulting in a complete separation/failure. In contrast, in the trapezoidal relationship (Tvergaard and Hutchinson, 1992), when the maximum traction is reached, the curve exhibits a plateau before it starts to decrease linearly. Typically, for each mode of loading, the two cohesive relationships require moduli (E), peak tractions (T or S), and the critical energy release rates (G_c), which represent the fracture toughness. In the trapezoidal relationship, each loading mode requires an additional parameter (fg) to describe the ratio of the area under the plateau region.

While the bi-linear cohesive relationship (Figure 13a) has been successfully used to represent brittle fracture response, structural toughened adhesive exhibiting some ductility would require a more accurate representation of the plasticity response during damage progression. Therefore, researchers utilized CZM with trapezoidal traction-separation relationship (Figure 13b) and reported excellent results and convergence rate when simulating structural toughened adhesives (Campilho *et al.*, 2013; Liao *et al.*, 2018; Trimiño and Cronin, 2016; Watson *et al.*, 2019; Zhang *et al.*, 2018).

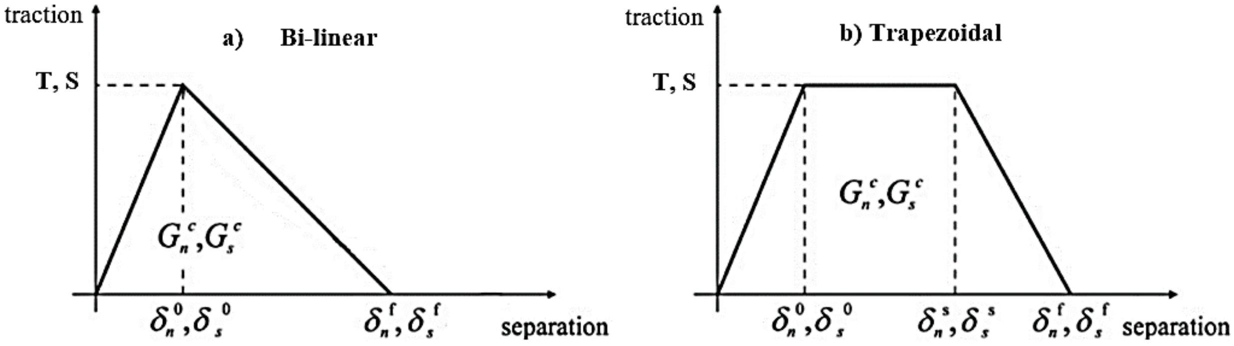

Figure 13: Traction-separation curves for the a) bilinear and b) trapezoidal cohesive relationships. Adapted from Campilho *et al.* (2013)

2.2.5 Adhesive Material Characterization and CZM Implementation

According to Adams (1990), there is no perfect test for determining the mechanical properties of the adhesive. Adhesives in the transportation industry are applied in thin layers, with typical bond line thickness in the range of 0.2 – 0.4 mm (Lanzerath and Pasligh, 2014), and are influenced by the adherend geometry, thickness, and mechanical properties. The adhesive bond line thickness and confinement in joint form were investigated and results suggest that the behaviour of bulk adhesives may not be directly related to the behaviour of adhesively bonded joints. Kinloch and Shaw (1981) compared the fracture toughness of a bulk, toughened, rubber adhesive and TDCB joints bonded with the same adhesive using a range of bond line thicknesses. In general, the fracture toughness of adhesively bonded joints was higher than or equal to the bulk adhesive and was dependent on the bond line thickness. The authors related the influence of bond line thickness to the radius of the plastic-deformation zone of a sharp crack (r_{Iy})

$$r_{Iy} = \frac{1}{2\pi}\frac{E_{adherend}G_{Ic}}{\left(\sigma_{\text{Yield,Tension}}\right)^2} \qquad \text{Equation 2}$$

When the bond line thickness was smaller than twice the radius of the plastic-deformation zone ($t_{adhesive} < 2r_{Iy}$), the plastic zone was too thin and adhesive constraints (stress and strain) were high, resulting in fracture energy lower than bulk adhesive. As the bond line thickness increased, the plastic zone increased and the constraint stress at the crack tip was lower, resulting in higher fracture energy. The fracture energy approached the maximum at $t_{adhesive} = 2r_{Iy}$, then decreased to reach the fracture energy of the bulk adhesive when the bond line thickness was substantially larger than $2r_{Iy}$, with almost no constraints and a small circular plastic zone. In general, adhesive joints in automotive applications are expected to demonstrate higher fracture energy than bulk adhesive, attributed to the plastic deformation zone developed due to the confinement of the thin adhesive layer by the high modulus adherends.

To measure the fracture toughness of adhesives and find the critical energy release rates, fracture tests are performed under Mode I (tensile opening mode) (Figure 14a), Mode II (in-plane shear mode) (Figure 14b), and mixed mode (a combination of Mode I and II, ranging between 30-75 degrees with 45 degrees as the most common). Ripling *et al.* (1971) introduced a double cantilever beam (DCB), which was described in the ASTM standard (ASTM D3433-99), and a tapered double cantilevered beam (TDCB) test specimens along with an analytical formula to measure the fracture toughness of adhesives under Mode I loading. The formula used to calculate the critical energy release rate in Mode I loading (G_{IC}), known as simple beam theory (SBT), was based on Irwin's energy method and Timoshenko beam theory under the assumptions that the DCB was clamped at the crack tip and the interface material was stiff and brittle. Later, the same authors showed that the SBT underestimated the measured crack length due to the crack tip rotation. The SBT concept was corrected by Blackman *et al.* (2005, 2003), who proposed a corrected beam theory (CBT), which was described in (BS ISO 25217:2009). Another widely used method to calculate the critical energy release rate, the so-called compliance-based beam method (CBBM), was developed by de Moura *et al.* (2009) to address the challenges of crack length measurement and account for the energy dissipated in the fracture process zone. Compared to Mode I fracture tests, Mode II and Mixed Mode tests are more complex. To determine the fracture toughness of adhesives under Mode II loading, the critical energy release rate, G_{IIC}, is commonly measured using end-notch flexure (ENF), end-loaded split (ELS) tests or 4-point End Notched Flexure (4-ENF).

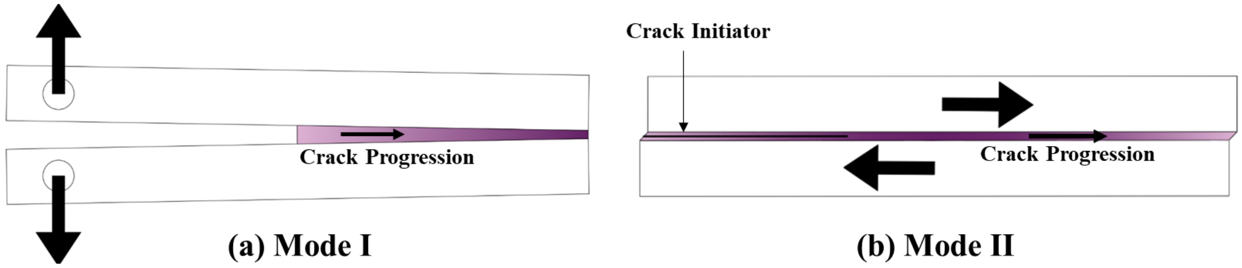

Figure 14: a) Mode I loading – opening mode and b) Mode-II loading – in-plane shear.

While characterizing the fracture toughness of adhesives under Mode I and Mode II loading configurations is essential to measure the fracture properties (*i.e.*, fracture energy release rate) and describe the damage evolution of bonded joints, failure strength tests are required to measure the elastic properties (*i.e.*, modulus of elasticity, peak stress, and separation at damage initiation under each mode of loading). These parameters are required to accurately describe the full cohesive relationship (traction-separation curve) which will enable capturing the behaviour of the adhesive joints numerically. The butt joint test specimen was widely used to determine the elastic properties of bonded joints under Mode I loading (Adams and Coppendale, 1979; Sauvage *et al.*, 2017). The same test specimen was used to determine the joint shear strength by applying torsion to account for the adherend deformation (Adams *et al.*, 1988). Recently, Spaggiari *et al.* (2019) presented a modified butt joint with relief grooves to characterize adhesive Mode I strength, claiming that the grooves lowered the stress concentration at the adhesive interface and throughout the bond-line thickness. Tests used for characterizing the Mode II elastic properties of adhesive joints include the napkin ring test under torsion loading, and the thick adherend shear test (TAST). Although the napkin ring is a standard test (ASTM E-229), manufacturing the test specimen and cleaning the adhesive spew have been reported to be challenging (da Silva *et al.*, 2018). TAST specimens have been the most popular shear failure strength tests for adhesively bonded joints because they were simple to make and test. Two different TAST geometry dimensions have been used according to ASTM D2095 and ISO 11003-2. However, the two geometries had limitations associated with stress concentration and edge effects, causing strength under-estimation (Cognard *et al.*, 2008; da Silva *et al.*, 2018).

Efforts were made to reduce the number of tests required to measure the parameters required for adhesive CZM implementation. Dastjerdi *et al.* (2013) presented a new test specimen, the so-called rigid double cantilever beam (RDCB), that was designed to maximize the second moment of area in the bending direction, resulting in a test specimen with rigid adherends. The advantage of this test specimen was two-fold: 1) the strain energy was only released due to crack propagation with no elastic energy storage due to adherends deflection, and 2) the analysis of crack opening was simplified, and crack opening measurement could be done along the bond-line length, without the need for advanced imaging capabilities. Liao *et al.* (2018) used the RDCB test specimen to characterize an automotive toughened structural epoxy adhesive, and by using a single test, they could obtain the data traditionally obtained from a fracture test (*e.g.,* DCB test) and a failure strength test (*e.g.,* butt joint test). Recently, Watson *et al.* (2018) performed a detailed FE analysis on the RDCB test specimen and revealed that a portion of the bond line length was under compression, which was not considered in the original analysis. Therefore, they extended the original analysis and validated the RDCB specimen using the ASTM D3433 TDCB. In addition to the improved analysis method, they optimized the geometry of the RDCB to further increase the second moment of the area resulting in improved adherends rigidity and minimizing the geometrical effects of the adherends (Figure 15a). The RDCB test specimen could potentially provide means to characterize the Mode I response of adhesively bonded joints using a single test rather than using fracture toughness and failure tests. The authors extended their work to Mode II characterization and developed the bonded shear specimen (BSS), which allowed measuring the Mode II traction separation curve from a single test while addressing the limitations of the end-notch flexure (ENF) test (Watson *et al.*, 2020). The BSS geometry, based on a concept similar to TAST, was optimized to maximize the second moment of area in the bending direction of the specimen, which confined all the deformations within the adhesive layer. Consequently, the BSS test analysis reduced the complex analysis required to account for adherend deformation and allowed direct measurement of the full traction-separation relationship (Watson *et al.*, 2020). Similarly, the RDCB geometry has been optimized to maximize the test specimen rigidity, minimizing the geometrical effects of the adherends. The BSS specimen was also adapted to characterize adhesives under mixed-mode loading. Without the requirement for additional failure strength testing, the RDCB and BSS tests measured the CZM traction-separation relationships efficiently and accurately. However, there is no single study that verified and validated adhesive FE models with CZM parameters measured from the RDCB and BSS tests.

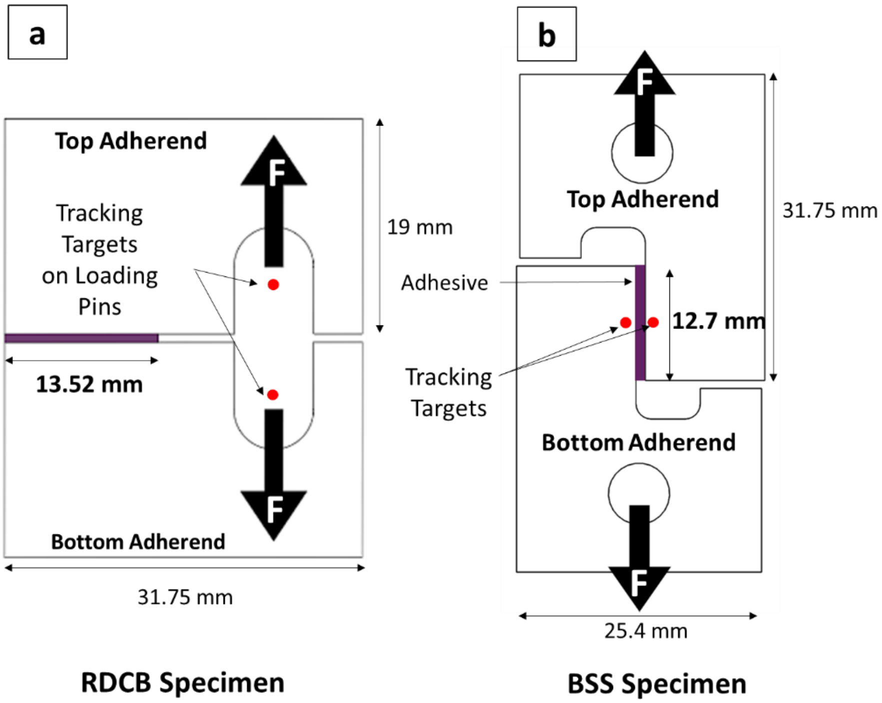

Figure 15: Adhesive characterization specimens for Mode I (RDCB, a) and Mode II (BSS, b). Adapted from Watson *et al.* (2020).

2.2.5.1 3M 07333 Adhesive Characterization Data

The CZM parameters for the structural epoxy adhesive (07333 IRS; 3M, Canada) used in this study have been characterized in the literature using the RDCB and BSS tests for a range of bond line thicknesses (0.18 - 0.64 mm) (Watson *et al.*, 2020). The authors reported that the RDCB and BSS specimens demonstrated a plateau when the peak traction was reached, indicating some adhesive ductility in Mode I and Mode II loading (Figure 16). Thus, the response of each RDCB and BSS test was fitted to a trapezoidal response using a least-squares fit, determining the stiffness, peak traction, area ratio (a parameter that controls the plateau region), separation at peak traction and separation at failure. The critical energy release rate was calculated by finding the area under each trapezoidal traction-separation response. The CZM parameters for a bond line thickness of 0.3 mm were used for the adhesive CZM implementation in this study (Table 4).

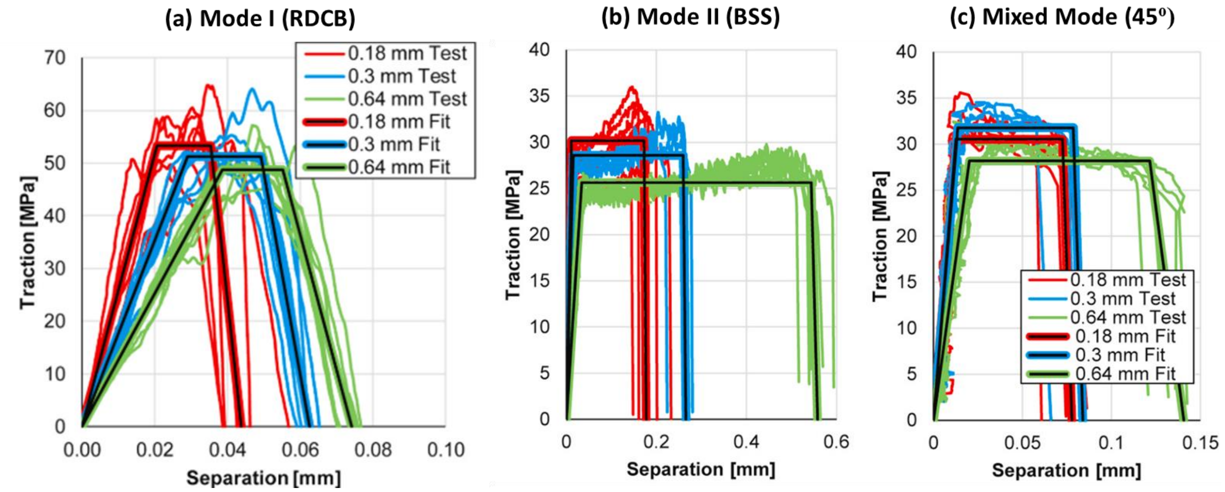

Figure 16: Cohesive traction-separation relationship in Mode I (a), Mode II (b) and mixed mode (c) for the 3M 07333 adhesive with a range of bond line thicknesses (0.18 mm to 0.64 mm). Adapted from (Watson *et al.*, 2020)

Table 4: Cohesive zone method parameters for the 3M 07333 adhesive with 0.3 mm bond line thickness.

Loading Direction	**Stiffness (MPa/mm)**	**Peak Traction (MPa)**	**Critical Energy Release Rate (kJ/mm^2)**	**Area Ratio**
Mode I	1762	51	2.13	0.49
Mode II	1880	29	7.28	0.96

2.2.6 Component-Level Response of Adhesively Joined Structures

Component-level testing of adhesive structures, which generally implies a large adhesive bond area with complex loading conditions and progressive joint failure, provides the loading conditions that are more relevant to a full vehicle (relative to what is represented at coupon scale tests). The large bonding area will distribute the loads and enable a better understanding of how the structure deformation influence crack initiation and progression. Understanding adhesive response at this level informs joint designers on how the scale influences the mechanical behaviour of the joint. Importantly, a component-level test is required to validate the FE model of the joint, confirming that the specimen-level testing could be used as a representative volume element to reproduce joint behaviour in a complex loading scenario.

Several authors used component-level axial crush tubes to evaluate adhesive joined structures and validate adhesive FE models. Yang *et al.* (2012) tested tubular tubes, comprising two 1.5mm-thick steel hat sections joined with a 0.25 mm-thick adhesive, using axial impact with a 276 kg rigid wall at a speed of 10.15 m/s. The component-level validation showed a good correlation in terms of load-displacement response, energy absorption, and deformation patterns. The tubes exhibited substantial deformation and the adhesive failed at one side of the tube causing asymmetrical deformation and separation on one side (single flange) (Figure 17a and Figure 17b).

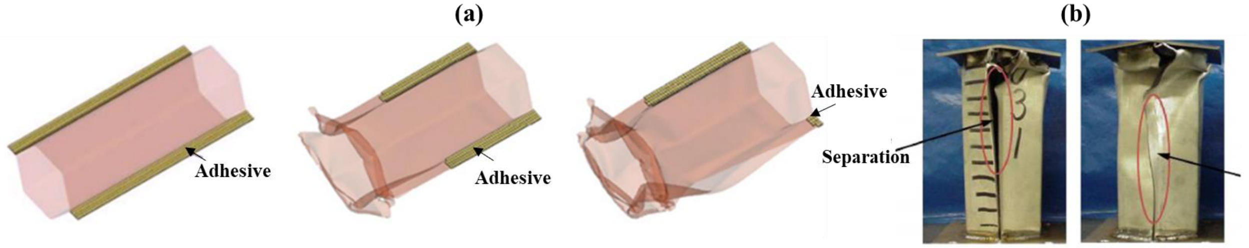

Figure 17: (a) Adhesively joined tubes under axial impact, (b) Tube deformation and adhesive failure. Adapted from Yang *et al.*, (2012)

Trimiño and Cronin (2014) used sub-scale axial crush tubes made of DP800 steel and a drop tower to axially impact the tubes. A key difference in their study was that the tubes had a square geometry and exhibited well-behaved deformations in the form of folding. The authors also investigated tubes with flanged geometries with an indented fold initiator and a notch to facilitate progressive folding. Gowda *et al.* (2017) used a drop tower, having a 134 kg impactor, to axially crush adhesively bonded and spot-welded steel tubes at a velocity of 4.3 m/s. The tubes were 250 mm long and were joined with spot welds spaced at ~40 mm or adhesives with a bond line thickness of 0.3mm. The peak load of the impact was 52.6 kN and 73.2 kN for the spot-welded and adhesively bonded tubes, respectively. However, the mean loads and energy absorbed for both joining methods were similar (less than 10% difference), which was likely attributed to the dominance of the base metal deformation on the overall response. Yamashita *et al.* (2013) studied the axial crushing of aluminum-bonded tubes. The author concluded that it was important to choose the aluminum sheet material with an appropriate strain hardening to achieve a well-behaved folding deformation (Figure 18a); otherwise, plastic instability will occur. Close-up images of the deformed tubes showed that the adhesive failure was randomly distributed along the flange (Figure 18b).

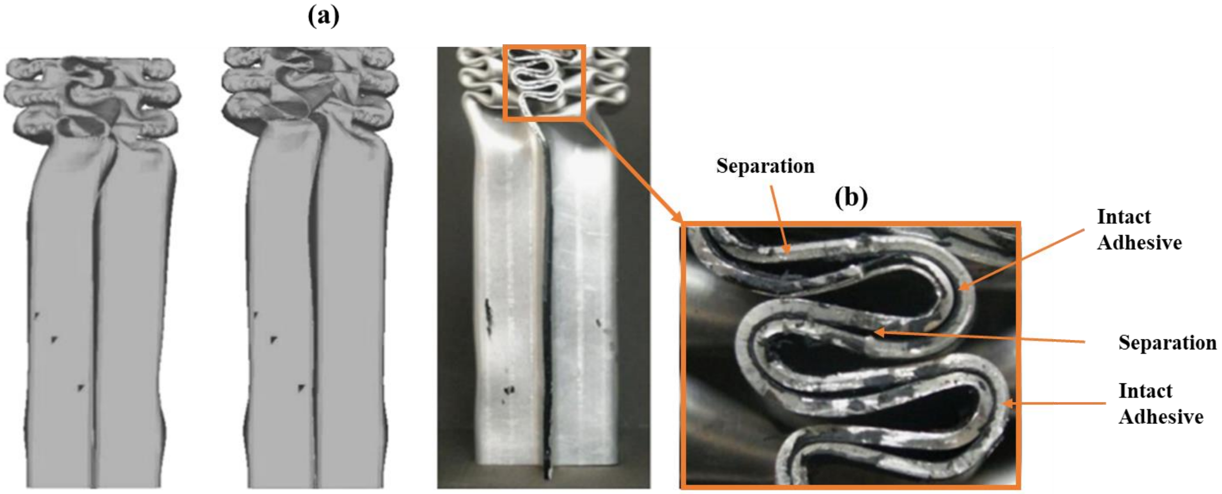

Figure 18: (a) Progressive folding of adhesively joined axial crush tubes, (b) Adhesive failure along the flanges. Adapted from Yamashita *et al.* (2013)

T-shaped components were also used to assess adhesively joined structures under various modes of loading. May *et al.* (2015) investigated adhesive computational model development, verification and validation. In their work, T-components made with 1.2 mm dual-phase steel were joined using an automotive adhesive (Betamate 1496V, Dow) and then tested under two modes of loading: front loading and side loading (Figure 19a). One key differentiator in this study was that the authors tried to primarily isolate the load to the adhesive joint, as opposed to the combined adhesive-structure deformation response. The T-components subjected to front impact loading exhibited limited structure deformation and failed by peel failure of the adhesive layers (Figure 19b). However, the side-loaded T-components exhibited localized plastic deformation at the contact area (1, Figure 19b) and at the junction, which formed a folding (3, Figure 19b) and tube debonding (4, Figure 19b). Tube rotation was encountered and joints exhibited peel loading at the top joint (2, Figure 19b) and shear loading at the side joint (5, Figure 19b).

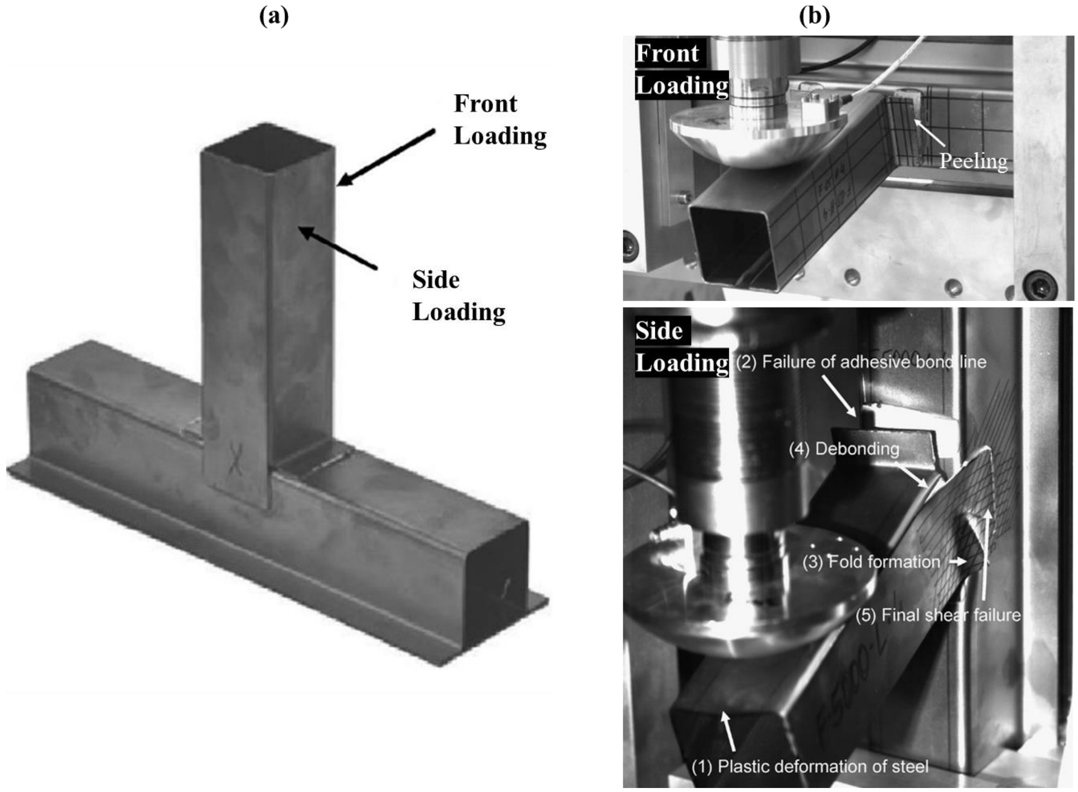

Figure 19: (a) T-Component test, (b) Adhesive joint failure under front and side loading. Reproduced with permission from May *et al.* (2015)

Similarly, Boqaileh (2015) used a T-component test sample, comprising two C-channels, to evaluate the adhesive joining performance and validate the adhesive CZM model (Figure 20a). The T-shaped component used in his work was originally developed for discrete joining (Hoang *et al.*, 2012), but the author refined the geometry for use with adhesives because it was simple and efficient to prepare and test in terms of cost and time. However, substantial plastic deformation in the fixed section was reported, which induced joint rotation (Figure 20b).

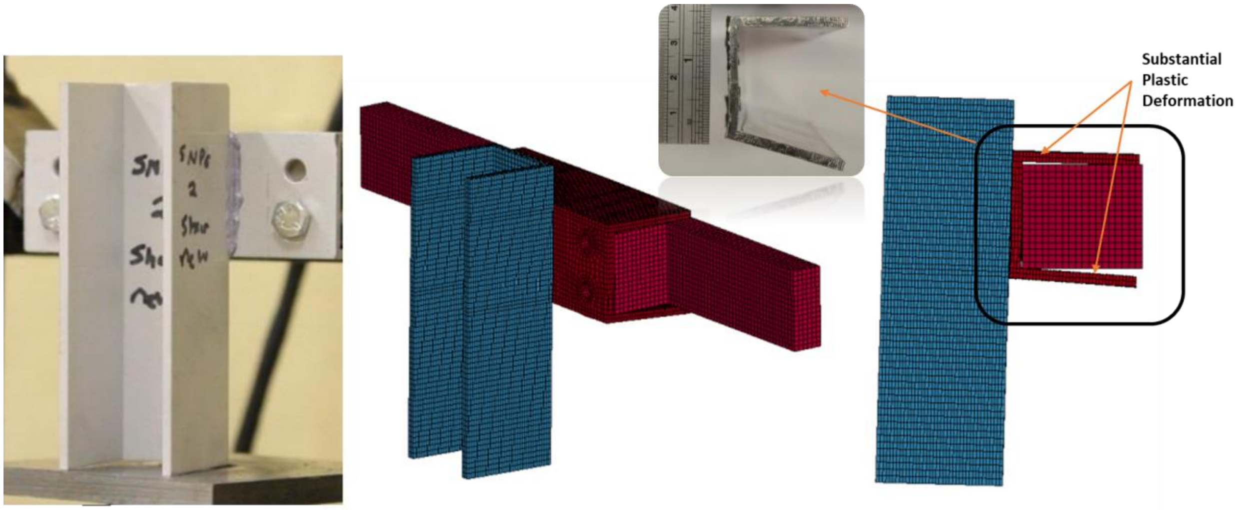

Figure 20: (a) T-shaped component made with C-channels, (b) deformation in the fixed C-channel. Adapted from Boqaileh (2015)

Limited studies have considered the 3-point bending test to evaluate the performance of adhesively joined components. Gowda *et al.* (2018) assessed the 250 mm-long adhesively joined tubes under 3-point bending. The authors compared flanged and square hollow tubes made with steel 250 mm long and reported the mechanical response and deformation behaviour results. The flanged tubes showed substantial localized deformation at the contact area and global bending deformation along the length of the tube resulting in abrupt adhesive failure and flange separation. The deformation in the hollow square tubes was localized and adhesive total separation was not encountered attributed to the lack of adhesive crack propagation. Liu (2019) used a 3-point bending test to assess adhesively joined structures made with UHSS sheet metal. The test was used to validate the adhesive FE model under shear loading; however, the author reported that the base material properties and deformation significantly influenced the overall response. When the tubes were made from softened hat sections, the overall response was significantly influenced by material softening and the adhesive remained intact because the structure exhibited substantial local and global bending deformation. Efforts were made to identify a component-level test for adhesively joined structures; however, the tests used in the literature have major limitations.

Previous studies often showed substantial deformation and/or failure in the base material, which could result in similar mechanical behaviour for different joining methods, masking their influence on the mechanical response and making joint performance comparison somewhat challenging. Also, the adhesive joint often experienced arbitrary crack initiation and unstable crack progression, making it impossible to isolate the load and energy absorbed by the joining method. Therefore, evaluating the global structure response and local joint response using measurable metrics was challenging with the previously discussed component-level tests. The Caiman test was originally developed to investigate the structural performance of discrete joining methods, particularly spot welds (O'Keeffe, 2018). Liu (2019) used the 'Caiman test' with structural adhesive joining and achieved a stable adhesive crack propagation with limited structure deformation until flange separation. The author applied 'local separation' and 'crack extension' metrics to validate the local adhesive response close to the adhesive free boundaries using the rate of adhesive crack progression (energy associated with adhesive fracture) (Figure 21). The test was used to compare two adhesively bonded structures having the same geometry but substantially different material properties. The author reported that for the same adhesive, the response was similar, highlighting that the response was dominated by the joining method (Liu, 2019).

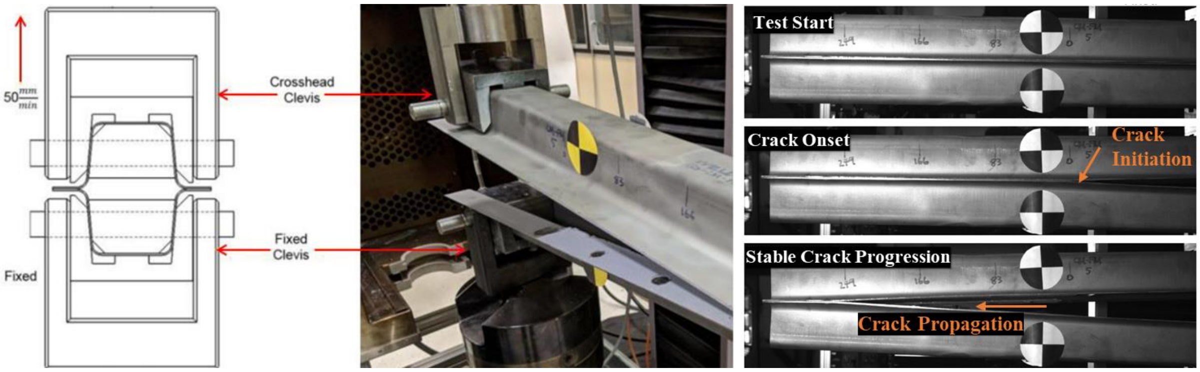

Figure 21: Caiman test geometry and setup, showing adhesive crack progression. Adapted from Liu (2019)

2.3 Self-Piercing Rivets

Self-piercing riveting is a high-speed, point-based, mechanical-fastening process that was developed for joining two or more sheets made of similar materials (*e.g.*, aluminum (Hoang *et al.*, 2012)) or dissimilar materials (*e.g.*, aluminum to steel (Meschut *et al.*, 2014), and aluminum to composites (Zhang and Yang, 2015)) using a tubular rivet. While traditional rivets require hole pre-drilling or pre-punching of the joined sheets, SPR is a one-step multi-process that does not require pre-joining preparation, resulting in a significantly lower footprint on the joined structures. SPR rivets can join two or more sheets of materials by creating a mechanical interlock between the rivet and the joined sheets (*i.e.*, stack). The SPR system is composed of a punch, a rivet, a die and a blank holder mounted on a c-clamp requiring access to both sides of the joint (Figure 22a). The following stages describe the SPR process (Figure 22b): (a) clamping, holding the sheets to be joined between the blank holder and the die; (b) piercing, perforating the top sheet(s) during the rivet insertion; (c) flaring, forming the rivet skirt into the bottom sheet using a die to create a mechanical interlock; (d) releasing, retraction of the insertion tool. During stages (b) and (c), significant plastic deformation is induced as the stack flows into the die and the rivet flares into the bottom sheet, creating a mechanical interlock.

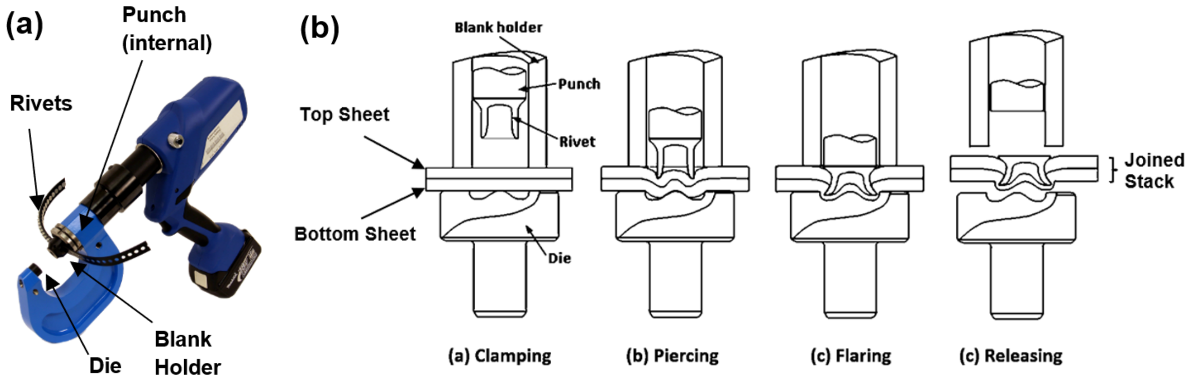

Figure 22: (a) SPR system, (b) a graphical representation demonstrating the four stages of SPR process. Adapted from Li *et al.* (2017)

Recently, Mori and Abe (2018) reviewed the mechanical techniques for sheet metal joining and gave special attention to SPR as one of the techniques that will likely become an essential component in lightweight applications. The author listed the advantages of SPR joining over other mechanical joining methods as extended tool life, simple equipment requirements, and short cycle time. Sarda and Srivastav (2017) and Li *et al.* (2017) outlined a comprehensive list of remarkable features that SPR offers, and some of those features were:

- compatibility with adhesive joining;
- fully automated process;
- environmental and user-friendly with no fumes, sparks, noise or waste material;
- non-damaging for protective coatings;
- applicable to similar and dissimilar materials;
- no pre-drilling or pre-punching requirements;
- superior joint strength and fatigue life;

- low energy requirements and low processing cost; and
- no surface preparation requirements.

Michalos *et al.* (2010) added that the possibility to manually apply SPR using a portable handheld insertion tool and the ability to achieve a leak-proof joint were among the advantages of SPR joining. On the other hand, Li *et al.* (2017) highlighted that there are limitations associated with SPR joining, which could prevent further light-weighting opportunities. These limitations could be summarized as non-uniform load distribution along the joint flange and the possibility of galvanic corrosion when joining dissimilar materials.

SPR joining has been investigated by the automotive industry over the last three decades to facilitate the production of aluminum-bodied premium and sport vehicle classes. In 1994, Audi led the evolution of vehicle-body structure by developing the aluminum space frame for their premium class vehicle (A8 model). The A8 used pre-clamping with an early technology of SPR for single-point joints. Early in the 2000s, Jaguar introduced an adhesive and SPR joined monocoque body structure, also known as a single shell, for the premium XJ sedan and XK sport car models (Mortimer, 2006). The Jaguar XJ X351, with its first production in 2010, used 3118 SPR rivets with 154 meters of adhesive to join the 313 body parts. Other premium vehicle manufacturers in the transportation industry, such as BMW, Daimler and Tesla, also adopted SPR joining as the primary joining method for aluminum structures (Li *et al.*, 2017). While SPR joining application was limited to the premium vehicle class, the 2015 Ford F-150 introduced an SPR-joined aluminum body at a high-volume production scale to achieve 317.5 kg of weight reduction compared to the previous model. Ultimately, SPR joining has been considered a strong alternative for RSW in future transportation applications (Mori and Abe, 2018).

When applying SPR joining, the morphology and physical attributes (*e.g.,* head height, bottom thickness, and mechanical interlock) of the formed joint (Figure 23a) depend on various factors (*e.g.,* SPR process parameters, material formability and ductility, sheet thickness, and the geometry of the rivet and die). According to Li *et al.* (2017), the physical attributes recommended for adequate mechanical interlock (*i.e.,* mechanical interlock (x) = [deformed rivet diameter (D_t) - initial rivet diameter (D_o)] / 2) and superior joint characteristics were achieved using: rivet head height (Y) close to zero; a minimum mechanical interlock of 0.4 mm; minimum bottom thickness (b) of 0.2 mm; an adequate top and bottom seals; and no rivet buckling or cracking (Figure 23b and Figure 23c).

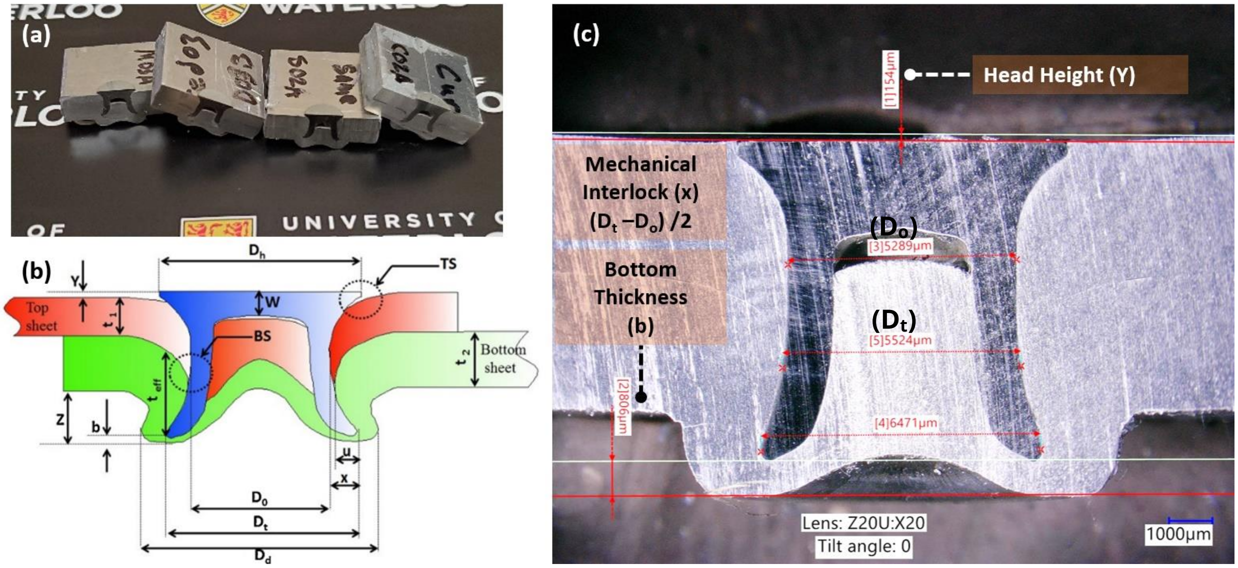

Figure 23: Cross-sectional view of SPR joints; (a) Sectioned joint ready for physical attributes measurements, (b) SPR cross-sectional parameters (Li *et al.*, 2017), and (c) physical attributes measurements.

Hahn and Wibbeke (2005) used the measurement of the physical attributes method to optimize the SPR process parameters and achieve a joint with improved mechanical interlock. Sun and Khaleel (2005) investigated the joint strength of CT test specimens from a joint cross-section perspective, and presented a model to predict failure mode and estimate the lower-bound strength of SPR joints under tension loading as follows,

$$F_h^T = \eta_h \beta_h t_1 \pi D_h \sigma_h \qquad \text{Equation 3}$$

$$F_t^T = \eta_t \beta_t t_{eff} \pi D_c \sigma_{t-s} \qquad \text{Equation 4}$$

where F^T is the rivet strength for the head (h) and tail (t) pull failures; η is the empirical coefficient to consider the degradation of material yield strength during the riveting process on head and tail sides; β is the empirical coefficient for sheet bending induced thickness reduction; t_1 is the sheet thickness on the head side; t_{eff} is the effective material thickness on the tail side; D_c is the diameter of the flared portion of the rivet tail; D_h is the rivet head diameter; σ_h is the yield strength of the material on the head side; σ_{t-s} is the yield strength in shear for the material on the tail side; and t_{eff} and D_c require measuring the physical attributes of the SPR joint cross-section. Hoang *et al.* (2013) replaced steel SPR rivets with aluminum AA7278-T6 rivets; and assessed the newly developed rivets by measuring the formed joint physical attributes, which revealed a fracture in the aluminum rivet during joining (2 + 2 mm) aluminum (AA6060-T6) sheets. Similarly, Meschut *et al.* (2014c) demonstrated that applying localized thermal conditioning, using induction or laser equipment, to UHSS will improve the formed SPR UHSS-aluminum joint, and confirmed that using cross-sectional imaging of the formed joints. Also, Haque (2018) suggested that measuring the cross-sectional physical attributes of SPR joints to evaluate joint quality could offer opportunities to develop new products (*i.e.*, rivets and dies) and optimize the SPR process.

2.3.1 Specimen Level Mechanical Response of SPR Joints

Similar to adhesive joints, SLJ, CT, and H-shaped test specimens were used to evaluate and assess the mechanical performance of SPR joints under shear and tension loading configurations. Han *et al.* (2010) adopted SLJ and CT test specimens made from aluminum (AA5754) to investigate the mechanical performance of SPR joints with symmetrical stacks (two or more joined sheets, illustrated in Figure 10). The SPR SLJ joints had peak loads of 2kN, 5kN and 8kN for the (1+1) mm, (2+2) mm and (3+3) mm stacks, respectively; while CT joints exhibited lower peak loads of 1.4 kN, 4kN and 5kN for the same stack thicknesses, respectively. All SLJ and CT test specimens failed by rivet tail pulling out of the bottom sheet (tail pull-out failure mode). In a similar work with different aluminum alloy (AA5052) and stack thicknesses, Zhao *et al.* (2015) reported SLJ peak loads of 3.11 kN, 4.48 kN and 5.44 kN for (1.5+1.5) mm, (2+2) mm, and (2.5+2.5) mm stacks, respectively. Additionally, SLJ and CT test specimens were also used to assess the mechanical performance of SPR joints made of dissimilar materials (aluminum (AA5052) and boron steel). For example, Mori and Abe (2012) testing results showed that SPR joints made with 1.5 mm thick sheets had an SLJ peak strength of ~5 kN (Figure 24a), while similar CT joints failed at ~2.8 kN (Figure 24b). Importantly, the CT specimens failed at a displacement of nearly 17 mm, demonstrating that the test specimen exhibited a substantial amount of deformation before joint failure, attributed to the high compliance of the CT specimen (Figure 24).

Khanna *et al.* (2006) and Zhao *et al.* (2015) demonstrated that sheet metal thickness affected SPR joint strength, failure mode, and fatigue life. Porcaro *et al.* (2006) used H-specimens to investigate SPR joints under shear, tension, and mixed-mode loading configurations. The experimental results data demonstrated a strong correlation between joint strength, aluminum alloy type (*e.g.*, yield strength) and sheet metal thickness. The authors reported that SPR joints possibly fail through one of the following failure modes: (a) tail pull out, (b) head pull out and (c) shearing of the bottom sheet. Hanssen *et al.* (2010) evaluated H-specimens made of aluminum (AA6060-T4, YS= 70 MPa) and (AA6060-T6, YS= 190 MPa) under shear and tension loading configurations. The experimental results data showed that the aluminum alloy with higher yield strength had 29-44% higher joint strength under normal loading, and 22-50% higher joint strength under shear loading. The increase in joint strength varied according to sheet metal thickness, indicating that there could be a significant interaction between the base material thickness and yield strength.

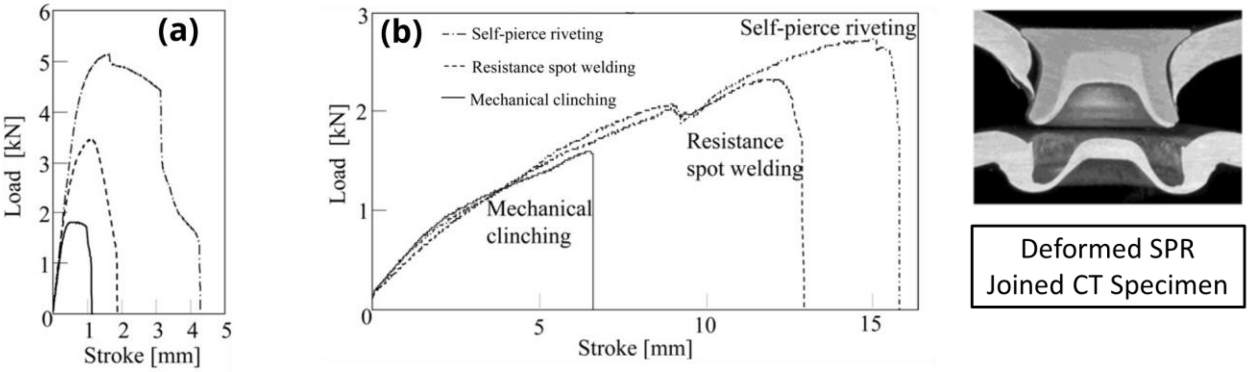

Figure 24: Force-displacement curve from (a) SLJ and (b) CT tests comparing SPR, RSW and clinching. Reproduced with permission from Mori *et al.* (2012)

2.3.2 Finite Element Modeling of SPR Joints

Initial efforts in modeling SPR joints followed some of the traditional approaches used for RSW, and included simple rigid links (Figure 25a), beam elements (Figure 25b), hexahedral (brick) elements (Figure 25c and Figure 25d), and node-to-node, node-to-surface and surface to surface constraints (Figure 25e). However, the joining mechanism of SPR is complex and different from that of RSW, which made most of these methods inapplicable for modeling the physical behaviour of SPR failure (Hoang *et al.*, 2012). For example, Porcaro *et al.* (2004) modelled SPR joints using a node-to-node constraint model and compared the simulation results with the experimental data, but the FE model could not obtain the softening behaviour of SPR rivets post damage initiation. To address this limitation, Porcaro *et al.* (2006b; 2008) considered simulating the SPR joining process and developed a 2D axisymmetric FE model of the riveting/insertion process, then mapped the resulting geometry to generate a 3D numerical model of the formed joint.

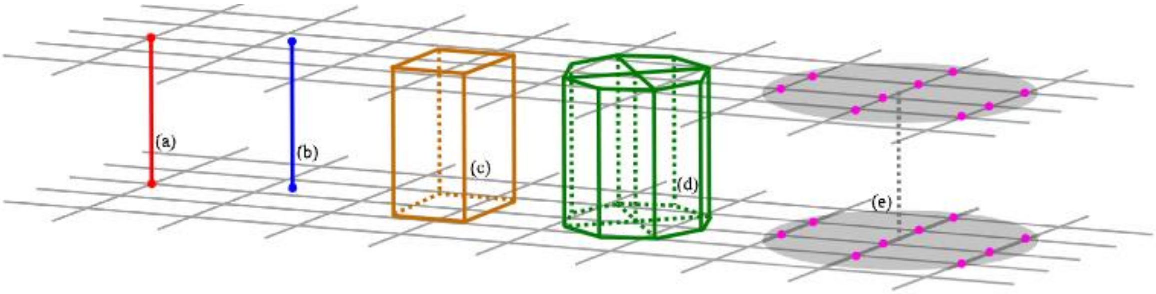

Figure 25: A graphical representation of SPR modeling techniques, demonstrating link elements (a), beam elements (b), hexahedral elements (c), cluster of hexahedral elements (d) and constraint (e). Reproduced with permission from Sønstabø *et al.* (2016)

After that, the meshed 3D model of the SPR joint was augmented into the structure model under investigation to simulate the structural response. Although the results were promising, the method was tedious and is not compatible with large-scale or full vehicle models incorporating shell elements. Hanssen *et al.* (2010) proposed a surface-to-surface constraint model that was specifically developed to mimic the physical behaviour of SPR rivets while taking into account the non-symmetrical deformation between the top and bottom joined sheets. The model was suitable for large-scale models (*e.g.*, full vehicle models) incorporating shell elements and was implemented in a commercial FE package (LS-DYNA). The model dealt with the asymmetric deformation between the top and bottom sheets (master and slave sheets) and included a plastic-like damage algorithm to capture the softening behaviour of rivet failure. The model orthogonally projects the constraint node to the master and slave sheets to be connected and create a group of nodes on each sheet (similar to spider elements) within the specified effective rivet diameter (Figure 26a). Two normal unit vectors ($\hat{n}_s, \hat{n}_m$) are defined for the slave and master sheets (Figure 26b) then assuming that the rivet translation and rotation follow the master sheet, the plane of the maximum opening is determined using the cross multiplication $\hat{n}_o = \hat{n}_s \, x \, \hat{n}_m$, and a tangential unit average vector is defined as $\hat{n}_t = \hat{n}_o \, x \, \hat{n}_m$. The normal and tangential forces (Figure 26e and Figure 26f) were calculated at the plane of maximum opening by lumping the forces at the nodes within the projected domain of influence. Therefore, the model allowed asymmetric deformation between the master and slave sheets, with the SPR rivet axially orthogonal to the master sheet. To find the parameters required for SPR modeling, the authors calibrated and verified the developed model using H-shaped specimens (Figure 26c and Figure 26d) under single and mixed loading configurations. The authors did not propose a characterization approach and suggested that calibration of the model parameters should be done using a trial and error or optimization approach with the help of reverse analysis of the force-displacement curves obtained from the mechanical testing. They suggested running hundreds of simulations to calibrate the following parameters: peak load in tension (f_n^{max}), peak load in shear (f_t^{max}), tangential separation at failure (δ_t^{fail}), normal separation at failure (δ_n^{fail}), fraction of failure displacement at peak load in tension (ξ_n), fraction of failure displacement at peak load in shear (ξ_t), effective rivet diameter (*D*), total stack thickness (*H*), and three dimensionless scaling parameters ($\alpha_1, \alpha_2, \alpha_3$). The model was used in the literature (Bier and Sommer, 2013; Hoang *et al.*, 2012; Sommer and Maier, 2011; Sønstabø *et al.*, 2016), and Hoang *et al.* (2012) validated the model using a T-components component-scale test under two loading cases.

To reduce the amount of experimental testing required to measure the SPR model parameters, Grujicic *et al.* (2014) proposed a three-step virtual characterization procedure to measure the parameters required for the Hanssen *et al.* (2010) constraint model. First, SPR insertion process was simulated, then the resulting joint geometry and material properties were mapped into the 3D FE model of the test specimen. Virtual testing of the test specimen was conducted under different loading cases to obtain the numerical force-displacement curves. Finally, the trial-and-error approach with reverse analysis of the force-displacement curves was carried out to calibrate the required parameters for the constrained SPR model. The proposed approach is reasonable and may reduce the experimental work; however, the accuracy of the SPR insertion/joining simulation remains a critical challenge. Hönsch *et al.* (2020) reported that the SPR forming model required including the strain dependency of SPR rivets, and the thermal effects exhibited by the aluminum sheets. Carandente *et al.* (2016) reported that modeling the SPR joining process using non-thermal FE models failed to capture the thermal softening of the sheet metal, which significantly affected the accuracy of the physical attributes of the numerically formed joint. Another important factor that affected the SPR forming simulation was incorporating strain hardening into the sheet metal material model. The results from the thermo-mechanical FE model demonstrated that neglecting thermal softening and strain hardening resulted in a joint morphology that did not match the experimental results (*e.g.,* the minimum bottom thickness was significantly over-predicted (up to 28%) when thermal effects were neglected). More recently, Hönsch *et al.* (2018) provided possible explanations for the disagreements between the simulations and the SPR joining process. They found that the limitations in SPR process simulation could potentially be attributed to the simplified two-dimensional axisymmetric SPR joint forming model, friction model, and accuracy of material models at high strain rates.

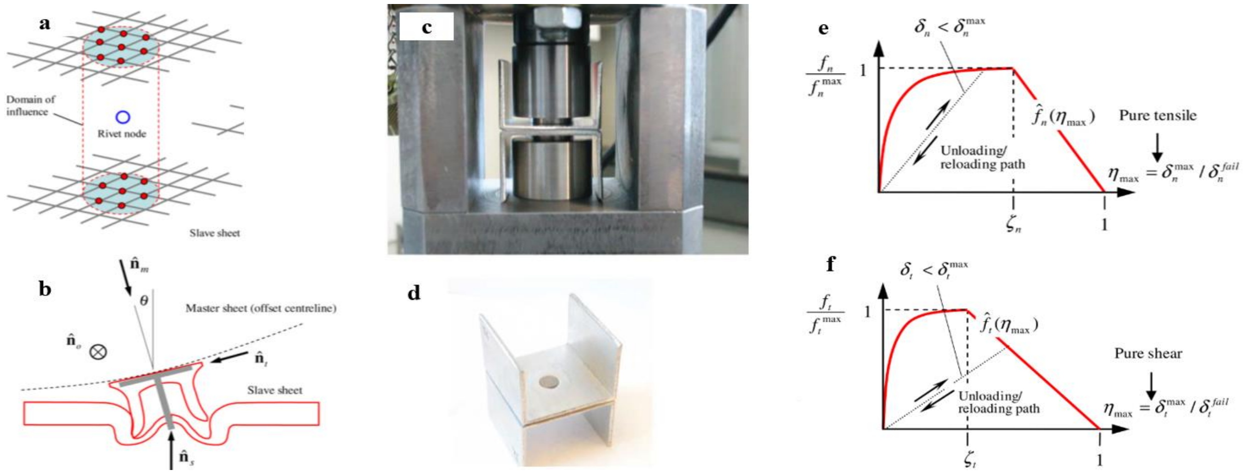

Figure 26: Hanssen *et al.* SPR model development illustrations (a,b), H-specimen verification (c,d), and force-displacement curves for (e) pure tension, and (f) pure shear. Reproduced with permission from Hanssen *et al.* (2010)

Large-scale FE models, such as full-vehicle models, are needed to support and accelerate vehicle development and optimization. An FE model of a medium sedan has more than 3 million elements, and a joint modelling approach with low computational efficiency could hinder or slow down vehicle development (Lanzerath and Pasligh, 2014). To improve the computational efficiency of SPR joint model, Pasligh *et al.* (2017) proposed an approach for modeling SPR joints using CZM. Their approach was verified using experimental results data from H-shaped experimental tests, then implemented in FE models of (a) hat-profile components under axial crush test and (b) full vehicle (fourth-generation Ford Taurus) frontal crash model to assess the applicability of the proposed approach for large FE models. The CZM model was simple and efficient to implement in a full-vehicle FE model. However, the computational time was not compared with other SPR models to quantify the improvement in computational efficiency. Five approaches for FE modeling of flow drilling screws were evaluated and compared, including CZM and Hanssen *et al.* (2010) models (Sønstabø *et al.*, 2016). The authors used 16 cohesive elements to represent the FDS in T-component test and reported that the CZM approach required 4 times the computational time relative to Hanssen *et al.* (2010) model. When the Hanssen *et al.* (2010) model was compared to other constraint-based models, it demonstrated the most appropriate physical behaviour for modeling FDS.

2.3.3 Component-level Response of SPR Joined Structures

SPR-joined structural components are joined using large groups of SPR rivets. A large number of rivets will distribute the loads, making the stress and deformation fields complex and unknown, especially when large plastic deformation and joint rotation are involved. Such complex behaviour may not be captured by a joint made of a single rivet (Sønstabø *et al.*, 2016). Thus, component-level testing of SPR-joined structures is critical to fully understand the mechanical response and structure deformation associated with discrete joining as it explains how the rivets interact and affect load capacity and failure modes. However, component-level testing of SPR-joined structures and discrete-joint FE models are not well documented in the literature. Reil *et al.* (2021) attributed that to two reasons: a) many component-level tests are dominated by the base material rather than the joint itself; b) the availability of many discrete joining technologies (*e.g.*, SPR (Ibrahim and Cronin, 2022), FDS (Sønstabø *et al.*, 2016), RIVTAC (Meschut *et al.*, 2014b)) and a range of materials (*e.g.,* aluminum (Ibrahim and Cronin, 2022), composites (Di Franco *et al.*, 2013), UHSS (Meschut *et al.*, 2014b)), made it difficult to build tests with high accuracy and precision.

Similar to adhesive joining, researchers used axial crush tubes to evaluate the structural behaviour of SPR joints. Lee *et al.* (2006) compared adhesively bonded and SPR joined tubes (Figure 27a), made with dissimilar materials (aluminum to steel) using 350 mm-long tubes which were tested using crushing test equipment having a weight of 215 kg and a velocity of 5.8 m/s. The authors reported three failure modes of SPR joined structures: a) rivet tail pull-out, b) rivet head pull-out, and c) base material failure. The tubes encountered substantial deformation (Figure 27b), and the SPR rivets did not fail progressively as the failure was dominated by the overall structure deformation (Figure 27c). The absorbed energy of SPR tubes was higher than that of similar adhesive tubes, which was attributed to premature adhesive failure due to the adhesive peeling induced by structure deformation.

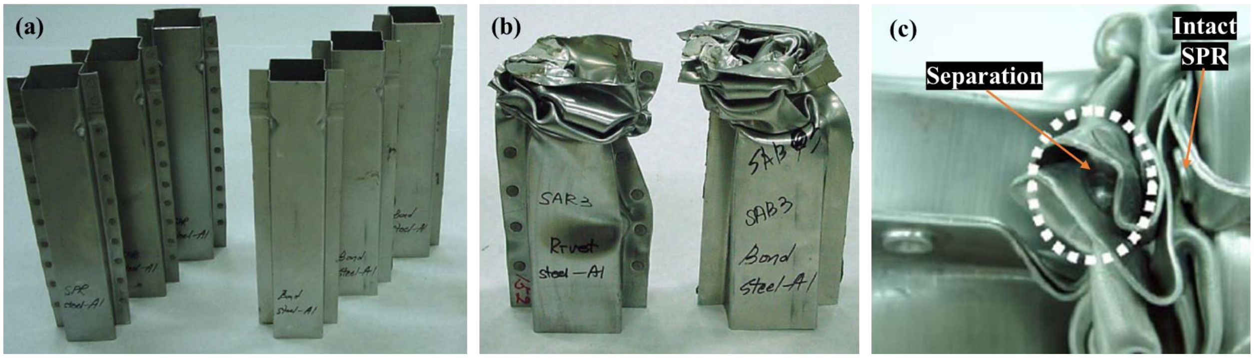

Figure 27: Adhesively bonded and SPR joined double hat crash tubes (a) showing post testing deformation patterns (b) and SPR failure modes (c). Adapted from Lee *et al.* (2006)

Hoang *et al.* (2012) evaluated the structural behaviour of self-piercing riveted joints using T-components made with two extruded aluminum C-channels, and assessed components joined using two rivet configurations (component R6 (6 rivets) and component R12 (12 rivets)) (Figure 28a and Figure 28b). The experimental results were used to validate the SPR FE model developed by (Hanssen *et al.*, 2010). The authors found that the T-component test results agreed well with the FE predicted force-displacement curves and rivet failure for cases with limited deformation (Figure 28c). However, for cases with complex loading conditions and large local deformations, the SPR model was not able to predict the structural behaviour. The reason was not quite understood, but the author explained that it was possibly due to aluminum anisotropy post-yielding.

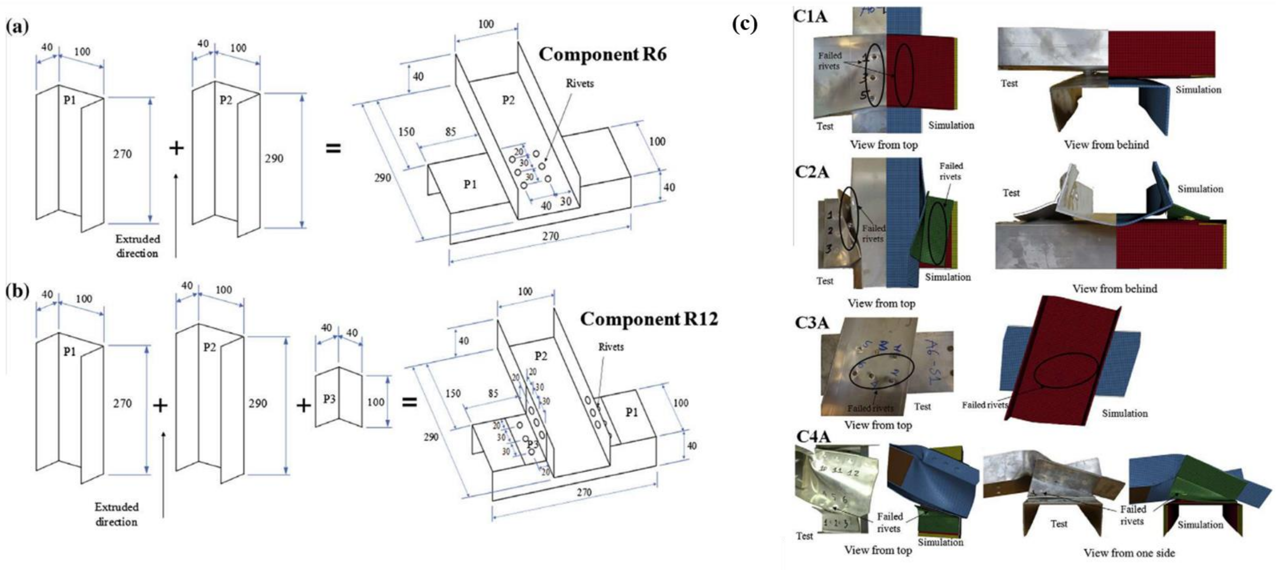

Figure 28: T-components jointed using 6 rivets (a) and 12 rivets (b), comparing the deformations in experimental and computational results (c). Adapted from Hoang *et al.* (2012)

2.4 Hybrid Joining

In hybrid joining, two joining techniques are simultaneously used to join sheet metal. Previous studies investigated various hybrid joining technologies, including SPR-adhesive (also known as riv-bonded) (Di Franco *et al.*, 2013), weld-bonded (Weiland *et al.*, 2019), clinch-bonded (Lei *et al.*, 2018), and fastener-bonded (Sadowski *et al.*, 2011) joints. Motivated by the advantages of adhesives and SPR joining, research on combining adhesives and SPR has found increasing interest in recent years (Di Franco *et al.*, 2012). Researchers argued that exploiting the lightweighting potential of future materials mandates combining adhesive and SPR (Meschut *et al.*, 2014). The hybrid joining enhanced joint strength, stiffness, energy absorption and leak-tightness (joint seal) (Li *et al.*, 2017). However, the work in this space is still limited, and the literature needs additional research on the strength, stiffness, and energy absorption of hybrid joints (Di Franco *et al.*, 2013).

The technique followed when applying hybrid joining is to apply SPR to the joint after mating the adherends during the adhesive work time (uncured adhesive) (Di Franco *et al.*, 2013; Meschut *et al.*, 2014b). Meschut *et al.* (2014b) reported that this technique reduced the bonding area of SLJ test specimens due to adhesive squeeze-out, reducing joint strength relative to adhesive-only joints. However, Di Franco *et al.* (2013) reported that hybrid joining the same application method when applied to composite-aluminum showed hybrid joints with improved strength relative to adhesive-only. Unfortunately, the lack of data about the mechanical response of hybrid joining and the influence of material type and sheet thickness on joint behaviour are key factors to advance our understanding and explain the inconsistent data reported in the literature. Also, the presence of uncured adhesive was reported negatively affect the SPR joint formation. Hahn and Wibbeke (2005) demonstrated that hybrid joining changed the joint morphology and developed joint cracks and faults in the SPR rivet and/or base material. The authors proposed adjusting the process parameters (*i.e.,* clamping force, rivet insertion velocity and rivet hardness) to achieve a sound joint. Their proposed process change was optimized for structures with a total sheet thickness of up to 1.5 mm; however, when substituting steel with aluminum, one of the key requirements is to match the bending stiffness, which demands increasing the aluminum thickness by a factor of about 1.45 (Pinlung, 2015). Thus, a stack thickness below 1.5 mm may not be suitable for automotive industry applications. The effect of hybrid joining on the morphology of joints with varying thicknesses remains an open question.

2.4.1 Finite Element Modeling of Hybrid Joints

There has been little discussion about the FE modeling of hybrid joints in the literature. This is not surprising, considering that the experimental work in this space needs attention, and the testing needed to verify and validate the developed FE models is limited and requires rigorous preparation. Lee *et al.* (2014) used a dual-layer of CZM elements to model hybrid (clinch-bonded) joints under shear and tension loading configurations. They calibrated the traction separation relationship parameters from the force-displacement curves using reverse analysis. The authors used SLJ and H-shaped specimens to calibrate the CZM parameters for clinched joints, while the adhesive CZM parameters were calibrated using SLJ and T-peel. The dual-layer CZM approach was verified, and the simulation results agreed well with the experimental data. The proposed approach could be extended to adhesive-SPR joints; however, calibrating the models to a particular test specimen is a critical limitation that needs to be addressed. El Zaroug *et al.* (2018) modelled bonded/bolted SLJ specimens by using the CZM approach for adhesive and the 3D continuum approach for the bolts. The FE simulations agreed well with the experimental results data; however, implementing this approach to hybrid adhesive-SPR joining would require simulating the SPR joining process to obtain the 3D continuum model. Thus, the model was not compatible with full vehicle models, or models incorporating shell elements. Yao *et al.* (2017) carried out a preliminary study to assess modeling blind rivets augmented with adhesives using a single layer of CZM elements having two different traction separation curves. The CZM parameters for the adhesive and the rivets were calibrated to match the force-displacement curves obtained from experimental results using SLJ and coach peel specimens. However, the models could not capture the softening that took place after the damage initiation phase. Similarly, Weiland *et al.* (2019) used a single layer of CZM elements, with two different traction separation relationships to model a hybrid (bonded-spot welded) H-specimens under shear and tension loading configurations. In their work, experimental data was used to reverse calculate the pseudo stiffness and the critical energy release rate, required for determining the traction-separation relationship. The work concluded that H-specimens were challenging to simulate under tension loading configuration, as discrepancies appeared between the FE and experimental results. They explained that the flexibility of the H-specimens was not captured properly due to the complexity of plastic deformation. However, no data about the stress or strain distribution was provided, leaving an unaddressed question about modeling the H-specimens under a tension loading configuration.

2.4.2 Component-level Response of Hybrid Joined Structures

Gowda *et al.* (2018) compared the response of adhesive, spot weld, and hybrid (weld-bond) joining at the structure scale using a three-point bending test. The joined double hat sections were subjected to lateral impact loading and the peak and mean loads were compared for the three joining methods. Hybrid joined tubes achieved peak and mean loads comparable to the spot-welded tubes, which were 9% and 5% higher than the adhesive tubes, respectively. Also, hybrid joining improved the overall structure response as hybrid joining structures did not encounter a full flange separation or the abrupt failure seen in adhesively joined tubes (Figure 29). A study associated with Ford Motor Company used a 4-point bending test on a single hat section joined with a flat sheet (Lanzerath and Pasligh, 2014) reported that adding adhesives to spot welding improved the energy absorption by 10-20%. The energy absorption improvement was dependent on the spot-weld pitch, material yield strength, part geometry and structure compliance. The study concluded that adhesive application to discrete joining must be evaluated for each case, and thus accurate computational models are required to support structural design.

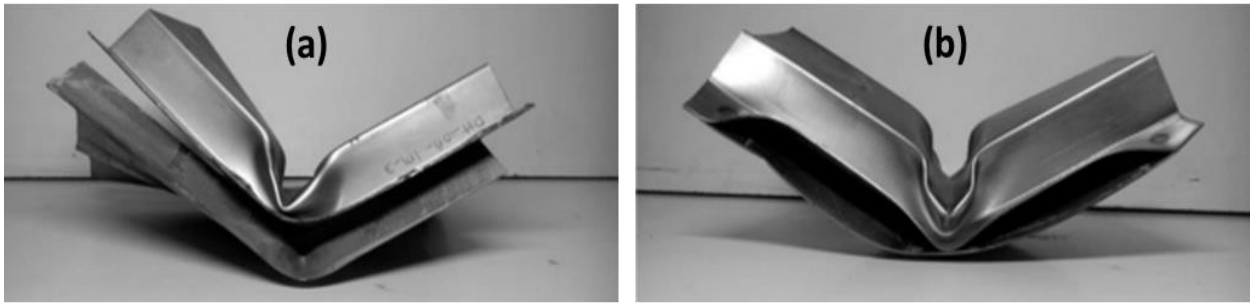

Adhesively Joined Hat Sections **Hybrid Joined Hat Sections**

Figure 29: Adhesive (a) and hybrid joined (b) double hat Sections subjected to lateral impact loading. Adapted from (Gowda *et al.*, 2018)

Reil *et al.* (2021) proposed two component-level structures, comprising double hat sections joined through the hats rather than the flanges, to validate hybrid (adhesive-SPR) joints using 3-point bending setup. The hat sections were made with different materials (aluminum and steel) having similar geometries but different heights for each section to assess the tension (Figure 30a) and shear (Figure 30b) responses of the hybrid joined structures. The results from the tests were used to validate the hybrid joining computational model, and the simulation results showed a good correlation with the force-displacement data (Figure 31a and Figure 31c). An important observation is that the peak load under shear and normal loading was the same (12 kN), which is quite low for a structural adhesive subject to shear loading, especially for such a large bonding area (15 mm x 400 mm). Automotive adhesives under shear loading generally have substantially higher strength than tension loading. For reference, an adhesive SLJ joint often achieves a peak load of more than 15 MPa (~10kN for a bonding area of 25.4 mm x 25.4 mm). Thus, there is a possibility that the shear test exhibited Mode I locally at the regions of crack initiation, which could be observed from the deformed samples as the rivets did not show localized shear deformations (Figure 31b).

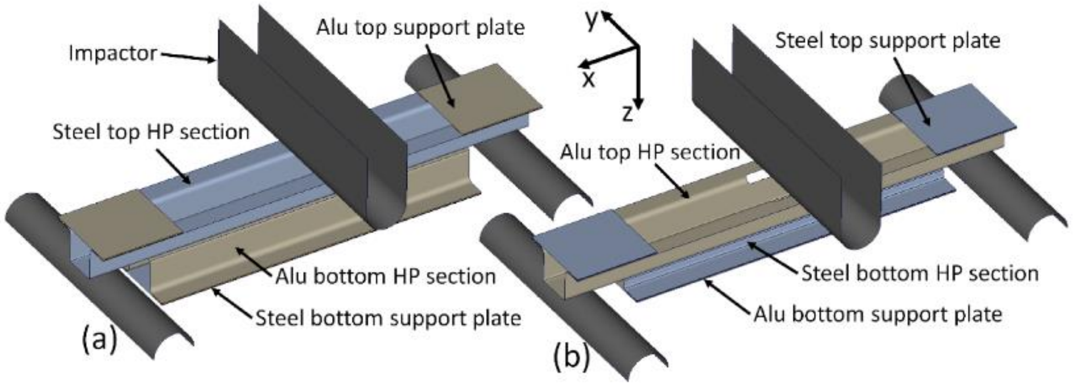

Figure 30: Double hat Sections under 3-point bending to assess tension (a) and shear (b) response of hybrid (adhesive-SPR) at component level. Adapted from Reil *et al.* (2021)

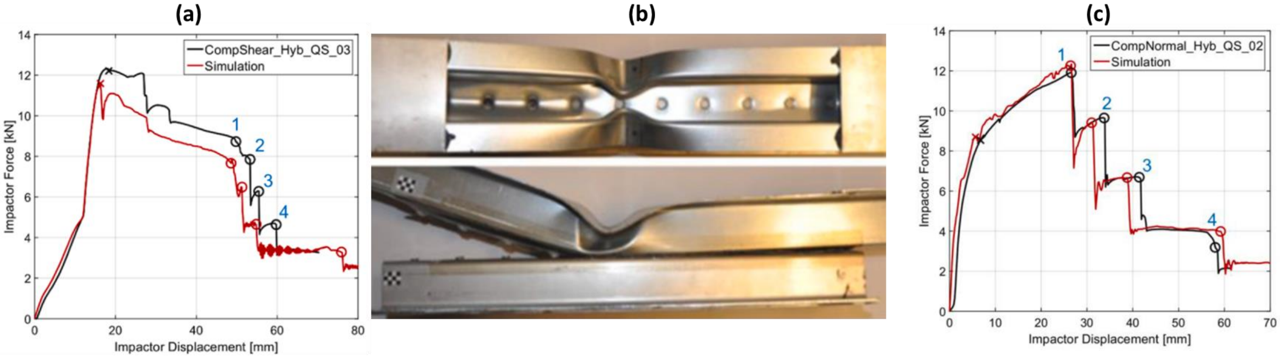

Figure 31: load-displacement response (a) and deformations (b) under shear loading, and load-displacement response under normal loading (c) for the 3-point bending test. Adapted from Reil *et al.* (2021)

2.4.1 Specimen-level Mechanical Response of Hybrid Joints

A study on adhesively bonded, SPR and hybrid joints was carried out by Meschut *et al.* (2014a) comparing the strength of each joining method using single-lap shear and LWF-KS2 (H-shaped specimen) test specimens made with aluminum (AA6016-T6) and press hardened steel. The study reported that adhesive-only SLJ specimens outperformed the SPR and the hybrid ones in terms of strength. They reported that SPR-only joints exhibited a 43% lower strength under tension loading compared to shear loading. However, this study did not consider evaluating the adhesive joints under tension loading or the energy absorption of any joining method. Meschut *et al.* (2014b) used SLJ specimens to compare the shear strength of aluminum-press hardened steel joints created using SPR, adhesive bonding, and hybrid joining. The authors reported that adhesive joints exhibited 19.5 kN; while SPR and hybrid joints had a peak load of 5.41 kN and 16.86 kN, respectively. The reduction in hybrid joining strength relative to adhesive-only joints was attributed to the adhesive. Di Franco *et al.* (2013) investigated the influence of SPR rivet spacing on the response of hybrid joined SLJ specimens made with aluminum and carbon fibre composites. The authors concluded that the rivet spacing did not influence the SLJ joint strength; However, the SLJ failure was reported to adherend failure in the composite panel, indicating that the joint strength was dominated by the adherend material as opposed to the joining method. The study would have been more interesting if it had avoided joint overdesigning. Di Franco *et al.* (2013b) compared the strength, energy absorption and stiffness of adhesive, SPR, and hybrid joints using multi-material SLJ joints made with aluminum (2024-T6) and carbon fibre composite. The hybrid joining exhibited the highest joint strength (~5 kN), compared to adhesive joints (~4.5 kN) and SPR joints (~3.5 kN). However, the failure mechanism of adhesive and hybrid joints was reported to be adhesion (interfacial) failure, indicating that the response was dominated by the interfacial strength (adhesive/parent material interface) rather than adhesive joint strength. Similar to the previous studies on adhesive and SPR joints, Li and Fatemi (2006) highlighted that sheet thickness had a direct correlation with the static strength of hybrid joints. However, the peak load reported using a coach peel specimen made with (3+3) mm aluminum stack was 1.4 kN, indicating that the adhesive used was not intended for structural applications, and the SPR rivet used was an early model.

So far, no previous study has investigated the mechanical performance of aluminum-aluminum hybrid joints under tension loading. Also, very limited work considered aluminum adhesively bonded joints under the same loading configuration, and that work used the CT test specimen, which was reported to prematurely fail due to compromised bending stiffness (Weiland *et al.*, 2019).

2.5 Summary

Adhesive bonding and SPR joining are expected to be widely adopted joining technologies in the automotive industry and are critical for the adoption of high-performance lightweight materials. Combining adhesives and SPR is expected to overcome the limitations of individual joining technologies, such as low adhesive strength in tension loading and SPR non-uniform load distribution. However, advanced characterization, mechanical response data and modeling techniques for individual and hybrid joints are key requirements to enable the design and optimization of future automotive structures (*e.g.*, BiW).

The mechanical response of adhesive and SPR joints is dependent on adherend thickness and material strength. The SLJ response showed strong co-dependence on adherend yield strength and sheet thickness. In adhesive joints with low yield strength adherend, increasing the sheet thickness reduced the amount of adherend plastic deformation. In contrast, increasing sheet thickness for adherends with higher yield strength increased the bending moment and led to a reduction in joint strength. However, the effect of sheet thickness and adherend strength were not assessed under tension loading, which requires using a low compliance test specimen to avoid adhesive joint strength reduction due to bending deformation at the adhesive boundaries. Similar to adhesive joints, SPR joints exhibited increased joint strength with increasing sheet thickness; however, the effect of adherend strength on the mechanical response of the joint was not systematically assessed. Material strength and ductility can influence the formation of the SPR joint and change the physical attributes (*e.g.*, mechanical interlock and bottom thickness); thus, the relationship between the material strength and joint morphology needs to be understood first.

In the current literature, there is a lack of experimental data on the mechanical behaviour of hybrid joining, and the data available is inconsistent in terms of the mechanical response relative to adhesive joints. Also, the influence of key joint design parameters, such as sheet thickness, material strength, and joint morphology, on the mechanical behaviour of hybrid joints has not been investigated. Therefore, there is a compelling need to advance our understanding of the mechanical behaviour of hybrid joints and explain the conflicting data in the literature regarding the strength of hybrid joints relative to adhesive-only joints.

Most researchers have calibrated the adhesive CZM parameters using experimental test results; however, the ability to directly integrate material-level properties of adhesives into FE models of different tests is currently somewhat limited. Similar to adhesive joints, instead of using experimentally measured SPR parameters to drive the FE model behaviour of SPR joints, numerous experiments and hundreds of simulations are needed to calibrate the SPR parameters using a trial-and-error approach. Thus, it is challenging and time-consuming to characterize the individual joining methods, and more importantly, it is impossible to extend the adhesive and SPR FE models to large-scale structures. Finally, the limitations associated with the FE modeling of adhesive and SPR joints need to be addressed to allow the development of a hybrid joining model.

The RDCB and BSS tests accurately characterized the traction-separation relationship under Mode I and Mode II loading, reducing the number of tests required to characterize adhesives.

However, the characterization data were not systematically verified at the coupon level under different modes of loading or validated using a structure scale test, which are key requirements for adhesive model implementation at full car scale. Also, the development of a methodology to measure the SPR parameters from the coupon-level joint tests represent a gap in the literature. Additionally, a robust validation procedure is important to ensure that the FE models can predict the complex joint behaviour with mixed modes of loading, commonly seen in automotive structures, enabling further analysis and optimization of vehicle components. The validation tests widely adopted in the literature showed substantial parent metal deformation, which often masked the influence of the joining method. Also, the joints did not often exhibit stable crack extension, making it challenging to measure validation metrics that assess the global (overall structure response) and local (joint-structure response) behaviours of the structure. Therefore, there is a need to identify a component-scale test and systematically validate the FE models of the individual and hybrid joining, allowing assessment and optimization of full car structures.

Chapter 3: Experimental Design and Methodology

3.1 Materials

3.1.1 Aluminum Sheet Metal (Adherend)

The work presented in this thesis used two cold-rolled aluminum alloys (AA6061-T6 and AA5052-H32), in sheet metal form. The AA6061 alloy, widely used in work related to the assessment of aluminum joining methods and weight reduction applications (Arnold and Altenhof, 2005; El-Batahgy and Kutsuna, 2009; Nguyen *et al.*, 2011; Prillhofer *et al.*, 2014), has been considered because it offered mechanical properties relatively similar (*i.e.*, yield strength, ultimate tensile strength, and elongation) to the automotive alloys in service. Another important factor is that the AA6061-T6 alloy is thermally stable and does not exhibit age hardening when subjected to additional heat treatment, making it suitable to undergo the adhesive curing process while retaining the original mechanical properties. According to Braun (2005), additional heat treatment of AA-6061-T6 at 120^{o}C for 1000 hours did not affect the tensile or microstructure of the alloy. The AA5052-H32 alloy, widely used in vehicle weight reduction related studies (Ufferman *et al.*, 2018; Wong, 1984), has been selected as a second alloy to assess the effect of alloy yield strength because it offered 42% lower yield strength compared to the AA6061-T6 alloy. To assess the influence of sheet metal thickness, three thicknesses (1 mm, 2 mm, and 3 mm), commonly used in automotive structures and panels, were considered for each alloy. Considering aluminum alloys with substantial yield strength difference and a variety of sheet thicknesses allowed to characterize and understand the mechanical response of joining methods with varying degrees of adherend deformation.

To determine the tensile properties and stress-strain relationships of the base sheet materials, the aluminum alloys (AA6061-T6 and AA5052-H32) were experimentally characterized for the three sheet thicknesses (1, 2, 3 mm) considered in this work. Tensile specimens were prepared and tested according to ASTM E8/E8M standard. The specimen geometry had a width of 12.5 mm (0.5 in) and a gauge length of 50 mm (2 in) and were extracted from sheet blanks using a water jet cutter with the rolling direction oriented along the length of the specimen, and then sanded using a 600 grit sandpaper. The specimens were cleaned with acetone and the average width and thickness were calculated from micrometre measurements (three measurements along the gauge length to calculate the average width and average thickness) (Table 5).

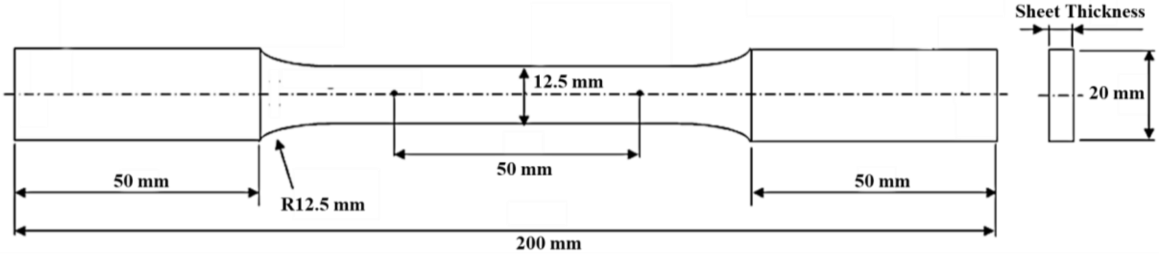

Figure 32: Aluminum base material (adherend) tensile specimen geometry.(ASTM E8/E8M, 2016)

Each tensile specimen was painted with a white base coat and then randomly speckled using a flat black spray paint for digital image correlation measurements. The specimens were tested using a servo-hydraulic tensile frame (Criterion Model 45, MTS) with proportional grips (hydraulic wedge grips) and a 100 kN load cell (Figure 33). The tests were conducted at room temperature using a cross-head displacement of 0.1 mm / s (strain rate of 0.002 s^{-1}). Displacement and surface strains were measured for all tests using a stereo DIC system, comprising two 2.0 MP cameras (Grasshopper GRAS-50S5M-C, Point Grey Research Inc.) fitted with 85 mm f/1.4 manual focus lenses (BOWER, USA). The cameras captured 5 images per second with a resolution of 16 pixels/mm using commercial DIC software (VIC SNAP 2009, Correlated Solutions, USA). The displacements and strains were analyzed and computed using commercial three-dimensional DIC analysis software (VIC-3D 7, Correlated Solutions, USA). The DIC post-processing used a subset size of 15, a step size of 1, and a strain filter of 7, which resulted in a virtual strain gauge length of 1.3 mm (21 pixels). The load data was acquired by the DIC system through an auxiliary cable to ensure that the load and DIC imaging are synchronized.

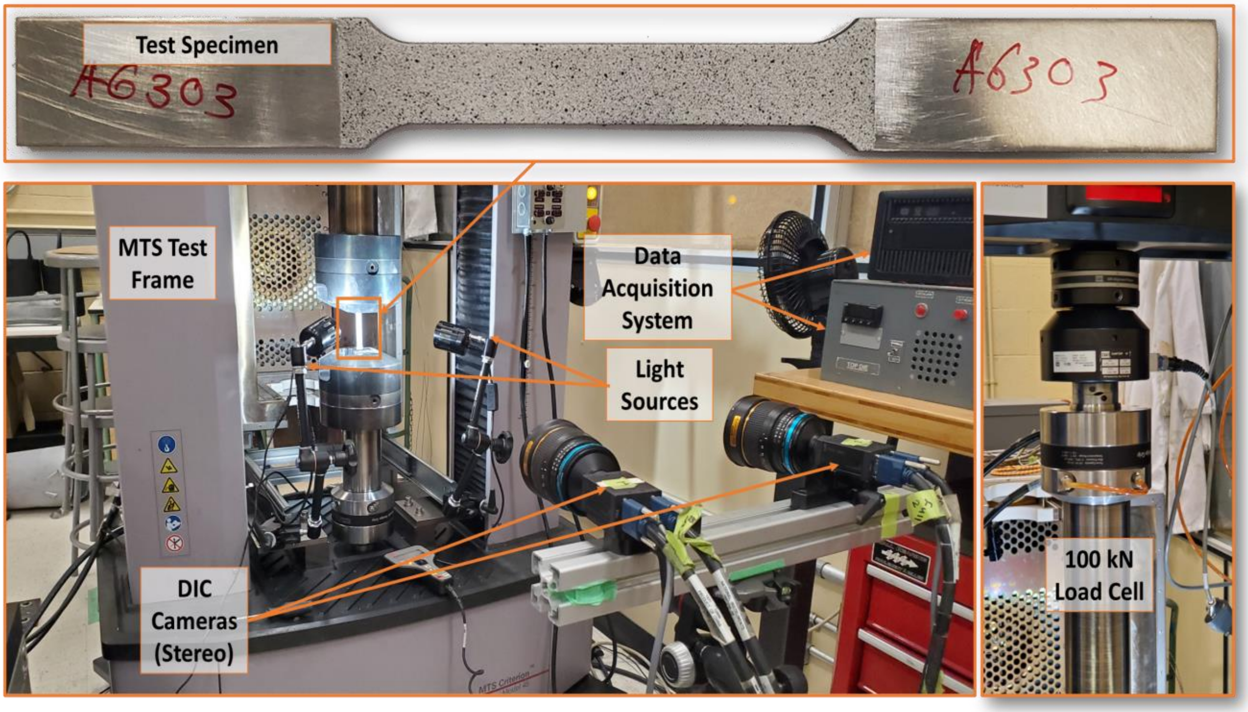

Figure 33: Aluminum base material characterization experimental setup (ASTM E8/E8M, 2016)

The engineering stress ($\sigma_{\text{engineering}}$) was calculated from the load data and average width and thickness measurements (Table 5), and the engineering strain ($\varepsilon_{\text{engineering}}$) was extracted from the DIC analysis software. The DIC system measured the full field strain and deformation values using the surface measurements, and then a virtual extensometer (virtual gauge length = nominal gauge length = 50 mm) was used to report the longitudinal engineering strains. The true stress (σ_{true}) and true strain ($\varepsilon_{\text{true}}$) were calculated from the engineering values using the following equations:

$$\sigma_{\text{true}} = \sigma_{\text{engineering}} \left(1 + \varepsilon_{\text{engineering}}\right) \qquad \text{Equation 5}$$

$$\varepsilon_{\text{true}} = \ln\left(1 + \varepsilon_{\text{engineering}}\right) \qquad \text{Equation 6}$$

And in the hardening region, the logarithmic (effective) plastic strain ($\varepsilon_{\text{effective}}^{\text{plastic}}$) required for the computational modeling was calculated as follows:

$$\varepsilon_{\text{effective}}^{\text{plastic}} = \varepsilon_{\text{true}}^{\text{total}} - \frac{\sigma_{\text{flow stress}}}{\text{Elastic Modulus}} \qquad \text{Equation 7}$$

Prior to using the material characterization data in the computational models, the data were fitted to a simplified Johnson-Cook model (power law curve excluding temperature and strain rate effects) using a MATLAB script (Available in Appendix A) to ensure that the tangent stiffness was positive through all the data points and discard the experimental data points post the ultimate tensile strength (UTS).

Table 5: Average gauge width and sheet thickness for the AA6061 alloy with three sheet thicknesses (average calculated from three measurements along the gauge length)

	1 mm		**2 mm**		**3 mm**	
	Gauge Width (mm)	Sheet Thickness (mm)	Gauge Width (mm)	Sheet Thickness (mm)	Gauge Width (mm)	Sheet Thickness (mm)
Specimen #1	12.23 ± 0.02	0.94 ± 0.01	12.51 ± 0.12	1.96 ± 0.01	11.93 ± 0.02	3.16 ± 0.01
Specimen #2	12.22 ± 0.02	0.94 ± 0.01	12.50 ± 0.01	1.96 ± 0.01	12.03 ± 0.07	3.16 ± 0.01
Specimen #3	12.23 ± 0.01	0.93 ± 0.01	12.51 ± 0.01	1.95 ± 0.01	12.26 ± 0.06	3.15 ± 0.01

3.1.1 Structural Adhesive

The adhesive used throughout this research is a two-part structural toughened epoxy adhesive (Impact Resistant Structural Adhesive (IRSA) 07333, 3M™, Figure 34a) specially formulated for automotive applications and used by major automotive manufacturers, such as Honda, General Motors, Jaguar/Land Rover, and Tesla in structural repair (3M, 2016). This adhesive (Figure 34b) is toughened using synthetic rubber and aluminum particles and aluminum flakes, confirmed under the opto-digital microscope (Figure 34c), to improve the impact response of bonded structures and provide tailored impact characteristics (3M, 2022). The nominal bond line thickness used throughout the study was 0.3 mm, which was within the range reported in automotive applications (0.2 to 0.4 mm) (Lanzerath and Pasligh, 2014), and was the same as the thickness used in a recent study on the same adhesive (Watson *et al.*, 2020). The mechanical properties of this adhesive were characterized using material-level tests for the bond line thickness used in this work, and the CZM traction separation relationships were measured (summarized in section 2.2.5.1). More details on the adhesive material-level characterization methods and analysis have been presented in the literature (Watson *et al.*, 2020, 2018). Readers should note that this study did not deal with environmental factors (*e.g.*, temperature) or strain rate effects, but the methods presented in this section will be used to address these aspects in future work.

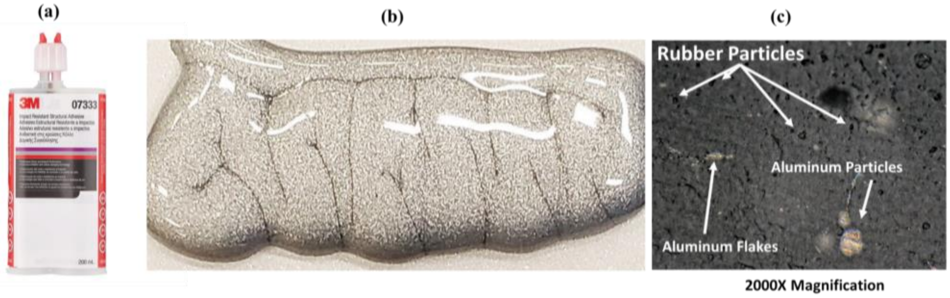

Figure 34: (a) 3M™ Impact Resistant Structural Adhesive (IRSA) 07333, (b) uncured adhesive and (c) rubber and aluminum content in the adhesive composition.

3.1.2 Self Piercing Rivets (SPR)

The SPR setting tool, rivets and dies were procured from Henrob Corp. (Atlas Copco, USA), which is a major SPR equipment supplier for automotive manufacturers. A handheld SPR rivet setting tool (Rivlite MK V, Henrob, Atlas Copco, USA) (Figure 35a), widely used in automotive repair and prototyping applications, has been selected to create the SPR joints in a lab environment. When the trigger is pulled, the hydraulic system drives the blank holder to clamp the sheets to be joined, and then the rivet insertion tool drives the rivet (Figure 35b) loaded through the 'rivet feed' (Figure 35a, rivet feed). The rivet pierces the top sheet, then flares into the bottom sheet while deforming the stack to occupy the die (Figure 35c) volume and forming the joint mechanical interlock (Figure 35d). Finally, the hydraulic system releases the rivet insertion tool when the load reaches the pre-selected insertion force (up to 50 kN). Three models of zinc-coated semi-tubular steel rivets (Figure 35b) with a diameter of 5 mm, and two models of dies with a domed pip (DP) profile (Figure 35c) were used to accommodate the varying sheet thicknesses. The following rivet/die/insertion force combinations have been used for each stack (Table 6).

Table 6: A summary of the rivets, dies and setting forces used for each joint configuration created in this study.

Stack Thickness (mm)	Material	Rivet	Die	Setting Force (kN)
1 + 1	Aluminum AA6061-T6 or AA5052-H32	C50541A	DP09-200	32
2 + 2		C50642A	DP09-200	40
3 + 3		K50844A	DP10-200	50

The rivet/die combination was identified according to manufacturer recommendations, and the insertion force was identified based on morphology assessment (Figure 35d), with initial values selected to achieve a head height closer to zero. The rivets, dies and insertion forces were used consistently to create the SPR and hybrid joints.

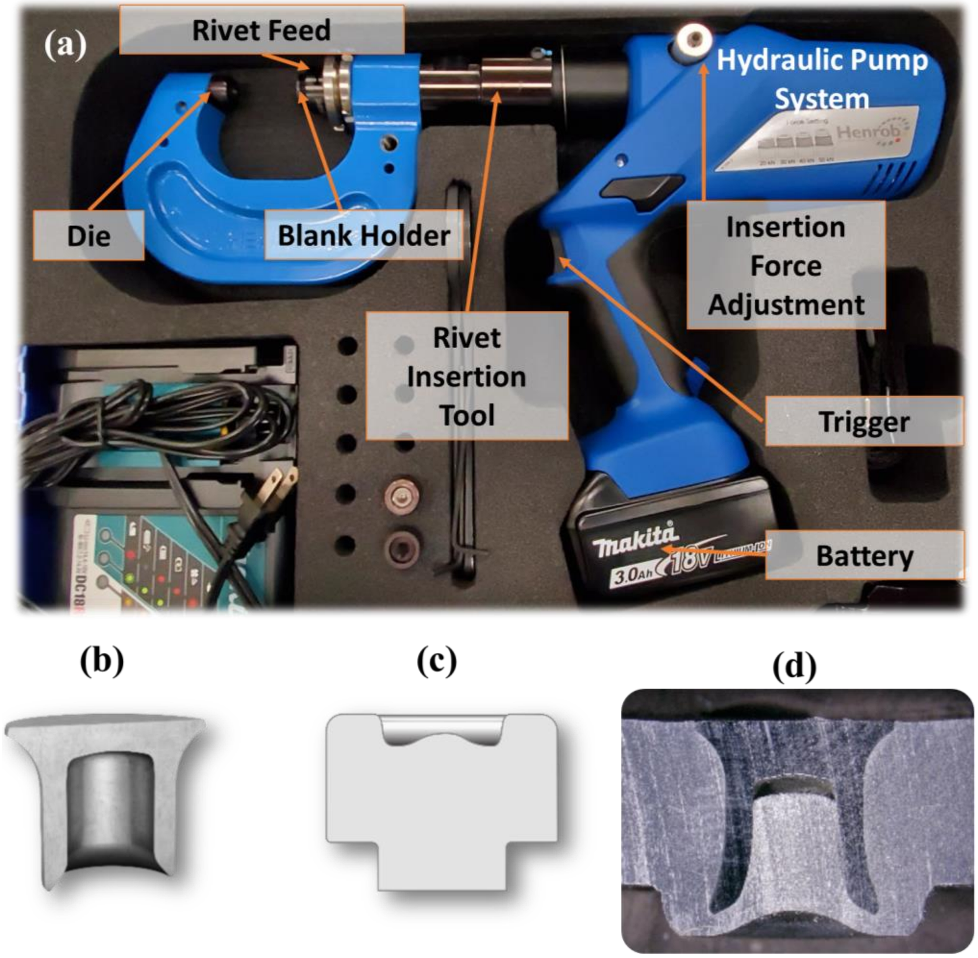

Figure 35: (a) Rivlite MK V Setting tool, (b) standard semi-tubular rivet, (d) a domed pip (DP) profile die and (d) SPR joint morphology showing a cross-section view of the formed joint.

3.2 Surface Preparation of Aluminum Sheet Metal

Identifying an adequate surface preparation technique that maximized aluminum joint strength for the particular adhesive used in this study was crucial to avoid premature joint failure due to interfacial debonding, which would compromise the comparison between the adhesive, SPR and hybrid joints. Six contemporary, lab-applicable surface treatments were assessed based on SLJ joint strength and failure surface. The surface treatments were selected for their potential in production and repair applications and covered a broad range of surface roughness (R_a) values. To fabricate the SLJ specimens, aluminum AA6061-T6 sheet metal blanks were cut using a shear cutter to the dimensions per ASTM D1002-10 (2019) (Figure 36). The aluminum SLJ adherends were degreased and decontaminated using acetone and a lint-free cloth. The adherends that were degreased and decontaminated but did not receive additional surface treatments were designated SD (solvent degreased). The SD adherends were subjected to six surface treatments, as follows:

- Abrading (SDA) - Surface abrading was conducted using Scotch-Brite nylon mesh cushioned sanding pads (7447, 3M™, USA, Figure 37a) in a cross pattern, and then dust was removed by repeating the degreasing and decontamination process. To ensure that the abrading process was consistent, the surface roughness arithmetic mean (Ra) was measured after each treatment.
- Grit blasting (SDGB) - Grit blasting was carried out in a cross-pattern using 80 grit aluminum oxide media at 65 psi, followed by degreasing and decontamination. Alumina impingement was avoided during the grit-blasting process by using a low grit blasting angle, low blasting pressure and relatively higher grit particle size. Grit blasting at a lower angle (30-40 degrees) promoted material removal by micro-cutting, as opposed to indentation. In contrast, grit blasting at angles close to 90 degrees was reported to result in material indentation, alumina impingement, and grit media getting embedded in the substrate (Poorna Chander *et al.*, 2009).
- Re-greasing (SDDR) - This process was carried out by applying an oil-based metal preservative, to mimic the process used in the automotive industry for corrosion protection and to assess the sensitivity of the adhesive used in this work to surface contamination. The adherends were dipped into a metal preservative (FERROCOTE ® 6130, Quaker, USA), widely used in the automotive industry, then left to drip until a thin uniform coat was achieved. The weight of the adherends was measured before and after the application to ensure that a consistent amount of surface coating was deposited into each adherend.

- Sol-gel (SDSG) - This process was carried out by applying a high-performance two-part sol-gel surface treatment (AC-130, 3M, USA, Figure 37b), widely used in the aviation industry (Fink *et al.*, 2010). The sol-gel was mixed for 30 minutes as per the manufacturer's recommendations. After that, adherends were dipped in the mixture for 2 minutes 30 seconds, then allowed to air-dry for 60 minutes prior to adhesive application. The sol-gel technology used a silica-based sol to deposit a hybrid inorganic/organic film with silicon, oxygen, and zirconium micro-nano structure on the aluminum substrate, modifying the surface chemistry of the aluminum substrate for better adhesion.
- Abrading followed by sol-gel (SDASG) – In this treatment, the abrading and sol-gel treatments were combined to assess if the removal of the weak hydroxylated oxides and the higher surface roughness improved the efficacy of the sol-gel treatment. Thus, the SDA preparation process was applied to the adherends, and then followed by SDSG process using the same methodologies explained above.
- Self-etching primer (SDSEP) – This process was carried out by applying three coats of a self-etching primer (39673, SEM, USA, Figure 37c) to the adherends with a flash time (the time between coats) of 7 minutes and a topcoat time (the time prior to applying the final (third) coat) of 4 hours. The applied primer was designed to provide excellent adhesion when applied to bare aluminum, so it was applied directly after solvent degreasing.

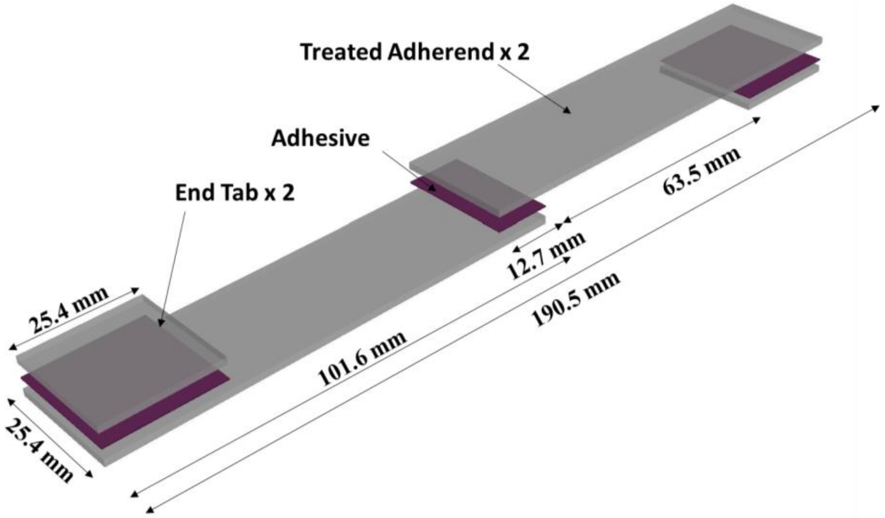

Figure 36: The SLJ geometry used to assess the adhesive joint strength of the treated adherends.

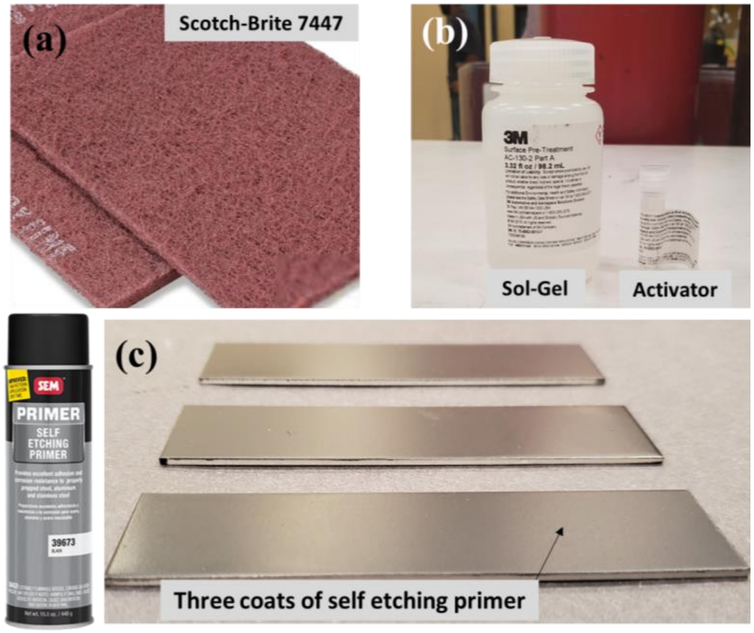

Figure 37: (a) SDA treatment using Scotch-Brite 7447, (b) SDSG treatment using Sol-gel with activator, (c) SDSEP treatment using self-etching primer.

3.2.1 SLJ Preparation, Testing and Surface Roughness Measurement

Five SLJ specimens for each surface treatment were bonded using a custom-made curing fixture to maintain a consistent bonding area of (12.7 ± 0.5) x (25.4 ± 0.25) mm^2. Teflon spacers were applied to the adherends to obtain a bond line thickness of 0.3 mm and to minimize the effect of spew adhesive (Figure 38a). Next, a continuous bead of adhesive was applied (Figure 38a), and then the top adherends were mated ensuring excess adhesive flowed through all the bond area boundaries (Figure 38b). Adhesive excess was found to reduce the likelihood of introducing porosity (air pockets) during the mating and curing processes. Finally, the top and bottom adherends were fixtured, and a uniform pressure was applied to the bonding area (Figure 38c). The specimens were cured in a convection oven 30 minutes after reaching a surface temperature of 80 ºC, and the fixture clamping was removed after a minimum of 4 hours (Figure 38d). Additionally, the dimensions necessary to ensure that the adhesively bonded SLJ specimens were consistent, such as joint overlap length and the bond line thickness were measured (Figure 39) using an opto-digital microscope (VHX-5000, Keyence Canada).

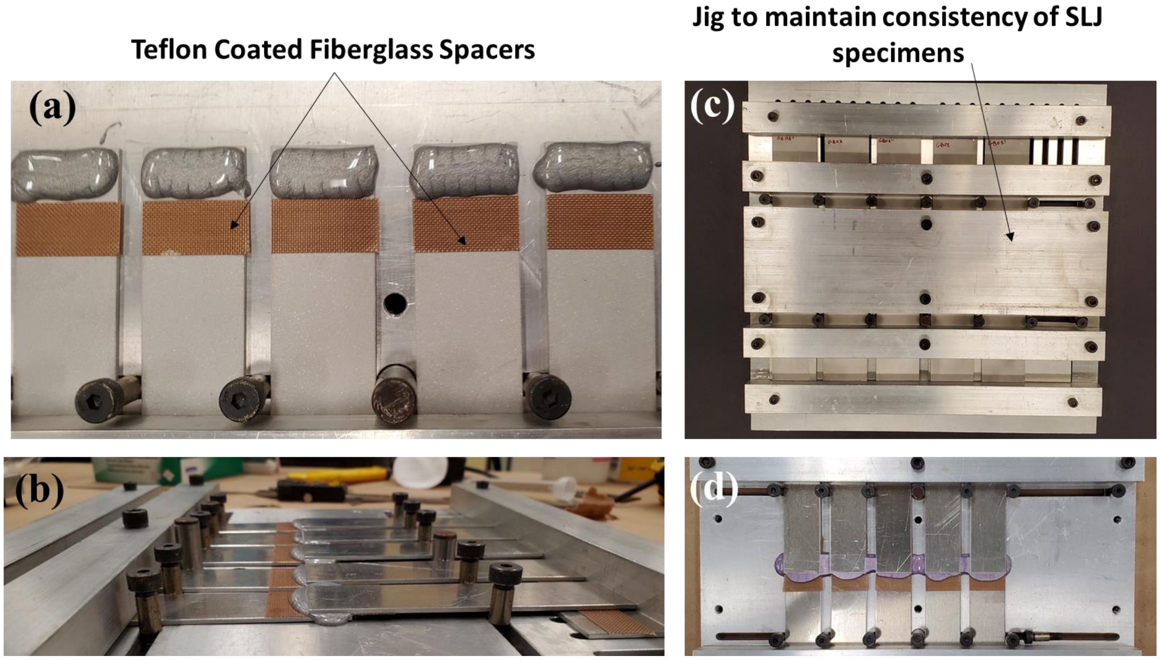

Figure 38: (a) SLJ adherends with adhesive beads and Teflon-coated fiberglass spacers applied, (b) Adherends mating with excess adhesive at the boundaries, (c) SLJ specimens assembled in the fixture, and (d) SLJ specimens after curing.

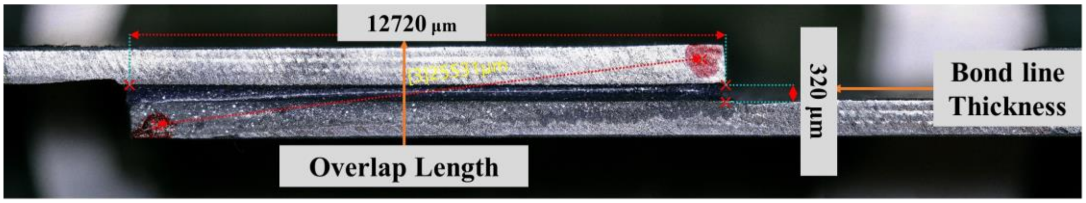

Figure 39: (a) SLJ overlap length and bond line thickness measurements.

The test matrix summarizing the SLJ testing is illustrated in Figure 40. Each set of SLJ specimens were tested on a custom-made hydraulic test frame controlled using an MTS controller (MTS 407, MTS, USA). A 100 kN load cell measured the load data while the cylinder displacement was measured using a linear variable differential transformer (LVDT) (Figure 41a). The data acquisition was carried out using a computer system having National Instruments USB-6211 data acquisition modules and LabVIEW 7.1 software (National Instruments, USA). The test was conducted at a constant crosshead speed of 0.1 mm/s (6 mm/min), and each test was recorded using a digital single-lens reflex (DSLR) camera (D3200, Nikon, Japan), fitted with a macro lens (105 mm f2.8, Sigma, Japan) to improve the pixel density and allow tracking the local behaviour of the adhesive joint. LED lighting panels with adjustable intensity were utilized to improve the lighting and reduce the light reflection of the aluminum adherends. SLJ joint rotation was measured by the change in the angle of the overlap, which was tracked using open-source software (Tracker, Open Physics Project). The change in the angle of an imaginary line connecting the two corners of the free ends was calculated. More details on the methods used to measure joint rotation were laid out in section 3.5. Immediately after testing, the failure surfaces of the adhesive joints were inspected, and images were captured for further visual analysis (Figure 41b).

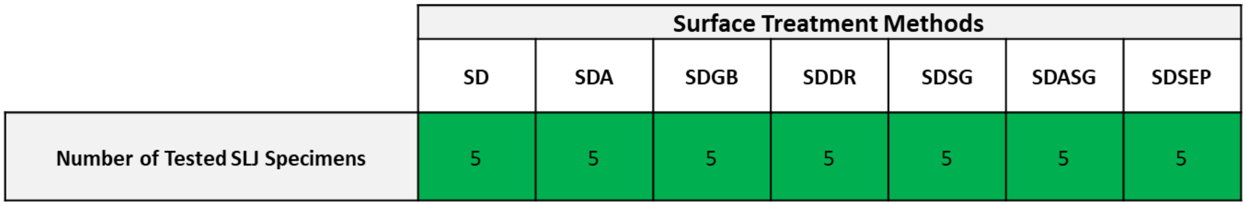

	Surface Treatment Methods						
	SD	SDA	SDGB	SDDR	SDSG	SDASG	SDSEP
Number of Tested SLJ Specimens	5	5	5	5	5	5	5

Figure 40: The test matrix summarizing the SLJ testing for surface treatment assessment.

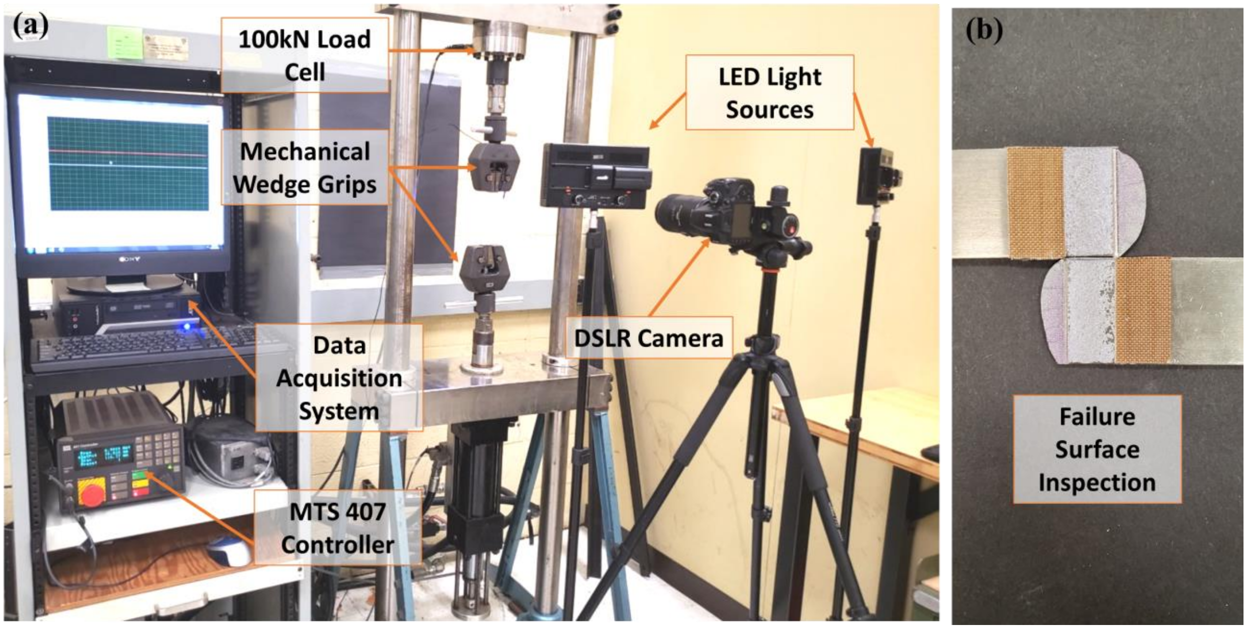

Figure 41: (a) The test setup for SLJ testing, and (b) the failure surface inspection and imaging post testing.

The surface roughness of treated specimens was measured using a profilometer (Surtronic 25, Taylor Hobson, UK). The mean arthimetic roughness (Ra) was used to evaluate the surface roughness of the specimens with a resolution of 0.01 μm. Measurements were performed using a cut-off length of 0.4 mm, an evaluation length of 8.0 mm and a measurement range of 100 μm. The cut-off length was selected according to ISO 4288-1996 for Ra values ranging from 0.1 to 2 μm.

3.2.2 Assessment of Wetting Behaviour and Surface Energy using Contact Angle Measurements

Surface treatments influence the wetting behaviour of the as-received aluminum substrate and consequently influence the intrinsic adhesion, which is required to achieve a high-quality bond and cohesive failure within the adhesive layer. To further understand the surface characteristics, the wetting behaviours of solvent-degreased (SD), grit-blasted (SDGB), and sol-gel (SDSG) treated aluminum substrates were evaluated using contact angle measurements. A customized apparatus with a built-in camera (Basler scA 1000-30 fm) was used to measure the static contact angle. A liquid droplet, the so-called sessile drop, was formed at the end of the syringe, and then the syringe was moved carefully to deposit the droplet on the aluminum surface. The images were taken 3 s after the deposition of the droplet at room temperature (20 °C) using a custom-built LabView software application. Then, the images were processed using an open-source software for processing and analyzing scientific images (ImageJ v.153, National Institutes of Health, USA) utilizing the 'Contact Angle' plug-in (developed by Marco Brugnar) to measure and report the contact angle based on 3 repeats (Figure 42). The droplet profile was manually input by selecting points along the edge of the drop, and the plug-in automatically fitted a circle and an ellipse to the cross-section of the sessile drop, drawing a line across the baseline of the drop connecting the left and right tri-phase points. The measured angle provided by the circle and ellipse approximations were comparable (±2°), which was expected because the volume of the droplet was small (3-5 microlitres).

When the deposited droplet reaches equilibrium, the interface molecular forces are balanced, and the equilibrium energy state is given by Young relation (Adams *et al.*, 1988):

$$\gamma_{solid} = \gamma_{solid-liquid} + \gamma_{liquid} \cdot \cos\theta \qquad \text{Equation 8}$$

Where θ is the contact angle measured, and γ represents the surface energy for solid-vapour (solid), solid-liquid and liquid-vapour (liquid) interfaces. Surface energy is a key parameter to characterize how the solid interact with other materials (*e.g.*, adhesives), which shed light on the adhesion and interface properties. The calculated surface energy generally depends on the model used, and in this study the commonly accepted Fowkes model was used, combining Young and Young-Dupree equations to calculate the dispersive and polar components of the surface energy (Kozbial *et al.*, 2014), as follows:

$$\frac{\gamma_{liquid}(\cos\,\theta+1)}{2} = (\gamma^{\mathrm{d}}_{liquid})^{1/2}(\gamma^{\mathrm{d}}_{\mathrm{solid}})^{1/2} + (\gamma^{\mathrm{p}}_{liquid})^{1/2}(\gamma^{\mathrm{p}}_{\mathrm{solid}})^{1/2} \qquad \text{Equation 9}$$

Where $\gamma^{\mathrm{d}}_{liquid}$ and $\gamma^{\mathrm{p}}_{liquid}$ are the liquid dispersive and polar components, respectively and $\gamma^{\mathrm{d}}_{\mathrm{solid}}$ and $\gamma^{\mathrm{p}}_{\mathrm{solid}}$ are the solid dispersive and polar components respectively, and thus finding $\gamma^{\mathrm{d}}_{\mathrm{solid}}$ and $\gamma^{\mathrm{p}}_{\mathrm{solid}}$ will allow us to calculate the total surface energy of the substrate using the following Fowkes theory assumption:

$$\gamma_{solid} = \gamma^{\mathrm{d}}_{\mathrm{solid}} + \gamma^{\mathrm{p}}_{\mathrm{solid}} \qquad \text{Equation 10}$$

First, a non-polar liquid (*i.e.*, diiodomethane, $\gamma^{\mathrm{p}}_{liquid} = 0$) was tested (Table 7), and the dispersive component of the surface energy was calculated from Equation 9, as follows:

$$(\gamma^{\mathrm{d}}_{\mathrm{solid}})^{1/2} = \frac{\gamma_{diiodomethane}(\cos\,\theta+1)}{2((\gamma^{\mathrm{d}}_{diiodomethane})^{\frac{1}{2}})} \qquad \text{Equation 11}$$

Second, a polar liquid (*e.g.*, de-ionized water) was tested (Table 7), and using Equation 9 while knowing $\gamma^{\mathrm{d}}_{\mathrm{solid}}$ the polar component of the surface energy ($\gamma^{\mathrm{p}}_{\mathrm{solid}}$) was calculated.

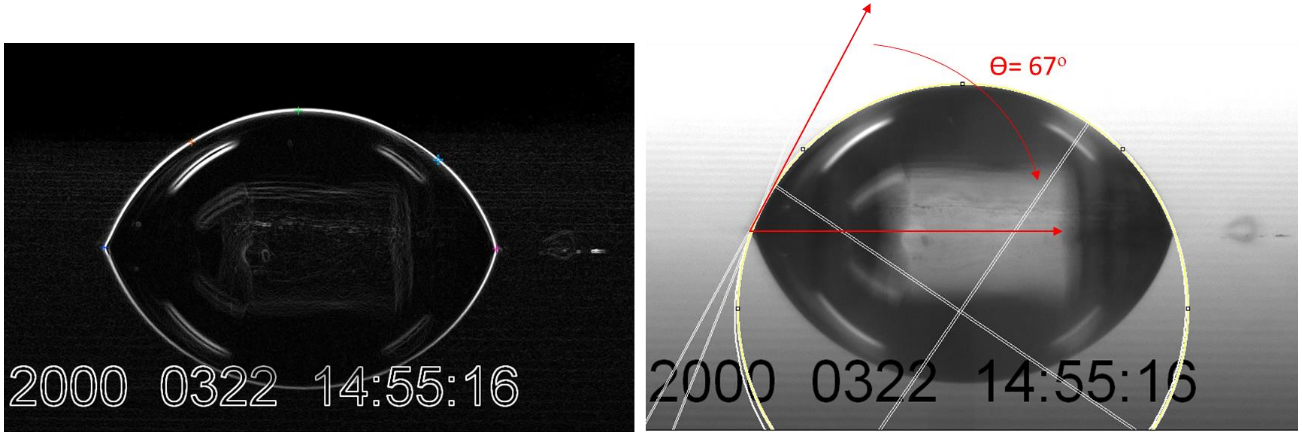

Figure 42: Contact angle measurement of a DI water droplet on a solvent-degreased aluminum substrate.

Table 7: Polar and dispersive surface energy components of the contact angle measurement liquids (Kozbial *et al.*, 2014)

	γ (mJ/m^2)	γ^p (mJ/m^2)	γ^d (mJ/m^2)
De-Ionized Water	72.8	51.0	21.8
Diiodomethane	50.8	0.0	50.8

3.3 Quantification of Joint Morphology and Physical Attributes

To assess the morphology of the joints, the physical attributes (*i.e.*, bond line thickness, mechanical interlock (rivet flaring), head height, bottom thickness) of the adhesive-only, SPR-only and hybrid joints were quantified. The bond line thickness of adhesive and hybrid joints was measured directly from the SLJ joints and H-specimens. The details on the manufacturing and preparation of the SLJ and H-specimens were presented in section 3.4 (H-specimen) and section 3.5 (SLJ). Measuring the rivet flaring, head height and bottom thickness, required sectioning the joints to reveal the physical attributes. Therefore, representative SPR and hybrid joints made from flat sheets were created. Twelve sets of joints, having three repeats each, were prepared from the two aluminum alloys (AA6061-T6 and AA5052-H32) with varying sheet metal thickness (1 mm, 2mm, and 3mm). Sheet metal was sheared into 28 x 40 mm flat substrates to create symmetrical stacks (1+1) mm, (2+2) mm, and (3+3) mm (Figure 43). Six sets (*i.e.*, two aluminum alloys with three sheet thicknesses each) were prepared using hybrid joining, and six sets were created using SPR-only joining. Next, the specimens were sectioned with a high precision, water-cooled cutter (ACCUTOM-50, Struers, USA) to maintain the integrity of the cross-section and retain the physical attributes. The physical attributes were measured using an opto-digital microscope (VHX-5000, Keyence Canada) under 20X magnification (Figure 44). Currently, there is no industry standard to guide the quality of SPR joints; however, the physical attributes required to create sound joints have been discussed in the literature (Haque, 2018; Li *et al.*, 2017). These guidelines were adopted in the industry to establish a reference force-displacement curve for the SPR rivet insertion parameters that achieved the required physical attributes. Then, the reference force-displacement curve could be used to monitor the joint consistency in an industrial environment (high volume), by comparing the production line process curve to the reference curve (Haque *et al.*, 2017; Haque and Durandet, 2017; Li *et al.*, 2017).

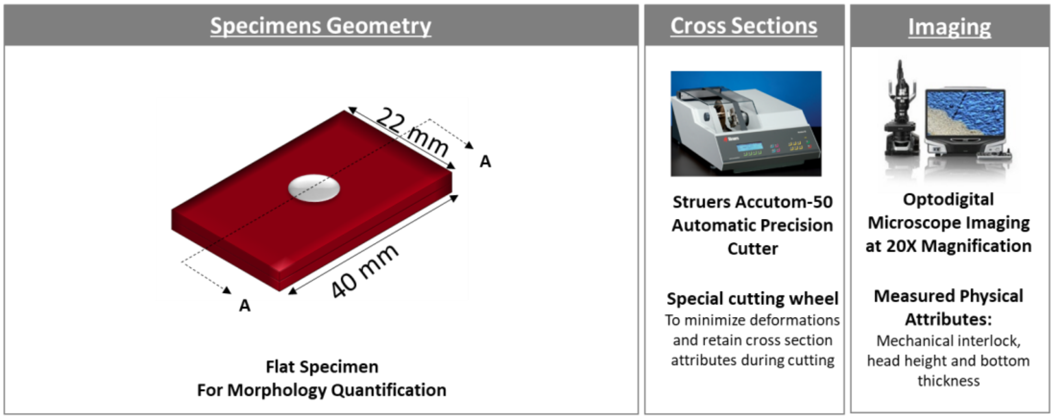

Number of Specimens		Morphology Flat Specimens		
		1 mm	2 mm	3 mm
SPR Joined	AA6061 Alloy	3	3	3
	AA5052 Alloy	3	3	3
Hybrid Joined	AA6061 Alloy	3	3	3
	AA5052 Alloy	3	3	3

Figure 43: Opto-digital microscope images showing bond line thickness measurements (left) and formed joint physical attributes (right).

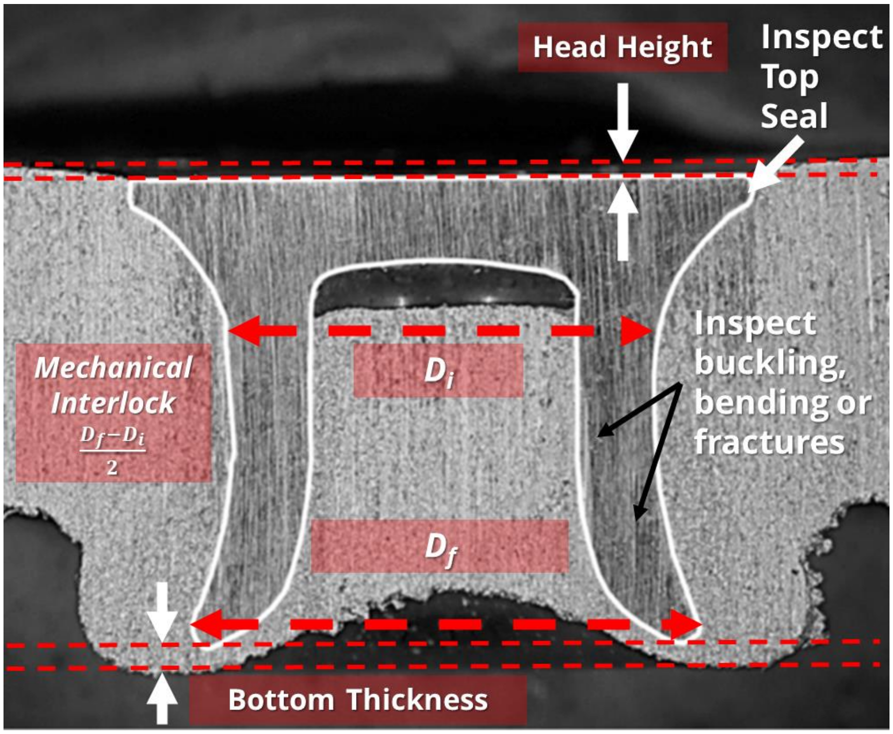

Figure 44: A typical cross-section of SPR and hybrid joints showing the physical attributes measurements using the opto-digital microscope.

3.4 H-Specimen Manufacturing, Preparation, and Testing

The H-specimen geometry, comprising two U-sections, was used to assess the mechanical performance of adhesive, SPR, and hybrid joints under tension loading. The test specimen geometry, similar to KS2, was re-designed with increased width to allow SPR application, and a larger bend radius to allow bending for the range of aluminum sheet thicknesses considered in this work (Figure 45). In order to fabricate the U-sections required for joining the H-specimens, sheet metal blanks were cut using a water jet cutter to the required dimensions (Figure 46a), then, bent into the final geometry (Figure 46b) using a compact hydraulic press brake. The U-sections were grit-blasted in a cross-pattern using 80 grit aluminum oxide media at 65 psi followed by acetone degreasing and air-drying (surface treatment identified based on the surface treatment study conducted in this work) (Figure 46c).

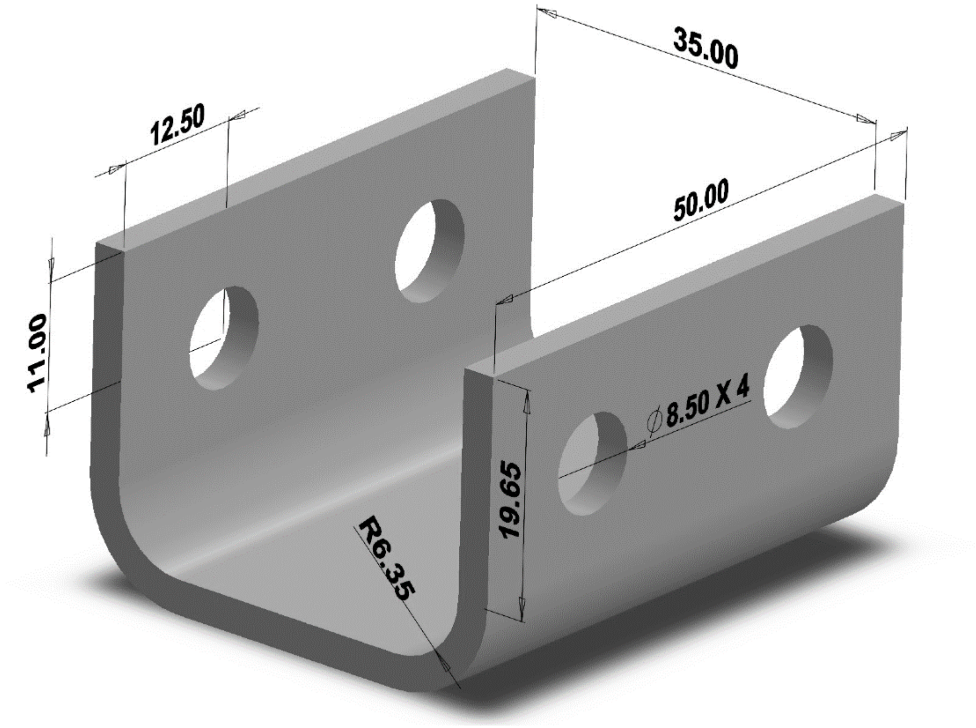

Figure 45: U-section geometry with dimensions in millimetres (mm).

Teflon spacers were applied at the adhesive boundaries to maintain a nominal bond line thickness of 0.3 mm, facilitate the removal of adhesive spew, and minimize edge effects (Figure 46d). To ensure contaminant-free adherends, the bonding area was cleaned with acetone immediately prior to bonding. A thick, continuous bead of adhesive was applied to the bonding area (18.5 ± 0.5) x (50 ± 0.5) mm^2 to match the standard width of flanges seen in transportation structures (Figure 46e); after that, the U-sections were mated and fixtured (Figure 46f). The adhesive curing was carried out in a convection oven (ED-53, Binder, Tuttlingen, Germany) for 30 min after the specimen reached 80^o Celsius (Figure 47a). The average weights of the 1, 2 and

3 mm adhesively bonded specimens were measured as 21.45 ± 0.03 grams, 42.26 ± 0.14 grams, and 68.40 ± 0.57 grams, respectively.

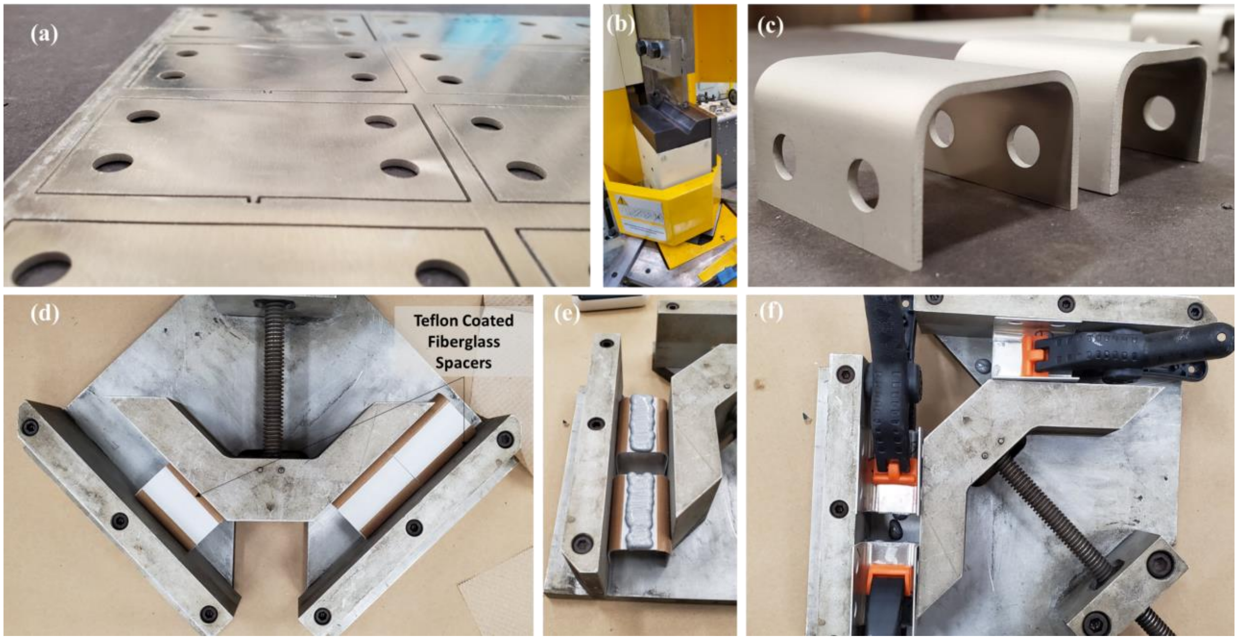

Figure 46: The H-Specimen manufacturing and preparation processes included waterjet cutting (a), sheet metal bending (b), grit blasting (c), and adhesive application and adherend mating (d-f).

SPR joining required precisely locating the SPR rivet at the center of the joining area. This was achieved using a 3D-printed template to position the SPR rivet within +/- 0.5 mm of the required location (Figure 47b). To create the SPR joints, the SPR setting tool (Rivlite MK V; Henrob, Atlas Copco, USA) was used with 5 mm zinc-coated semi-tubular steel rivets and domed pip dies (Henrob, Atlas Copco, USA). The SPR setting forces for the 1+1, 2+2 and 3+3 mm were 32 kN, 40 kN and 50 kN, respectively. The weights of the 1, 2 and 3 mm specimens were -3.0%, -0.6% and -0.4% relative to the adhesive joints with similar sheet thickness, highlighting that the final adhesive and SPR test specimens were comparable in terms of weight (Figure 47c).

Adhesive and SPR joining were used together to join the U-sections, creating hybrid joints. First, the specimens were joined using the adhesive bonding process discussed earlier in this section and then, the SPR rivet was applied to the uncured adhesive joint (Meschut *et al.*, 2014b; Ufferman *et al.*, 2018). The SPR rivet, die and setting force for each joint thickness were identical in both SPR and hybrid joints, and the hybrid joined specimens were cured using the same method for adhesive joints. The weights of the 1-, 2- and 3-mm hybrid joined specimens were +4.5%, +1.6% and +1.0% relative to the adhesive joints with similar sheet thickness, indicating that the weight gain with hybrid joining was less than 5%.

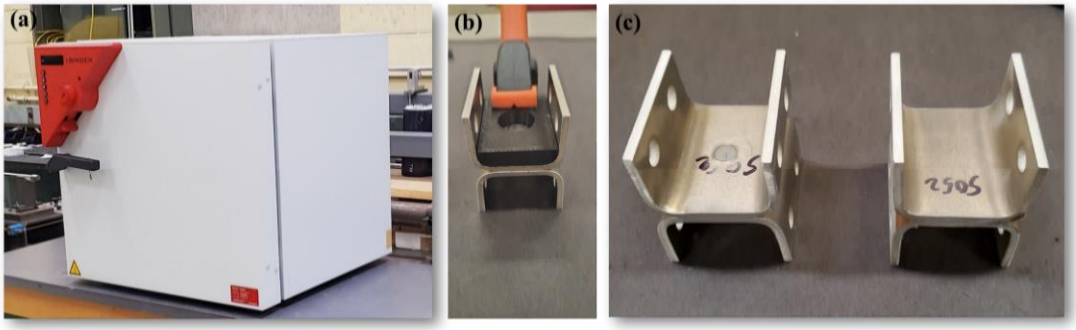

Figure 47: Adhesively joined specimens were cured in the oven (a), SPR joined specimens used a 3D printed template (b) and the final H-specimens were consistent (c).

Adhesively bonded, SPR and hybrid joined H-specimens (Figure 48) were tested using a hydraulic load frame having a 4” bore x 6” stroke cylinder (Cylinders and Actuators; Parker Canada) controlled using a commercial controller (MTS 407; MTS USA). Fifty-four (54) quasi-static tests (18 test sets with 3 repeats each, Figure 49) were conducted at room temperature using a constant crosshead velocity of 6 mm/min with displacement control and feedback from a linear variable differential transformer (LVDT). The load data was measured using a 90kN load cell (Transducer Techniques SWP 20 k; California, USA). A high-resolution digital single-lens reflex (DSLR) camera (D3200, Nikon Japan) fitted with a 105 mm f2.8 macro lens was used to record each test and optically track the localized separation of the H-specimens. The load data was acquired using a National Instruments Daqpad-6015 DAC system and LabVIEW software, and specimen displacement was measured from the imaging data using open-source software (Tracker Video Analysis and Modeling Tool, Open-Source Physics (OSP) project). The joint performance was assessed using peak load, joint stiffness (slope of the loading curve), and energy absorption (area under the force-displacement curve).

Figure 48: Experimental setup for H-specimen test, showing a hybrid joined H-shaped test specimen (left), the testing frame (middle), and a close up view of a mounted test specimen (right).

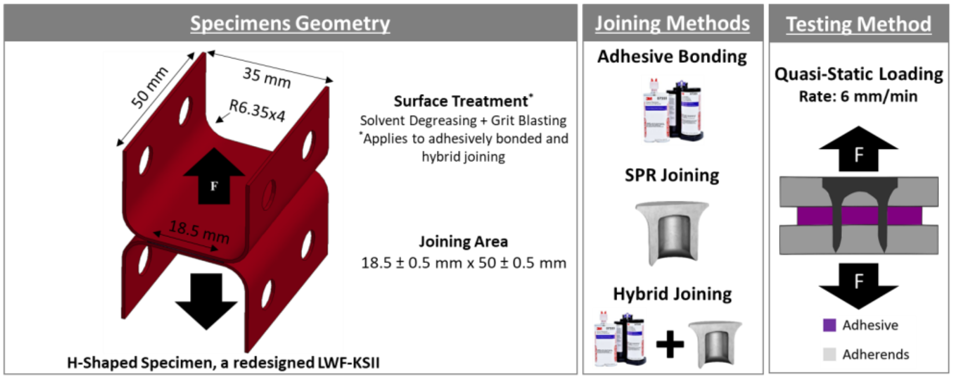

Joining Method	Adherend Type	Number of H-specimens Tested		
		1 mm	2 mm	3 mm
Adhesively Bonded	AA6061 Alloy	3	3	3
	AA5052 Alloy	3	3	3
SPR Joined	AA6061 Alloy	3	3	3
	AA5052 Alloy	3	3	3
Hybrid Joined	AA6061 Alloy	3	3	3
	AA5052 Alloy	3	3	3

Figure 49: Test matrix of the H-specimen testing applied to adhesive, SPR and hybrid joints (54 tests in total).

3.5 Single Lap Shear (SLJ) Specimen Manufacturing, Preparation and Testing

The single lap shear tests were carried out using a test specimen similar to the ASTM D1002 standard. The SLJ specimen geometry was redesigned to have 40 mm wide and 108 mm long adherends (Figure 50), while keeping the free length the same as the one in the ASTM D1002 (63.5 mm) (Karachalios *et al.*, 2013b, 2013a). The specimen width was increased from 25.4 mm to 40 mm to represent an SPR rivet spacing of 40 mm and ensure that the bond area was sufficient to observe adhesive morphology (*e.g.,* adhesive squeeze-out) variations in hybrid joints. Similar to the H-specimen, the adherend materials were 6061 and 5052 aluminum alloy sheets considering thicknesses of 1 mm, 2 mm, and 3 mm. The aluminum adherends were sheared from sheet blanks, then degreased using acetone and wiped using a lint-free cloth. The SLJ joints were created in symmetrical configuration (1 + 1 mm, 2 + 2 mm, and 3 + 3 mm), and joined using three joining methods (adhesive, SPR and hybrid joining).

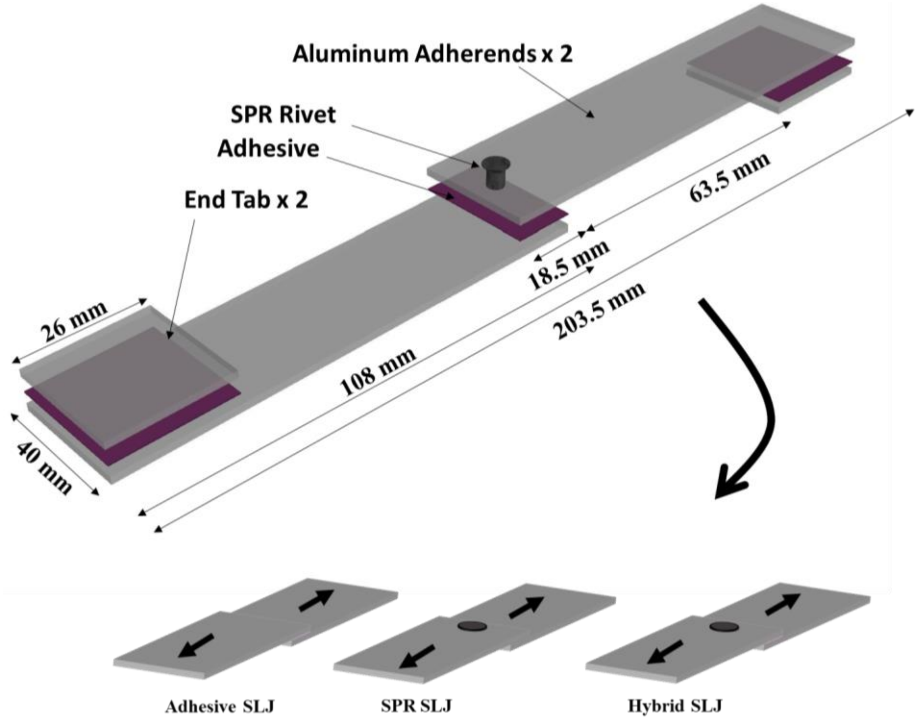

Figure 50: SLJ specimen geometry with end tabs to reduce load eccentricity.

The adhesively joined SLJ adherends were grit-blasted in a cross-pattern using 80 grit aluminum oxide media at 65 psi followed by acetone degreasing and air-drying (the same process followed for the H-specimen). The adhesive layer length was maintained at 18.5 mm, using a custom-made precisely ground curing fixture (Figure 51a), and two Teflon-coated fibreglass spacers were applied at the adhesive boundaries to facilitate the removal of adhesive spew and minimize edge effects (Figure 51b). Karachalios *et al.* (2013b) showed that having an adhesive layer length below 20 mm resulted in a joint response that was not substantially influenced by the adherend properties (*i.e.*, adherend yielding), emphasizing the response of the joining method. To ensure contaminant-free adherends, the bonding area was cleaned with acetone immediately prior to bonding. A continuous bead of adhesive was applied to the bonding area (18.5 ± 0.5 mm x 40 ± 0.5 mm), and the bead size was identified to ensure proper coverage and avoid the formation of voids (Figure 51b). After the adhesive application, the top adherends were mated, and then the curing fixture was assembled in a way that applied a uniform clamping pressure to the bonding area. The assembled curing fixture was put in a convection oven (ED-53, Binder, Tuttlingen, Germany) to cure the adhesive SLJ specimens for 30 min after the specimen reached 80^{o} Celsius (90 minutes in total). After that, the excess adhesive was removed using a sharp blade and a file, and square tabs (40 mm x 25 mm) were glued to the clamping areas of each test specimen to improve alignment and avoid load eccentricity. Bond line thickness measurements were carried out on the side of the SLJ specimens using an opto-digital microscope (VHX-5000, Keyence, Japan) to ensure the consistency of bond line thickness, which could substantially influence the mechanical response of adhesive joints. The measured bond line thickness of the SLJ specimens had an average of 0.516 ± 0.011 mm. The bond line length was controlled prior to adhesive application and the average bond line length was measured at 12.60 ± 0.10 mm. The average weights of the 1, 2 and 3 mm adhesively bonded specimens were measured as 24.10 ± 0.07 grams, 45.77 ± 0.17 grams, and 73.89 ± 0.37 grams, respectively.

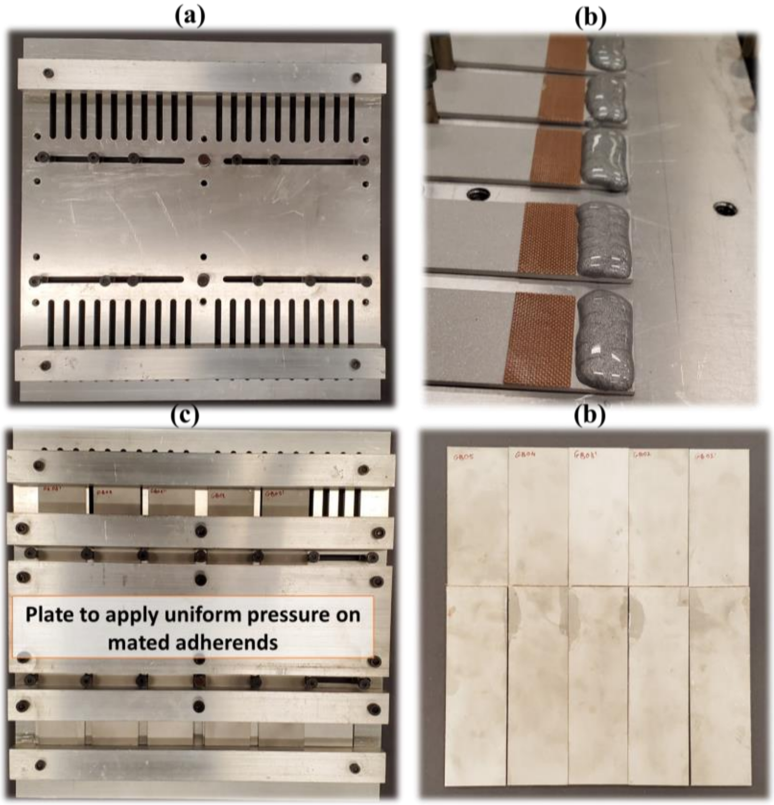

Figure 51: (a) SLJ sample preparation jig, (b) Teflon-coated spacer and adhesive application, (c) assembled jig, and (d) SLJ specimens prior to adding end tabs.

The SPR SLJ joints were created using the same methods used to create the H-specimens. The handheld SPR setting tool (Rivlite MK V, Henrob, USA) was used with 5 mm zinc-coated semi-tubular steel rivets and domed pip dies. The insertion force for the 1-, 2- and 3-mm joints was ~32 kN, 40 kN and 50 kN, respectively. The insertion force was identified to ensure sound joints with a morphology that met the standard guidelines published in the literature. To ensure that the SPR rivet was located precisely at the center of the SLJ overlap, three fixtures were designed and created using 3D printing to accommodate the difference in adherend thickness (one fixture for each adherend thickness, Figure 52a). The weights of the 1, 2 and 3 mm SPR specimens were +0.55%, +0.92% and +0.62% relative to the adhesive joints with similar sheet thickness, highlighting that the final adhesive and SPR test specimens were comparable in terms of weight (similar to the H-specimens). To create the hybrid joined SLJ, the adherends were prepared using the same methods used for the adhesive-only joints, and then the SPR rivets were applied to uncured adhesive following the methods discussed earlier for the SPR-only joints (Figure 52b). The SPR insertion process induced some deflection in the adherends, depending on the sheet thickness, which was more pronounced near the boundaries of the joining area. The bond line thickness of the adhesive was measured along the side of the SLJ side edge to check the bond line thickness along the bond area (Figure 52c-d). The 1 mm joints showed a substantial increase in bond line thickness at the adhesive free ends, attributed to the substantial deflection in 1 mm aluminum substrates (Figure 52c). The weights of the 1-, 2- and 3-mm hybrid joined specimens were +2.4%, +0.8% and +0.89% relative to the adhesive joints with similar sheet thickness, indicating that the weight gain with hybrid joining was less than 3%.

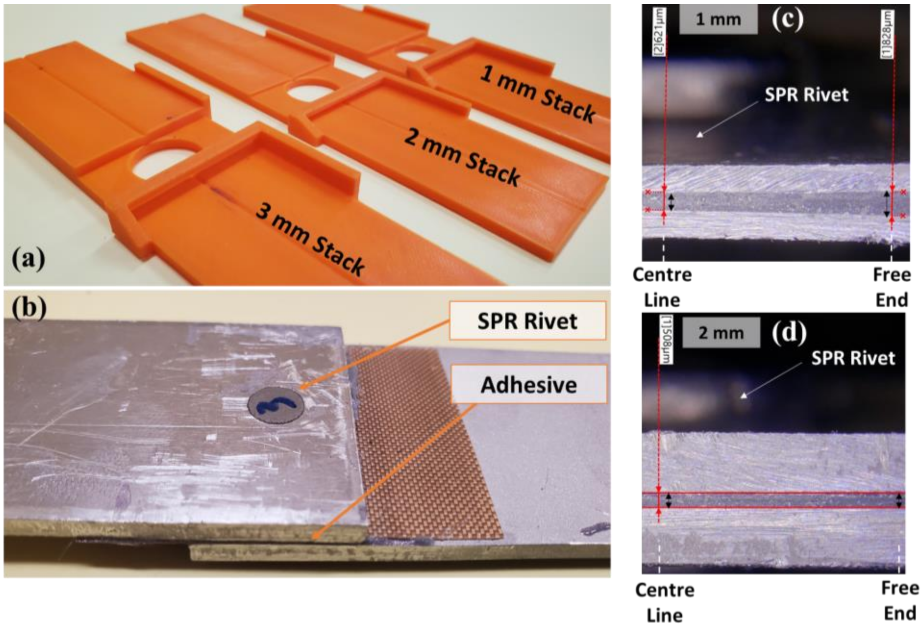

Figure 52: (a) 3D printed assembly template for SPR and hybrid joints, (b) Hybrid joined SLJ specimen, (c-d) hybrid joining affecting bond line thickness depending on sheet thickness.

The SLJ specimens were tested using a custom-made hydraulic tensile frame with an MTS hydraulic controller (MTS 407, MTS, USA) (Figure 53a). The test load was measured using a 100 kN load cell and the cylinder displacement was measured using a linear variable differential transformer (LVDT) while conducting the test at a crosshead speed of 6 mm/min. SLJ testing utilized a 105 mm macro lens to track the joint overlap rotation with a resolution of 66 pixel/mm in the area of interest (Watson *et al.*, 2019). SLJ overlap rotation was measured by the change in the angle of the line connecting points ‘A’ and ‘B’ (Figure 53b), which was tracked using open-source software (Tracker, Open Physics Project). A total of fifty-four (54) SLJ tests were conducted to assess the mechanical response of the three joining methods using two aluminum alloys having three sheet thicknesses each (Figure 54).

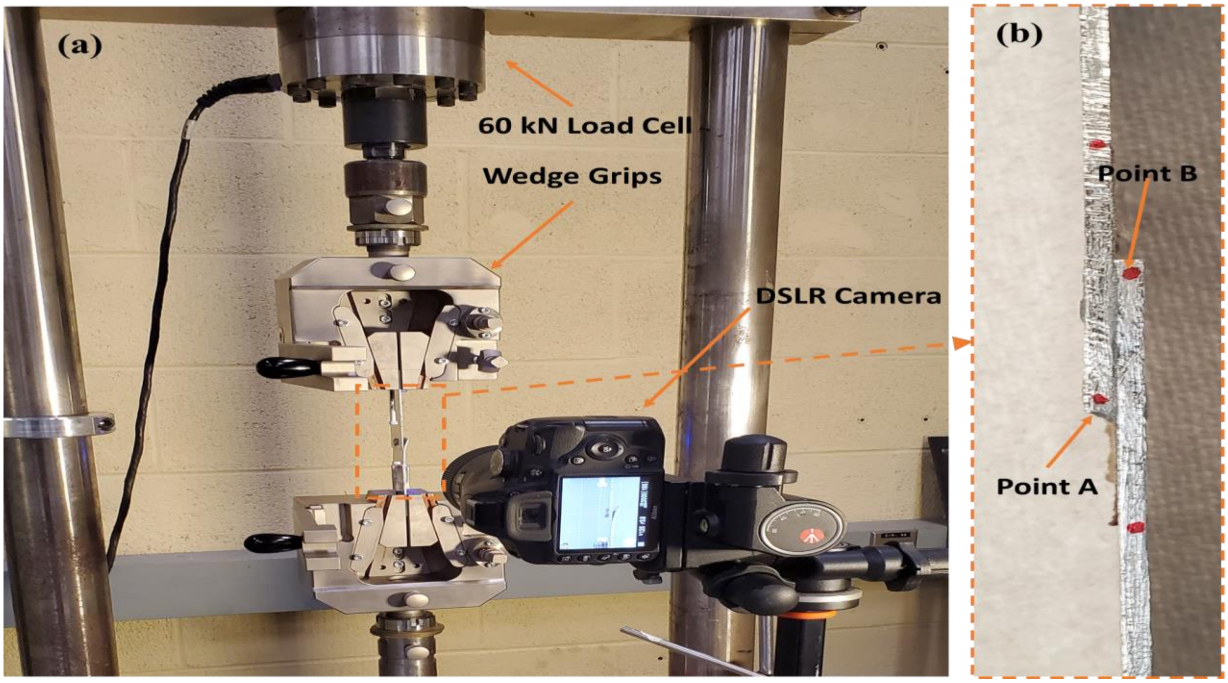

Figure 53: (a) Test setup for the tensile testing of adhesive, SPR and hybrid joined SLJ specimens and (b) the optical tracking targets on the side of the SLJ specimen.

The change in the angle of the line connecting ‘A’ and ‘B’ was calculated used the following equation,

$$\text{Rotation Angle } (\theta) = \left[\tan^{-1}\left(\frac{y_i^A - y_i^B}{x_i^A - x_i^B}\right) - \tan^{-1}\left(\frac{y_o^A - y_o^B}{x_o^A - x_o^B}\right)\right] \qquad \text{Equation 12}$$

Where y is the y-coordinate, x is the x-coordinate, the subscript ‘i’ is the time, the subscript ‘o’ denotes the time at the beginning of the test, and the superscripts denote the point location (points ‘A’ or ‘B’). The joint rotation measurement served as a local validation metric for the computational models and allowed to quantify the amount of adherend bending during each test.

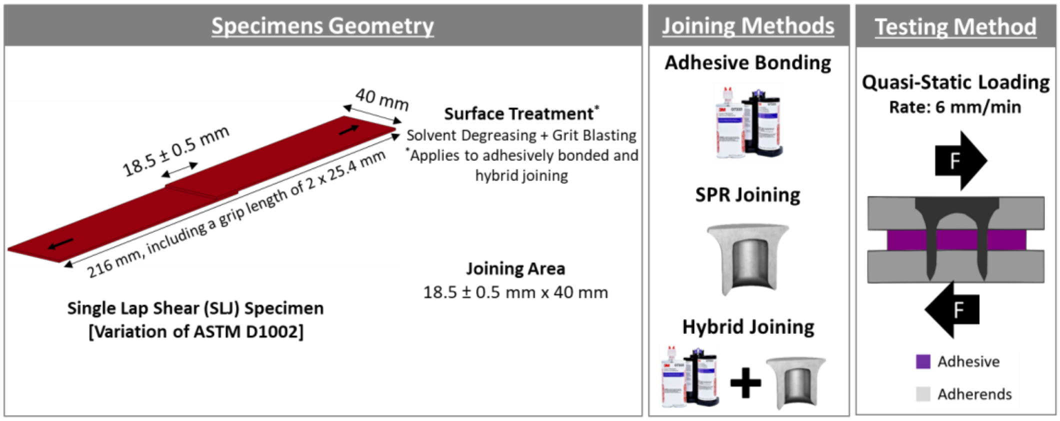

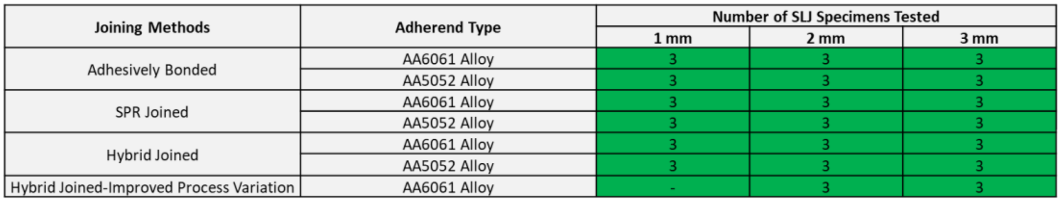

Joining Methods	Adherend Type	Number of SLJ Specimens Tested		
		1 mm	2 mm	3 mm
Adhesively Bonded	AA6061 Alloy	3	3	3
	AA5052 Alloy	3	3	3
SPR Joined	AA6061 Alloy	3	3	3
	AA5052 Alloy	3	3	3
Hybrid Joined	AA6061 Alloy	3	3	3
	AA5052 Alloy	3	3	3
Hybrid Joined-Improved Process Variation	AA6061 Alloy	-	3	3

Figure 54: Test matrix of the SLJ testing applied to adhesive, SPR and hybrid joints (54 tests in total).

3.6 Mechanical Response Improvement using Hybrid Joining Process Variations

Researchers used measurements of the physical attributes to improve the mechanical interlock and predict the performance of SPR-only joints (Hahn and Wibbeke, 2005; Sun and Khaleel, 2005). Also, adhesive morphology (*i.e.*, bond line thickness) was reported to affect the mechanical performance of adhesive and hybrid joints (Dillard, 2010; Ibrahim and Cronin, 2022). The measurement of physical attributes was used in this study to investigate three variations of hybrid joining processes while assessing how the process modifications influenced the morphology of the adhesive and SPR joint formation.

To identify hybrid joining process variations that would have the potential to improve the mechanical performance of joints was assessed using H-specimen and SLJ testing, and a thorough analysis of the failure mechanisms was conducted. Consequently, three hybrid joining process variations with the potential to enhance the adhesive layer morphology within a hybrid joint were identified. First, adopting a 0.17 mm-thick brass spacer (shim), placed at the location of the rivet, was investigated because it could allow for increased bond line thickness, and reduce the amount of adhesive squeeze out. The brass spacer was cut using a punch to a diameter of 8 mm, which was greater than the maximum diameter of the flared rivets (~7.3 mm) (Figure 55a). Second, applying the SPR rivet after curing the adhesive joint at room temperature (Ufferman *et al.*, 2018) was investigated because the process variation could result in uniform bond line thickness without adhesive squeeze out or air porosity. However, with no data published in the literature, it was not clear whether adhesive damage could be initiated during the SPR insertion process, affecting the mechanical performance of the joint. The third process variation was applying the SPR rivet to the adhesive at the end of the curing process at the curing temperature. Banea and Da Silva (2010) reported that a toughened epoxy adhesive had 57% lower strength, 40% lower Young’s modulus, and 43% higher tensile strain when the temperature was elevated from 25 ºC to 80 ºC. Therefore, this study investigated applying an SPR rivet to adhesive at an elevated temperature to reduce adhesive susceptibility to cracking and improve the SPR formation. For each process variation, flat specimens (Figure 55b) were prepared according to the methods laid out earlier in this section.

The flat specimens were cross-sectioned and polished (Figure 55c), and the measurements were taken using the opto-digital microscope considering three repeats (Table 8).

Table 8: Number of specimens assessed for the three hybrid joining process variations using the measurements of physical attributes.

Sheet Thickness	**Hybrid Joining Traditional Method with a Brass Spacer (Shim)**	**Hybrid Joining Post Curing – Room Temperature**	**Hybrid Joining End of Curing Process – Curing Temperature (80 ^{o}C)**
2 mm + 2 mm	3	3	3
3 mm + 3 mm	3	3	3

Figure 55: (a) 0.17 mm thick brass shims (8 mm diameter) applied to the centre of the joining area, (b) Specimens prepared using variations of the traditional hybrid joining technique, and (c) cross-sectioned specimens.

Next, SLJ specimens were prepared and tested to verify the mechanical response improvement, and the hybrid joining process variation that provided the best improvement in joint morphology was used to prepare the specimens. The SLJ specimen preparation and testing were undertaken following the same methods explained in section 3.5. Two sets of test specimens (SLJ made with 2 mm and 3 mm thicknesses) were used to verify the improvement in joint strength and quantify the strength improvement relative to the hybrid SLJ joints prepared using the traditional method.

3.7 Caiman Component-Level Manufacturing, Preparation and Testing

The focus of this work was to assess the mechanical response of aluminum structures joined using adhesives, SPR and hybrid joining to understand how large adhesive bond area and groups of SPR rivets behave and influence the mechanical response of a large-scale test. In addition, incorporating a structural-level test into this research allowed for the investigation of key joining aspects, such as SPR rivet spacing and hybrid joining process variation, comparing the structural-scale response of the traditional hybrid joining method and a process variation that achieved potential improvement. Thus, five tube-shaped components, comprising double aluminum hat channels, were prepared to create adhesively bonded tubes, an SPR joined tubes, a hybrid joined tubes, hybrid joined tubes with SPR rivets applied post curing, and hybrid joined tubes with SPR rivets applied post curing using double the rivet spacing (50 mm versus 25 mm). These different configurations were used to compare how each joining method affected the overall response of the structure under Mode I loading while measuring local metrics pertinent to each joining methods (*e.g.*, rate of crack propagation for adhesive and localized separation for SPR rivets).

The hat sections were formed from aluminum AA6061-T6 blanks having 3 mm thickness. The sheet thickness was selected according to FE modeling simulations, which confirmed that using a sheet thickness below 3 mm would encounter plastic deformation (bending) in the base metal. The formed hats had a length of 600 mm, a hat width of 67.5 mm, and total width of 130.5

mm (Figure 56). The bend radius used for all the bends was 7.9 mm (~2.5 times the sheet thickness) with a bend angle of 85º, which allowed the bending of the AA6061-T6 alloy. The hat sections had two holes (R8.75 mm) at the top of the hat to allow bolting the fixturing components to the section, and two side holes to allow loading the hat section using a pin while distributing the load to the section profile along a length of 110 mm (more details in section 3.7).

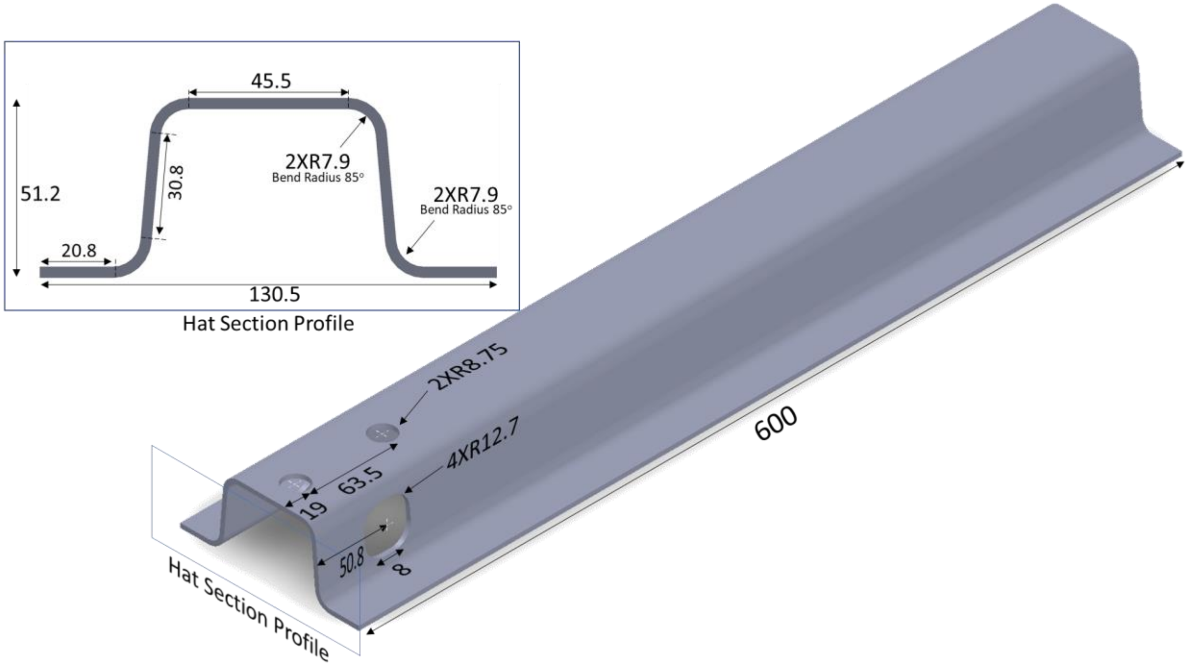

Figure 56: The geometry of the Caiman hat section, illustrating the hat section profile.

When joining large structures with flanges, it is important to ensure that the top and bottom flanges have proper squareness and flatness. The flatness of the flange would ensure adequate mating along the joining area and facilitate achieving the bond line thickness required. Also, the squareness of the flanges would ensure that the joining area is not skewed, and that tube is symmetrical (the mated flanges on both sides have comparable bonding area). Thus, the hat section fabrication process plays a key role in the quality of the joint and can affect the mechanical response of the structure. In a previous work by Liu (2019) on hat sections with similar geometry but made of UHSS, the author reported that the flanges had a gap of 8.5 mm when mated, and that achieving squareness during the forming process was a challenge (Figure 57a). The author addressed the gap by using C-clamps along the flanges while adjusting the clamping pressure to achieve adequate mating. To avoid these challenges, the fabrication of the aluminum hat sections in this work used computer-aided advanced bending equipment with laser correction for accuracy. In addition, several trials were conducted to identify the required load and fabrication parameters and a trial sample was created as a first article inspection (Figure 57b).

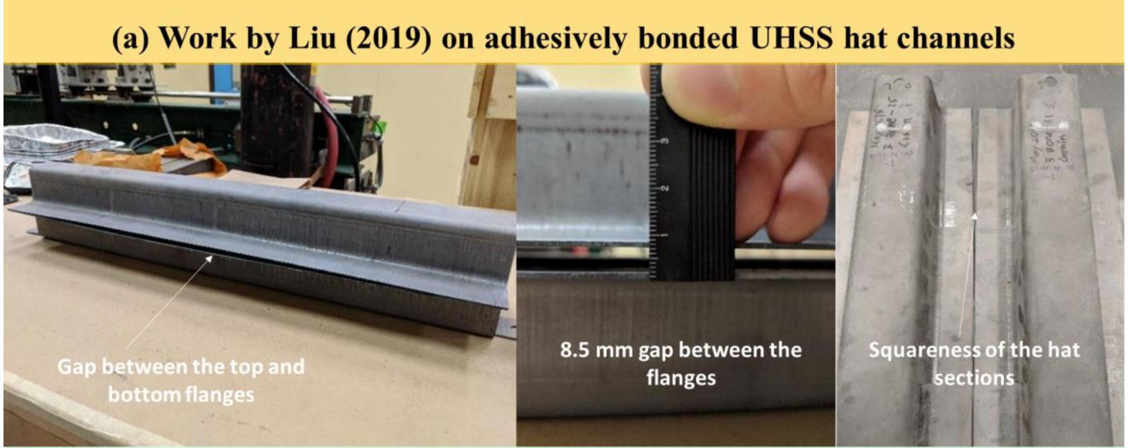
(a) Work by Liu (2019) on adhesively bonded UHSS hat channels


(b) A trial component prepared to address the reported challenges

Figure 57: (a) Challenges reported for hat section fabrication (Liu, 2019), and (b) a trial sample created as a first article inspection prior to fabrication.

The hat section fabrication process consisted of four steps. To start, the pre-formed blank was cleaned, and a forming lubricating was applied. Next, the blank was loaded to a high-precision computer-aided hydraulic press brake (Xpert 250, Bystronic Laser, Switzerland) (Figure 58a) with laser angle measuring system and bend angle automatic correction (Figure 58b and Figure 58c). The blank was precisely bent using laser measurements to create the four required bends. After that, the blank was machined using a CNC-operated 5-axis vertical machining center (Matsuura, USA) to create the two top holes and two side holes while using high-pressure machining coolant (Figure 58d-f). The final hat sections weighed 985.9 ± 2.0 grams (< 0.02% difference) and was manufactured to a dimensional precision of ± 0.01 mm (Figure 58).

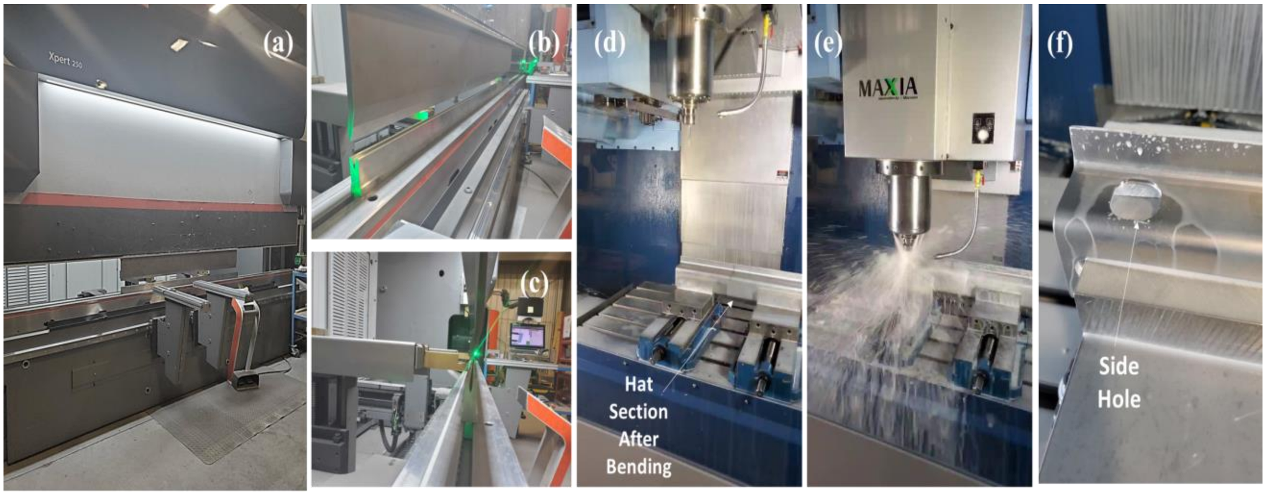

Figure 58: Fabrication of the Hat section using a high precision press brake (a) with laser alignment (b) and bend angle automated correction (c), and then machining on a CNC-operated 5-axis vertical machining center (d-f).

Figure 59: The weight measurements of the hat section to ensure weight precision.

Similar to the specimen-level specimen preparation, an important aspect of the component-level testing was to achieve cohesive failure within the adhesive. With large bonding area, careful preparation of the flange surface was required to ensure proper intrinsic adhesion along the length of the tubes. The surface treatment study completed in this work showed that the strength of single lap shear specimens was maximized and achieved consistent cohesive failure using grit blasting, followed by cleaning the surface with a solvent (*i.e.*, acetone) immediately prior to the application of adhesive. In addition to improving the surface roughness for mechanical interlocking, another function of grit blasting was that it removed the weak hydrated oxides, which was reported to weaken the interfacial adhesion (Cavezza *et al.*, 2020). Therefore, all flanges of the hat sections were grit blasted with 80 grit aluminum oxide at 65 psi in a cross pattern and then cleaned with acetone prior to bonding (the same surface preparation process used for SLJ and H-specimens) (Figure 60a). Prior to grit blasting, the bonding area was scribed using a digital gauge and a scribe tool, and the boundaries were masked using masking tape. After grit blasting, Teflon-coated fiber-glass spacers were applied along the inner bond area boundaries to reduce the edge effect and influence of the adhesive spew (Figure 60b).

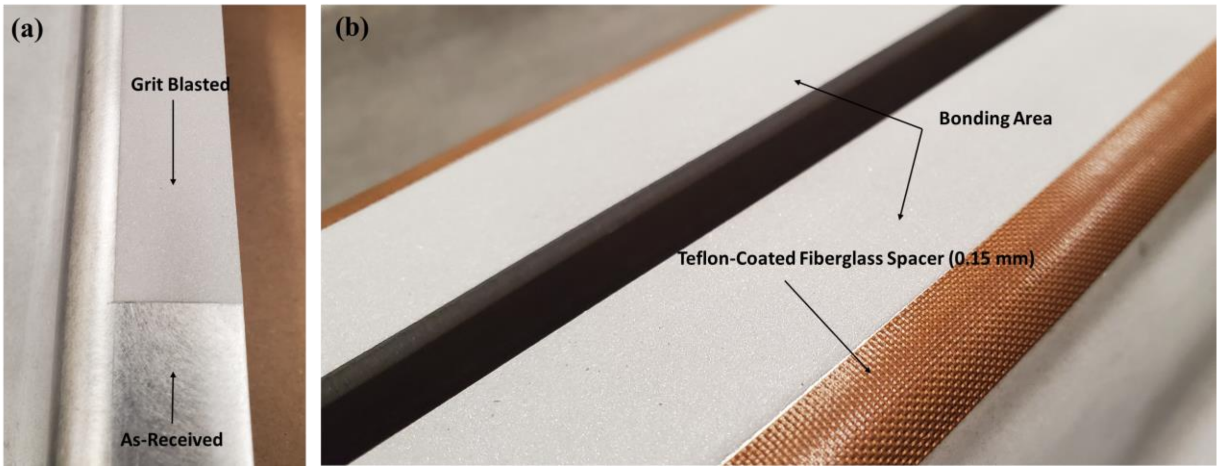

Figure 60: (a) Flange grit-blasting, and (b) application of Teflon-coated spacers along the inner boundaries of the adhesive.

The Caiman component, originally developed by O'Keeffe (2018) for spot welds and adopted for adhesives by Liu (2019), used a free length of 243 mm and an effective joining length of 357 mm (59.5% of the total length, 600 mm). In the work by Liu (2019), controlling the bond line thickness along the adhesive joining area was achieved by applying six circular shims (11.12 mm (7/16") dia) with equal spacing (three on each flange spaced at 83.5 mm) on one side of the joined hat sections (Figure 61a). The total area of the shims was 582.7 mm^2, which resulted in an 8% reduction in the effective joining area. However, area reduction was not desirable in this work as it could mask the difference in mechanical response between adhesive joining (area reduction due to shims) and hybrid joining (area reduction due to adhesive squeeze out). Thus, the bond line thickness was controlled using Teflon-coated fiberglass spacers applied to the free length (the length of the tube that was not joined, Figure 61b). The spacers were applied to one side of the hat sections (Figure 62a and Figure 62b) and facilitated reducing the edge effects at the location of adhesive crack initiation.

(a) Adhesively Joined Caiman Configuration used by Liu (2019)

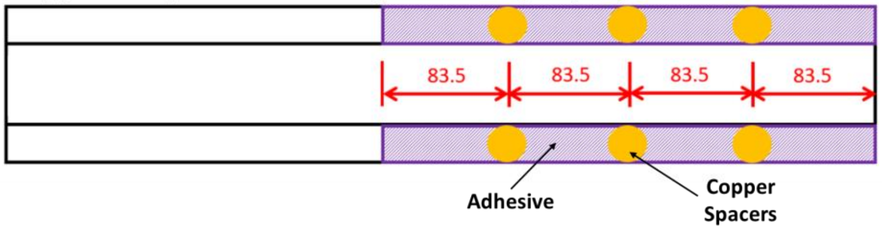

(b) Adhesively Joined Caiman Configuration used in this study

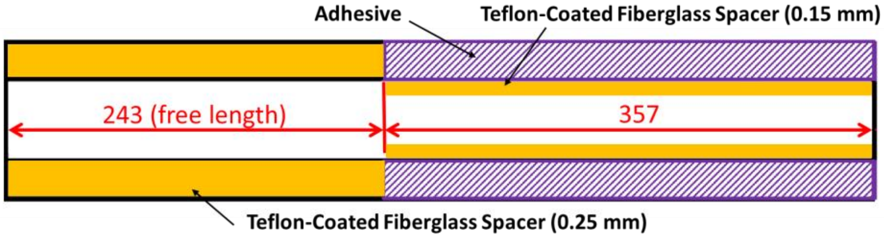

Figure 61: (a) Reduced effective joining area due to copper spacers used to maintain the bond line thickness in the literature (Liu, 2019), (b) Teflon-coated spacers applied at the free length and inner boundaries of the adhesive allowed maintaining bond line thickness without area reduction.

Figure 62: (a) Teflon-coated spacers to maintain bond line thickness and reduce edge effects and adhesive spew, (b) Hat section ready for adhesive or hybrid joining application.

A thick continuous bead of adhesive was applied to the joining area of one hat section for each tube (Figure 63a), and then the other hat section was placed over the first one in a way that achieved adequate mating with minimum adjustment/movement. Initial trials showed that excessive movement during the mating process could result in air voids and non-uniform adhesive distribution along the bond area. Another important aspect to ensure proper coverage of adhesive within the bond area was to apply and ensure excess adhesive flowed through all adhesive boundaries (Figure 63b). Next, four C-clamps (2” jaw opening) were applied to the free length of the tube to fixture the hat sections together (Figure 63c). The C-clamps were hand tightened, plus half turn to apply consistent clamping pressure to all tubes. Using C-clamps on one side of the joined tube acted as a hinge and resulted in opening a gap at the free end of the adhesive (the other end of the tube). Therefore, four spring clamps (two on each side of the flanges) were applied to the tube (two 3” clamps at the adhesive free end and two 2” claps at the mid point of the joining area length) because this type of clamp could result in consistent and more uniform pressure along the bond area. Also, representative flat aluminum substrates were used to verify that applying the 3” spring clamp did not result in a bond line thickness below 0.3 mm. After that, the assembled tube was cured in a large convection oven for 30 min after the surface temperature reached 80^{o} C. After curing, the flange edge was cleaned using a sharp blade and a file (Figure 63d).

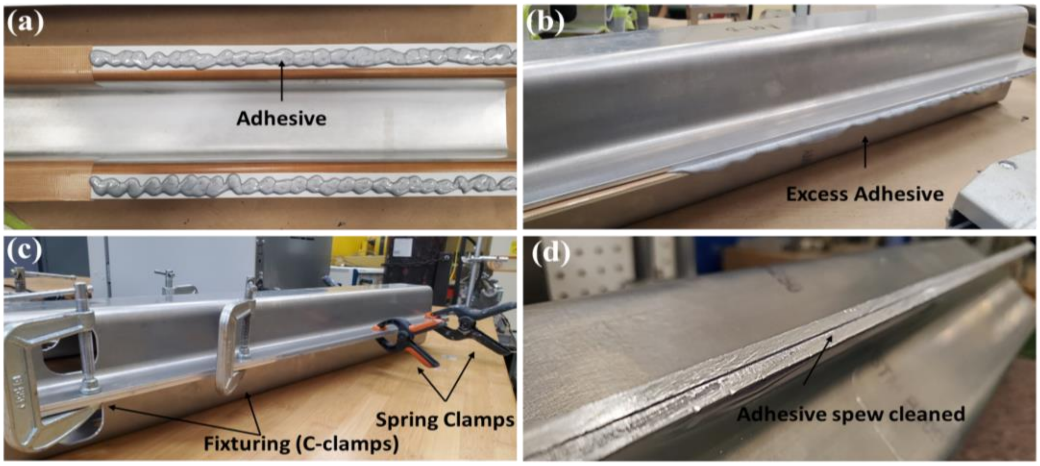

Figure 63: (a) thick continuous bead of adhesive applied to the hat section, (b) mating of hat sections ensuring excess adhesive, (c) fixturing the hat sections using C-clamps and spring clamps, and (d) flange edge after adhesive cleaning.

The SPR joining was applied to the effective length using two rivet configurations, 25 mm rivet spacing (Figure 64a) and 50 mm rivet spacing (Figure 64b). The tubes joined using SPR-only used 25 mm spacing and had 13 rivets on each flange (26 rivets in total). The hybrid joined tubes used a spacing of 25 mm and 50 mm, with the 50 mm spacing requiring 7 rivets on each flange (14 rivets in total). The SPR rivets (K50844A, Henrob, USA) were used with a domed-pip due (DP10-200, Henrob, USA) and the SPR forming process was completed using a handheld setting tool (Rivlite MK V, Henrob, USA), repeating the same methodology followed for the specimen-level tests. To precisely locate the SPR rivets, two templates were designed for each rivet spacing (one template for each side of the flanges) (Figure 65a), and the templates were 3D printed to avoid the time and cost associated with fabrication. The templates were applied to each flange using double-sided adhesive film prior to the SPR application (Figure 65b), allowing the SPR rivets to be precisely located within +/- 0.25 mm (Figure 65c).

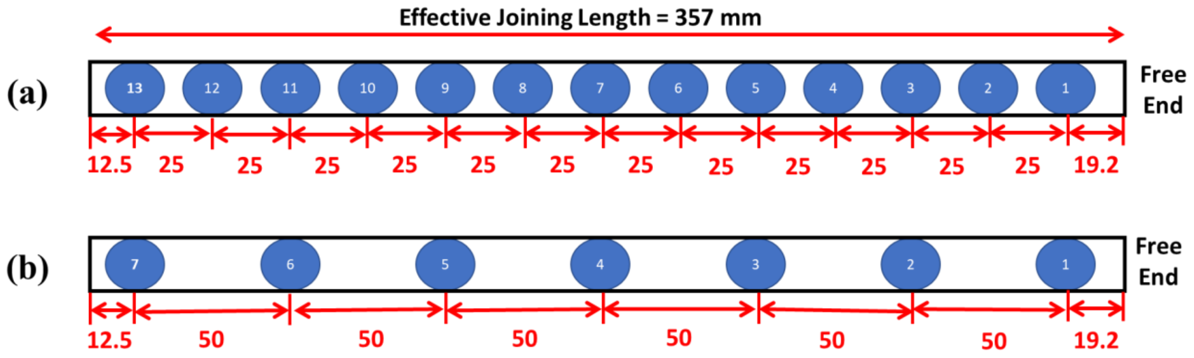

Figure 64: SPR rivet configurations along the effective joining length using (a) 25 mm rivet spacing and (b) 50 mm rivet spacing.

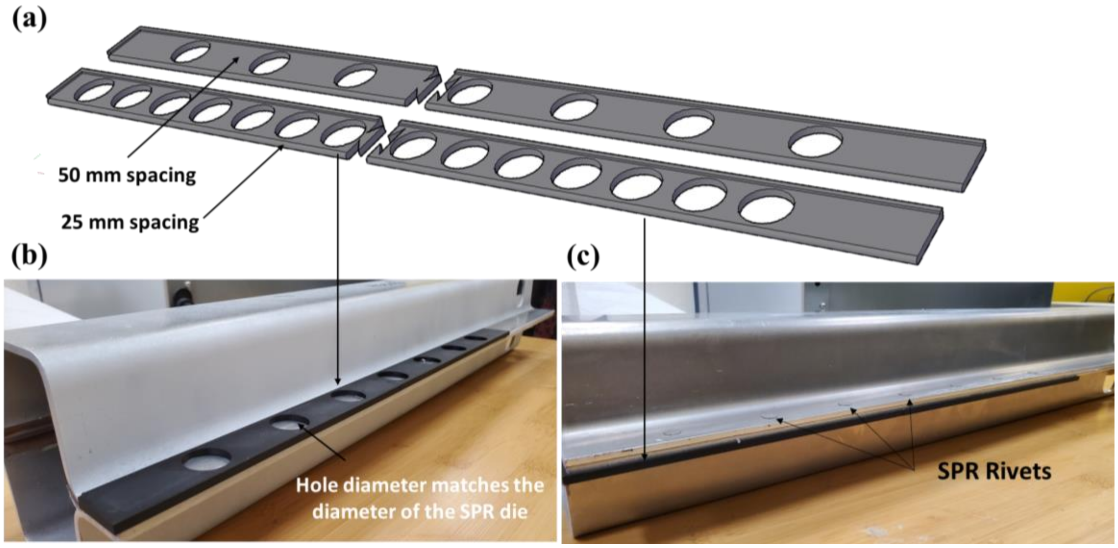

Figure 65: (a) SPR riveting templates for 25 mm and 50 mm spacing (designed as 2-part assembly due to the 3D printer size limitation, (b) SPR template applied to a flange, and (c) SPR rivets applied using the 3D template for positioning.

Hybrid joining was applied to the hat section using the traditional method (*i.e.*, SPR rivets applied to uncured adhesive) (Meschut *et al.*, 2014b; Ufferman *et al.*, 2018), and using the method that was identified in this work to provide improved adhesive morphology and increased joint strength (*i.e.,* SPR rivets applied to cured adhesive at room temperature). The hybrid joining followed the same methodology for the adhesive-only tubes and utilized the 3D printed template to precisely locate the SPR rivets. The hybrid joined tubes received the same heat curing process (30 minutes after reaching 80 degrees) as the adhesive-only tubes and the specimen-scale hybrid joints (SLJ and H-specimens). Although the specimen preparation process of SLJ and H-specimens did not clearly show the formation of air voids and increased porosity within the adhesive, the formation of air voids was observed along the flange of the hybrid joined tubes. Large air pockets formed during the SPR insertion process and became visible as the adhesive squeezed out (Figure 66a). The heat curing process allowed some of the entrapped air pockets to escape, and additional voids were observed at the end of the adhesive curing process (Figure 66b).

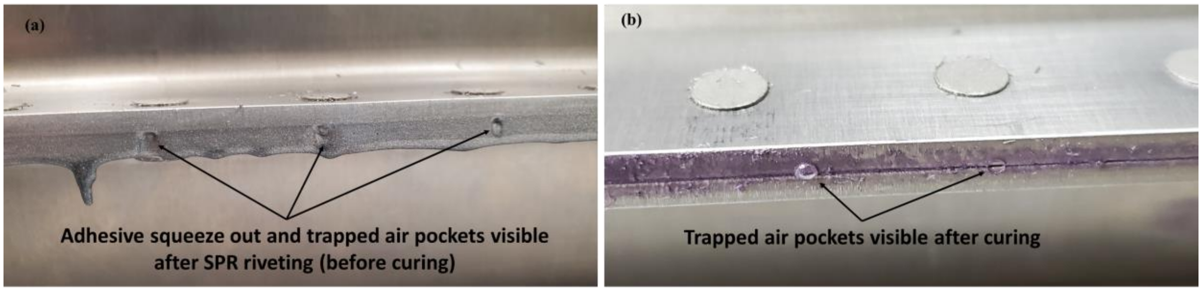

Figure 66: Porosity and air voids within the adhesive layer were observed during the SPR insertion process (a) and continued until the end of the curing process (b).

The Teflon-coated spacers applied at the inner boundaries of the joining area negated the effect of the adhesive spew inside the hollow section of the adhesive-only and hybrid joined tubes tube (Figure 67a). It was reported that spew at the inner boundaries increased the variability in the mechanical response; however, the spew was not possible to remove due to the confinement inside the section profile (Liu, 2019). Next, the tubes were prepared for optical tracking using a flat white spray paint to reduce the light reflections off aluminum surface (Figure 67b), and then optical tracking targets were added. For each tube, the beginning of the adhesive bond area received an optical mark, and each rivet location had an optical target on the top flange and another one on the bottom flange (Figure 67c).

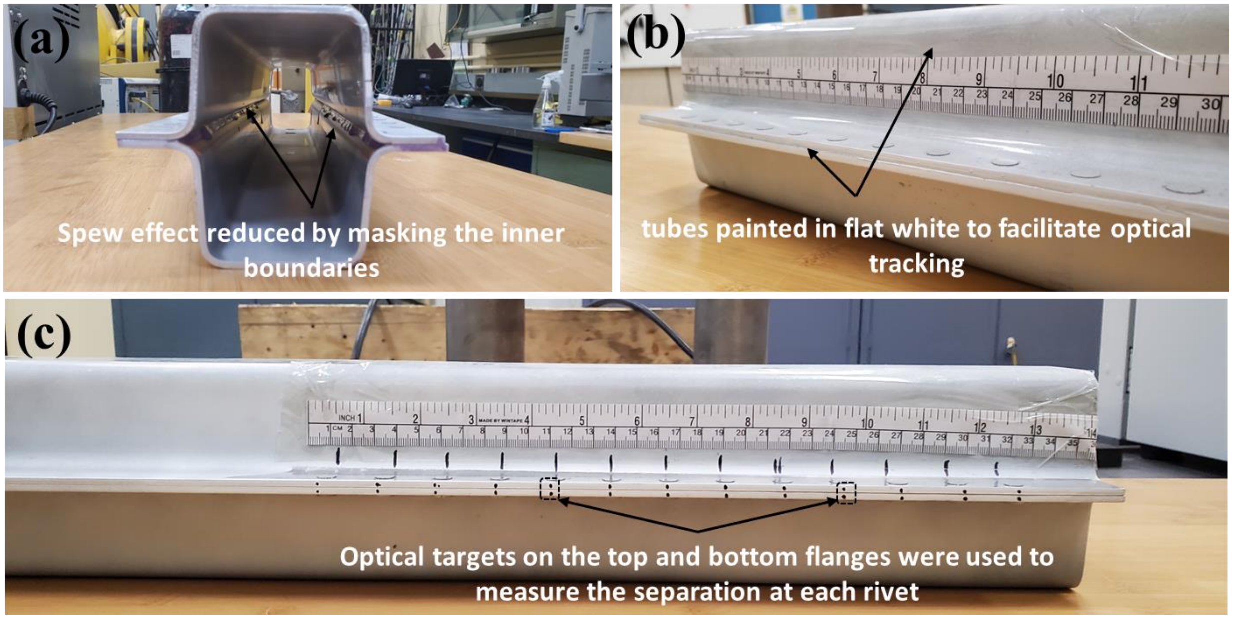

Figure 67: (a) Teflon-coated spacers reduced edge effects, (b) tube painted in flat white to improve optical tracking, and (c) optical tracking targets on the side of the tube.

3.7.1 Caiman Component Testing and Analysis

The Caiman tubes were assembled with the fixturing components required for tensile frame mounting (Figure 68a). Then, the tubes were tested using a hydraulic tensile frame (Criterion Model 45, MTS, USA), and the load was measured using a 100 kN load cell (Figure 68b). A top and bottom clevis were mounted to the frame, such that the bottom clevis was clamped to the hydraulic grip using a pressure of 3000 psi and the top clevis was threaded directly into the load cell. The fixturing components consisted of two sets of bosses that clamped the Caiman tube, each set comprised an inner and an outer boss that were bolted together (Figure 68c). The loaded clevis applied a displacement to the 19.05 mm diameter pin passing through the inner boss of the loaded hat section. The other pin was fixed to the fixed clevis, and both pins are allowed to rotate to induce a progressive separation within the top and bottom hat channels as the joining method failed because of Mode I loading (Figure 69). The loaded clevis was displaced at a rate of 25 mm/min, initiating a joint failure that propagated until the Caiman component was completely separated (Figure 69). Two DIC cameras with LED lighting, one on each side, were used to simultaneously capture images of the failure initiation and propagation of the joining method at intervals of 400 milliseconds. The captured images were acquired using the DIC software (VIC SNAP 2009, Correlated Solutions, USA) and were synchronized to the force and displacement of each test. In addition, a DSLR camera was used to record the tests using a wider field of view, which allowed for understanding the global behaviour of the structure deformation.

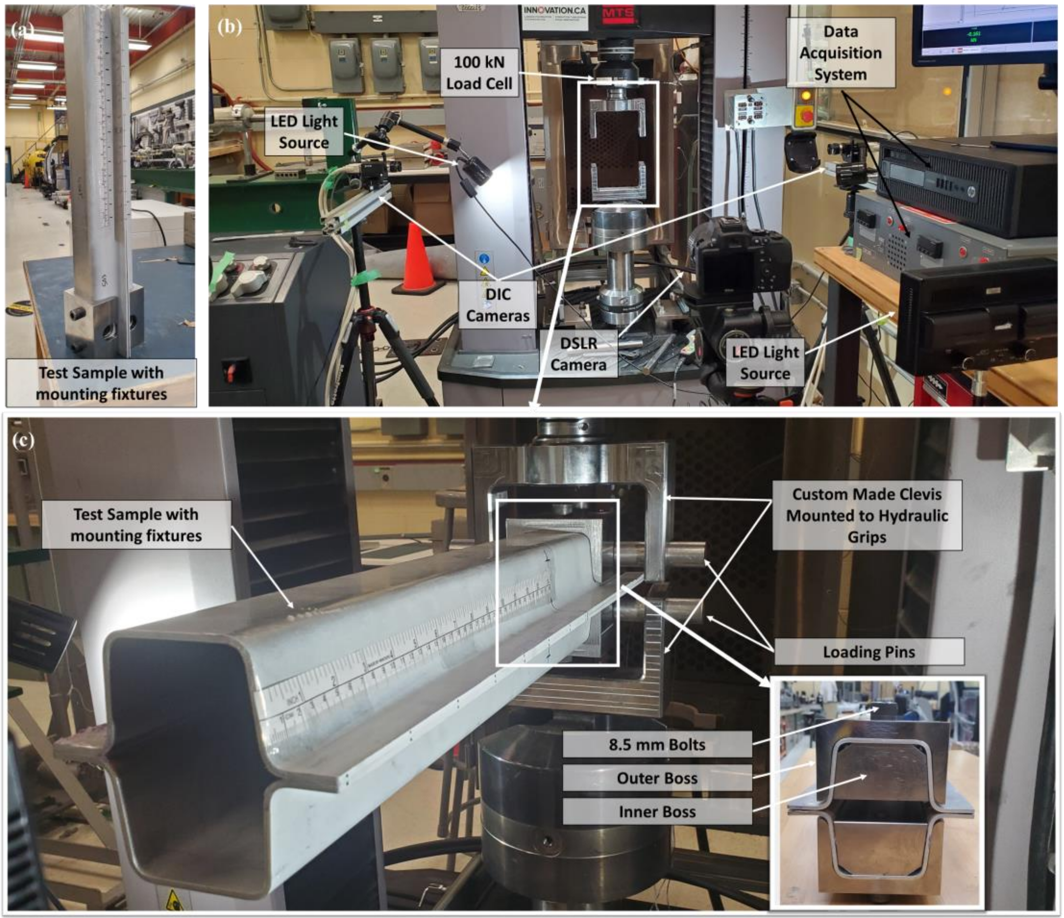

Figure 68: (a) Caiman tube assembled with the fixturing components and ready for testing, (b) Tensile frame setup, and (c) Caiman component frame mounting details.

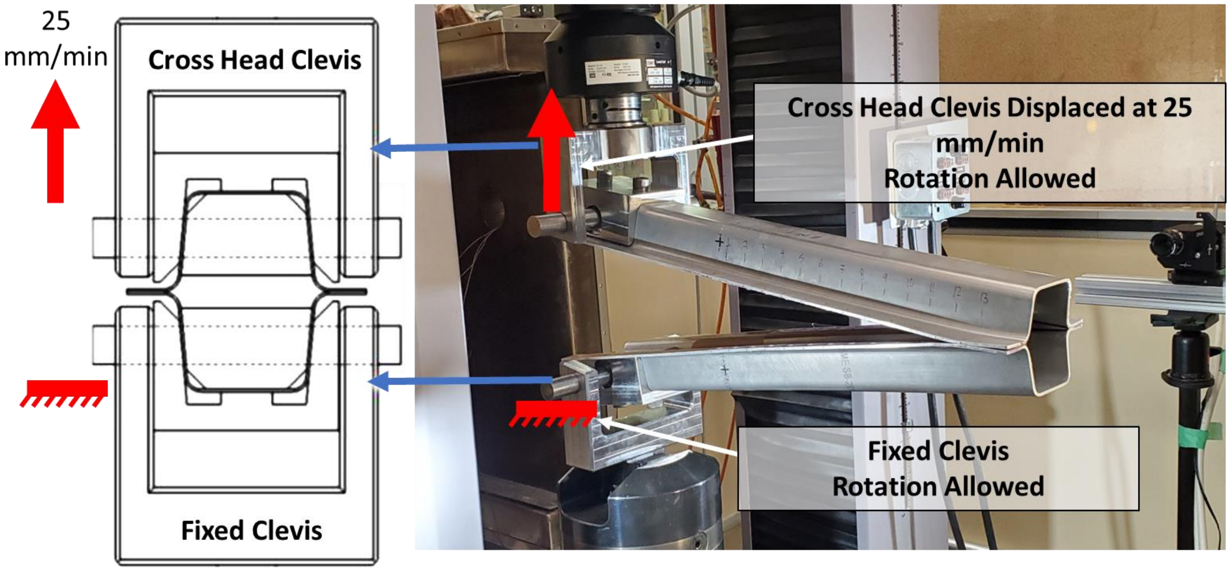

Figure 69: The Caiman test used a pin joint to progressively fail the joining method and separate the hat sections.

A summary of the Caiman test matrix is presented in Figure 70, showing the fifteen (15) tests conducted on Caiman tubes joined using adhesive-only, SPR-only, hybrid joining, hybrid joining with SPR rivets applied post adhesive curing, and hybrid joining with double-spaced SPR rivets applied post adhesive curing. Throughout each test, the crack extension was measured using optical methods, and the local separation at the location of each rivet was measured by tracking the coordinates of the tracking targets on the top and bottom hat sections during loading, using commercial motion analysis software (ProAnalyst 1.6, Xcitex, USA) (Figure 71). The adhesive tubes weighed 2003.3 g ± 4.0 g on average, which was similar to the average weight of SPR joined tubes (2005.7 g ± 2.1 g). The average weight of hybrid joined tubes was only +1.2% relative to the adhesive-only tubes, indicating that the weight difference was negligible even at the structure scale.

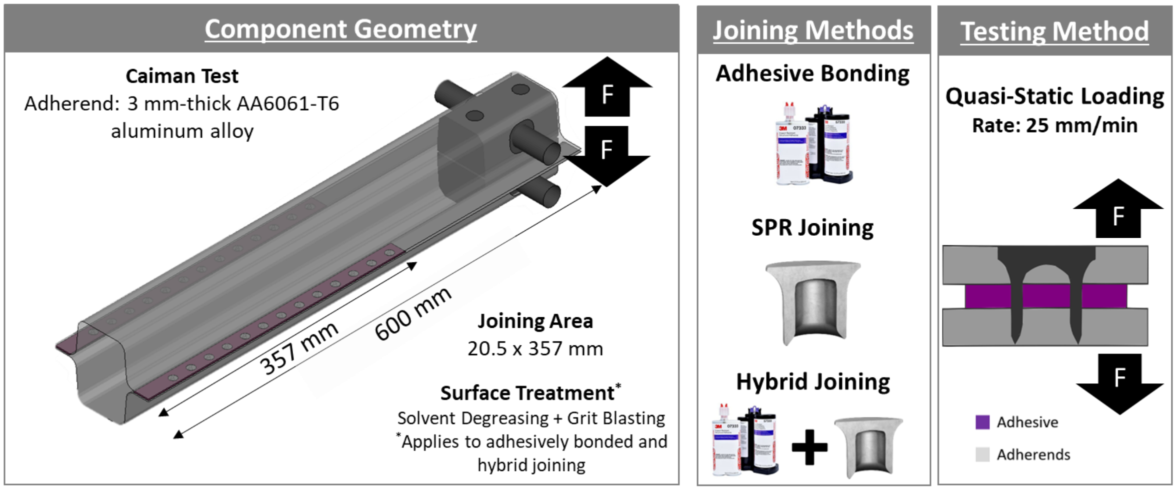

	Joining Method				
	Adhesively Bonded	SPR Joined	Hybrid Joined	Hybrid Joined Post Curing (HPC)	Hybrid Joined Post Curing with Double Rivet Spacing (HPCD)
Number of tests	3	3	3	3	3

Figure 70: Caiman component test matrix, illustrating the component geometry, joining methods used, and number of repeats for each joining method.

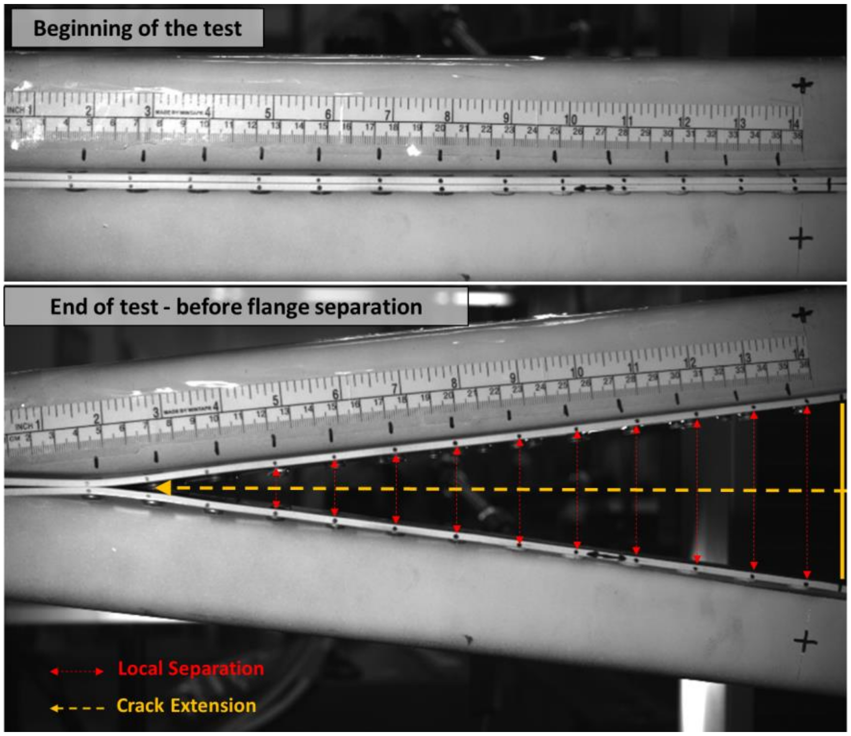

Figure 71: Measurements of crack extension and local separation throughout a Caiman test.

Chapter 4: Experimental Results and Discussion

4.1 Aluminum Sheet Metal (Adherend) Material Characterization

The mechanical properties, in particular the stress-strain relationship, of the AA5052-H32 and AA6061-T6 alloys were characterized at a quasistatic rate that mimics the specimen and component level experimental loading rate for the three sheet thicknesses (1 mm, 2 mm, and 3 mm) considered in this work. The material characterization aimed to improve the accuracy of the computational modeling of these materials. Tensile test specimens, according to ASTM E8, were undertaken in uniaxial tension tests to determine the material properties. DIC techniques were used to measure the strain optically using a virtual extensometer applied to the gauge length (50 mm). The engineering stress was calculated from the force, measured from the tensile frame load cell, and the average initial cross-section area, measured using a micrometre before the test. The engineering stress versus strain curves for the AA6061-T6 alloy showed good consistency and repeatability for all the tested sheet thicknesses (1 mm, 2 mm and 3 mm) with somewhat higher variability in the strain at failure for the 3 mm sheet material (Table 9). Young's modulus for all the tested sheets was consistent and ranged between 70.15 GPa and 70.72 GPa. Importantly, the transition from elastic to plastic behaviour, the ultimate tensile strength (UTS) and the strain at failure were sheet thickness dependant, and the UTS and strain at failure were inversely related to sheet thickness. The 1 mm sheets showed the highest UTS and strain at failure of 346.9 MPa and 0.146, respectively, while the 3 mm sheets showed the lowest UTS and strain at failure of 318.6 MPa and 0.0102, respectively. Finally, the engineering stress-strain curves for the 1 mm, 2 mm, and 3 mm sheets (Figure 72) were used to determine the relationship between the flow stress and equivalent plastic strain curves for computational modeling fitting and implementation (details presented in section 5.1).

Table 9: The mechanical properties of the aluminum AA6061-T6 alloy

Mechanical Properties	AA6061 Sheet Thickness		
	1 mm	2 mm	3 mm
Young's Modulus (GPa)	70.46 ± 0.76	70.15 ± 0.67	70.72 ± 0.42
Yield Strength (MPa)	290.82 ± 2.63	266.55 ± 2.40	277.02 ± 0.56
UTS (MPa)	346.90 ± 1.88	320.10 ± 1.99	318.60 ± 4.44
Strain at Failure	0.146 ± 0.004	0.138 ± 0.003	0.102 ± 0.014

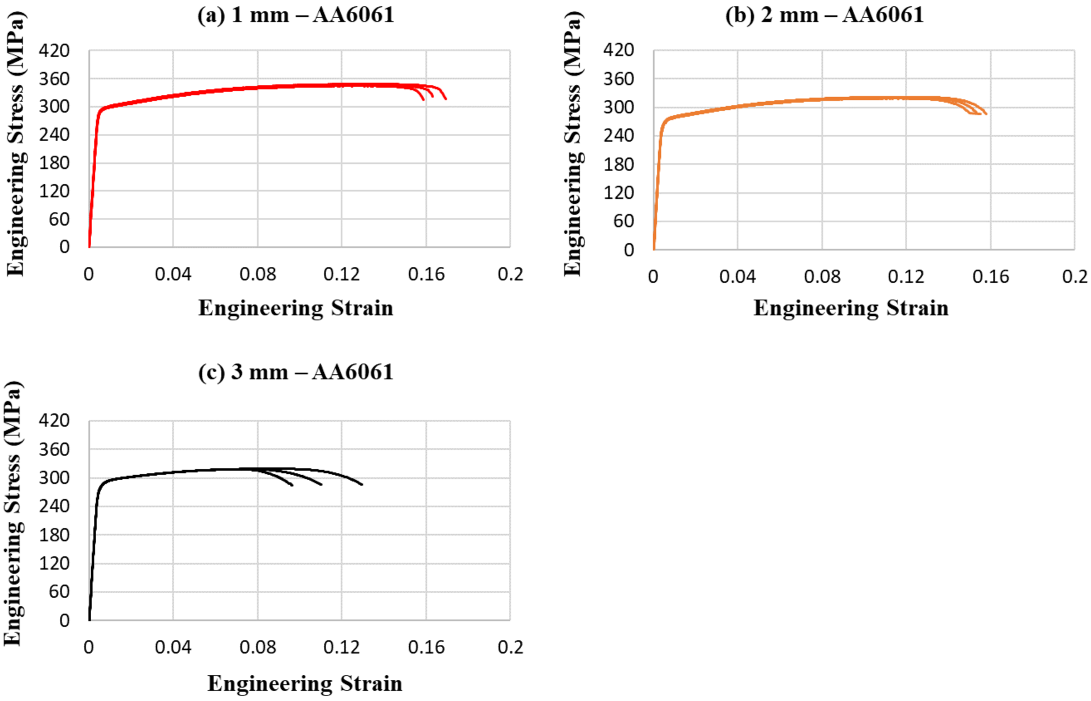

Figure 72: The engineering stress-strain curves for the cold-rolled AA6061-T6 sheet material with 1 mm (a), 2 mm (b) and 3 mm (c) thick cold-rolled sheets.

The engineering stress versus strain curves for the AA5052-H32 alloy also showed good consistency and repeatability for all the tested sheet thicknesses (1 mm, 2 mm and 3 mm) (Table 10). Young’s modulus for all the tested sheets was consistent and ranged between 69.63 GPa and

69.97 GPa. Similar to the AA6062-T6 sheet material, the ultimate tensile strength (UTS) and the strain at failure were sheet thickness dependent, and the UTS and strain at failure were inversely related to sheet thickness. The 1 mm sheets showed the highest UTS and strain at failure of 282.54 MPa and 0.102, respectively. The engineering stress-stress curves for the 1 mm, 2 mm, and 3 mm sheets (Figure 73) clearly showed that the AA5052-H32 experienced discontinuous yielding behaviour at room temperature, associated with Portevin-Le Chaterlier (PLC) deformation bands, which was observed in the data acquired from the tensile frame and the DIC imaging.

Table 10: The mechanical properties of the aluminum AA5052-H32 alloy

Mechanical Properties	**AA5052-H32 Sheet Thickness**		
	1 mm	2 mm	3 mm
Young's Modulus (GPa)	69.97 ± 0.67	69.63 ± 0.49	68.75 ± 0.40
Yield Strength (MPa)	190.96 ± 5.86	176.37 ± 0.12	165.20 ± 3.01
UTS (MPa)	282.54 ± 5.73	266.01 ± 1.16	237.61 ± 0.62
Strain at Failure	0.102 ± 0.001	0.101 ± 0.003	0.088 ± 0.006

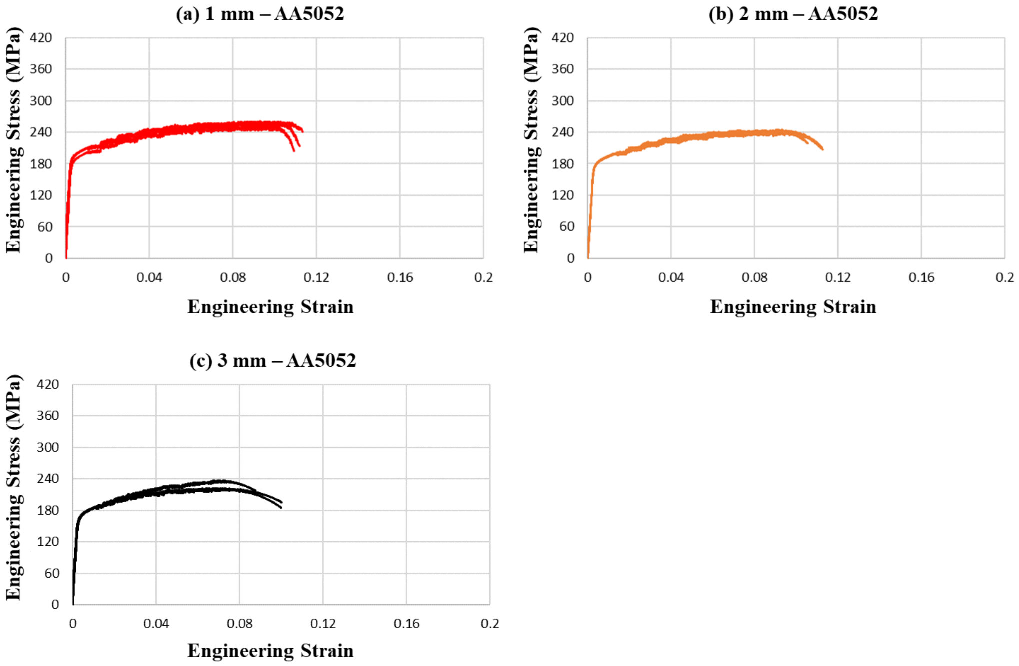

Figure 73: The engineering stress-strain curves for the cold-rolled AA5052-H32 sheet material with 1 mm (a), 2 mm (b) and 3 mm (c) thick cold-rolled sheets.

4.2 Effect of Surface Preparation on Aluminum SLJ Joint Strength and Failure Mode

Seven contemporary surface treatments including, mechanical and chemical methods were assessed using adhesively bonded aluminum SLJ tests, according to ASTM D1002-10 (2019), made with AA6061-T6 alloy. The surface treatments that maximized joint strength and achieved cohesive failure were identified and the most suitable for a lab environment was used in this study to avoid reduced adhesive joint strength due to interfacial failure, which would lead to a flawed comparison between adhesive, SPR and hybrid joints throughout the study. Additionally, the surface treatments with maximum joint strength and cohesive failure were compared to the non-treated solvent-degreased aluminum (baseline) to understand how surface roughness and wettability behaviour influenced the SLJ joint strength and failure mode.

The mechanical testing of the SLJ specimens revealed that the SLJ joint strength varied substantially according to the method used to prepare the adherend surface before adhesive application. The average peak load of the SLJ joints was substantially higher (nearly seven times) for the four sets of SLJ tests treated using SDA (Solvent Degreased – Abraded), SDGB (Solvent Degreased – Grit Blasted), SDASG (Solvent Degreased – Abraded – Sol-gel) and SDSG (Solvent Degreased – Sol-gel) relative to other surface treatments (*i.e.*, SD (Solvent Degreased, baseline), SDSEP (Solvent Degreased - Self Etching Primer), SDDR (Solvent Degreased – Regreased)). The average peak load of the SLJ joints ranged between < 1 kN and 7.54 kN (Figure 74), with the four top-performing surface treatments (SDA, SDGB, SDSG, and SDASG) producing joints that met or exceeded the strength specifications provided by the manufacturer (horizontal dashed red line in Figure 74). One-way analysis of variance (ANOVA) was conducted, and the results showed that there was no statistically significant difference (p = 0.326) between the SDA, SDGB, SDASG and SDSG data sets, indicating that the four surface treatments improved joint strength at similar levels. In contrast, the SD (baseline), SDDR, and SDSEP surface treatments had a significantly low average peak load of less than 1 kN, emphasizing the importance of surface preparation to avoid premature joint failure. The considerably low joint strength caused some of the SD, SDDR and SDSEP specimens to fail during mounting on the test frame and led to high variability in strength.

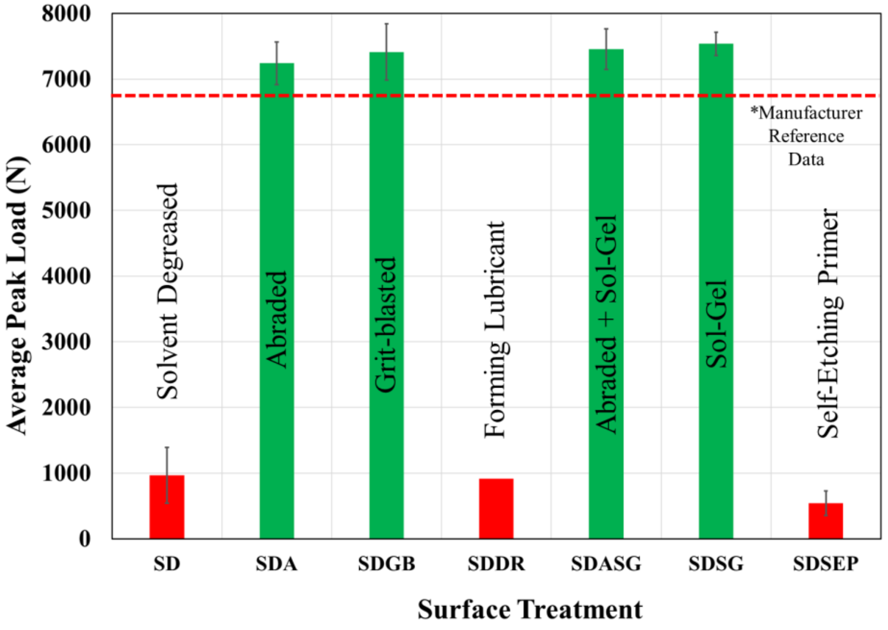

*3M 07333 IRSA Technical Data Sheet, (3M, 2022)

Figure 74: The SLJ average peak load for seven contemporary surface treatments.

Bond line thickness was reported to play a key role in adhesive joint response (Davies *et al.*, 2009; Watson *et al.*, 2020); thus, it was important to ensure consistency in bond line thickness among the test samples. Opto-digital microscope imaging and measurements showed that the bond line thickness variability was low for each set of specimens and had a difference of less than 0.1 mm between surface treatments (Table 11). In addition, the average overlap length for all the SLJ test sets was rigorously maintained at 12.68 mm ± 0.26 mm, to minimize the influence of joint geometry on stress distribution within the adhesive layer (da Silva *et al.*, 2009).

Table 11: Bond line thickness and length measurements

Surface Treatment	Average Bond Line Thickness (mm)	Average Overlap Length (Bond Line Length) (mm)
SD (baseline)	0.377 ± 0.018	12.97 ± 0.17
SDA	0.389 ± 0.023	12.30 ± 0.28
SDGB	0.421 ± 0.073	12.82 ± 0.20
SDDR	0.357 ± 0.009	12.26 ± 0.28
SDASG	0.305 ± 0.018	12.71 ± 0.44
SDSG	0.320 ± 0.037	12.86 ± 0.41
SEP	0.338 ± 0.019	12.84 ± 0.05

Examining the failure surfaces of the tested SLJ specimens provided additional insight into the failure modes and measured response (Figure 75). The SD, SDDR, and SDSEP specimens exhibited interfacial failures, explaining the reason behind poor joint strength and premature joint failure. In contrast, the SDA, SDGB, SDASG and SDSG specimens exhibited varying degrees of cohesive failure (crack propagated within the adhesive layer). The SDA specimens showed non-uniform cohesive failure with a fracture surface near the interface and most of the adhesive bonded to one of the adherends with a thin layer of adhesive on the other adherend (SDA, Figure 75). The SDGB specimens showed uniform adhesive coverage and visually equal adhesive thickness on the mated adherends (SDGB, Figure 75), improving the adhesive fracture surface characteristics. Several studies have used grit blasting to prepare adhesive joints used from similar and dissimilar materials, including aluminum, steel and magnesium, and reported that grit blasting could achieve a cohesive failure, and maximized adhesive joint strength (Ibrahim and Cronin, 2022; Watson *et al.*, 2018). The SDASG and SDSG specimens exhibited similar cohesive failure, which was surprising for the single-step SDSG treatment. Both treatments showed porosity-like features at the boundaries of the adhesive free ends, but those features were smaller in size and more scatted within the bond area of the SDSG specimens. The mechanism behind how and why the porosity-like features formed was not yet understood; however, it could be speculated that the porosity-like features might have been formed during the adherend mating process due to the adhesive spread out.

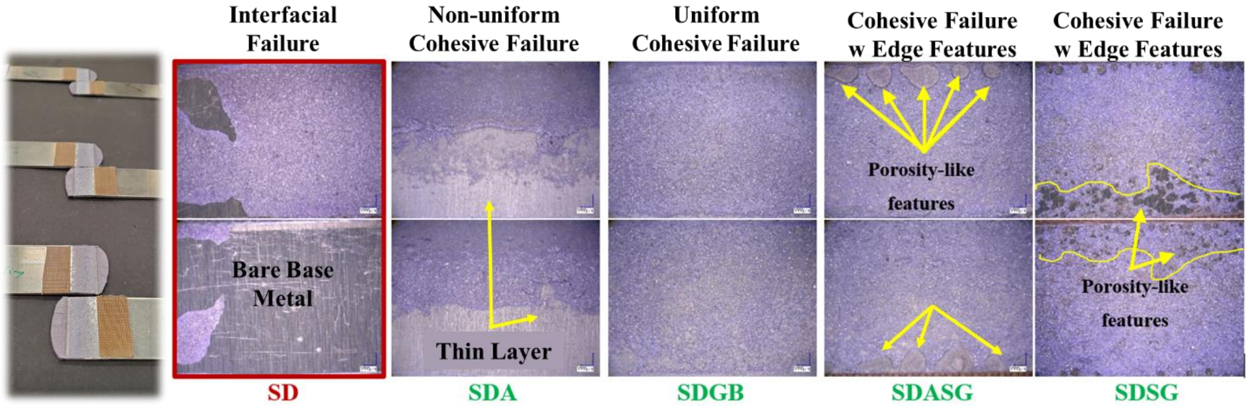

Figure 75: SLJ joint failure surfaces for SD, SDA, SDGB, SDAGB and SDSG surface treatments.

4.2.1 Effect of Surface Roughness and Morphology on SLJ Joint Strength and Rotation

The surface treatments considered in this work resulted in a range of surface roughness, with an arithmetic mean (R_a) ranging from 0.20 μm to 3.47 μm (Table 12). The SDA, SDGB, SDASG and SDSG specimens exhibited comparable average peak load but a substantially different mean arithmetic surface roughness, demonstrating that the adhesive used in this work responded well to both chemical and mechanical surface treatments and spread out well on surfaces with a variety of surface roughness values. The SDGB and SDSG were of particular interest because the average surface roughness of SDSG was ~17 times that of the SDSG; however, the joint strength was comparable (Figure 76). The sol-gel treatment (SDSG) increased the joint strength by a factor of 7 compared to the SD specimens, while both treatments had the same surface roughness, highlighting that surface chemistry played a key role in improving epoxy-based adhesive interfacial strength (Figure 76). Boutar *et al.* (2016) studied the effect of surface roughness on the strength of SLJ joined using epoxy adhesive and observed that changes in the roughness were not enough to explain joint strength improvement because other factors, such as the interface chemistry, needed to be taken into account, supporting the findings of this study.

Table 12: Surface roughness measurement for treated adherends

Surface Treatment	**Surface Roughness Arithmetic Mean R_a (µm)**
SD	0.28 ± 0.04
SDA	0.57 ± 0.02
SDGB	3.47 ± 0.16
SDDR	-
SDASG	0.48 ± 0.17
SDSG	0.20 ± 0.03
SEP	0.96 ± 0.19

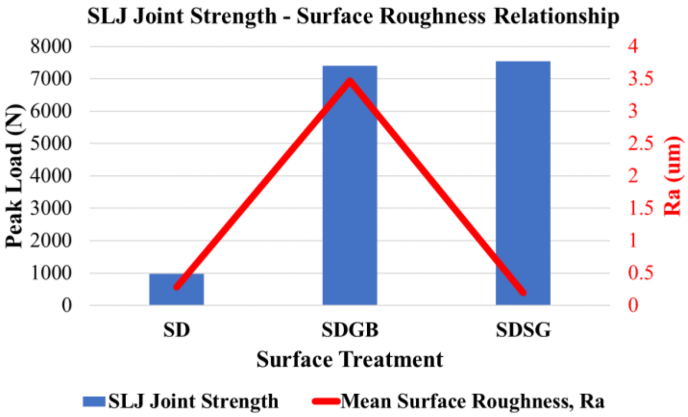

Figure 76: SLJ joint strength and mean surface roughness for adherends treated using solvent degreased (SD), grit-blasting (SDGB, mechanically treated adherend), and sol-gel (SDSG, chemically treated adherend).

The surface morphology of the SD baseline, SDGB and SDSG specimens was further assessed using an opto-digital microscope. The surface images showed that grit blasting changed the surface morphology creating a large number of ridges and valleys of various sizes (SDGB,

Figure 77). The mechanical theory attributed the improved adhesion to the increase in the adherend surface porosity and roughness (Cavezza *et al.*, 2020). The surface imaging showed that grit-blasted surfaces exhibited a change in the surface colour, from brownish (oxidized) to greyish aluminum colour, indicating a potential change in surface chemistry as well (SDGB versus SD, Figure 77). Surface imaging on the sol-gel treated surfaces showed a minor change in the surface colour compared to the solvent-degreased baseline aluminum substrate (SDSG versus SD, Figure 77). The sol-gel treatment (SDSG) deposited a coating with hybrid inorganic-organic compounds on the aluminum substrate, which achieved converted the surface chemistry without noticeable changes in surface colour or morphology.

The through-thickness imaging was undertaken to look at the near-surface deformed layer (NSDL) formed during the rolling process of the aluminum sheets. The through-thickness imaging of the aluminum sheet metal was undertaken for the SD baseline, SDGB and SDGB. The imaging analysis revealed that the grit blasting process removed the NSDL (Figure 78a and Figure 78b), which was reported to be a key factor that help increase the interfacial strength (Cavezza *et al.*, 2020). The chemical treatment (sol-gel) did not remove the NSDL; however, maximizing joint strength was still possible, leaving an open question about how the sheet metal rolling process plays an important role in aluminum sheet surface quality.

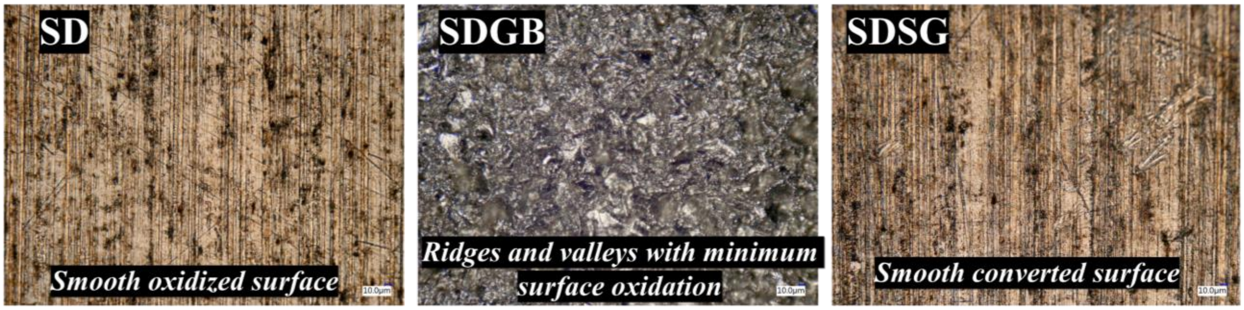

Figure 77: Surface imaging of aluminum sheet metal treated using SD, SDGB and SDSG.

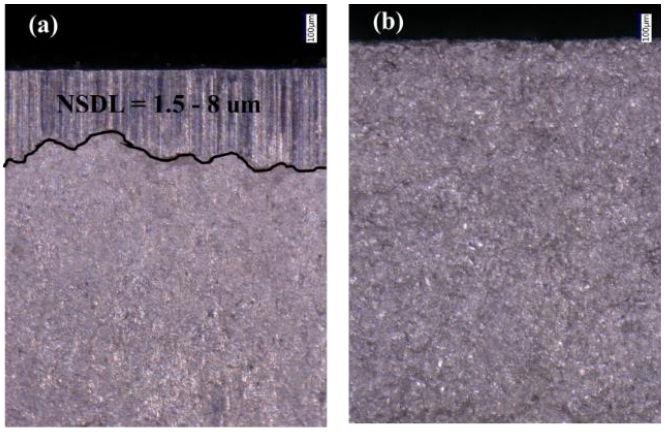

SD with Near Surface Deformed Layer (NSDL)

SDGB with NSDL Removed

Figure 78: Through thickness imaging of the aluminum substrate with near-surface deformed layer (NSDL) (a) versus grit-blasted substrate (b) with NSDL removed.

4.2.2 Effect of Wettability Behaviour on SLJ Joint Strength

The wettability of a surface is an indicator of the suitability of a surface for adhesive bonding, and in this section, the effect of wettability on SLJ joint strength was investigated for grit-blasted (SDGB) and sol-gel (SDSG) treated surfaces and compared with the baseline solvent-degreased (SD) aluminum adherends. In theory, the wettability of a liquid (*i.e.,* adhesive) can be quantified by measuring the contact angle of the liquid on the surface of a solid (aluminum alloy sheet in this work). However, the contact angle of adhesive is challenging to measure because epoxy has a high viscosity and poor mobility, making it difficult to place a sessile drop on the aluminum sheet without pressure (Xu *et al.*, 2016). Thus, the contact angle was measured for de-ionized (DI) water and Diiodomethane to measure the polar and dispersive surface energy components for the aluminum substrate after surface treatment application (Zheng *et al.*, 2015).

The measurements showed that the de-ionized water contact angle of the baseline SD and SDGB treatments were similar ($66.4^o \pm 7.5^o$, and $70.7^o \pm 1.5^o$, respectively), while the SDSG treatment decreased the water contact angle to $35.9^o \pm 1.9^o$ (Figure 79). The diiodomethane contact angles of the SD, SDGB and SDSG treatment were 55.0º ± 7.0º, 44.9º ± 2.3º, and 44.6º ± 0.7º, respectively (Figure 79). It was clear that the baseline aluminum substrate exhibited higher variability than the surfaces treated using grit blasting or sol-gel, attributed to the lower consistency of the untreated surfaces compared to the rigorously treated sheet metal. After calculating the surface free energy for each surface treatment (Figure 80), it was evident that the grit-blasting process used did not contribute to increasing the surface wettability (the overall surface free energy of the SD and SDGB was comparable (<3.1%)). The wettability of a grit-blasted substrate was reported to depend on several factors including the composition and size of abrasive media used during the process (Harris and Beevers, 1999), so the results should not be generalized. The surface free energy characterization value reported in the literature for grit blasted aluminum adherends (42.8 mJ/m^2) matched the value measured in this work (44.7 mJ/m^2) (Figure 80a) (Miturska-Barańska *et al.*, 2021). In contrast, the sol-gel treatment increased the surface free energy by (48.6%) relative to the baseline SD treatment, attributed to the sol-gel effect on the polar surface energy component (Figure 80a). Although the SDGB treatment showed an overall lower surface energy compared to the SDSG treatment, the average SLJ joint strengths were comparable and not statistically different (Figure 80b).

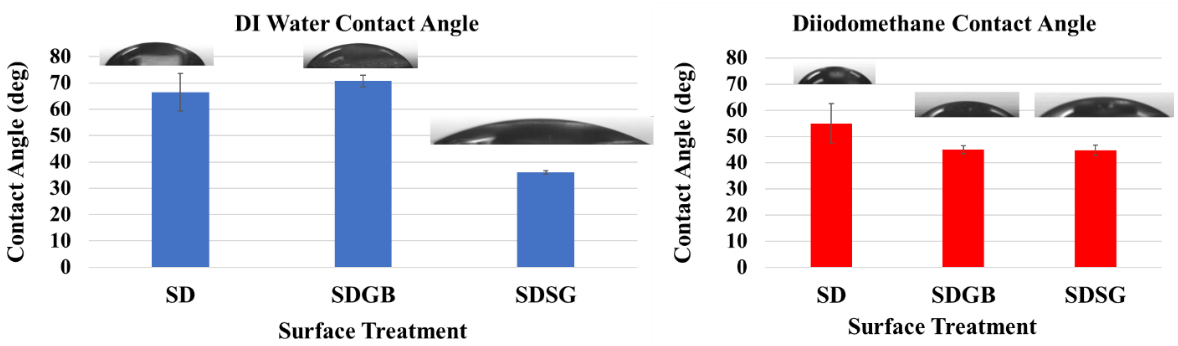

Figure 79: De-ionized (DI) water and diiodomethane contact angle measurements on treated aluminum AA6061-T6 substrates.

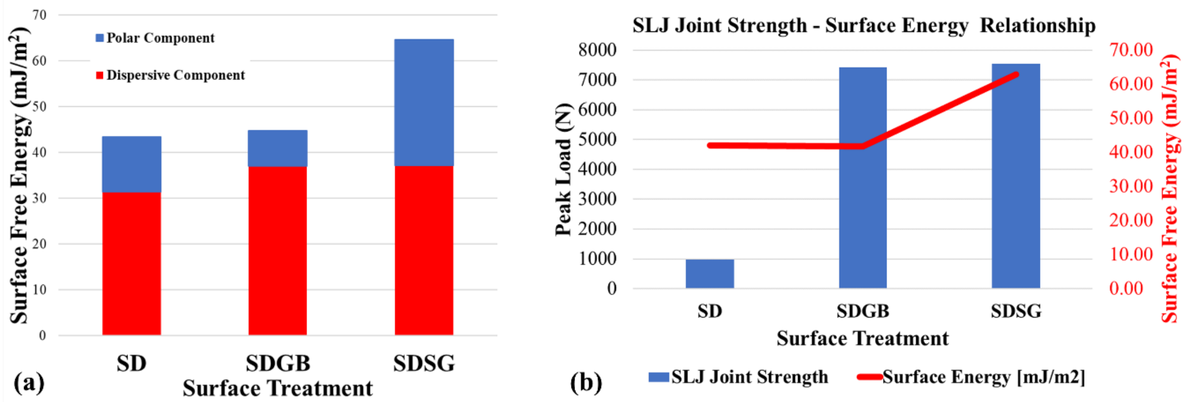

Figure 80: The surface free energy values for the SD, SDGB and SDSG treatments (a) and SLJ joint strength (b).

The effect of the polar and dispersive components of the surface energy on the SLJ joint strength was assessed for the baseline SD, SDGB and SDSG treatments. The results showed that the SDSG and SDGB treatments increased the dispersive components of the surface free energy, which could indicate that there could be a minimum threshold of dispersive surface free energy required to achieve proper adhesion (Figure 81b). According to the adsorption theory, the increase in dispersive energy increased the van der Waals forces, such as the London force, which are inherently weak but were reported to be important for adhesive bonding (Szewczak and Łagód, 2022). Thus, it was likely that grit-blasting has improved the SLJ joint strength and achieved cohesive failure due to a combination of improved mechanical interlocking, removed NSDL and higher van der Waals forces. The sol-gel treatment provided a surface that was ready for chemical bonding with improved polar surface energy and higher van der Waals forces. Also, it converted the weak hydroxylated oxides with a coat of organic-inorganic hybrid sol-gel, introducing an interface with a chemical composition ready for bonding.

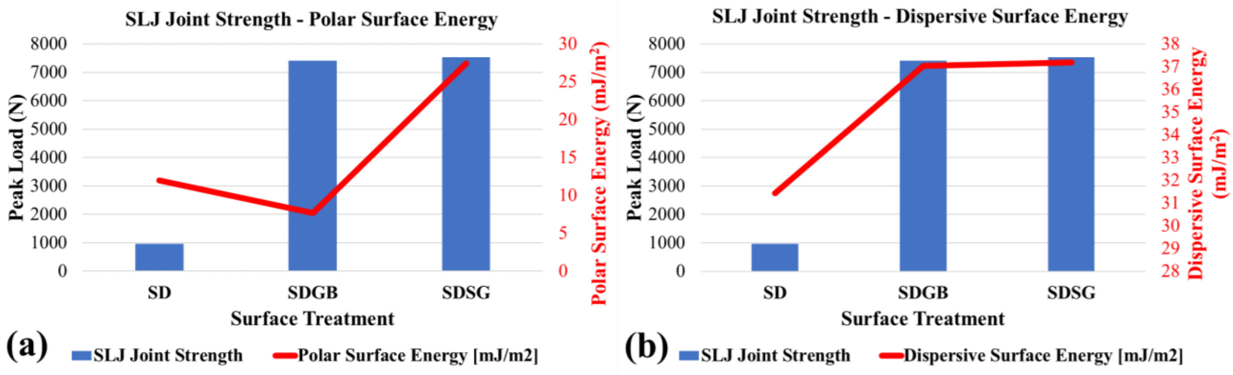

Figure 81: The SLJ joint strength versus the polar (a) and dispersive (b) components of the surface free energy.

One could conclude from the results that the SDGB and SDSG treatments had similar effectiveness but different mechanisms in achieving better adhesion. Grit blasting was deemed to be the appropriate method for this study because it was convenient, cost-efficient, and could be applied consistently in a lab environment. Importantly, grit blasting was reported to provide consistent reliability for adhesive joints, indicating that grit blasted adherends were less likely to fail due to interfacial failure (Liu and Dawood, 2017). For large bond areas or large-volume applications, one could argue that the SDSG treatment could be a strong candidate for surface treatment because it is a one-step method that does not require another pre-treatment method (*e.g.*, grit blasting) or the use of hazardous chemicals (*e.g.*, chromate), making it suitable for industrial environments. Industrial applications could require assessing the influence of environmental conditions, such as moisture, contamination and temperature, on the surface treatment to ensure adhesive joint reliability in service (Borges et al., 2021).

4.3 Quantification of Adhesive, SPR and Hybrid Joint Morphology and Physical Attributes

4.3.1 Measurement of SPR and Hybrid Joined Physical Attributes using Flat Specimens

Cross sections of flat specimens joined using SPR-only and hybrid joining were evaluated using the opto-digital microscope. The 20x zoomed images allowed for the measurement of the rivet's physical attributes, and comparison to literature guidelines (Haque, 2018; Li *et al.*, 2017) relevant to the automotive industry. The guidelines recommended a head height close to zero, a bottom thickness larger than 0.2 mm, a mechanical interlock ([final flared rivet diameter - initial undeformed rivet diameter] / 2) larger than 0.4 mm and a rivet leg with no buckling (Haque, 2018; Li *et al.*, 2017) (Figure 44). After assessing the physical attributes, it was important to understand how hybrid joining influenced these attributes in addition to the adhesive layer morphology within the vicinity of the rivet. First, the imaging of the SPR and hybrid joints made with AA5052-H32 alloy with varying sheet thicknesses is presented for the three sheet thicknesses used in this work (1 mm, 2 mm, and 3 mm) to assess the joints according to literature guidelines and understand the effect of hybrid joining on the SPR rivet attributes.

The 1 mm – 1 mm SPR and hybrid joints met the literature guidelines, and it was clear that the presence of the adhesive did not influence the SPR rivet formation (both joints showed similar measurements within < 10%) (Figure 82). Importantly, the adhesive squeeze-out resulted in a non-uniform bond line thickness, such that the bond line thickness increased moving away from the centre of the rivet. The adhesive was observed after 6 mm from the centre of the rivet diameter and the adhesive bond line thickness increased almost linearly to 0.269 mm (at 13.5 mm) (Figure 83).

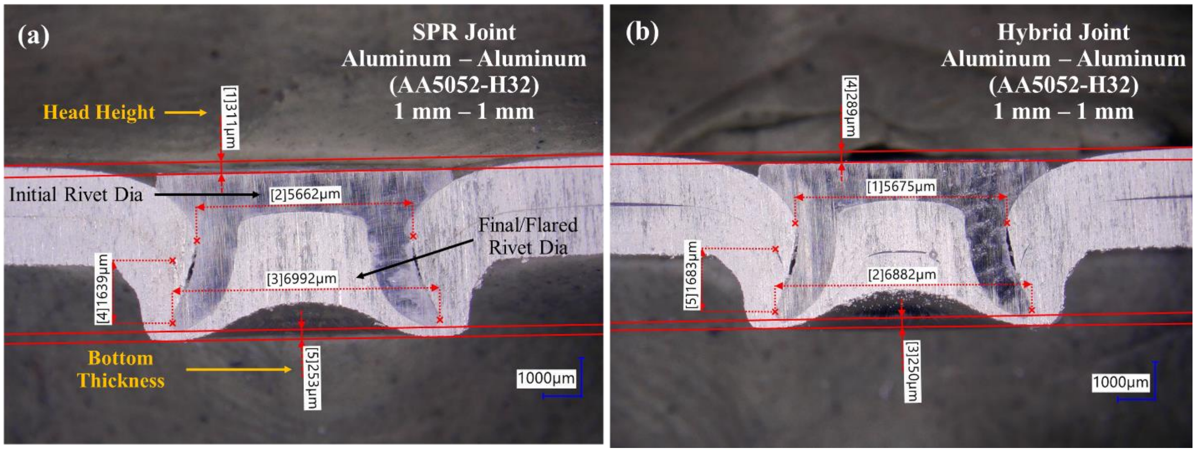

Figure 82: Cross-sectional imaging of SPR (a) and hybrid joints (b) made with 1 mm-thick aluminum AA5052-H32 alloy, showing the measured physical attributes.

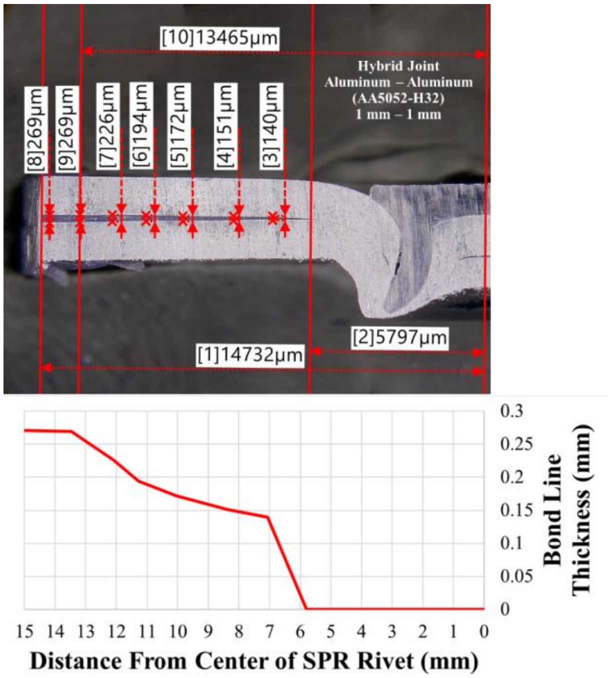

Figure 83: Bond line thickness measurements on hybrid joints made with 1 mm-thick aluminum. AA5052-H32 alloy

The 2 mm – 2 mm SPR and hybrid joints met the literature guidelines, and the adhesive presence did not affect the mechanical interlock, the bottom thickness or the head height (Figure 84). The adhesive squeeze-out increased compared to the 1 mm – 1 mm joints, and consequently, the maximum adhesive bond line thickness decreased to 0.183 mm (-31.9% relative to the 1 mm

– 1 mm joints) at ~15 mm from the centre of the rivet (Figure 85). The 3 mm – 3 mm SPR and hybrid joints also met the literature guidelines, and the bond line thickness experienced further reduction, resulting in a complete adhesive squeeze out (no adhesive observed in the hybrid joints even at 15 mm from the centre of the rivet) (Figure 86).

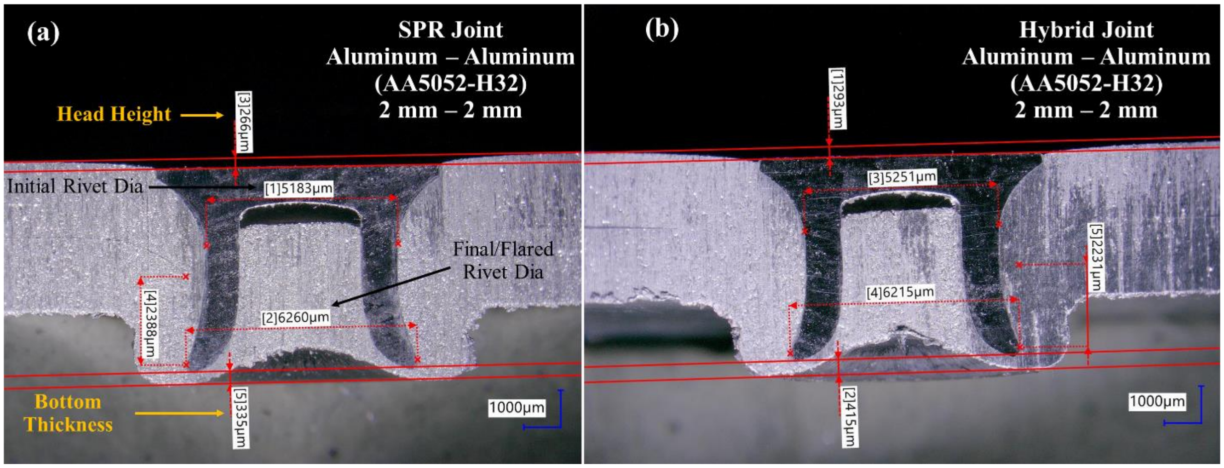

Figure 84: Cross-sectional imaging of SPR (a) and hybrid joints (b) made with 2 mm-thick aluminum AA5052-H32 alloy, showing the measured physical attributes.

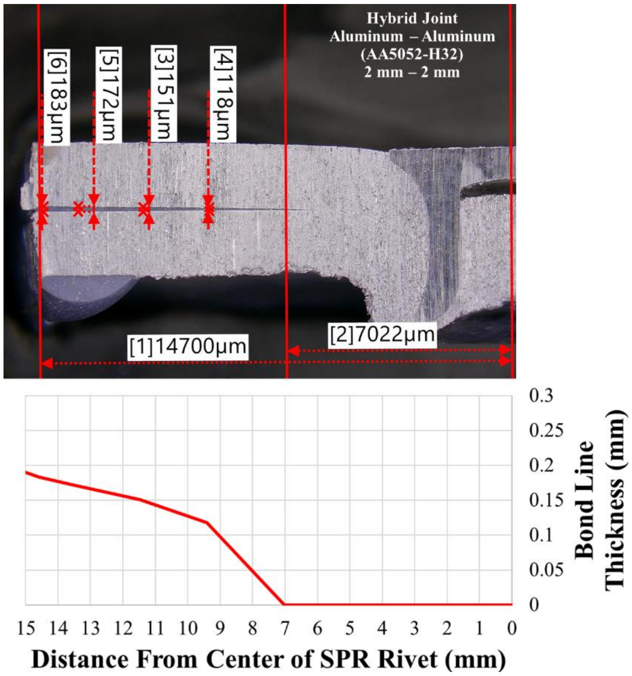

Figure 85: Bond line thickness measurements on hybrid joints made with 2 mm-thick aluminum AA5052-H32 alloy.

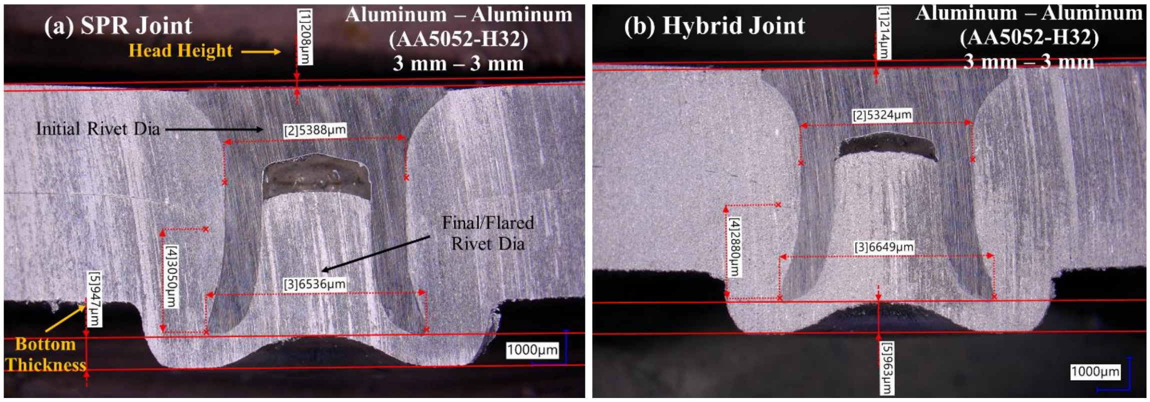

Figure 86: Cross-sectional imaging of SPR (a) and hybrid joints (b) made with 3 mm-thick aluminum AA5052-H32 alloy, showing the measured physical attributes.

In general, the mechanical interlock measurements of the SPR-only joints were relatively consistent for the three sheet thicknesses with a mean value of 0.62 mm, 0.54 mm and 0.57 for the 1 mm, 2 mm, and 3 mm sheets, respectively. The mechanical interlock measurements of the hybrid joints were the same as the SPR-only joints for the 1 and 2 mm joints, and within 0.1 mm for the 3 mm joints (Figure 87a). The bottom thickness measurements were also compared for the two joining methods, and it was observed that the SPR-only and hybrid joints were generally within 0.06 mm (Figure 87b). Thus, the measurements and general observations indicated that hybrid joining did not have a substantial effect on the SPR rivet formation for the joints made with AA5052 among the sheet thicknesses considered.

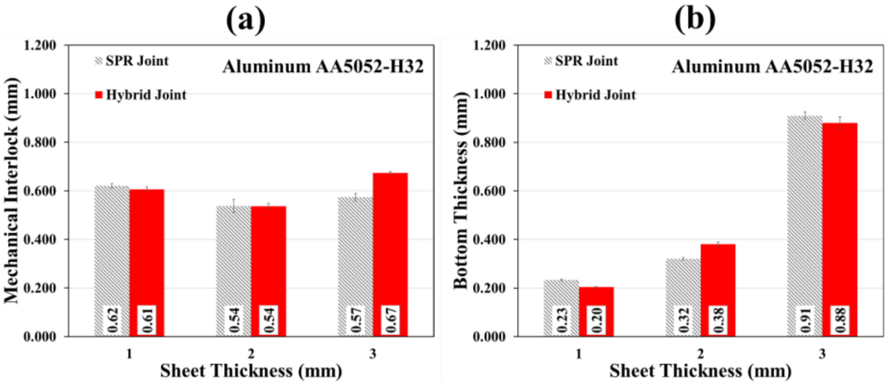

Figure 87: Mechanical interlock (a) and bottom thickness (b) measurements for SPR and hybrid joints made with aluminum AA5051-H32 for varying sheet thicknesses.

The joints created with the AA6061-T6 alloy showed some similarities to the joints made with the AA5052 alloy. The adhesive bond line thickness was non-uniform and increasing sheet metal thickness resulted in a higher degree of adhesive squeeze-out (Figure 88). The mechanical interlock measurements of the SPR-only joints were relatively consistent for the three sheet thicknesses with a mean value of 0.89 mm, 0.90 mm and 0.95 for the 1 mm, 2 mm and 3 mm sheets, respectively (Figure 89a). The mechanical interlock measurements for hybrid joints were the same as the SPR-only measurements for the 1 and 3 mm joints (within 0.02 mm), and somewhat lower for the 2 mm hybrid joints (within 0.2 mm) (Figure 89a). The reduction of the mechanical interlock by 0.2 mm could reduce the upper bound of the expected peak load (Haque and Durandet, 2016; Sun and Khaleel, 2005). The bottom thickness measurements for the SPR-only and hybrid joints were generally within 0.05 mm (Figure 89b), except for the 3 mm joints showing 0.38 mm higher bottom thickness for the hybrid joints (+19.7% relative to SPR-only joints). The higher strength, thicker alloy resisted deformation and had a substantially larger volume of material; however, only a limited material volume could flow within the constant die volume. Thus, the presence of the adhesive increased the head height by ~0.25 mm, and consequently, the bottom thickness increased by an amount close to the value of the increased head height. The increase in bottom thickness could decrease joint strength in the case of an SPR rivet tail pull-out because the volume of effective material within the mechanical interlock (also known as effective thickness) will be lower (Haque and Durandet, 2016; Sun and Khaleel, 2005). Importantly, the SPR rivets in the hybrid joints did not exhibit cracks, as has been observed in other hybrid joining studies (Haque, 2018).

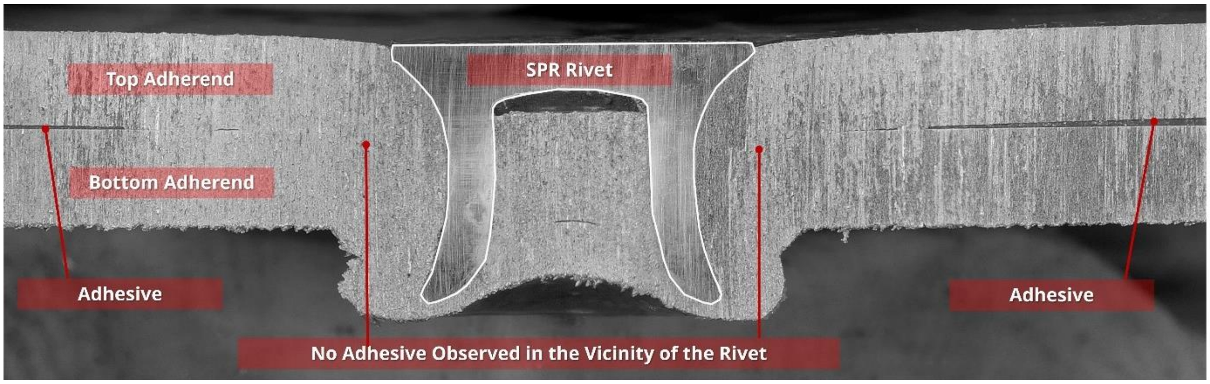

Figure 88: Hybrid joint made with 2 mm thick aluminum AA6061-T6 alloy, showing bond line thickness non-uniformity.

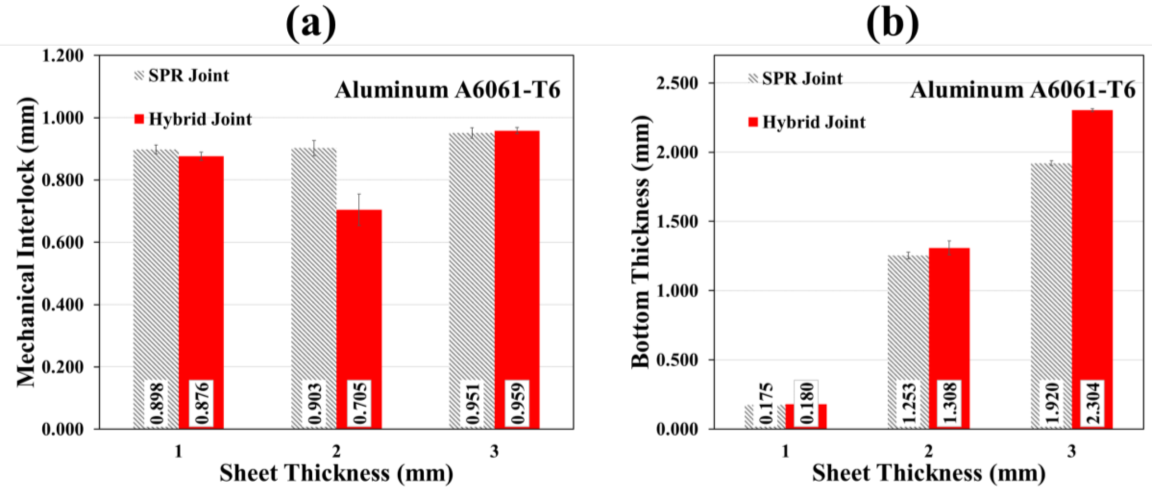

Figure 89: Mechanical interlock (a) and bottom thickness (b) measurements for SPR and hybrid joints made with aluminum AA6061-T6 for varying sheet thicknesses.

The cross-section imaging also allowed identifying that the joints were susceptible to joint formation flaws, such as the joint flaws due to inadequate SPR rivet insertion force. For instance, the 2 mm joints made with the AA6061 alloy experienced base material cracking in the bottom sheet when the SPR insertion force was increased by 25% (10 kN) (Figure 90), supporting early work by Hahn and Wibbeke (2005). The joint flaw (*i.e.,* bottom sheet cracking) was not visually detectable, highlighting that cross-section imaging was not only necessary to ensure that the joints met the literature guidelines but also to identify the adequate SPR sitting force for each sheet thickness.

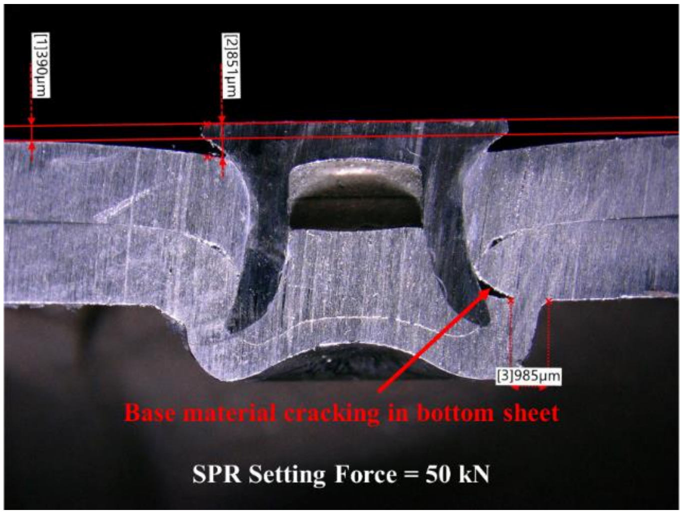

Figure 90: SPR joint made with 2 mm-thick aluminum AA6061-T6 alloy showing base material cracking when setting force was increased by 10 kN (25%).

In general, the SPR and hybrid joints made with AA6061 alloy exhibited higher mechanical interlock relative to the AA5052 alloy (37% on average, Figure 87a and Figure 89a). The riveting parameters, such as insertion force, rivet characteristics, and die material and geometry, were identical for both alloys, so it could be inferred that the difference in mechanical interlock was caused by the mechanical properties of the alloy (*i.e.*, ductility and formability). The higher strength, lower ductility alloy had greater resistance to deformation and penetration, which increased rivet flaring during the SPR cold forming process. Importantly, the presence of the adhesive in the hybrid joint did not generally affect the SPR rivet formation for the joints made with AA6061 or AA5052 alloys. The joint morphology and physical attributes measurements carried out on adhesive, SPR and hybrid joints made with varying sheet thicknesses and aluminum alloys enabled quantifying the influence of hybrid joining on the SPR and adhesive morphologies.

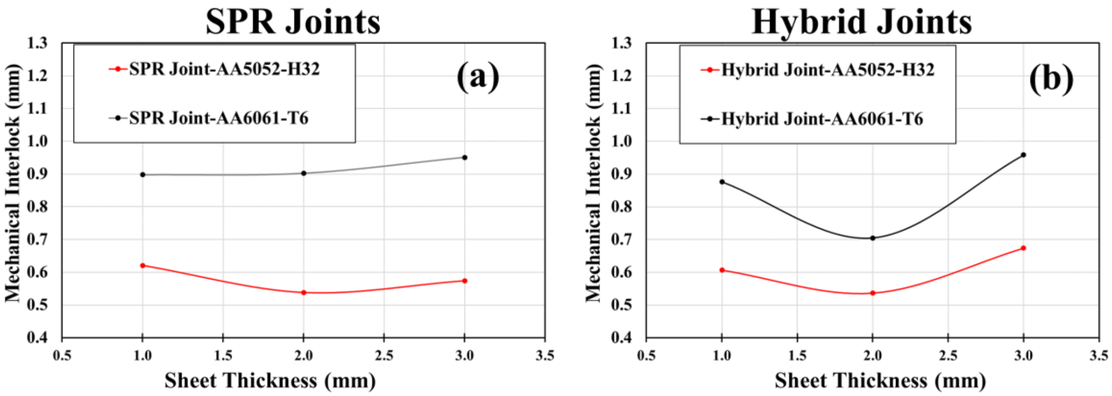

Figure 91: Mechanical interlock of SPR and hybrid joints made with aluminum AA5052-H32 and AA6061-T6 alloys.

4.3.2 Measurement of Bond Line Thickness in Adhesive and Hybrid Joined H-shaped and SLJ Specimens

Imaging and measurements of adhesive and hybrid joined H-specimens made from the two aluminum alloys (*i.e.*, AA6061 and AA5052) demonstrated that the bond line thickness of the adhesive and hybrid joints was consistent, and ranged from 0.406 mm to 0.493 mm for adhesive joints and 0.248 mm to 0.373 mm for hybrid joints (Figure 92a and Figure 92b). Adhesive bond line thickness has been reported to influence the mechanical response of adhesives (Davies *et al.*, 2009). Therefore, it was crucial to measure adhesive bond line thickness in adhesive and hybrid joints, and assess its effect on the joint strength. The average adhesive bond line thickness in hybrid joints was 38% lower (on average) than in adhesive joints made with the AA6061 alloy. Similarly, the hybrid joints made with the AA5052 alloy were affected by the bond line thickness reduction, but the effect was less pronounced than the AA6061-T6 (average bond line thickness was 27.5% lower than adhesive joints) and showed more variability. It was obvious that hybrid joining generally decreased the bond line thickness of adhesive, attributed to adhesive squeeze out during the SPR insertion process, which requires high loads ranging between 30-50 kN. An important observation was that the bond line thickness reduction varied according to sheet thickness. For example, the AA5052 alloy had limited influence on 1 mm joints but a considerable influence on the 3 mm joints and the same observation was made for the AA6061 alloy as well.

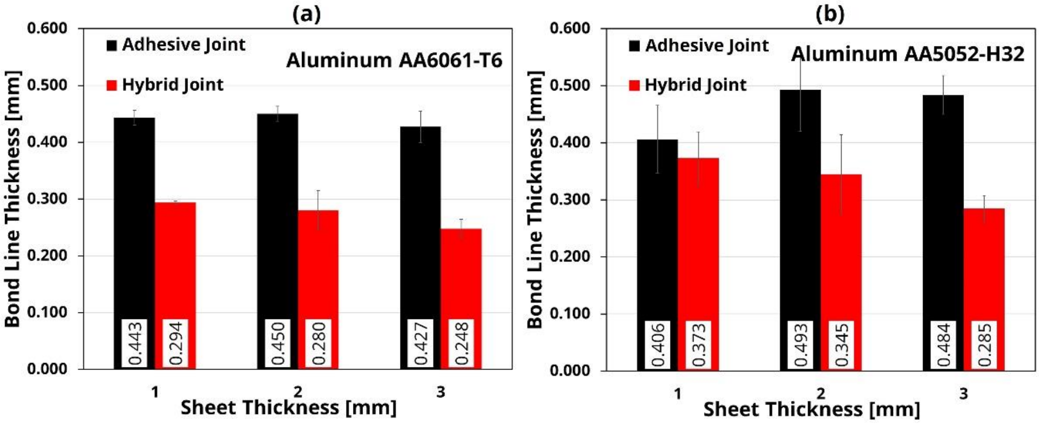

Figure 92: Bond line thickness measurements of adhesive-only and hybrid joints made with aluminum AA6061-T6 (a) and AA5052-H32 (b)

Similar measurements were undertaken on the side of the SLJ specimens, made with the AA6061-T6 alloy and joined using adhesive-only and hybrid joining. The adhesive-only joints demonstrated that the bond line thickness of the adhesive joints ranged from 0.489 mm to 0.519 mm, which was within <0.1 mm of the measurements of H-specimens, highlighting that the bond line thickness was rigorously maintained for all the joints used in this study. The bond line thickness of the hybrid joints showed a substantially larger range (0.287 mm to 0.685). In particular, the 1 mm joints showed larger bond line thickness relative to adhesive-only joints (+40%) because the sheet material deformed during the rivet insertion process (Figure 93), resulting in a non-uniform bond line thickness. On the other hand, the thicker 3 mm sheet material resisted deformation causing a substantial amount of adhesive to squeeze out during the rivet insertion process, which reduced the bond line thickness by 44% relative to the adhesive-only joints (Figure 93). It was clear that hybrid joining generally induced adhesive squeeze-out and non-uniform bond line thickness. A similar observation was reported by Meschut *et al.* (2014), but their study did not quantify these effects.

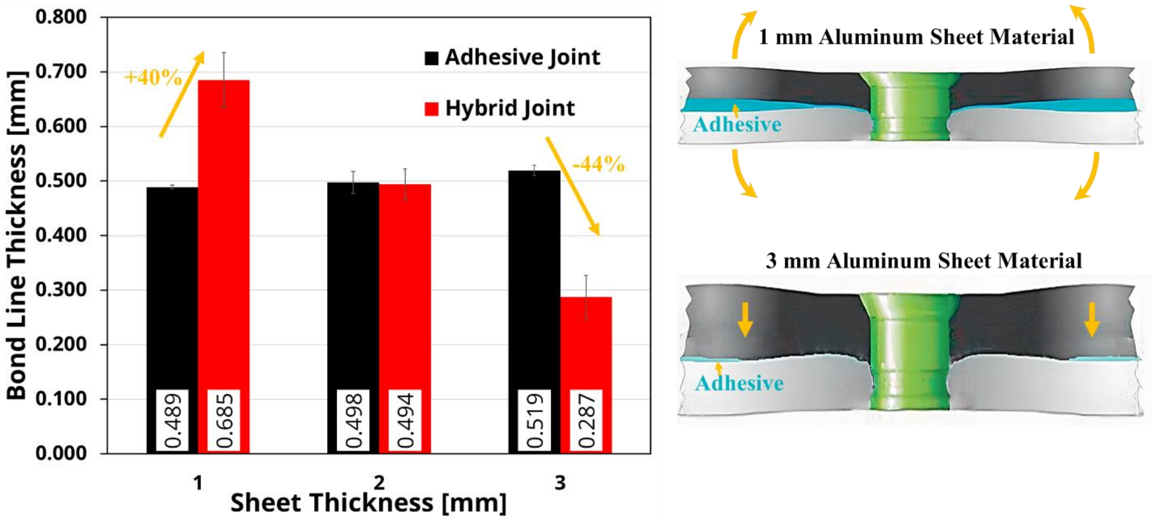

Figure 93: Bond line thickness measurements of the adhesive-only and hybrid joined SLJ specimens made with aluminum AA6061-T6. Illustrations adapted from Meschut *et al.* (2014)

4.4 H-Specimen Testing of Adhesive, SPR and Hybrid Joints

4.4.1 Mechanical Response of Joints Made with AA6061-T6 Alloy

The mechanical response of adhesive-only, SPR-only and hybrid joints was assessed under tension loading using H-specimen tests. Adhesive joints exhibited an average peak load of 2.06 kN for the (1+1) mm joint, 4.92 kN for the (2+2) mm joint (139% increase over 1 mm joints), and 8.39 kN for the (3+3) mm joints (307% and 71% increase over the 1 mm and 2 mm joints, respectively) (Table 13). The load was initially distributed along the two 50 mm adhesive edges, which induced bending deformation at the bend radii of the U-section and initiated a crack along the adhesive edges. The initial crack extension was followed by a crack arrest, causing the load to increase again. After that, the crack rapidly progressed toward the centerline as the load reached its peak, indicating some adhesive ductility. The joint failed abruptly after reaching the peak load, and cohesive failure was observed for all test specimens. Importantly, adhesive joints generally demonstrated higher peak load and stiffness when compared to SPR joints. In contrast, the displacement at failure for adhesive joints was significantly lower than SPR and hybrid joining, attributed to the higher stiffness response and limited specimen deformation prior to failure. Therefore, adhesive joints showed the lowest energy absorption (Table 13), owing to the marginal contribution of specimen deformation and relatively low energy for adhesive crack propagation.

SPR joints failed at higher displacements relative to the adhesive joints, but generally demonstrated lower average peak loads of 1.84 kN, 4.66 kN and 6.96 kN for the (1+1) mm, (2+2) mm and (3+3) mm joints, respectively (Table 13). The average peak loads were 11%, 5.3%, and 17% lower than those of the (1+1) mm, (2+2) mm, and (3+3) mm adhesive joints, respectively. The force-displacement curves (Figure 94b) demonstrated a smooth, gradual degradation in stiffness up to the peak load, and unloading also continued with gradual softening until ultimate failure. The joints exhibited significant localized plastic deformation around the rivet, and the rivet tail lost the mechanical interlock with the bottom sheet, failing in a tail pull-out mode. While SPR joint stiffness was significantly lower compared to adhesive joints, the plastic strain energy stored during the localized specimen deformation increased the overall energy absorption of the SPR joints relative to adhesive joints (up to 352%).

The response of the hybrid joints appeared to follow those of the adhesive joints initially; however, when adhesive damage extended to the SPR rivet, the load dropped sharply, then the load-displacement response followed those of the SPR joints. The hybrid joints generally failed at displacement values close to those of the SPR joints. The average peak load of the hybrid joints made with 1- and 2-mm sheet material was comparable to the adhesive joints (difference of less than 8%) with no statistically significant difference (Table 13).

Table 13: Mechanical performance and joint-level morphology summary for the adhesive, SPR and hybrid joints made with aluminum AA6061-T6 alloy.

Joining Method	**Adhesive Joining**			**SPR Joining**			**Hybrid Joining**		
	(1+1) mm	**(2+2) mm**	**(3+3) mm**	**(1+1) mm**	**(2+2) mm**	**(3+3) mm**	**(1+1) mm**	**(2+2) mm**	**(3+3) mm**
Peak Load (N)	2,065 ± 202	4,925 ± 507	8,397 ± 736	1,841 ± 71	4,663 ± 143	6,966 ± 179	2,225 ± 76	4,533 ± 180	7,128 ± 199
Stiffness (N/mm)	6,392 ± 1063	13,959 ± 971	22,109 ± 4930	1,235 ± 252	2,674 ± 189	10,607 ± 1056	6,869 ± 737	14,348 ± 1104	13,728 ± 3456
Energy Absorption (J)	3.84 ± 0.40	4.20 ± 0.96	4.83 ± 1.06	5.98 ± 1.35	19.00 ± 3.23	11.40 ± 0.59	9.18 ± 0.55	18.33 ± 0.10	13.79 ± 0.80
Bond line Thickness (mm)	0.443 ± 0.022	0.450 ± 0.023	0.427 ± 0.048	-	-	-	0.294 ± 0.005	0.280 ± 0.061	0.248 ± 0.029
Mechanical Interlock (mm)	-	-	-	0.898 ± 0.025	0.903 ± 0.043	0.951 ± 0.029	0.876 ± 0.022	0.705 ± 0.087	0.959 ± 0.018
Bonding Area (mm^2)	928	928	928	-	-	-	829 (-10.7%)	809 (-12.8%)	763 (-17.8%)
Specimen Weight (grams) (% relative to adhesive joints)	21.45 ± 0.03	42.26 ± 0.14	68.40 ± 0.57	-3.0%	-0.6%	-0.4%	+4.5%	+1.6%	+1.0%

The peak load corresponded to adhesive failure, suggesting that the mechanical interlock of the SPR rivet is more relevant to the displacement at failure and energy absorption of the joint rather than the peak load. Thus, the variation in the SPR physical attributes due to hybrid joining (reported in section 4.3.1 for the 2- and 3-mm AA6061-T6 joints) did not influence the hybrid joint peak load. The load response demonstrated two rapid decreases due to the discontinuity of the adhesive layer around the rivet, which was caused by adhesive squeeze out during rivet insertion. Importantly, the hybrid joints demonstrated the highest energy absorption, owing to the combined energy absorption mechanisms of adhesive and SPR joints. Another important aspect was that the mechanical performance benefits of hybrid joining were realized with a weight increase of less than 5% (as low as 1%) relative to individual joints (Table 13).

In general, the H-specimen test showed good repeatability and consistency (Figure 94) with somewhat higher variability in the displacement at failure for SPR joints (Figure 94b) and stiffness for the 3 mm hybrid joints (Figure 94c). The displacement at failure variability of the SPR joints could be attributed to the progressive change in the H-specimen compliance as the SPR joint gradually lost the mechanical interlock after reaching the peak load. Hybrid joints with 3 mm sheet material demonstrated mechanical response variability, owing to the variability in adhesive morphology (*e.g.,* adhesive squeeze out, bond line thickness non-uniformity and reduction, induced adhesive porosity) during the application of SPR rivet with uncured adhesive. The variability in the mechanical response of hybrid joints may explain a limitation and the high process variability in the commonly adopted (traditional) SPR-adhesive hybrid joining application.

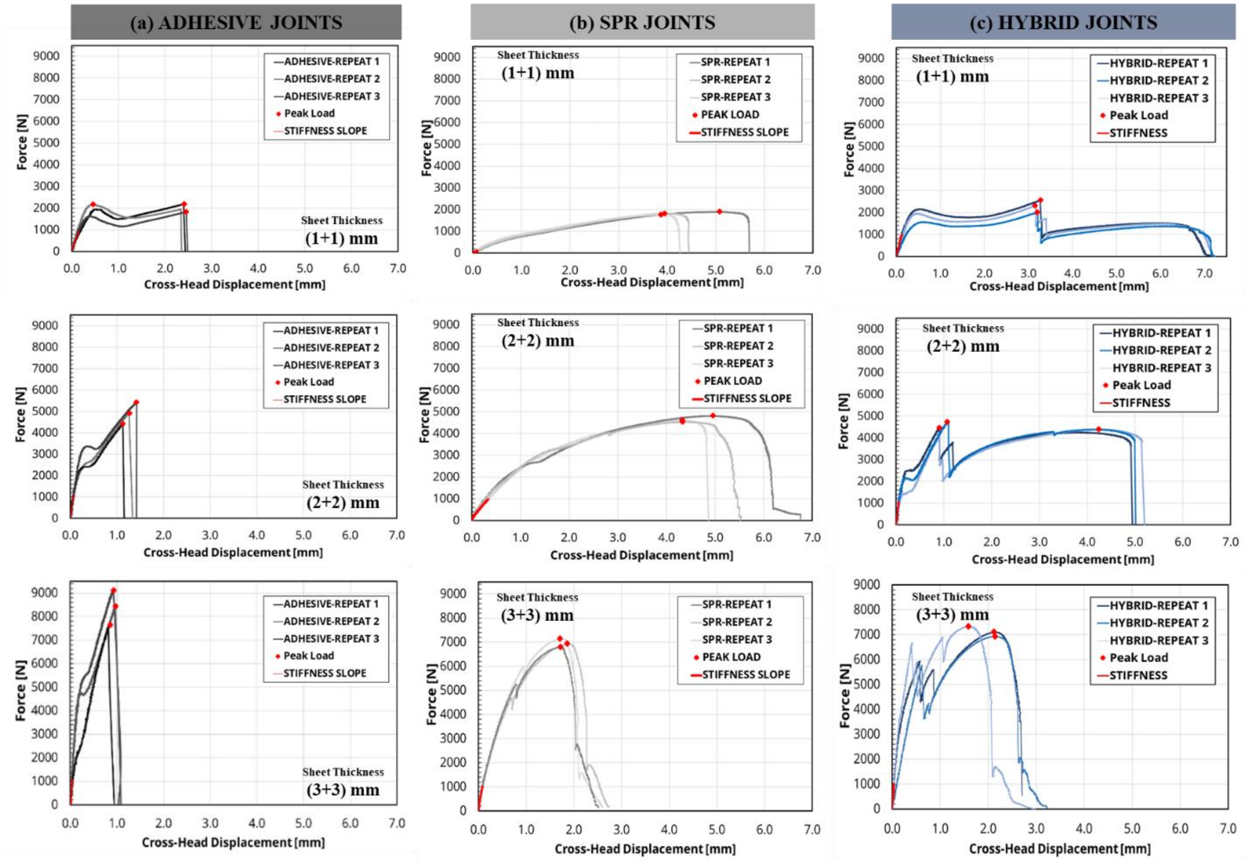

Figure 94: Force-displacement response measurement of adhesive (column a), SPR (column b) and hybrid (column c) joints made with aluminum AA6061-T6 alloy.

4.4.1.1 Failure Surface Analysis

The failure surfaces demonstrated that adhesive specimens achieved a cohesive failure; thus, the strength of the adhesive was maximized for the joints assessed in this study. A crack initiated in the adhesive at the edges along the length of the specimen; then progressed toward the centre leading to joint abrupt separation (Figure 95a). SPR specimens exhibited tail pull-out failure, indicating that the SPR mechanical interlock played a key role in determining SPR joint strength (Han *et al.*, 2010) (Figure 95b). Hybrid joints exhibited crack initiation and progression similar to adhesive joints, followed by a rivet tail pull-out similar to SPR joints, combining the deformation mechanisms seen in adhesive and SPR joints. The failure surfaces of hybrid joints revealed a reduction in effective bonding area as a circular area around the SPR rivet showed no adhesive, attributed to adhesive squeeze out during SPR rivet insertion (Figure 95c).

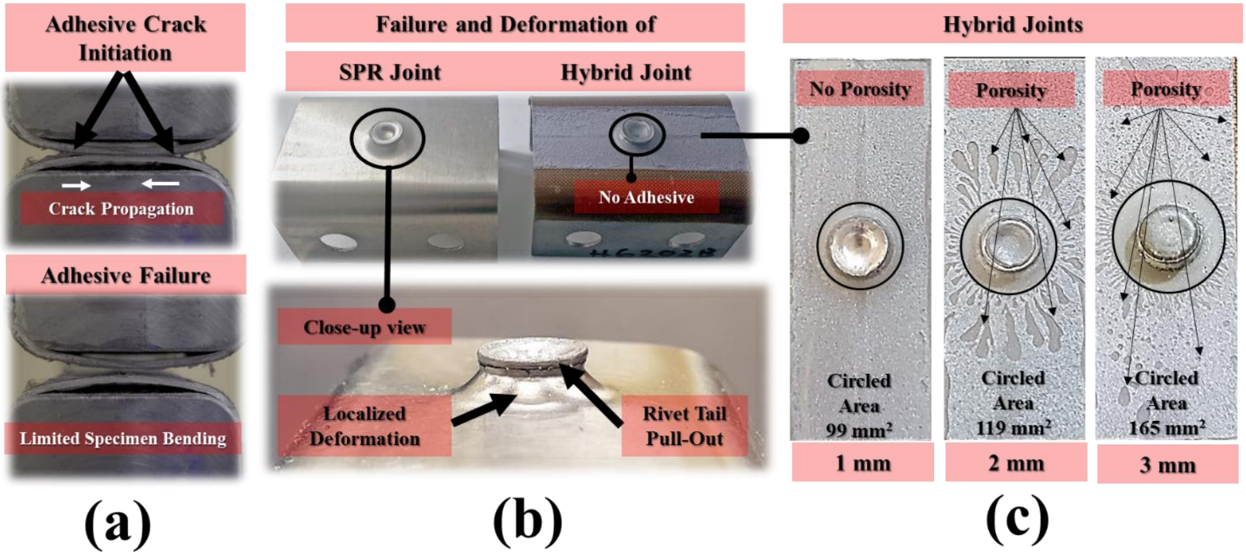

Figure 95: Adhesive crack initiation and progression (a), localized deformation in SPR and hybrid joints (b) and failure surfaces of hybrid joints with three sheet thicknesses.

The amount of squeeze-out varied according to the sheet thickness. The (1+1) mm joint experienced a 10.7% (99 mm^2) reduction in the bonding area, while the (2+2) mm and (3+3) mm joints exhibited an area reduction of 12.8% (119 mm^2) and 17.8% (165 mm^2), respectively. Importantly, the failure surface evaluation showed that the (2+2) mm joints exhibited porosity (air cavities) within the adhesive layer in the vicinity of the rivet, which was likely induced during the SPR insertion process. The higher SPR insertion force, required by the (3+3) mm joints, induced higher porosity within the adhesive layer, smaller in size but scattered throughout the bonding area. Importantly, the bonding area reduction did not significantly affect the hybrid joint peak load of the (1+1) and (2+2) mm joints. However, the (3+3) mm joints experienced a statistically significant reduction in joint strength and stiffness, which was attributed to the combined effect of reduced bonding area, reduced bond line thickness below the recommended manufacturer value

(0.25 mm), and scattered porosity closer to the boundaries of the adhesive. The porosity was likely induced by air pockets entrapped during adhesive flow (*i.e.,* squeeze out). In addition, Kaufmann *et al.* (2023), who have recently studied adhesive flow to achieve a bond without trapped air pockets using adhesive squeeze flow experiments, have reported phenomena called viscous fingering, which produced similar air pockets to the ones seen in this study.

4.4.1.2 Effect of Joining Method and Sheet Thickness on Mechanical Response

Two-way repeated-measures analysis of variance (ANOVA) revealed that the joining method and sheet thickness had significant effects on joint strength ($p < .05$, $\eta_p{}^2{}_{\text{joining method}} = .511$, $\eta_p{}^2{}_{\text{sheet thickness}} = .936$), stiffness ($p < .05$, $\eta_p{}^2{}_{\text{joining method}} = .849$, $\eta_p{}^2{}_{\text{sheet thickness}} = .856$) and energy absorption ($p < .05$, $\eta_p{}^2{}_{\text{joining method}} = .936$, $\eta_p{}^2{}_{\text{sheet thickness}} = .889$). A significant interaction was reported between the two independent variables, meaning that the effect of sheet metal thickness on joint strength, stiffness and energy absorption changed according to the joining method. To isolate the statistical differences, Tukey post hoc pairwise comparison with Sidak correction for multiple comparisons was undertaken.

The post hoc comparison showed that the peak load values of the (1+1) and (2 + 2) mm joints were not significantly different among the three joining methods ($p > 0.4$, Figure 96). However, the joint strength of adhesive joints was significantly higher for the (3+3) mm joints, achieving 20.5% and 18% higher average peak load compared to SPR and hybrid joints, respectively. Interaction plots showed that adhesive, SPR and hybrid joints exhibited a relatively linear increase in joint strength with increasing sheet metal thickness (Figure 99a). A similar relationship was reported for adhesive SLJ joints by da Silva *et al.* (2009), which suggests that the influence of adherend thickness on the strength of adhesive joints is likely linear regardless of loading orientation.

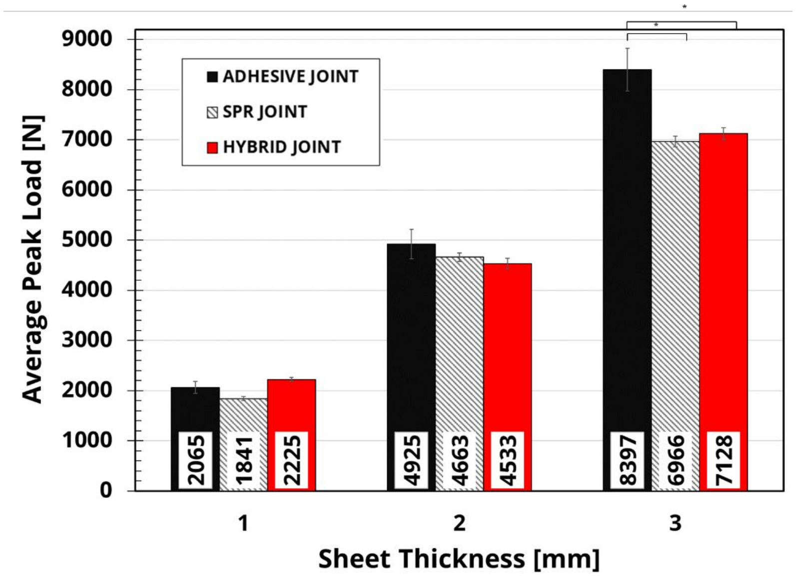

Figure 96: A comparison of average peak load for adhesive, SPR and hybrid joints made with aluminum AA6061-T6 alloy (*statistically significant different groups are marked and error bars represent the standard error)

The stiffness response of adhesive joints was significantly higher than those of SPR (108%) and hybrid joints (61%) for the (3+3) mm joints; however, for the (1+1) and (2+2) mm joints, adhesive and hybrid joining were not statistically different ($p_{(1\ mm)}$= 0.990 and $p_{(2\ mm)}$= 0.995) (Figure 97), demonstrating significantly higher stiffness (up to 422%) compared to SPR joints. The stiffness of the adhesive joints increased linearly with sheet thickness, which reduced the overall specimen compliance and displacement at failure. Although the load at failure increased, the reduction in specimen deformation and displacement at failure damped the energy absorption capabilities of the adhesive joints. In contrast, SPR joints showed a nonlinear trend with a significant stiffness increase for the 3 mm joints. The SPR joints made with 2 mm sheet material demonstrated significant localized deformation and slower rivet tail pull-out progression, which led to somewhat higher displacement at failure relative to the 1 mm SPR joints. However, when sheet thickness was increased to 3 mm, the SPR joint stiffness was about an order of magnitude larger than 1 mm joints and localized yielding was considerably reduced, which led to a rivet tail pull-out at lower displacement at failure. In hybrid joints, an increase in stiffness was observed from 1 to 2 mm, but from 2 to 3 mm, the stiffness was similar (Figure 99b), highlighting the influence of morphology (*e.g.*, bond line thickness reduction and scattered porosity) on the mechanical performance of joints with thicker adherends.

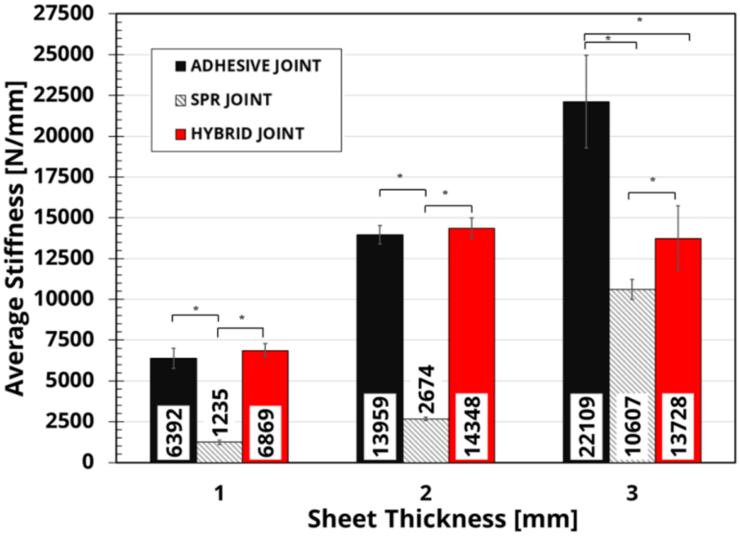

Figure 97: The average stiffness of adhesive, SPR and hybrid joints made with aluminum AA6061-T6 alloy (*statistically significant different groups are marked and error bars represent the standard error)

The energy absorption values of SPR and hybrid joints were significantly higher relative to adhesive joints ($p < 0.05$), demonstrating up to 352% higher energy absorption for the range of sheet thicknesses considered (Figure 98). Sheet thickness did not show a statistically significant effect on the energy absorption of the adhesive joints. In contrast, the energy absorption of SPR and hybrid joints varied significantly according to sheet thickness and showed a maximum value for (2+2) mm joints (Figure 99c). The 2 mm material demonstrated significant localized deformation around the rivet and maintained the mechanical interlock with the rivet tail. On the contrary, the 3 mm material did not exhibit considerable deformation prior to failure, leading to a reduction in the overall energy absorption of the joint.

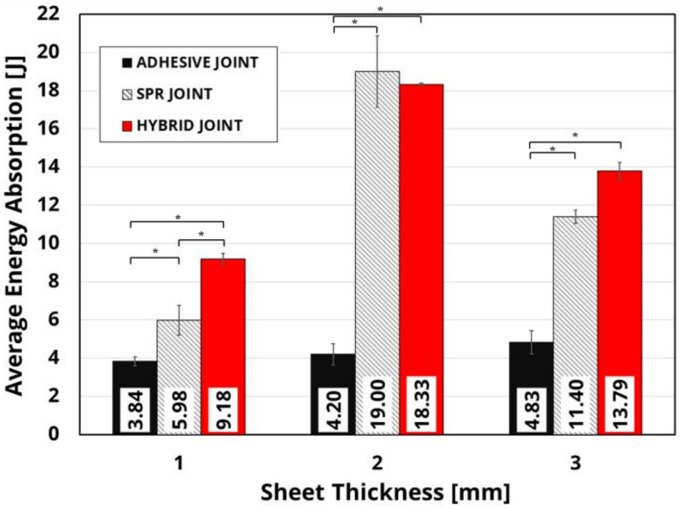

Figure 98: The average energy absorption for adhesive, SPR and hybrid joints made with aluminum AA6061-T6 alloy (*statistically significant different groups are marked and error bars represent standard error)

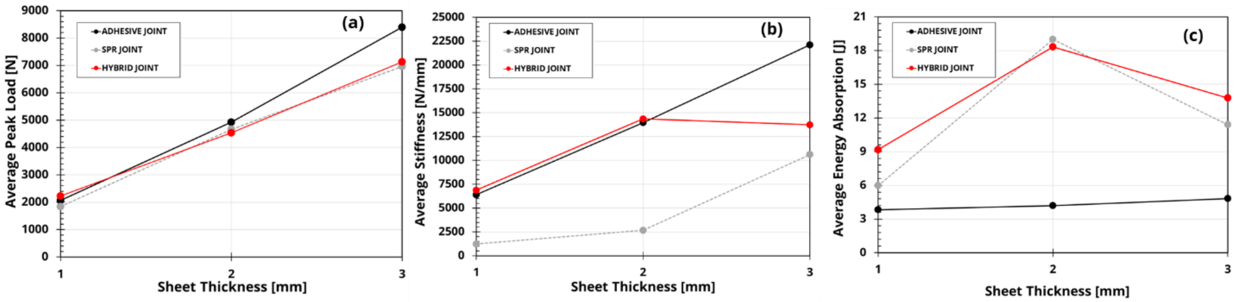

Figure 99: Interaction plots of average peak load (a), stiffness (b), and energy absorption (c) for adhesive, SPR and hybrid joints made with aluminum AA6061-T6 alloy.

4.4.2 Effect of Alloy Type on Mechanical Response

In this section, the effect of alloy type on the peak load and energy absorption was assessed for each joining method. The effect of alloy type on each joining method was quantified while highlighting the interaction effects of sheet thickness.

4.4.2.1 Adhesive Joints

Alloy type showed a statistically significant effect on adhesive joint strength ($p < 0.05$), and joints with AA6061 alloy generally exhibited higher joint strength than the AA5052 joints (Figure 100a). For example, the (2+2) mm joints with AA6061 had a 37% higher peak load compared to AA5052 joints. The 1 mm joint was a special case because the AA5052 alloy exhibited early yielding within the U-section bend radius, which reduced the adhesive edge effects and consequently delayed adhesive crack initiation, resulting in higher joint strength relative to AA6061 joints. Alloy type did not show a statistically significant effect on energy absorption or joint stiffness ($p = 0.603$ and 0.136, respectively). The energy was primarily absorbed to create new adhesive fracture surfaces, with limited energy required for specimen bending or plastic deformation; therefore, the effect of sheet material properties on energy absorption was not significant (Figure 100b). Considering adhesive joints made with both alloys (statistical analysis applied to the results data from both alloys), sheet thickness showed a strong correlation with joint strength (Spearman's correlation (ρ) = 0.939), moderate correlation with stiffness ($\rho = 0.657$) and weak correlation ($\rho = 0.376$) with energy absorption.

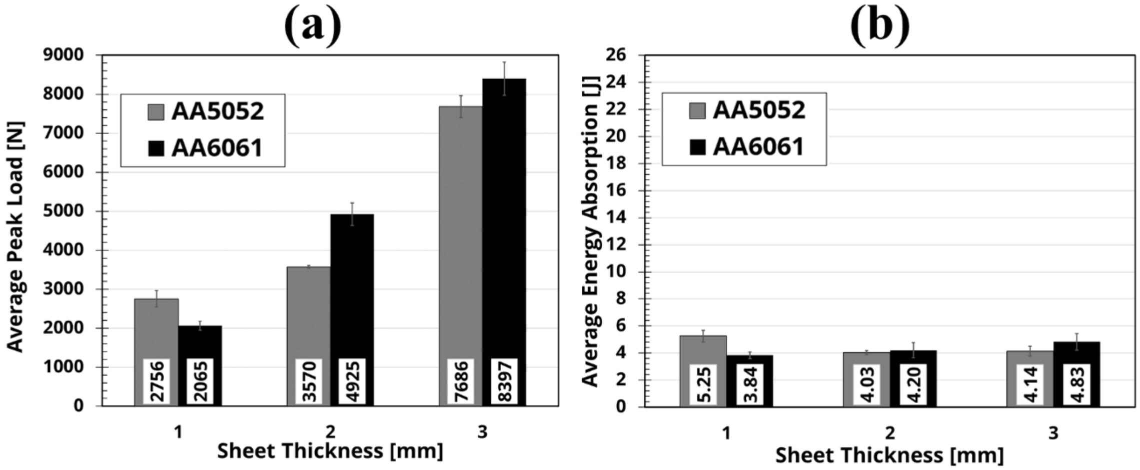

Figure 100: Peak load (a) and energy absorption (b) for adhesive joints made with AA6061-T6 and AA5052-H32 alloys.

To assess the compliance of H-specimens, the adhesive H-specimen data from this study was compared to adhesive CT test specimens reported in the literature (Ufferman *et al.*, 2018). The (1+1) mm H-specimen made with AA5052 demonstrated a maximum displacement at failure of ~2.6 mm with a peak load of 2.75 kN, while similar CT specimens made with AA5052 sheet thickness (1.6+1.6 mm) failed at ~6.7 mm (more than 2.5 times) with a peak load of 1.77 kN (-35.5%). The CT specimens are known to be more compliant compared to other geometries due to the bending of the adherends (Weiland *et al.*, 2019), which leads to higher loading at the boundaries of the adhesive and earlier crack initiation due to peeling.

4.4.2.2 SPR Joints

Similar to the adhesive joints, the SPR joints made with AA6061 alloy generally exhibited higher joint strength than the AA5052 joints. SPR joints with the AA5052 alloy generally demonstrated lower peak load (-13%, -33% and -16% for the 1, 2 and 3 mm joints, respectively, Figure 101a), which in part can be attributed to the lower mechanical interlock of the AA5052 joints. The effect of alloy type on joint stiffness was not statistically significant ($p=0.138$), but it had a significant effect on the energy absorption of the SPR joints ($p < 0.05$)). The energy absorbed in SPR joints was attributed to the localized plastic deformation within the vicinity of the rivet, and the lower strength, higher ductility alloy allowed for increased deformation prior to joint failure. The AA5052 alloy demonstrated higher energy absorption, relative to the AA6061 joints (Figure 101b), with the largest increase in energy absorption associated with the 3 mm sheet (89% increase). The AA6061 alloy with 3 mm sheet thickness exhibited significantly lower localized deformation relative to the AA5052 and higher stiffness relative to the other sheet thicknesses, which led to early loss of rivet mechanical interlock and joint failure. Considering SPR joints made with both alloys, sheet thickness showed a strong correlation with joint strength (ρ = 0.947) and stiffness (ρ = 0.913), and moderate correlation (ρ = 0.620) with energy absorption.

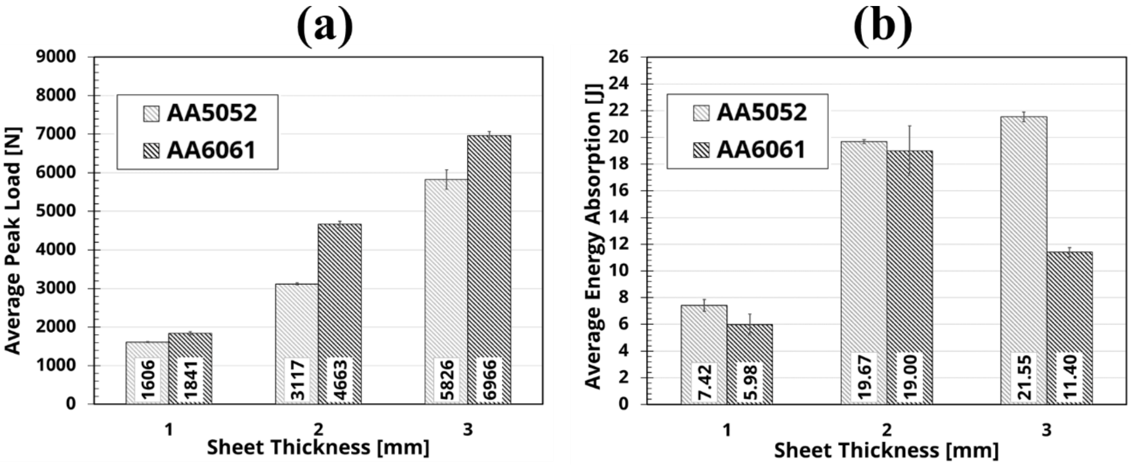

Figure 101: Peak load (a) and energy absorption (b) for SPR joining of AA6061-T6 and AA5052-H32 aluminum alloys

4.4.2.3 Hybrid Joints

Alloy type had a statistically significant effect on the peak load, stiffness, and energy absorption of hybrid joints ($p < 0.05$ for peak load, stiffness, and energy absorption). Similar to adhesive joints, hybrid joining joints made with A6061 alloy generally exhibited higher strength compared to AA5052 joints (Figure 102a). Also, hybrid joints showed a strong interaction effect between sheet thickness and alloy type, meaning that the effect of alloy type on the mechanical response varied according to sheet thickness. The statistical analysis showed that sheet thickness had a strong correlation with joint strength (ρ = 0.982), stiffness (ρ = 0.828), and energy absorption (ρ = 0.737). The AA5052 hybrid joints demonstrated up to 70% (13.79 J versus 23.46 J) higher energy absorption, relative to the AA6061 joints. The AA5052 joints exhibited increasing energy absorption with sheet thickness and the maximum energy absorption was achieved by 3 mm joints (23.46 J) (Figure 102b), attributed to increased deformation in the vicinity of the rivet, prior to ultimate joint failure. In comparison, the AA6061 joints exhibited the maximum energy absorption for 2 mm joints, owing to the reduced deformation and early loss of mechanical interlock in 3 mm joints. In general, hybrid joining improved the energy absorption of the joints for both alloys relative to the adhesive and SPR joints.

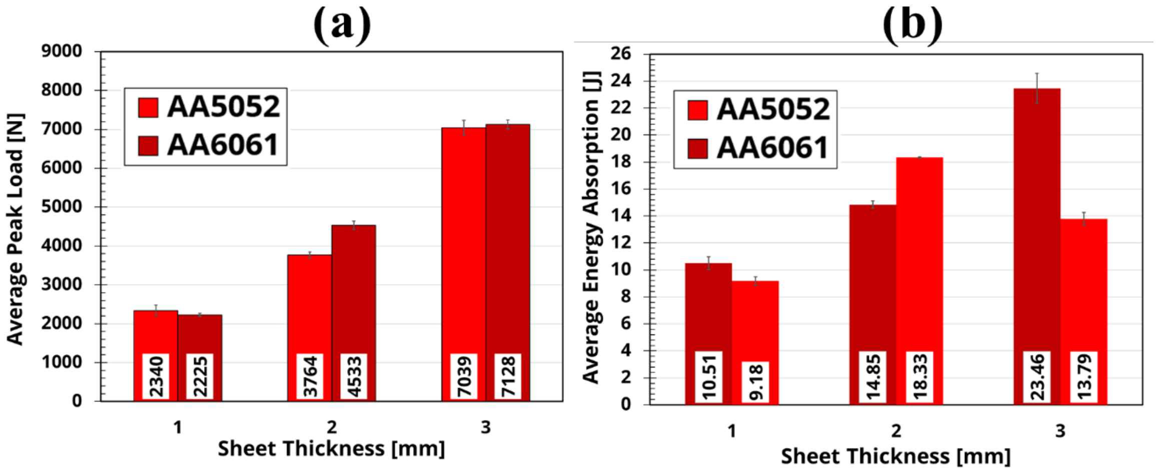

Figure 102: Peak load (a) and energy absorption (b) of hybrid joints with AA6061-T6 and AA5052-H32 alloys.

Comparing the strength data of adhesive and hybrid joints highlighted that the effect of alloy type on the strength of hybrid joints was less pronounced compared to adhesive joints (Figure 103). The 2 mm hybrid joints with AA6061 exhibited 20.43% higher strength relative to AA5052 joints (3.76 kN versus 4.53 kN), while similar adhesive joints exhibited 37.95% higher strength for the same alloy. However, the 3 mm hybrid joints with AA6061 exhibited only +1.25% higher joint strength compared to joints made with AA5052, while the same increase in adhesive joints was +9.25%. Using the AA5052 alloy with higher ductility reduced the effect of hybrid joining on adhesive morphology, which was obvious with the 3 mm sheet material.

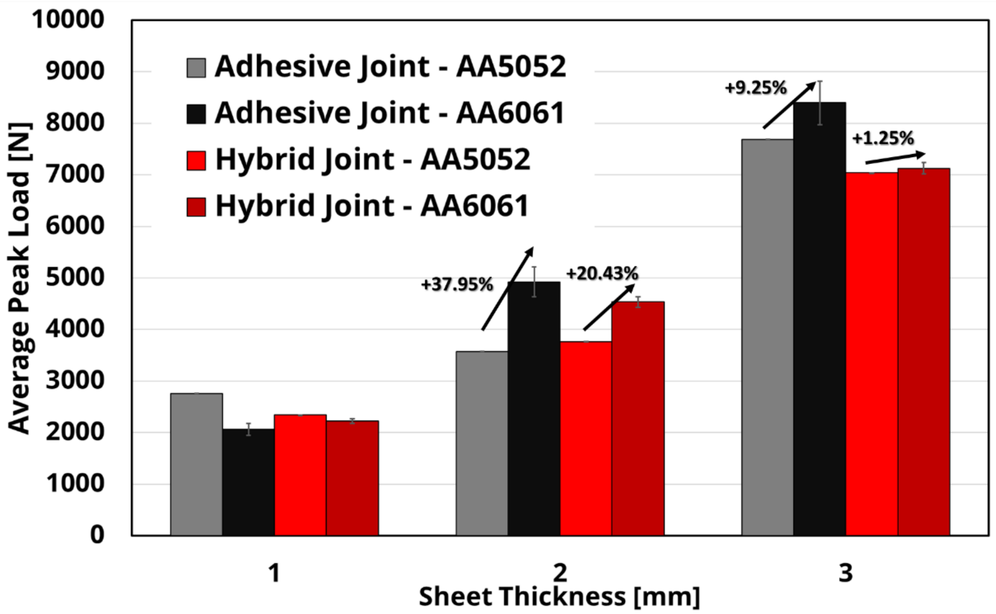

Figure 103: Peak load comparison between the adhesive and hybrid joining applied to AA6061-T6 and AA5052-H32 alloys.

4.4.3 Mechanical Response and Statistical Analysis Summary (AA6061-T6 and AA5052-H32)

The H-specimens redesigned and used in this study provided reduced compliance relative to commonly used CT specimens, enabling the comparative assessment of three joining methods (adhesive, SPR and hybrid) while reducing the influence of adherend deformation. The study showed that aluminum joined with structural adhesive exhibited higher joint strength than SPR joining, for tension loading. On the other hand, SPR joints demonstrated higher energy absorption capabilities compared to adhesive joints, attributed to the localized plastic deformation in the vicinity of the rivet. Hybrid joints achieved improved overall mechanical performance (strength, stiffness, and energy absorption) for joints made with 1 mm and 2 mm sheets, demonstrating peak load and stiffness comparable to adhesive joints and energy absorption equal to, or higher than, the SPR joints. In the case of 3 mm material, hybrid joining adversely affected the adhesive bond area, and bond line thickness, and resulted in adhesive porosity leading to a lower joint strength (up to -15%) and stiffness (up to -38%) compared to similar adhesive joints.

Increasing sheet metal thickness significantly increased the peak load for all three joining methods (Table 14). In contrast, the effect of sheet thickness on energy absorption was complex and depended on alloy type and joining method. For example, it was insignificant in adhesive joints, adverse in AA6061 SPR and hybrid joints, when increased from 2 mm to 3 mm sheets, and desirable in AA5052 SPR and hybrid joints (Table 14).

Alloy type had a significant effect on the peak load of adhesive, SPR and hybrid joints. The higher strength alloy (AA6061) improved joint strength for all three joining methods, while the joints with the lower strength and more ductile alloy (AA5052) generally demonstrated higher energy absorption capabilities for SPR and hybrid joints. The alloy type did not have a significant effect on the energy absorption of adhesive joints, attributed to the limited specimen deformation during the test. Importantly, the hybrid joints demonstrated a non-monotonic co-dependence on alloy type and thickness, and the mechanical performance gain due to hybrid joining was inversely related to alloy strength and sheet thickness.

Table 14: Two-way ANOVA and Tukey post hoc results testing the effect of sheet thickness and alloy type for each joining method.

Joining Method	**Effects (Factors)**	**Two-Way ANOVA** **Statistical Significance Effects**		
		Peak Load	**Energy Absorption**	**Stiffness**
Adhesive	**Sheet Thickness**	**Significant** $p < 0.05$	Not Significant $p = 0.223$	**Significant** $p < 0.05$
	Alloy Type	**Significant** $p=0.05$	Not Significant $p = 0.603$	Not Significant $p = 0.136$
SPR	**Sheet Thickness**	**Significant** $p < 0.05$	**Significant** $p < 0.05$	**Significant** $p < 0.05$
	Alloy Type	**Significant** $p < 0.05$	**Significant** $p < 0.05$	Not Significant $p = 0.138$
Hybrid	**Sheet Thickness**	**Significant** $p < 0.05$	**Significant** $p < 0.05$	**Significant** $p < 0.05$
	Alloy Type	**Significant** $p < 0.05$	**Significant** $p < 0.05$	**Significant** $p < 0.05$

4.5 Single Lap Shear (SLJ) Specimen Testing of Adhesive, SPR and Hybrid Joints

4.5.1 Mechanical Response of Joints Made with AA6061-T6 Alloy

The mechanical response of adhesive-only, SPR-only and hybrid joints was assessed using SLJ tests to characterize the joints under varying degrees of shear loading (Mode II). The results of the SLJ joints made with AA6061 alloy showed good repeatability and low variability in terms of peak load (the highest standard deviation among all datasets was 10.85% relative to the mean) (Table 15). Similar to the tension-loaded joints (H-specimens), some higher variability was associated with hybrid joints, which was more pronounced in the 2 mm and 3 mm joints attributed to the influence of adhesive squeeze-out affecting joint morphology and the quality of the adhesive at the bond area boundaries to varying degrees.

Adhesive joints exhibited an average peak load of 13.58 kN for the (1+1) mm joint, 17.52 kN for the (2+2) mm joint (28.9% increase over 1 mm joints), and 18.09 kN for the (3+3) mm joints (33.18% and 3.3% increase over the 1 mm and 2 mm joints, respectively) (Table 15). The joints showed varying degrees of joint rotation with localized bending plastic deformation, which generally initiated cracks at the adhesive leading and trailing ends due to mixed mode loading and then progressed rapidly until the joint failed abruptly due to shear loading. Cohesive failure was observed for all test specimens. Similar to the joints under tension loading (H-specimens), the adhesive joints generally demonstrated higher peak load and stiffness when compared to SPR and hybrid joints. Unlike the tension-loaded joints, the displacement at failure for adhesive SLJ joints varied depending on the sheet thickness, which influenced the overall energy absorption of the joint. Adhesive joints made with 2 mm and 3 mm adherends showed the lowest energy absorption among the three joining methods, owing to the marginal contribution of specimen deformation and relatively low energy for adhesive crack propagation compared to SPR rivets. On the contrary, the adhesive joints with 1 mm adherends exhibited substantial yielding and plastic deformation, which drastically increased the energy absorbed during the test. The adherends exhibited substantial yielding and plastic deformation, which affected the geometry of the specimen (bending, stretching and width reduction) resulting in somewhat inconsistent displacement to failure.

Table 15: Mechanical performance summary for the adhesive, SPR and hybrid SLJ joints made with aluminum AA6061-T6 alloy.

Joining Method	**Adhesive Joining**			**SPR Joining**			**Hybrid Joining**		
	(1+1) mm	**(2+2) mm**	**(3+3) mm**	**(1+1) mm**	**(2+2) mm**	**(3+3) mm**	**(1+1) mm**	**(2+2) mm**	**(3+3) mm**
Peak Load (N)	13,589 ± 194	17,520 ± 622	18,099 ± 217	2,952 ± 306	7,359 ± 49	10,248 ± 205	12,905 ± 69	15,522 ± 1,126	14,899 ± 1,618
Stiffness (N/mm)	6,786 ± 897	12,332 ± 1,614	19,733 ± 2,339	3,446 ± 1,024	9,694 ± 1,318	14,395 ± 1,614	6,883 ± 737	9,308 ± 689	15,477 ± 3,899
Energy Absorption (J)	158.99 ± 2.54	13.03 ± 0.83	8.83 ± 1.44	10.62 ± 3.69	27.42 ± 2.44	36.31 ± 5.51	75.97 ± 17.65	37.15 ± 2.44	59.14 ± 6.29

Relative to the adhesive joints, the SPR joints demonstrated substantially lower average peak loads of 2.95 kN, 7.35 kN and 10.24 kN for the (1+1) mm, (2+2) mm and (3+3) mm joints, respectively (Table 15). The average peak loads were 78.3%, 57.9%, and 43.3% lower than those of the (1+1) mm, (2+2) mm, and (3+3) mm adhesive joints, respectively. Similar to the SPR tension-loaded joints, the force-displacement curves demonstrated a smooth, gradual degradation in stiffness up to the peak load, and unloading continued with gradual softening until ultimate failure. The joints exhibited significant localized plastic deformation around the rivet, and the rivet tail lost the mechanical interlock with the bottom sheet, failing in a tail pull-out mode. The plastic strain energy stored during the localized specimen deformation (deformation localized in the vicinity of the rivet) increased the overall energy absorption of the SPR joints relative to adhesive joints up to 311%.

The hybrid joined SLJ reached the peak load at the adhesive damage initiation; then the load abruptly dropped during adhesive damage progression. When the adhesive failed, the load was rapidly transferred to the SPR rivet, causing a sudden drop in load followed by a gradual load increase similar to the SPR-only joint response. The peak load of hybrid joints increased with sheet thickness and demonstrated a peak load of 12.9 kN, 15.5 kN and 14.9 kN for the 1 mm, 2 mm, and 3 mm joints, respectively. The average peak load of the hybrid joints made with 1 mm sheet material was comparable to the adhesive joints (difference of less than 5%, 12.9 kN versus 13.5 kN). The 2 mm hybrid joints had a moderately lower peak lower compared to adhesive only (-11.4%, 15.5 kN versus 17.5 kN), and the 3 mm joints demonstrated further strength reduction relative to similar adhesive joints (-17.6%, 14.9 kN versus 18.1 kN). Similar to the tension-loaded H-specimens, the hybrid joints demonstrated the highest energy absorption among all joining methods, owing to the combined energy absorption mechanisms of adhesive and SPR joints. The hybrid joints generally failed at displacement values higher than those of the adhesive and SPR joints.

4.5.1.1 Failure Surface Analysis

The failure surface of adhesive SLJ was typical to what was reported in the literature for adhesive SLJ made with aluminum and an overlap length closer to 20 mm. The crack initiated at the leading and trailing edges of the adhesive and the crack path progressed from both ends along the bond line length toward the center, which resulted in a sharp transition zone near the centre line of the bond line length (shear failure, Figure 104a) (Ibrahim *et al.*, 2023). The failure process was illustrated by (Cui *et al.*, 2020), who explained how the shear failure progressed within aluminum joints with relatively long overlap lengths (Figure 105).

The SPR joints exhibited a rivet tail pull-out with substantial deformation within the vicinity of the rivet. The top sheet exhibited a considerable amount of bending deformation causing a partial head pullout; while the bottom sheet was deformed plastically in-plane and demonstrated base material failure (Figure 105b). The rivet body did not show signs of deformation.

The hybrid joints experienced the same failure modes as the adhesive joints (shear failure with a sharp transition zone near the centre of the overlap length), and after adhesive failure, the SPR rivet exhibited a tail pull-out (Figure 105c).

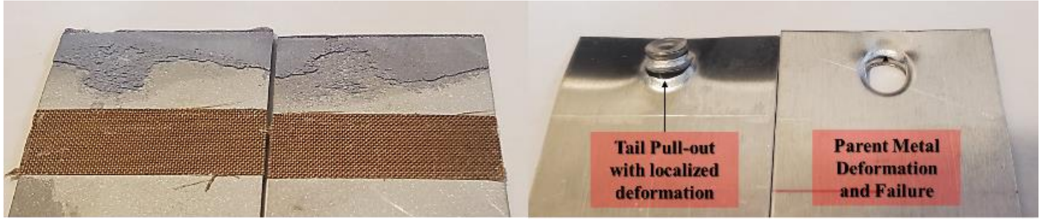

(a) Adhesive SLJ Failure **(b) SPR SLJ Failure**

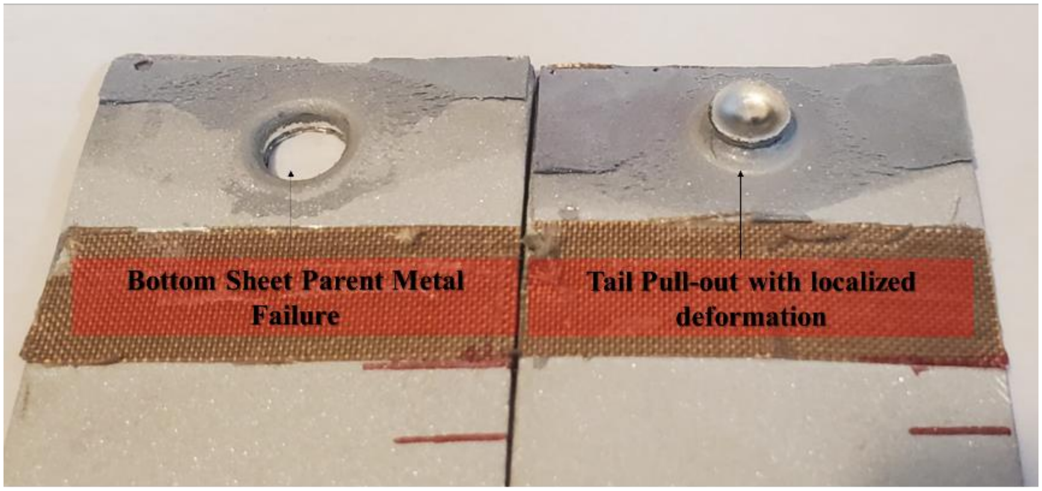

(c) Hybrid SLJ Failure

Figure 104: SLJ failure surfaces of adhesive (a), SPR (b) and hybrid joints (c)

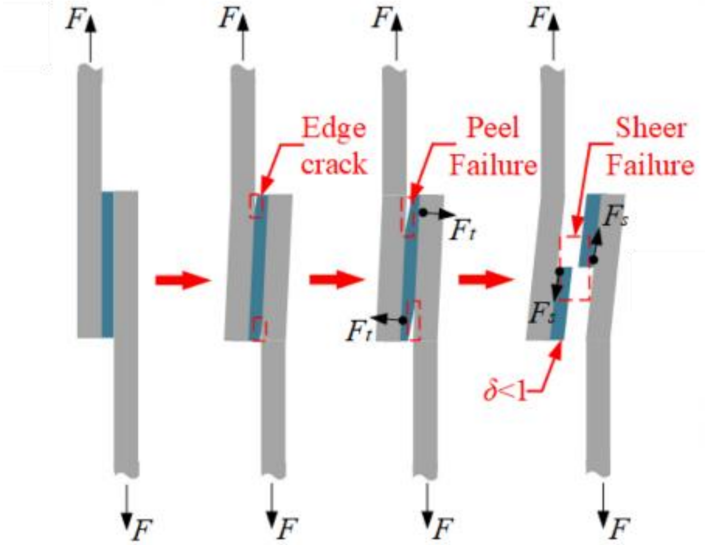

Figure 105: The crack propagation within an adhesive SLJ joint made with aluminum and an overlap length closer to 20 mm (Cui *et al.*, 2020).

4.5.1.2 Effect of Joining Method and Sheet Thickness on Mechanical Response

Two-way repeated-measures analysis of variance (ANOVA) revealed that the joining method and sheet thickness had significant effects on the SLJ joint strength ($p < .05$, $\eta_p^2{}_{\text{joining method}} = .981$, $\eta_p^2{}_{\text{sheet thickness}} = .922$), stiffness ($p < .05$, $\eta_p^2{}_{\text{joining method}} = .508$, $\eta_p^2{}_{\text{sheet thickness}} = .892$) and energy absorption ($p < .05$, $\eta_p^2{}_{\text{joining method}} = .612$, $\eta_p^2{}_{\text{sheet thickness}} = .786$). The effect of sheet metal thickness on joint strength, stiffness and energy absorption varied according to the joining method with a significant statistical interaction (similar to tension-loaded joints).

The peak load data for the adhesive, SPR and hybrid joined SLJ tests showed statistically significant differences ($p < 0.05$) and sheet thickness had a significant influence on the peak load of all types of joints. The post hoc comparison showed that the peak load values of the (1+1), (2+2) and (3+3) mm joints were significantly different among the three joining methods ($p < 0.03$, Figure 106). For the (1+1) joints, adhesive and hybrid joining were not statistically different ($p= 0.582$). In contrast, for the (2+2) mm joints, the adhesive joints had 138.0% and 12.8% higher average peak load compared to SPR and hybrid joints, respectively. Similarly, the joint strength of adhesive joints was significantly higher for the (3+3) mm joints, achieving 76.6% and 21.4% higher average peak load relative to SPR and hybrid joints, respectively. The SPR and hybrid joints exhibited a relatively linear increase in joint strength by increasing sheet metal thickness; however, adhesive joints did not show strength improvement when sheet thickness was increased from 2 mm to 3 mm (Figure 106).

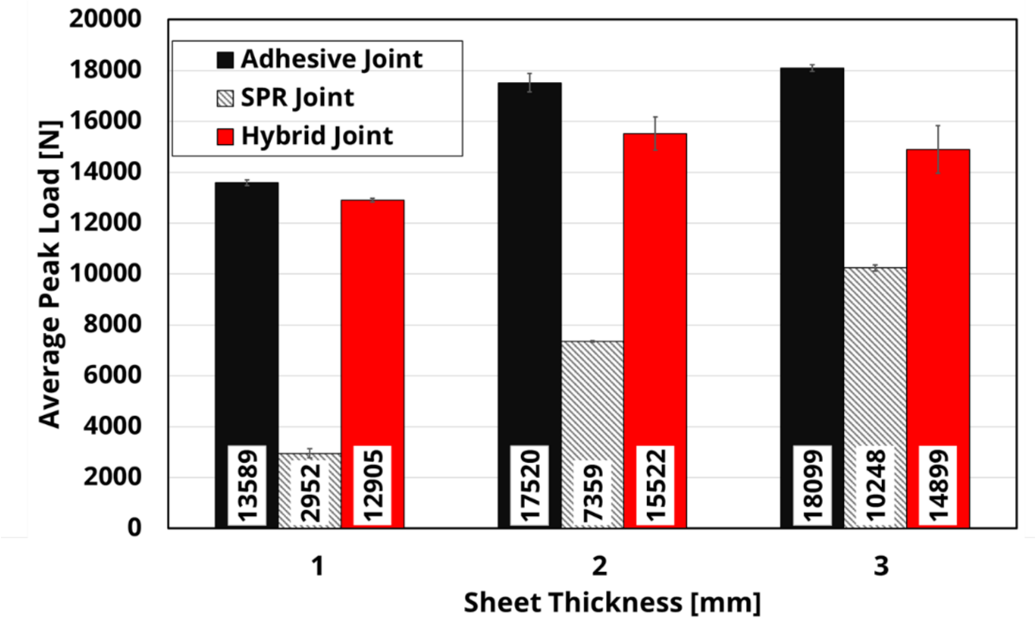

Figure 106: Average peak load for adhesive, SPR and hybrid joints made with aluminum AA6061-T6 alloy (error bars represent the standard error).

The adhesive joint strength generally correlated with adherend thickness and material strength (Spearman's correlation coefficients > 0.5). The 1 mm joints had an average peak load of 13.58 kN, 2.95 kN and 12.90 kN for the adhesive, SPR and hybrid joints respectively. The 2 mm joints generally had a stiffer response and increased the peak load by +28.9%, +149.2%, and +20.2% for the adhesive, SPR and hybrid joints, respectively. Previous work in the literature (da Silva *et al.*, 2009), reported that the influence of adherend thickness on the strength of adhesive joints is likely linear, and this study has shown that strength improvement of adhesive and hybrid joints with sheet thickness has an upper threshold value and further sheet thickness increase may not be beneficial. Adhesively joined SLJ made with thick adherends and relatively long overlap generally exhibit shear strains within the adhesive layer (Karachalios *et al.*, 2013a), and for low ductility adhesives, the strains will be similar regardless of the adherend thickness, thus, a strength increase with sheet thickness may not be achieved.

The stiffness response of adhesive joints was significantly higher than those of SPR (up to 37.0%) and hybrid joints (up to 27.4%) for the (2+2) and (3+3) mm joints. However, for the (1+1) joints, adhesive and hybrid joining were not statistically different ($p > 0.9$) (Figure 107), and both demonstrated significantly higher stiffness (up to 99.7%) compared to SPR joints. The adhesive squeeze-out and bond line thickness reduction affected the stiffness of the hybrid joints when the sheet thickness was increased. Thus, hybrid joining usually experienced an upper limit equal to the stiffness of a similar adhesive joint and a lower limit equal to a similar SPR joint.

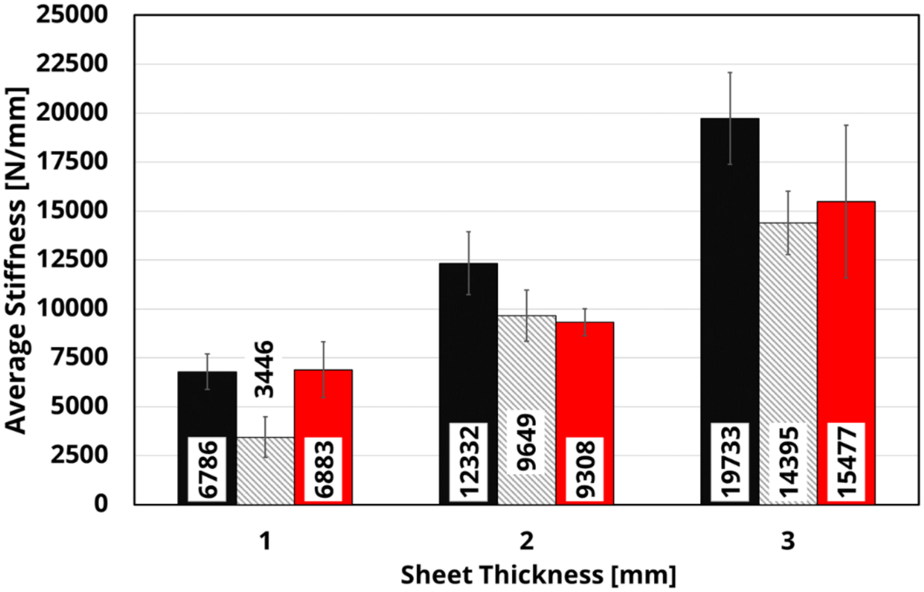

Figure 107: Average stiffness for adhesive, SPR and hybrid joints made with aluminum AA6061-T6 alloy (error bars represent the standard error)

Although the stiffness and peak load of the adhesive joint generally improved with sheet thickness, the reduction in specimen deformation and displacement at failure reduced the energy absorption capabilities of the joints (Figure 108). Unlike tension-loaded joints (H-shaped specimens), sheet thickness showed a statistically significant effect on the energy absorption of the adhesive joints, because the higher adhesive strength under shear loading resulted in adherend yielding, which contributed to the overall joint energy absorption. Thus, adhesive and hybrid joints achieved the maximum energy absorption for the 1 mm joints, attributed to the combined energy absorption mechanisms of joint damage and adherend deformation. In contrast, SPR joints experienced an increase in energy absorption by increasing sheet thickness. The SPR joints made with thicker sheets demonstrated a significant increase in joint strength while demonstrating localized deformation and slower rivet tail pull-out progression, which led to somewhat higher displacement at failure relative to SPR joints made with thinner sheets. In general, the energy absorption values of hybrid joints were significantly higher than adhesive joints ($p < 0.05$), except for the 1 mm joints which showed substantial adherend yielding in the adhesive joints (energy was absorbed in adherend deformation not by the joining method). Hybrid joints demonstrated 185% and 569% higher energy absorption than adhesive joints with 2 and 3 mm adherends, respectively. In addition, hybrid joints showed considerably higher energy absorption capabilities compared to SPR joints across the range of sheet thicknesses considered (+615%, + 35% and +62% for the 1-, 2- and 3-mm joints, respectively).

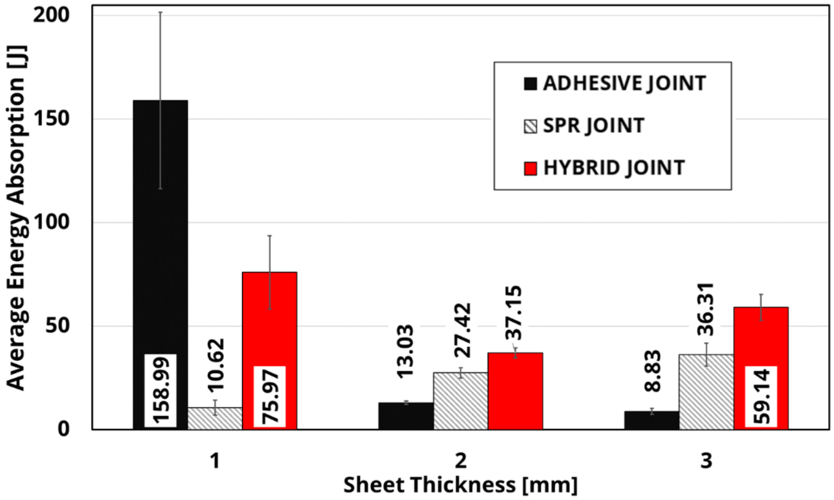

Figure 108: Average energy absorption for adhesive, SPR and hybrid joints made with aluminum AA6061-T6 alloy (error bars represent the standard error)

4.5.1.2.1 SLJ Joint Rotation

The deformation characteristics of the adherends were reported to highly influence the joint response of SLJ tests (Ibrahim *et al.*, 2023; Watson *et al.*, 2019). All SLJ joints exhibited localized joint rotation within the joint overlap region and the bending deformation of the adherend varied according to sheet thickness and joining method (Figure 109).

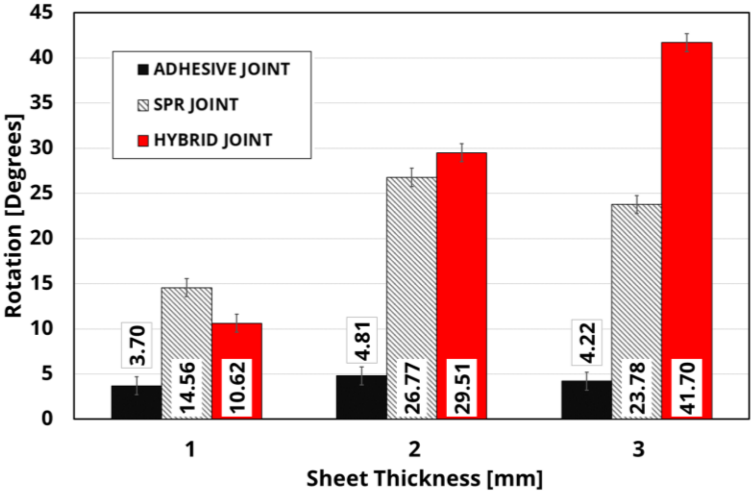

Figure 109: SLJ joint strength and mean surface roughness for adherends treated using solvent degreased, grit-blasting (mechanically treated adherend), and sol-gel (chemically treated adherend).

Measuring joint rotation during the SLJ tests facilitated quantifying the bending deformation of adherends. The adhesive SLJ joint with 1 mm adherends did not show a fair bit of rotation as the adherend encountered in-plane yielding (stretching and width reduction), and the joint failed at a rotation angle of 3.7 degrees (Figure 110). During loading of 1 mm SLJ adhesive joints, the whole length of the adhesive was involved in transferring the load due to the global yielding within the adhesive and adherends (Karachalios *et al.*, 2013b), which reduced joint rotation and resulted in localized shear strains within the adhesive layer. The adhesive joints with 2 and 3 mm adherends showed higher joint rotation, because the higher sheet thickness reduced the global yielding, and thus, the joints exhibited a crack initiation due to peel loading at the adhesive free ends. The adhesive joints with 3 mm adherends had higher flexural stiffness due to the increase in moment of inertia compared to the 2 mm joints which reduced the rotation angle at failure.

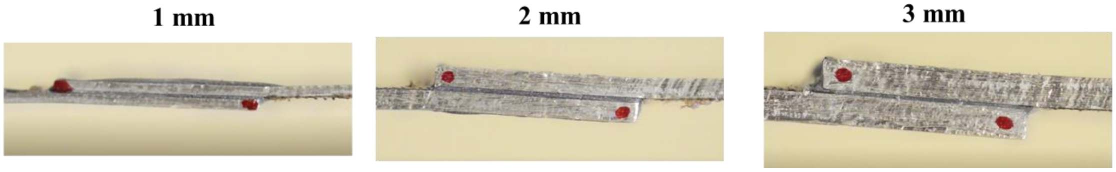

Figure 110: Joint rotation of adhesive joined SLJ joints for varying sheet thicknesses.

Unlike adhesive joints, the SPR SLJ joints showed asymmetrical rotation as the top (head-side) and bottom (tail-side) sheets exhibited different degrees and modes of deformation. For all sheet thicknesses, the top sheet exhibited substantial bending deformation while the bottom sheet exhibited localized plastic deformation as the interlocked portion of the SPR rivet was under shear loading (Figure 111). Therefore, although the joint encountered a substantial amount of joint rotation the bottom sheet did not contribute to the joint kinematics, as the SPR rivet axis followed the rotation of the top sheet. The reader should note that this observation may not be generalized to other failure modes (*i.e.*, rivet head pull-out).

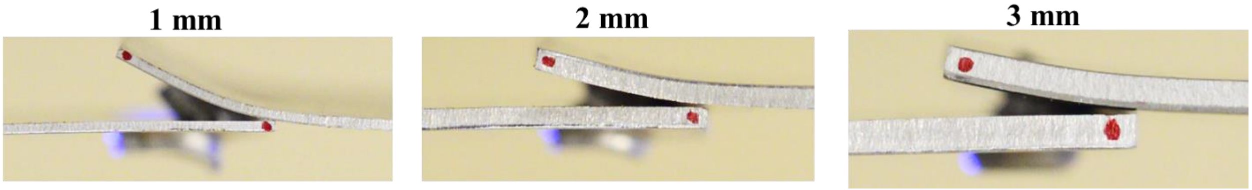

Figure 111: Joint rotation of SPR joined SLJ joints for varying sheet thicknesses.

The hybrid SLJ joints exhibited adherend bending and joint rotation similar to the adhesive joints during the initial loading phase (Figure 112). After adhesive failure, the joint kinematics were similar to the SPR-only joints. The joint rotation combined the two rotation mechanisms, which resulted in a joint rotation that was generally higher than the joint rotation of individual joints. In the case of the hybrid joints made with 1 mm sheet, the abrupt and substantial drop in load from ~13.5 kN to ~2.9 kN due to adhesive failure resulted in instant SPR rivet failure, which reduced the deformation associated with SPR rivet damage progression and consequently the overall joint rotation (Figure 109).

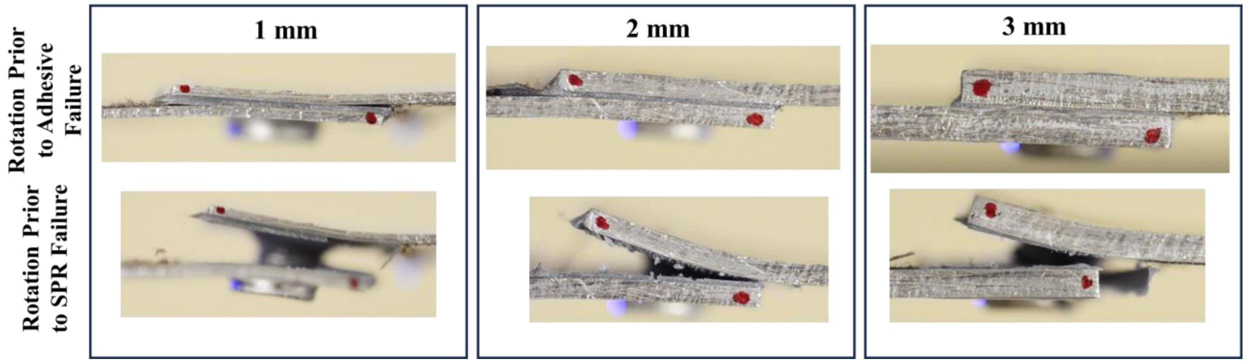

Figure 112: Joint rotation of hybrid joined SLJ joints for varying sheet thicknesses.

4.5.2 Effect of Alloy Type on Mechanical Response

In this section, the effect of alloy type on the peak load and energy absorption was assessed for each joining method. The effect of alloy type on each joining method was quantified while highlighting the interaction effects of sheet thickness.

4.5.2.1 Adhesive Joints

Similar to the tension-loaded joints, alloy type showed a statistically significant effect on adhesive joint strength, and the joints made with AA6061 alloy exhibited higher joint strength than the AA5052 joints (Figure 113a). Alloy type showed a statistically significant effect on energy absorption for the 1 mm joints ($p < 0.05$), a marginal statistically significant difference for the 2 mm joints ($p = 0.05$) and no statistically significant difference for the 3 mm joints (Figure 113b). Although the energy was primarily absorbed to create new adhesive fracture surfaces, the 1 mm joints made with AA6061 had substantially higher joint peak load which increased the energy absorption by 167% compared to the AA5052 alloy. The SLJ joints made with 1 mm AA5052 alloy exhibited significantly lower joint strength and energy absorption because the base material failed prematurely at a peak load of 7.1 kN (Figure 114). The 2 mm joints made with the 5052 alloy showed a slightly lower peak load compared to the AA6061 joints; however, these joints exhibited somewhat higher energy absorption due to adherend yielding. When sheet thickness was increased to 3 mm, the energy absorption for both alloys was similar, because the AA6061 alloy provided higher strength but the AA5052 contributed to the energy absorption with more adherend deformation.

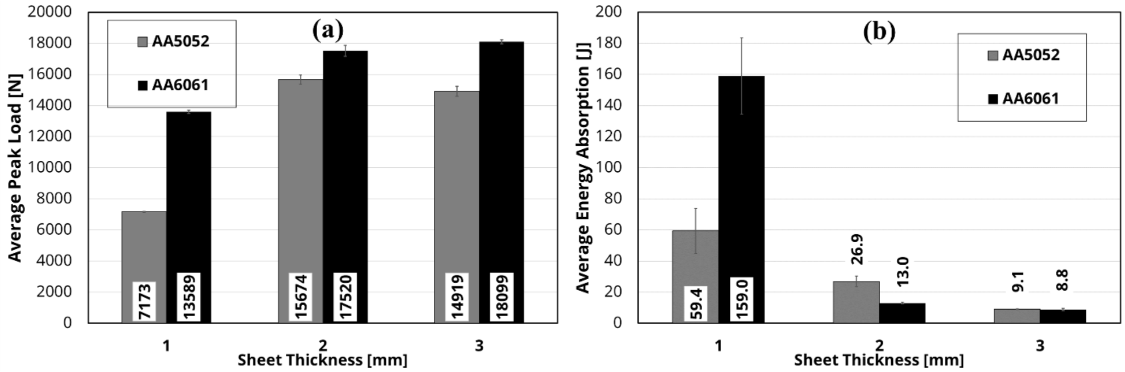

Figure 113: Peak load (a) and energy absorption (b) for adhesive joints made with AA6061-T6 and AA5052-H32 alloys.

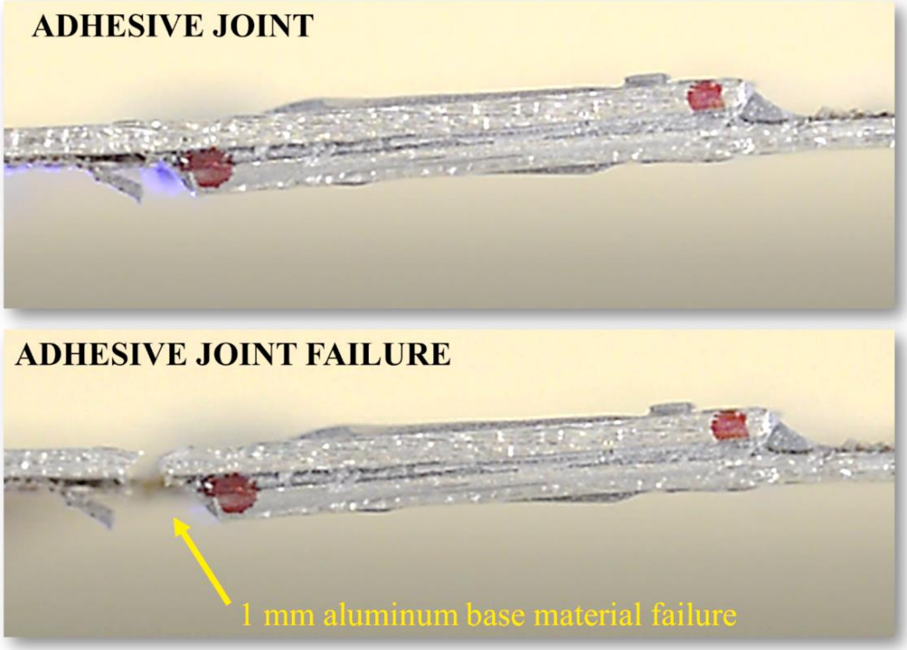

Figure 114: Adhesive SLJ joints made with 1 mm AA5052 alloy exhibited adherend failure.

4.5.2.2 SPR Joints

Similar to adhesive joints, the SPR joints made with the AA6061 alloy generally experienced higher peak load than the ones with AA5052 (joints made with AA5052 lower by 10%, 23% and 31% for the 1, 2 and 3 mm joints, respectively, Figure 115a). The higher strength of the AA6061 joints can in part be attributed to the higher mechanical interlock of the AA6061 joints. Unlike the tension-loaded joints, the alloy type had no significant effect on energy absorption of SPR SLJ joints ($p = 0.75$). In the tension-loaded joints, the energy absorbed in SPR joints was attributed to localized plastic deformation of the sheet material around the rivet; however, the SLJ joints primarily experienced adherend yielding. Thus, the higher ductility of the AA5052 alloy and the higher joint strength of the joints made with the AA6061 alloy balanced out the difference in the energy absorbed (Figure 115b).

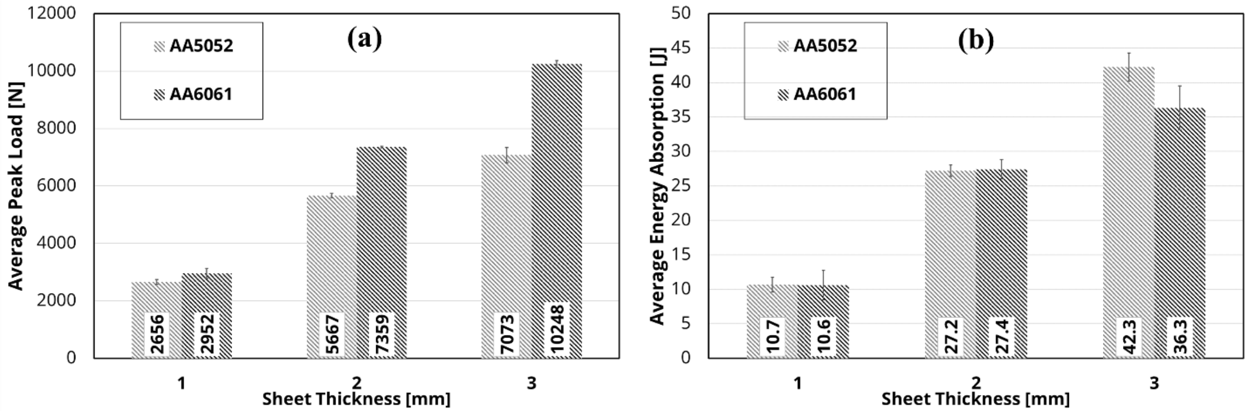

Figure 115: Peak load (a) and energy absorption (b) for SPR joints made with AA6061-T6 and AA5052-H32 alloys.

4.5.2.3 Hybrid Joints

Alloy type had a statistically significant effect on the peak load ($p < 0.05$), but not on the energy absorption of hybrid joints ($p = 0.399$). Hybrid joining showed strong interaction effects between sheet thickness and alloy type, and joints made with AA6061 alloy generally exhibited higher strength compared to the AA5052 joints. The AA6061 hybrid joints demonstrated up to 80% (12.90 kN versus 7.18 kN) higher joint strength, relative to the AA5052 joints. In contrast, the AA5052 and AA6061 joints exhibited comparable energy absorption and the maximum energy absorption was achieved by 1 mm joints made with AA5052 alloy (92.9 J) (Figure 116b), attributed to increased deformation in the adherends, prior to aluminum sheet metal failure. Importantly, hybrid joining improved energy absorption of the joints regardless of the alloy relative to the adhesive and SPR joints.

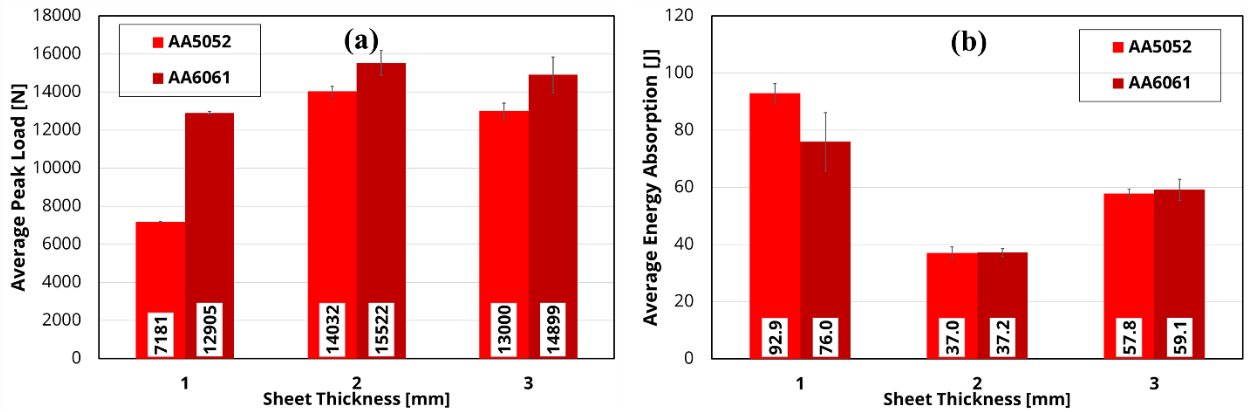

Figure 116: Peak load (a) and energy absorption (b) for hybrid joints made with AA6061-T6 and AA5052-H32 alloys.

4.5.3 Mechanical Response and Statistical Analysis Summary (AA6061-T6 and AA5052-H32)

The SLJ joints used in this study enabled the comparative assessment of adhesive, SPR and hybrid joining methods (adhesive, SPR and hybrid) under primarily shear loading. The study showed that aluminum joined with structural adhesive exhibited higher joint strength than SPR joining. On the other hand, SPR joints demonstrated higher energy absorption capabilities compared to adhesive joints, attributed to the localized plastic deformation in the vicinity of the rivet. Hybrid joints achieved improved overall mechanical performance (strength, stiffness, and energy absorption) for joints made with 1 mm sheet thickness, demonstrating peak load and stiffness comparable to adhesive joints and energy absorption equal to, or higher than, the SPR joints. In the case of 2- and 3-mm material, hybrid joining adversely affected the adhesive bond area, and bond line thickness, and resulted in adhesive porosity leading to a lower joint strength (up to -17.6%) and stiffness (up to -21.5%) compared to similar adhesive joints.

Increasing sheet metal thickness did not significantly increase the peak load for all three joining methods (Table 16). The strength improvement of adhesive and hybrid joints with sheet thickness had an upper threshold value and sheet thickness increase from 2 mm to 3 mm was not beneficial. In contrast, SPR joining showed a significant increase, following an almost linear trend, with sheet thickness. Similar to tension-loaded joints, the effect of sheet thickness on energy absorption was complex and depended on alloy type and joining method. It was generally insignificant in adhesive and SPR joints when sheet thickness increased from 1 to 2 mm or from 2 to 3 mm, but significant when the thickness was increased from 1 to 3 mm (Table 16). sheet thickness had a strong effect on the energy absorption of hybrid joints.

Alloy type had a significant effect on the peak load of adhesive, SPR and hybrid joints. Similar to tension-loaded joints, the higher strength alloy (AA6061) improved joint strength for all three joining methods. The alloy type demonstrated a significant effect on the energy absorption of adhesive joints because the SLJ joints made with 1 mm joints exhibited adherend failure with AA5052 alloy but substantial adherend yielding and joint failure with AA6061 alloy (different failure modes). In contrast, alloy type had no significant effect on the energy absorption of SPR joints, as the higher ductility of the AA5052 alloy and the higher joint strength of the joints made with the AA6061 alloy balanced out the difference in the energy absorbed by the SLJ specimen. Similar to tension-loaded joints, the hybrid joints demonstrated a non-monotonic co-dependence on alloy type and sheet thickness, and the mechanical performance gain due to hybrid joining was inversely related to alloy strength and sheet thickness.

Table 16: Two-way ANOVA and Tukey post hoc results testing the effect of sheet thickness and alloy type for each joining method.

Joining Method	**Effects (Factors)**	**Two-Way ANOVA** **Statistical Significance Effects**	
		Peak Load	**Energy Absorption**
Adhesive	**Sheet Thickness**	**Case Dependant** **$p < 0.05$ for 1 mm to 2 mm** $p = 0.991$ for 2 mm to 3 mm	**Case Dependant** **$p < 0.05$ for 1 mm to 2mm** $p = 0.375$ for 2 mm to 3 mm
	Alloy Type	**Significant** $p=0.05$	**Case Dependant** $p < 0.05$ for 1 mm
SPR	**Sheet Thickness**	**Significant** $p < 0.05$	**Case Dependant** $p = 0.089$ for 1 mm to 2mm $p = 0.306$ for 2 mm to 3 mm **$p < 0.05$ for 1 mm to 3 mm**
	Alloy Type	**Significant** $p < 0.05$	Not Significant $p = 0.75$
Hybrid	**Sheet Thickness**	**Significant** $p < 0.05$	**Significant** $p < 0.05$
	Alloy Type	**Significant** $p < 0.05$	Not Significant $p = 0.399$

4.6 Mechanical Response Improvement Using Hybrid Joining Process Variations

It was evident from the mechanical response data that hybrid joining improved the energy absorption over both adhesive-only and SPR joints regardless of the mode of loading. However, sheet thickness played a key role in the strength and stiffness of hybrid joints as it affected the morphology of the adhesive layer, resulting in strength and stiffness degradation relative to adhesive-only joints. Although hybrid joints achieved better overall performance relative to SPR-only joints, there was room to improve the strength and stiffness aspects of hybrid joints. The 2 and 3 mm SLJ hybrid joints exhibited 11.4% and 17.7% lower joint peak loads, respectively, compared to similar adhesive joints (Figure 117a). Strength degradation was also observed under tension loading (H-specimens) to a lesser extent, as the 2 and 3 mm hybrid joints experienced 7.9% and 15.1% strength reduction, respectively, compared to similar adhesive joints (Figure 117b). On the contrary, when hybrid joining was applied to 1 mm sheet material, the strength reduction was negligible (5% and not statistically significant); thus, the possibility of recovering the strength and stiffness reductions associated with hybrid joints applied to 2- and 3-mm sheet materials was assessed in this section.

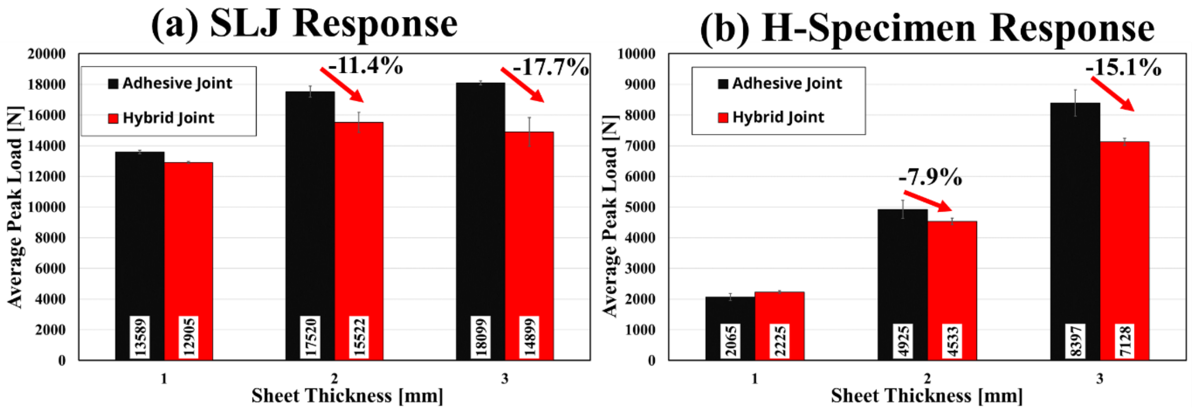

Figure 117: A comparison between the average peak load (joint strength) of adhesive-only and hybrid joints using SLJ (a) and H-specimen (b) tests.

To recover the strength and stiffness reduction observed in hybrid joints with thicker sheet metal due to adhesive morphology reduction, three variations of the widely used hybrid joining process (hereinafter referred to as traditional hybrid joining) were investigated. The first process variation included applying a 0.17 mm-thick circular brass shim (diameter = 9 mm) at the location of the SPR rivet to reduce the adhesive squeeze out. The cross-sectioned joint showed that the shim application did not reduce adhesive squeeze out and no adhesive was observed in the vicinity of the rivet (Figure 118a). The shim was pierced and encountered substantial deformations during the riveting process, and the formed joint showed a head height of 0.55 mm, affecting joint aesthetics and increasing the bottom thickness (Figure 118a). Interestingly, using a shim between the two joined sheets affected joint symmetry (the rivet tail was 0.385 mm higher on one side, Figure 118a). It was concluded that this process variation could not enhance the joint morphology and introduced a variability factor to the process as it affected the rivet formation and required high accuracy while positioning the shim at the centre of the rivet, which might be time-consuming in a production environment.

The second process variation was applying the SPR at the end of the adhesive curing process at the adhesive curing temperature (80° C) to reduce adhesive squeeze-out and porosity. Adhesive ductility was reported to increase with temperature while the adhesive strength decreased (Banea and Da Silva, 2010); thus, riveting at the adhesive cure temperature was expected to facilitate piercing the adhesive layer and reduce adhesive cracking/microcracking. The cross-section imaging showed that the adhesive layer was present in the rivet vicinity and an adhesive bond line thickness of 0.263 mm was measured outside the rivet head diameter (Figure 118b). A bond line thickness of 0.175 mm was observed at the centre of the rivet (below the rivet), indicating substantial adhesive ductility and flexibility. Importantly, the joint physical attributes met the guidelines established in the literature (Haque, 2018; Li *et al.*, 2017) and no major cracks were observed. Goglio *et al.* (2008) reported that epoxy adhesives exhibited substantial ductility under compression at both quasistatic and high strain rates, and in their work adhesive under quasi-static compression loading exhibited a total strain of 45% without failure or cracking.

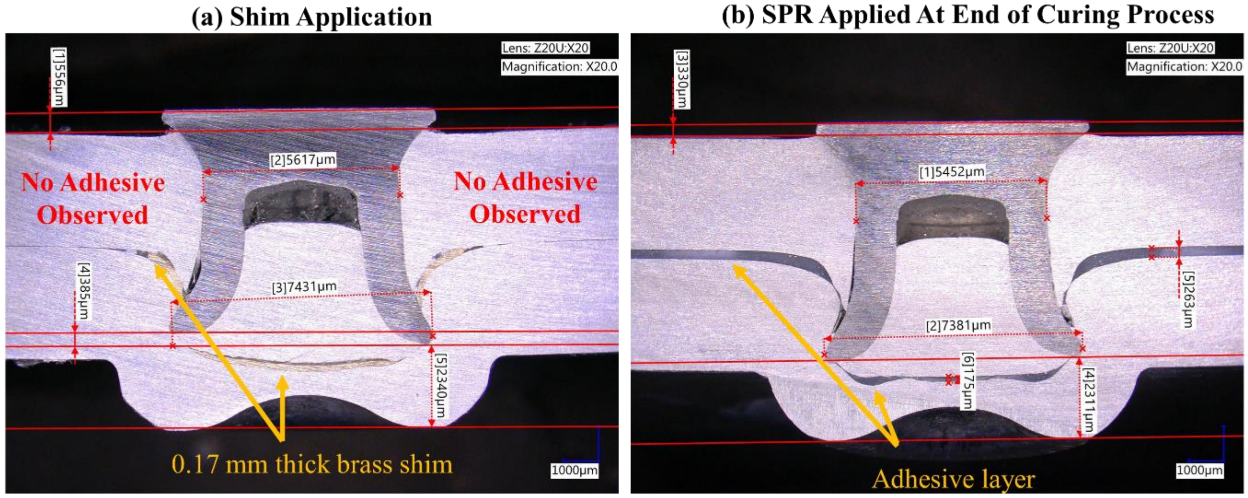

(a) Shim Application

(b) SPR Applied At End of Curing Process

Figure 118: Cross-section of hybrid joining process including a 0.17 mm-thick brass shim (a) and rivet application following adhesive curing (b)

The third hybrid joining process variation was applying the SPR after completing the adhesive curing process at room temperature (Figure 119a). This process variation did not require applying the SPR rivet instantly at the end of the curing process, making it more convenient for production environment implementation. The joint cross-sections showed similar measurements to the joints created by applying the SPR rivet at curing temperature with one less step (keeping the adhesive joint at an elevated temperature).

The bond line thickness measured varied according to the distance from the centre of the rivet and reached a maximum of 0.317 mm (Figure 119b). Compared to traditional hybrid joining, this process variation resulted in improved adhesive coverage (no reduction in the bond area due to squeeze-out), increased bond line thickness and eliminated adhesive porosity. While the reported improvements could be sufficient to improve joint strength and stiffness, it was important to have a closer look at the adhesive within the rivet diameter to assess the quality of the adhesive layer remaining. Within the rivet diameter, the adhesive layer encountered substantial deformation, especially below and above the rivet tail (Figure 119c and Figure 119d); thus, regions experiencing the maximum deformations were inspected for cracking at 2000X magnification. The rivet tail pierced through the adhesive layer and substantially deformed the adhesive to plastically form the aluminum sheets into the joint, creating the mechanical interlock. The SPR forming process reduced the adhesive bond line thickness to 33 μm below the rivet tail (Figure 119c). Generally, the adhesive showed excellent ductility, and because the riveting process primarily applied compression loading, no extended or large cracks were observed (Figure 119c and Figure 119d). A single microcrack was observed when the adhesive thickness was lower than 33 μm (Microcrack, Figure 119c); however, it did not extend along the aluminum-epoxy interface or through the depth of the adhesive layer.

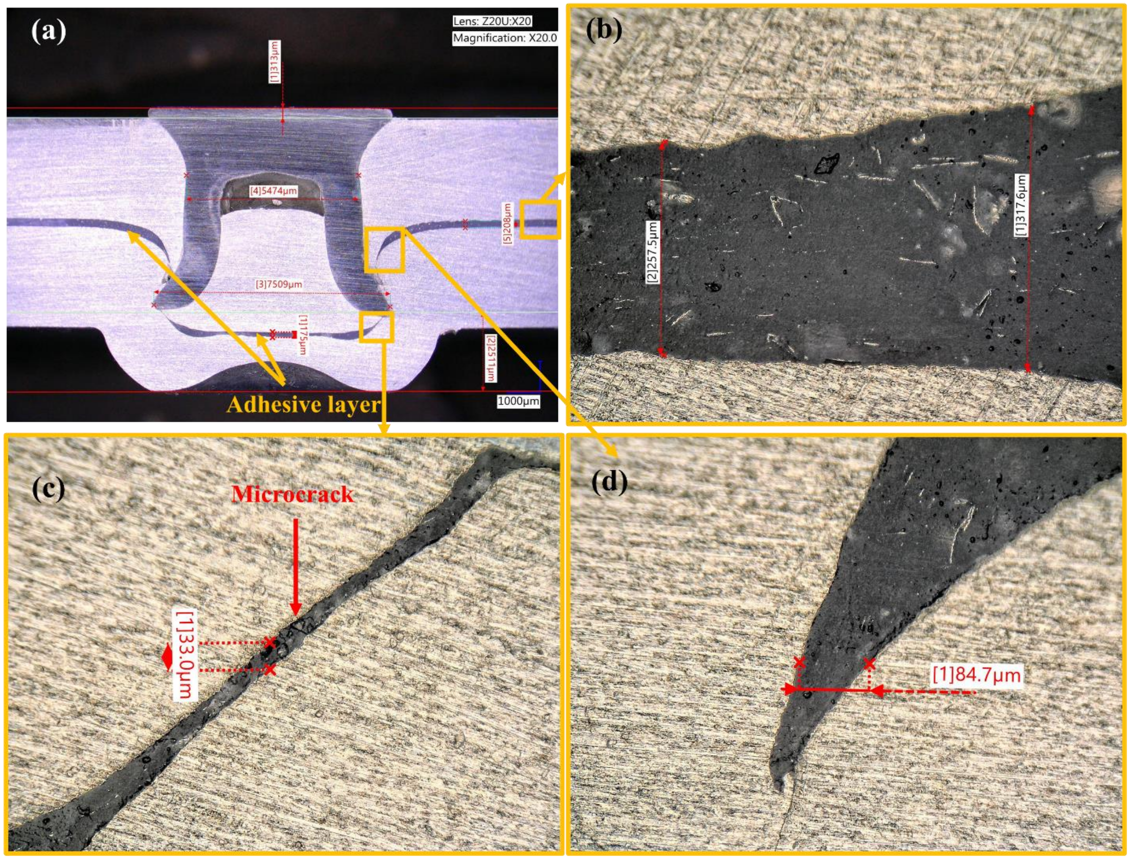

Figure 119: Cross-section imaging of hybrid joining process with SPR rivet applied after curing the adhesive at room temperature (a) with 2000X magnified images in regions of high deformations (b-d).

It was important to assess the physical attributes of the formed SPR joints using the hybrid joining process variations. The measurements taken from cross-sectioned joints created using the traditional process, SPR applied to cured joint at room temperature (cured), SPR applied and the end of curing process at curing temperature (end of curing) and shim application (shims) were compared. The measurements showed that the process variations did not have a considerable effect on the mechanical interlock of the SPR rivet. The mechanical interlock measurements of the traditional and the process variations were within 0.1 mm (Figure 120a). A similar observation was made to the bottom thickness measurements (Figure 120b), indicating that the process variations had a more pronounced influence on the adhesive rather than the SPR joint formation. Readers should note that the shim application has affected joint symmetry and joint aesthetics due to the increase in head height.

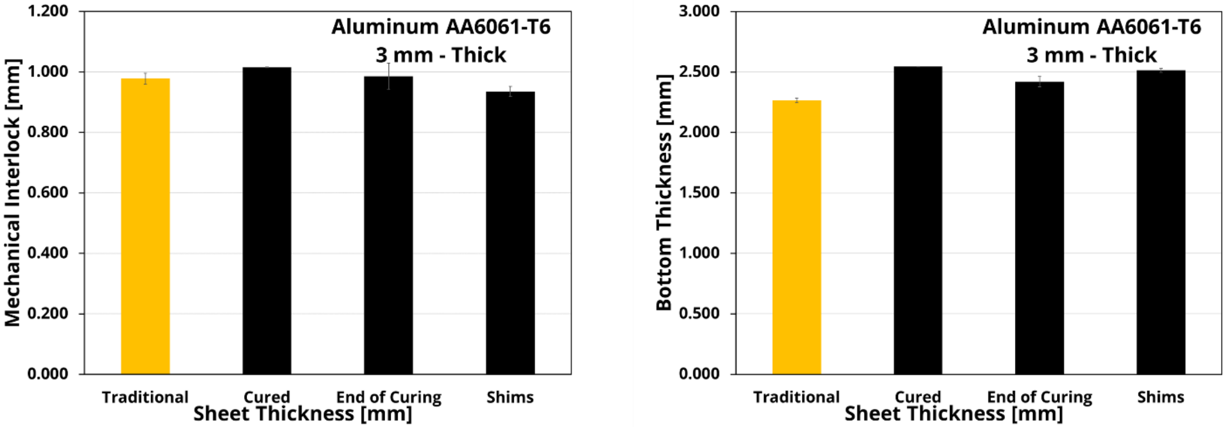

Figure 120: Mechanical interlock (a) and bottom thickness (b) measurements of hybrid joints created using the traditional approach and three process variations (cured, end of curing and shims).

The application of the SPR rivet at room temperature produced the same joint morphology as applying the rivet at the end of the curing process at an elevated temperature. The former offered more flexibility and compatibility with industrial applications adoption, so it was considered for further verification. SLJ specimens were prepared and joined using hybrid joining applied after adhesive curing at room temperature according to the methods discussed earlier (section 3.5). The SLJ test applied varying degrees of mode mixity to the adhesive layer and experienced a higher reduction in peak load and stiffness relative to adhesive joining when compared to similar H-specimens. Because the strength and stiffness reduction with hybrid joints was not observed with the 1 mm joints, the SLJ joints were made with 2 mm and 3 mm adherends, and the alloy considered was AA6061 alloy because it exhibited a more pronounced effect on adhesive morphology compared to the more ductile AA5052 alloy. The force-displacement curves showed excellent repeatability and consistency among the three repeats (Figure 121) for each hybrid joining sheet thickness (2 mm and 3 mm). The peak load corresponded to adhesive crack initiation and the adhesive failed consistently at the same load and displacement. Similar to traditional hybrid joints, the load was abruptly transferred to the SPR rivet and the peak load and displacement at the failure of the SPR rivet were also consistent in all the tests (Figure 121a and Figure 121b). The average peak load of the SLJ joined was improved for both the 2 mm and 3 mm joints, and the improvement over the traditional method was +11.8% and +15.5% for the 2 mm and 3 mm joints, respectively (Figure 122a). Also, the stiffness reduction observed with traditional hybrid joined SLJ was addressed, using the hybrid joining process variation, and the average stiffness for the 2 mm and 3 mm joints improved by 13.5% and 8.3%, respectively (Figure 122b). Importantly, the joints created using the proposed hybrid joining variation resulted in a joint with improved overall mechanical performance compared to the individual joining methods.

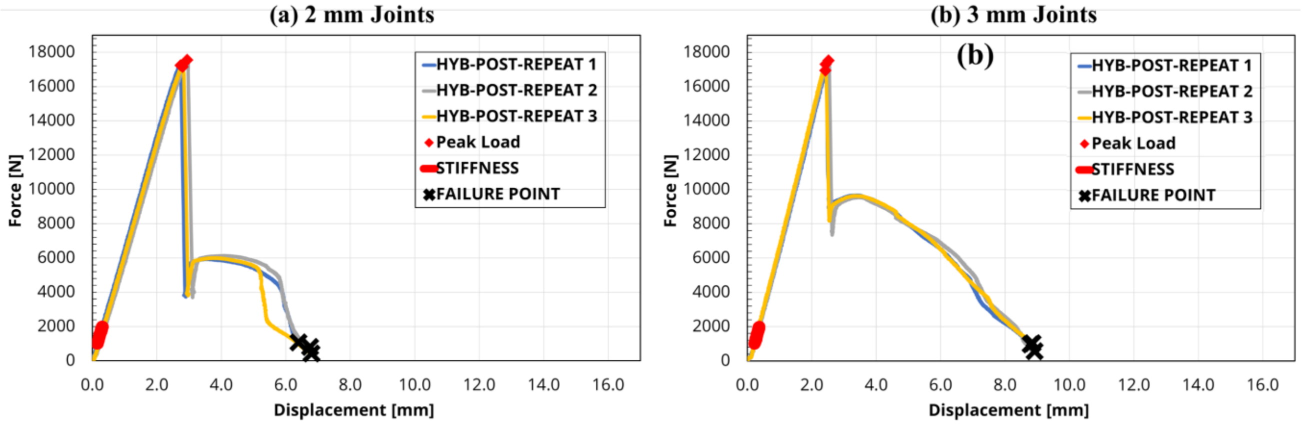

Figure 121: The SLJ force-displacement response for hybrid joints made with 2 mm (a) and 3 mm (b) adherends.

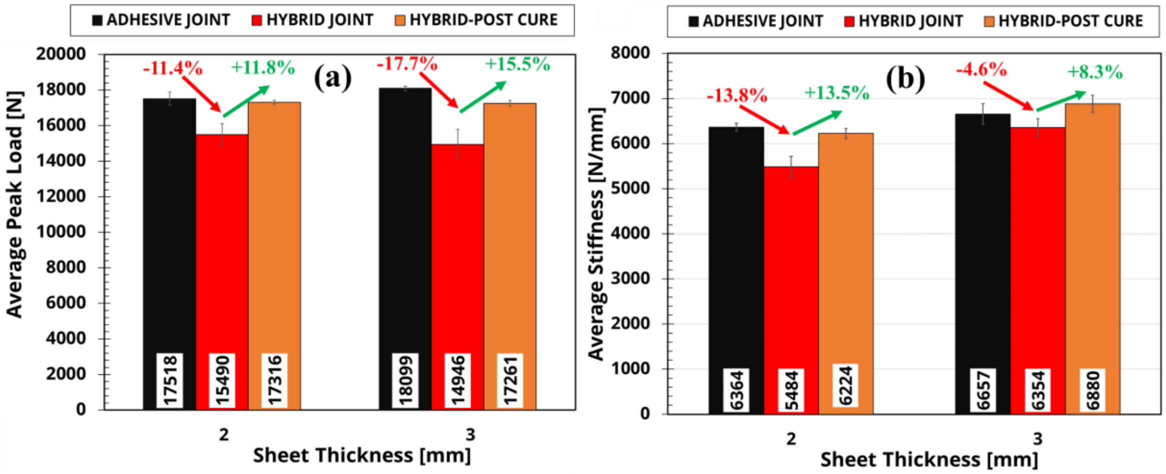

Figure 122: Stiffness (a) and peak load (b) comparison between the SLJ response of adhesive-only, hybrid (traditional), hybrid-post cure (post-curing at room temperature) joints made with 2 mm and 3 mm adherends.

4.7 Caiman Component-Level Testing of Adhesive, SPR and Hybrid Joints

Component-level tests, using the Caiman test (Liu, 2019; O'Keeffe, 2018), were conducted to assess the mechanical response (peak load, stiffness and energy) of adhesive, SPR and hybrid joining at a larger scale relevant to automotive assemblies. The Caiman component allowed testing of the joining method under primarily Mode I loading. Given that the primary objective was to assess the overall structure response dominated by the joining methods, it was important to ensure that the response was not substantially influenced by the parent metal deformation or the overall compliance of the Caiman component. A scoping FE study was conducted to identify the sheet thickness required to minimize parent metal deformation and provide sufficient compliance to retain the hat profile geometry throughout the tests. The aluminum AA6061-T6 alloy in 3 mm thickness was found to achieve the expected peak loads without experiencing substantial plastic deformation or change in hat profile geometry. The 3 mm sheet aluminum sheets could be a potential alternative to the 1 - 1.8 mm thick steel sheets, commonly used in automotive structures, based on structural stiffness and bending moment equivalency (Li *et al.*, 2020).

4.7.1 Adhesive Joined Caiman Test Results and Analysis

The adhesive-joined Caiman components showed a consistent load-displacement response with an average peak load of 2.67 kN (Figure 123a) and a low standard deviation of 2.5%. The peak load corresponded to the adhesive crack initiation, which took place at an average pin displacement of 5.7 mm (Table 17). The structure stiffness was 0.63 kN/mm and the energy absorbed to separate the hat sections under tension (normal) loading was 30.32 J (Figure 123b). After reaching the peak load, the load gradually dropped as the crack propagated along the adhesive layer (along the length of the hat sections). The crack extension, measured optically, increased almost linearly with pin displacement (constant crack extension rate); then the slope plummeted as the crack extension propagated at a slower rate at the other end (free end) of the Caiman test tubes prior to the complete separation (Figure 124).

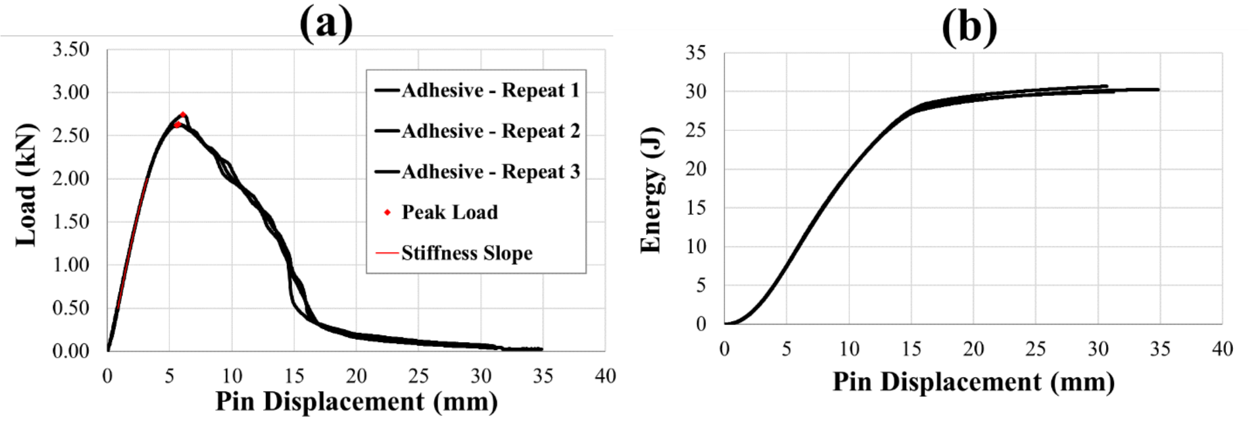

Figure 123: The load-displacement and energy-displacement responses of the adhesive joined Caiman test specimen.

Table 17: The mechanical performance summary of the adhesive joined Caiman component.

	Average Value	**Standard Deviation, Std Dev**	**Std Dev %**
Peak Load, kN	2.67	0.07	2.5
Stiffness, kN/mm	0.63	0.01	1.8
Displacement at Peak Load, mm	5.77	0.26	4.6
Energy, J	30.32	0.35	1.2

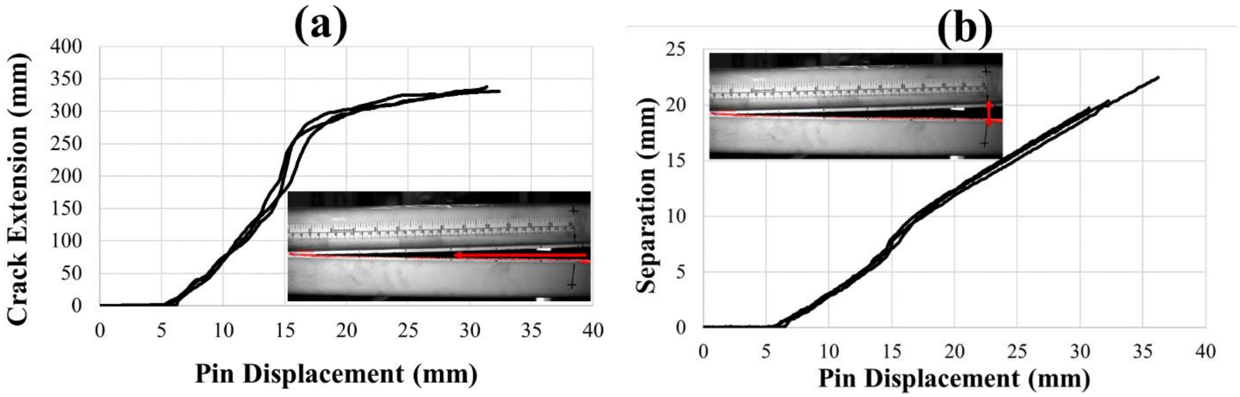

Figure 124: The adhesive crack extension (a) and the flange separation at the adhesive crack tip (b) as a function of the pin displacement.

The separation at the adhesive crack tip, measured optically, showed consistent behaviour and increased linearly with pin displacement. The separation value at the adhesive crack tip was lower than the pin displacement value due to the frame and test component compliance, and somewhat adhesive ductility. Importantly, all components showed a uniform, consistent cohesive failure along the flanges (Figure 125). Overall, there was no noticeable difference in the progressive adhesive joint failure, and all repeats showed no deformations in the hat sections, attributed to the adhesive crack progression dominating the test response (Figure 126). Liu (2019) tested adhesive joined Caiman components made with ultra-high-strength steel (YS = 1500 MPa, 1.2 mm thick) comprising hat sections with two different tailored flange properties, such that the flange yield strength was reduced from 1500 MPa to ~500 MPa. Tailoring the hat profile material properties did not result in a difference in the Caiman test peak load (2.9 kN versus 3.0 kN), indicating that the test was likely dominated by the joining method rather than the parent metal properties and deformations.

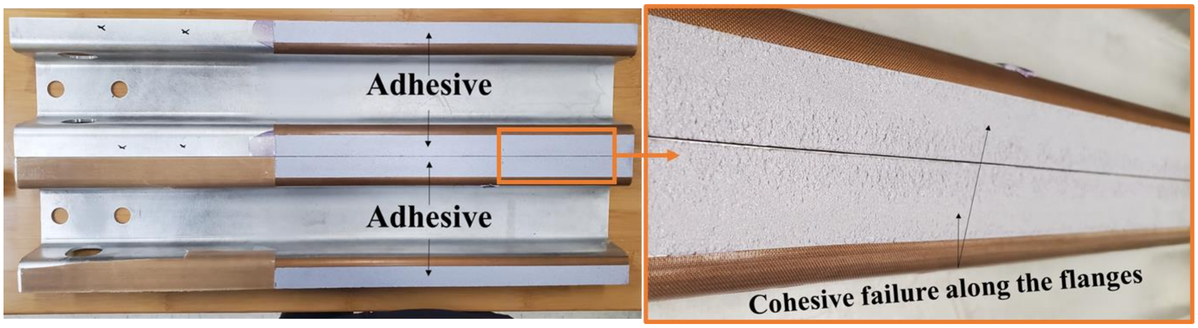

Figure 125: Failure surface of adhesive joined Caiman components.

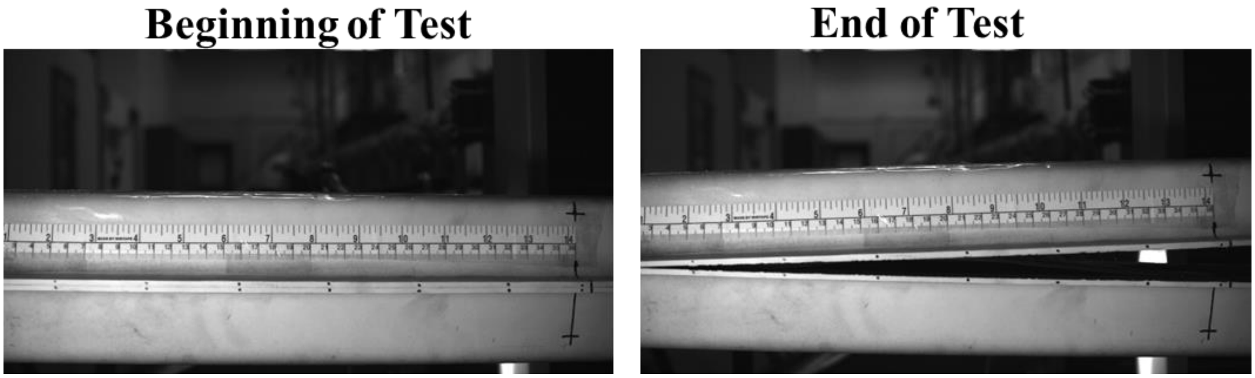
Beginning of Test

End of Test

Figure 126: The deformation of the adhesive joined Caiman component.

4.7.2 SPR Joined Caiman Test Results and Analysis

The SPR-joined Caiman components showed consistent load-displacement response with an average peak load of 8.89 kN (+234% increase over adhesive joints) and a standard deviation of 5.5% (Table 19). The peak load corresponded to the failure initiation of the first row of SPR rivets, which took place at an average pin displacement of 25.9 mm (+354% increase over adhesive joints) (Figure 127a). The substantial increase of displacement at peak load relative to adhesive could be explained by (a) the higher overall compliance of mechanically interlocked SPR rivets, and (b) the localized deformation encountered in the vicinity of the rivet during the progressive joint damage up to failure. The overall structure stiffness was 0.42 (-32.6% reduction relative to adhesive joints), indicating that even at a rivet spacing of 25 mm, SPR joining could not result in a joint stiffness comparable to a continuous joining method (adhesive). The energy absorbed to fail a total of twenty-six rivets (thirteen rivets on each flange) and separate the hat sections under Mode I loading was 442.84 J (Figure 127b), increasing the energy absorbed by 1361.0% over adhesive joints.

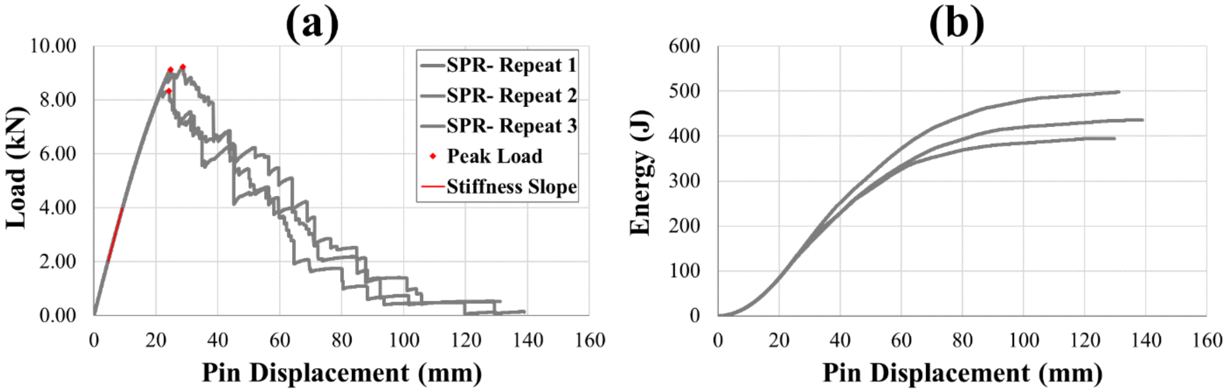

Figure 127: The load-displacement and energy-displacement responses of the SPR joined Caiman component.

Table 18: The mechanical performance summary of the SPR joined Caiman component.

	Average Value	**Standard Deviation, Std Dev**	**Std Dev %**
Peak Load, kN	8.89	0.49	5.5
Stiffness, kN/mm	0.42	0.01	1.4
Displacement at Peak Load, mm	25.90	2.46	9.5
Energy, J	442.84	51.90	11.7

Unlike adhesive joints, the crack extension, measured optically, did not increase linearly with pin displacement due to the crack arrests encountered after rivets failure as a result of the discrete nature of SPR joining (Figure 128a). The separation at the first row of SPR rivets, measured optically, showed consistent behaviour and was influenced by the progress of rivets failure (seen as small dips (crack arrests) in Figure 128b).

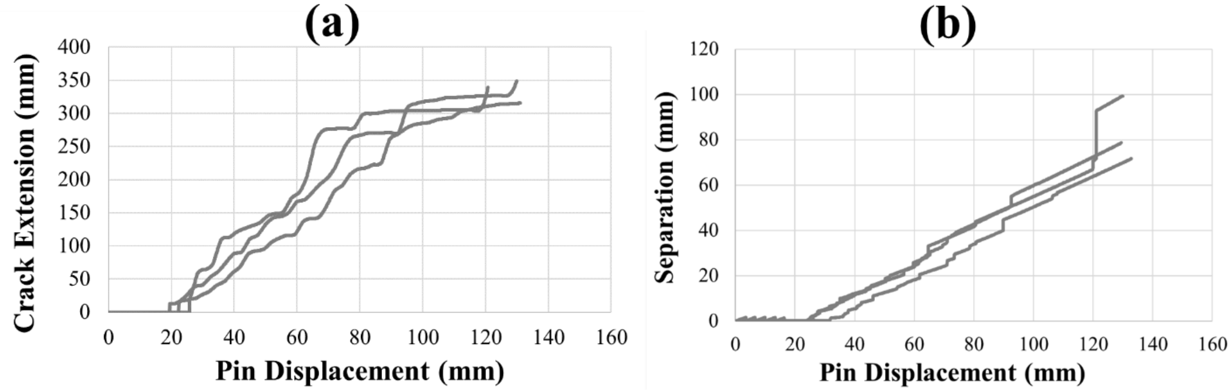

Figure 128: The flange crack extension (a) and flange separation at the first row of rivets (b) as a function of the pin displacement.

Importantly, the separation data for each rivet along the flange shed light on the local separation at each rivet, which could be used to verify the kinematics of the computational model locally for each SPR rivet (Figure 129). All the rivets consistently exhibited a tail pull-out (Figure 130), and deformation images at the beginning and end of the test showed that the majority of the strain energy was absorbed by the SPR joining, causing localized deformation in the vicinity of the rivet and propagating a crack along the flange (Figure 131). OKeeffe (2018) tested spot-welded Caiman components made with ultra-high-strength steel (YS = 1500 MPa, 1.6 mm thick), and their results showed that the variability with spot weld crack progression was quite high, and the peak loads were substantially lower than the SPR joined aluminum Caiman components (peak loads ranged between 2.5 kN to 7.5 kN).

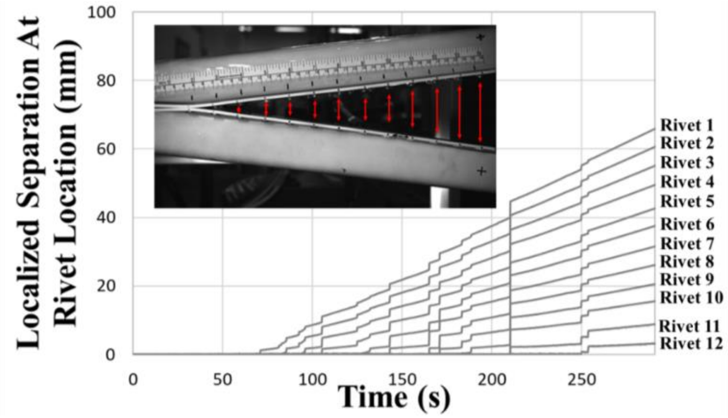

Figure 129: The flange separation at each rivet (13 rivets in total with rivet 1 starting at the right).

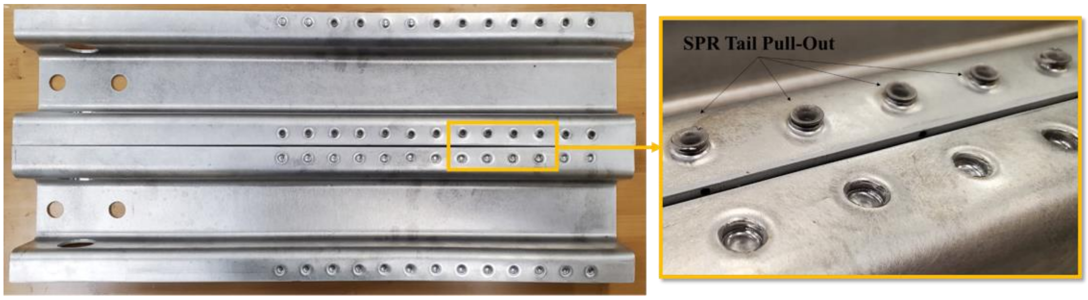

Figure 130: Consistent SPR rivet tail pull-out failure along the flanges

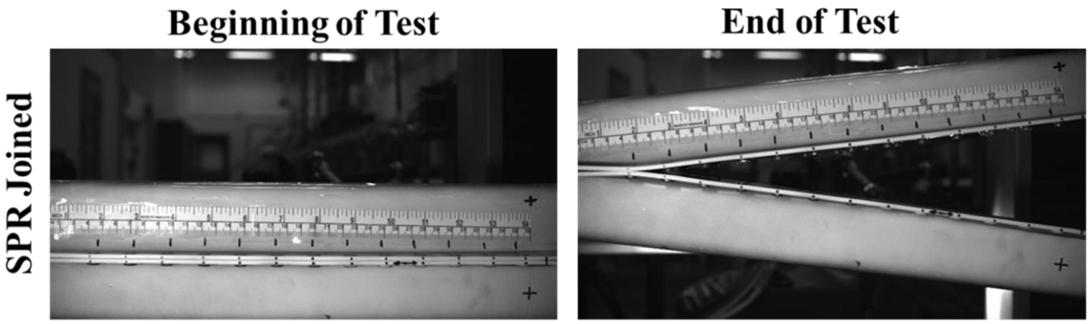

Figure 131: The deformation of the SPR joined Caiman component.

4.7.3 Hybrid Joined Caiman Test Results and Analysis

The hybrid joined Caiman components showed a consistent load-displacement response with an average peak load of 9.19 kN (Figure 132a) and a standard deviation of 5.8% (Table 19). A drop in the loading slope, observed during the initial loading, corresponded to the adhesive crack initiation, which reduced overall structure stiffness from 0.61 kN/mm to 0.42 kN/mm (adhesive presence enhanced the initial stiffness response). The peak load was substantially higher than the peak load of adhesive joints (+244.5%). The peak load was similar to the one of the SPR joints (difference of +3.2% relative to SPR joints) and corresponded to the failure of the first row of SPR rivets. The energy absorbed to separate the hat sections under tension (normal) loading was 473.38 J (Figure 132b), improving the energy absorption of SPR joining by 6.9% and adhesive joining by 1461.4%.

Table 19: The mechanical performance summary of the hybrid joined Caiman component.

	Average Value	Standard Deviation	Std Dev %
Peak Load, kN	9.19	0.53	5.8
Stiffness, kN/mm	0.61	0.019	3.1
Displacement at Peak Load, mm	32.50	1.88	5.8
Energy, J	473.38	45.89	9.7

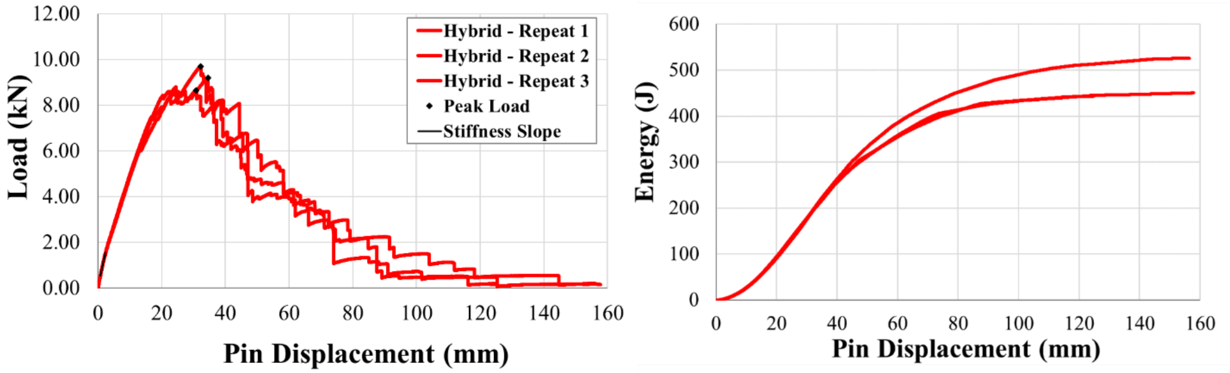

Figure 132: The load-displacement and energy-displacement responses of the hybrid joined Caiman component.

The crack extension and localized separation at the SPR rivets exhibited behaviour similar to what was reported for the SPR joining. The deformation images at the beginning and end of the test showed that the majority of the strain energy was absorbed by the SPR joining, causing localized deformation in the vicinity of the rivet; while the adhesive presence slowed down the crack propagation along the flange (Figure 133). Importantly, the larger bond area and substantially higher adhesive volume, relative to specimen-level joining, reduced the influence of adhesive squeeze-out and porosity inclusion (Figure 134). Hybrid joining achieved an overall better mechanical performance over the adhesive and SPR joints, improving the peak load, stiffness, and energy absorption of individual joints.

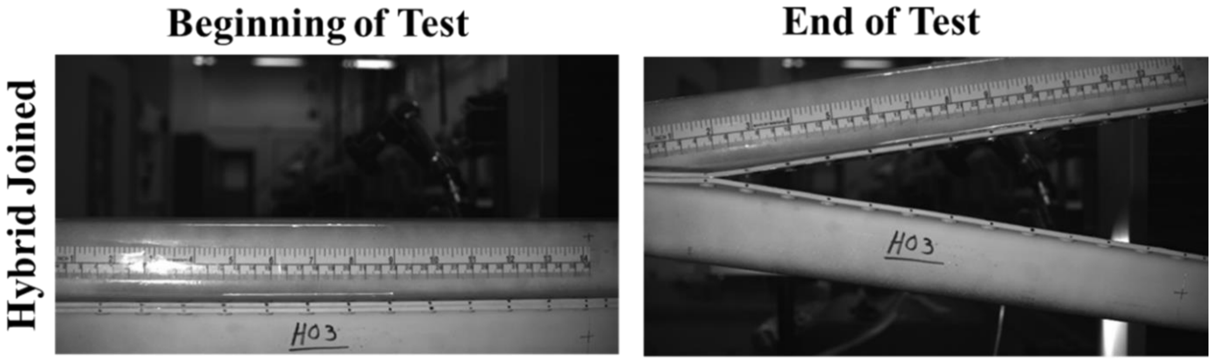

Figure 133: The deformation of the hybrid joined Caiman component.

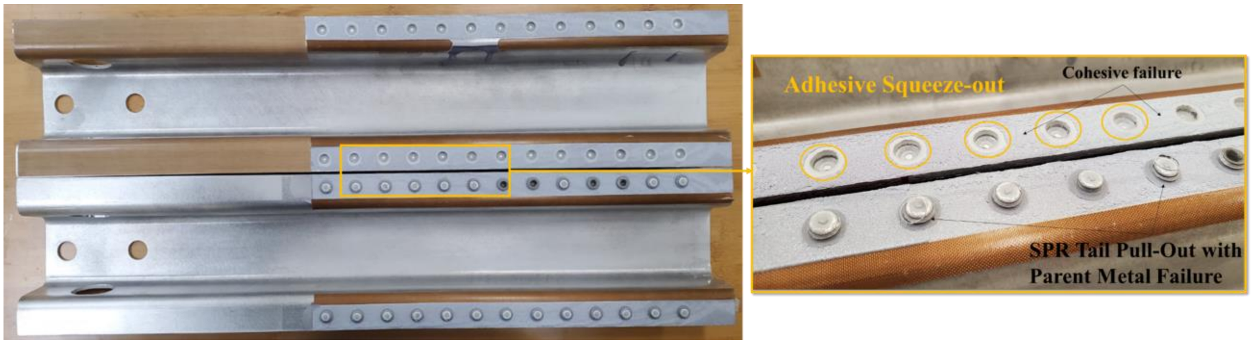

Figure 134: The failure modes of the hybrid joined Caiman component.

It was evident that hybrid joining could address the challenges associated with individual joining methods while improving the mechanical response, yet the weight implications due to hybrid joining have been rarely quantified in the literature. At the specimen level, it was shown that hybrid joining increased the weight of the test specimen between 1% to 4.5%, depending on sheet thickness (Ibrahim and Cronin, 2022). However, measuring the weight increase due to hybrid joining per meter of joining line would be more relevant to structural joining and would provide a reasonable estimate of the weight increase in a vehicle structure. For example, an automotive designer would be able to estimate the weight increase due to hybrid joining in the 2014 Lexus IS, which uses 25 meters of adhesive bonding (Toyota Canada Inc., n.d.). The Caiman component, total joining length of 714 mm (2 flanges x 357 mm), allowed measuring the weight associated with the adhesive, SPR and hybrid joining (Table 20).

The average weight of the adhesive, SPR and hybrid joining was 18.0 ± < 1 g, 32.0 ± < 1 g, 44.3 ± < 1 g. Thus, hybrid joining increased the weight of the structure by 36.8 g per meter and 17.2 g per meter compared to adhesive and SPR joining, respectively. For instance, a 2014 Lexus IS with 25 m of adhesive joining would add 920 grams to improve the mechanical response by switching to hybrid joining.

Table 20: Weight measurements of the Caiman Components joined using adhesive, SPR and hybrid joining (T and B indicate the top and bottom hat sections, respectively)

	Weight of Hat Sections before Joining (grams)	Weight of Caiman Tubes after Joining and Cleaning (grams)	Weight of Joining Method (grams)
Adhesive Joined Caiman Components			
A01T	995	2,000	19
A01B	986		
A02T	991	2,009	19
A02B	999		
A03T	997	2,001	17
A03B	987		
Average	**992.5**	**2,003.3**	**18.0**
Std Dev	**4.9**	**4.0**	**<1**
SPR Joined Caiman Components			
S01T	987	2,003	31
S01B	985		
S02T	986	2,006	32
S02B	988		
S03T	985	2,008	33
S03B	990		
Avg	**986.8**	**2,005.7**	**32.0**
Std Dev	**1.8**	**2.1**	**<1**
Hybrid Joined Caiman Components			
H01T	987	2,027	45
H01B	995		
H02T	984	2,024	44
H02B	996		
H03T	992	2,031	43
H03B	996		
Avg	**991.7**	**2,027.3**	**44.0**
Std Dev	**4.6**	**2.9**	**<1**

4.7.4 Effect of Hybrid Joining Process Variation

The mechanical response of Caiman components, prepared using the hybrid joining process variation (SPR rivets applied post-curing the adhesive at room temperature) that resulted in improved morphology and increased SLJ strength, was compared to the ones prepared using the widely used hybrid joining process (SPR rivets applied to the uncured adhesive). The results data for the Caiman components prepared using the hybrid joining process variation, hereafter denoted as ‘Hybrid – Cured’, showed improved consistency and repeatability in the load-displacement response compared to the traditional hybrid joining. The ‘Hybrid – Cured’ Caiman tubes exhibited an average peak load of 8.14 kN (Figure 132a) with a low standard deviation of 2.3%, and the unloading curve showed less variability during the crack progression due to SPR rivet failure. The peak load corresponded to the damage initiation within the first row of rivets and was lower than the peak load of the traditional hybrid joints (a difference of -11.4% relative to hybrid joints). Similar to the traditional hybrid joined components, an initial drop in the stiffness was observed, which corresponded to the adhesive crack initiation and reduced the overall structure stiffness from 0.62 kN/mm to 0.44 kN/mm. The energy absorbed to separate the hat sections was 300.75 J (Figure 132b), lower than the energy absorption of traditional hybrid joints by 36.4%.

Table 21: The mechanical performance summary of the ‘Hybrid – Cured’ Caiman components with SPR rivets, spaced at 25 mm, applied post adhesive curing at room temperature.

	Average Value	**Standard Deviation, Std Dev**	**Std Dev %**
Peak Load, kN	8.14	0.19	2.3
Stiffness, kN/mm	0.62	0.02	3.6
Displacement at Peak Load, mm	20.90	1.80	8.6
Energy, J	300.75	5.15	1.7

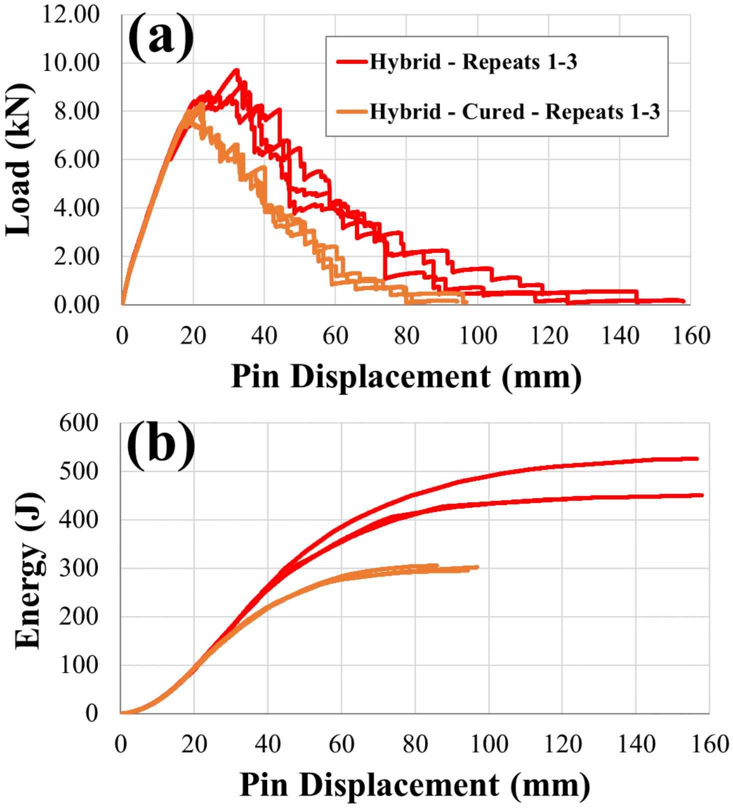

Figure 135: The load-displacement (a) and energy-displacement (c) responses of the hybrid joined Caiman component with SPR rivets applied post curing at room temperature.

Using the process variation with improved adhesive morphology did not improve the mechanical performance of the hybrid joints at a component scale. Although the process variation achieved the desired outcomes at the specimen level, the same outcomes were not attainable when the hybrid joint was subjected to Mode I (peel) loading. At the specimen level, the joining methods were subjected to tension (H-specimens) and shear (SLJ) loading, and the peak load corresponded to the adhesive crack initiation. The hybrid joining process variation improved the peak load and stiffness relative to the traditional hybrid joining process because it improved the adhesive morphology. However, the Caiman test applied peel loading (Mode I). Adhesives showed a substantial reduction in strength under peel loading, and the adhesive crack was initiated early during the initial loading, which resulted in an early adhesive failure and peak load corresponding to the damage propagation of the SPR rivet (first row of rivets). Therefore, the process variation, which focused on improving the adhesive morphology, did not contribute to the peak load of the joint. On the contrary, the improved adhesive morphology weakened the mechanical interlock of the SPR rivet (Figure 136a). The adhesive separation during crack progression resulted in a loss of contact between the top and bottom sheets, which reduced the confinement of the mechanical interlock and allowed relative motion within the interlocked joint. Thus, the joint experienced a lower strength relative to traditional hybrid joining and adhesive hackles were observed in the vicinity of the rivet indicating that the crack path has likely moved closer to the parent metal as it progressed toward the rivets (Figure 136b).

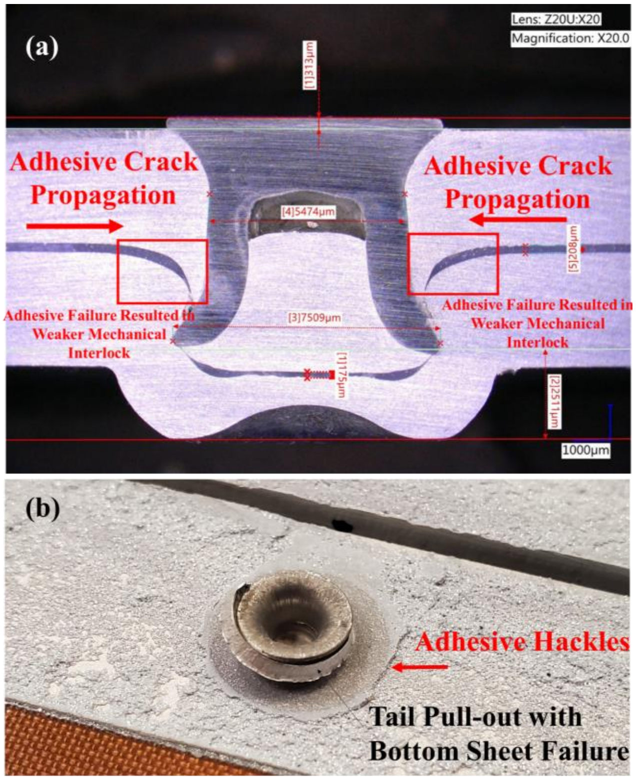

Figure 136: Adhesive crack propagation (a) resulted in a weaker mechanical interlock and consequently reduced the hybrid joint strength, and adhesive hackles (b) indicated a change in the characteristics of adhesive crack propagation.

Finally, it could be concluded that the process variation worked well when the peak load corresponds to the adhesive failure; however, in joints with an early adhesive crack initiation, the process variation may reduce the SPR rivet joint interlock and consequently the peak load. The findings reported in this section encouraged evolving the research plan to include a FE investigation to assess the performance of adhesive, SPR and traditional hybrid joining under Mode I (peel) loading at the specimen level (section 5.6.2).

4.7.5 Effect of Rivet Spacing on Hybrid Joined on Mechanical Response

To assess the effect of rivet spacing, the Caiman components were joined using hybrid joining with SPR rivets applied post curing at double the rivet spacing (50 mm spacing), hereafter denoted as 'Hybrid – Cured – Double'. The force-displacement response was compared to the results data of Caiman components joined using the same process variation discussed in the previous section ('Hybrid – Cured'), which used the standard rivet spacing of 25 mm. In comparison, the 'Hybrid – Cured – Double' results data showed the same consistency and repeatability in load-displacement response, with an average peak load of 6.16 kN (Figure 137a) and a standard deviation of 2.3% (Table 22).

Table 22: The mechanical performance summary of the hybrid joined Caiman component with SPR rivets. spaced at 50 mm, applied post adhesive curing at room temperature.

	Average Value	**Standard Deviation, Std Dev**	**Std Dev %**
Peak Load, kN	6.16	0.06	1.0
Stiffness, kN/mm	0.63	0.02	3.9
Displacement at Peak Load, mm	15.16	0.16	1.0
Energy, J	144.85	6.34	4.4

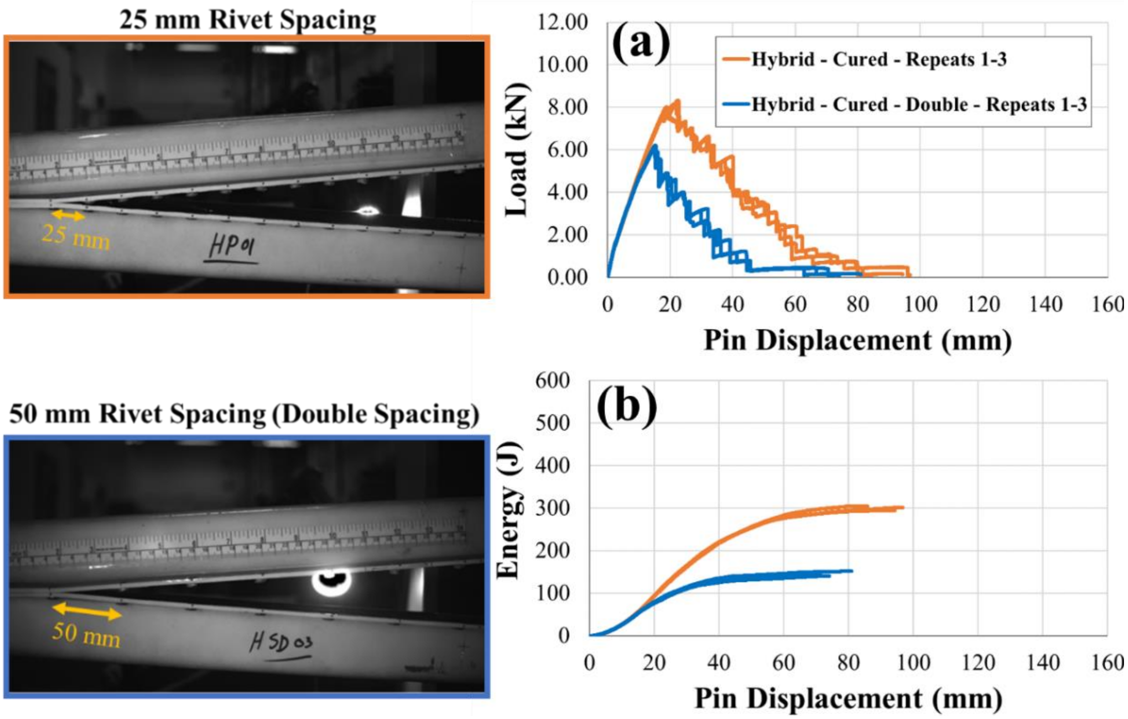

Figure 137: The load-displacement (a) and energy-displacement (c) responses of the hybrid joined Caiman component with SPR rivets applied post curing at room temperature using single and double rivet spacings (25 mm and 50 mm).

Increasing the rivet spacing decreased the number of rivets which led to a lower peak load (-24.3% relative to the ‘Hybrid – Cured’). Also, the energy absorption was 144.85 J only, which was 36.4% lower than the ‘Hybrid – Cured’ (Figure 137b). On the other hand, increasing the rivet spacing did not influence the structural stiffness (0.63 ± 0.02 kN/mm versus 0.62 ± 0.02 kN/mm), indicating that the initial loading stiffness was dominated by the first row of rivets and adhesive crack tip. The rivet spacing did not influence the failure modes and all tests exhibited consistent SPR rivet tail pull-out (Figure 138).

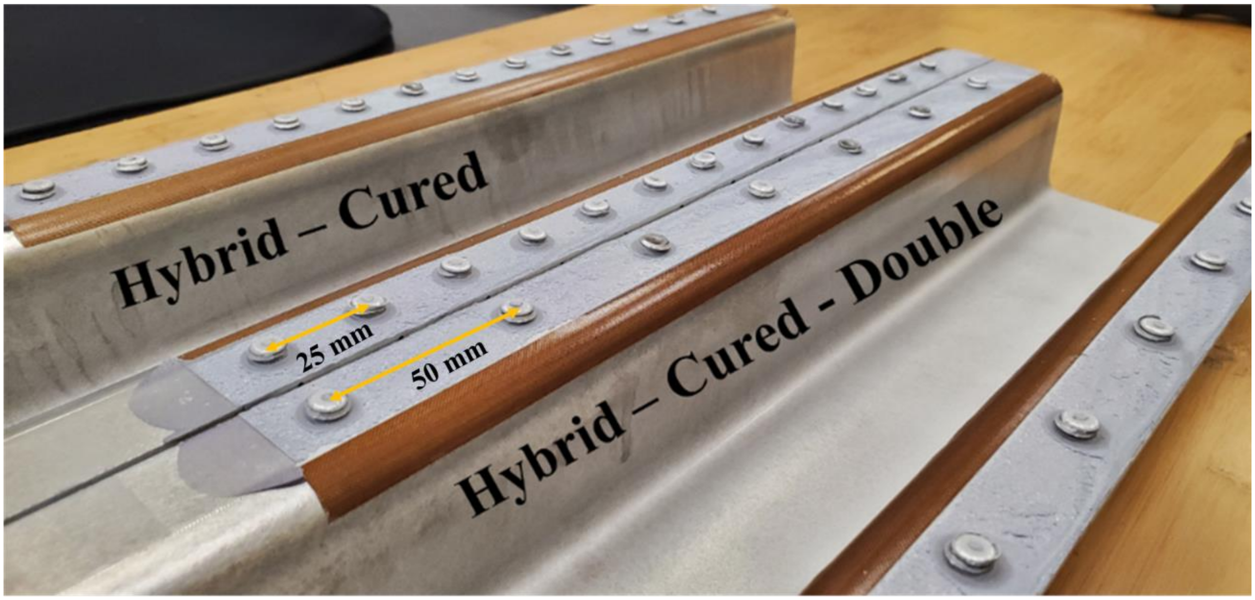

Figure 138: The failure modes of the hybrid joined Caiman components prepared using single ‘Hybrid – Cured’ and double ‘Hybrid – Cured - Double’ spaced SPR rivets.

In addition, the weight saving due to increasing rivet spacing was assessed to determine the feasibility of the approach for lightweight applications. By increasing the rivet spacing from 25 mm to 50 mm, the weight of the hybrid joining method was reduced from 49.3 g to 27.0 g (-45.2%) (Table 23). While the reduction value is significant in terms of percentage, it was important to look at the weight-saving value using the context of weight reduction per meter of joining method. Given that the total joining length of the Caiman component was 714 mm (2 x 357 mm), the total weight reduction was 22.3 g per 714 mm, corresponding to 31.2 g per meter of joining. For example, doubling the rivet spacing on a 2014 Lexus IS, which has 25 meters of joining, would save only ~780 grams, but joint strength and energy under Mode I loading would be reduced by 24.3% and 36.4%, respectively.

Table 23: Weight measurements of the Caiman Components joined using ‘Hybrid – Cured - Double ’ and ‘Hybrid – Cured’ (T and B indicate the top and bottom hat sections, respectively)

	Weight Prior to Bonding (grams)	**Weight Post Adhesive Application (grams)**	**Weight Post Riveting and Cleaning (grams)**	**Weight of Joining Method (grams)**
Hybrid - Cured - Double (HCD)				
HCD01T	987	1997	2013	29
HCD01B	997			
HCD02T	993	1997	2013	27
HCD02B	993			
HCD03T	992	1998	2014	25
HCD03B	997			
Avg	**993.1**	**1997.3**	**2013.3**	**27**
Std Dev	**3.3**	**0.4**	**0.4**	**1.6**
Hybrid - Cured				
HC01T	988	2006	2038	49
HC01B	1001			
HC02T	984	1997	2029	48
HC02B	997			
HC03T	982	1998	2030	51
HC03B	997			
Avg	**991.5**	**2000.3**	**2032.3**	**49.3**
Std Dev	**7.1**	**4.0**	**4.0**	**1.2**

The comparison was further extended, and the ‘Hybrid – Cured – Double’ was compared to the adhesive, SPR and traditional hybrid joining cases. Concerning peak load, the ‘Hybrid – Cured – Double’ demonstrated a peak load increase of 130.9% relative to adhesive joining, but a peak load reduction of 44.3% and 49.0% compared to the SPR and traditional hybrid joining, respectively. The same trend was observed with energy absorption, showing an increase relative to adhesive joining (+377.9%) and a reduction relative to SPR (-67%.2%) and hybrid (-69.3%) joints. Concerning the weight, the ‘Hybrid – Cured – Double’ was heavier than the adhesive, SPR and traditional hybrid joining by 173.8%, 54.0%, and 12.0%, respectively. Although the ‘Hybrid

– Cured – Double' had double the rivet spacing compared to traditional hybrid joining, it was still 12% heavier because it did not experience any adhesive squeeze out. Importantly, the traditional hybrid joining enhanced the performance of adhesive-only and SPR-only joining. Using the process variation worked well under shear and tension loading because the peak load corresponded to adhesive joining. However, the process variation exhibited a reduced mechanical performance under Mode I loading in addition to increased weight.

Chapter 5: Finite Element Modeling Methodology

Following the experimental testing carried out to characterize adhesive, SPR and hybrid joints made with aluminum sheet metal at specimen and component levels, finite element models were developed to simulate the mechanical response of the joining methods. First, the adhesive characterization data from the literature (Watson *et al.*, 2020) was implemented into a cohesive zone model to simulate adhesive joint crack initiation, progression and failure. The adhesive CZM model was validated under tension and shear loading using the experimental data for the adhesively joined H-shaped and SLJ joints. The verification of the models included the range of sheet thicknesses, considered in the experimental investigation, and commonly used in the automotive industry (1, 2, and 3 mm), to incorporate varying degrees of adherend yielding and plasticity.

Second, two approaches were considered for modeling and calibrating SPR rivets. The SPR constraint model developed by Hanssen *et al.* (2010) was calibrated and verified using the H-specimens and SLJ experimental data undertaken in this work for joints made with three sheet thicknesses (1, 2, and 3 mm). Then, an alternative SPR modeling approach using CZM was adopted and the calibrated CZM model of the SPR rivet was verified using the same using H-specimen and SLJ experimental data for a single sheet thickness (3 mm).

Next, the adhesive and SPR joint models were integrated to develop the hybrid joining models. The hybrid joining models considered the adhesive morphology changes measured experimentally, mapping the adhesive squeeze out into the adhesive CZM model to capture the effect of adhesive porosity and reduced bond line thickness. The hybrid joining model, combining adhesive CZM and SPR constraint models, was validated using the specimen-level test results (H-specimens and SLJ) for three sheet thicknesses. In addition, an alternative hybrid joining model, combining adhesive CZM and SPR CZM models, was validated using the H-specimens and SLJ joints made with 3 mm thick sheets. Finally, the adhesive, SPR and hybrid joint models were implemented in structural scale Caiman models, and each model (one model for adhesive, two models for SPR rivet, and two models for hybrid joining) was validated using experimental at a structural level. The structure scale models were validated using the load-displacement response of the experimental data, and optically measured local validation metrics, such as crack extension, and local separation between the flanges.

5.1 Aluminum Sheet Metal (Adherend) Modeling

The H-specimen, SLJ and Caiman geometries were conceptualized by developing 3D CAD parts of the adherends geometries using commercial CAD design software (Solidworks 2019, Dassault Systèmes, USA). The SLJ specimen comprised flat sheets, which were modeled using 3D cubes with the required dimensions. The H-specimen and Caiman components required drawing the profile of each section (U-section for H-specimen and Hat section for Caiman) and then extruding the section along the length of the part. After that, the features (*i.e.*, holes) were added. The 3D solid parts of the adherends (U-section, flat sheet or hat section) were then exported into a commercial finite element meshing software (Hypermesh 2018, Altair, USA) to assemble the H-specimen, SLJ and Caiman component from the 3D parts. The parts were mirrored and then positioned according to sheet thickness and joining method to be used. All adherends were modeled using shell elements, to provide computational efficiency and compatibility with large-scale models. Therefore, the 3D parts were converted into mid-plane surfaces prior to meshing. After meshing, shell offset was considered to account for the thickness of the sheet and adhesive.

Then, the element and nodal definitions were exported to a FE preprocessor software (LS-PrePost 4.8, LST/Ansys, USA) to define the material models, joint models, load, and boundary conditions, and then generate the input files for each test configuration. The models were solved using a commercial FE package (LS-DYNA Multiphysics Solver R9.7, LST/Ansys, USA) running on a high-performance computing cluster (Graham Cluster, Digital Research Alliance of Canada). The simulation output data were post-processed in a FE postprocessor (LS-PrePost 4.8, LST/Ansys, USA) to extract, analyze and visualize the computational results.

Fully integrated 4-node shell elements (shell type 16 in LS-DYNA) were used because of their high accuracy in capturing large strains and rotations using a single element through the thickness. The shell elements had a formulation based on the Reissner-Mindlin kinematic assumption with five degrees of freedom (DOF) in a local coordinate system that yields six DOF globally. The elements had 2x2 integration points in the plane of the shell, seven integration points through the thickness and activated warpage stiffness (hourglass control type 8 in LS-DYNA). The shell reference surface was coincident with the mid-surface of the sheet metal. A shell element size of 2 mm x 2 mm was used for the SLJ and Caiman models, and 1 mm x 1 mm was used for the H-specimen models. Previous research studies used shell element sizes ranging from 1 to 2.5 mm for similar SLJ models (Ibrahim *et al.*, 2023; Watson *et al.*, 2019) and Caiman hat sections (Liu, 2019). The H-specimen experimental tests showed localized deformation within the bend region, so the models used a 1 mm element size to ensure a sufficient number of elements within the bend region and achieve a smooth curved geometry (Appendix A, A.3). However, further refinement (1 mm to 0.5 mm elements) was not necessary and did not improve the response of the joints (Appendix A, A.3).

The aluminum adherends were modelled using a piecewise linear elastic-plastic material model with isotropic hardening (*MAT_24 in LS-DYNA). The material model parameters (*i.e.*, elastic properties and flow stress-plastic strain data) were obtained from material characterization tensile tests at a quasi-static loading rate. The material models of the adherends did not require a failure criterion because the failure occurred within the joint (adhesive, SPR or hybrid) in all the tests with the AA6061-T6 alloy. The stress-effective plastic strain curves for the 1 mm, 2 mm and 3 mm sheets were fitted to a power-law curve (simplified Johnson-Cook (JC) flow stress expression) in MATLAB using non-linear regression. The fitted data were exported in a tabulated format using a sufficient number of data points to provide a smooth curve with positive tangent stiffness (100 data points were used) (Figure 74). The piecewise linear elastic-plastic material model (Mat_24 in LS-DYNA) was used over the simplified JC material model (Mat_98 in LS-DYNA) because it is widely used in automotive, can be extended to account for rate dependency, and is compatible with complex failure criteria used in crash applications (*e.g.,* Generalized Incremental Stress-State dependent Damage Model, GISSMO).

To verify the material model implementation within the commercial FE package (LS-DYNA), a series of single-element simulations were carried out, incorporating the 1 mm, 2 mm and 3 mm sheet material thicknesses. A single 1 mm x 1 mm 4-node shell element was assigned the average measured sheet thickness. The two nodes of the fixed edge of the shell element were constrained in all translational degrees of freedom, while a prescribed displacement was applied to the other two nodes of the element to load it uniaxially. The shell element used the piecewise linear elastic-plastic material model with the fitted stress-strain data presented in Figure 74 for each sheet thickness.

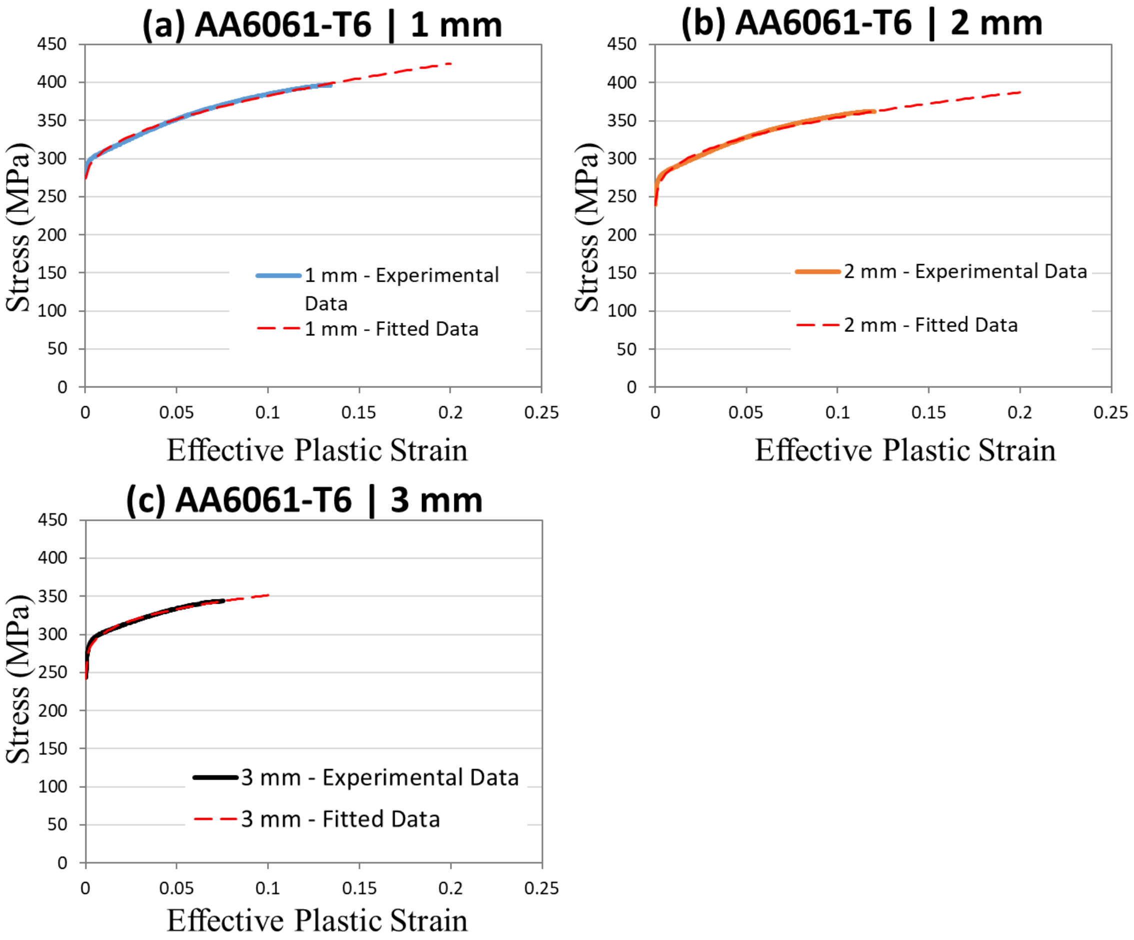

Figure 139: The aluminum AA6061-T6 alloy material characterization data fitted to the Johnson-Cook model with three sheet thicknesses: 1 mm (a), 2 mm (b), and 3 mm (c).

5.2 Modeling and Validation of Adhesive Joints (Cohesive Zone Modeling)

The adhesive was modeled using eight-node 3D CZM elements (Figure 140) with a single layer of elements having a thickness equal to the physical bond line thickness (0.3 mm) (Figure 141a). One of the important aspects of 3D cohesive element modeling is the local coordinate system of each element, which is defined by the numbering sequence of the nodes. The 3D cohesive elements are assumed to be under normal loading (Mode I loading) if the traction/separation was applied to the top (n5, n6, n7, n8 in Figure 140) or bottom faces (n1, n2, n3, n4 in Figure 140). Therefore, it was important to number the nodes of each cohesive element to properly define the normal direction and achieve a proper local coordinate system for each cohesive element. The node numbering was done during the preprocessing phase, in particular during meshing (discretization), of the model development in the FE pre-processing software (Hypermesh 2018, Altair, USA). A custom-made script facilitated batch processing of all the cohesive elements and applied the node numbering scheme to all adjacent cohesive elements based on a reference element. The node renumbering redefined the normal direction (element orientation) with respect to the global coordinate system of the model, aligning the normal orientation of the element with Mode I loading. The script was coded in TCL and a copy of the script was made available within this document (Appendix A).

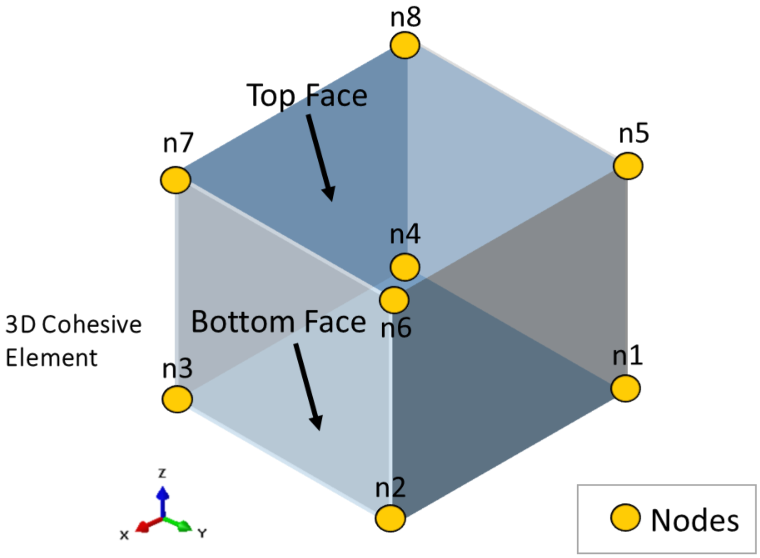

Figure 140: 3D cohesive element node numbering to determine the top and bottom faces.

The top and bottom surfaces of CZM elements were connected to the adherend shell elements using a tied constraint accounting for the shell thickness offset (Figure 141b). The tied constraint allowed using cohesive elements without matching the adherend shell elements mesh (without shared nodes) while accounting for translational and rotational degrees of freedom to transfer the loads and moments between the shell and cohesive elements. The cohesive elements were assigned an element formulation that allowed for the moments to be transferred using the defined tied constraint (element formulation 19 in LS-DYNA). First, the shell elements (mid-plane) were positioned at the center of the adherend thickness, and the top and bottom surfaces of the cohesive elements were then constrained to their adjacent shells using two tied constraints (*TIED_SHELL_EDGE_TO_SURFACE_CONSTRAINED_OFFSET in LS-DYNA) (Figure 141b).

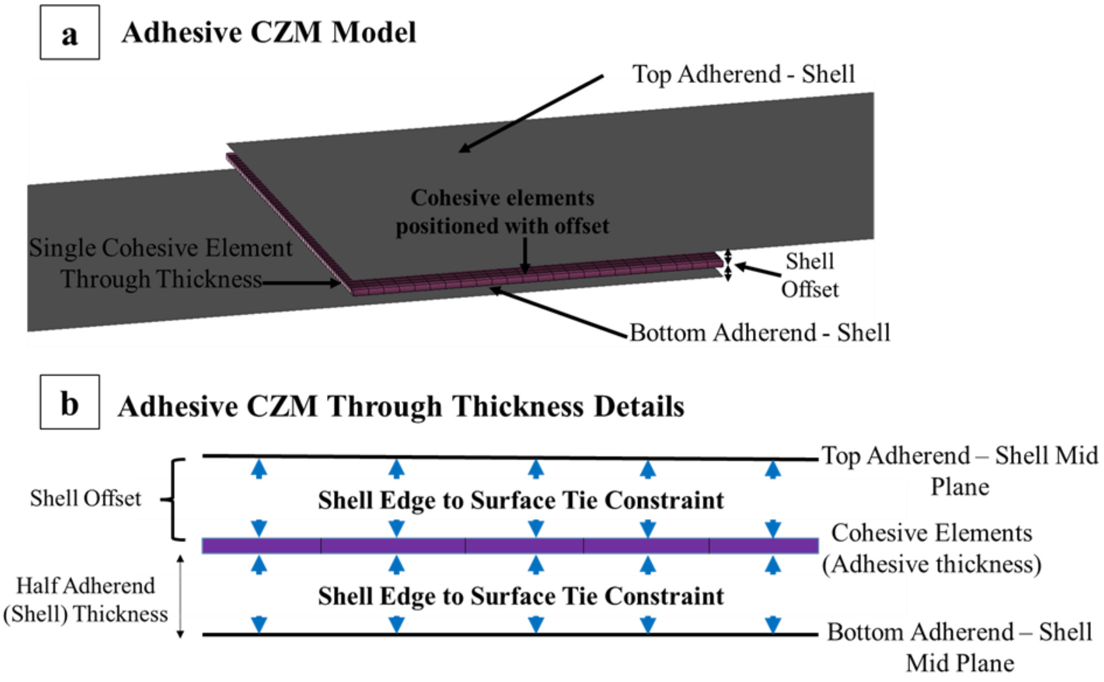

Figure 141: (a) Adhesive modeled with CZM elements and (b) a through-thickness schematic of the adhesive bond line model accounting for shell thickness.

The Mode I and Mode II CZM traction-separation parameters were obtained from the literature (Watson *et al.*, 2020) for the same adhesive and bond line thickness used in this work (Table 4). The material model definition (*MAT_240) contained the parameters that defined the traction-separation law for both Mode I and Mode II loading conditions (Table 25). In the material model, *emod* and *gmod* are the tensile and shear elastic moduli, respectively, *t0* and *s0* are the peak tractions, *fg1* and *fg2* are the ratios of the area under plateau to the total area, and *g1c_0* and *g2c_0* are the critical energy release rates under Mode I and Mode II loading, respectively (Figure 142).

Table 24: Cohesive zone method parameters for the 3M 07333 adhesive with 0.3 mm bond line thickness (Watson *et al.*, 2020).

Loading Mode	Stiffness (MPa/mm)	Peak Traction (MPa)	Critical Energy Release Rate (kJ/mm^2)	Area Ratio
Mode I	1,762	51	2.13	0.49
Mode II	1,880	29	7.28	0.96

Table 25: *MAT_240 keyword card used in this study for the 3M 07333 adhesive.

Variable	**mid**	**ro** (Kg/mm³)	**roflg**	**intfall**	**emod** (GPa)	**gmod** (GPa)	**thick**
Value	2	1.2e-9	0	1	1762	1880	1
Variable	**g1c_0** (N/mm)	**g1c_inf**	**edot_g1**	**t0** (MPa)	**t1**	**edot_t**	**fg1**
Value	2.13	0	0	51	0	0	0.49
Variable	**g2c_0** (N/mm)	**g2_inf**	**edot_g2**	**s0** (MPa)	**s1**	**edot_s**	**fg2**
Value	7.28	0	0	29	0	0	0.96

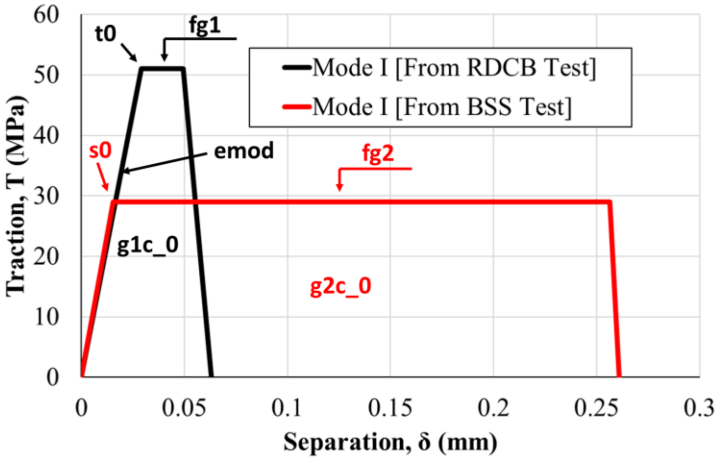

Figure 142: Trapezoidal traction-separation relationship for 3M 07333 adhesive with annotated CZM parameters.

A cohesive element size of 1 mm x 1 mm was used for the specimen-level models (SLJ and H-specimens) (Ibrahim *et al.*, 2023; Watson *et al.*, 2020), and 1.5 mm x 1.5 mm was used for the Caiman models. Marzi *et al.* (2008) showed that a cohesive element of 2 mm generally converged well when modeling adhesives in large-scale FE models, but adding mass scaling to the problem may require cohesive element mesh refinement. In this work, 1.5 mm cohesive elements were assessed with and without selective mass scaling, and the simulation results for the adhesively joined Caiman simulations were presented in section 6.5.1.

5.2.1 Single Lap Shear Joint Validation (CZM Model under Shear Loading)

The SLJ models comprised two flat aluminum substrates representing the adherends, which were discretized using 2160 fully integrated shell elements, and a layer of adhesive represented by 1248 cohesive elements (Table 26). Separate models were developed for each sheet thickness (1 mm, 2 mm and 3 mm), and the shell offset was adjusted according to shell thickness (Figure 141b). To model the end conditions of the SLJ test, axial displacement and rotation of the model were fixed at the top and bottom surfaces of the clamping (grip) area at one end (Constrained Grip, Figure 143). The top and bottom surfaces of the clamped area at the opposite end of the specimen were prescribed a displacement and fixed in the other two translation degrees of freedom (Translating Grip, Figure 143). The maximum prescribed displacement rate was (5 mm/s), scaling the experimental test loading rate by ~50 times, which is known as time scaling. Time scaling has been suggested in the literature when modeling quasistatic tests using an explicit FE formulation to increase computational efficiency (Gulavani *et al.*, 2014), and was used in this work to achieve the target simulation runtime (less than 12 hours). The kinetic, internal and total energies were monitored, ensuring that the ratio of kinetic energy to internal energy was less than 5% (Gulavani *et al.*, 2014), and the simulation results were compared to a simulation that was time scaled by 25 times (time scale was halved) to confirm that the inertial forces were absent. The force data were extracted from the models by extracting the loads acting on the fixed nodes within the fixed grip. The SLJ joint rotation was calculated by extracting the coordinates of the nodes marked with red points (Figure 143).

Table 26: Assembly summary of the adhesively joined SLJ FE models.

Part	Geometry	Number of Nodes	Number of Elements	Type of Elements
Adherends	2D Surface	1,155 x 2	1,080 x 2	Fully integrated 4-node shell elements
Adhesive	3D Solid	2,650	1,248	cohesive elements

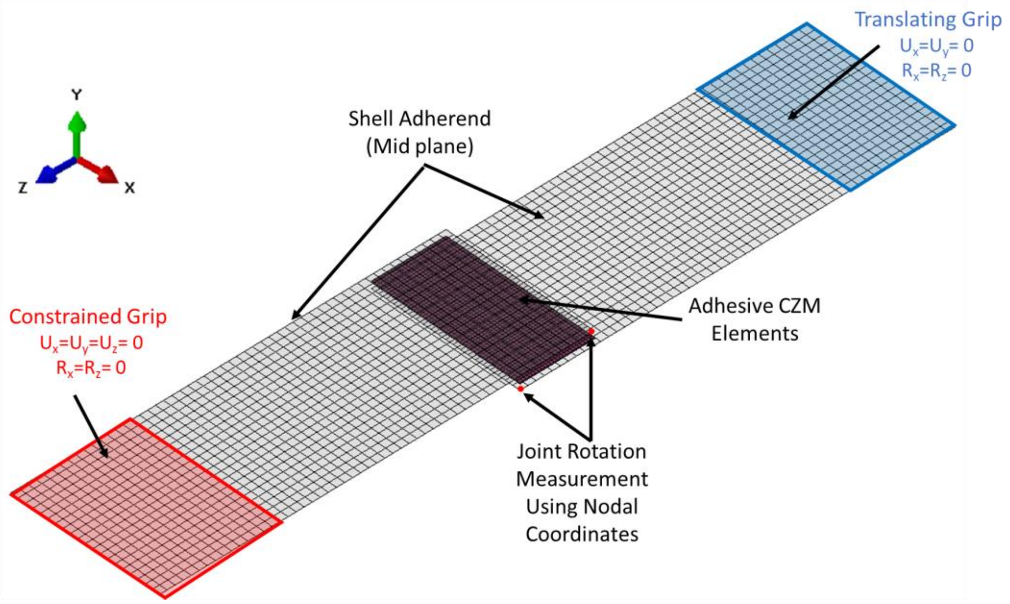

Figure 143: The SLJ model, made with 2 mm sheet material and joined using the adhesive CZM, with the boundary conditions applied. (Similar models were created for each adherend sheet thickness)

5.2.2 H-Specimens Validation (CZM Model under Tension Loading)

The H-specimen models comprised two aluminum U-sections representing the adherends, which were discretized using 4300 fully integrated shell elements (Figure 6). Three models were developed to consider each sheet thickness and incorporate adequate shell offset (Figure 144). The fixturing blocks were also modeled using shells with the same number and type of elements (Fixturing Blocks, Figure 144). The fixturing blocks were treated as rigid parts and used the material properties of steel (Density = 7850 kg/m3). The bottom fixturing block was fixed while the top one was assigned a displacement through a prescribed boundary motion to load the joint (displacement rate = 3 mm/s, time scaled by ~30 times). Similar to the SLJ joints, the aim was to model the quasi-static process using an explicit formulation scheme with a target simulation run time of under 12 hours. Time scaling (increased rate of loading) allowed for achieving the target simulation run, while inertial (dynamic) effects due to scaling were monitored throughout the simulation (total, kinetic and internal energies) and the ratio of kinetic energy to internal energy was typically less than 5% (Gulavani *et al.*, 2014). Readers should note that changing the time scaling factor should not change the simulation results unless it was increased to a limit that introduced inertial forces.

The clamped regions of the adherends (U-sections of the H-specimen) were constrained to the fixtures using rigidly constrained nodes (*EXTRA_NODES_SET in LS-DYNA) applied to the area of the clamping plates (blue and red highlighted regions, Figure 144). The rigidly constrained nodes represented the bolts, clamping plates, and initial pre-load between the plates and experimental test specimens. Two surface-to-surface contacts were defined between the U-sections and the fixturing blocks using a soft constraint formulation and a friction coefficient of 0.15 (static and dynamic). The contact definition was required to avoid nodal penetration within the bend regions as the U-sections deformed during loading. The force data were extracted from the models by monitoring the loads on the fixed fixture block, and the displacement data was extracted from the nodal displacement of the translating block.

Table 27: Assembly summary of the adhesively joined H-specimen FE models.

Part	Geometry	Number of Nodes	Number of Elements	Type of Elements
U-section	2D Surface	4,437 x 2	4,300 x 2	Fully integrated 4-node shell elements
Adhesive	3D Solid	1,938	900	Cohesive elements
Fixturing Blocks	2D Surface	4,437 x 2	4,300 x 2	Fully integrated 4-node shell elements with rigid definition

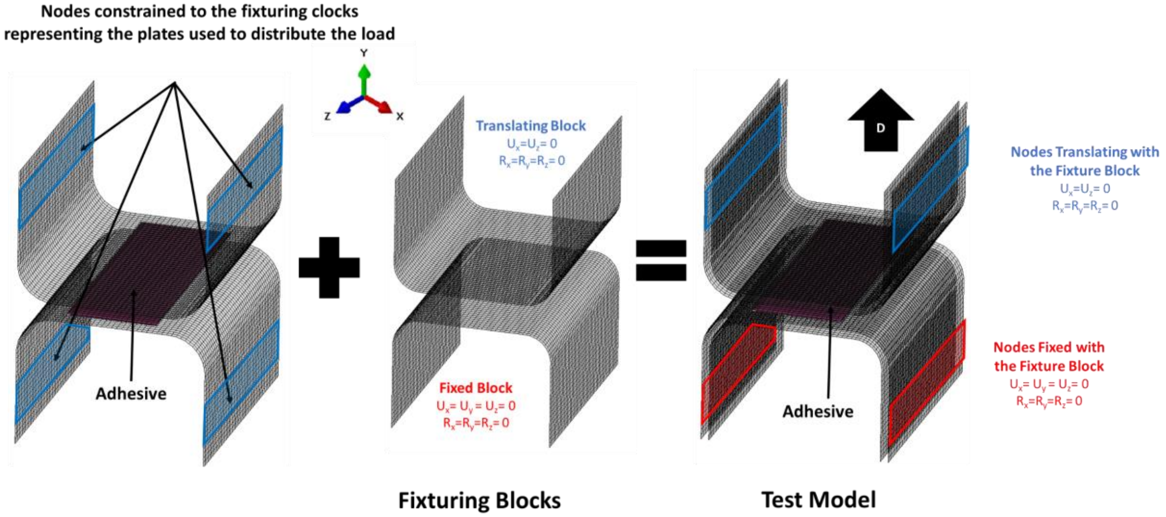

Figure 144: The H-specimen model, made with 2 mm sheet material and joined using adhesive CZM, showing the adherends and fixturing parts with boundary conditions. (Similar models were created for each adherend sheet thickness)

5.3 Modeling and Calibration of SPR Riveted Joints (Constraint and CZM Models)

Two SPR rivet modeling approaches were evaluated: (1) a meshless SPR constraint model based on the work proposed by Hanssen *et al.* (2010) and (2) a CZM model with trapezoidal traction-separation curve (*MAT_240 in LS-DYNA). The goal of the SPR rivet calibration process was to find the parameters required to accurately predict the mechanical behaviour of the SPR joints (*i.e.*, peak load, stiffness and energy absorption values) independent of loading conditions or model scale. The proposed calibration procedure was similar for both modeling approaches (constraint and CZM), requiring the load-displacement data for the SPR joint and optical measurements to determine the local separation. The two models of the SPR rivet were calibrated to the SLJ (shear/tangential) and H-specimen (normal/axial) experimental data, unlike the adhesive CZM parameters which were characterized at the material level. After verifying the models using the specimen level test data, the models were validated using Caiman test data without using a different set of parameters or re-calibration to the component level.

The SPR constraint model uses a meshless approach and does not require element discretization, which made this model convenient to adopt and use with large-scale models (Hoang *et al.*, 2012). To model SPR rivets, each rivet was defined by a node, positioned at the rivet location between the two shell elements representing the sheet materials to be joined. The node, representing the rivet, projected two spider elements (one spider element for each sheet) within the specified rivet radius of influence (Figure 145a). Each spider element connected the nodes within the specified radius of influence to a single node at the center using rigid beam elements. The central nodes of the top and bottom spider elements were connected using a beam element to transfer the forces and moments with the spider element on the master sheet controlling the joint kinematics during failure (Figure 145b).

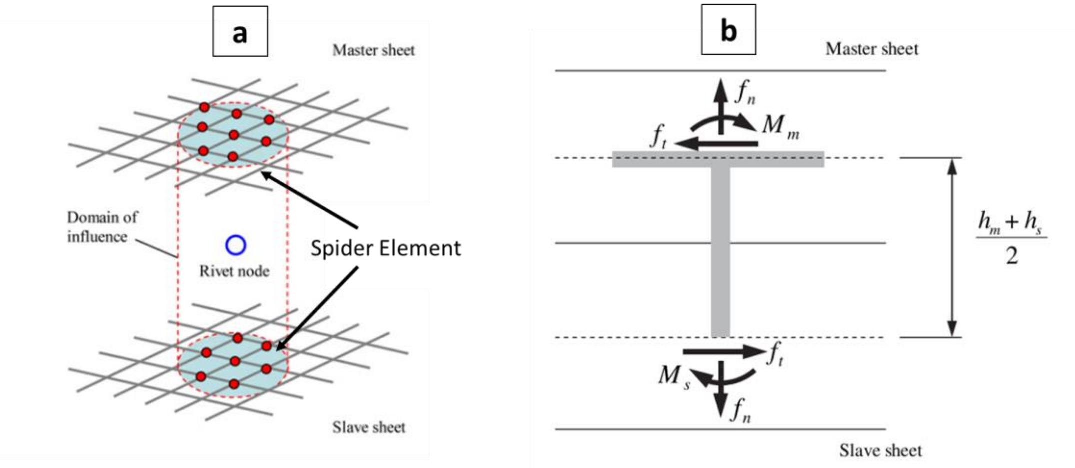

Figure 145: SPR constraint model spider elements projected to the master and slave sheets within the radius of influence (a), and account for the forces and moments acting on both sheets but follow the kinematic of the master sheet (b). Reproduced with permission from Hanssen *et al.* (2010)

The following parameters were required for the model: peak load in tension (f_n^{max}), peak load in shear (f_t^{max}), tangential separation at failure (δ_t^{fail}), normal separation at failure (δ_n^{fail}), the fraction of failure displacement at peak load in tension (ξ_n), the fraction of failure displacement at peak load in shear (ξ_t), effective rivet diameter (*D*), total stack thickness (*H*), and three dimensionless scaling parameters ($\alpha_1, \alpha_2, \alpha_3$) (Figure 146). The scaling parameters can be used to correct the force in peeling and oblique loading cases and α_1 and α_2 were recommended to have a value below 1 (Hanssen *et al.*, 2010). The parameters were used to construct normalized force-separation relationships for normal (Figure 146a) and shear (Figure 146b) loading, similar to the traction-separation relationship used in the cohesive zone modeling. The normal and shear parameters were calibrated to the H-specimen and SLJ test data, respectively, and the process was repeated for each sheet thickness.

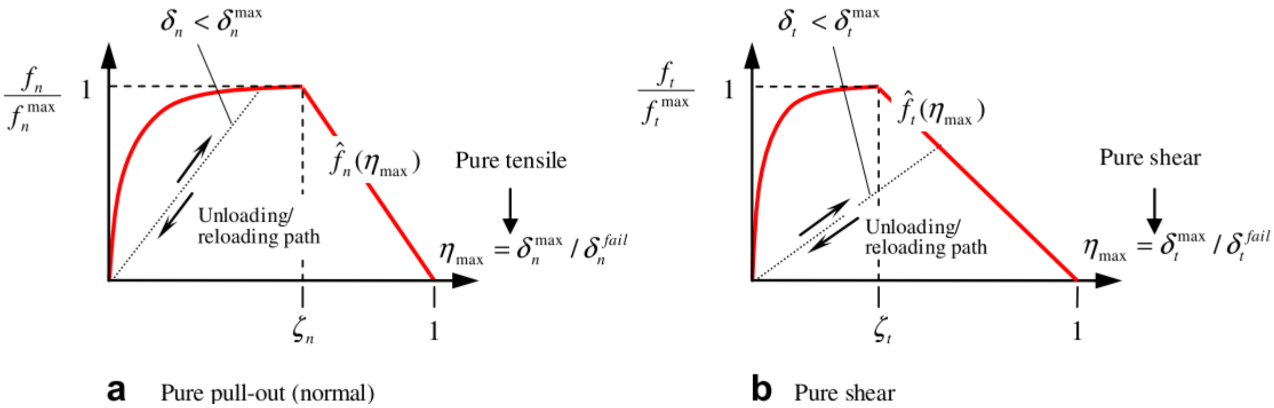

Figure 146: The SPR constraint model normalized force-separation relationship under (a) normal and (b) shear loading. Reproduced with permission from Hanssen *et al.* (2010)

The peak loads used in the SPR force-separation relationship for normal (f_n^{max}) and tangential (shear) (f_t^{max}) loads were determined by calculating measured average peak loads from the experimental tests. On the other hand, the separation at failure parameters in tangential (δ_t^{fail}) and normal (δ_n^{fail}) directions did not directly relate to the experimental load-displacement data because the displacement data was influenced by the testing frame compliance and adherend yielding. The separation at failure was measured locally within the vicinity of the SPR rivet using optical measurements. A DSLR camera with a macro lens (experimental setup details available in Chapter 3) was used throughout the experimental testing to determine the local SPR rivet separation at failure under normal (H-specimens) and tangential (SLJ) loading. The separation at failure in the tangential direction (δ_t^{fail}) was measured by tracking two targets on the side of the SLJ specimen during the test. The targets were located across the SLJ overlap region, which allowed computing the local separation across the overlap by measuring the distance between the targets at the beginning of the test and joint (rivet) failure (Figure 147). The two measurements were subtracted to determine the local separation, considering that the measurement at joint failure was aligned with the flat adherend to limit the effect of joint rotation and measure the separation in the direction of the applied load (tangential direction). Similarly, the separation at failure in the normal direction (δ_n^{fail}) was measured optically from zoomed images of the tests to measure the local separation at the instant of rivet failure (Figure 148). Tracking targets on the side of the specimen was considered; however, it did not provide the correct separation measurements because it took into account the localized yielding in the vicinity of the rivet under normal loading, resulting in substantially higher separation values (+60% higher than local separation measured at the rivet) (Figure 148). The fraction of failure separation at peak load in normal (ξ_n) and tangential (shear) (ξ_t) directions were calculated as ratio between the optically measured separations at peak load and separation at failure using,

$$\xi_i = \frac{\delta_i^{Peak\ load}}{\delta_i^{fail}} \qquad \text{Equation 13}$$

where i is the loading mode (normal or tangential).

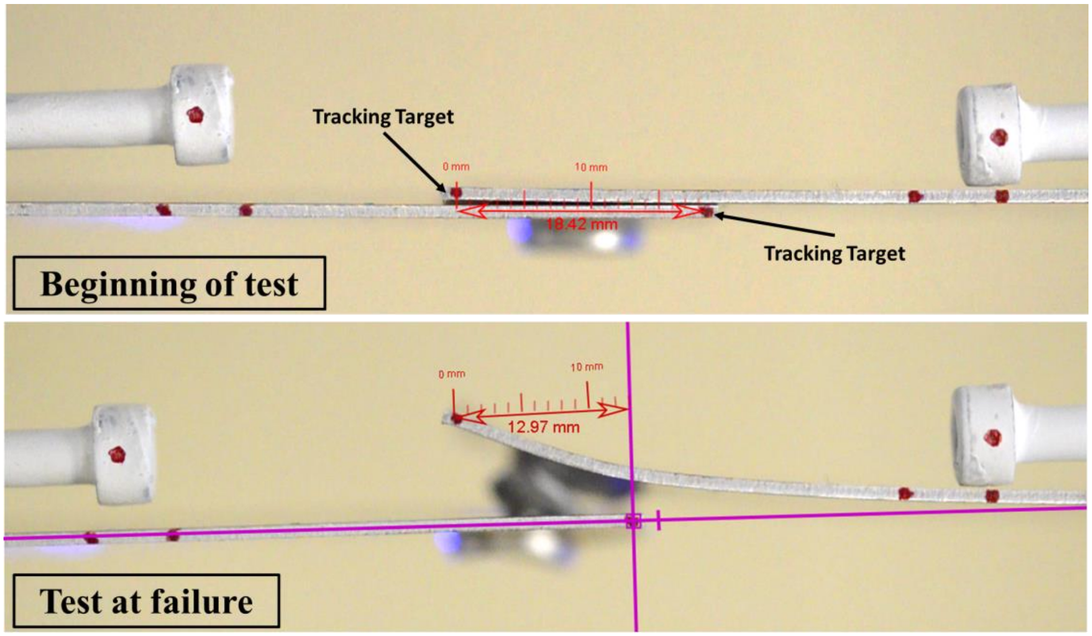

Figure 147: The measurements of the separation at failure in tangential (δ_t^{fail}) direction using optical methods tracking two targets on the side of the SLJ specimen during the test.

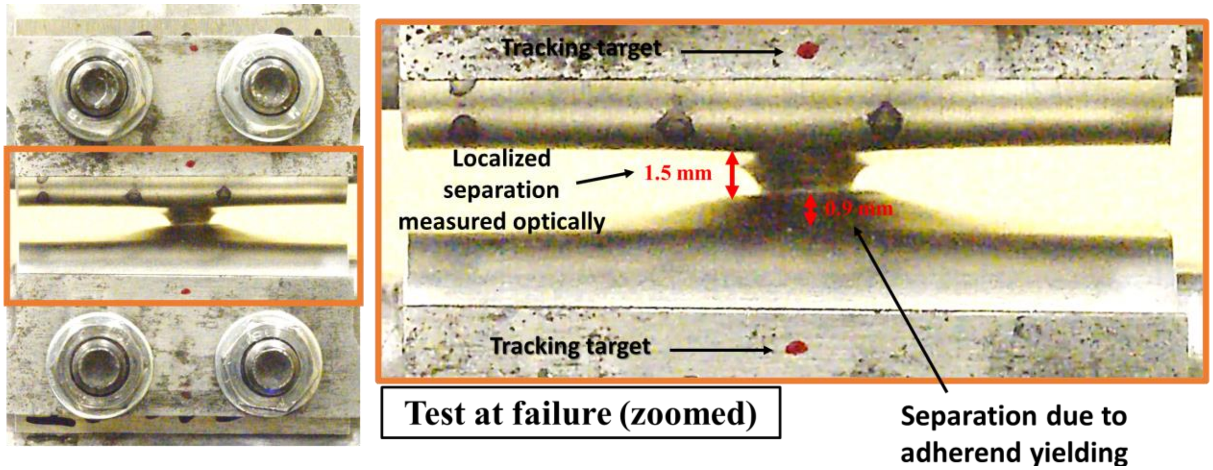

Figure 148: The separation at failure measurement under normal loading (δ_n^{fail}) using optical methods.

Another important aspect that needed to be addressed when using the SPR constraint model was determining the effective rivet diameter (radius of influence). Optimally, the effective rivet diameter should be equal to the measured diameter of the rivet head or flared tail depending on SPR rivet failure mode. However, care should be taken when following this approach as the adherend mesh size plays an important role in the overall SPR joint response. With a coarse adherend mesh, using the measured diameter of the flared rivet may not provide enough nodes to distribute the loads and moments to a sufficient number of adherend shell elements (Figure 13a). To address the challenge associated with localized loads and moments, artificially increasing the effective rivet diameter to cover a sufficient number of adherend nodes was suggested (Hanssen *et al.*, 2010). In this work, The diameter of the rivet head was measured as 7.8 mm so a 15% larger effective rivet diameter was used (9 mm) to provide a sufficient number of nodes including corner nodes and a fairly symmetrical distribution for the adherend mesh size used in the specimen and component (2.0 mm elements) level models (Figure 13b). The effective rivet diameter value is embedded into the calibrated response of the SPR rivet model and small changes to this value may not change the SPR rivet response.

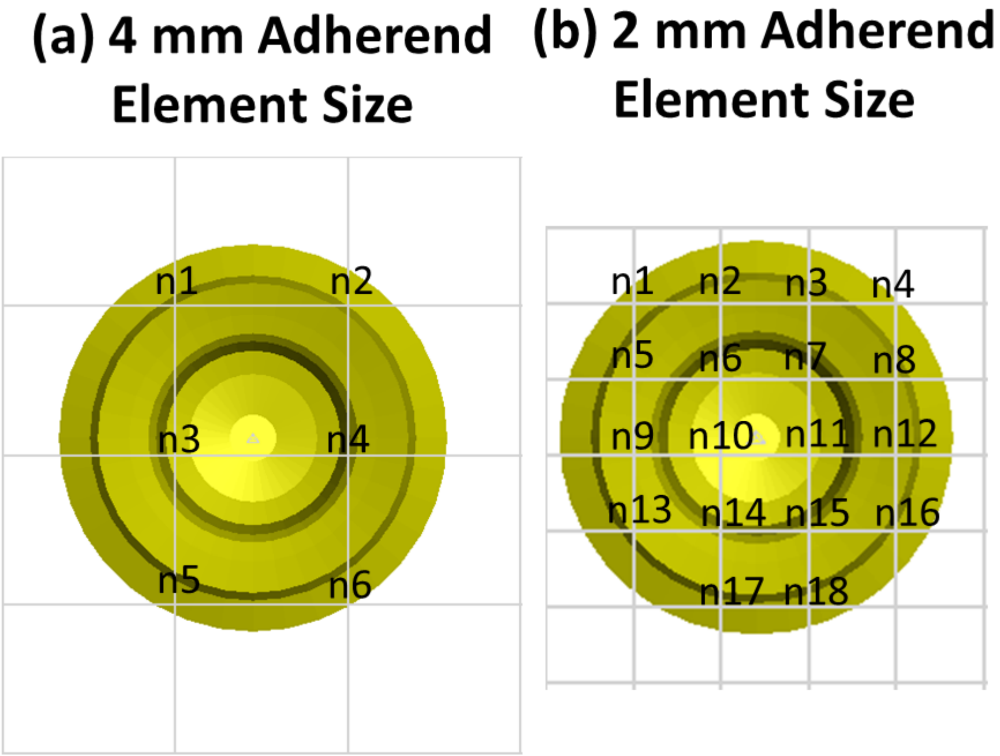

Figure 149: The number of adherend nodes attached to an SPR rivet constraint model, with 9 mm effective radius, for adherends with a shell element size of 4 mm (a) and 2 mm (b).

The SPR constraint model (*Constraint_SPR2 in LS-DYNA) parameters calibrated to the SLJ and H-specimen test data and optical tracking for each sheet thickness (1-, 2- and 3- mm) were summarized (Table 5) and the complete input card required for the FE package (LS-Dyna) were included in Appendix A. Although the SPR constraint model did include specific parameters for the energy dissipated by the SPR rivet during unloading/damage progression, the model parameters defined the area under the force-separation relationship (Figure 146), which indirectly determined the fracture energy.

Table 28. The constraint model parameters used in this study for SPR joints with 1-, 2- and 3-mm thick sheets.

Sheet Thickness	**Effective Radius (mm)**	**Normal Peak Load f_n^{max} (N)**	**Tangential Peak Load f_t^{max} (N)**	**Normal Separation at failure δ_n^{fail} (mm)**	**Tangential Separation at failure δ_t^{fail} (mm)**	**Scaling parameter $\alpha_1, \alpha_2, \alpha_3$**	**Fraction of normal failure separation ξ_n**	**Fraction of tangential failure separation ξ_t**
1 + 1 mm	9	1,841	2,952	2.0	5.5	0.15,0.65,1.7	0.95	0.85
2 + 2 mm		4,530	7,359	4.0	6.0	0.55,0.8,1.0	0.85	0.50
3 + 3 mm		6,860	10,250	1.5	7.0	0.45,0.5,0.7	0.85	0.33

The use of the constraint model required applying a drilling rotation constraint (artificial rotational stiffness) to the adherend shell elements because the default shell element formulation does not offer rotational stiffness about the element's normal axis and relies on the bending stiffness of the neighbouring elements to provide resistance to torsional rotation. It was reported in the literature that constraint and connector models, such as the models used for SPR and spot welds, could experience unphysical nodal rotations and could encounter numerical instabilities when flat or curved elements are loaded in the normal direction (Erhart and Borrvall, 2013) (Figure 150).

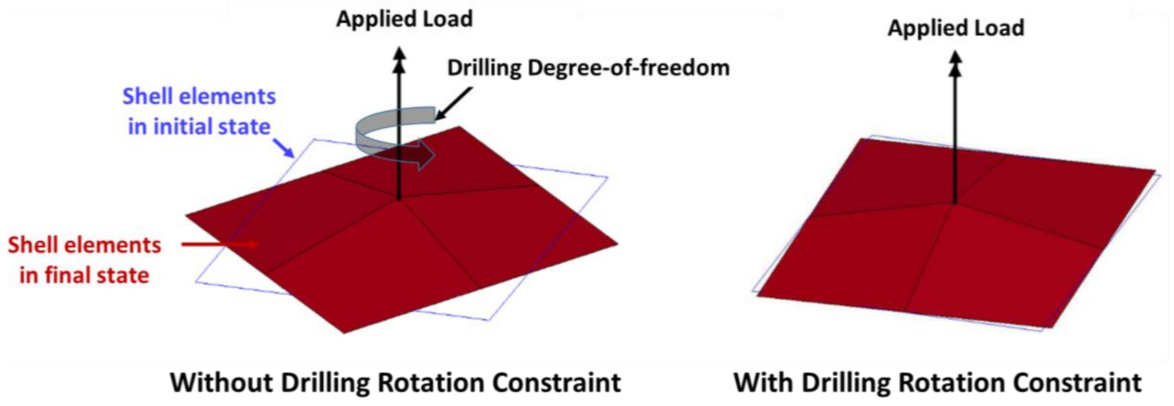

Figure 150: Drilling rotation constraint corrected the lack of stiffness in drilling degree-of-freedom. Adapted from Erhart and Borrvall (2013)

5.3.1 Modelling and Calibration of the CZM Model

The alternative SPR rivet modelling approach used cohesive zone modeling, and the SPR rivet was modeled using cohesive elements. The CZM approach was reported to be mesh dependent and it was suggested in the literature to use a minimum of three elements within the fracture process zone (Turon *et al.*, 2007). The SPR rivet was modeled using a hex-shaped assembly (Figure 151a) of cohesive elements. Using a single element was examined in an attempt to improve the computational efficiency (Figure 151b), but the simulation results showed that the model with a single element could not provide a gradual damage progression (red curve, Figure 152), attributed to the low number of tied nodes. In contrast, using the hex-shaped assembly of cohesive elements resulted in a physical behaviour similar to the rivet progressive failure seen in the experimental tests, therefore, the predicted load was lower and matched the experimental results of an SLJ test (blue curve, Figure 152). Similar findings were reported when a cohesive zone modeling approach was used to model spot welds. The shell elements of the adherend contacted each other through the single cohesive element, attributed to the low number of tied points and low stiffness of the cohesive element relative to the adherend material (Tolton, 2020).

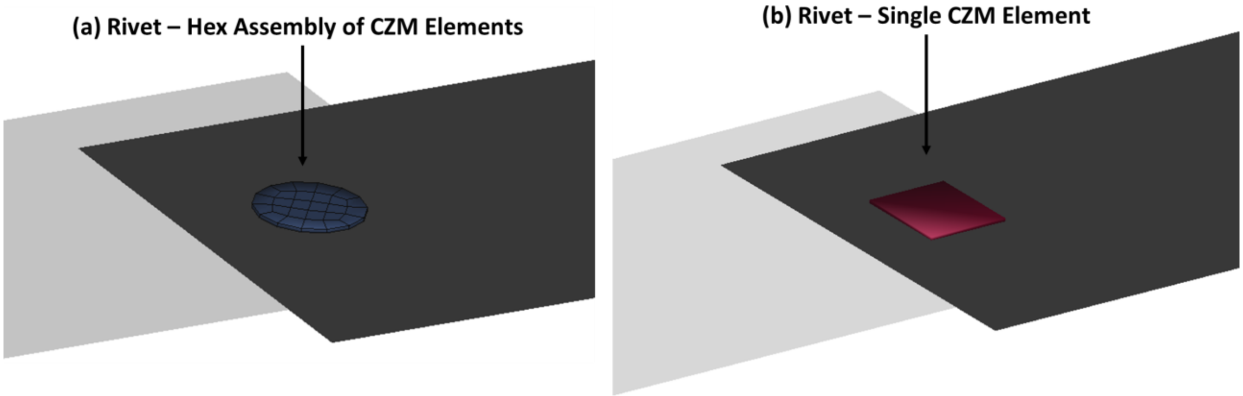

Figure 151: The SLJ model using SPR rivet modeled with a single CZM element (a) and a CZM hex assembly (b).

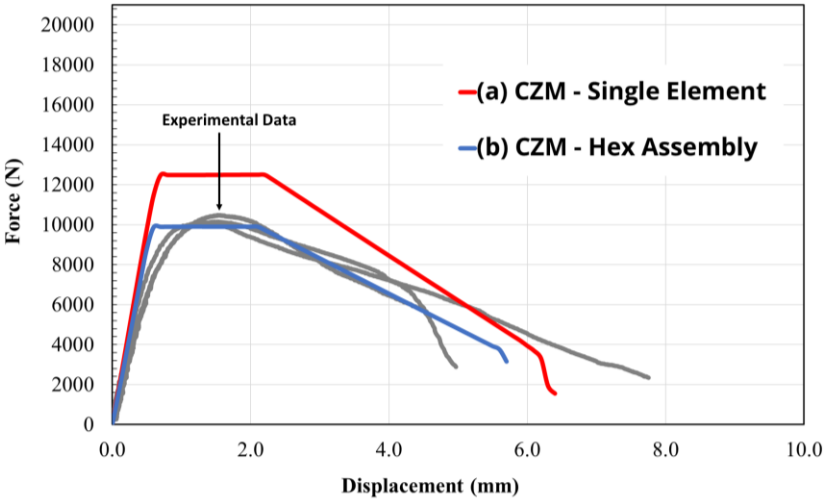

Figure 152: The simulation results of the SLJ model with SPR rivet modeled a single CZM element (a) and a CZM hex assembly (b).

The traction-separation relationships under normal loading (Mode I) and shear loading (Mode II) required calibrating the following traction-separation parameters: *emod*, *gmod*, *t0*, *s0*, *fg1*, *fg2*, *g1c_0*, and *g2c_0* (Figure 142). The elastic and shear modulus parameters (*emod* and *gmod*) representing the stiffness of the CZM traction separation curves were calibrated to ~1 GPa. The elastic modulus parameters showed limited influence on the overall joint response because the stiffness of the adherends was substantially larger the stiffness of the overall joint ($E_{adherend} >> 20 \times E_{joint}$), and therefore the value was calibrated to a value slightly lower than the value measured in adhesive joints. The elastic modulus provided the stiffness to avoid numerical instabilities rather than controlling the overall structural response. The elastic and shear parameters, representing the interface stiffness, had a limited influence on the model behaviour and increasing the value of the parameter up to 20 times barely influenced the joint stiffness response (blue and green curves, Figure 153), agreeing with the results reported by Turon *et al.* (2007). When the value was reduced by an order of magnitude the element stiffness was not sufficient and caused numerical instability (red curve, Figure 153). Small changes in these parameters did not influence the overall response, and a value range of 0.8 GPa to 20 GPa was assumed to be appropriate for metal joining as it provided enough stiffness and was not large enough to dominate the overall joint response.

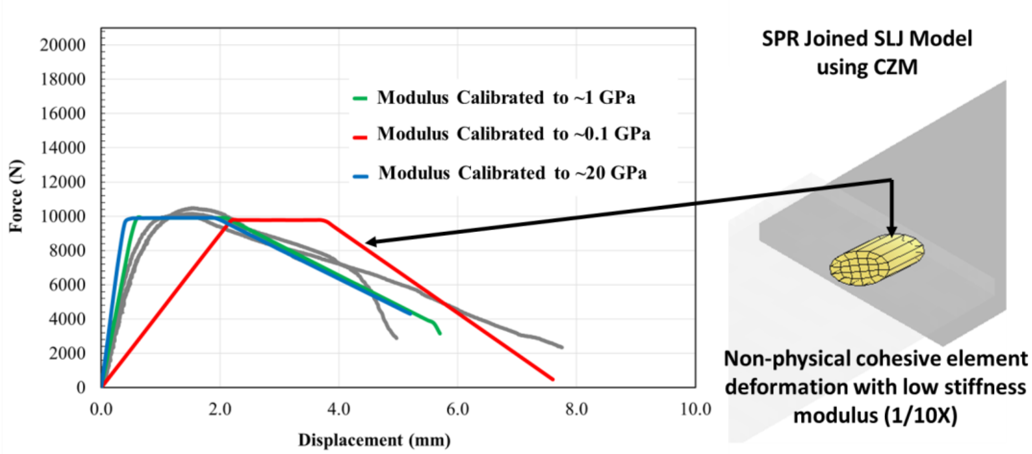

Figure 153: The influence of CZM elastic and shear modulus parameters was limited above a certain value (~1 GPa) that provided numerical stability in the SLJ joint simulation.

The traction parameters (*t0* and *s0*) were determined from the experimental force-displacement data by dividing the average measured peak force of the H-specimen and SLJ tests by the total area of the hex assembly. The length of the plateau at peak traction (*fg1* and *fg*2) was measured from the experimental data by calculating the ratio between the separation at damage initiation and separation at failure, allowing the model to incorporate some ductility during the damage progression, as opposed to sudden softening. The SPR joined H-specimens and SLJ joints experienced gradual softening during the loading and unloading, thus it was somewhat challenging to determine the exact point of damage initiation. Given that the gradual softening was linearized in the trapezoidal traction-separation relationship, it was found that the separation at damage initiation separation could reasonably be estimated by determining the point of intersection between the line extending the initial loading slope and a horizontal line at the peak load value. The parameters controlling the fracture energy within the model are *g1c_0* (Mode I, determined from the H-specimen tests), and *g2c_0* (Mode II, determined from the SLJ tests). These parameters controlled the overall energy absorbed by the SPR rivet during the rivet damage phase. To identify these parameters, a numerical solver (Generalized reduced gradient) was used. The solver determined the area under the traction separation curve to achieve the calibrated elastic modulus, the calculated peak traction, and the determined length of the plateau while maintaining a separation at failure value (δ_t^{fail} for shear and δ_n^{fail} for normal direction) equal to the optically measured value (Figure 147 for shear (SLJ) and Figure 148 for normal direction (H-specimen)). The calibration approach was applied in this study for the SPR joints made with 3 mm adherends, using the load-displacement responses of the H-specimen and SLJ joints, and applying optical measurements and numerical tools to determine the required parameters (Figure 154).

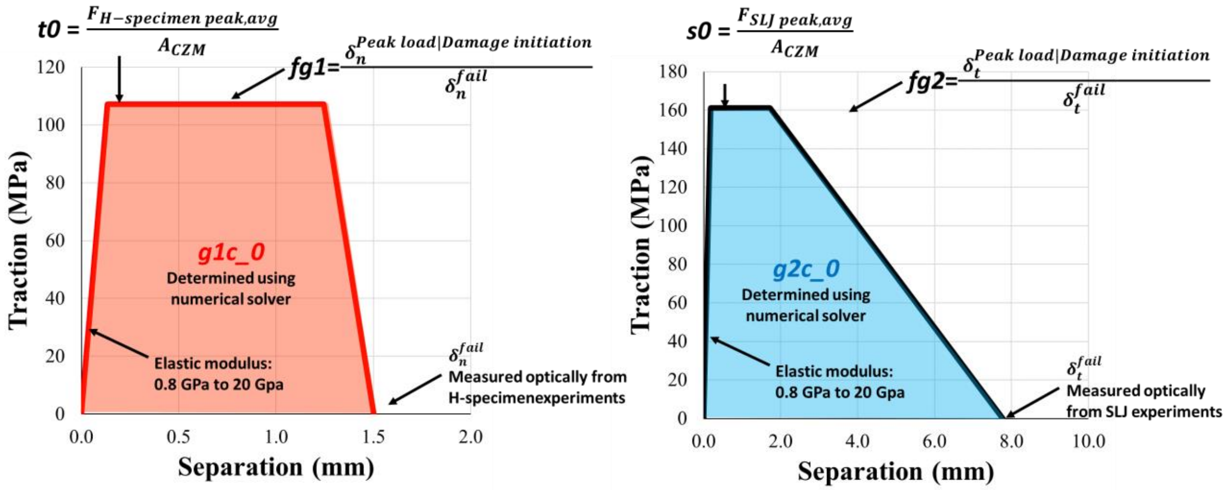

Figure 154: The CZM traction-separation relationship under Mode I and Mode II loading for the SPR rivet applied to 3 + 3 mm thick joints.

Table 29. The trapezoidal traction-separation parameters used in this study for the SPR rivet applied to 3 + 3 mm thick joints.

Variable	**mid**	**ro** (Kg/mm³)	**roflg**	**intfall**	**emod** (GPa)	**gmod** (GPa)	**thick**
Value	2	7.8e-9	0	1	800	880	1
Variable	**g1c_0** (N/mm)	**g1c_inf**	**edot_g1**	**t0** (MPa)	**t1**	**edot_t**	**fg1**
Value	140	0	0	107.2	0	0	0.85
Variable	**g2c_0** (N/mm)	**g2_inf**	**edot_g2**	**s0** (MPa)	**s1**	**edot_s**	**fg2**
Value	750	0	0	161.09	0	0	0.33

5.3.2 Single Lap Shear Joint Verification (Constraint and CZM Models under Shear Loading)

The SPR SLJ models were generally similar to the adhesive SLJ models presented in section 5.2.1 and used the same mesh size for the adherend shell elements (2 mm). Three models were developed using the constraint model of the SPR to consider the three sheet thicknesses tested in this work. The boundary conditions, loading rate and adherend material model were identical to the adhesive models. A single node, representing the SPR rivet, was defined at the centre of the overlap area between the top and bottom adherends to initialize the SPR constraint model (Figure 155). The force data were extracted from the models by extracting the loads acting on the fixed nodes within the fixed grip, and the SLJ joint rotation was calculated by extracting the coordinates of the nodes marked with red points (Figure 155). The SLJ models comprised 2160 shell elements for the adherends and a constraint model representing the SPR rivet (Table 30).

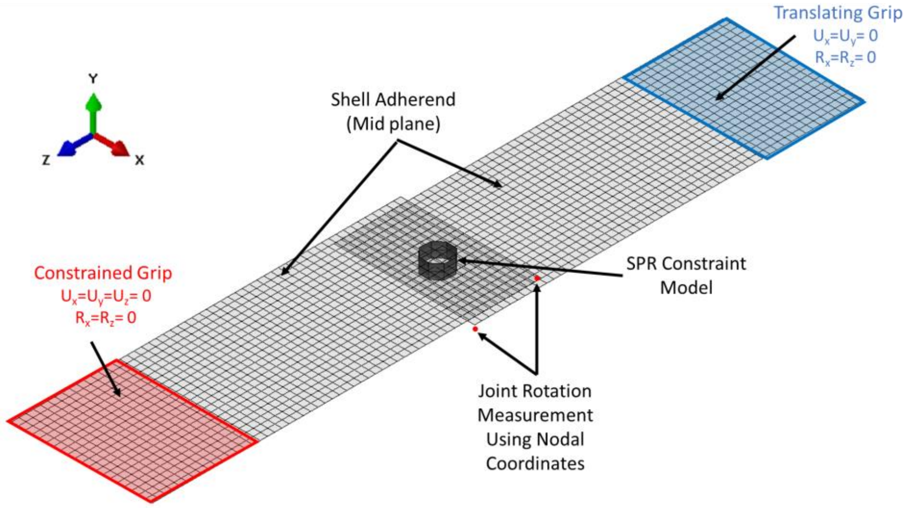

Figure 155: The SLJ model developed with 2 mm thick sheet material and joined using the SPR constraint model, illustrating the applied boundary conditions. (Similar model was developed for each adherend sheet thickness)

Table 30: Assembly summary of the SPR joined SLJ FE models.

Part	Geometry	Number of Nodes	Number of Elements	Type of Elements
Adherends	2D Surface	1,155 x 2	1,080 x 2	Fully integrated 4-node shell elements
SPR Rivet	Connector	1	-	Mesh-independent constraint model
	or			
	3D Hex Assembly	68	26	Cohesive elements

The alternative CZM modeling approach was applied to the joints with 3 mm adherend thickness, using the same methods presented earlier in this section. The SPR constraint model (initialization node and constraint definition) was substituted for the hex-assembly of cohesive elements and an additional tie constraint with an offset was used (Figure 156). All the SLJ models joined using the SPR constraint or CZM model had the drilling rotation constraint applied (DRCSPID in *CONTROL_SHELL control card, LS-DYNA).

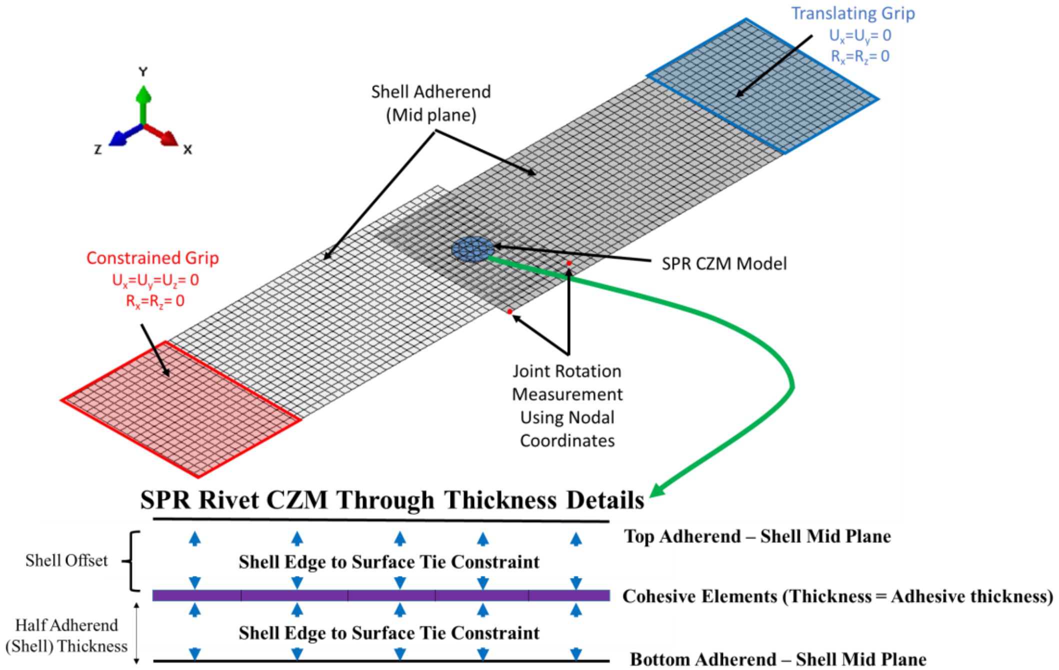

Figure 156: The SLJ model developed with 3 mm thick sheet material and joined using the SPR CZM model, illustrating the boundary conditions applied and the CZM through thickness details.

5.3.3 H-Specimens Verification (Constraint and CZM Models under Tension Loading)

The SPR H-specimen models used the same adherend shell element size, boundary conditions, loading rate, and adherend material model of the adhesive H-specimen models (Figure 144, section 5.2.2). Three H-specimen models were created to account for the 1-, 2- and 3- mm thick adherends, and each model comprised 4300 shell elements for the U sections, 4300 shell elements for the fixturing blocks and a constraint model of the SPR rivet with the calibrated parameters corresponding to the sheet thickness of the joint (Table 31). The force data were extracted from the models by extracting the loads acting on the fixed fixture block. The alternative CZM modeling approach was applied to the joints made with 3 mm thick adherends by substituting the SPR constraint model (initialization node and constraint definition) for the hex-assembly of cohesive elements tied to the adherends using a tied constraint with offset (Figure 156). Similar to the SPR SLJ models, all the H-specimen models joined using the SPR constraint or CZM model had the drilling rotation constraint applied.

Table 31: Assembly summary of the SPR joined H-specimen FE models.

Part	**Geometry**	**Number of Nodes**	**Number of Elements**	**Type of Elements**
U-section Adherends	2D Surface	4,437 x 2	4,300 x 2	Fully integrated 4-node shell elements
SPR Rivet	Connector	1	-	Mesh-independent constraint model
	or			
	3D Hex Assembly	68	26	Cohesive elements
Fixturing Blocks	2D Surface	4,437 x 2	4,300 x 2	Fully integrated 4-node shell elements with rigid material model

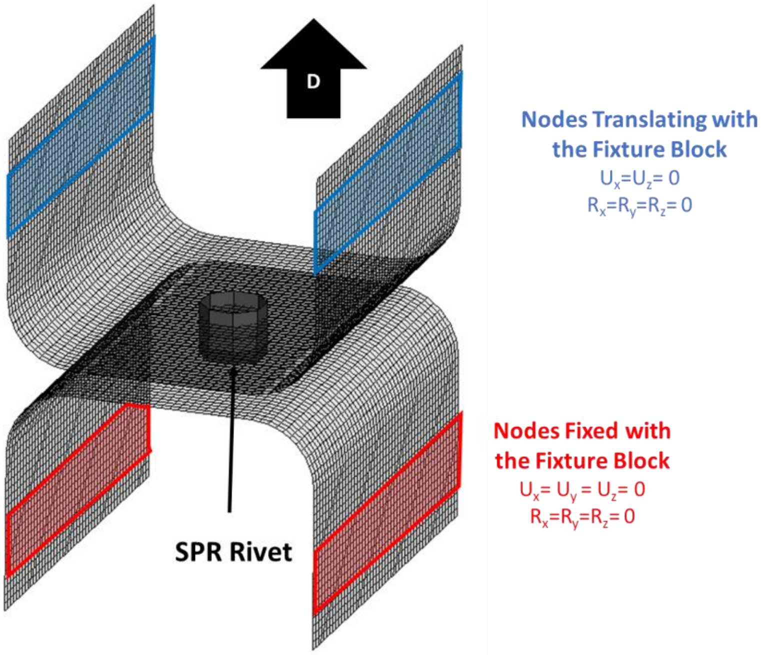

Figure 157: The H-specimen model, developed with 2 mm thick sheet material and joined using the SPR constraint model, illustrating the applied boundary conditions. (Similar model was developed for each adherend sheet thickness)

5.4 Modeling and Validation of Hybrid Joints (CZM-Constraint and CZM-CZM Models)

Two hybrid joint modeling approaches were examined. The adhesive was modeled using CZM with traction-separation relationships from the material-level characterization. The adhesive CZM model was integrated with (a) the constraint model (CZM-Constraint) or (b) the CZM model (CZM-CZM) of the SPR rivet to formulate a hybrid joint model. To achieve proper integration, the morphological effect of hybrid joining was considered and adhesive squeeze-out was mapped into the adhesive CZM model before the SPR model was introduced at the rivet location. The SPR rivet parameters calibrated to the SPR specimen-level tests were directly implemented, computationally linking the hybrid joint mechanical response to the intrinsic response of the individual joints. In this section, the integration process between the adhesive CZM and SPR constraint model is presented (Figure 158). The separation at failure (δ_n^{fail}) in normal direction required considering the cohesive element thickness (adhesive thickness = 0.3 mm), such that:

$$\delta_{n,\,\text{hybrid joint}}^{fail} = \delta_{n,\text{SPR joint}}^{fail} + \text{thickness}_{\text{cohesive element}} \qquad \text{Equation 14}$$

The constraint model calculated the local separation of the from the physical separation between the top and bottom adherend shell elements. Therefore, the thickness of the adhesive CZM element needed to be considered into the δ_n^{fail} to achieve the separation at failure measured from the SPR-only H-specimen experiments.

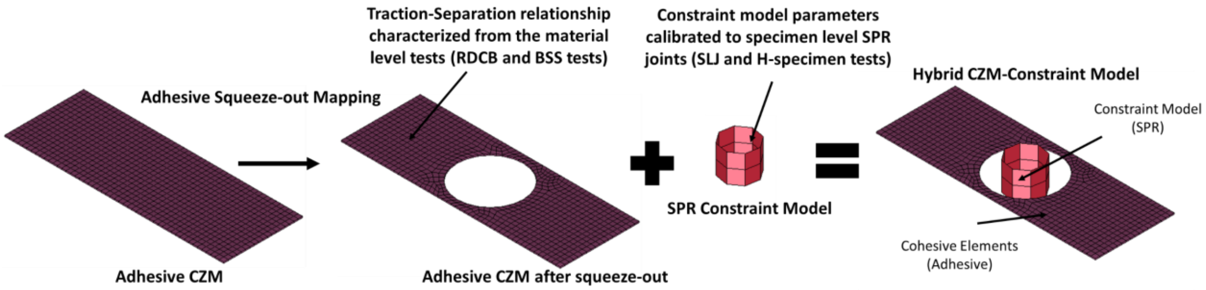

Figure 158: The adhesive CZM model integration with SPR constraint model to develop a hybrid joining model.

Integrating the adhesive CZM and SPR constraint models, introduced numerical oscillations into the model, which was addressed by adding numerical control measures. The abrupt failure of the adhesive CZM model released a fair amount of energy and required a sudden load transfer to the constraint model (Figure 159). The numerical controls did not influence the response but reduced the susceptibility of shell elements to oscillations and increased the stability of the constraint model. Damping was applied to the adherends shell elements (*DAMPING_PART_STIFFNESS in LS-DYNA) to diminish the high-frequency oscillations using Rayleigh damping (coefficient of 0.05). Bulk viscosity for shell elements was invoked, and the energy dissipated by the bulk viscosity of shell elements was added to the energy calculations to ensure energy balance. Finally, the calculated time step was scaled down by a factor of 0.5 to improve the numerical stability of the constraint model and allow sudden load transfer within the neighbouring nodes after adhesive failure. These numerical controls were suggested for numerical instability associated with sudden energy release or high-velocity events (shocks, contact or impact) (Bala and Day, 2012), and were assessed in this work to understand how they affected the simulation results (details discussed in section 6.5.4).

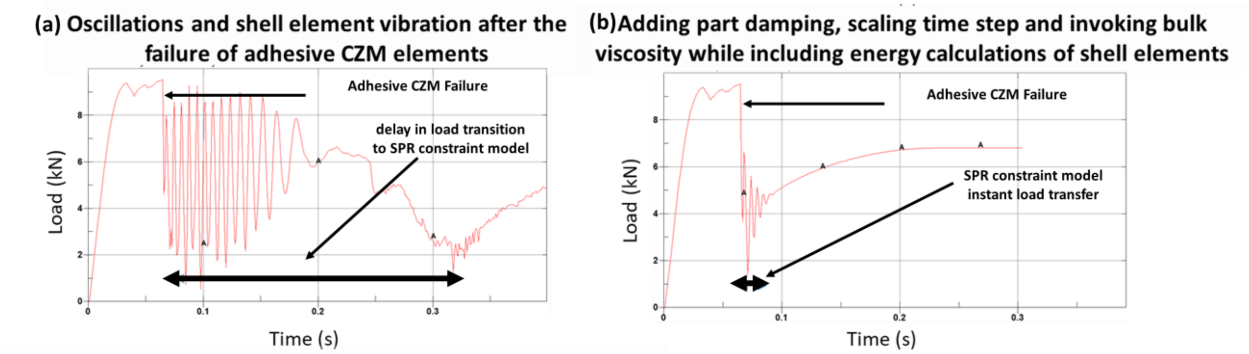
(a) Oscillations and shell element vibration after the failure of adhesive CZM elements

(b)Adding part damping, scaling time step and invoking bulk viscosity while including energy calculations of shell elements

Figure 159: Numerical oscillations encountered post adhesive CZM failure (top) were substantially reduced using numerical controls (bottom).

5.4.1 Integration of the Dual CZM (CZM-CZM) Model

The alternative hybrid joint modeling approach used a dual CZM-CZM model, such that both adhesives and SPR rivet were modeled using cohesive elements. The SPR rivet was modeled using a hex-shaped assembly (an assembly of hexahedral-shaped elements) of cohesive elements using the parameters calibrated to the SPR-only joints (discussed previously in section 5.3.1). The dual CZM-CZM approach used cohesive elements with two different sets of parameters (traction-separation relationship) to model hybrid joint model (Figure 160). The hex assembly of cohesive elements used the same physical thickness of the adhesive layer (0.3 mm). The CZM-CZM modeling approach was validated using the SLJ and H-specimen experimental test data of the 3 mm thick joints. Importantly, this modeling approach did not require numerical control cards, which could improve the computational efficiency relative to the CZM-Constraint model.

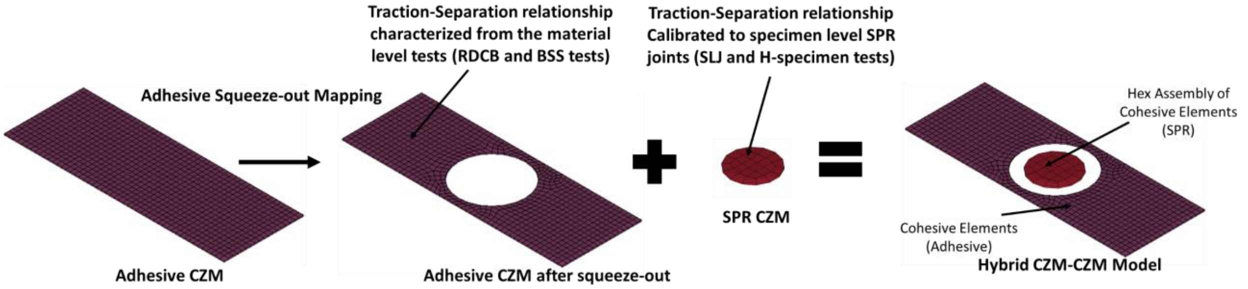

Figure 160: The dual CZM - CZM model development to simulate the hybrid joint response.

5.4.2 Single Lap Shear Joint Validation (CZM-Constraint and CZM-CZM Models under Shear Loading)

The hybrid joined SLJ models were similar to the adhesive and SPR SLJ models presented in sections 5.2.1 and 5.3.2, and used the same mesh size for the adherend shell elements (2 mm). Three models were developed for the CZM-Constraint model to consider the SPR parameters and adhesive squeeze-out effect according to sheet thickness. The boundary conditions, loading rate, element formulations, and adherend material model were identical to the adhesive and SPR models. The model used a tied constraint for adhesive CZM model, and a single node, representing the SPR rivet, was defined at the centre of the bonding area between the top and bottom adherends to initialize the SPR constraint model (Figure 161). The CZM-Constraint model adopted numerical controls to reduce the model susceptibility to oscillations as discussed earlier in section 5.4. The force data were extracted from the models by extracting the loads acting on the fixed nodes within the fixed grip, and the joint rotation was calculated by extracting the coordinates of the nodes marked with red points (Figure 161). The CZM-Constraint models comprised 2160 shell elements representing the adherends, up to 554 cohesive elements representing the adhesive layer (depending on adhesive squeeze-out encountered with each sheet thickness), and a constraint model to represent the SPR rivet (Table 32).

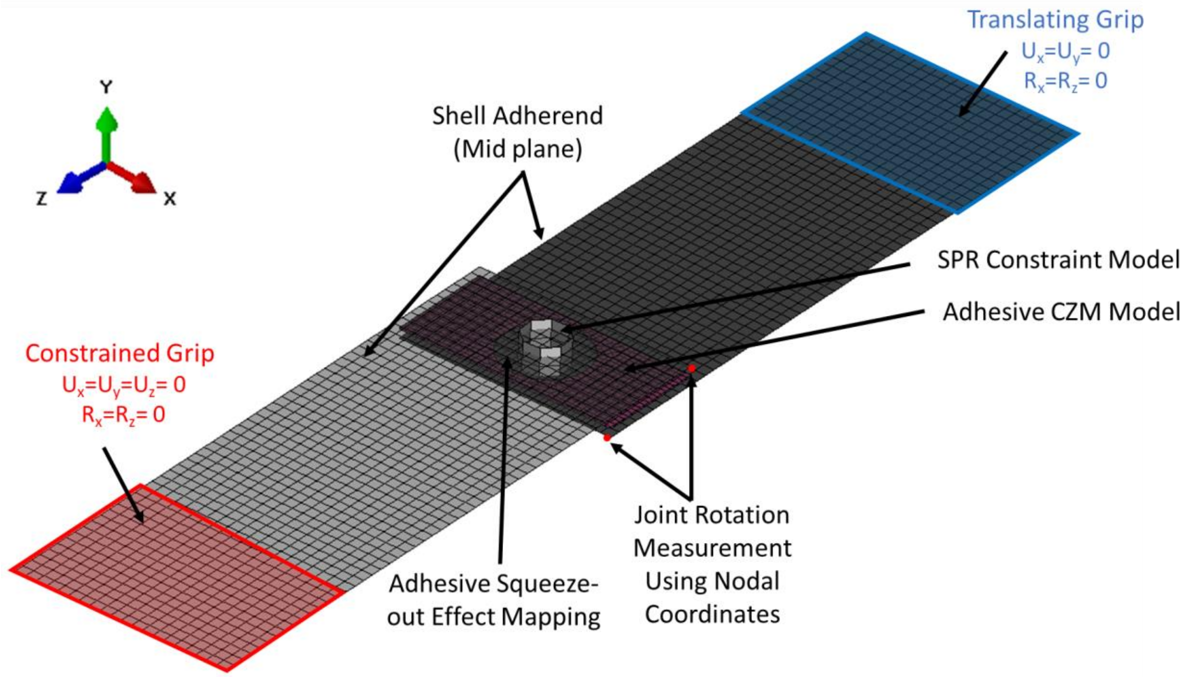

Figure 161: The hybrid joined SLJ model, developed with 2 mm sheet material, was joined using the integrated CZM-Constraint model, highlighting the applied boundary conditions. (Similar model was developed for each adherend thickness)

Table 32: Assembly summary of the hybrid joined SLJ FE models.

Part	Geometry	Number of Nodes	Number of Elements	Type of Elements
U-section	2D Surface	1155 x 2	1080 x 2	Fully integrated 4-node shell elements
Adhesive	3D Solid	1272	554	cohesive elements
SPR Rivet	Connector or	1	-	Mesh independent constraint model
	3D Hex Assembly	68	26	cohesive elements

The dual CZM-CZM modeling approach was applied to the joints made with 3 mm thick adherends, using the same methods presented for the SLJ model joined using the CZM-Constraint model (Table 32). The SPR constraint model (initialization node and constraint definition) was substituted for the hex-assembly of cohesive elements (Figure 162a), and an additional tie constraint with offset was used to transfer the loads and moments at the adherend-CZM interface (Figure 162b). All the SLJ hybrid joined models had the drilling rotation constraint applied.

(a) Implementation of the Hybrid Joining dual CZM-CZM Model

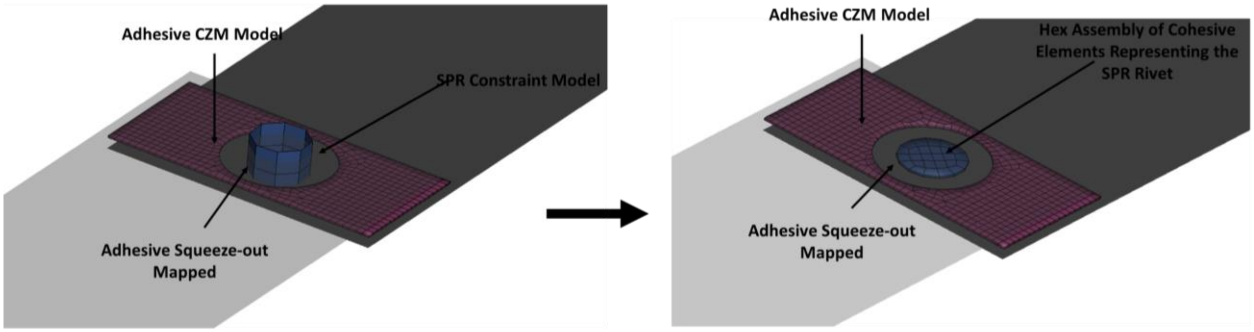

(b) Hybrid CZM-CZM Model Through Thickness Details

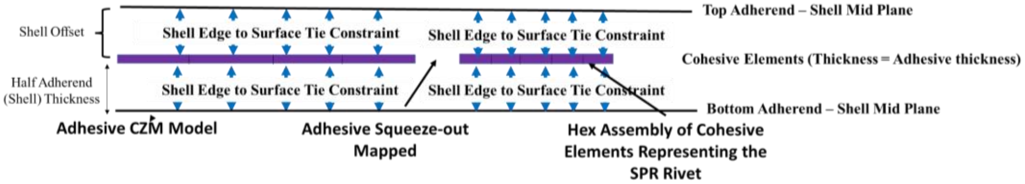

Figure 162: The hybrid CZM-CZM SLJ model, developed with 3 mm sheet material (a), showing the through thickness details of the CZM-CZM model (b).

5.4.3 H-Specimens Validation (CZM-Constraint and CZM-CZM Models under Tension Loading)

The hybrid joined H-specimen models were similar to the adhesive and SPR models presented in sections 5.2.2 and 5.3.3. The H-specimen models used the same mesh size for the adherend shell elements (1 mm), and three models were developed using the CZM-Constraint model considering the SPR calibrated parameters and adhesive squeeze-out effect according to sheet thickness. Similar to the SLJ models, the CZM-Constraint model used additional numerical controls to reduce the model susceptibility to oscillations. The force data were extracted from the models by monitoring the loads on the fixed fixture block, and the displacement data was extracted from the nodal displacement of the translating block (Figure 163). The H-specimen models with CZM-Constraint model comprised 4300 shell elements for the U sections, 4300 shell elements for the fixturing blocks, up to 744 cohesive elements representing the adhesive layer, and a constraint model to represent the SPR rivet (Table 33).

Table 33: Assembly summary of the hybrid joined H-specimen FE models.

Part	Geometry	Number of Nodes	Number of Elements	Type of Elements
U-section	2D Surface	4437 x 2	4300 x 2	Fully integrated 4-node shell elements
Adhesive	3D Solid	1672	744	cohesive elements
SPR Rivet	Connector	1	-	Mesh independent constraint model
	or			
	3D Hex Assembly	68	26	cohesive elements
Fixturing Blocks	2D Surface	4437 x 2	4300 x 2	Fully integrated 4-node shell elements with rigid material model

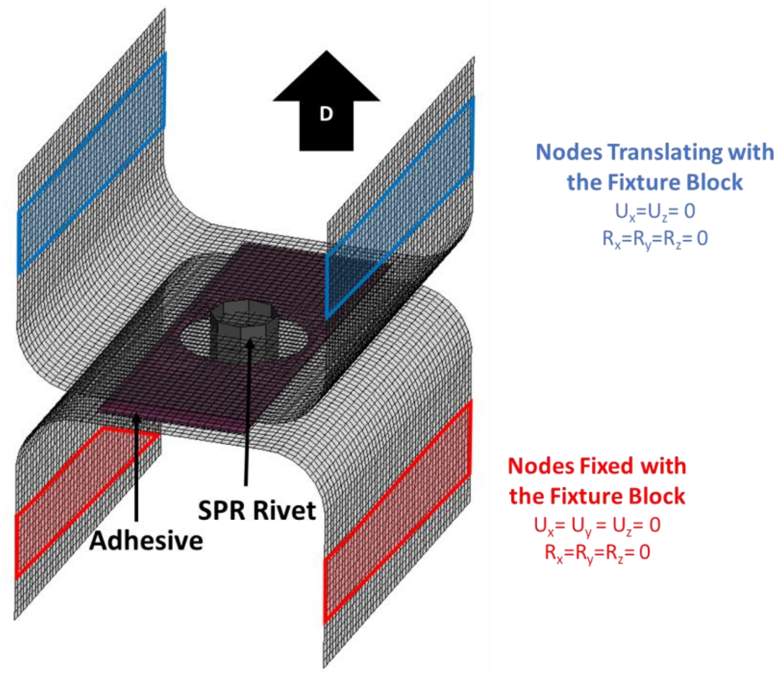

Figure 163: The H-specimen model made with 2 mm sheet material and joined using the CZM-Constraint model, showing the adherends and fixturing parts with boundary conditions. (Similar models were created for each adherend sheet thickness)

The dual CZM-CZM modeling approach was applied to the joints with 3 mm thickness, by substituting the CZM-Constraint model for the hex-assembly of cohesive elements (Figure 162a), following the method discussed in the previous section for hybrid CZM-CZM SLJ model (section 5.4.2). All the hybrid joined H-specimen models had the drilling rotation constraint applied.

5.5 Component-Level Caiman Modeling and Analysis

In this section, the adhesive, SPR and hybrid joining models were used at a structural scale to simulate the component-level Caiman tests undertaken in this study. The Caiman component, comprising two double hat sections with flanges, allowed for assessing a large bond area and groups of rivets under primarily Mode I loading. Note that the FE model validation process used quasistatic loading conditions; however, the models developed in this work could be extended to high-strain rate applications for crash modelling (further discussion in Chapter 7).

The Caiman model included 3 mm thick AA6061-T6 aluminum alloy sheet metal (3.12-3.16 mm measured thickness). The hat sections were modelled following the methods in section 5.1 (fully integrated shell elements with a piecewise linear plasticity material model incorporating the material properties measured in this study). The model representing the adhesive joined Caiman used CZM to model adhesive joining (section 5.2). Two models were developed for the SPR joined Caiman test, modeling the SPR rivets using the constraint model (section 5.3) or CZM approach (5.3.1). Similarly, two models were developed for the hybrid joined Caiman test (Figure 164a and Figure 164b). The adhesive was modeled using CZM while SPR rivets were modeled using the constraint model (CZM-Constraint, Figure 164a) (more details in section 5.4) or CZM approach (CZM-CZM, Figure 164b) (more details in section 5.4.1). To be consistent with the specimen-level models, the Caiman models, joined using SPR or hybrid joints, had the drilling rotation constraint applied (DRCSPID in *CONTROL_SHELL control card, LS-DYNA). Also, the hybrid joint models utilizing the constraint model (CZM-Constraint model only) for the SPR rivet required numerical stability controls, such as part stiffness damping, time step scaling, and bulk viscosity of shell elements.

(a) Caiman Model with CZM-Constraint Model

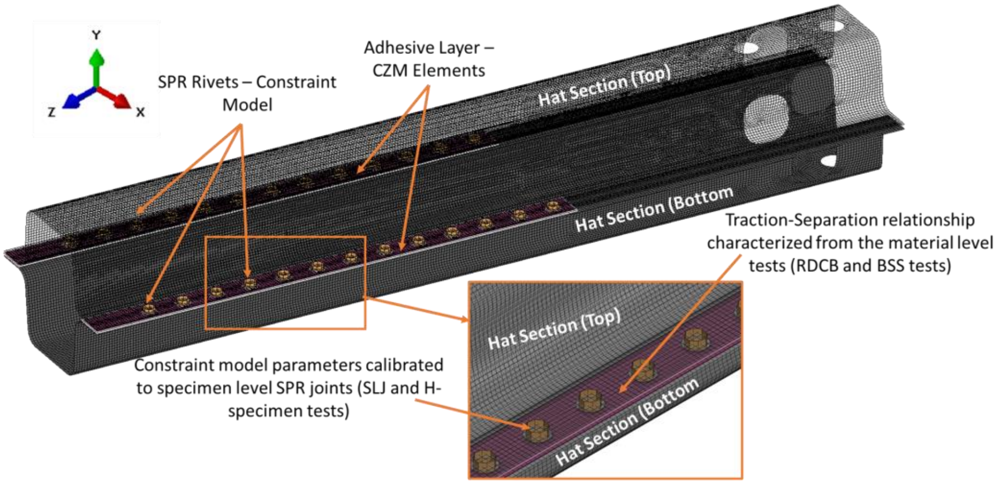

(b) Caiman Model with CZM-CZM Model

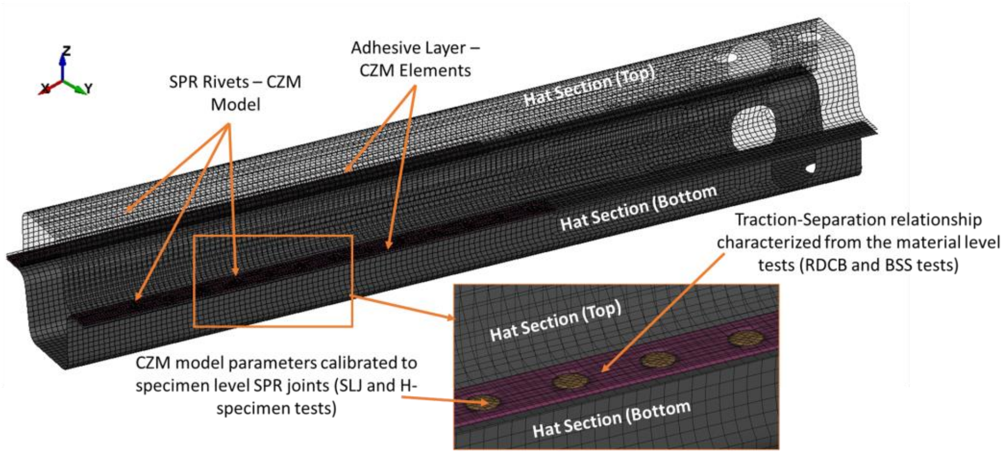

Figure 164: Caiman hat sections modeled using shell elements for the hat sections (adherends), which were joined using CZM elements for adhesive and constraint model (a) or CZM approach (b) for SPR rivets.

The fixturing components were modeled as rigid parts using shell elements, because the steel inner bosses and the pins (Figure 165) did not experience any deformations and the inertial forces were absent at quasistatic loading rate. The top pin was assigned a prescribed displacement of 25 mm/s (loaded pin), while x, y, and z translational constraints were applied to the bottom pin (fixed pin). The rotation of the pins was not constrained around their axis and contact between the inner bosses and the mated pins was defined using a static and dynamic friction coefficient of 0.4

(Liu, 2019; O’Keeffe, 2018). The contact definition allowed the bosses to rotate relative to the pins while the loaded pin was translated to apply the load. In the experiments, a 110 mm length of each hat section was secured to the fixturing components, so to model the boundary condition of the front portion of the tubes, the nodes of the tube secured to the fixture assembly were constrained to the inner bosses, using a rigid constraint (*CONSTRAINED_EXTRA_NODES) (Figure 166).

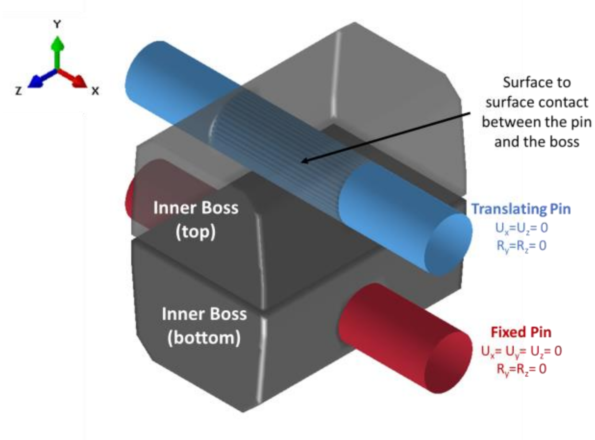

Figure 165: The fixturing components for the Caiman models with boundary conditions.

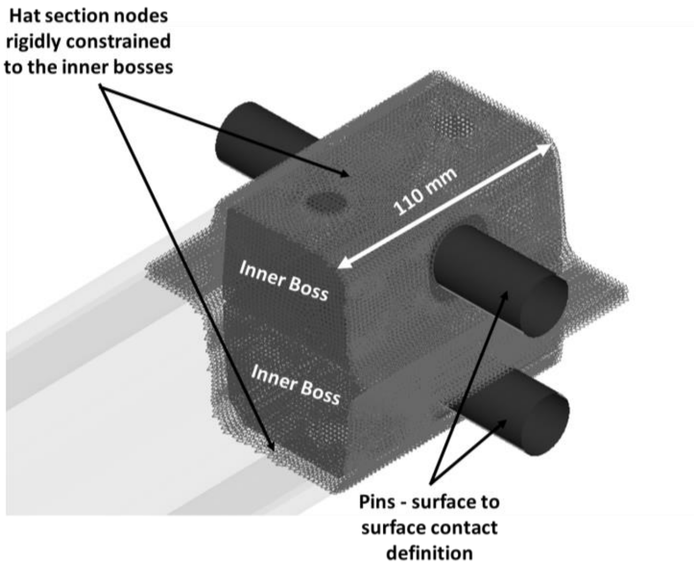

Figure 166: The Caiman model with the hat section nodes rigidly constrained to the inner bosses.

Mass scaling and time scaling have been widely used in the literature to increase computational efficiency and reduce simulation time in automotive-related applications (Lorenz and Haufe, 2008; Pirondi and Moroni, 2009; Sadowski *et al.*, 2011). Also, time scaling, which was used at the specimen level for the SLJ and H-specimen models, was used at the component level to apply the explicit FE formulation to quasistatic simulations and achieve the target simulation run time (Gulavani *et al.*, 2014). In this study, selective mass scaling (DT2MS in LS-DYNA) was applied to maintain the minimum timestep size to 1×10^{-6} by artificially adding mass to only the elements that caused the timestep to decrease below the specified time step size. Additionally, 60x time scaling was applied by increasing the load rate (the velocity of the loading pin) to achieve the target simulation run time (below 48 hours). The mass and energies were monitored to ensure the absence of inertial effects and unphysical mass addition. The load applied in the direction the crosshead moved was extracted from the fixed pin using the boundary conditions database output (bnd output in LS-DYNA), and the simulation was terminated after the hat sections were completely separated. The pin displacement was assumed to be equal to the crosshead displacement of the frame and was recorded in the simulation by tracking the rigid body motion of the loaded pin. The displacement-time and force-time responces were cross-plotted to generate the force-displacement curves to be compared with experimental data from the tensile frame. The SPR rivet failure time was obtained from the constraint model by enabling the ‘swforce’ database output. For each rivet, the failure parameter output data were extracted to identify the timestep (and time) at which the rivet completely failed, which allowed for determining the load and pin displacement corresponding to the failure. The Caiman models comprised 29,210 shell elements representing the hat sections, up to 6,664 cohesive elements representing the adhesive layer, a constraint model or CZM model to represent the SPR rivets, and 21,478 rigid shell elements for the fixturing components (bosses) and pins (Table 34).

Table 34: Mesh details for the Caiman FE models

Part	Geometry	Number of Nodes	Number of Elements	Type of Elements
Hat Sections	2D Surface	15163 x 2	14605 x 2	Fully integrated 4-node shell elements
Adhesive	3D Solid	7144 (hybrid joining) 14340 (adhesive-only)	3024 (hybrid joining) 6664 (adhesive-only)	cohesive elements
SPR Rivet	Connector	1	-	Mesh-independent constraint model
	or			
	3D Hex Assembly	68	26	cohesive elements
Inner Bosses	3D Solid	7887 x 2	7889 x 2	Fully integrated 4-node shell elements with rigid material model
Pins	2D Surface	2888 x 2	2850 x 2	Fully integrated 4-node shell elements with rigid material model

To ensure that there were no dimensional differences between the current model and the physical hat sections, the dimensions of the physical hat section were cross-checked with the FE models (Figure 167). The measurements were taken at both ends of the hat section, and the bend radius was measured with radius gauges in 0.5 mm increments. All hat sections had consistent dimensions and all the measurements were within 2% of the dimensions used in the FE models (Table 35).

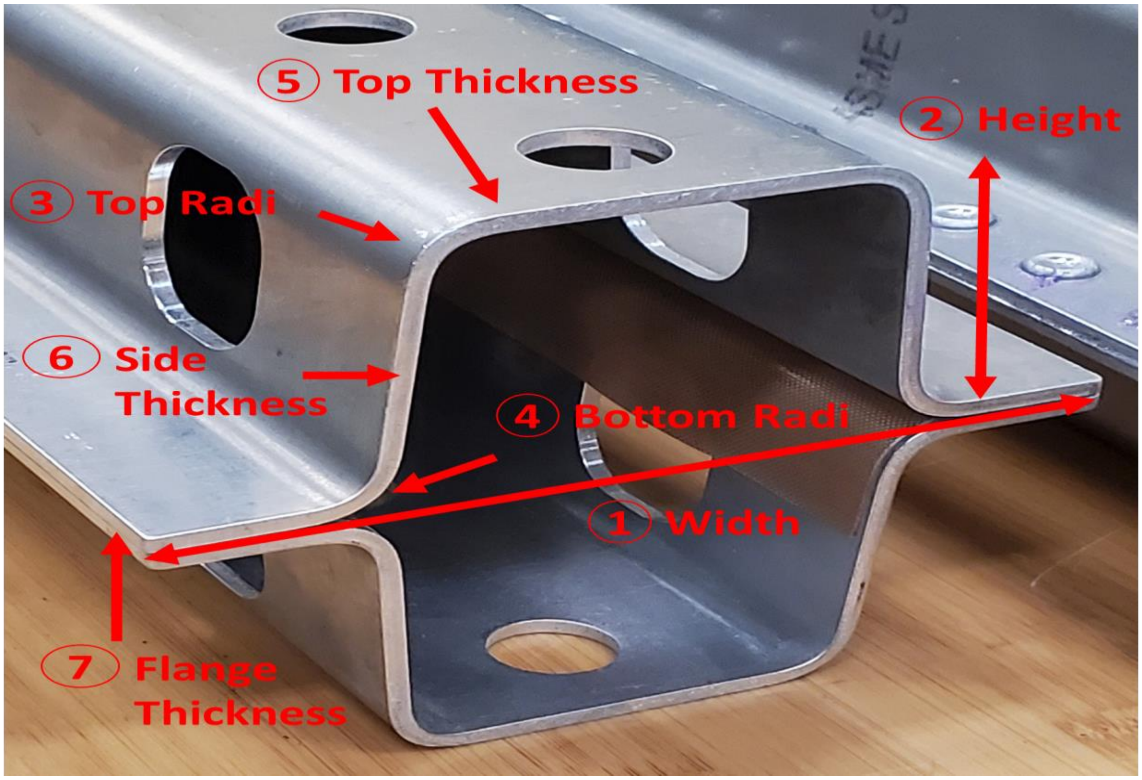

Figure 167: Geometry measurements conducted on the Caiman hat sections.

Table 35: Dimensions of the Caiman test hat sections (measured versus FE model)

	①	②	③	④	⑤	⑥	⑦
Average Measured Dimensions	131.34 ± 1.41	48.13 ± 0.11	8.5	8.5	3.12 ± 0.05	3.11 ± 0.04	3.10 ± 0.04
FE Model Dimensions	130.24	48.00	8.66	8.66	3.16	3.16	3.16
% Difference	-0.8%	-0.28%	+1.88%	+1.88%	+1.17%	+1.49%	+1.9%

5.6 Computational Investigations of Joint Attributes and Loading Mode

5.6.1 Influence of Number of SPR Rivets on Mechanical Responses of SLJ and H-specimen

It was reported that the response of SPR joints is strongly tied to the configuration and number of rivets used (Rudawska and Wahab, 2019). Thus, a parametric study was carried out on SLJ and H-Specimen joints to demonstrate the capability of the developed SPR models and shed light on the influence of the number of rivets under different modes of loading. SLJ and H-specimen models with two SPR rivets, made with 3 mm base material, were developed, simulated and compared to the validated models with one SPR rivet. The geometries of the SLJ and H-specimen were identical to the validated models used in this work (sections 5.3.2 and 5.3.3) with a second rivet added by using a rivet spacing of 25 mm (Figure 168).

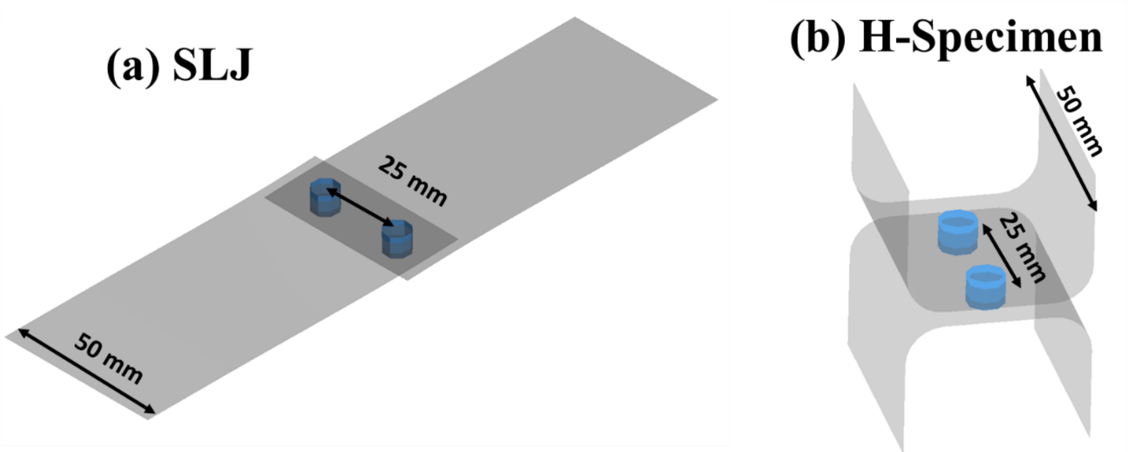

Figure 168: The SLJ (a) and H-specimen (b) joined using two rivets with a rivet spacing of 25 mm

5.6.2 Joint Behaviour under Peel (Mode I) Loading Mode

Adhesives are generally sensitive to peel loading (bending loading), and recently Zhang *et al.*(2022) have reported that an adhesively joined coach-peel test specimen failed at a peak load that was nearly 10% of that of the SLJ test. Thus, the H-specimen models, made with 3 mm thick sheets, were re-designed into a coach-peel test by trimming one of the curved sections from the top and bottom U-sections (trimmed part highlighted in red, Figure 169a), while keeping the same dimensions and joining area (Figure 169b), The coach peel models used the same fixturing blocks, boundary conditions, material models, and numerical controls presented for H-specimen joined using adhesives (section 5.2.2), SPR (5.3.3) and hybrid joining (section 5.4.3). The mechanical response of adhesive coach peel joint response was compared to the SLJ and H-specimen responses, highlighting the influence of loading mode on adhesive joining. Additionally, the load-displacement response was compared for the adhesive, SPR and hybrid joining to understand the influence of peel loading on each joining method.

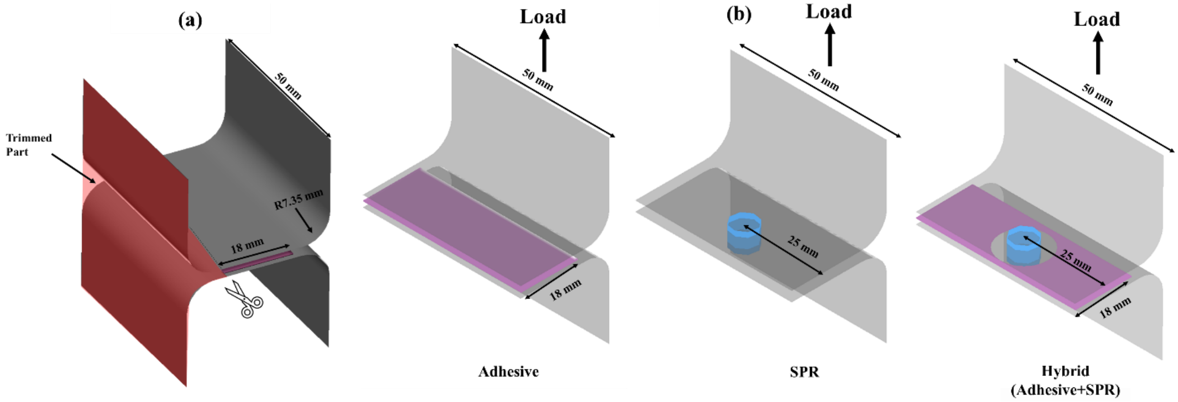

Figure 169: The re-designed H-specimen geometry (a) used to develop the adhesive, SPR and hybrid joining coach-peel models (b).

5.6.3 Effect of Adhesive Area Reduction on Caiman Mechanical Response

Hard spacers, such as shims, have been used to maintain the adhesive bond line thickness (Campbell, 2004; Licari and Swanson, 2005). In large-scale structures, maintaining a uniform bond line thickness may require using spacers within the adhesive bonding area, which reduces the total area available for bonding (Liu, 2019). To assess the effect of adhesive area reduction and understand its relationship with peak load and energy, the validated Caiman model joined using adhesive CZM (Figure 33a) was adopted. Thirteen holes were added to each flange (diameter = 10 mm) achieving a total adhesive area reduction of 1963 mm^2 (-26.5%) (Figure 170), mimicking using circular spacers spaced at 25 mm. The boundaries of the adhesive were kept the same so that the crack tip and damage initiation points are identical, which allowed for assessing the influence of area reduction while isolating the interaction of the crack tip effect. The Caiman model with the reduced adhesive area used the same boundary and loading conditions as the validated adhesively joined Caiman model (discussed in section 5.5). The load-displacement and energy-displacement responses were compared to the validated adhesively joined Caiman model to quantify the effect of area reduction.

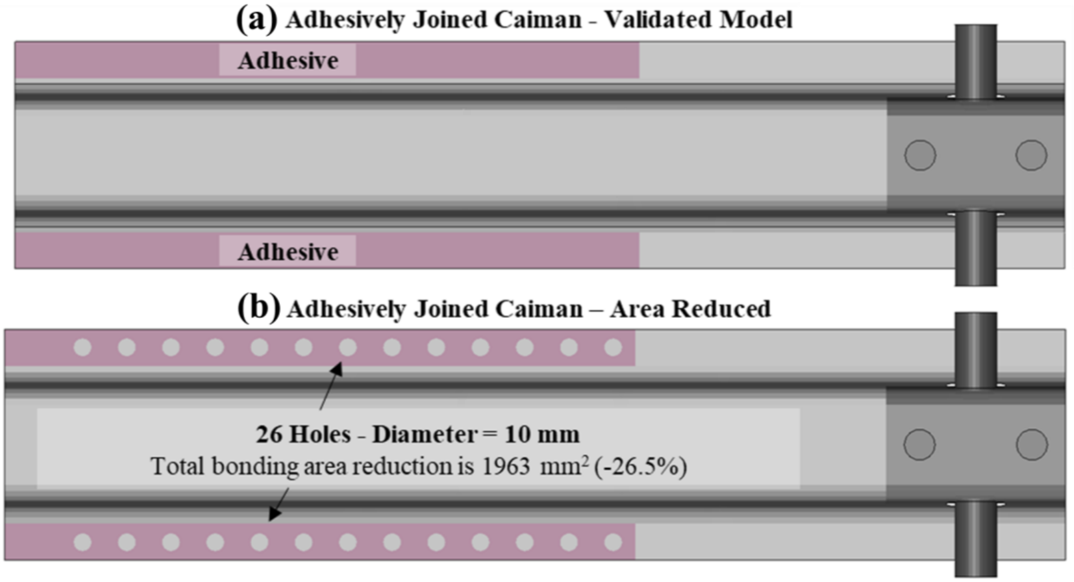

Figure 170: The validated adhesively joined Caiman model (a) was adapted to investigate the influence of adhesive area reduction while maintaining the adhesive boundaries (b).

5.6.4 Joint Enhancement of Adhesively Joined Caiman Components

Researchers attempted to enhance the mechanical response of adhesive joints, by optimizing adhesive joint configuration, joint design parameters, substrate stiffness and strength or adhesive selection (Mallick, 2020). It was observed in the experiments conducted in this work on adhesively joined Caiman components that the peak load corresponded to adhesive crack initiation. Therefore, a joint enhancement with a reinforced adhesive crack tip was incorporated into the validated FE model. The Caiman joint design was improved by reinforcing the crack tip using two 3 mm thick sheets (one sheet on each side of the tube). The reinforcement sheets were joined to the Caiman component internally using four SPR rivets (two rivets for each sheet) (Figure 171). The SPR rivets were aligned with the adhesive crack tip so that the reinforcing sheets and SPR rivets could carry the load prior to initiating a crack at the adhesive crack tip. The reinforced joint could be created in an actual bonded structure where the crack tip is at the free ends of the joined hat sections. The reinforcing sheets were 55 mm wide, but the dimensions of the sheets are not expected to have a substantial influence on the mechanical response unless the width was too narrow and allowed yielding. The load-displacement and energy-displacement responses of the reinforced model were compared to the validated adhesively bonded Caiman simulation results.

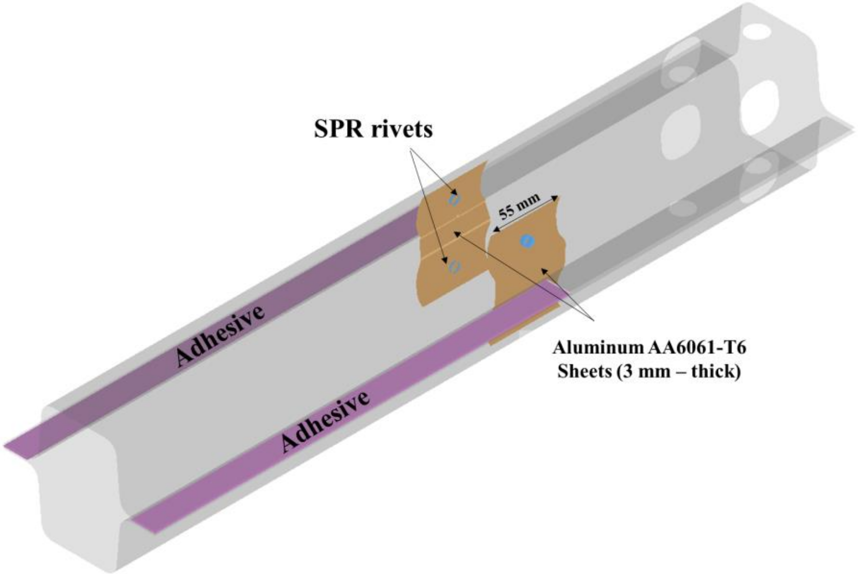

Figure 171: Adhesively joined Caiman component reinforced using two 3 mm sheets (one sheet on each side of the tube), which were joined to the inner hollow section of the tube using four SPR rivets.

Chapter 6 Finite Element Modeling Results and Discussion

The developed FE computational models were assessed using three joint configurations (SLJ, H-Specimen and Caiman), three modes of loading (shear, tension and Mode I loading) and varying adherend thickness (1, 2 and 3 mm thick sheets), for a total of twenty-seven models made with aluminum AA6061-T6 adherends. First, the constitutive model of the aluminum adherends was verified for each sheet thickness by comparing the single-element FE model response to the experimental characterization data.

Next, the material-level traction-separation relationships of the adhesive (Watson *et al.*, 2020, 2018) were implemented into a CZM model, and then the adhesively joined H-specimens and SLJ joints were modelled, simulated and validated using the experimental results of the joints made with 1, 2 and 3 mm thick sheets (Chapter 44.4 and 4.5). Second, the SPR parameters, measured and calibrated to the SLJ joints and H-specimens (SPR rivet calibration methods in 5.3) for each sheet thickness, were implemented into a constraint model available in a commercial code (Constraint_SPR2 in LS-DYNA, developed by Hanssen *et al*. (2010)) and a CZM-based model. The constraint model of the SPR rivet was verified for joints made with 1, 2 and 3 mm thick sheets (Chapter 4, sections 4.4 and 4.5), while the CZM model was verified for the joints made with 3 mm thick sheets to avoid redundancy. After that, the models of the adhesive (CZM) and SPR rivet (constraint or CZM) were integrated and validated with the response of the hybrid joined H-specimen and SLJ experimental tests. Similar to the SPR models, the CZM-Constraint model was validated for joints made with 1, 2 and 3 mm thick sheets, while the CZM-CZM model was validated for the joints made with 3 mm thick sheets.

To validate the models at the component level, the adhesive, SPR and hybrid joint models were directly implemented and simulated using the Caiman test, without any modification to the adhesive CZM properties or the parameters of the SPR models. Finally, the Caiman model was used to investigate variables including rivet spacing, adhesive bond area, and augmenting adhesive joint design with reinforcement.

6.1 Aluminum Sheet Metal (Adherend) Material Model Single Element Verification

The aluminum sheet material was modeled using a piecewise linear elastic-plastic with isotropic hardening and was verified using single-element FE models. Aluminum AA6061-T6 sheet material anisotropy was reported to have almost no effect on yield strength and a small effect on the hardening response (difference less than 10 MPa between the 0 and 90-degree responses) (Tardif and Kyriakides, 2012), so using isotropic hardening was deemed appropriate. The simulation results were compared to the experimental data of the aluminum AA6061-T6 uniaxial tensile specimens for the three sheet thicknesses (1, 2 and 3 mm). The material model accurately predicted the tensile behaviour of the sheet materials, providing an excellent fit to the average experimental data including the yield point and hardening behaviour for the three sheet thicknesses (Figure 172). The yield strength difference was within 2% of the measured experimental data. Post-yield, the FE-predicted hardening curve demonstrated an excellent match with the experimental data for all sheet thicknesses (Figure 172a, Figure 172b and Figure 172c). The hardening curve of the aluminum sheet materials under quasistatic uniaxial loading was within a difference of 1.5% (measured at an effective plastic strain of 0.05). Failure was not incorporated into the material models because adherend failure was not observed during the experimental tests. Importantly, the sheet thickness effect on the aluminum hardening response (*i.e.,* reduced UTS with increasing thickness) was measured and incorporated into the material models.

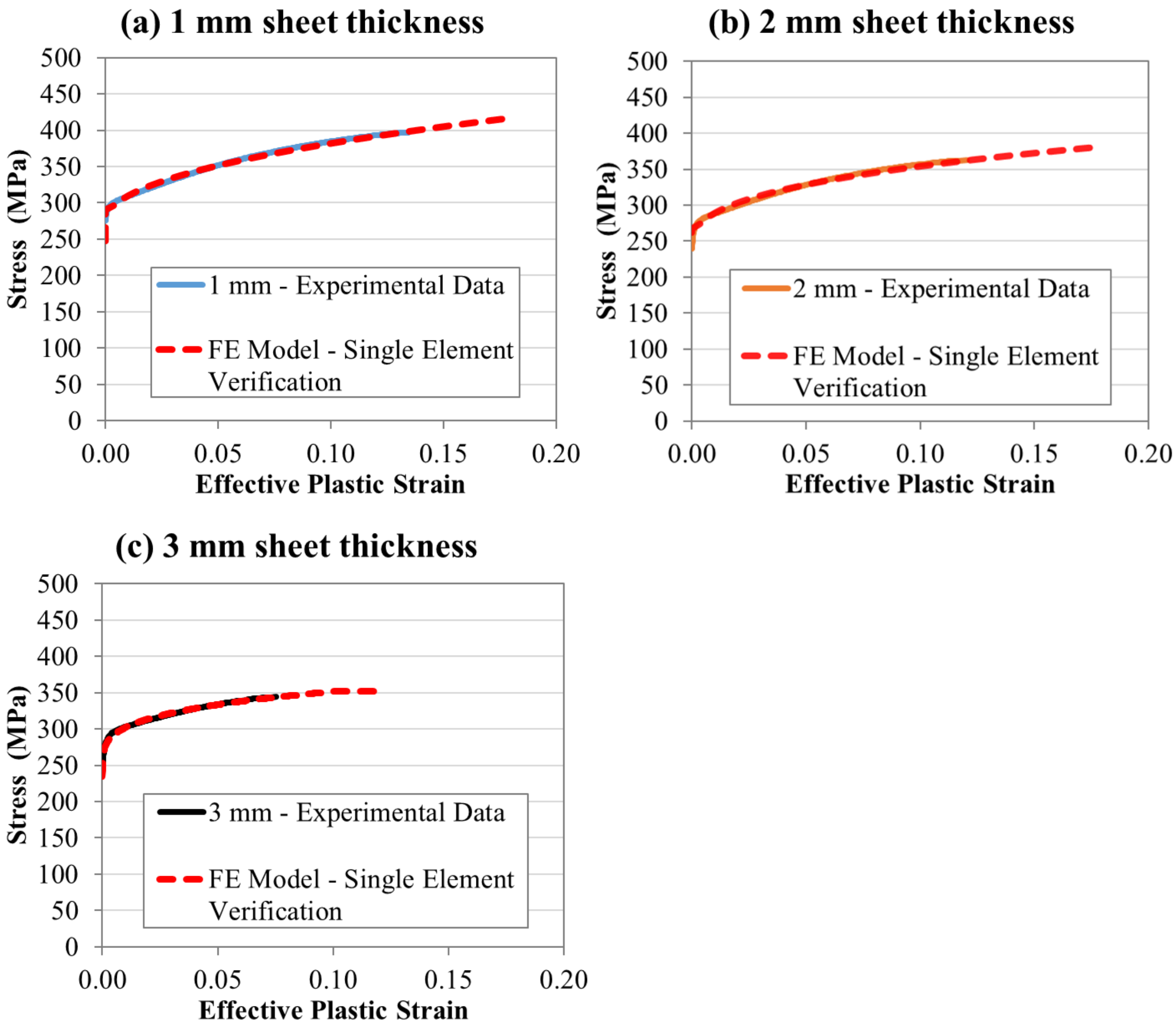

Figure 172: Simulation results of a single-element model for the AA6061-T6 alloy having 1 mm (a), 2 mm (b) and 3 mm (c) thick sheets compared to the experimental uniaxial tension tests.

6.2 Adhesive Cohesive Zone Model Validation Using Coupon-Level Data

The adhesive CZM model was developed based on material-level adhesive characterization tests (RDCB and BSS) (Watson *et al.*, 2020, 2018) and the measured traction-separation curves (Mode I and Mode II loading) were implemented into the model to represent the adhesive crack initiation and damage progression. In this section, the CZM model validation was presented for two different specimen-level tests (SLJ and H-specimen) having three different sheet thicknesses each.

6.2.1 Single Lap Shear Joint CZM Model Validation (three sheet thicknesses)

The SLJ FE model with 1 mm adherends predicted the measured load-displacement (Figure 173a) and rotation-displacement (Figure 173b) responses, validating the overall response and the local kinematics of the joint. The predicted peak load matched the measured peak load (< 3%), with somewhat higher predicted stiffness in the linear loading region. The models captured the adherend bending deformation of the SLJ joint and showed a joint rotation of ~2 degrees prior to joint failure mimicking the local joint kinematics observed in the test (based on optical measurements, Figure 173b). The bending moment within the adherend, which induced joint rotation, was coupled with adherend yielding at a load of ~11.5 kN. The adherends plastically deformed (in-plane deformation/stretching) and after substantial hardening, cohesive element failure was initiated at the leading and trailing ends of the adhesive layer (red regions in Figure 173c). The damage progressed rapidly through the CZM layer, and the model matched the bending and in-plane deformations seen in the experimental test throughout the test, up to adhesive damage initiation and joint failure (Figure 173c).

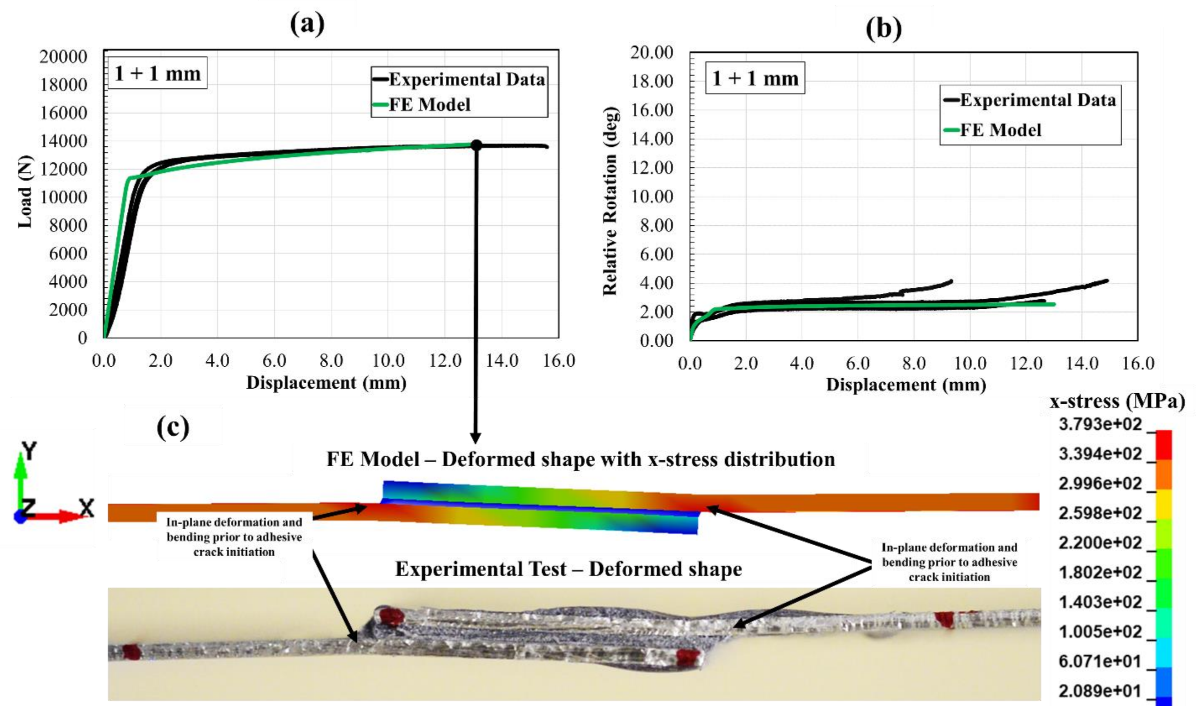

Figure 173: The SLJ model made with 1 mm adherends compared to experimental load-displacement response (a), joint rotation (b), and the deformed adherends showed bending and in-plane plastic deformation at the adhesive damage initiation (c), matching the experiments.

Similarly, the SLJ FE model made with 2 mm thick adherends was validated for the overall response and local kinematics of the joint. The predicted and measured load-displacement responses (Figure 174a) showed that the peak loads agreed within a difference of 16%, and similar to the 1 mm models, the predicted stiffness in the linear loading region was somewhat higher. The joint rotation measurements from the SLJ tests were compared to the simulation results (Figure 174b), and the joint failed at a relative rotation of 4.8°. The ultimate failure of the joint happened due to a damage initiation within the CZM elements at the adhesive leading and trailing edges (free ends) followed by abrupt damage progression through the CZM layer (CZM damage progression within one time-step, Figure 174c). Prior to joint failure, the adherend showed concentrated plastic bending deformation adjacent to the adhesive leading and trailing edges, as observed in the experimental data (Figure 175).

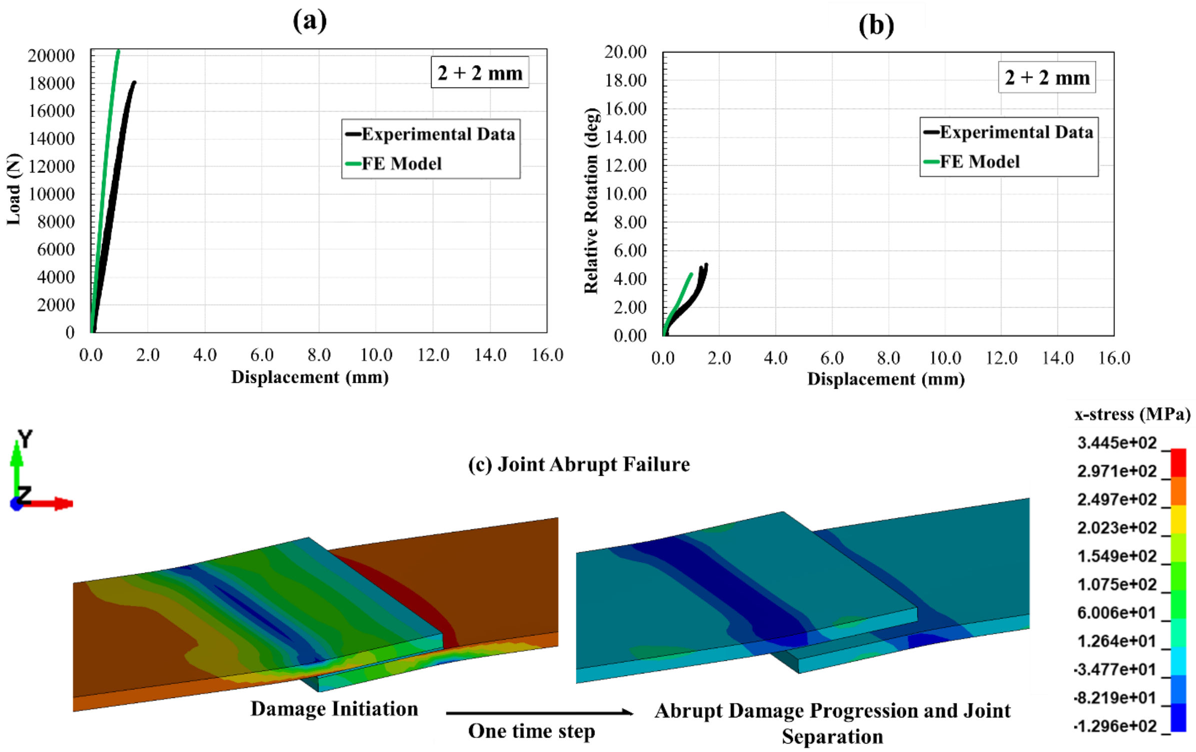

Figure 174: Simulation results of the SLJ model made with 2 mm adherends, illustrating load-displacement (a), joint rotation (b) responses with abrupt adhesive joint failure (c).

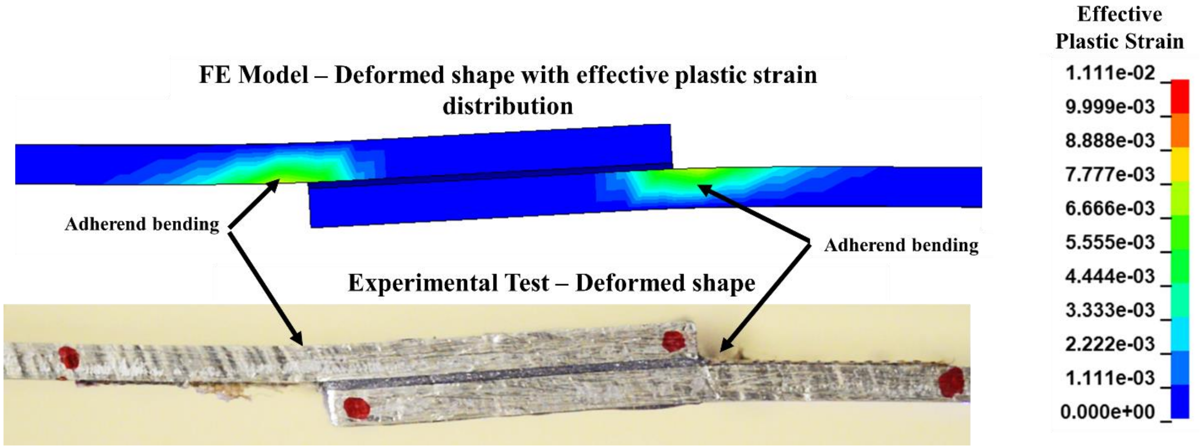

Figure 175: The SLJ model experienced a concentrated bending moment adjacent to the leading and trailing edges of the adhesive, as seen in the experimental test. (comparison at adhesive damage initiation)

The SLJ model, made with 3 mm adherends, showed good agreement with peak load (<12.3% difference) and displacement at failure (<0.5 mm difference) (Figure 176a). Similar to the 1 mm and 2 mm models, the response of the FE model was somewhat stiffer compared to the experiments. The models captured the adherend bending deformation, resulting in SLJ relative joint rotation (Figure 176b). The overall deformation of the model agreed well with the experimental test and the bending moment within the adherends was concentrated adjacent to the adhesive leading and trailing edges (Figure 176c), similar to the SLJ joints with 2 mm but with a lower effective plastic strain value.

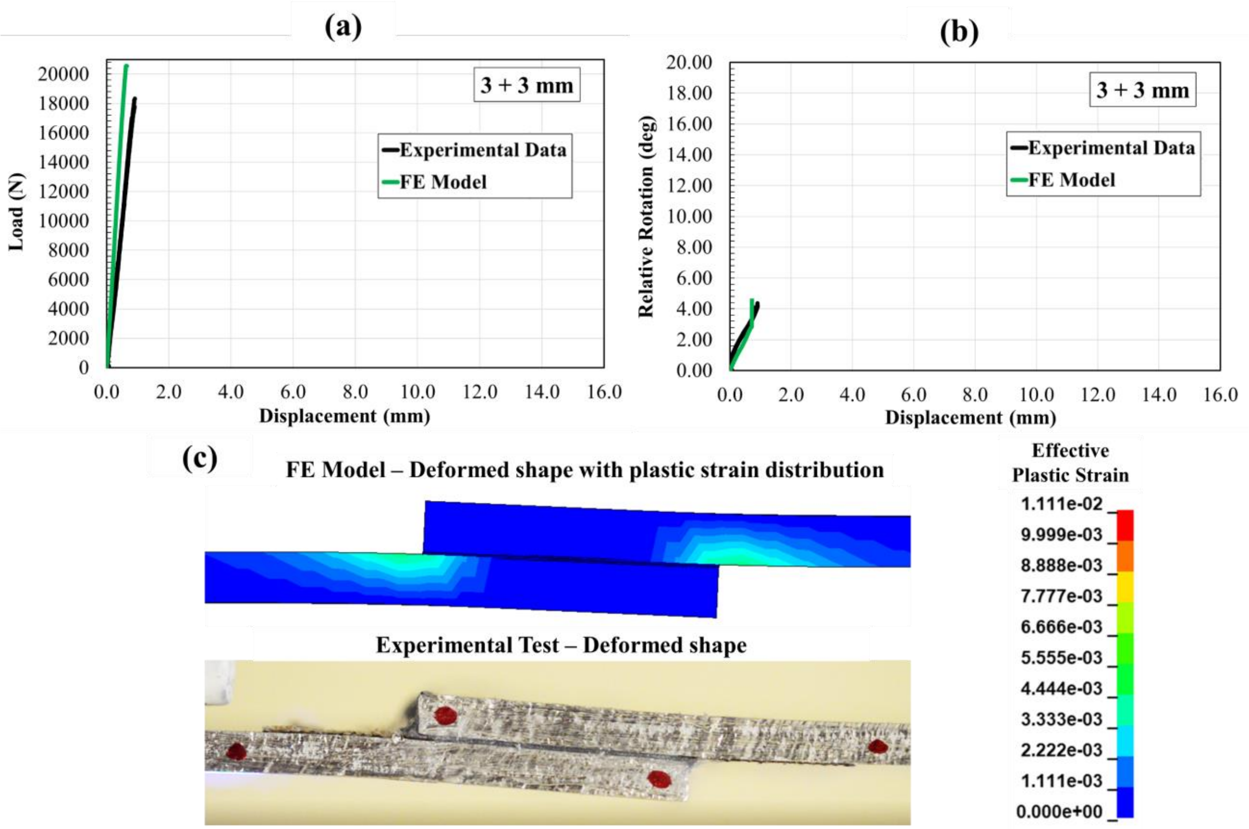

Figure 176: The SLJ model made with 3 mm adherends predicted the load-displacement (a) and rotation-displacement (b) responses, demonstrating localized adherend bending that matched the experimental test.

The SLJ models with 1 mm adherends experienced plastic deformation (stretching) that started locally adjacent to the adhesive ends and then gradually progressed globally within the adherends. During plastic deformation, the force plateaued as the adherends experienced strain hardening and the shear strains localized within the adhesive boundaries. As the adherends resisted further plastic deformation, a small increase in load resulted in a substantial increase in the localized adhesive strains and initiated an abrupt CZM failure, matching the literature observation made using strain gauges applied to similar SLJ joints experiencing substantial plastic deformation within the adherends (Karachalios et al., 2013a). The substantial adherend plastic deformation was also manifest in the joint rotation. The joint rotated two degrees then plateaued because the adherend yielding localized the deformations in-plane rather than increasing the bending moment. Ultimately, the 1 mm joint response was dominated by the adherend material properties, and the crack initiation mechanism was due to localized strains at the adhesive boundaries. Increasing the sheet thickness to 2 or 3 mm reduced the adherend yielding resulting in increased Mode I loading on the adhesive. The 2 and 3 mm models failed at a substantially lower displacement of (< 2 mm) compared to the 1 mm owing to extensive yielding and plastic deformation in the 1 mm adherends. The CZM crack initiation was abrupt due to mixed mode loading, which was followed by a progressive failure within the adhesive CZM layer due to shear loading. The SLJ model with 3 mm adherends experienced slightly lower adherend bending than the 2 mm joint, which was also seen in the experimental joint rotation measurements (4.2° versus 4.8°).

All three SLJ FE models demonstrated a slightly stiffer response compared to the experiments, which is consistent with the literature (Harintho and Gould, 1991; Hartlen *et al.*, 2020; Ibrahim *et al.*, 2023; Watson *et al.*, 2019). One of the shortcomings of shell elements based on the Reissner-Mindlin plate theory is that these elements experience overly stiff behaviour under displacement-based membrane loading due to the constrained boundaries effect (Harintho and Gould, 1991), as occurred in the SLJ models. The constrained boundaries induced localized bending and out-of-plane strains early during the loading (displacement of ~ 0.5 mm), exacerbating the need for capturing the shell thickness changes. The 2 mm model showed that the out-of-plane (through-thickness) strains of a critical element within the localized bending region were almost in the same order of magnitude as the in-plane (membrane) strains (Figure 177). Additionally, the setup relied on the tied constraint to transfer the moment between the adhesive CZM elements and adherend shell elements to avoid using coincident nodes of the shell and cohesive elements. It has been noted that cohesive element formulation 19 in LS-DYNA suffers from stiffness increase in these circumstances (Hartlen *et al*., 2020). A different element formulation that allowed moment transfer at the cohesive element nodes is available (Element formulation 20 in LS-DYNA); however, this particular formulation showed an unphysical unloading behaviour (rapid crack propagation with stiffness degradation) under Mode I loading (Hartlen *et al*., 2020), and therefore was not used in the present study.

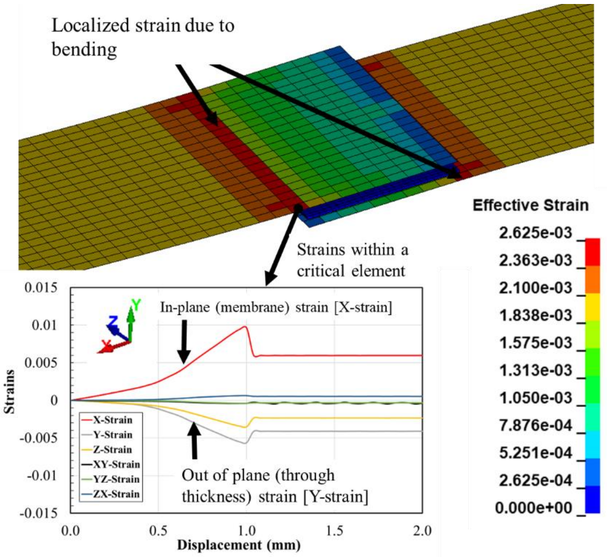

Figure 177: The SLJ model with 2 mm adherend exhibited substantial through-thickness strain within the localized bending region.

The CZM tractions (stresses within the adhesive CZM layer) under Mode I and Mode II were compared for the SLJ models made with 1, 2 and 3 mm adherends. Increasing the adherend thickness generally reduced the localization of both peel and shear loads (Figure 178a and Figure 178b). The 1 mm joints did not experience substantial peel loading, and the shear loading at the adhesive boundaries was the primary crack initiation mechanism, attributed to the plastic deformation in the adherends enabling joint reorientation to primarily load the joint in shear and localize the shear strains at the boundaries. In the 2 and 3 mm joints, the localized bending moment adjacent to the adhesive leading and trailing edges introduced some degree of mode mixity, and both models (2 and 3 mm) experienced a similar magnitude of Mode I traction (~20 MPa, Figure 178a). A Mode I traction of 20 MPa was below the peak traction value of this adhesive (51 MPa), therefore although the joints failed due to mixed mode loading, the primary crack initiation was due to shear loading, which reached the peak value for this adhesive at damage initiation (29 MPa, Figure 178b). Thus, the 3 mm models failed at a load similar to that of the 2 mm, explaining the experimental results and highlighting that increasing sheet thickness may not always be associated with higher adhesive joint strength.

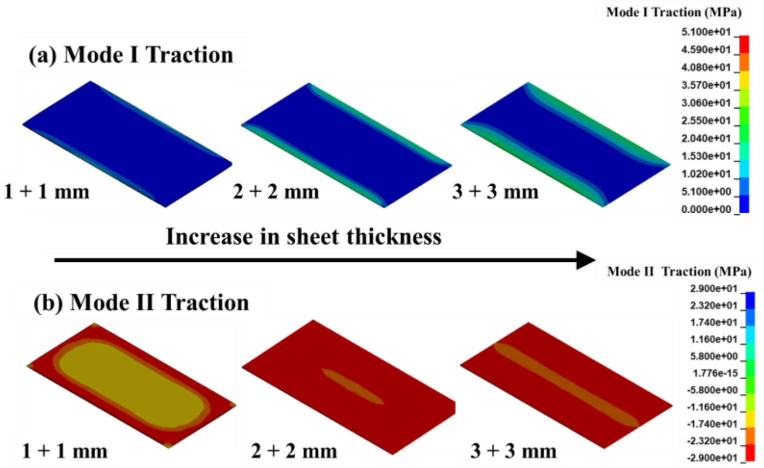

Figure 178: Mode I (a) and Mode II (b) traction distribution within the adhesive layer for the joints made with 1+1, 2+2 and 3+3 mm adherends.

6.2.2 H-Specimen CZM Model Validation (three sheet thicknesses)

The 1 mm adherend H-specimen model showed good agreement with peak load (<12% difference), initial stiffness (<5% difference) and the overall behaviour (*i.e.*, the shape of the response curve) (Figure 179). However, the displacement at failure was somewhat overpredicted (1 mm difference). In the model, the displacement of the top fixturing block induced localized Mode I traction at the adhesive free ends (Figure 180), which failed the CZM elements in that location and resulted in the load observed during the initial loading, and also seen in the experimental response. As the damage propagated within the cohesive elements reducing the CZM width, the moment arm of the load acting at the adhesive free ends increased and consequently the bending moment around the radius of the U-section.

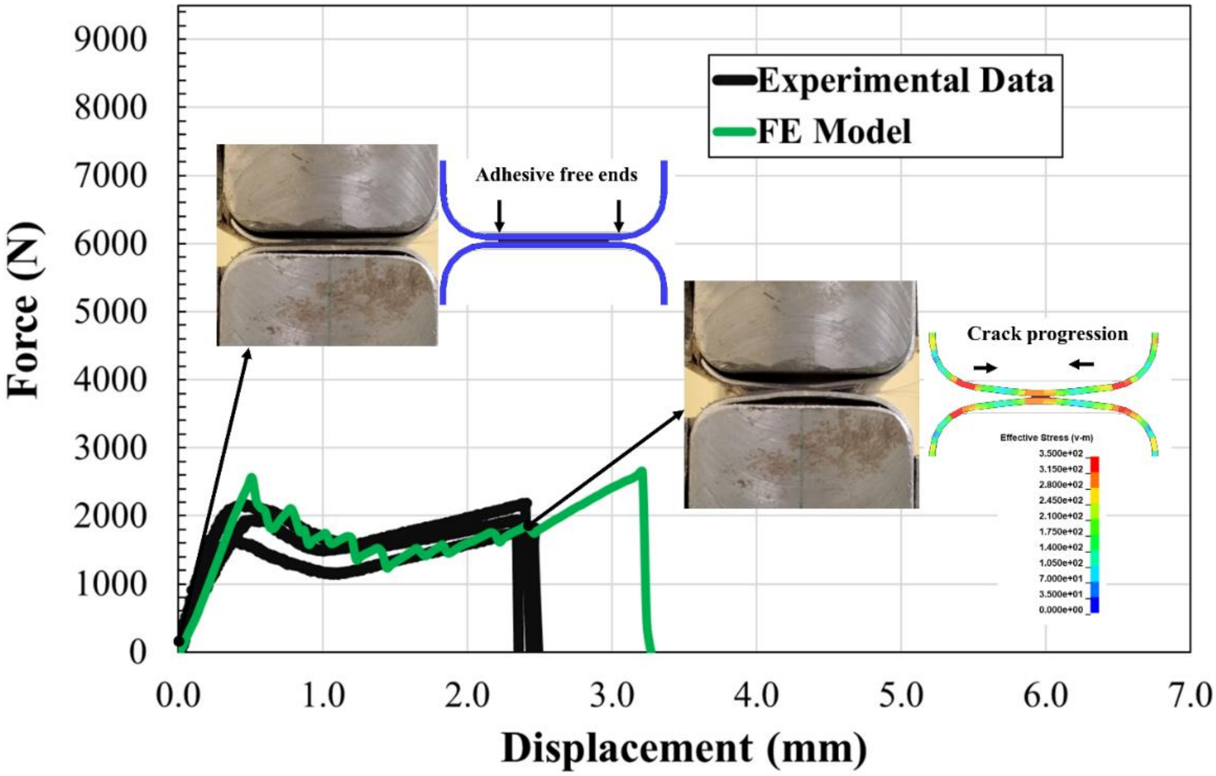

Figure 179: Simulation results of the H-specimen model made with 1 mm adherends, illustrating load-displacement response, illustrating that the deformations seen in the experiment and model were similar at the failure of the experimental test.

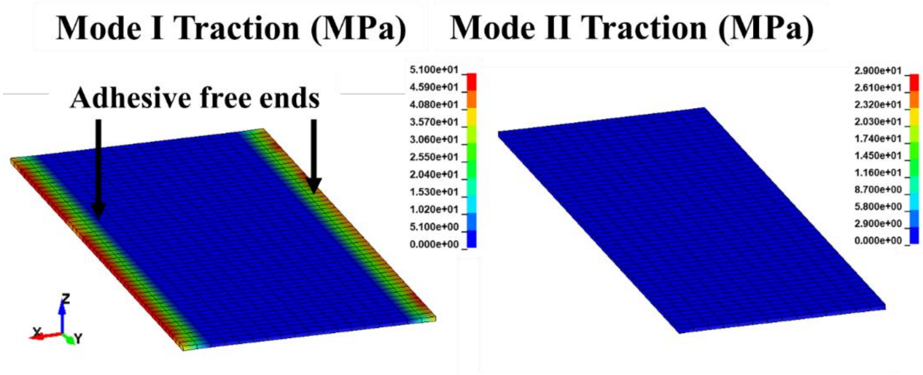

Figure 180: The Mode I and Mode II traction distribution within the CZM layer of the 1 mm adherend H-specimen showed that the adhesive failure was initiated due to Mode I loading at the adhesive free ends.

Therefore, the U-sections exhibited a gradual increase in bending deformation, and the effective stresses were localized at the radius of the U-section (Figure 181a). As the loading continued, the radius geometry deformed into the fixturing blocks and acted as a boundary condition which increased the adherend localized stresses within the bond area (Figure 181a). Thus, the bond area and radius geometry experienced highly localized plastic deformations which dominated the response prior to failure and resulted in a reduction in the traction applied on the adhesive CZM, delaying the failure of the last row of CZM elements (Figure 181b).

A previous study reported that capturing the stiffness of adhesively joined H-specimens made with thin sheet metal was challenging due to the geometry of the U-section (Weiland *et al.*, 2019). The authors attributed the model limitation to the material model; however, in the same work, the material model could predict the response of spot-welded H-specimens. Spot welds are generally more ductile and induce deformations locally within the welding regions, such as the heat-affected zone, thus, the stress distribution was different with very little stresses localized along the length of the joining area or radius of the U-section. However, the adhesively bonded H-specimen experienced highly localized membrane stress within the bond area, which was intensified after adhesive damage progression (Figure 182), which localized the plastic deformations, and consequently over-predicting the displacement at failure.

(a) Effective Stress

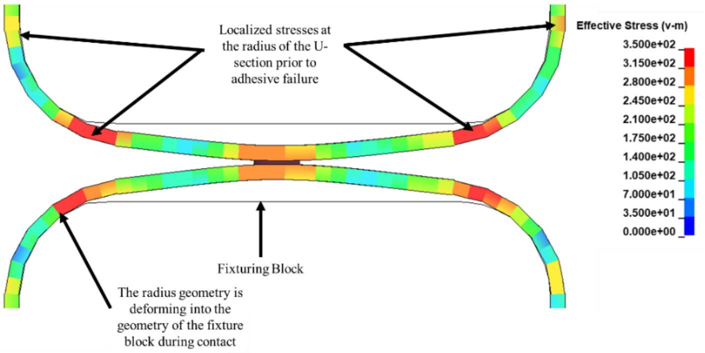

(b) Effective Strain

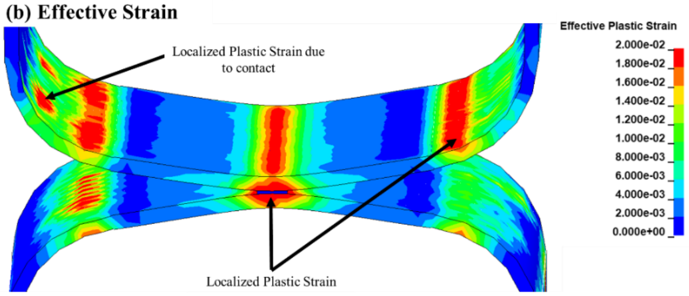

Figure 181: The H-specimen experienced highly localized stresses (a) and strains (b) within the radius of the U-section and the bond area delaying the adhesive CZM failure.

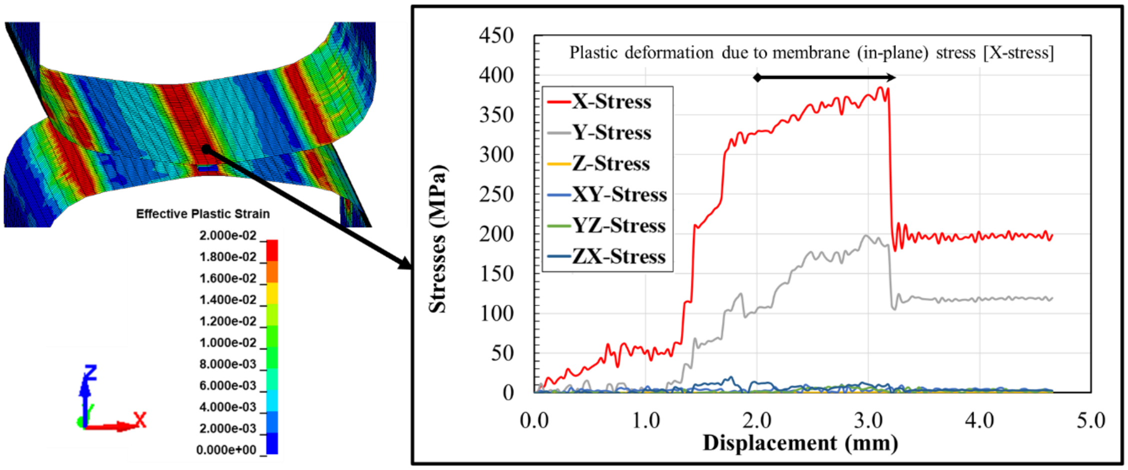

Figure 182: The H-specimen experienced bending as the adhesive damage initiated, which resulted in localized in-plane (membrane) stress within the bond area later in the loading (prior to adhesive CZM failure).

The 2 mm adherend model showed good agreement with the failure load (<7% difference), and initial stiffness up to a load of 2-3 kN (<5% difference) (Figure 183a). The model accurately predicted the displacement at failure, but the initial loading behaviour showed a load spike corresponding to adhesive damage initiation, which was followed by a sudden drop in load, as opposed to the smooth gradual softening observed in the experiments at a load of 2-3 kN (Figure 183a). In the experimental tests, the U-section experienced elastic deformation at the radius as it bent into the shape of the fixturing blocks filling the gap and creating full contact with the fixturing blocks along the length (Figure 183b). As the radius of the U-sections elastically deformed, a smooth gradual reduction in force took place due to a localized damage initiation at the adhesive free ends adjacent to the radius, which created some variability in the experimental response (Figure 183a). The model predicted the same overall behaviour, such that the crack initiated at the adhesive free ends and progressed toward the centre of the adhesive until ultimate failure led to joint separation. However, in the model, the CZM damage initiation was symmetrical on both sides of the full length of the CZM layer (50 mm) (Figure 183c), as opposed to multiple localized crack initiation points. The load softening seen in the experimental results during the loading phase requires modeling the adherends and adhesive using highly refined solid elements to capture the localized crack initiation at the adhesive edges (Cognard, 2008).

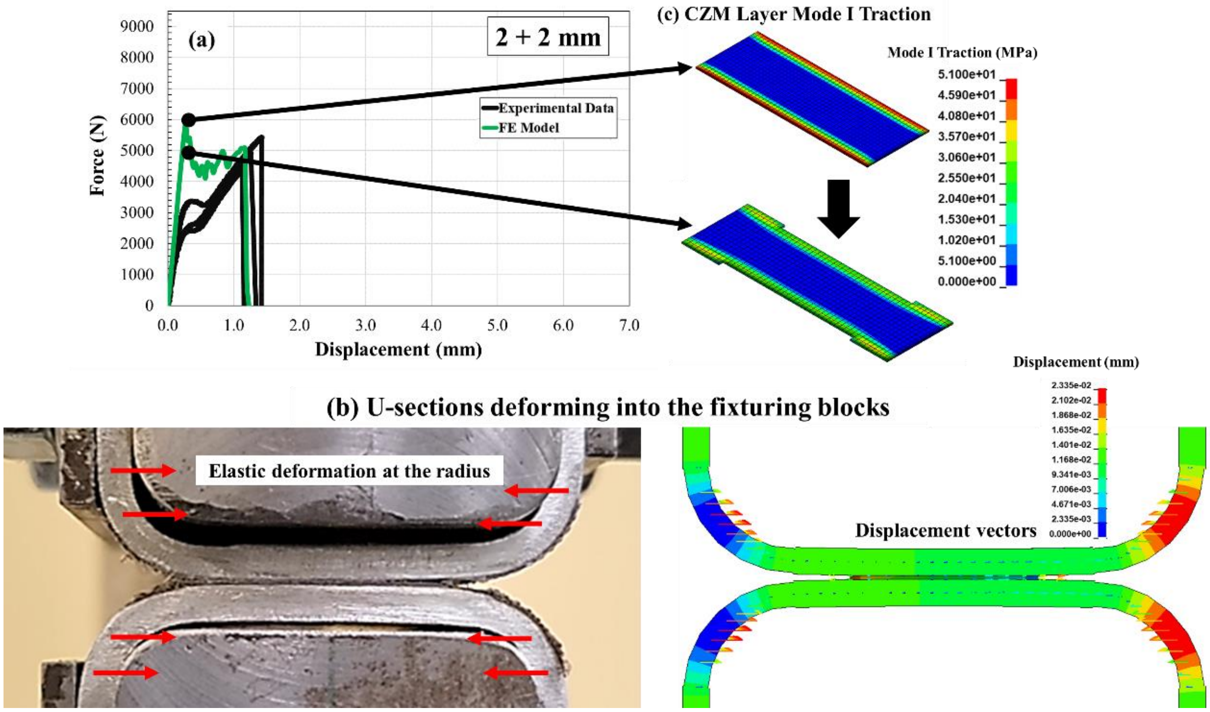

Figure 183: The 2 mm adherend H-specimen model, illustrating load-displacement response (a), deformation of the U-sections during early loading (b), and the symmetrical 2D (rows of elements) failure of CZM layer due to Mode I loading.

The model showed that prior to the adhesive damage initiation, the effective stresses were localized adjacent to the adhesive free ends and at the radius of the U-section (Figure 184). The radius of the U-section experienced localized in-plane (membrane), out-of-plane, and transverse shear stresses with a peak that corresponded to the adhesive damage initiation (Figure 184a). The stresses at a highly stressed adherend element adjacent to the adhesive free edges showed that the adherends experienced predominantly localized in-plane (membrane) stress with a peak value that corresponded to the adhesive damage initiation (Figure 184b). Overall, the effective stresses were highly localized, but the stress state within the radius was more complex because it was in contact with the fixturing block. The contact interface sliding energy from the model confirmed that the radius geometries of the U-section and the fixturing blocks experienced nodal penetration (Figure 185b), which further exacerbated the localized stresses at the contact interface. One of the methods that reduced the stress localization effect was updating the shell thickness based on the through-thickness strains (ISTUPD option in LS-DYNA), which improved the stress state at the radius and consequently resulted in better load-displacement prediction (Figure 185b).

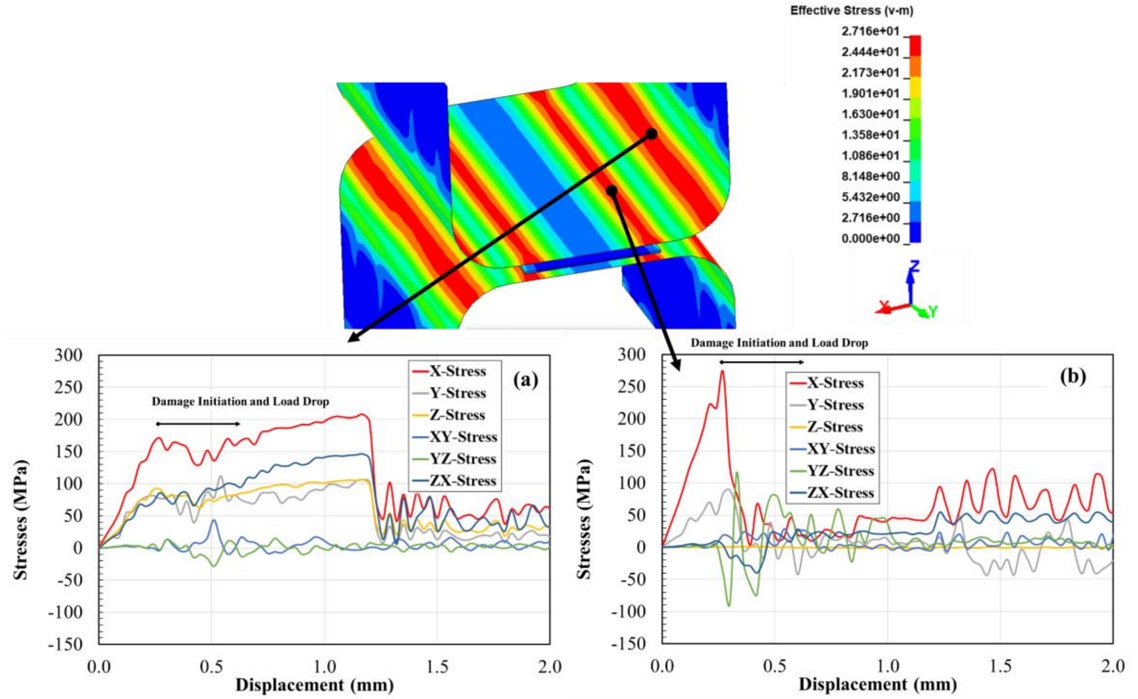

Figure 184: The effective stress distribution within the H-specimen showed stress localization adjacent to the adhesive free ends and at the radius, and the stresses at local points showed that the stresses were generally membrane stresses.

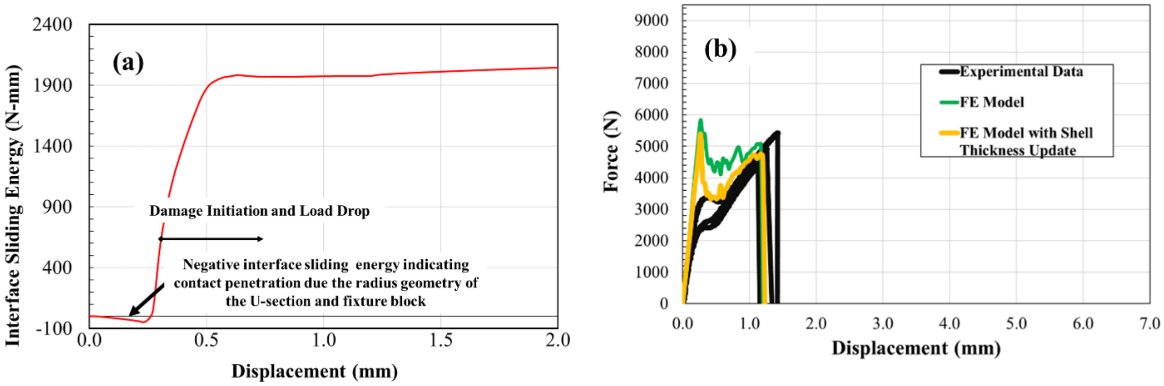

Figure 185: Localized stresses at the radius induced contact penetration, which resulted in higher membrane stresses. Enabling the shell thickness update reduced stress localization at the radius, which improved the FE model predicted response after adhesive damage.

The model with the 3 mm adherends showed good agreement with the load at failure (<5% difference) and initial stiffness up to a load of 2-5 kN (<4% difference). The model reasonably predicted the displacement at failure, but similar to the 2 mm model, the initial loading behaviour showed a load spike at the adhesive damage initiation as opposed to the smooth gradual softening observed at a load of 2-5 kN in the experiments (Figure 186a). The 3 mm adherends were more resistant to deformation, relative to the 2 mm adherends, which further exacerbated the stress concentration at the bend radius and reduced the membrane load adjacent to the adhesive free ends (Figure 186b). A highly stressed element within the radius of the U-section showed that, similar to the 2 mm model, the radius experienced localized in-plane (membrane), out-of-plane and transverse shear stresses, but the peak value did not correspond to the adhesive damage initiation (Figure 187a). The contact interface sliding energy confirmed that the radius of the U-section and the fixturing blocks experienced nodal penetration during damage initiation and continued up to the joint failure (Figure 187b), thus, the load did not drop and was dominated by the contact stress distribution at the radius.

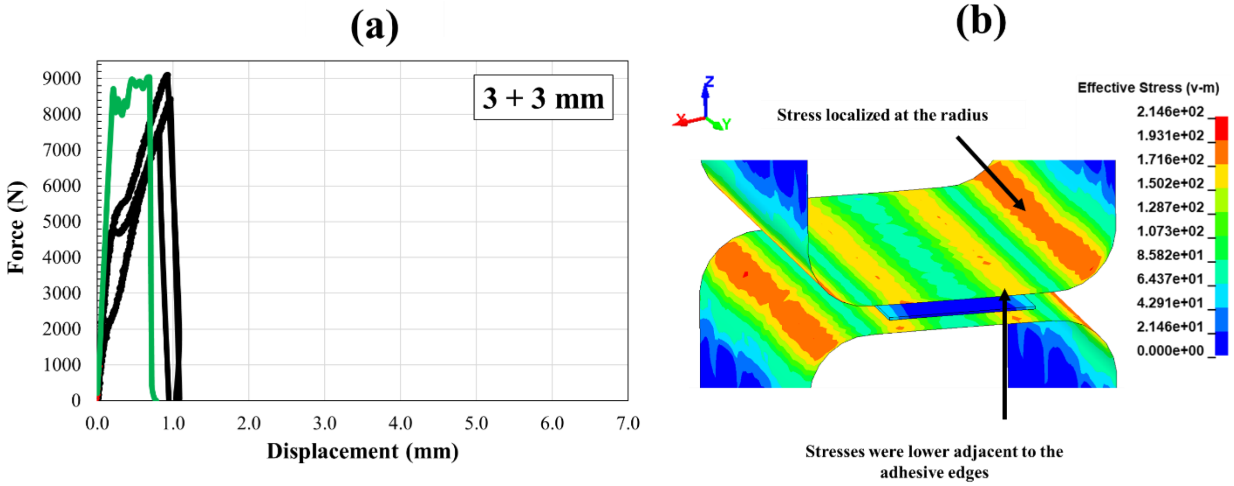

Figure 186: The H-specimen model made with 3 mm adherends, illustrating load-displacement response(a), and effective stress distribution at the adhesive damage initiation (b).

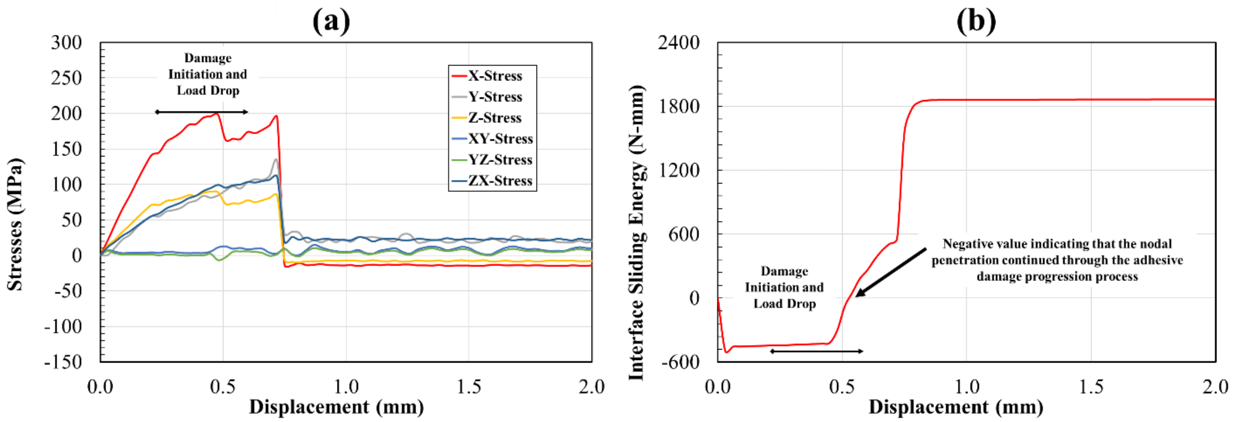

Figure 187: The stress distribution at the bend radius showed that the H-specimen experienced localized stresses (membrane, out of plane and transverse shear) (a), due to the localized contact stress and nodal penetration (b).

6.3 SPR Rivet Model Calibration and Verification

The SPR calibration aimed to use a physics-based fitting approach, as opposed to inverse fitting, and was applied to three SPR rivet/material thickness combinations, which were necessary to accommodate the difference in total joint thickness (1 + 1 mm, 2 + 2 mm and 3 + 3 mm). The SPR rivet constraint model was calibrated to the data obtained from the load-displacement response and the optical measurements conducted on the H-specimen and SLJ joints tests. The calibrated parameters for each sheet thickness (1, 2 and 3 mm) were implemented into the corresponding specimen-level models to verify the response, including joint kinematics, rivet damage initiation and damage progression.

6.3.1 Single Lap Shear Joint SPR Constraint Model Verification (three sheet thicknesses)

The 1 mm adherend SLJ FE model predicted and measured load-displacement response (Figure 188a) to verify the joint response. The predicted peak load matched the measured peak load (1%), and the model predicted the joint stiffness reduction with a high level of accuracy. The ultimate failure of the joint happened after substantial local yielding within the vicinity of the rivet (in-plane deformation) (Figure 188b), which was accompanied by gradual damage progression in the constraint model. The models captured the adherend bending deformation and the SLJ joint rotation to an extent (Figure 188c), demonstrating asymmetrical joint rotation (bending was only observed in the head-side sheet) and mimicking the local joint kinematics of the SPR joint but underpredicting the rotation angle.

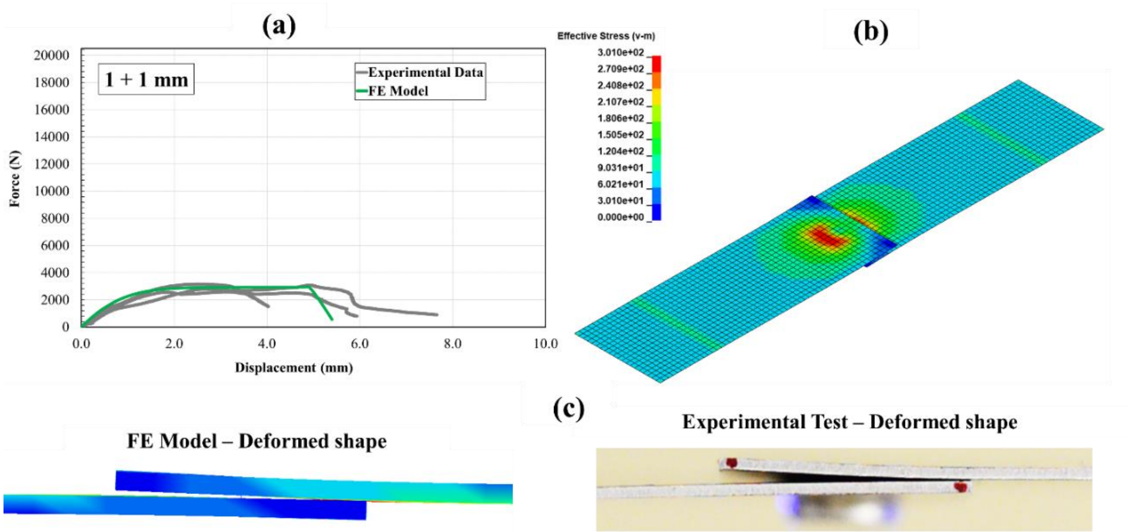

Figure 188: Simulation results of the SLJ model made with 1 mm base material, illustrating load-displacement (a), effective stress distribution at peak load (b) and deformed shape comparison at peak load (c).

Similarly, the load-displacement response of the SLJ model, using the set of calibration parameters for the joints with 2 mm adherends, agreed well with the measured experimental response (Figure 189a), suggesting that the calibration process worked consistently for joints of different sheet thickness and rivet models. The predicted peak load and displacement at failure matched the measured peak load (~1%) and displacement at failure. Increasing the adherend thickness from 1 mm to 2 mm resulted in a similar stress distribution within the vicinity of the rivet (Figure 189b). The model captured the local joint rotation behaviour (Figure 189c) with a difference of ~3 degrees during the early elastic loading (load < 6 kN); however, the model did not capture the substantial joint rotation due to physical sheet separation later during the rivet damage progression.

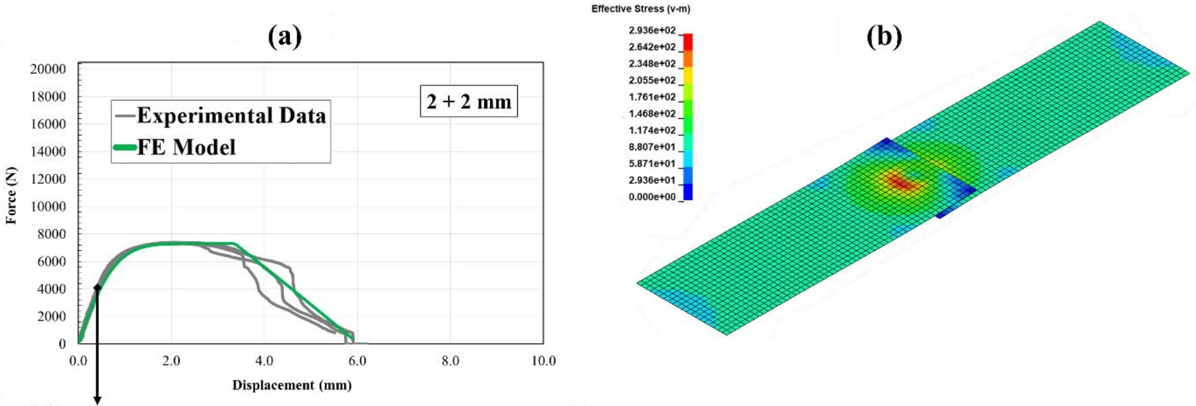

(c) **FE Model – Joint rotation during early elastic loading**

(d) Experimental Test – Joint rotation during early elastic loading

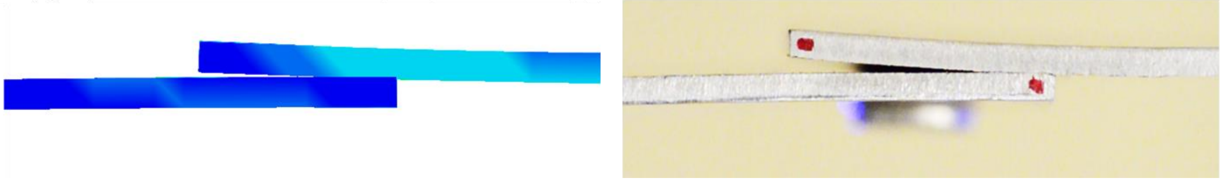

Figure 189: The SLJ model made with 2 mm adherends, illustrating load-displacement response (a), effective stress distribution at peak load (b), and joint rotation during elastic loading (at a load of 4 kN) (c-d).

The 3 mm adherend SLJ FE model showed excellent agreement with the measured load-displacement response (Figure 190a). The predicted peak load and displacement at failure matched the measured peak load (<3%) and measured displacement at failure. Similar to the 1 mm and 2 mm models, the predicted stiffness exhibited a gradual stiffness reduction, and the adherends exhibited localized stresses and yielding within the vicinity of the rivet (in-plane deformation) (Figure 190b), which was followed by linear unloading due to the damage propagation within the SPR constraint model.

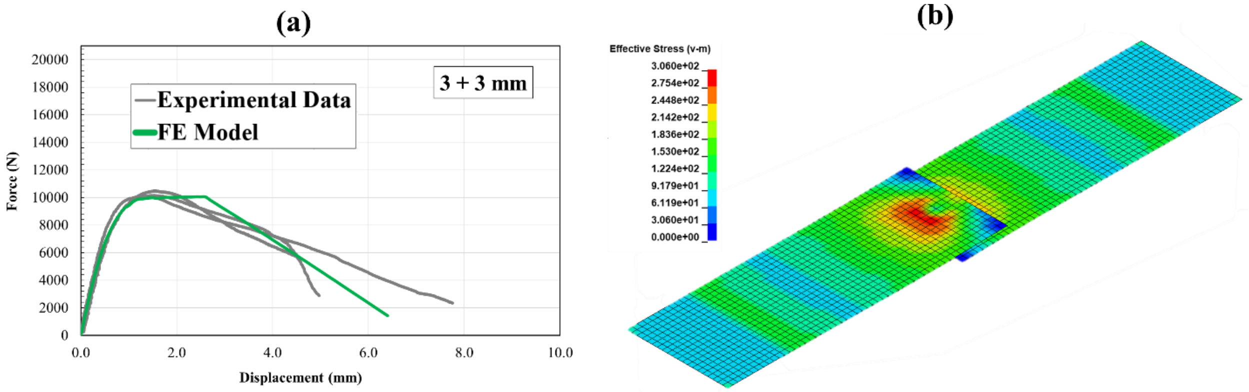

Figure 190: Simulation results of the SLJ model made with 3 mm base material, illustrating load-displacement response (a), and effective stress distribution (b).

In all the SLJ experimental tests, the SPR rivet tail pulled out, and during the rivet damage progression, the rivet rotated while sliding out of the tail-side sheet, attributed to the bending moment generated due to the shear loading eccentricity and physical sheet separation (Figure 191a and Figure 191b). The FE model showed increasing joint rotation, but the rotation in the experimental SLJ tests was higher, and the difference increased substantially later during the SPR rivet damage progression (Figure 191c). The constraint model used a beam element to represent the SPR rivet body, which could not physically represent the separation between the joined sheets during rivet pull-out. Also, the model assumed that the moment arm value remained constant throughout the simulation (moment arm equal to half the thickness of the joint); however, as the rivet pulled out of the tail-side sheet the moment arm increased, reaching a maximum moment roughly equal to the length of the deformed rivet.

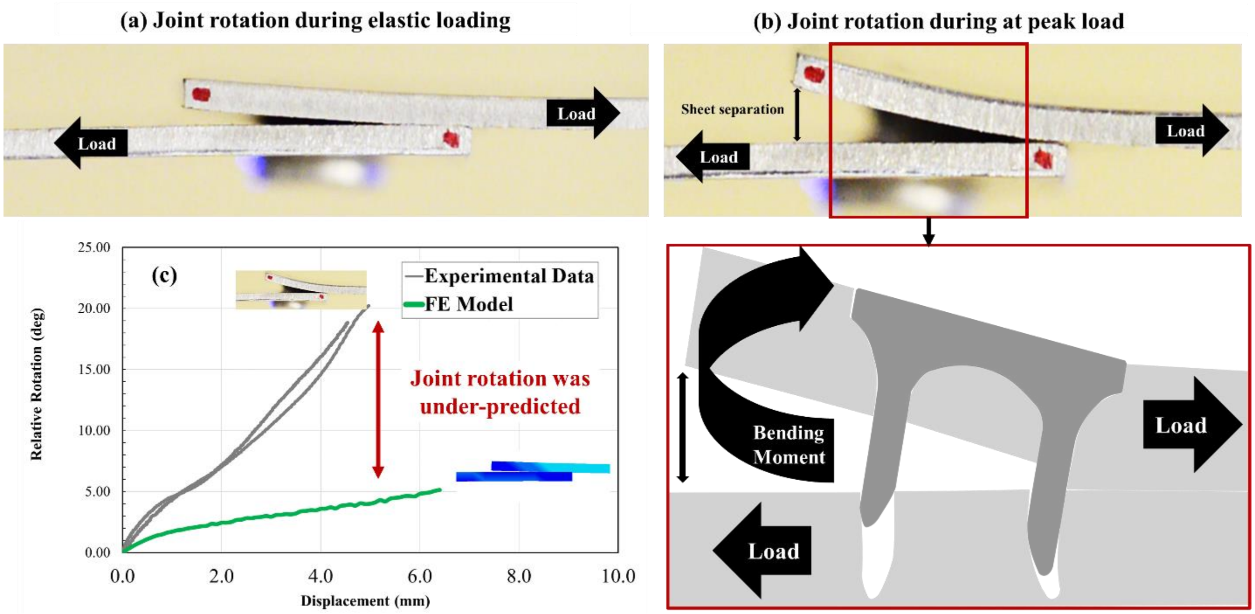

Figure 191: The rotation of the SPR joint with 2 mm adherends increased due to shear loading eccentricity and physical sheet separation (a, b), which was not fully captured in the FE model prediction (c).

The axial load (load acting on the axis of the rivet no the axis of the test specimen), shear load, and bending moment acting on the SPR rivet were extracted from the constraint model for the models with 1 mm (light line weight, Figure 192), 2 mm (medium line weight, Figure 192) and 3 mm (heavy line weight, Figure 192) thick adherends. It was evident that the SPR rivets exhibited shear loading that was equal to the joint peak load (red curve, Figure 192), and a bending moment that increased with shear load and sheet thickness (green curves, Figure 192). However, the axial loading was negligible (black curves, Figure 192). Prior to rivet damage initiation, the model used an equilibrium with equal moment magnitude on the top and bottom sheets but as the rivet damage progressed the model gradually transferred the moment to the top sheet (head side) to mimic the asymmetrical damage resulting from rivet pull out, and the bottom sheet became a moment free hinge (Hanssen et al., 2010). The authors used that approach because it represented the physical behaviour of SPR failure mechanism. However, the joint rotation measurements validation confirmed that the bending moment, which was calculated as half the joint thickness times the shear load, was conservative and the model under-predicted the adherend bending (joint rotation). Such a limitation leaves an aspect to be addressed within the implementation of the model; however, updating the bending moment to account for the increase in moment arm during rivet pull-out is a complex task that requires implementing details about the SPR physical attributes and rivet failure mode into the FE model.

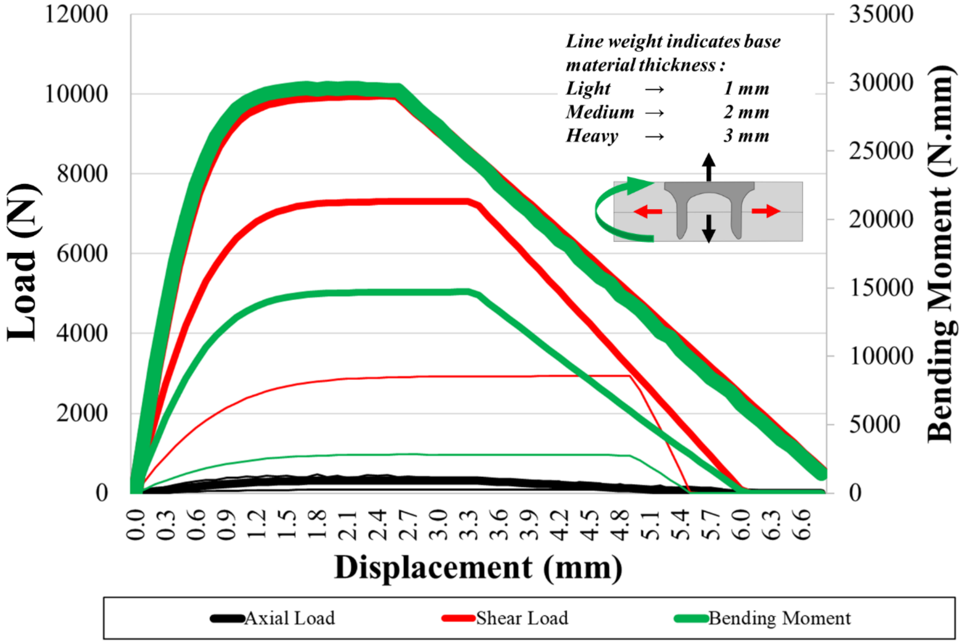

Figure 192: The axial and shear loads, and bending moment acting on the SPR rivets predicted by the SLJ models, made with 1, 2, and 3 mm base material.

6.3.1 H-Specimen SPR Constraint Model Verification (three sheet thicknesses)

The H-specimen FE model made with 1 mm adherends showed good agreement with peak load (2% difference), stiffness (5% difference) and the overall behaviour (*i.e.*, the shape of the response curve) (Figure 193a). The displacement at failure was within the range of the experimental data. Prior to SPR rivet failure, the 1 mm adherends exhibited localized plastic deformation as the rivet tail gradually pulled out of the bottom sheet, and the model captured the SPR rivet damage progression up to failure and complete separation. It was clear from the stress distribution in the H-specimen that during the rivet damage progression that the stresses were localized within the rivet vicinity and did not extend to the radius of the U-section (Figure 193b). Thus, the model response was dominated by the SPR rivet model and the local material properties within the SPR rivet vicinity. The measured and predicted local separation showed excellent agreement and highlighted that the SPR rivets under tension did not encounter joint rotation (Figure 193c).

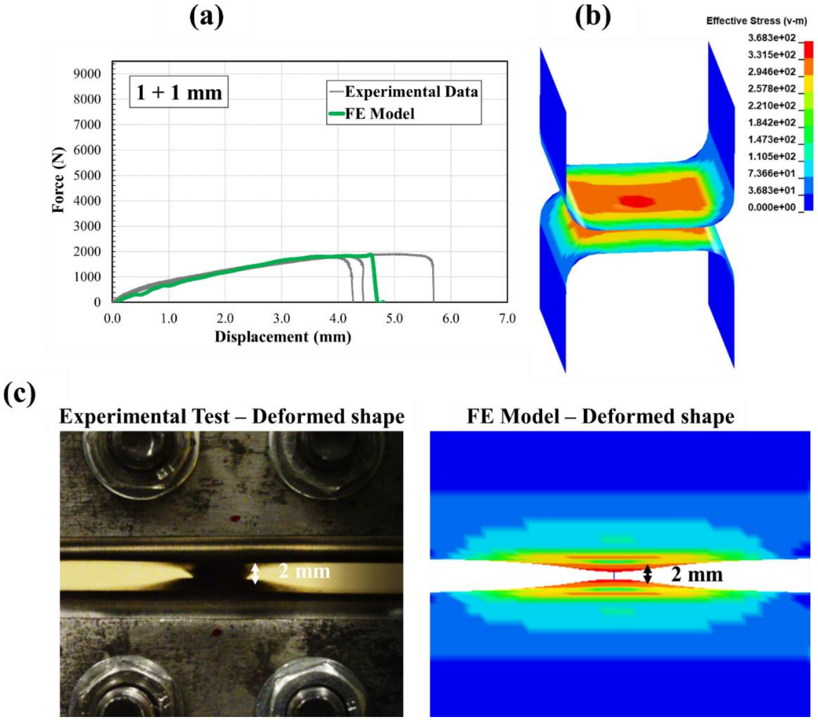

Figure 193: The simulation results of the 1 mm adherend H-specimen model were within the experimental results range for the load-displacement (a), deformation behaviour during rivet damage progression based on effective stress distribution (b), and the measured and predicted local separation (c).

The FE model for the joints made with 2 mm base material showed good agreement with peak load (5% difference), and stiffness (5% difference) (Figure 194a). Similar to the 1 mm model, the 2 mm model exhibited localized plastic deformation corresponding to the rivet tail gradually pulling out of the bottom sheet, and the model captured the SPR rivet damage during the loading phase. The stress distribution in the U-sections during the SPR rivet damage progression showed that the stresses were localized within the vicinity of the rivet (Figure 194b).

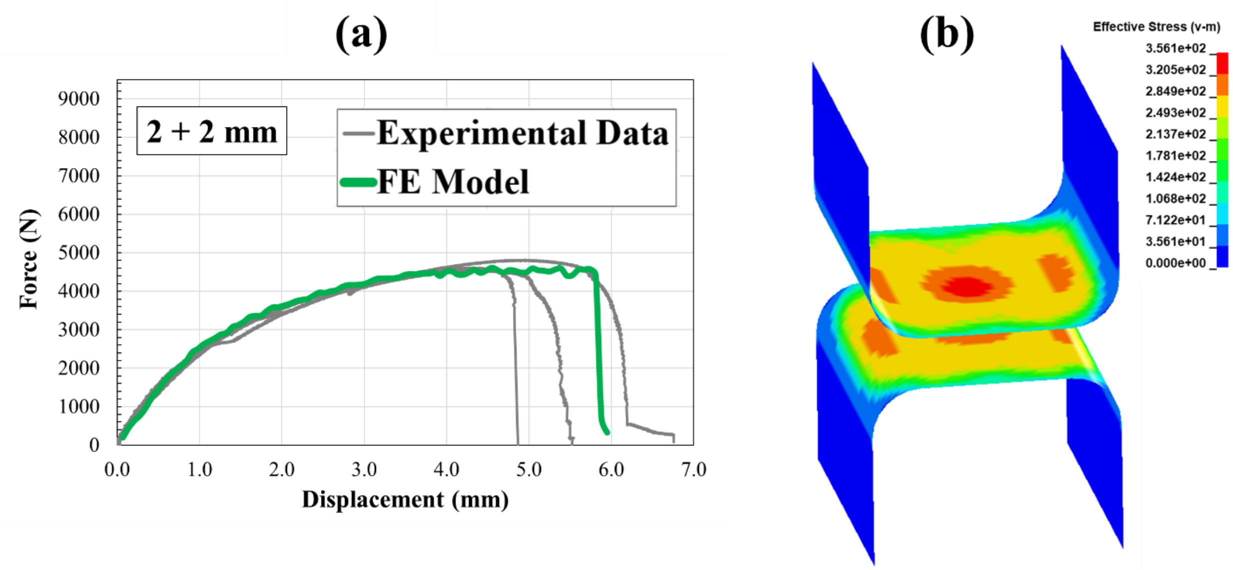

Figure 194: The simulation results of the H-specimen model made with 2 mm adherends were within the experimental results range for the load-displacement (a), and deformation behaviour during rivet damage progression based on effective stress distribution (b).

The constraint model predicted the response of the H-specimens made with 3 mm adherends and showed good agreement with the measured peak load (5% difference) and stiffness (5% difference) (Figure 195a). Similar to the 1 mm and 2 mm models, the 3 mm model exhibited localized plastic deformation within the vicinity of the rivet as the rivet tail gradually pulled out of the bottom sheet. The model captured the gradual stiffness reduction during the SPR rivet damage up to failure, and the stress distribution in the U-sections prior to the rivet failure was similar to what was seen in the 1 and 2 mm models (Figure 195b). The H-specimen separation measured from the nodal coordinates matched measured optical measurements, confirming that models not only captured the global behaviour but also the local joint kinematics (Figure 195c).

Ultimately, the H-specimen geometry provided adequate compliance, stress distribution and deformation to test and model the SPR joining method.

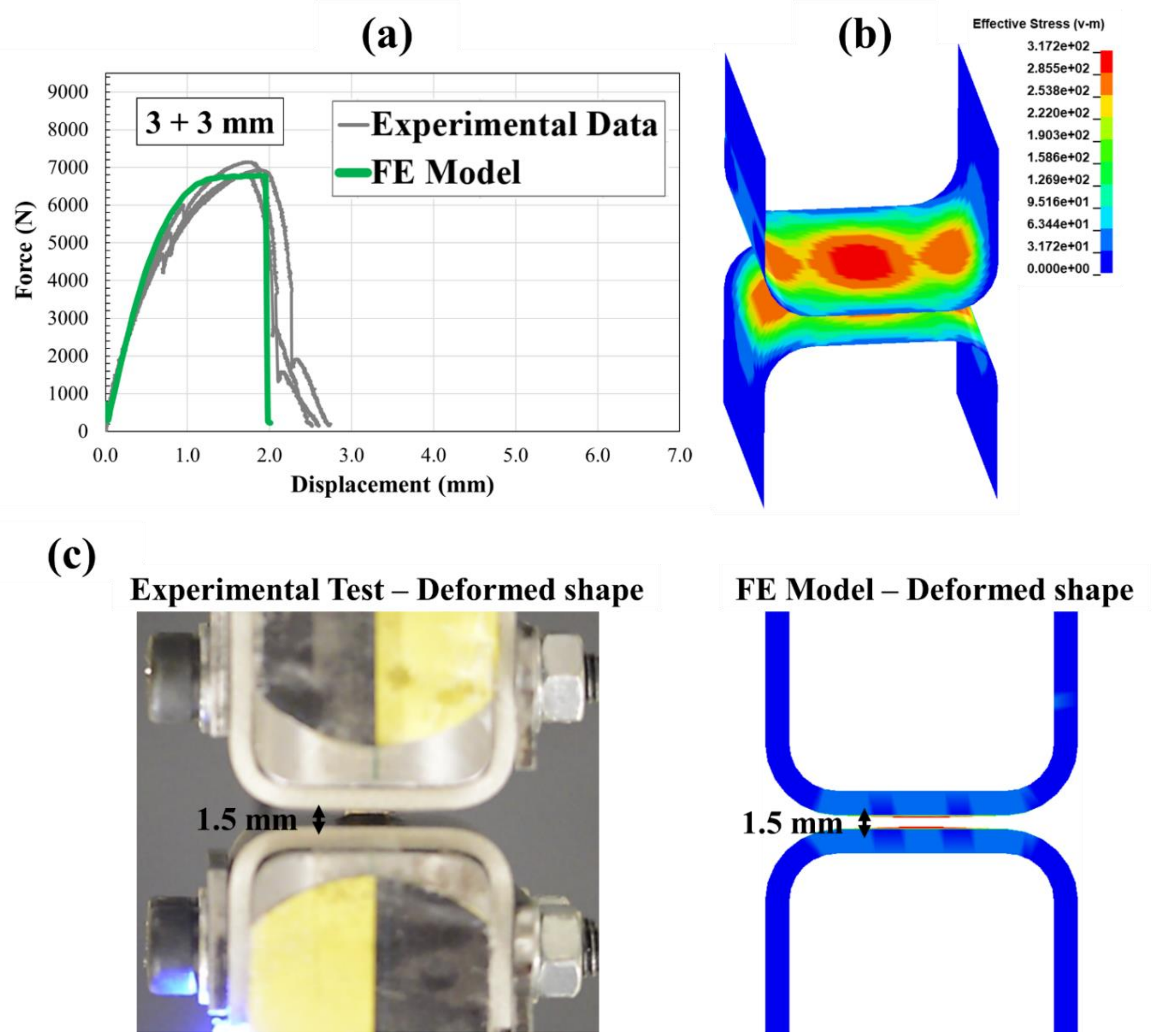

Figure 195: The simulation results of the 3 mm adherend H-specimen model were within the experimental results range for the load-displacement (a), deformation behaviour during rivet damage progression based on effective stress distribution (b), and the measured and predicted local separation (c).

The axial load, shear load, and bending moment acting on the SPR rivet were extracted from the SLJ and H-specimen models with 3 mm adherends to compare to the loads and moments acting on the SPR rivet (Figure 196a and Figure 196b, respectively). Unlike the SPR rivet in the SLJ model, which exhibited shear load and bending moment, the SPR rivet in the H-specimen model encountered pure axial (normal) loading (Figure 196a). The rivet damage progressed due to axial loading, and the model was able to predict the measured response. The SPR rivets under pure axial loading resulted in an abrupt failure, such that the load rapidly dropped, therefore, the model did not experience the bending moment limitation observed in the SLJ joints.

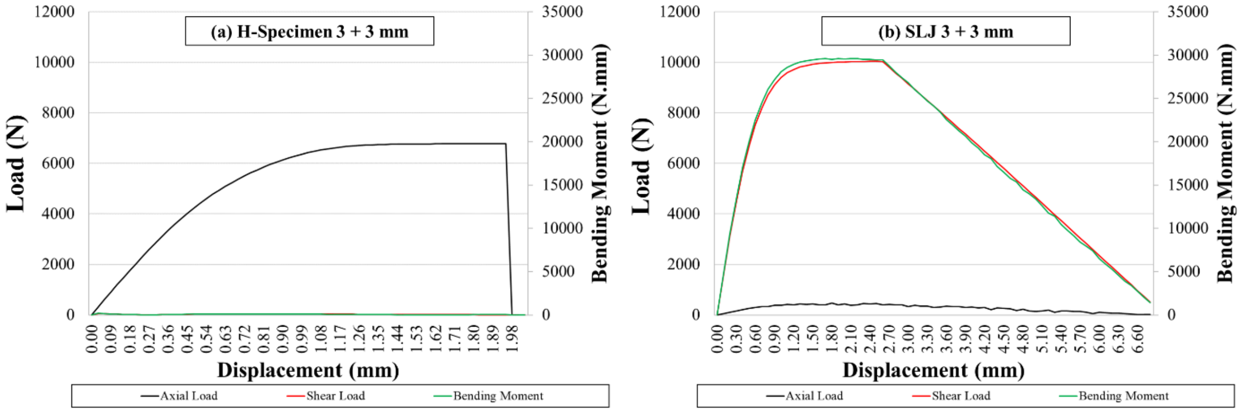

Figure 196: The loads and moment acting on the SPR rivet joining H-specimen (a) and SLJ (b) made with 3 mm base material.

6.3.2 Single Lap Shear Joint and H-specimen SPR CZM Model Verification (3 mm thick adherends)

The simulation results of the single lap shear and H-specimen models joined using an assembly of cohesive elements, representing the SPR rivet, are presented in this section. The SPR rivet behaviour followed the traction-separation relationships calibrated to the experimental tests of the SLJ joints and H-Specimens made with 3 mm adherends. The simulation results of both the SLJ and H-specimen models showed good agreement with the measured peak load (<3% difference) and stiffness (<5% difference) (Figure 197a and Figure 197b). Due to the linearity of the trapezoidal traction-separation relationship, the gradual softening observed prior to reaching the peak load (rivet damage initiation) was linearized (blue curves Figure 197a and Figure 197b).

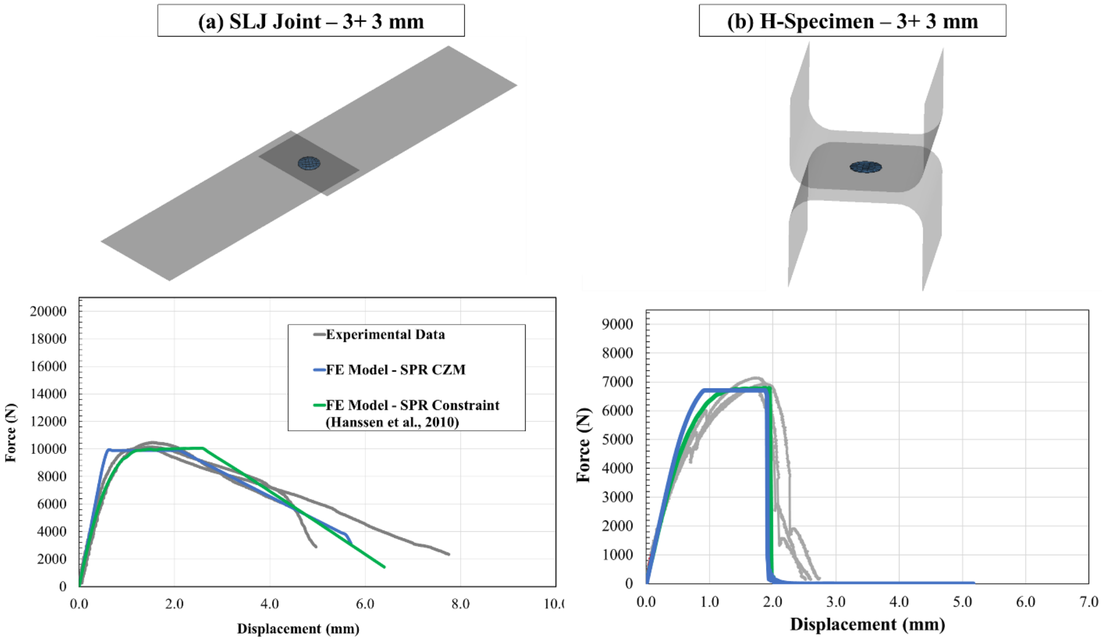

Figure 197: Comparison between the accuracy of the predictions of the SPR CZM and SPR constraint models using SLJ and H-specimen.

The SLJ model showed that the assembly of cohesive elements, representing the SPR rivet, exhibited pure Mode II loading which initiated the rivet damage (Figure 198a). The CZM assembly was substantially deformed during the rivet damage progression to simulate the rivet sliding observed in the experimental test, which allowed absorbing a considerable amount of energy prior to rivet failure, matching the SPR joint energy measured in experimental testing. All the cohesive elements within the assembly experienced an equal level of damage that gradually increased until the separation under Mode II loading reached a value that achieved the critical fracture energy release rate and the whole assembly failed at the same time. The cohesive assembly within the H-specimen model, experienced Mode I loading and showed substantial deformation mimicking the SPR rivet tail pull-out (Figure 198b). The whole assembly failed at the same time after all the elements attained the calibrated critical fracture energy release rate under Mode I, highlighting that the cohesive elements could maintain their numerical stability even after experiencing a large amount of deformation regardless of the mode of loading. Similar to the constraint model, the CZM representation of the SPR rivet underpredicted the SLJ joint rotation (Figure 199a). The interface between the cohesive elements and adherend shell elements experienced loads and moments that were equal at the top and bottom sheets, causing symmetrical joint rotation. Ultimately, both the constraint and CZM models were shown to provide a good representation of the SPR rivets, and while both modeling techniques need to be enhanced to be able to represent the SPR rivet rotation during the failure progression under shear loading, this limitation may not be critical because large structures usually fail due to tension or Mode I loading. Interestingly, both the models (constraint and CZM models) had similar computational efficiency as both models required similar total CPU time when eight CPU cores were used on a high-performance computing cluster (Figure 199b).

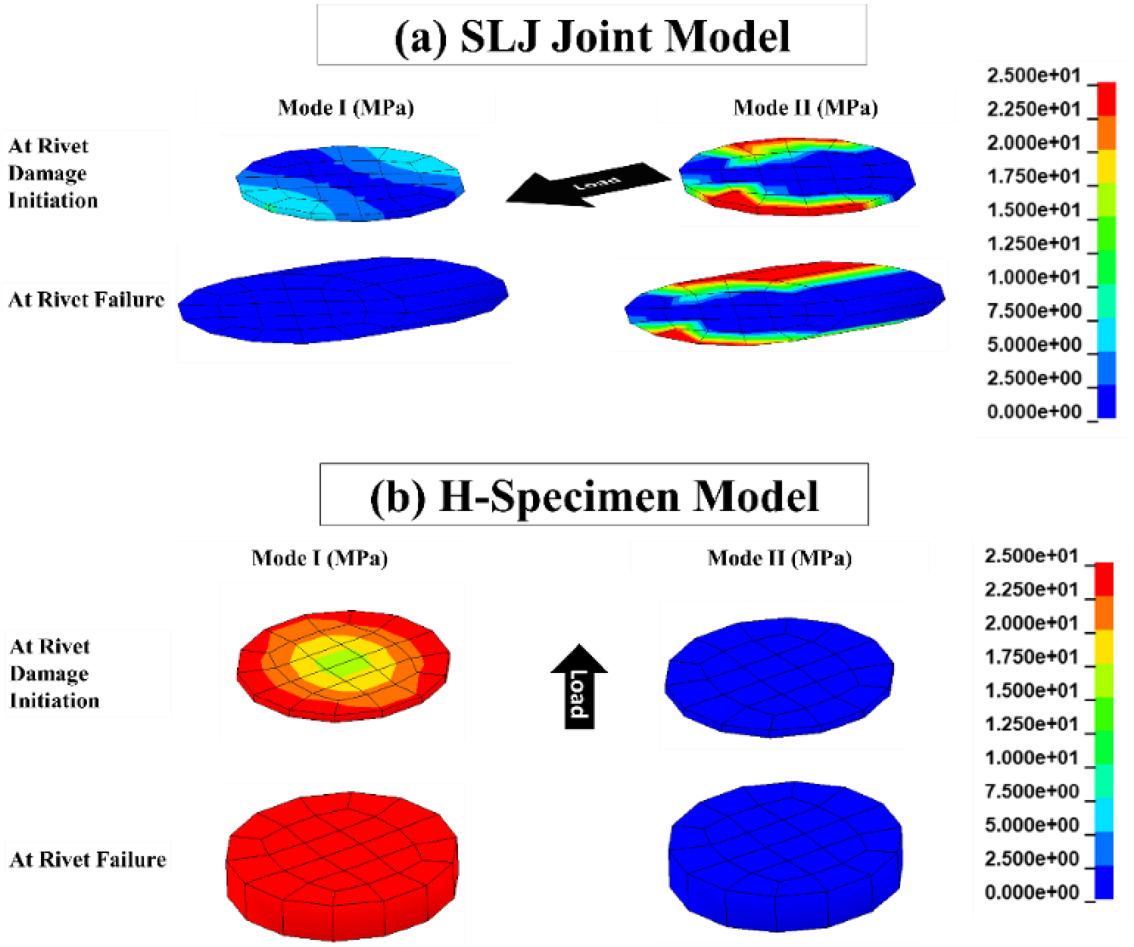

Figure 198: The assembly of cohesive elements representing the SPR rivet in the SLJ (a) and H-specimen (b) models experienced large deformations (separation) to mimic the large energy absorbed during SPR rivet damage.

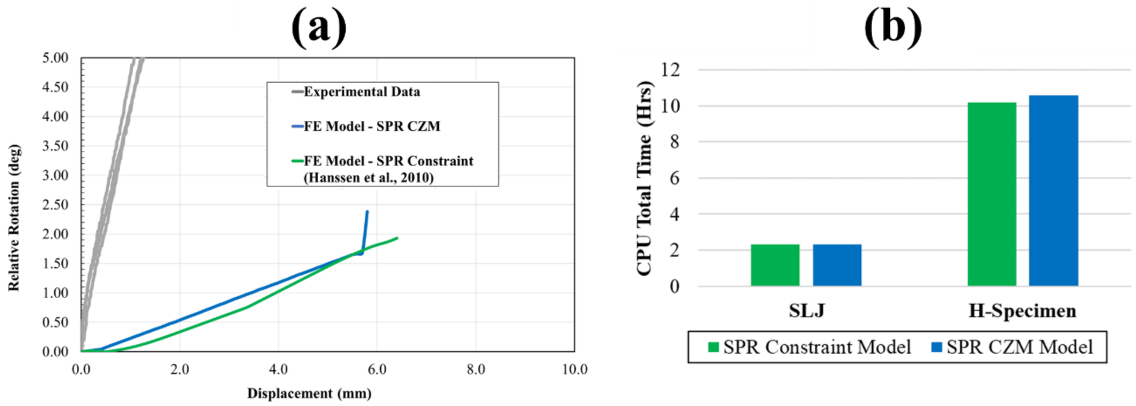

Figure 199: The constraint and CZM models of the SPR rivet showed limited capability in predicting the local rotation of the rivet and consequently the joint rotation (a). Both models showed similar computation efficiency (b).

6.4 Hybrid Joint Model Validation

The adhesive CZM and SPR constraint models were integrated to develop the hybrid joint model without using calibration parameters, mimicking the intrinsic responses of the individual joining methods. In this section, the hybrid CZM-constraint model validation is presented for two different models (SLJ and H-specimen) having three different sheet thicknesses each to assess the efficacy of the models under different modes of loading and with increasingly complex hybrid joining joint morphology effects. After that, the CZM-CZM model, using adhesive CZM and an assembly of cohesive elements representing the SPR rivet, was validated for SLJ joints and H-specimens made with 3 mm thick adherends.

6.4.1 Single Lap Shear Joint Hybrid CZM-Constraint Model Validation (three sheet thicknesses)

The 1 mm adherend FE CZM-Constraint SLJ model predicted the measured load-displacement response accurately (Figure 200a), validating the overall hybrid joint response. The predicted peak load matched the measured peak load (<5%), while the predicted stiffness was somewhat higher in the linear loading region, which was inherited from the adhesive-only models (due to the intrinsically stiff behaviour of constrained shell elements coupled with tied constraint). Similar to the adhesive-only joints, the ultimate failure of the joint happened after substantial yielding (stretching/in-plane deformation), which was followed by sudden damage initiation in the CZM elements at the adhesive leading and trailing ends. After damage initiation, the CZM damage progression caused a rapid drop in the load, and the SPR rivet model failed abruptly with a flick in the load response, matching the experiments. As discussed earlier in section 6.2.1, the SLJ model with 1 mm adherends experienced substantial plastic deformation (tied to the global stress distribution within the adherends, Figure 200b), thus, the response was dominated by the material properties and hardening curve. The presence of the SPR rivet did not influence the adhesive CZM traction distribution or failure mechanism. The peel stresses at the adhesive ends were the same as in the adhesive-only model (Mode I traction value of ~10 MPa which is about 20% of the critical peak traction, Figure 200b). Therefore, the damage in the cohesive layer was initiated due to localized shear at the adhesive boundaries, matching what was observed in the experiments.

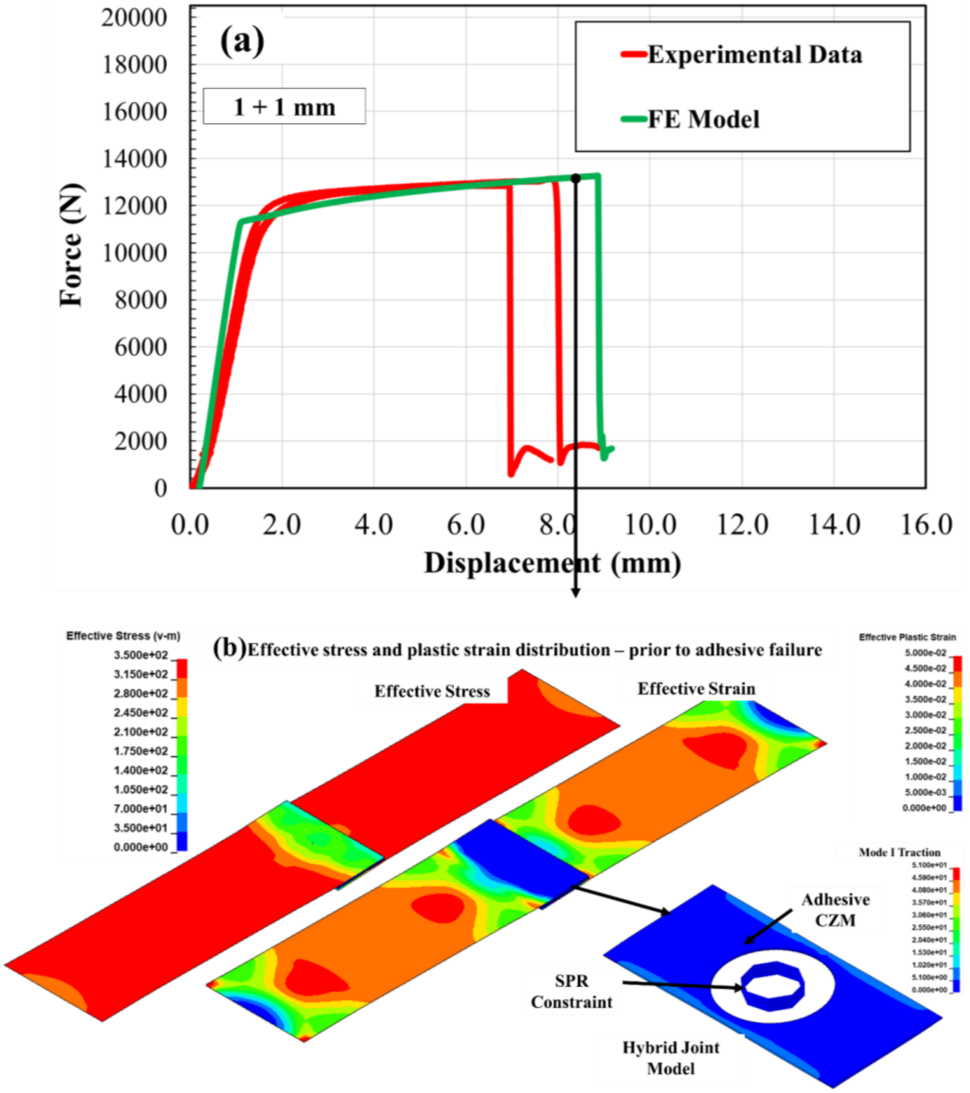

Figure 200: Simulation results of the SLJ model made with 1 mm adherends, illustrating the load-displacement response (a), and effective stress and strain distribution within the adherends, illustrating the Mode I traction distribution within the adhesive layer.

The SLJ FE model made with 2 mm was validated, and the predicted load-displacement response was within the experimental data with the peak load within 6% (Figure 201a). The intrinsically stiffer response of the FE model setup compared to the experimental setup was manifest in the displacement at which the adhesive failed (lower by about 0.5 mm). The initial response was similar to the adhesive-only models with localized adherend bending, which induced peel stresses within the adhesive free ends (Figure 201b). The damage initiation was due to mixed mode loading (primarily shear) with adhesive damage progression due to shear load, which was also seen in the adhesive-only joints and was not surprising given that the joint overlap length was relatively large (18 mm).

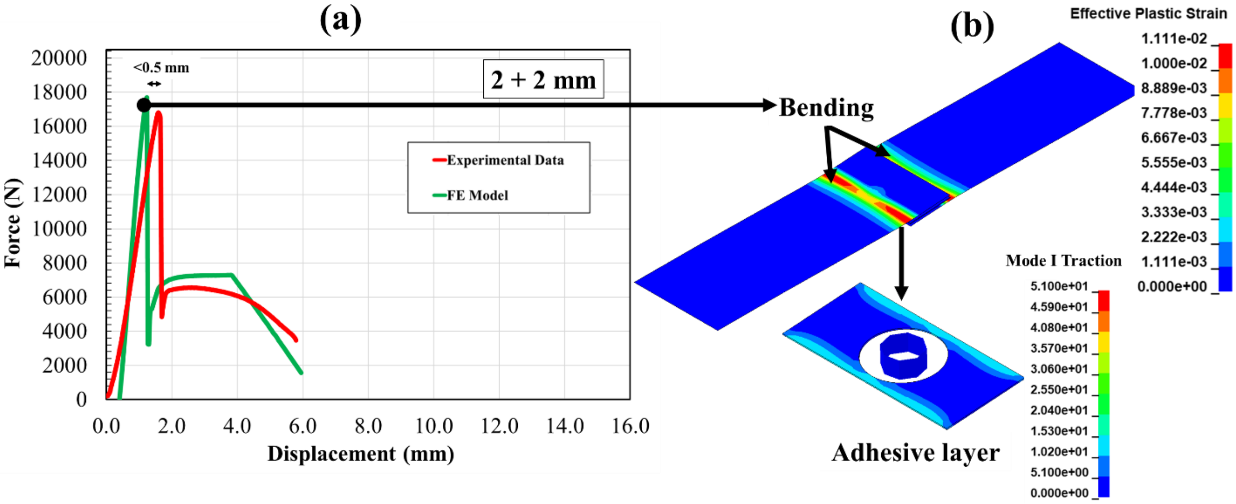

Figure 201: Simulation results of the SLJ model made with 2 mm base material, illustrating load-displacement (a), and effective stress distribution within the base material, illustrating the Mode I traction distribution within the adhesive layer.

The behaviour of the CZM crack initiation and propagation matched the experiments, such that the adhesive failed abruptly causing a substantial load drop coupled with a smooth load transfer from the failing cohesive elements to the constraint model of the SPR rivet. It was observed that the model had a generally higher load prediction (<10%) during the loading of the

SPR rivet. The hybrid joint with the 2 mm thick sheet experienced a slight reduction in the mechanical interlock (section 4.3.1) relative to SPR-only joints, reducing the experimental load response of the hybrid compared to SPR-only joints. Considering that the SPR rivet was calibrated to the SPR-only joint, the difference was manifest, but a difference of less than 10% was trivial given that the joint overall energy was within the range of the experimental data (<9.5%) (Figure 202).

The influence of the numerical controls, adopted to control the numerical instability and shell element oscillation on the model prediction, was assessed. The numerical controls enabled smooth load transition between the CZM and constraint models. The effect of the numerical controls on the energy balance was negligible (Figure 202). The kinetic, internal, and total energies were stable, and the total energy agreed with the total energy calculated from the experimental data (<9.5%). Also, the kinetic to internal energy ratio did not increase above 1% at adhesive failure.

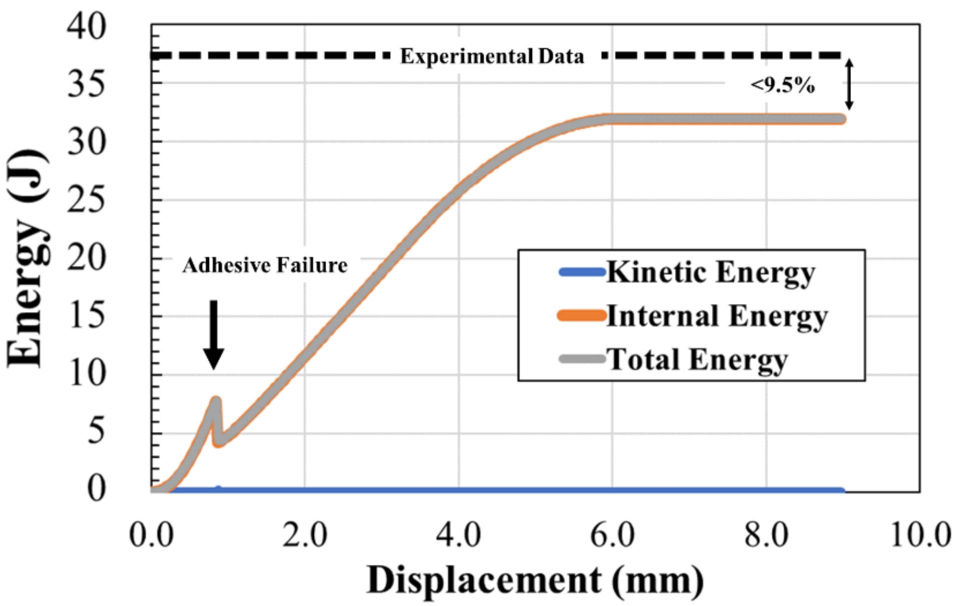

Figure 202: The kinetic, internal, and total energies of the FE model with total energy demonstrating good agreement with experimental data.

The SLJ model made with 3 mm thick adherends overpredicted the peak load (~ 33%) corresponding to the adhesive crack initiation, but agreed well with the measured load-displacement curve after the adhesive failure (Figure 203a). The effective plastic deformation within the adherends, due to bending, was localized adjacent to the edges of the adhesive (Figure 203b). Similar to the 2 mm joints, the bending induced adhesive peel stresses at the free ends (12.6 MPa versus 14.0 MPa for 2 mm joints, Figure 203b) and the CZM abrupt damage progression was due to shear loading.

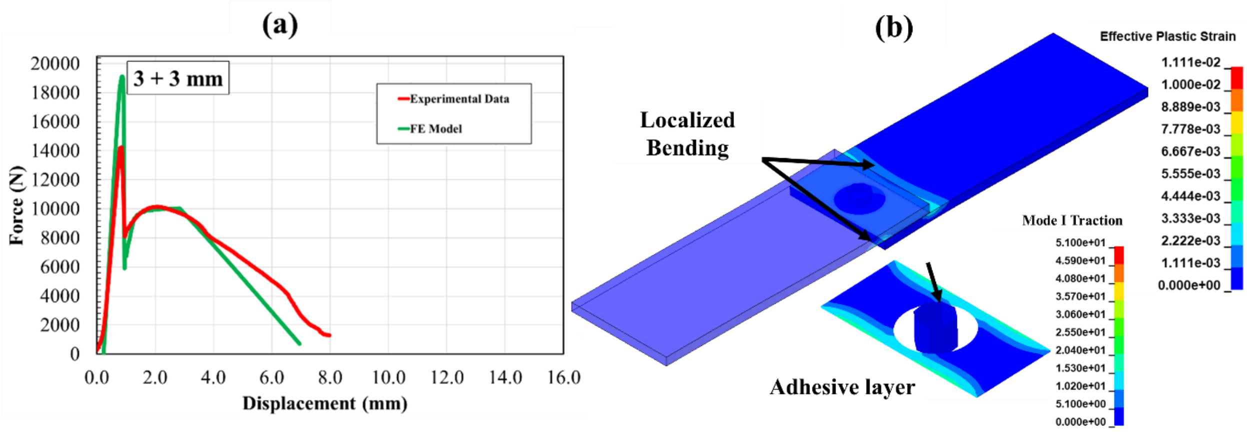

Figure 203: Simulation results of the SLJ model made with 3 mm base material, illustrating load-displacement response (a), and effective stress distribution within the base material, illustrating the Mode I traction distribution within the adhesive layer (b).

It was not surprising that the model overpredicted the peak load of the joint because the experimental test results and optical imaging confirmed that the joints with 3 mm adherends experienced substantial degradation in the adhesive morphology in the form of bond line thickness reduction, adhesive squeeze out and air inclusions (porosity). The adhesive squeeze-out was modeled by mapping the adhesive area reduction in the CZM model; however, the air inclusions and bond line thickness reduction were complex to model as they affected the material-level properties. To incorporate the morphological effects into the model, a methodology to calibrate the material-level traction-separation relationships was developed and assessed. The Mode I and Mode II traction-separation relationships, based on material-level properties, were calibrated based on the degradation observed in the hybrid joined H-specimen and SLJ experimental data. The calibration methodology used the adhesive-only experimental data as a baseline and reduced the traction separation relationships by the same percentage difference calculated between the adhesive-only joints and hybrid joints, such that Mode I and Mode II reductions corresponded to the difference in H-specimen and SLJ joint responses, respectively. The calibration method reduced the peak traction, the separation at failure, and the *fg* parameter, which resulted in a lower critical fracture energy release rate (Figure 204). The CZM stiffness was kept constant because the influence of the stiffness on the overall response was found to be trivial (detailed discussion in section 5.3.1) since the stiffness of the adherend is almost two orders of magnitude that of the CZM. The *fg* parameters were reduced, such that the ratio between the plateau region and the total separation was maintained. In other words, the ratio of the lengths of the blue lines and the ratio of the lengths of the yellow lines were identical (Figure 204). Finally, the degraded traction-separation relationships were implemented into the adhesive CZM model. The peak traction was reduced by 28.6% under Mode I and 17.6% under Mode II, and the separation at failure was reduced by 22.8% under Mode I and 5.5% under Mode II (Table 36). These values represented the percentage difference calculated for the load and displacement (separation) at failure in the experimental data (hybrid joint versus adhesive-only joints).

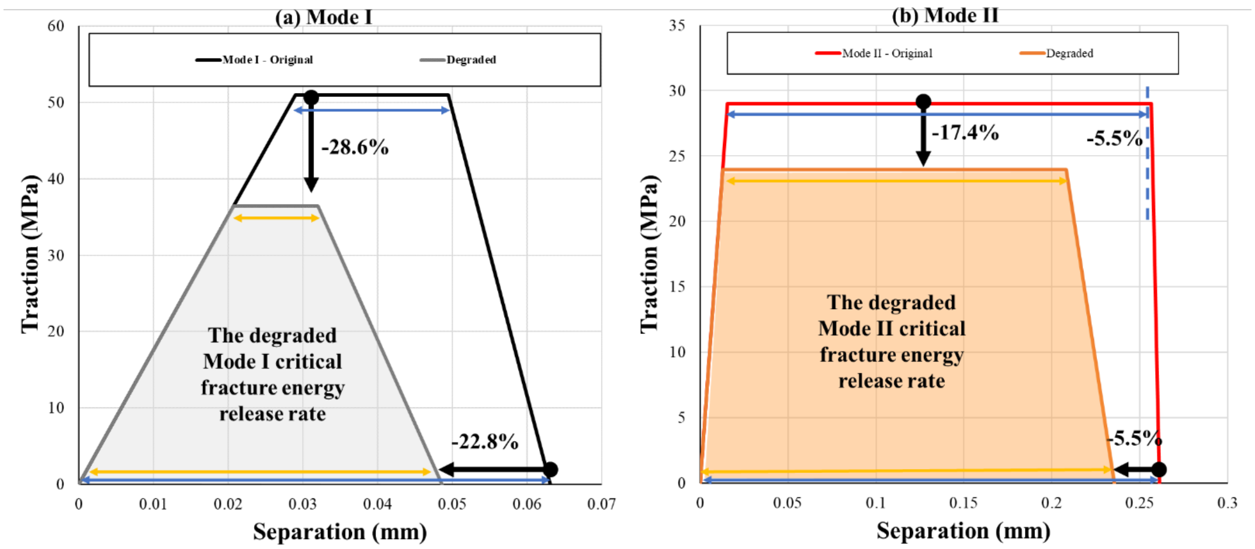

Figure 204: The degraded adhesive traction-separation calibration process under Mode I (a) and Mode II (b).

Table 36: The degradation percentages calculated from the experimental data of the SLJ joints and H-specimens

	Mode of Loading	Adhesive Only	Hybrid Joint	% Difference
Adhesive Peak Load, N	**Mode I**	8397	5993	-28.6
Adhesive Separation at Failure, mm	***H-Specimen***	0.92	0.71	-22.8
Adhesive Peak Load, N	**Mode II**	18099	14899	-17.6
Adhesive Separation at Failure, mm	***SLJ Joint***	0.90	0.85	-5.5

The degraded CZM parameters predicted the peak load within 6.9% of the experimental measurement and the displacement at failure within <0.5 mm (green curve, Figure 205), substantially improving the accuracy over the non-calibrated model. An interesting observation was that the change in the adhesive CZM model only influenced the initial joint response up to adhesive failure with no influence on the SPR constraint model response, indicating the SPR river was not influenced by the load distribution prior to adhesive CZM failure.

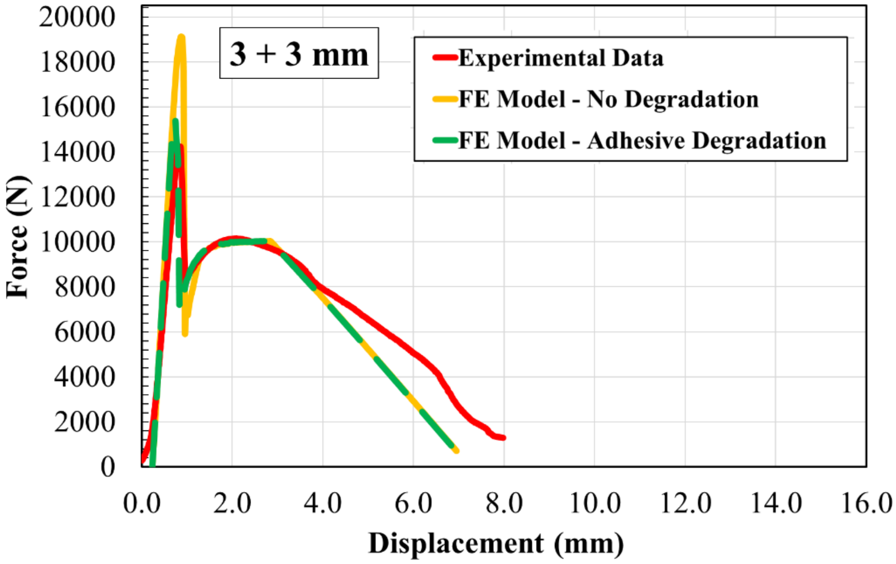

Figure 205: Simulation results of the SLJ model made with 3 mm adherend, incorporating the degraded adhesive traction separation relationship.

To shed some light on the loads exhibited by the SPR rivets in hybrid joints, the loads and moments predicted from the SPR rivet model were extracted and compared to the data extracted from the SPR-only model. The comparison showed that both the models experienced the same shear load (Figure 206) and that the rivet damage initiation occurred at the same local separation value. In hybrid joints, the presence of the adhesive layer only influenced the initial loading, reducing the initial load on the rivet to ~2.2 kN at a displacement of 0.5 mm while the SPR-only joints exhibited close to ~8 kN at the same displacement (Figure 206). The bending moment predicted by the hybrid joint was slightly higher (+9.8%) as the increase in the joint thickness by 0.3 mm (adhesive bond line thickness) increased the moment arm of the shear load (Figure 206b). Importantly, the models confirmed that the loads and moments acting on the SPR rivet in SPR-only and hybrid joints were fairly similar, explaining the similarity seen in the SPR rivet response of the experimental data. Also, the increase of the loads and moment acting on the SPR rivet at adhesive failure was stable, indicating adequate numerical stability within the integrated hybrid joined model (Figure 206b).

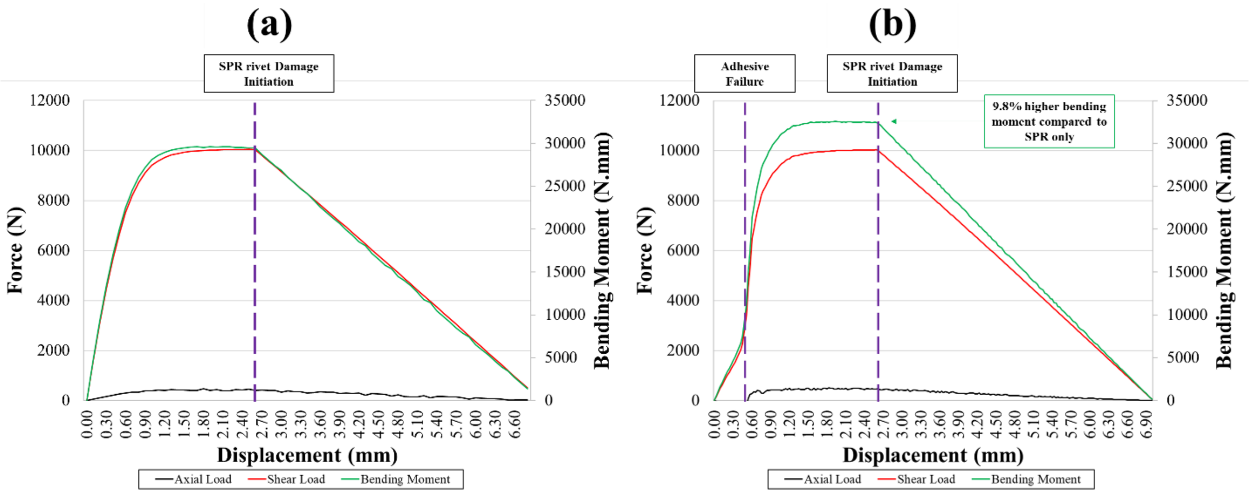

Figure 206: The loads and moments exhibited by the rivet in the SPR-only (a) and hybrid (b) joined SLJ models.

6.4.2 H-Specimen Hybrid Joint CZM-Constraint Model Validation (three sheet thicknesses)

The H-specimen FE model made with 1 mm adherends predicted the peak load (<10% difference), initial loading stiffness (<5% difference) and the general shape of the response comparable to the experimental test, but overpredicted the displacement at failure (Figure 207a). The adhesive CZM failed first and then the load was transferred to the SPR constraint model, causing a sharp drop in load as observed in the experimental test. The adhesive displacement at failure was overpredicted by ~0.75 mm due to the concentrated membrane loading adjacent to the adhesive free ends prior to the onset of adhesive failure, attributed to the localized stresses at the radius of the U-section (detailed explanation in section 6.2.2) (Figure 207b). The higher adhesive displacement at failure was manifested in the overall response, resulting in higher displacement at failure. After adhesive failure, the adherends exhibited plastic deformation within the vicinity of the rivet as the rivet tail gradually pulled out of the bottom sheet, which changed the stress and strain distribution within the U-section, reducing the effect of the localized stresses and nodal penetration at the bend radius (Figure 207c). The hybrid CZM-constraint model predicted the SPR rivet peak load (< 3% difference), and the damage progression (unloading) behaviour up to joint separation.

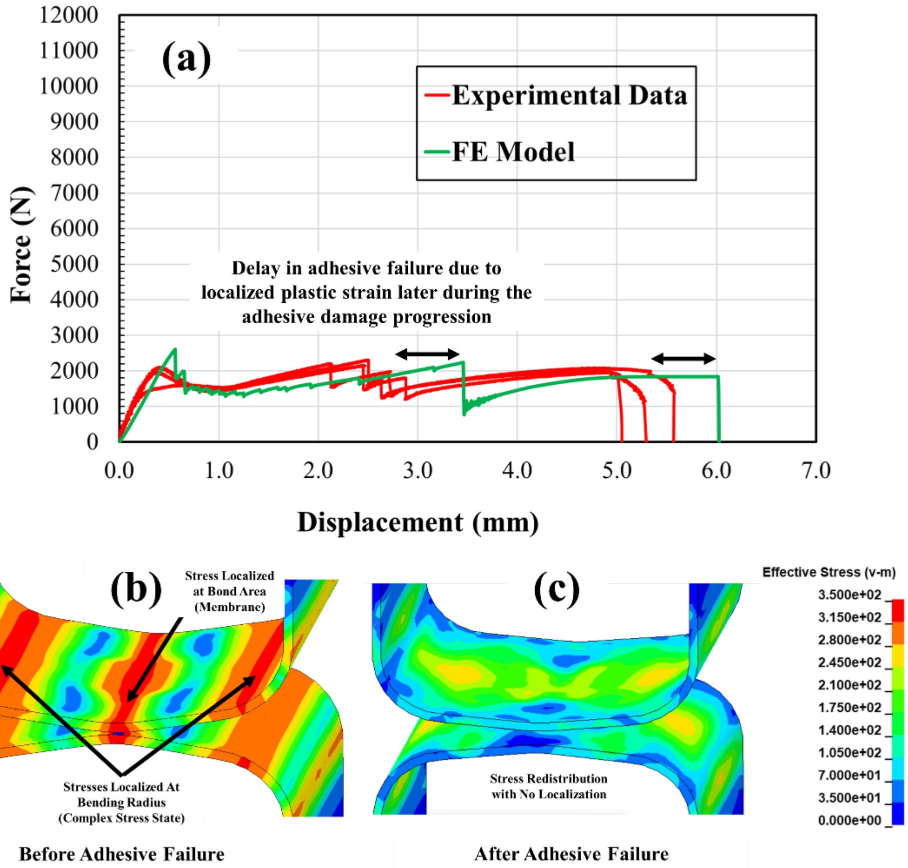

Figure 207: Simulation results of the 1 mm adherend H-specimen model illustrating the load-displacement response (a), and effective stress distribution before (b) and after (c) adhesive failure.

The model with the 2 mm thick adherends predicted the adhesive failure load (< 2% difference), adhesive failure displacement, SPR peak load (<4% difference), and SPR failure displacement. The overall behaviour of the joint, including the load transition from the adhesive CZM model to the SPR constraint model and gradual loading to SPR rivet failure (green curve,

Figure 208a) matched the experimental test; however, the slope change in the loading response observed at a load of 1.5-2.5 kN was not predicted, similar to with the adhesive model. The load spike during the initial loading (Figure 208b) was attributed to the symmetrical initiation of damage along a line of elements, rather than localized initiation at a point. The load spike was also observed in the adhesive model with 2 mm adherends.

Numerical controls were used in the hybrid CZM-Constraint models to reduce shell element oscillations observed as the load transitioned from the CZM to the constraint model (section 5.4). The effect of Rayleigh damping, needed to reduce the high-frequency shell oscillations, was investigated by increasing the damping coefficient from 0.05 to 0.10. The response was the same and no change was observed in the predicted force-displacement curve (yellow curve, Figure 208a), indicating that the response was insensitive to arbitrary changes to the numerical controls.

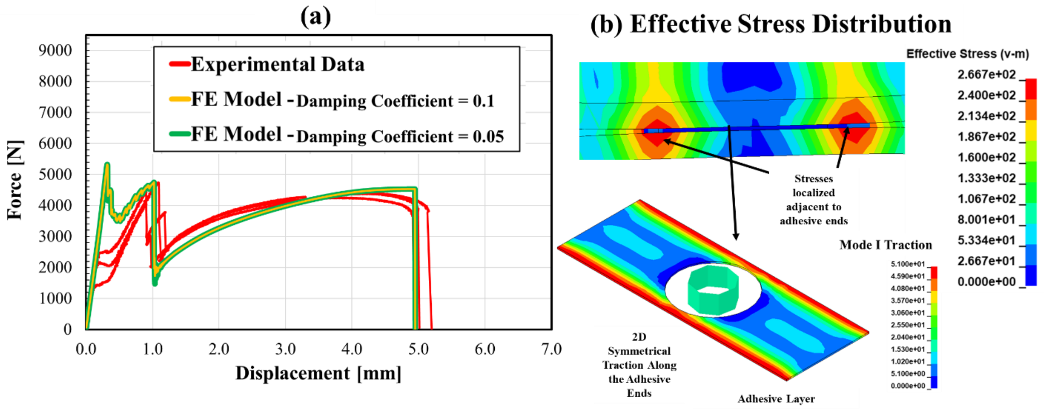

Figure 208: Simulation results of the H-specimen model made with 2 mm adherends, illustrating load-displacement response (a), and the effective stress distribution within the adherends and Mode I traction distribution within the adhesive (b). (just before the adhesive CZM failure initiation)

The H-specimen model made with 3 mm thick adherends predicted the adhesive failure displacement, SPR peak load, joint failure displacement, and the overall behaviour of the joint including the load transfer from the adhesive to SPR joining. Similar to the 2 mm joints, the slope change in the loading response observed at a load of 2.5 kN was not predicted. A spike in load corresponded to a symmetrical failure initiation of the adhesive CZM adjacent to the adhesive free ends. After adhesive failure initiation, the stresses decreased and were distributed within the vicinity of the rivet (yellow curve, Figure 209b). The stress redistribution promoted deformation within two different regions of the adherends, which increased the total energy of hybrid joining relative to individual joints as reported in the experimental tests. Thus, the model showed the physical behaviour observed in the experimental tests and highlighted the energy absorption mechanism of hybrid joints. The stress redistribution, showing reduced stress localization after adhesive failure, explained why the same models have better prediction with SPR joints compared to adhesive joints.

Similar to the hybrid joined SLJ models, a key limitation that needed to be addressed for the 3 mm model was the overprediction of the load corresponding to adhesive failure initiation. Thus, the degraded adhesive traction separation relationship calibrated based on the approach proposed earlier (Figure 204, details in section 6.4.1) was assessed. The calibrated traction separation curve with degraded CZM parameters yielded increased model prediction accuracy and agreement with the experiments. The adhesive peak load was accurately predicted (green curve versus yellow curve, Figure 209a) within 12% and the total energy of the model was within the range of the experimental results. The traction separation degradation approach demonstrated strong potential in addressing the challenges associated with capturing adhesive response, where substantial morphology effects were present, regardless of the mode of loading.

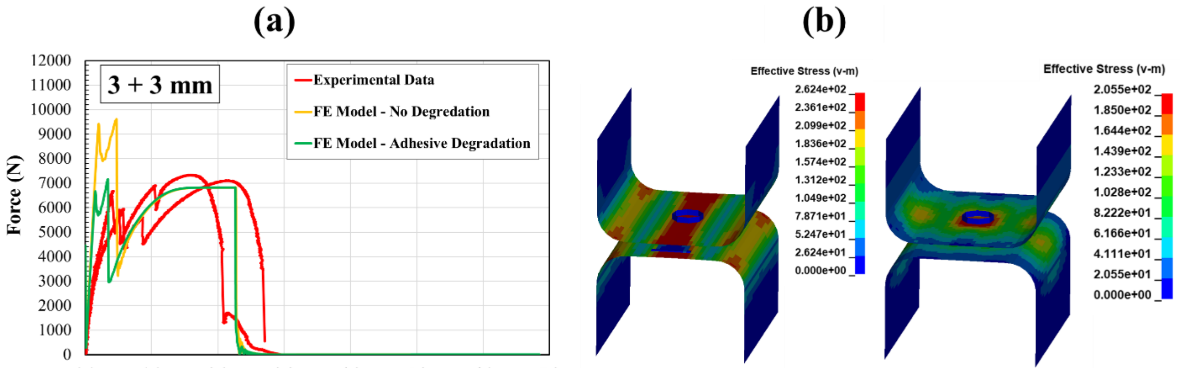

Prior to adhesive failure **Post adhesive failure**

Figure 209: Simulation results of the 3 mm adherend H-specimen model illustrating load-displacement response (a), and effective stress distribution before and after adhesive failure (b).

6.4.3 Single Lap Shear Joint and H-specimen CZM-CZM Model Validation (3 mm thick adherends)

The validated adhesive CZM model (section 6.2) was integrated with the verified SPR CZM rivet model (section 6.3.2), and the hybrid CZM-CZM model was used to predict the response of the H-specimens and SLJ joints made with 3 mm thick adherends (Figure 210). The predicted response was similar to that of the CZM-Constraint model for both the SLJ (section 6.4.1) and H-specimen (section 6.4.2) models. Predicting the adhesive portion of the response with a good level of accuracy required using the degraded traction-separation relationships, which were calibrated to account for the reduction in adhesive bond line thickness and adhesive porosity (section 6.4.1). The adhesive CZM damage progression was followed by a smooth load transition to the SPR cohesive elements, and the difference in the traction separation relationships between the adhesive CZM and SPR CZM allowed for predicting the substantial load drop observed in the experiments at adhesive failure. Interestingly, the smooth load transition between the adhesive CZM and SPR CZM models was achieved without the use of the numerical control cards (*e.g.*, part damping), potentially improving the computational efficiency over the CZM-Constraint model. The SLJ CZM-CZM model predicted the adhesive peak load (<5%), SPR peak load (<3%) and the displacement at failure for the adhesive and SPR rivet (joint separation) (Figure 210a). The SPR loading and unloading (softening) behaviour was predicted reasonably well but somewhat lacked the gradual loading nature of the SPR owing to the linearity of the trapezoidal traction separation curve used in this study. Similarly, the H-specimen CZM-CZM model predicted the adhesive peak load (<12%), SPR peak load (<7%) and the displacement at failure for the SPR rivet (joint separation) (Figure 210b).

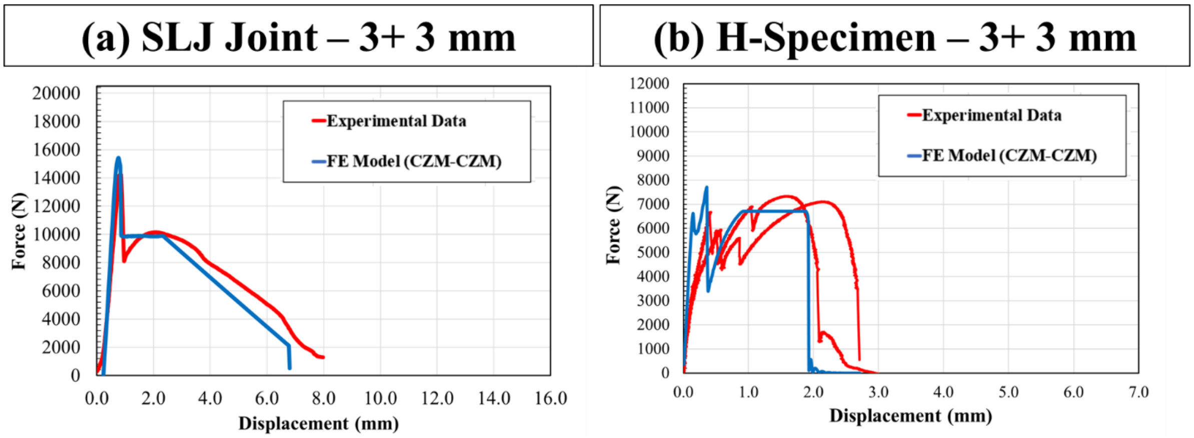

Figure 210: The response of the hybrid joint CZM-CZM model for the SLJ joint (a) and H-specimen (b) made with 3 mm thick adherends.

After adhesive failure, the models joined using the CZM-CZM model showed similar stress distribution within the adherends to the stresses reported in the models with CZM-Constraint. Both the CZM-CZM and CZM-Constraint models predicted localization of the stresses within the vicinity of the rivet, demonstrating a distinct kidney-shaped stress localization around the rivet within the SLJ adherends (Figure 211a). After SPR failure (complete separation), the models using CZM-CZM and CZM-Constraint models demonstrated the same amount and distribution of plastic deformation (Figure 211b). In general, The CZM-CZM and CZM-Constraint models reasonably predicted the hybrid joint behaviour; however, the CZM-CZM model allowed a smooth load transition of the load between the adhesive CZM to the SPR model models without requiring the use of numerical controls (*i.e.,* part damping), which could improve the computational efficiency in large-scale models. The computational efficiency of both models was examined by comparing the total simulation runtime (*i.e.*, total CPU time) for the component level Caiman test (section 6.5.1).

(a) Effective Stress Distribution After Adhesive Failure

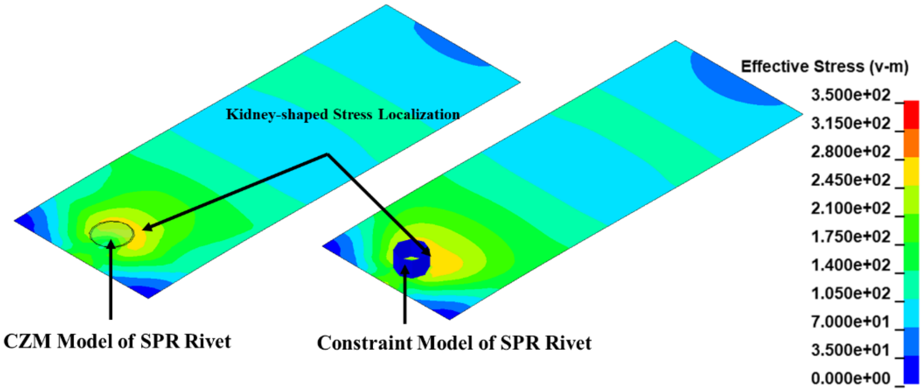

(b) Effective Plastic Strain Distribution After SPR Failure (Joint Separation)

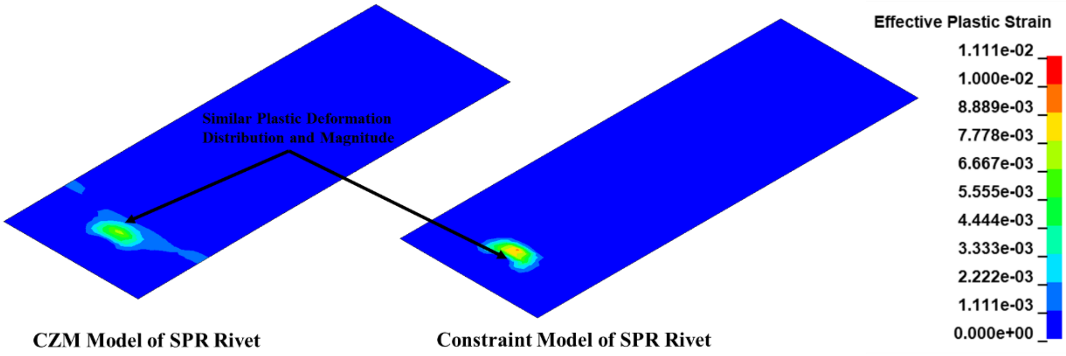

Figure 211: The CZM-CZM hybrid joint model showed similar effective stress distribution (a) and plastic deformation (b) within the 3 mm adherends, compared to the CZM-Constraint model.

6.5 Component-Level Caiman Models Validation

6.5.1 Adhesively Bonded Caiman CZM Model Validation

The adhesively bonded Caiman CZM model response was validated using the load-displacement and energy-displacement responses of the experimentally measured data (Figure 212). The initial stiffness, peak load, and adhesive damage initiation (displacement at peak load) were predicted with a high level of accuracy (the peak load predicted within <4%), and the total energy was predicted within -14% (Table 37). During the loading and unloading phases, the joining method (adhesive) dominated the overall response as the adherends experienced limited plastic deformation. During the unloading, the adhesive damage increased the compliance of the Caiman component and the tension in the system (experimental setup and Caiman component) decreased, allowing the influence of the slack present within the experimental setup (*i.e.*, clevises, loading pins and fixturing blocks) to creep in. Thus, the experimental data measurements for the pin displacement were somewhat higher (2 – 3 mm) for the same load value during the unloading, and increased the measured energy, owing to energy stored in the compliant system.

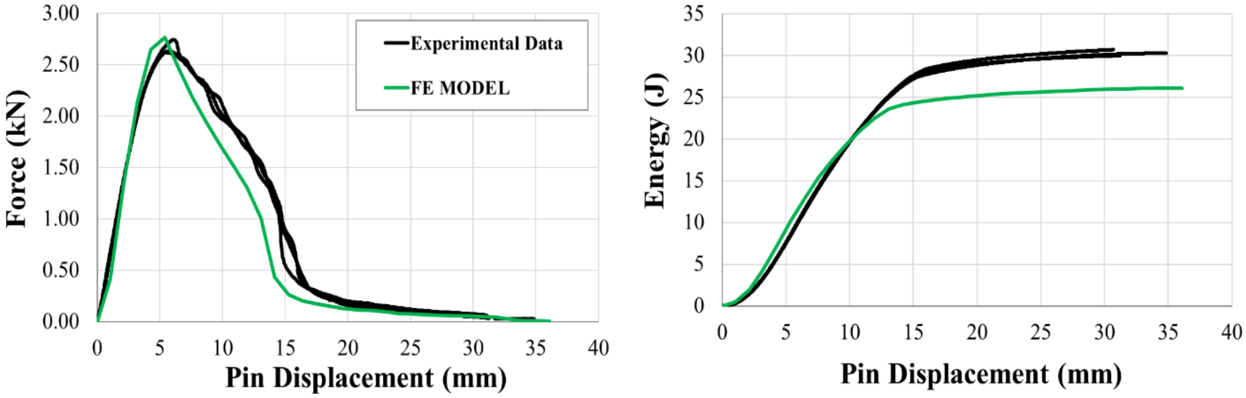

Figure 212: Comparison of the adhesive CZM Caiman model and experiments, force-displacement (left) and energy-displacement (right).

Table 37: A comparison between the adhesively bonded Caiman experimental measurements and FE predictions using adhesive CZM model.

	Experimental Measurement (Average)	**FE Model Prediction**	**% Difference**
Peak Load, kN	2.67	2.76	+3.37
Displacement at Peak Load, mm	5.77	5.39	-6.58
Energy, J	30.32	26.06	-14.05

To further assess the adhesive CZM model and reduce the effect of the experimental setup, two local metrics were used to directly validate the localized joint behaviour of the model (Figure 213a and Figure 213b). The first local metric was the crack propagation optically measured on the side of the Caiman component, which represented the rate of adhesive crack progression along the bond line. The experimental test videos were analyzed, and the crack propagation data were extracted using commercial software (ProAnalyst Motion Analysis Software, version 1.6), and then compared with the simulation data. Optical scale calibration was done by defining a pixel-to-mm conversion using an object, located at the same depth of required measurements and with pre-known dimensions, within the field of view of the camera capturing the experimental videos. The model predicted adhesive crack extension matched the experimental data, which demonstrated consistent adhesive crack propagation over three tests (Figure 213a). The adhesive crack and propagation started a pin displacement of ~5 mm, followed by a linear increase in the crack extension up to a pin displacement of ~17 mm, and after that, the rate of crack propagation decreased, corresponding to the slope change in the unloading curve. The CZM FE predicted and measured crack extension showed the same behaviour with an initial linear increase in crack extension, followed by a reduction in the crack propagation rate after ~17 mm of pin displacement.

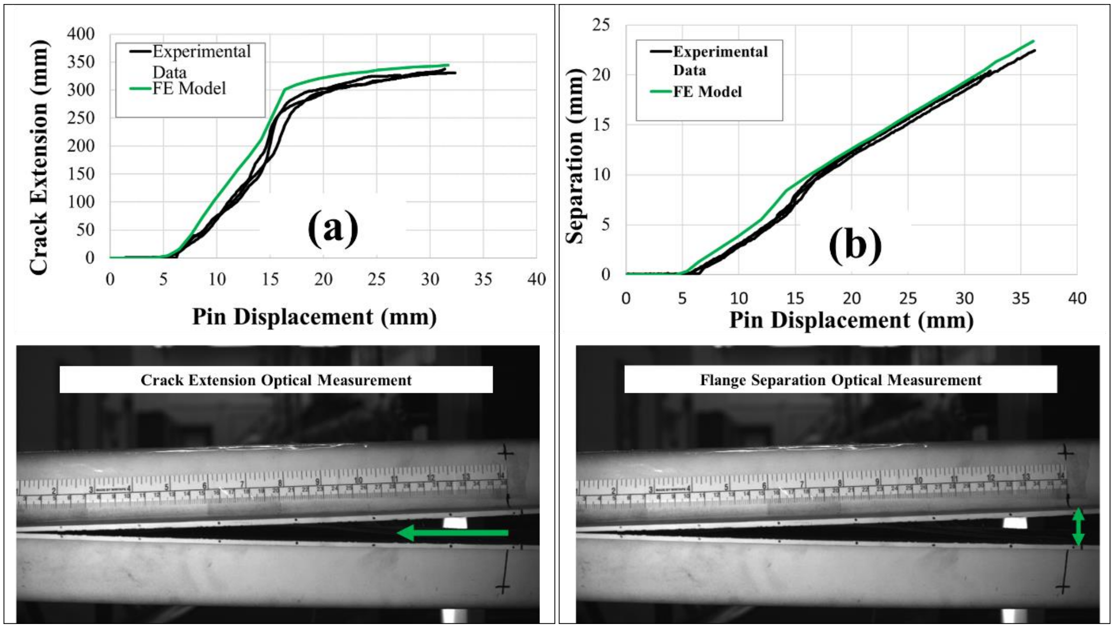

Figure 213: Simulation results of the adhesively joined Caiman model compared to the optically measured crack extension (a) and flange separation (b).

The second localized metric considered for the joint validation was the vertical separation of the flanges at the crack tip (Figure 213b). The separation was optically measured from the test videos and compared with the predicted separation calculated by tracking the nodal coordinates on the shell element at the adhesive crack tip. The predicted separation showed good agreement with the measured separation, indicating that the FE model predicted the vertical opening at the crack tip. Next, the FE model was used to analyze the CZM elements along the Caiman flange. The CZM tractions showed that the adhesive crack tip was under Mode I loading, localized at the adhesive inner boundary at the crack tip corner (Crack initiation point, Figure 214). On each flange, the adhesive damage initiated at the inner corner and then propagated along the flange length and width with a higher crack propagation rate along the adhesive length (Figure 214).

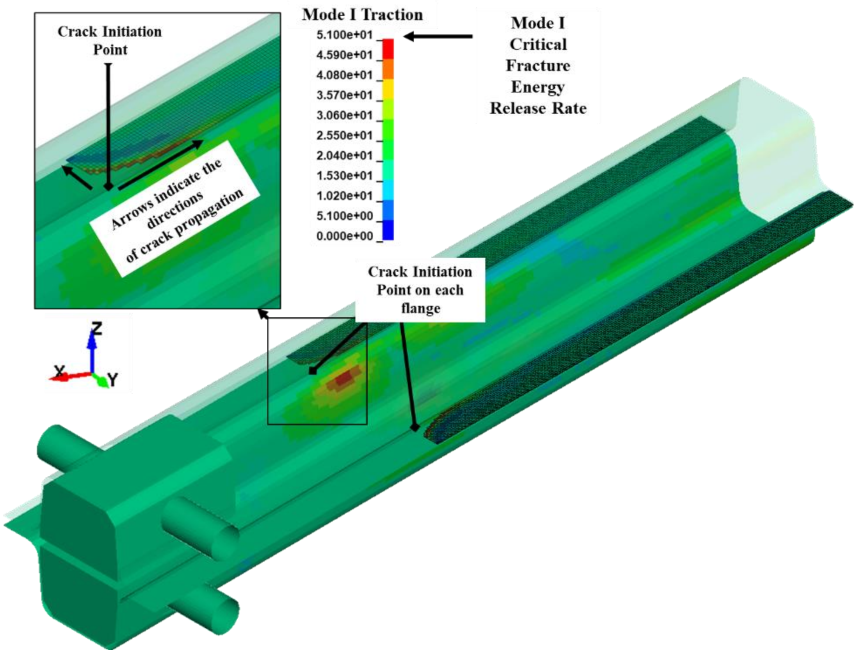

Figure 214: The Caiman adhesive crack initiation and propagation under Mode I loading, illustrating the damage initiation location and direction of crack propagation.

The component-level FE models used a combination of selective mass scaling and time scaling to achieve a target simulation run time below 48 hours. Thus, it was important to ensure that the inertial effects did not influence the response of the models and that the models were not sensitive to small changes applied to the time scaling factor. The validated adhesively bonded Caiman models were simulated with no mass scaling and the simulation results showed that both selective mass scaling did not change the predicted force-displacement response (Figure 215a). Similarly, the previously used time scaling factor of 60 was reduced to 30 (by half) and the predicted force-displacement response did not change (Figure 215b). Overall, there was no effect on the peak load, overall behaviour, or displacement at failure, indicating that the inertial effects were negligible and that the models were not sensitive to selective mass scaling or reasonable changes in the time scaling factor.

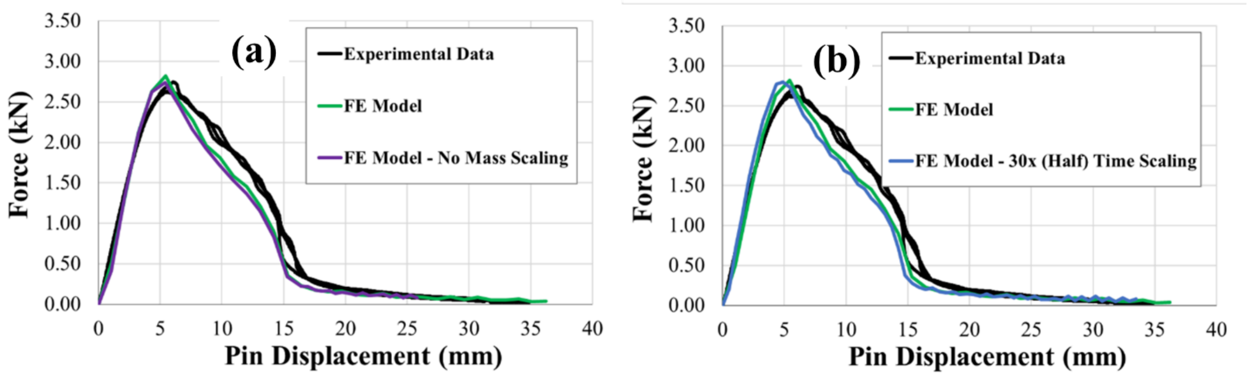

Figure 215: The influence of selective mass scaling (a) and time scaling (b) was assessed to ensure that the inertial effects were negligible.

In summary, the predictions of the adhesively joined Caiman model were within the range of the experiment results in terms of the loading response, deformation pattern, and local joint kinematics (*e.g.,* crack propagation behaviour). The peak load and displacement were predicted with a difference of <4% and <7%, respectively. The total energy had a reasonable prediction demonstrating a 14% lower energy value due to the deformation and slack within the experimental setup, which could be addressed by using local optical measurements on the test component.

6.5.2 SPR Joined Caiman Constraint Model Validation

The SPR constraint model was able to accurately predict the load-displacement and energy-displacement responses of the Caiman test (Figure 216) with the initial stiffness, peak load, and failure of the first rivet (displacement at peak load) matching the measured experimental data. The model directly implemented the calibration parameters obtained from the specimen-level tests, and predicted the peak load within a difference of 6.74%. The predicted energy was somewhat higher (+30% from average, and +17% from maximum), which was clear in the predicted energy curve after a pin displacement of 80 mm (Figure 216). In the Caiman experimental tests, the progressive failure of the rivets along the flanges was not perfectly symmetrical (rivets on the right and left flanges did not fail at the same instant). However, in the FE model, the rivets failed in a symmetrical manner, which contributed to the higher load spikes observed in the force-displacement curve and slightly delayed the failure of each row of rivets.

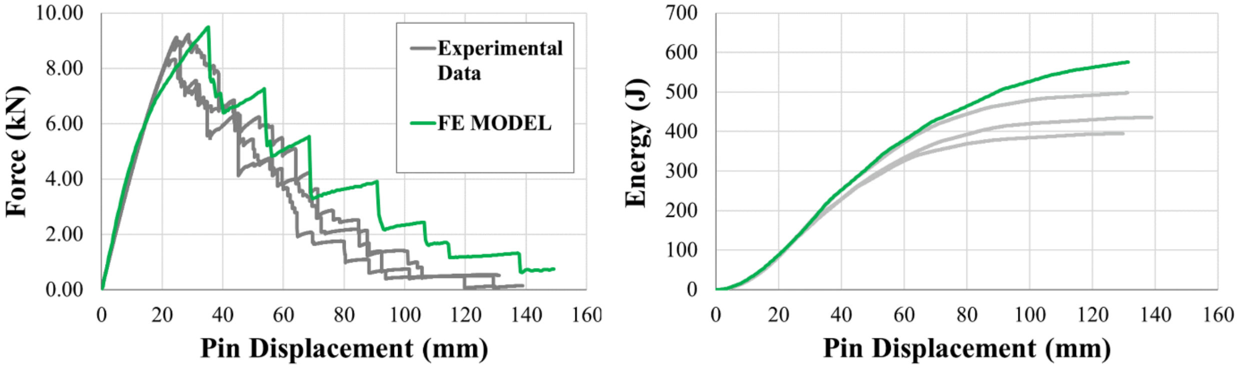

Figure 216: Simulation results of the SPR joined Caiman model (constraint model), compared to the load-displacement (left) and energy-displacement (right) responses of the experiments.

Two local metrics were used to validate the localized joint behaviour of the model. The first local metric was the optically tracked crack extension along the flange, which represented the rate at which the rivet failure progressed. The experimental test videos were analyzed, and the crack extension data were extracted using commercial software (ProAnalyst Motion Analysis Software, version 1.6), and then compared with the simulation data. From the simulation results, the time at which each rivet failed was extracted and then plotted versus the pin displacement and flange separation. The predicted crack extension showed good agreement with the optically measured data, which demonstrated fairly consistent SPR rivet failure over three tests (Figure 217). The second localized metric considered for the joint validation was the vertical separation of each rivet along the flange (11 rivets along the flange excluding the last two rivets, which exhibited substantial bending deformation and section geometry changes prior to failure). The separation at each rivet was optically measured from the test videos and compared with the predicted separation calculated by tracking the nodal coordinates on the shell element at each rivet. The predicted separations showed good agreement with the measured separations, indicating that the FE model predicted the vertical opening at which each rivet failed (Figure 218).

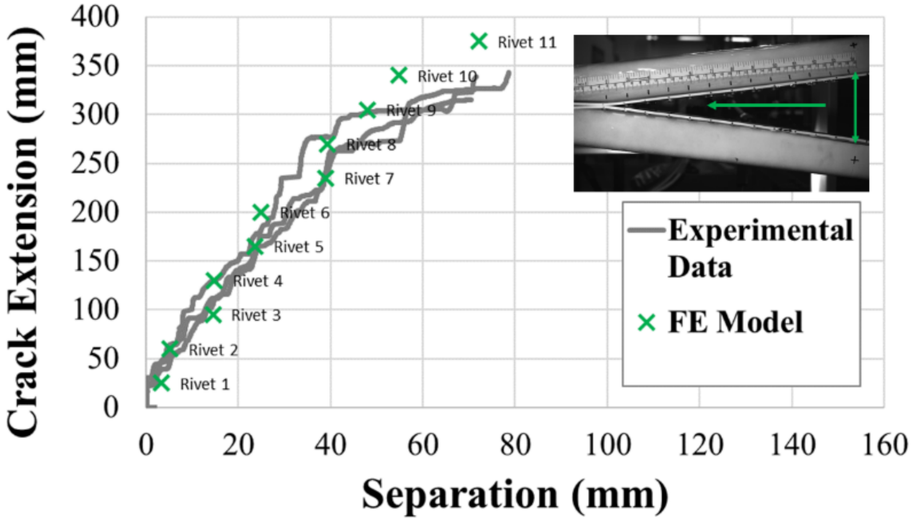

Figure 217: The measured crack extension compared to predicted rivet failure progression in the SPR constraint Caiman model.

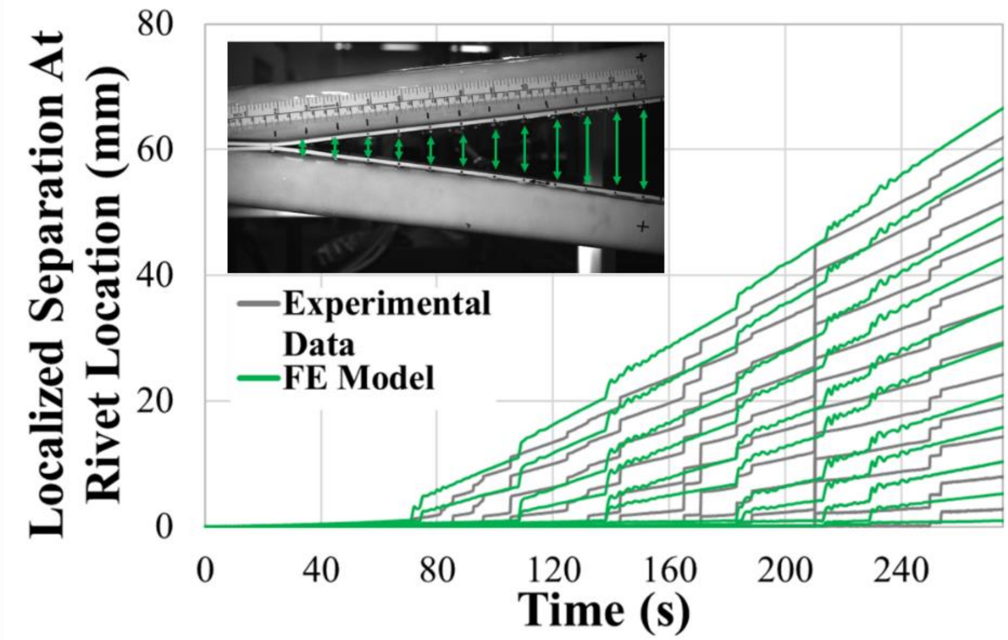

Figure 218: The measured local vertical flange separation compared to predicted rivet failure progression in the SPR constraint Caiman model.

Overall, the SPR constraint model captured the response including the damage and failure of a large number of rivets, including the progressive rivets failure (unzipping) along the flange. The model was used to analyze the loads within the rivets at peak load. The first few rivets experienced pure Mode I loading (Rivets experiencing failure, Figure 219a), which loaded the Caiman component under tension. The tension loading on the Caiman component was localized within the first few rivets along the flange, which imposed a boundary condition along the flange and acted as a centre of rotation (Centre of Rotation, Figure 219a). Therefore, the remainder of the flange experienced compression loading at the interface between the loaded and fixed hat sections. As the rivet failure propagated along the flange, the centre of rotation moved toward the free end and the next row of loaded rivets experienced pure Mode I loading (Figure 219b). Interestingly, the last rivet farthest from the load point (free end) of the Caiman component experienced tension loading (Figure 219b). The tension loading acting on the free end of the Caiman component was more pronounced after rivet failure progression. As the test progressed and the rivets failed along the flange, the tension, and compression loadings moved closer to the free end of the Caiman component, resulting in a boundary effect at the free end in the form of flange separation (Figure 220).

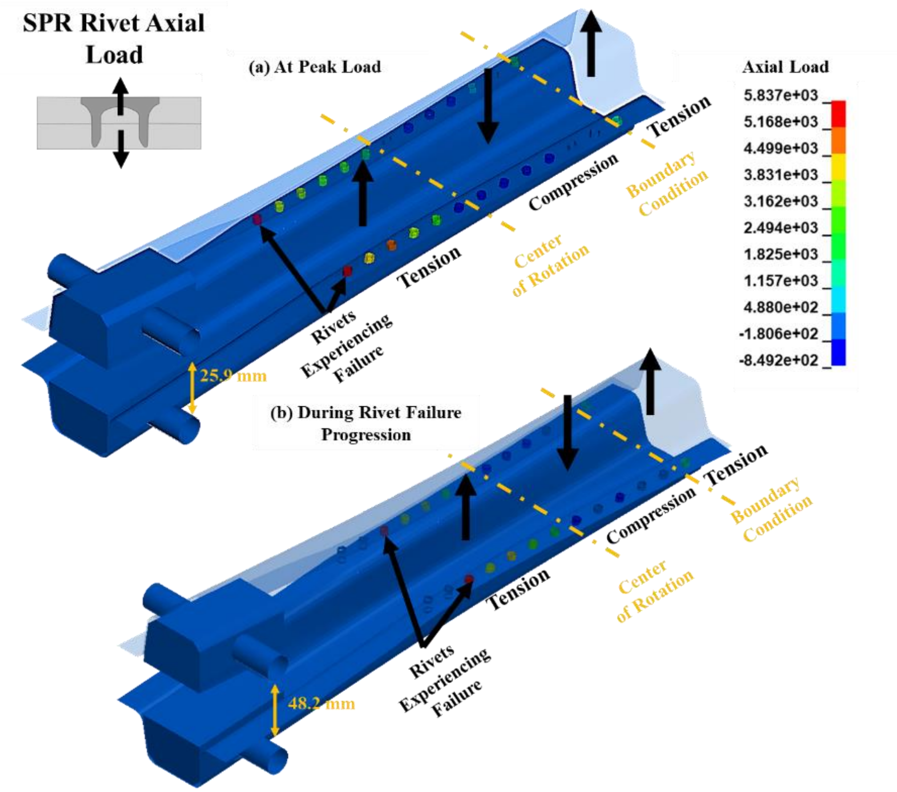

Figure 219: Peak load corresponded to the failure of the first row of rivets under Mode I (axial) loading (a), and failure propagation continued under Mode I loading with boundary effect at the unloaded (free) end (b).

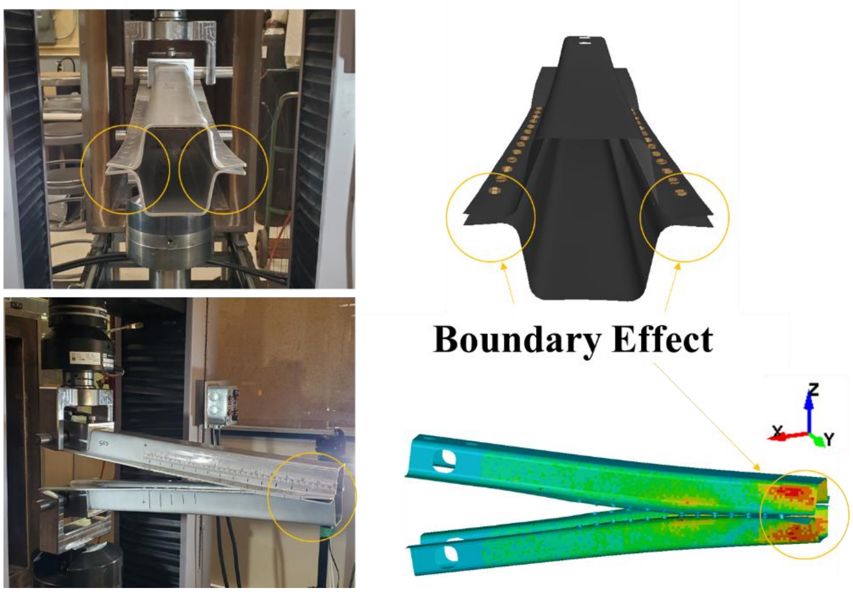

Figure 220: Flange separation at the unloaded (free) end of the Caiman was captured by the FE model.

In summary, the predictions of the SPR constraint Caiman model were in good agreement with the experiments in terms of the loading response, deformation pattern, and crack extension behaviour. The peak load was predicted within a difference of <7%, while the total energy load was somewhat overpredicted, due to the perfectly symmetrical rivet failure (Table 38).

Table 38: A comparison between the SPR-joined Caiman experimental measurements and FE predictions using SPR constraint model.

	Experimental Measurement (Average)	**FE Model Prediction**	**% Difference**
Peak Load, kN	8.89	9.49	+6.74
Energy, J	442.84	576.17	+30.10

6.5.3 SPR Joined Caiman CZM Model Validation

The SPR CZM model was able to accurately predict the load-displacement and energy responses (Figure 221) of the Caiman test with the initial stiffness, peak load, and failure of the first rivet (displacement at peak load) matching the measured experimental data. The SPR CZM model captured the behaviour of the structure, predicting the peak load within a difference of 3.93% (Table 39). Unlike the SPR constraint model, the overall energy had better accuracy (difference within 18%) and that was clear in the predicted energy curve.

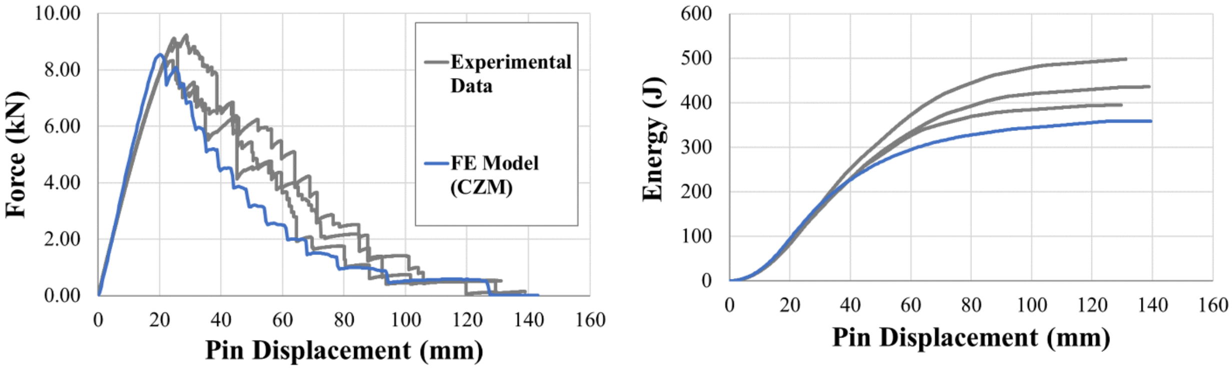

Figure 221: Simulation results of the SPR joined Caiman model (CZM model), compared to the load-displacement and energy-displacement responses of the experiments

Table 39: A comparison between the SPR-joined Caiman experimental measurements and FE predictions using SPR CZM model.

	Experimental Measurement (Average)	**FE Model Prediction**	**% Difference**
Peak Load, kN	8.89	8.54	-3.93
Energy, J	442.84	359.13	-18.90

The damage progression within the CZM model was based on the energy value calculated from the nodal displacements, and the CZM approach modeled rivet damage using local damage within the cohesive elements coupled with progressive cohesive element deletion to model the rivet pull-out (Figure 222). On the contrary, the constraint model did not allow for progressive failure in the same way as it maintained the effective area of the rivet while exhibiting rivet damage, such that the damage was linearly distributed across the total effective area (local damage but no element deletion). Therefore, the CZM model predicted lower energy, relative to the constraint model, when used for a large group of rivets (local damage coupled with progressive element failure versus local damage only). Similar to the experimental tests, as the rivets failure progressed along the flange, a boundary condition effect at the free end resulted in flange separation, which was predicted by the FE model (Boundary Effect, Figure 222).

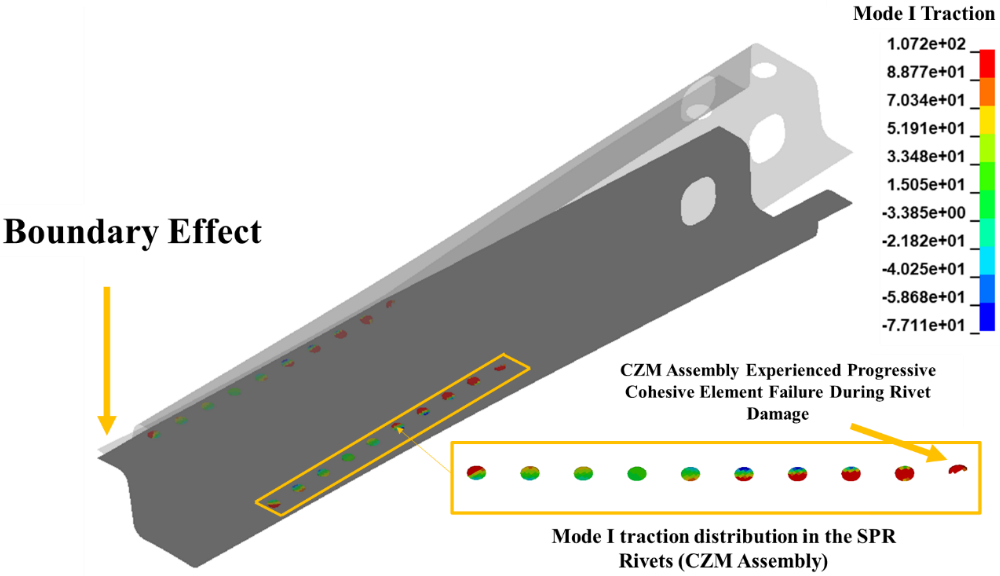

Figure 222: Mode I traction distribution within the CZM elements for each rivet, highlighting the progressive failure of the CZM model of the SPR rivet during the rivet damage progression.

6.5.4 Hybrid Joined Caiman CZM-Constraint Model Validation

The hybrid CZM-Constraint Caiman model was able to predict the load-displacement and energy responses of the Caiman test with the initial stiffness, peak load, and failure of the first rivet (displacement at peak load) matching the measured experimental data (Figure 223). The energy agreed well with the experimental data within 8.3% and the peak load was within a difference of 21.3% (Table 40)

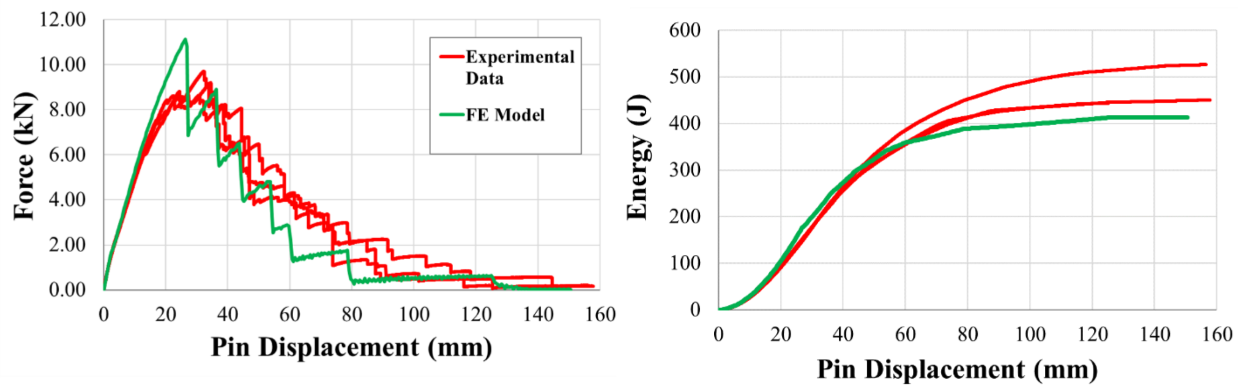

Figure 223: Simulation results of the hybrid joined Caiman model (CZM-Constraint model), compared to the load-displacement and energy-displacement responses of the experiments

Table 40: A comparison between the hybrid joined Caiman experimental measurements and FE predictions using hybrid CZM-Constraint model.

	Experimental Measurement (Average)	**FE Model Prediction**	**Difference**
Peak Load, kN	9.19	11.14	1.95 (+21.3%)
Energy, J	473.38	434.17	39.21 (-8.3%)

During the loading, the CZM damage initiation and progression resulted in a slight change in initial stiffness (observed in the experimental data) (Figure 224a), and loading continued until the peak load was reached causing a failure of the first row of SPR rivets. After the failure of each row of rivets, the load dropped and the CZM failure progression continued until the crack extended to the next row of SPR rivets, which arrested the CZM crack and caused an increase in the load. This behaviour continued during the unloading until the flanges separated) (Figure 224b and Figure 224c). The model also predicted that the free end of the Caiman component remained intact until complete separation (Figure 224c). Thus, the model accurately predicted the failure progression (crack extension) observed in the experiments (Figure 225).

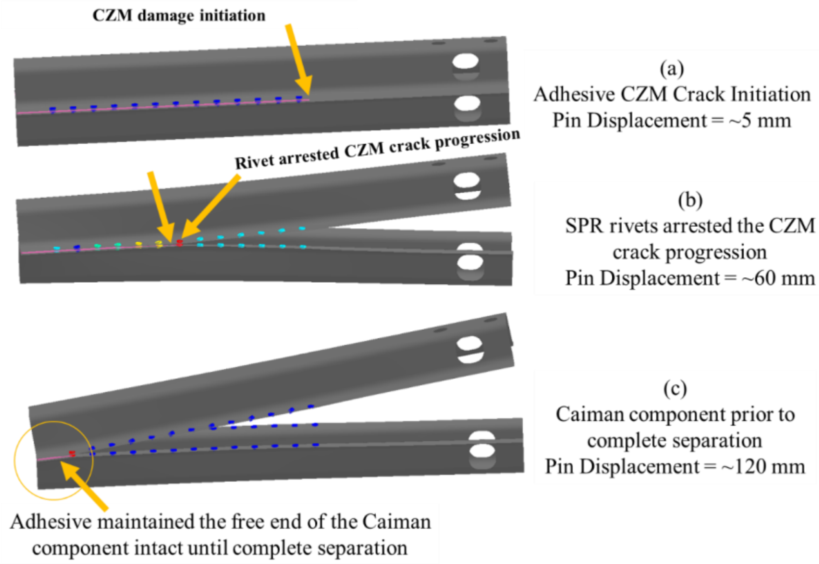

Figure 224: Adhesive and rivet failure propagation along the Caiman flanges at adhesive CZM crack initiation (a), during crack progression along the flange (b) and just before complete separation (c).

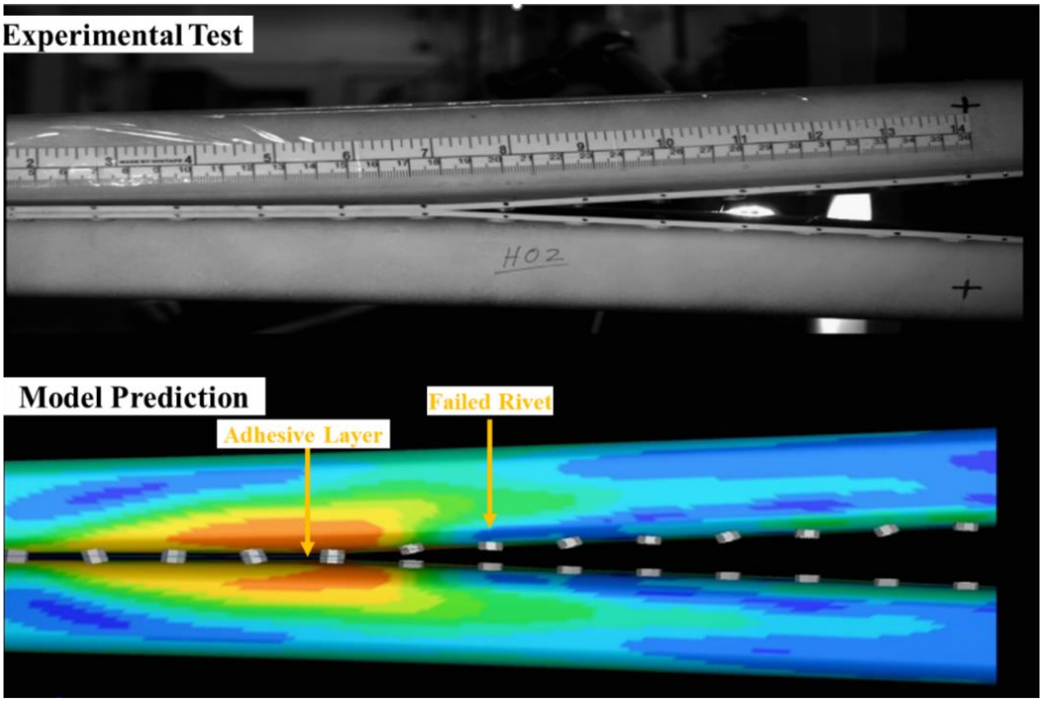

Figure 225: Side view of the experimental test (top) and simulation (bottom) showing rivet failure progression (crack extension).

To determine why the CZM-Constraint model somewhat overpredicted the peak load of the hybrid joined Caiman test, the damage progression and failure of the first row of rivets were investigated. While the adhesive CZM model exhibited a damage propagation early during the loading (between 2 to 3 kN) and was not expected to influence the peak load of the model, it was found that integrating the adhesive CZM model contributed to the peak load increase observed. The adhesive CZM crack initiated at the inner corner of the crack tip (Adhesive damage initiation point, Figure 226) and propagated toward the first rivet, as the load transferred to the SPR constraint model. The SPR rivet arrested the crack propagation and acted as a plastic hinge, thus the adhesive CZM elements at the other side of the rivet did not fail and experienced compression loading (Adhesive CZM under compression, Figure 226). Although crack progression behaviour was physical and matched what was observed in the experiments, the cohesive elements under compression influenced the SPR constraint model kinematics, reducing the relative separation and rotation between the top and bottom sheets (flanges) which increased the rivet failure load, owing to the constraining effect on one side of the rivet model. To validate our findings, the loads and moments acting on the first rivet were extracted and compared with the loads and moments acting on the same rivet in the SPR-only Caiman model. The rivet models in the hybrid and Caiman models were the same and used the same parameters, so the failure load and separation of the SPR-only and hybrid were expected to be similar. However, the first rivet in the hybrid CZM-Constraint model failed at a lower pin displacement and higher axial load relative to the SPR-only model (Figure 227). Interestingly, after the failure of the first rivet, the moment arm increased and consequently the adhesive damage progressed rapidly along the flange length and width due to peel (Mode I) loading, which improved the failure prediction of the constraint model.

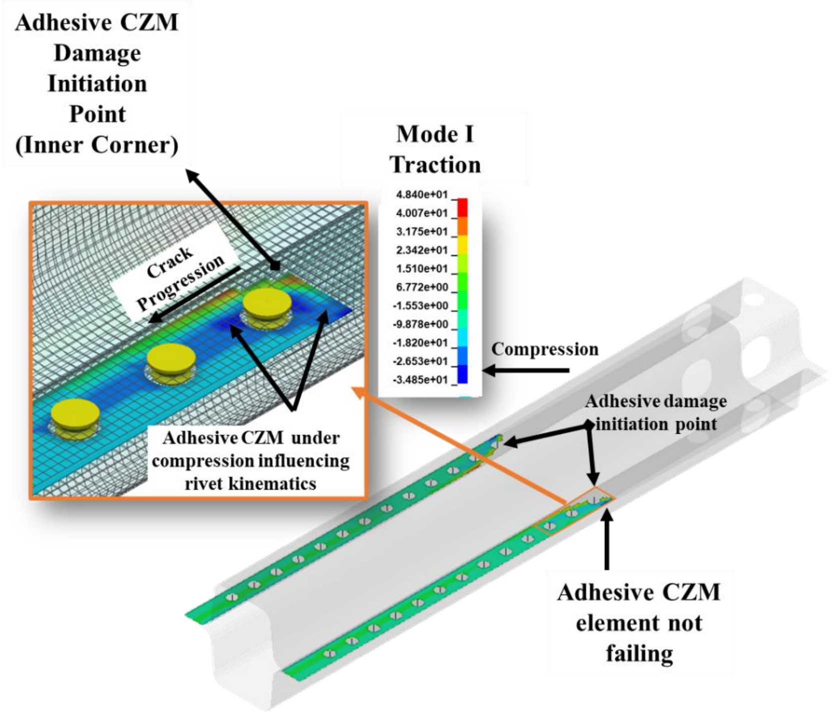

Figure 226: The adhesive CZM crack initiation at the inner corner of the crack tip and propagated toward the first SPR rivet constraint model which arrested the crack and acted as a hinge, applying compression loading on the cohesive elements at the other corner.

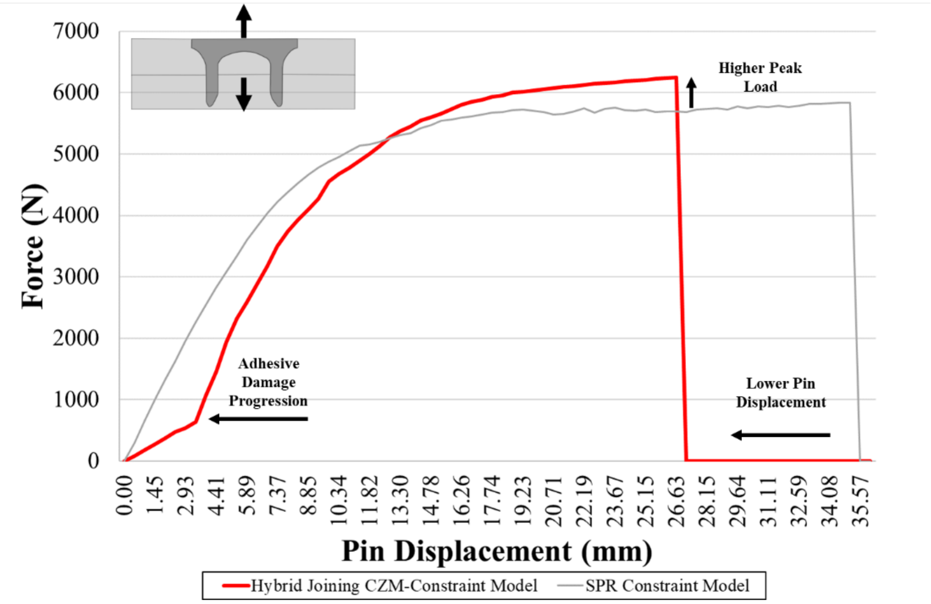

Figure 227: A comparison between the axial loads, acting on the first SPR rivet, in the SPR and hybrid joined Caiman models

6.5.1 Hybrid Joined Caiman CZM-CZM Model Validation

The integrated CZM-CZM model was able to accurately predict the load-displacement and energy responses of the Caiman test with the initial stiffness, peak load, and failure of the first rivet (displacement at peak load) matching the measured experimental data (Figure 228). The peak load was accurately predicted within a difference of 9.5%. Similar to the hybrid CZM-Constraint model, the adhesive CZM damage initiated at the corner and then propagated toward the SPR CZM rivet model. The adhesive CZM elements at the other corner of the crack tip experienced compression and did not fail, which constrained the kinematics of the rivet CZM model (Figure 229). Because the CZM constitutive model uses a damage progression criterion based on the fracture energy, the peak load was predicted with a high level of accuracy (<10% difference) (Table 41), unlike the constraint model which uses a load-based damage criterion. However, the

CZM-CZM model somewhat overpredicted the total energy by 28.3% compared to the average experimental data.

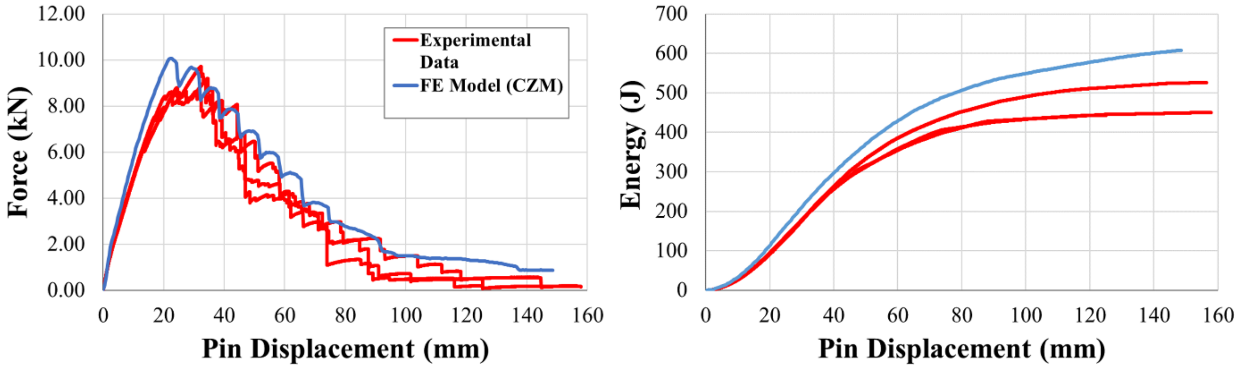

Figure 228: Simulation results of the hybrid joined Caiman model (CZM-CZM model), compared to the load-displacement and energy-displacement responses of the experiments

Table 41: A comparison between the hybrid joined Caiman experimental measurements and FE predictions using hybrid CZM-CZM model.

	Experimental Measurement (Average)	**FE Model Prediction**	**Difference**
Peak Load, kN	9.19	10.06	0.87 (+9.5%)
Energy, J	473.38	608.21	134.83 (+28.3%)

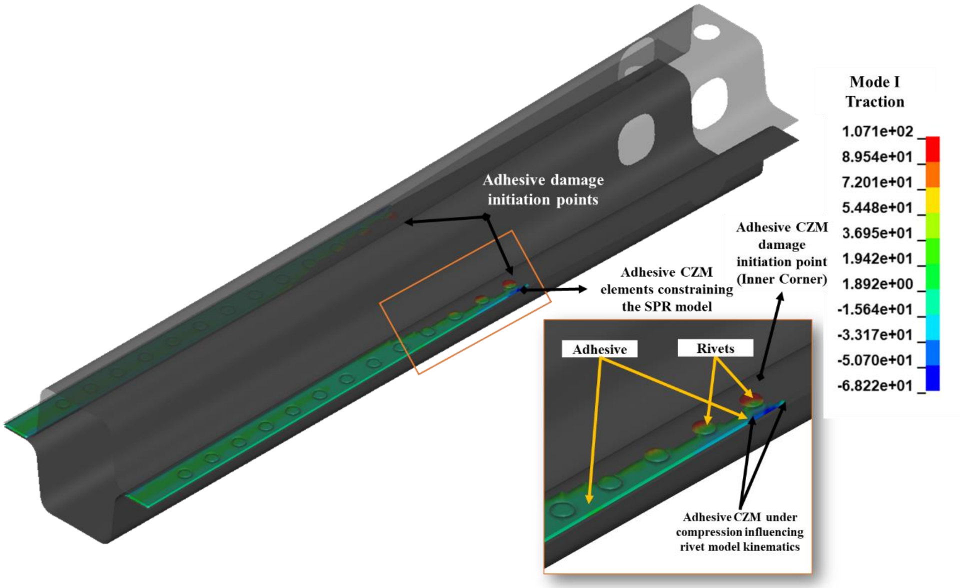

Figure 229: The adhesive CZM elements at the other corner of the crack tip experienced compression and did not fail, which constrained the kinematics of the rivet CZM model at peak load.

In general, while both the CZM-Constraint and CZM-CZM models showed reasonable accuracy in predicting the hybrid joint behaviour, the CZM-CZM showed a better overall response. Importantly, the CZM-CZM model had a three times higher computational efficiency when implemented in large-scale models as it reduced the total simulation time from 29 hours to less than 10 hours. The CZM-Constraint model required numerical control cards to ensure a smooth transition of the load between the CZM to constraint model and attenuate the shell oscillations after adhesive CZM damage, which substantially increased the simulation run time. Therefore, the CZM-CZM model is recommended for large-scale models and is expected to support the design and optimization of hybrid joined structures.

6.6 Computational Investigations of Joint Attributes and Loading Mode

The ultimate goal of this research was to support the weight reduction of future vehicles by enabling the design and optimization of aluminum structures joined using adhesive, SPR and hybrid joining. In this section, the validated joining models (adhesive, SPR and hybrid joining) were used to conduct computational investigations of (a) the influence of the number of SPR rivets on the mechanical response of SLJ and H-specimens, (b) joint behaviour under peel loading mode, (c) the effect of adhesive area reduction on Caiman mechanical response, and (d) an improved joint enhancement for the adhesively joined Caiman component.

6.6.1 Influence of Number of SPR Rivets on Mechanical Responses of SLJ and H-specimen

The SLJ and H-specimen models, using the original geometry with no changes to dimensions, were joined and simulated using two rivets spaced at 25 mm rather than a single rivet. The simulation results showed that increasing the number of rivets to two increased the SLJ peak load by 103.78% (20.48 kN versus 10.05 kN) and initial loading stiffness while maintaining the energy absorption (Figure 230a). The H-specimen peak load increased by 105.6% (13.94 kN versus 6.78 kN) with substantially higher initial loading stiffness and energy absorption (Figure 230b). Similar results were reported in the literature for aluminum SLJ tests joined using blind rivets (Rudawska and Wahab, 2019). The authors reported that when the number of blind rivets was increased from one to two the joint strength almost doubled.

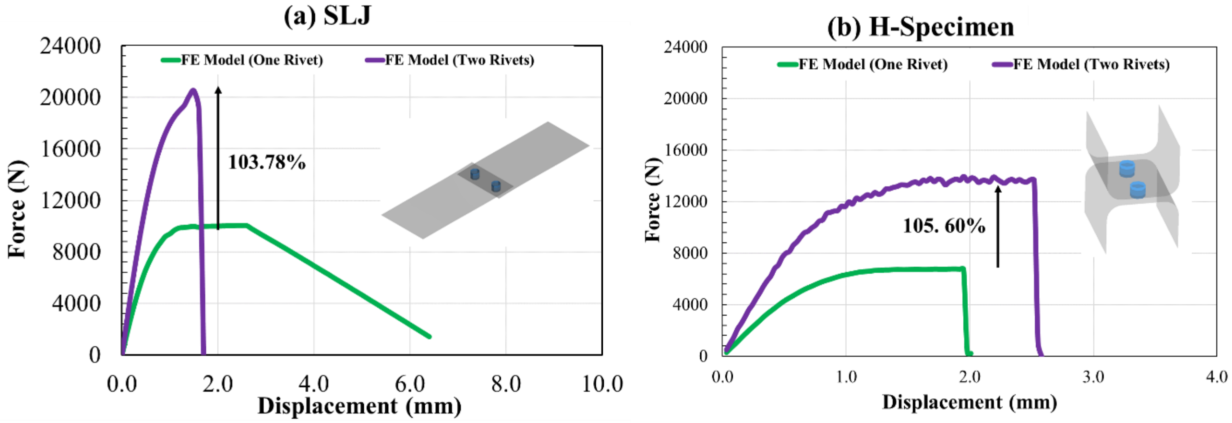

Figure 230: The mechanical response of SLJ (a) and H-specimen (b) joined using one and two rivets

The SLJ and H-specimen joined using two SPR rivets and made with 3 mm adherends were compared to similar adhesive joints (Figure 231). Both adhesive and SPR joints with two rivets demonstrated similar SLJ strength (difference of +2.55%), while the SPR-joined H-specimen demonstrated a 54.20% higher peak load. Importantly, the higher SPR joint strength was associated with additional weight, as the two rivets weighed 2.24 grams while the adhesive layer weighed only 1.34 grams. Although the use of two rivets could provide higher strength under tension loading relative to adhesive joining, it increased the weight of the joining method by 71.37%, highlighting that adhesives could provide a higher strength-per-weight ratio.

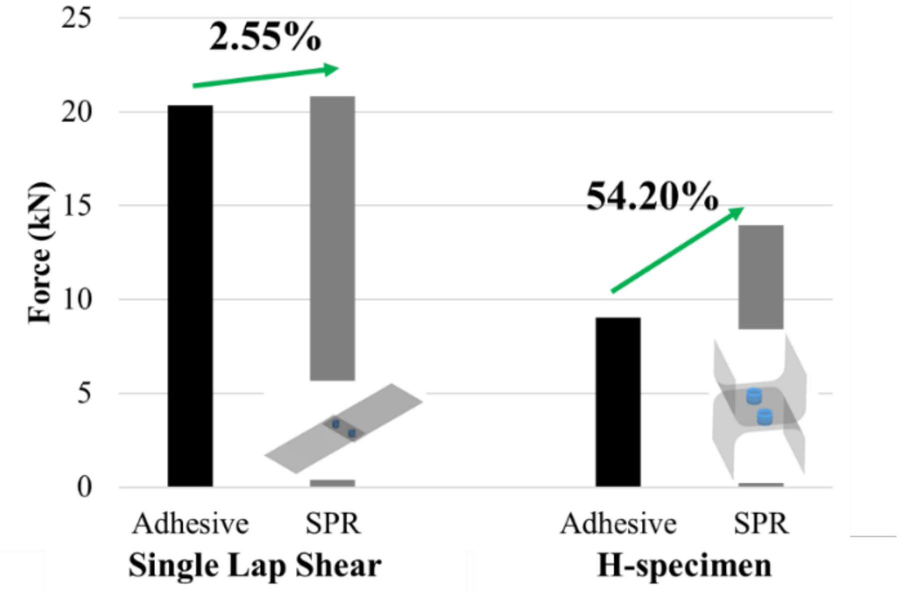

Figure 231: A comparison between adhesive and SPR (two rivets) joints peak load using SLJ and H-specimens.

6.6.2 Joint Behaviour under Peel (Mode I) Loading Mode

The H-specimen and SLJ showed that adhesive joining generally resulted in the highest peak load among the three joining methods. A study by Zhang *et al*. (2022) reported that adhesive SLJ joints could have +900% higher joint strength relative to similar adhesive coach peel joints, highlighting the effect of loading mode on the adhesive joint mechanical response. The adhesively bonded coach peel was compared to the adhesively joined SLJ and H-specimens to assess adhesive sensitivity to the mode of loading. The comparison showed that the coach-peel joints had substantially lower peak load (3.01 kN) compared to the SLJ (+575%) and H-specimen (+200%) joints (Figure 232a). The adhesive exhibited a localized Mode I loading along the adhesive edge (Figure 232b), which initiated a crack early during the loading. The crack progressed until adhesive failure was encountered, causing full separation of the joint.

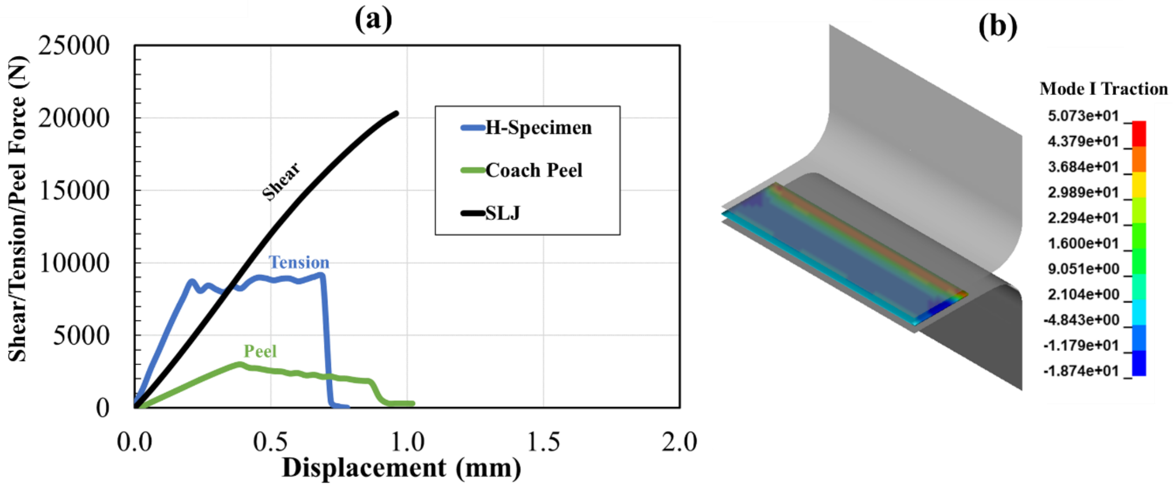

Figure 232: A comparison between the load response of adhesively joined H-specimen, SLJ and coach peel models (a), illustrating the adhesive coach-peel Mode I traction distribution (b).

The SPR and hybrid joining were also simulated using the coach peel model made with 3 mm thick adherends to assess the sensitivity of hybrid joining to peel loading and quantify its performance benefits relative to the adhesive-only and SPR-only joints. The hybrid joint model demonstrated the highest peak load as the simulation results showed that the adhesive failed during the loading phase and the peak load corresponded to SPR rivet failure, similar to the Caiman test. The peak load of the adhesive, SPR and hybrid joined coach-peel joints was 3.01 kN, 3.38 kN and 3.39 kN (12.3% higher than adhesive joints), respectively (Figure 233). Ultimately, the FE results suggested that adhesively bonded structures, subjected to peel loading could achieve a significant benefit from hybrid joining. Given that adhesives and SPR performance highly depended on the mode of loading, it could be concluded that another key advantage of hybrid joining over the individual joining methods was its ability to achieve the best mechanical response regardless of loading mode (less sensitive to the mode of loading).

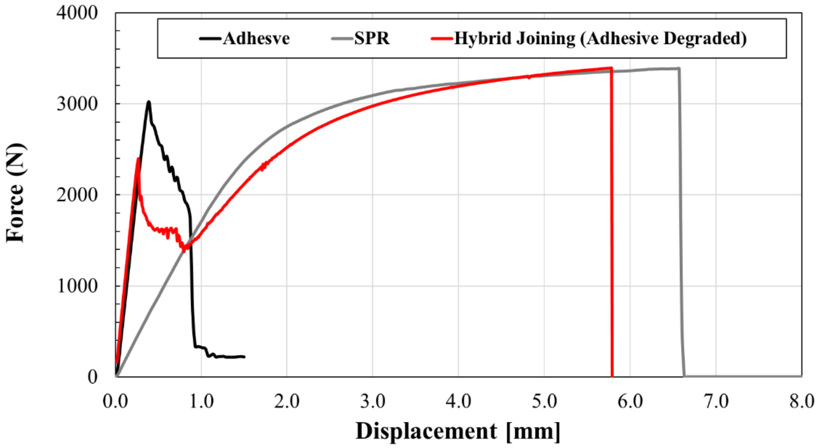

Figure 233: The coach-peel simulations load-displacement response for adhesive, SPR (constraint model) and hybrid joining (CZM-Constraint model)

6.6.3 Effect of Adhesive Area Reduction on Caiman Mechanical Response

Spacers, such as shims, have been used to maintain the adhesive bond line thickness (Campbell, 2004; Licari and Swanson, 2005), and in large-scale structures, maintaining a uniform bond line thickness may require using spacers within the adhesive bonding area, which reduces the total area available for bonding (Liu, 2019). The influence of adhesive area reduction due to the use of adhesive spacers was assessed using the validated adhesively joined Caiman model. The simulation results of the Caiman model showed that a 26.5% reduction in the bond area resulted in a 10.5% drop in peak load and a 23.7% drop in the total energy), highlighting the implications associated with the use of spacers to maintain adhesive bond line thickness. The reductions in adhesive bond area and total energy were comparable (26.5% versus 23.7%), as reducing the bond area required less energy to create new fracture surfaces. The direct influence of adhesive area reduction on the peak load was complex as it depended on the stress distribution and deformation localization within the adhesive and adherends, which could be influenced by several joint parameters, such as the geometry of the bond area and the location of the reduced area relative to the adhesive boundaries (crack tip). Therefore, the adhesive model developed and validated in this work could be extended to identify the spacer locations with minimum influence on load response.

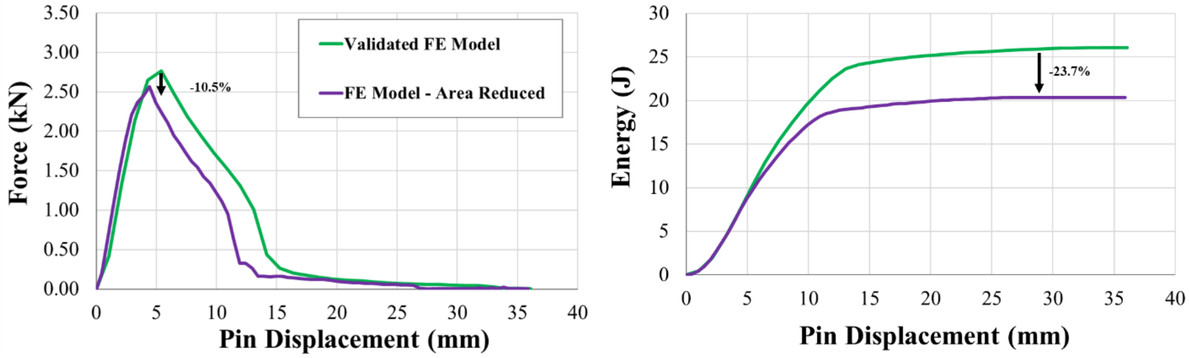

Figure 234: Comparison of the validated adhesive CZM Caiman models with and without area reduction to mimic the use of 13 spacers on each flange, force-displacement (left) and energy-displacement (right).

6.6.4 Joint Enhancement for Adhesively Joined Caiman Components

Researchers attempted to enhance the mechanical response of adhesive joints, by optimizing adhesive joint configuration, joint design parameters, substrate stiffness and strength or adhesive selection (Mallick, 2020). The Caiman test results highlighted that adhesives experienced a substantially low joint strength under peel loading (2.66 kN) relative to SPR and hybrid joining (9.18 kN). From a practical point of view, adhesively bonded structures likely fail due to peel loading because loading a structure or an assembly under pure shear or tension loading may require complex loading and boundary conditions. Therefore, the Caiman model could be a reasonable representation of a bonded structure used in an automotive assembly. The Caiman model with reinforced adhesive crack tip was simulated and the results were compared to the validated adhesively bonded Caiman model. Reinforcing the crack tip using aluminum plates joined to the hat sections using SPR rivets (Figure 235a) enhanced the mechanical performance of the Caiman model. The reinforced joint design increased the Caiman peak load by 4.16 times (4.16x) and the total energy by 4.31 times (4.31x) (Figure 235b). The peak load corresponded to the failure of SPR rivets joining the reinforcing sheets to the Caiman component, and the adhesive damage was only initiated after the failure of the rivets. Thus, it could be concluded that adhesive crack tip could benefit from the reinforcement methodology proposed, which could be integrated into a real design since SPR rivets do not require surface preparation, fixturing, or curing. Ultimately, several joint reinforcement techniques, such as different reinforcement materials, and the number or configuration of rivets, could be assessed using the models developed and validated in this work to further achieve a tailored mechanical response.

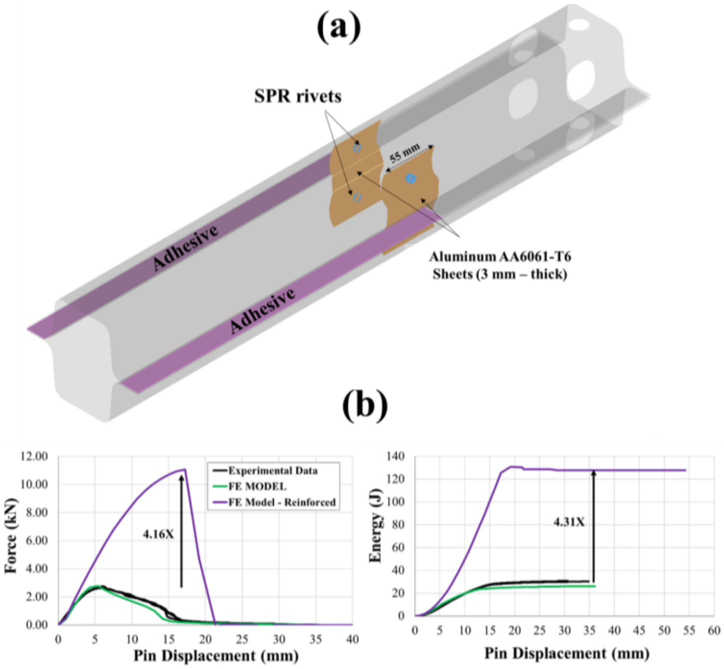

Figure 235: The adhesively joined Caiman component reinforced using aluminum sheet material and SPR rivet (a), and a comparison of the adhesive CZM Caiman models with and without reinforcement, force-displacement (left) and energy-displacement (right).

Chapter 7: Conclusions and Future Work

The current research aimed to advance our understanding and FE modelling capability of the mechanical behaviour and characteristics of hybrid (adhesive-SPR) joints, shedding light on the mechanical response benefits relative to the individual joining methods. The present study was designed to determine the effect of key parameters (*i.e.*, sheet thickness and alloy strength) on the joint morphology and the mechanical response of adhesive, SPR and hybrid joints under different modes of loading. In addition, this work described a multi-scale approach toward the development, verification and validation of a hybrid joint model, compatible with large-scale models (*e.g.*, models of full vehicles) and extendable to crash applications. Collectively, the outcomes from this research contribute to the body of knowledge surrounding the mechanical behaviour of adhesive, SPR and hybrid joints and support the implementation of hybrid joining technology to enable modern lightweight high-performance materials and multi-material systems in automotive structures. Importantly, there are five key strengths with novelty aspects that this study presents:

1. Adhesive, SPR and hybrid joints were assessed under the same test conditions, which allowed for quantifying the mechanical performance benefits of hybrid joints relative to individual joints while investigating the effect of aluminum sheet metal thickness and alloy type.
2. Adhesive, SPR and hybrid joints were characterized under tension loading using a low compliance test specimen, reducing the influence of adherend deformation and peel loading on the mechanical response.

3. The hybrid joining mechanical behaviour was related to the joint-level morphology and intrinsic behaviour of the individual joining methods, which allowed for an understanding of how hybrid joints improve the mechanical response of the individual joints.
4. A hybrid joining process variation was proposed and assessed, which enhanced the mechanical response of hybrid joining applied to thick aluminum adherends (3 mm), relative to the traditional hybrid joining process.
5. Finally, a key strength of this research lies in the multi-scale development, verification and validation of the hybrid joint FE model. The use of material-level adhesive characterization and the proposed specimen-level SPR calibration technique allowed for the modeling of hybrid joints without requiring calibration parameters, mimicking the intrinsic response of the individual joining methods.

7.1 Conclusions

From the experimental results and discussion, we can draw the following main conclusions:

The surface preparation study identified surface treatment methods that achieved cohesive failure and maximized joint strength for bonding aluminum sheet material using an automotive structural adhesive. The grit blasting (SDGB) treatment increased the surface roughness and bonding area by introducing ridges and valleys to the aluminum surface, removed the near-surface-deformed-layer (NSDL), potentially changed the interface chemistry (not measured in this work but reported in the literature (Cavezza et al., 2020) and observed as a change in the oxide layer colour), and increased the van der Waals forces. The sol-gel (SDSG) treatment improved the polar surface energy, and more importantly, converted the weak hydroxylated aluminum oxides using an interlayer of organic-inorganic silane coating which was deposited by the solution gelation process without altering the surface roughness. Ultimately, the grit-blasting and sol-gel surface treatments increased the interfacial strength, which improved SLJ joint strength compared to baseline by almost seven times (SD). The sol-gel application method has the potential to be implemented in a high-volume production environment enabling the treatment of large sheet material and bond area, and the cost-efficient grit-blasting method could be applied in a lab environment.

The joint morphology and physical attribute of adhesive, SPR and hybrid joints were quantified. The adhesive bond line thickness measured on the specimen-level joints showed excellent consistency for all sheet thicknesses, attributed to the use of Teflon-coated fibreglass spacers and assembly jigs for creating the joints. The mechanical interlock of the SPR joints created in this work was shown to be consistent and agreed with the guidelines in the literature. The mechanical properties of the aluminum sheets (*i.e.*, ductility and formability) had a substantial effect on the physical attributes of the formed SPR joint. Hybrid joining had marginal to no effect on the SPR rivet formation for the joints made with 1, 2 and 3 mm thick sheets regardless of alloy strength. On the contrary, hybrid joining affected adhesive morphology, resulting in a non-uniform adhesive bond line thickness and air inclusions within the adhesive layer to a degree that depended on material thickness and alloy type.

The H-specimens provided reduced compliance relative to commonly used CT specimens, enabling the comparative assessment of joining methods under tension loading while reducing the influence of adherend deformation. The SLJ joints enabled the comparative assessment of the joining methods under primarily shear loading and allowed visual access to observe and validate the local joint kinematics for each joining method. Importantly, adhesive joints generally demonstrated higher joint strength and stiffness than SPR joints under tension and shear loading, while SPR joints demonstrated higher energy absorption capabilities, attributed to the localized plastic deformation in the vicinity of the rivet. Hybrid joining improved the mechanical response for joints made with 1 mm and 2 mm sheets, demonstrating peak load and stiffness comparable to adhesive joints and energy absorption equal to or higher than the SPR joints.

Sheet (adherend) thickness and alloy type (*i.e.,* strength and ductility) were shown to be critical factors in the mechanical response of adhesive, SPR and hybrid joints. Under tension loading, increasing sheet thickness generally increased the peak load for all three joining methods. In contrast, the SLJ strength improvement observed in adhesive and hybrid joints with increasing sheet thickness had an upper limit and sheet thickness increase above 2 mm was not beneficial because increasing the adherend thickness did not reduce the primary crack propagation driver (*i.e.,* shear stress) within the adhesive layer. The alloy type had a significant effect on the peak load of adhesive, SPR and hybrid joints. The higher-strength alloy (AA6061) improved joint strength for all three joining methods, while the joints made with the lower-strength and more ductile alloy (AA5052) generally demonstrated higher energy absorption. In general, the energy absorption gains realized by adopting hybrid joining demonstrated co-dependence on sheet thickness and aluminum alloy type (*i.e.,* strength and ductility). For adhesives, sheet thickness and alloy strength were inversely related to the energy absorbed in SLJ joints while the effect on H-specimen was insignificant. For SPR and hybrid joining, increasing sheet thickness generally increased the energy absorption, except for special cases where the aluminum alloy with low ductility did not allow sufficient deformation within the vicinity of the rivet prior to joint failure

(3 mm thick sheets with AA6061 alloy). Although hybrid joining generally improved the overall mechanical performance of the joints regardless of loading mode, sheet thickness or alloy type, it was shown that some degree of strength and stiffness degradation, relative to adhesive-only, could be expected with 3 mm thick sheets owing to the reduced adhesive morphology.

The Caiman component-level test enabled assessing the response of large adhesive bond areas and groups of SPR rivets under primarily Mode I loading, addressing the mechanical response of the joints at a large scale. Unlike tension- and shear-loaded specimens, the peak load and energy absorption of adhesive joints under Mode I loading were considerably lower than those of SPR and hybrid joints, highlighting that adhesive joints were highly influenced by the mode of loading and did not perform well under peel loading. Hybrid joining demonstrated the best overall mechanical response, improving the peak load and energy absorption of the adhesively joined Caiman test by 244% and 1461%, respectively.

In summary, hybrid joining combined the advantages of the individual joining method to achieve a joint with well-rounded mechanical characteristics, substantially improving the overall performance of adhesive and SPR joints under tension, shear and Mode I (peel) loading. Under shear and tension loading, hybrid joining improved the energy absorption of adhesive joints and the strength, stiffness and energy absorption of SPR joints. Under Mode I loading, hybrid joining improved the strength and energy absorption of adhesive joints, and the stiffness of SPR joints. Additionally, hybrid joining can address the challenges associated with individual joining methods, such as the adhesive bonding fixturing requirements and SPR joining galvanic corrosion.

From the computational modeling results and discussion, we can draw the following conclusions:

The cohesive zone modeling approach enabled predicting the response of adhesive joints with a reasonable level of accuracy, providing a computationally efficient means to simulate adhesive joints in large-scale FE models (*i.e.,* models of automotive components or full cars). The material-level adhesive properties, determined from the RDCB and BSS tests and implemented into a trapezoidal-shaped traction-separation relationship, were shown to be representative of a relatively ductile structural adhesive used in automotive. The adhesive CZM model validation, presented for two different specimen-level tests (SLJ and H-specimen) having three different sheet thicknesses each, showed good agreement with the experimental data, predicting the overall mechanical response and joint kinematics (*e.g.,* SLJ joint rotation). The H-specimen was somewhat challenging to simulate as it required simulating the localized deformation at the bend radius with a substantial amount of stress localization and nodal penetrations. In addition, the symmetrical CZM 2D line damage at the free ends caused a load spike that overpredicted the load response of experiments which experienced multiple localized adhesive crack initiation points.

The constraint model of the SPR rivet, developed based on the measurements conducted on the specimen-level tests for each adherend thickness, captured the damage initiation and damage progression of the SPR joints under shear and tension loading. The verification of the SPR constraint model, presented for two different specimen-level tests (SLJ and H-specimen) having three different sheet thicknesses each, showed good agreement with experimental data, predicting the overall mechanical response, including the gradual softening observed during the loading and unloading. Furthermore, the proposed approach to use CZM to simulate SPR rivets enabled predicting the response of the H-specimens and SLJ joints made with 3 mm thick adherends and showed good agreement with the measured peak load, stiffness and displacement at failure. Both models (constraint and CZM models) of the SPR rivets had fairly similar computational efficiency, indicating that both models have strong potential to be implemented in large-scale models. The CZM approach linearized the response due to the constitutive traction-separation relationship, and both models model captured joint kinematics (*e.g.,* SLJ joint rotation) until substantial rivet damage occurred. Both models underpredicted joint rotation, such that the moment applied to the tail-side sheet was quite low; however, such limitation could be trivial in large-scale structures since they do not generally undergo shear loading.

The development of a hybrid joining model focused on integrating the validated adhesive CZM model with the verified SPR models (constraint and CZM models), incorporating a multi-scale approach that systematically used the models of the individual joining methods to simulate the combined intrinsic responses of the individual joints. The hybrid joint model mapped the adhesive squeeze out into the adhesive CZM model, and the models with 3 mm thick sheets, which experienced substantial morphological effects, required incorporating the influence of adhesive air inclusions and bond line thickness reduction into the CZM traction-separation relationships. The hybrid CZM-Constraint model showed a major limitation associated with numerical oscillations and stability, which required the use of computationally expensive numerical controls. On the other hand, the CZM-CZM hybrid joint model allowed a smooth transition of the load from the adhesive CZM to the SPR model without requiring additional numerical controls, substantially improving the computational efficiency of the model, which is critical for implementation in large-scale models. The predictions of the adhesive, SPR and hybrid joined Caiman models were generally in good agreement with the experiments in terms of the loading response, deformation pattern, and local joint kinematics (*e.g.,* adhesive crack propagation behaviour or rivet failure progression). Ultimately, the FE modeling methodologies developed in this work demonstrated a significant improvement in the ability to model hybrid joints under varying modes of loading and with varying degrees of base material deformation. Also, the FE investigations conducted using the validated models showed that the number of SPR rivets in a specimen-level test had a substantial influence on the mechanical response and could substantially improve the behaviour of SPR riveted joints. Also, it could be concluded that the reduction in the adhesive area while maintaining the same bonding area boundaries (crack tip), mimicking the use of the spacers used to maintain bond line thickness, was linearly related to the energy absorption, but will require case-specific computational investigation to minimize the effect of spacers location on the peak load of the joint. Interestingly, the coach-peel simulation results confirmed that adhesives showed substantially lower joint strength under peel loading, highlighting the benefits of hybrid joints for adhesive joints experiencing peel loading. Finally, combining adhesives and self-piercing rivets was shown to be an effective method to incorporate innovative joint design into adhesively bonded structures, reinforcing adhesive crack tips and improving the mechanical response.

Ultimately, the experimental and computational results highlighted important parameters in terms of automotive structure design trade-offs (*e.g.,* joining methods, mechanical performance, joining method, joint morphology, sheet thickness and alloy strength) and provided evidence that hybrid joining can enhance the strength, stiffness and energy absorption of adhesive and SPR joined structures regardless of loading mode. The results from the present study support and facilitate the design and optimization of future lightweight automotive structures made with aluminum and multi-material systems.

7.2 Future Work

The experimental work undertaken and FE models developed in this work could be extended to quantify and study the effect of elevated loading rate on the hybrid joints. The dynamic response of joining methods plays a significant role in crash loading scenarios, which motivated researchers to investigate adhesives and SPR joints at elevated loading rates (Dagorn *et al.*, 2020; Leconte *et al.*, 2020; Morin *et al.*, 2013). However, hybrid joints have not been investigated in the literature under dynamic loading. The specimen-level tests (SLJ and H-specimens) and component-level Caiman test, used in this work, can be adapted to study the rate effect on joint behaviour (Beule *et al.*, 2022; Liu, 2019; Zhang *et al.*, 2015). The adhesive material level characterization used in this work and SPR calibration methodology developed in this work could be used at elevated loading rates to determine the parameters required for the adhesive CZM and SPR CZM models. Then, the hybrid CZM-CZM model could be extended to simulate hybrid joints for automotive crash applications.

Further experimental investigation into the effect of environmental factors, such as temperature and humidity on the mechanical response of hybrid joining should be undertaken to identify challenges that hybrid joints may experience during their service life. The mechanical properties of adhesives were been reported to be temperature dependent and elevated service temperature reduced adhesive joint strength (Banea and Da Silva, 2010), but it is still not clear how service temperature and humidity affect the mechanical response of SPR and hybrid joining.

A deeper investigation into the effect of manufacturing factors, such as fillet size, adhesive curing process, SPR process parameters, and SPR rivet and die design, may be of great interest to the automotive industry and can shed light on novel methods to improve the hybrid joint response.

Understanding the uncertainty associated with manufacturing factors imparts to the joining process design and consequently the relationship between joining process design and the mechanical response of the joint. Future work could first assess the effect of manufacturing factors at the joint morphology level, and then conduct SLJ and H-specimen tests to compare the mechanical response relative to the data presented here. Also, future work may consider using thicker spacers in hybrid joints, relative to adhesive joints, to account for the reduction in bond line thickness and attempt to increase the thickness at the adhesive boundaries.

Finally, the durability of adhesive, SPR and hybrid joints was not addressed in this work. The approach followed in this work could be extended to evaluate the fatigue life of the joints. Adhesive joints were reported to have excellent fatigue life under shear loading, demonstrating higher fatigue life compared to spot welds and weld-bonded joints (Pereira *et al.*, 2014); however, the joint fatigue life under peel and tension loading can be considerably low. Also, the fatigue life of SPR joints was reported to be associated with fretting wear (Zhang *et al.*, 2016). Importantly, hybrid joining was shown to substantially improve the peel-loading capacity of adhesives and could address the fretting wear associated with SPR, thus, it is expected that hybrid joining will likely improve the durability of individual joints. The hybrid CZM-CZM could be updated to incorporate a damage accumulation parameter due to cyclic loading, which will facilitate predicting the fatigue life of hybrid joints.

Letters of Copyright Permissions

This Agreement between University of Waterloo -- Ahmed Ibrahim ("You") and John Wiley and Sons ("John Wiley and Sons") consists of your license details and the terms and conditions provided by John Wiley and Sons and Copyright Clearance Center.

License Number
5515461282957
License date
Mar 24, 2023

Licensed Content
Licensed Content Publisher
John Wiley and Sons
Licensed Content Publication
Materialwissenschaft und Werkstofftechnik
Licensed Content Title
Methods to increase the toughness of structural adhesives with micro particles: an overview with focus on cork particles
Licensed Content Author
A. Q. Barbosa, L. F. M. Silva, M. D. Banea, et al
Licensed Content Date
Apr 15, 2016
Licensed Content Volume
47
Licensed Content Issue
4
Licensed Content Pages
19

Order Details
Type of use
Dissertation/Thesis
Requestor type
University/Academic
Format
Print and electronic
Portion
Figure/table
Number of figures/tables
2
Will you be translating?
No

About Your Work
Title Experimental Assessment and Computational Modeling of Adhesive, Self Piercing Rivets (SPR), and Hybrid (Adhesive-SPR) Joints: Enhancing Joint Performance for Aluminum Sheet Material
Institution name University of Waterloo
Portions Figure 4

This Agreement between University of Waterloo -- Ahmed Ibrahim ("You") and John Wiley and Sons ("John Wiley and Sons") consists of your license details and the terms and conditions provided by John Wiley and Sons and Copyright Clearance Center.

Your confirmation email will contain your order number for future reference.

License Number
5515470673022
License date
Mar 24, 2023

Licensed Content

Licensed Content Publisher
John Wiley and Sons
Licensed Content Publication
Materialwissenschaft und Werkstofftechnik
Licensed Content Title
Methods to increase the toughness of structural adhesives with micro particles: an overview with focus on cork particles
Licensed Content Author
A. Q. Barbosa, L. F. M. Silva, M. D. Banea, et al
Licensed Content Date
Apr 15, 2016
Licensed Content Volume
47
Licensed Content Issue
4
Licensed Content Pages
19

Order Details

Type of use
Dissertation/Thesis
Requestor type
University/Academic
Format
Print and electronic
Portion
Figure/table
Number of figures/tables
1
Will you be translating?
No

About Your Work

Title Experimental Assessment and Computational Modeling of Adhesive, Self Piercing Rivets (SPR), and Hybrid (Adhesive-SPR) Joints: Enhancing Joint Performance for Aluminum Sheet Material
Institution name University of Waterloo
Expected presentation date Jun 2023

Additional Data

Portions Figure 10

The effect of temperature on the mechanical properties of adhesives for the automotive industry

Author:
M D Banea, L F M da Silva
Publication:
Proceedings of the Institution of Mechanical Engineers, Part L: Journal of Materials: Design and Applications
Publisher:
SAGE Publications
Date:
2010-04-01

Gratis Reuse

Permission is granted at no cost for use of content in a Master's Thesis and/or Doctoral Dissertation, subject to the following limitations. You may use a single excerpt or up to 3 figures tables. If you use more than those limits, or intend to distribute or sell your Master's Thesis/Doctoral Dissertation to the general public through print or website publication, please return to the previous page and select 'Republish in a Book/Journal' or 'Post on intranet/password-protected website' to complete your request.

Effect of Cure Temperature on the Glass Transition Temperature and Mechanical Properties of Epoxy Adhesives

Author:
R. J. C. Carbas, , E. A. S. Marques, et al
Publication:
Journal of Adhesion
Publisher:
Taylor & Francis
Date:
Jan 2, 2014
Rights managed by Taylor & Francis

Thesis/Dissertation Reuse Request

Taylor & Francis is pleased to offer reuses of its content for a thesis or dissertation free of charge contingent on resubmission of permission request if work is published.

This Agreement between University of Waterloo -- Ahmed Ibrahim ("You") and Elsevier ("Elsevier") consists of your license details and the terms and conditions provided by Elsevier and Copyright Clearance Center.

Your confirmation email will contain your order number for future reference.

License Number
5515471227863
License date
Mar 24, 2023

Licensed Content

Licensed Content Publisher
Elsevier
Licensed Content Publication
Applications of Surface Science
Licensed Content Title
Oxide morphologies on aluminum prepared for adhesive bonding
Licensed Content Author
J.D. Venables,D.K. McNamara,J.M. Chen,T.S. Sun,R.L. Hopping
Licensed Content Date
Jul 1, 1979
Licensed Content Volume
3
Licensed Content Issue
1
Licensed Content Pages
11

Order Details

Type of Use
reuse in a thesis/dissertation
Portion
figures/tables/illustrations
Number of figures/tables/illustrations
3
Format
both print and electronic
Are you the author of this Elsevier article?
No
Will you be translating?
No

About Your Work

Title Experimental Assessment and Computational Modeling of Adhesive, Self Piercing Rivets (SPR), and Hybrid (Adhesive-SPR) Joints: Enhancing Joint Performance for Aluminum Sheet Material
Institution name University of Waterloo
Expected presentation date Jun 2023

Additional Data

Portions Figures 2, 5 and 7

This Agreement between University of Waterloo -- Ahmed Ibrahim ("You") and Elsevier ("Elsevier") consists of your license details and the terms and conditions provided by Elsevier and Copyright Clearance Center.

Your confirmation email will contain your order number for future reference.

License Number
5515480029444

License date
Mar 24, 2023

Licensed Content

Licensed Content Publisher
Elsevier

Licensed Content Publication
International Journal of Adhesion and Adhesives

Licensed Content Title
Study on the role of laser surface irradiation on damage and decohesion of Al/epoxy joints

Licensed Content Author
Marco Alfano,Gilles Lubineau,Franco Furgiuele,Glaucio H. Paulino

Licensed Content Date
Dec 1, 2012

Licensed Content Volume
39

Licensed Content Issue
n/a

Licensed Content Pages
9

Order Details

Type of Use
reuse in a thesis/dissertation

Portion
figures/tables/illustrations

Number of figures/tables/illustrations
1

Format
both print and electronic

Are you the author of this Elsevier article?
No

Will you be translating?
No

About Your Work

Title Experimental Assessment and Computational Modeling of Adhesive, Self Piercing Rivets (SPR), and Hybrid (Adhesive-SPR) Joints: Enhancing Joint Performance for Aluminum Sheet Material

Institution name University of Waterloo

Expected presentation date Jun 2023

Additional Data

Portions Figure 2

This Agreement between University of Waterloo -- Ahmed Ibrahim ("You") and Elsevier ("Elsevier") consists of your license details and the terms and conditions provided by Elsevier and Copyright Clearance Center.

Your confirmation email will contain your order number for future reference.

License Number
5515501027152

License date
Mar 24, 2023

Licensed Content

Licensed Content Publisher
Elsevier

Licensed Content Publication
International Journal of Adhesion and Adhesives

Licensed Content Title
Modelling adhesive joints with cohesive zone models: effect of the cohesive law shape of the adhesive layer

Licensed Content Author
R.D.S.G. Campilho,M.D. Banea,J.A.B.P. Neto,L.F.M. da Silva

Licensed Content Date
Jul 1, 2013

Licensed Content Volume
44

Licensed Content Issue
n/a

Licensed Content Pages
9

Order Details

Type of Use
reuse in a thesis/dissertation

Portion
figures/tables/illustrations

Number of figures/tables/illustrations
1

Format
both print and electronic

Are you the author of this Elsevier article?
No

Will you be translating?
No

About Your Work

Title Experimental Assessment and Computational Modeling of Adhesive, Self Piercing Rivets (SPR), and Hybrid (Adhesive-SPR) Joints: Enhancing Joint Performance for Aluminum Sheet Material

Institution name University of Waterloo

Expected presentation date Jun 2023

Additional Data

Portions Figure 3

This Agreement between University of Waterloo -- Ahmed Ibrahim ("You") and Elsevier ("Elsevier") consists of your license details and the terms and conditions provided by Elsevier and Copyright Clearance Center.

Your confirmation email will contain your order number for future reference.

License Number
5515501201067
License date
Mar 24, 2023

Licensed Content

Licensed Content Publisher
Elsevier
Licensed Content Publication
International Journal of Adhesion and Adhesives
Licensed Content Title
Quantification of mixed mode loading and bond line thickness on adhesive joint strength using novel test specimen geometry
Licensed Content Author
Brock Watson,Michael J. Worswick,Duane S. Cronin
Licensed Content Date
Oct 1, 2020
Licensed Content Volume
102
Licensed Content Issue
n/a
Licensed Content Pages
1

Order Details

Type of Use
reuse in a thesis/dissertation
Portion
figures/tables/illustrations
Number of figures/tables/illustrations
4
Format
both print and electronic
Are you the author of this Elsevier article?
No
Will you be translating?
No

About Your Work

Title Experimental Assessment and Computational Modeling of Adhesive, Self Piercing Rivets (SPR), and Hybrid (Adhesive-SPR) Joints: Enhancing Joint Performance for Aluminum Sheet Material
Institution name University of Waterloo
Expected presentation date Jun 2023

Additional Data

Portions Figures 2,3,5 and 6

License Number
5515501498596
License date
Mar 24, 2023

Licensed Content

Licensed Content Publisher
Elsevier
Licensed Content Publication
International Journal of Adhesion and Adhesives
Licensed Content Title
Modeling of high strength steel joints bonded with toughened adhesive for vehicle crash simulations
Licensed Content Author
Xin Yang,Yong Xia,Qing Zhou,Pei-Chung Wang,Kathy Wang
Licensed Content Date
Dec 1, 2012
Licensed Content Volume
39
Licensed Content Issue
n/a
Licensed Content Pages
12

Order Details

Type of Use
reuse in a thesis/dissertation
Portion
figures/tables/illustrations
Number of figures/tables/illustrations
3
Format
both print and electronic
Are you the author of this Elsevier article?
No
Will you be translating?
No

About Your Work

Title Experimental Assessment and Computational Modeling of Adhesive, Self Piercing Rivets (SPR), and Hybrid (Adhesive-SPR) Joints: Enhancing Joint Performance for Aluminum Sheet Material
Institution name University of Waterloo
Expected presentation date Jun 2023

Additional Data

Portions Figures 20, 22 and 23

This Agreement between University of Waterloo -- Ahmed Ibrahim ("You") and Elsevier ("Elsevier") consists of your license details and the terms and conditions provided by Elsevier and Copyright Clearance Center.

Your confirmation email will contain your order number for future reference.

License Number
5515510201122
License date
Mar 24, 2023

Licensed Content

Licensed Content Publisher
Elsevier
Licensed Content Publication
Thin-Walled Structures
Licensed Content Title
Dynamic crush behavior of adhesive-bonded aluminum tubular structure—Experiment and numerical simulation
Licensed Content Author
Minoru Yamashita,Hiromasa Kenmotsu,Toshio Hattori
Licensed Content Date
Aug 1, 2013
Licensed Content Volume
69
Licensed Content Issue
n/a
Licensed Content Pages
9

Order Details

Type of Use
reuse in a thesis/dissertation
Portion
figures/tables/illustrations
Number of figures/tables/illustrations
2
Format
both print and electronic
Are you the author of this Elsevier article?
No
Will you be translating?
No

About Your Work

Title Experimental Assessment and Computational Modeling of Adhesive, Self Piercing Rivets (SPR), and Hybrid (Adhesive-SPR) Joints: Enhancing Joint Performance for Aluminum Sheet Material
Institution name University of Waterloo
Expected presentation date Jun 2023

Additional Data

Portions Figures 22 and 23

This Agreement between University of Waterloo -- Ahmed Ibrahim ("You") and Elsevier ("Elsevier") consists of your license details and the terms and conditions provided by Elsevier and Copyright Clearance Center.

Your confirmation email will contain your order number for future reference.

License Number
5515510350411
License date
Mar 24, 2023

Licensed Content

Licensed Content Publisher
Elsevier
Licensed Content Publication
Engineering Fracture Mechanics
Licensed Content Title
Rate dependent behavior of crash-optimized adhesives – Experimental characterization, model development, and simulation
Licensed Content Author
Michael May,Olaf Hesebeck,Stephan Marzi,Wolfgang Böhme,Jörg Lienhard,Sebastian Kilchert,Markus Brede,Stefan Hiermaier
Licensed Content Date
Jan 1, 2015
Licensed Content Volume
133
Licensed Content Issue
n/a
Licensed Content Pages
26

Order Details

Type of Use
reuse in a thesis/dissertation
Portion
figures/tables/illustrations
Number of figures/tables/illustrations
3
Format
both print and electronic
Are you the author of this Elsevier article?
No
Will you be translating?
No

About Your Work

Title Experimental Assessment and Computational Modeling of Adhesive, Self Piercing Rivets (SPR), and Hybrid (Adhesive-SPR) Joints: Enhancing Joint Performance for Aluminum Sheet Material
Institution name University of Waterloo
Expected presentation date Jun 2023

Additional Data

Portions Figures 28, 29 and 30

Self-piercing riveting-a review

Author:
Dezhi Li et al
Publication:
The International Journal of Advanced Manufacturing Technology
Publisher:
Springer Nature
Date:
Mar 20, 2017

Creative Commons

This Agreement between University of Waterloo -- Ahmed Ibrahim ("You") and Elsevier ("Elsevier") consists of your license details and the terms and conditions provided by Elsevier and Copyright Clearance Center.

Your confirmation email will contain your order number for future reference.

License Number
5515531161507
License date
Mar 24, 2023

Licensed Content

Licensed Content Publisher
Elsevier
Licensed Content Publication
Journal of Materials Processing Technology
Licensed Content Title
Mechanism of superiority of fatigue strength for aluminium alloy sheets joined by mechanical clinching and self-pierce riveting
Licensed Content Author
K. Mori,Y. Abe,T. Kato
Licensed Content Date
Sep 1, 2012
Licensed Content Volume
212
Licensed Content Issue
9
Licensed Content Pages
6

Order Details

Type of Use
reuse in a thesis/dissertation
Portion
figures/tables/illustrations
Number of figures/tables/illustrations
2
Format
both print and electronic
Are you the author of this Elsevier article?
No
Will you be translating?
No

About Your Work

Title Experimental Assessment and Computational Modeling of Adhesive, Self Piercing Rivets (SPR), and Hybrid (Adhesive-SPR) Joints: Enhancing Joint Performance for Aluminum Sheet Material
Institution name University of Waterloo
Expected presentation date Jun 2023

Additional Data

Portions Figures 5 and 7

This Agreement between University of Waterloo -- Ahmed Ibrahim ("You") and Elsevier ("Elsevier") consists of your license details and the terms and conditions provided by Elsevier and Copyright Clearance Center.

Your confirmation email will contain your order number for future reference.

License Number

5515531401284

License date

Mar 24, 2023

Licensed Content

Licensed Content Publisher

Elsevier

Licensed Content Publication

Thin-Walled Structures

Licensed Content Title

Macroscopic modelling of flow-drill screw connections in thin-walled aluminium structures

Licensed Content Author

Johan Kolstø Sønstabø,David Morin,Magnus Langseth

Licensed Content Date

Aug 1, 2016

Licensed Content Volume

105

Licensed Content Issue

n/a

Licensed Content Pages

22

Order Details

Type of Use

reuse in a thesis/dissertation

Portion

figures/tables/illustrations

Number of figures/tables/illustrations

1

Format

both print and electronic

Are you the author of this Elsevier article?

No

Will you be translating?

No

About Your Work

Title Experimental Assessment and Computational Modeling of Adhesive, Self Piercing Rivets (SPR), and Hybrid (Adhesive-SPR) Joints: Enhancing Joint Performance for Aluminum Sheet Material

Institution name University of Waterloo

Expected presentation date Jun 2023

Additional Data

Portions Figure 1

Your confirmation email will contain your order number for future reference.

License Number
5515550385708

License date
Mar 24, 2023

Licensed Content

Licensed Content Publisher
Elsevier

Licensed Content Publication
Thin-Walled Structures

Licensed Content Title
Crushing test of double hat-shaped members of dissimilar materials with adhesively bonded and self-piercing riveted joining methods

Licensed Content Author
Myeong-Han Lee,Heon-Young Kim,Soo-Ik Oh

Licensed Content Date
Apr 1, 2006

Licensed Content Volume
44

Licensed Content Issue
4

Licensed Content Pages
6

Order Details

Type of Use
reuse in a thesis/dissertation

Portion
figures/tables/illustrations

Number of figures/tables/illustrations
3

Format
both print and electronic

Are you the author of this Elsevier article?
No

Will you be translating?
No

About Your Work

Title Experimental Assessment and Computational Modeling of Adhesive, Self Piercing Rivets (SPR), and Hybrid (Adhesive-SPR) Joints: Enhancing Joint Performance for Aluminum Sheet Material

Institution name University of Waterloo

Expected presentation date Jun 2023

Additional Data

Portions Figures 2,3 and 7

This Agreement between University of Waterloo -- Ahmed Ibrahim ("You") and Elsevier ("Elsevier") consists of your license details and the terms and conditions provided by Elsevier and Copyright Clearance Center.

Your confirmation email will contain your order number for future reference.

License Number

5515550663218

License date

Mar 24, 2023

Licensed Content

Licensed Content Publisher

Elsevier

Licensed Content Publication

International Journal of Solids and Structures

Licensed Content Title

Structural behaviour of aluminium self-piercing riveted joints: An experimental and numerical investigation

Licensed Content Author

N.-H. Hoang,A.-G. Hanssen,M. Langseth,R. Porcaro

Licensed Content Date

Nov 15, 2012

Licensed Content Volume

49

Licensed Content Issue

23-24

Licensed Content Pages

13

Order Details

Type of Use

reuse in a thesis/dissertation

Portion

figures/tables/illustrations

Number of figures/tables/illustrations

2

Format

both print and electronic

Are you the author of this Elsevier article?

No

Will you be translating?

No

About Your Work

Title Experimental Assessment and Computational Modeling of Adhesive, Self Piercing Rivets (SPR), and Hybrid (Adhesive-SPR) Joints: Enhancing Joint Performance for Aluminum Sheet Material

Institution name University of Waterloo

Expected presentation date Jun 2023

Additional Data

Portions Figures 1 and 10

A novel tests set-up for validation of connector models subjected to static and impact loadings

Author:
Matthias Reil,David Morin,Magnus Langseth,Octavian Knoll
Publication:
International Journal of Impact Engineering
Publisher:
Elsevier
Date:
December 2021

Creative Commons

Taylor & Francis
Taylor & Francis Group
The Journal of Adhesion

Mode I traction-separation measured using rigid double cantilever beam applied to structural adhesive

Author:
Brock Watson, , Chi-Hsiang Liao, et al
Publication:
Journal of Adhesion
Publisher:
Taylor & Francis
Date:
Jun 10, 2020
Rights managed by Taylor & Francis

Thesis/Dissertation Reuse Request

Taylor & Francis is pleased to offer reuses of its content for a thesis or dissertation free of charge contingent on resubmission of permission request if work is published.

From: PermissionsFrance <permissionsfrance@elsevier.com>
Sent: Monday, May 15, 2023 12:56 PM
To: Ahmed Ibrahim <ahmed.ibrahim1@uwaterloo.ca>
Subject: RE: Request to reuse figures

Dear,
As per your request below, we hereby grant you permission to reprint the material detailed in your request at no charge **in your thesis** subject to the following conditions:

1.If any part of the material to be used (for example, figures) has appeared in our publication with credit or acknowledgement to another source, permission must also be sought from that source. If such permissions are not obtained then that materials may not be included in your publication.
2.Any modification of the material is likely to harm the moral right of the authors and therefore should be first submitted and approved by the authors who are the sole owner of the moral right.
3.Suitable and visible acknowledgement to the source must be made, either as a footnote or in a reference list at the end of your publication
4.Your thesis may be submitted to your institution in either print or electronic form.
5.Reproduction of this material is confined to the purpose for which permission is hereby given.
6.This permission is granted for non-exclusive world **English** rights only. For other languages please reapply separately for each one required. Permission excludes use in an electronic form other than submission. Should you have a specific electronic project in mind please reapply for permission.
7.Should your thesis be published commercially, please reapply for permission.
Yours sincerely,
Permissions France

A large-scale finite element point-connector model for self-piercing rivet connections

Author:
A.G. Hanssen,L. Olovsson,R. Porcaro,M. Langseth
Publication:
European Journal of Mechanics - A/Solids
Publisher:
Elsevier
Date:
July–August 2010

References

3M, 2016. 3M^{TM} Impact Resistant Structural Adhesive 07333 / 57333 Technical Data Sheet [WWW Document]. (accessed 10.11.22).

3M, 2022. 3M^{TM} Impact Resistant Structural Adhesive 07333 / 57333 Safety Data Sheet [WWW Document]. (accessed 12.07.23).

Abrahami, S.T., de Kok, J.M.M., Terryn, H., Mol, J.M.C., 2017. Towards Cr(VI)-free anodization of aluminum alloys for aerospace adhesive bonding applications: A review. Front. Chem. Sci. Eng. 11, 465–482.

Adams, R., 1990. Failure strength tests and their limitations. In: Materials, A.S. for (Ed.), Engineered Materials Handbook. Metals Park, pp. 325–335.

Adams, R., Comyn, J., Wake, W., 1988. Structural adhesives in engineering, International Journal of Adhesion and Adhesives. Chapman and Hall.

Adams, R.D., Coppendale, J., 1979. The Stress-Strain Behaviour of Axially-Loaded Butt Joints. J. Adhes. 10, 49–62.

Adibeig, M.R., Marami, G., Saeimi-Sadigh, M.A., da Silva, L.F.M., 2020. Experimental and numerical study of polyethylene hybrid joints: Friction stir spot welded joints reinforced with adhesive. Int. J. Adhes. Adhes. 98, 102555.

Alfano, M., Lubineau, G., Furgiuele, F., Paulino, G.H., 2012. Study on the role of laser surface irradiation on damage and decohesion of Al/epoxy joints. Int. J. Adhes. Adhes. 39, 33–41.

Arnold, B., Altenhof, W., 2005. Finite element modeling of the axial crushing of AA6061 T4 and T6 and AA6063 T5 structural square tubes with circular discontinuities. SAE Tech. Pap.

ASTM E8/E8M, 2016. standard test methods for tension testing of metallic materials. ASTM Stand.

Bagheri, R., Pearson, R.A., 1996. Role of particle cavitation in rubber-toughened epoxies: 1. Microvoid toughening. Polymer (Guildf). 37, 4529–4538.

Bala, S., Day, J., 2012. General guidelines for crash analysis in LS-DYNA. Livermore Softw. Technol. Corp.

Banea, M.D., Da Silva, L.F.M., 2010. The effect of temperature on the mechanical properties of adhesives for the automotive industry. Proc. Inst. Mech. Eng. Part L J. Mater. Des. Appl. 224, 51–62.

Banea, M.D., Rosioara, M., Carbas, R.J.C., da Silva, L.F.M., 2018. Multi-material adhesive joints for automotive industry. Compos. Part B Eng. 151, 71–77.

Barbosa, A.Q., Da Silva, L.F.M., Banea, M.D., Öchsner, A., 2016. Methods to increase the toughness of structural adhesives with micro particles: An overview with focus on cork particles. Materwiss. Werksttech. 47, 307–325.

Bascom, W.D., Cottington, R.L., 1976. Effect of Temperature on the Adhesive Fracture Behavior of an Elastomer-Epoxy Resin. J. Adhes. 7, 333–346.

Beule, F., Teutenberg, D., Meschut, G., 2022. Directional dependence of the mechanical properties of structural adhesive joints with curing-induced pre-deformations. Proc. Inst. Mech. Eng. Part D J. Automob. Eng.

Bier, M., Sommer, S., 2013. Simplified modeling of self-piercing riveted joints for crash simulation with a modified version of *CONSTRAINED_INTERPOLATION_SPOTWELD. 9th Eur. LS-DYNA Conf.

Blackman, B.R.K., Hadavinia, H., Kinloch, A.J., Paraschi, M., Williams, J.G., 2003. The calculation of adhesive fracture energies from double-cantilever beam and tapered double cantilever beam test specimens. Eng. Fract. Mech. 70, 233–248.

Blackman, B.R.K., Kinloch, A.J., Paraschi, M., 2005. The determination of the mode II adhesive fracture resistance, GIIC, of structural adhesive joints: An effective crack length approach. Eng. Fract. Mech. 72, 877–897.

Boqaileh, K., 2015. Experimental Testing and Modelling of Adhesively Joined T-structures. University of Waterloo.

Borges, C.S.P., Marques, E.A.S., Carbas, R.J.C., Ueffing, C., Weißgraeber, P., Silva, L.F.M.D., 2021. Review on the effect of moisture and contamination on the interfacial properties of adhesive joints. Proc. Inst. Mech. Eng. Part C J. Mech. Eng. Sci. 235, 527–549.

Boutar, Y., Naïmi, S., Mezlini, S., Ali, M.B.S., 2016. Effect of surface treatment on the shear strength of aluminium adhesive single-lap joints for automotive applications. Int. J. Adhes. Adhes. 67, 38–43.

Braun, R., 2005. Effect of thermal exposure on the microstructure, tensile properties and the corrosion behaviour of 6061 aluminium alloy sheet. Mater. Corros. 56, 159–165.

Campbell, F.C., 2008. Elements of Metallurgy and Engineering Alloys, ASM International.

Campbell, F.C.C., 2004. Chapter 8 - Adhesive Bonding and Integrally Cocured Structure: A Way to Reduce Assembly Costs through Parts Integration. In: Campbell, F.C. (Ed.), Manufacturing Processes for Advanced Composites. Elsevier Science, Amsterdam, pp. 241–301.

Campilho, R.D.S.G., Banea, M.D., Neto, J.A.B.P., Da Silva, L.F.M., 2012. Modelling of single-lap joints using cohesive zone models: Effect of the cohesive parameters on the output of the simulations. J. Adhes. 88, 513–533.

Campilho, R.D.S.G., Banea, M.D., Neto, J.A.B.P., Da Silva, L.F.M., 2013. Modelling adhesive joints with cohesive zone models: Effect of the cohesive law shape of the adhesive layer. Int. J. Adhes. Adhes. 44, 48–56.

Campilho, R.D.S.G., Banea, M.D., Pinto, A.M.G., Da Silva, L.F.M., De Jesus, A.M.P., 2011. Strength prediction of single- and double-lap joints by standard and extended finite element modelling. Int. J. Adhes. Adhes. 31, 363–372.

Carandente, M., Dashwood, R.J., Masters, I.G., Han, L., 2016. Improvements in numerical simulation of the SPR process using a thermo-mechanical finite element analysis. J. Mater.

Process. Technol. 236, 148–161.

Carbas, R.J.C., Marques, E.A.S., Da Silva, L.F.M., Lopes, A.M., 2014. Effect of cure temperature on the glass transition temperature and mechanical properties of epoxy adhesives. J. Adhes. 90, 104–119.

Cavezza, F., Boehm, M., Terryn, H., Hauffman, T., 2020. A review on adhesively bonded aluminium joints in the automotive industry. Metals (Basel). 10, 1–32.

Choi, W., Tuteja, A., Mabry, J.M., Cohen, R.E., McKinley, G.H., 2009. A modified Cassie-Baxter relationship to explain contact angle hysteresis and anisotropy on non-wetting textured surfaces. J. Colloid Interface Sci. 339, 208–216.

Ciardiello, R., Greco, L., Miranda, M., Sciullo, F. Di, Goglio, L., 2020. Experimental investigation on adhesively bonded U-shaped metallic joints using the Arcan test. J. Adv. Join. Process. 1, 100010.

Cognard, J.Y., 2008. Numerical analysis of edge effects in adhesively-bonded assemblies application to the determination of the adhesive behaviour. Comput. Struct. 86, 1704–1717.

Cognard, J.Y., Créac'hcadec, R., Sohier, L., Davies, P., 2008. Analysis of the nonlinear behavior of adhesives in bonded assemblies-Comparison of TAST and Arcan tests. Int. J. Adhes. Adhes. 28, 393–404.

Cox, R.G., 1983. The spreading of a liquid on a rough solid surface. J. Fluid Mech. 131, 1–26.

Crook, R.A., Sinclair, J.W., Poulter, L.W., Schulte, K.J., 1998. An environmentally-friendly process for bonding aluminum using aqueous metasilicate sol-gel and silane adhesion promoters. J. Adhes. 68, 315–329.

Cui, J., Wang, Shuhao, Wang, Shaoluo, Chen, S., Li, G., 2020. Strength and failure analysis of adhesive single-lap joints under shear loading: Effects of surface morphologies and overlap zone parameters. J. Manuf. Process. 56, 238–247.

Czerwinski, F., 2021. Current trends in automotive lightweighting strategies and materials. Materials (Basel). 14.

da Silva, L.F.M., Campilho, R.D.S.G., 2012. Advances in numerical modelling of adhesive joints, SpringerBriefs in Applied Sciences and Technology. Springer Berlin Heidelberg, Berlin, Heidelberg.

da Silva, L.F.M., Carbas, R.J.C., Critchlow, G.W., Figueiredo, M.A.V., Brown, K., 2009. Effect of material, geometry, surface treatment and environment on the shear strength of single lap joints. Int. J. Adhes. Adhes. 29, 621–632.

da Silva, L.F.M., Critchlow, G.W., Figueiredo, M.A. V., 2008. Parametric Study of Adhesively Bonded Single Lap Joints by the Taguchi Method. J. Adhes. Sci. Technol. 22, 1477–1494.

da Silva, L.F.M., Öchsner, A., Adams, R.D., 2018. Handbook of Adhesion Technology: Second Edition, Handbook of Adhesion Technology: Second Edition. Springer Heidelberg.

Dagorn, N., Portemont, G., Joudon, V., Bourel, B., Lauro, F., 2020. Fracture rate dependency of an adhesive under dynamic loading. Eng. Fract. Mech. 235, 107082.

Davies, P., Sohier, L., Cognard, J.Y., Bourmaud, A., Choqueuse, D., Rinnert, E., Créac'hcadec, R., 2009. Influence of adhesive bond line thickness on joint strength. Int. J. Adhes. Adhes. 29, 724–736.

Di Franco, G., Fratini, L., Pasta, A., 2012. Influence of the distance between rivets in self-piercing riveting bonded joints made of carbon fiber panels and AA2024 blanks. Mater. Des. 35, 342–349.

Di Franco, G., Fratini, L., Pasta, A., 2013. Analysis of the mechanical performance of hybrid (SPR/bonded) single-lap joints between CFRP panels and aluminum blanks. Int. J. Adhes. Adhes. 41, 24–32.

Di Franco, Giuseppe, Fratini, L., Pasta, A., Ruisi, V.F., 2013. On the self-piercing riveting of aluminium blanks and carbon fibre composite panels. Int. J. Mater. Form. 6, 137–144.

Dillard, D.A., 2010. Advances in structural adhesive bonding, Advances in Structural Adhesive Bonding. Woodhead Publishing.

dos Reis, M.Q., Banea, M.D., da Silva, L.F.M., Carbas, R.J.C., 2019. Mechanical characterization of a modern epoxy adhesive for automotive industry. J. Brazilian Soc. Mech. Sci. Eng. 41, 1–11.

El-Batahgy, A., Kutsuna, M., 2009. Laser beam welding of AA5052, AA5083, and AA6061 aluminum alloys. Adv. Mater. Sci. Eng. 2009.

El Zaroug, M., Kadioglu, F., Demiral, M., Saad, D., 2018. Experimental and numerical investigation into strength of bolted, bonded and hybrid single lap joints: Effects of adherend material type and thickness. Int. J. Adhes. Adhes. 87, 130–141.

Erhart, T., Borrvall, T., 2013. Drilling rotation constraint for shell elements in implicit and explicit analyses. 9th Eur. LS-DYNA Conf. 2013 8.

European Aluminum Association (EAA), 2013. Aluminium in Cars. Unlocking the Light-Weighting Potential. J. Chem. Inf. Model. 53, 1689–1699.

Ezzine, M.C., Amiri, A., Tarfaoui, M., Madani, K., 2018. Damage of bonded, riveted and hybrid (bonded/riveted) joints, Experimental and numerical study using CZM and XFEM methods. Adv. Aircr. Spacecr. Sci. 5, 595–613.

Fink, A., Camanho, P.P., Andrés, J.M., Pfeiffer, E., Obst, A., 2010. Hybrid CFRP/titanium bolted joints: Performance assessment and application to a spacecraft payload adaptor. Compos. Sci. Technol. 70, 305–317.

Fu, M., Mallick, P.K., 2003. Fatigue of self-piercing riveted joints in aluminum alloy 6111. Int. J. Fatigue 25, 183–189.

Goglio, L., Peroni, L., Peroni, M., Rossetto, M., 2008. High strain-rate compression and tension behaviour of an epoxy bi-component adhesive. Int. J. Adhes. Adhes. 28, 329–339.

Gonçalves, J.P.M., De Moura, M.F.S.F., De Castro, P.M.S.T., 2002. A three-dimensional finite element model for stress analysis of adhesive joints. Int. J. Adhes. Adhes. 22, 357–365.

Gould, J.E., 2012. Joining aluminum sheet in the automotive industry - A 30 year history. Weld. J. 91.

Gowda, S., Deb, A., Kurnool, G., Chou, C., 2017. Prediction of the Behaviors of Adhesively Bonded Steel Hat Section Components under Axial Impact Loading. SAE Tech. Pap. 2017-March.

Gowda, S., Deb, A., Kurnool, G., Chou, C.C., 2018. Behavior of Adhesively Bonded Steel Double-Hat Section Components under Lateral Impact Loading. SAE Tech. Pap. 2018-April, 1–8.

Grujicic, M., Snipes, J.S., Ramaswami, S., Abu-Farha, F., 2014. Self-Piercing Riveting Process and Joint Modeling and Simulations. Solids Struct. 3.

Gulavani, O., Hughes, K., Vignjevic, R., 2014. Explicit dynamic formulation to demonstrate compliance against quasi-static aircraft seat certification loads (CS25.561) -Part I: Influence of time and mass scaling. Proc. Inst. Mech. Eng. Part G J. Aerosp. Eng. 228, 1982–1995.

Hahn, O., Meschut, G., Bergau, M., Matzke, M., 2014. Self-pierce riveting and hybrid joining of boron steels in multi-material and multi-sheet joints. Procedia CIRP 18, 192–196.

Hahn, O., Wibbeke, T.M., 2005. Application of low-heat hybrid joining technologies for the joining of thin-walled sheet materials. Weld. Cut. 4, 208–214.

Han, L., Thornton, M., Shergold, M., 2010. A comparison of the mechanical behaviour of self-piercing riveted and resistance spot welded aluminium sheets for the automotive industry. Mater. Des. 31, 1457–1467.

Hanssen, A.G., Olovsson, L., Porcaro, R., Langseth, M., 2010. A large-scale finite element point-connector model for self-piercing rivet connections. Eur. J. Mech. A/Solids 29, 484–495.

Haque, R., 2018. Quality of self-piercing riveting (SPR) joints from cross-sectional perspective:

A review. Arch. Civ. Mech. Eng.

Haque, R., Durandet, Y., 2016. Strength prediction of self-pierce riveted joint in cross-tension and lap-shear. Mater. Des. 108, 666–678.

Haque, R., Durandet, Y., 2017. Investigation of self-pierce riveting (SPR) process data and specific joining events. J. Manuf. Process. 30, 148–160.

Haque, R., Wong, Y.C., Paradowska, A., Blacket, S., Durandet, Y., 2017. SPR characteristics curve and distribution of residual stress in self-piercing riveted joints of steel sheets. Adv. Mater. Sci. Eng. 2017.

Harintho, H., Gould, P.L., 1991. Static and dynamic analyses of plates and shells: theory, software and applications, Engineering Structures.

Harris, A.F., Beevers, A., 1999. Effects of grit-blasting on surface properties for adhesion. Int. J. Adhes. Adhes. 19, 445–452.

Harris, J.A., Adams, R.A., 1984. Strength prediction of bonded single lap joints by non-linear finite element methods. Int. J. Adhes. Adhes. 4, 65–78.

Hartlen, D.C., Montesano, J., Cronin, D.S., 2020. Cohesive Zone Modeling of Adhesively Bonded Interfaces: The Effect of Adherend Geometry, Element Selection, and Loading Condition. 6 th Int. LS-DYNA ® Users Conf. .

Henriksson, F., Johansen, K., 2016. On material substitution in automotive BIWs-From steel to aluminum body sides. Procedia CIRP 50, 683–688.

Hirsch, J., 2014. Recent development in aluminium for automotive applications. Trans. Nonferrous Met. Soc. China (English Ed. 24, 1995–2002.

Hoang, N.H., Hanssen, A.G., Langseth, M., Porcaro, R., 2012. Structural behaviour of aluminium self-piercing riveted joints: An experimental and numerical investigation. Int. J. Solids Struct. 49, 3211–3223.

Hoang, N.H., Hopperstad, O.S., Langseth, M., Westermann, I., 2013. Failure of aluminium self-piercing rivets: An experimental and numerical study. Mater. Des. 49, 323–335.

Hönsch, F., Domitner, J., Sommitsch, C., Götzinger, B., 2020. Modeling the Failure Behavior of Self-Piercing Riveting Joints of 6xxx Aluminum Alloy. J. Mater. Eng. Perform. 29, 4888–4897.

Hönsch, F., Domitner, J., Sommitsch, C., Götzinger, B., Kölz, M., 2018. Numerical simulation and experimental validation of self-piercing riveting (SPR) of 6xxx aluminium alloys for automotive applications. In: Journal of Physics: Conference Series.

Hu, P., Han, X., Li, W.D., Li, L., Shao, Q., 2013. Research on the static strength performance of adhesive single lap joints subjected to extreme temperature environment for automotive industry. Int. J. Adhes. Adhes. 41, 119–126.

Huang, L., Guo, H., Shi, Y., Huang, S., Su, X., 2017. Fatigue behavior and modeling of self-piercing riveted joints in aluminum alloy 6111. Int. J. Fatigue 100, 274–284.

Ibrahim, A.H., Cronin, D.S., 2021. Evaluation and Comparison of the Mechanical Performance of Adhesively Bonded and Self-Piercing Riveted Aluminum Joints Under Tension Loading. Conf. Proc. Soc. Exp. Mech. Ser. 7, 21–26.

Ibrahim, A.H., Cronin, D.S., 2022. Mechanical testing of adhesive, self-piercing rivet, and hybrid jointed aluminum under tension loading. Int. J. Adhes. Adhes. 113, 103066.

Ibrahim, A.H., Watson, B., Jahed, H., Rezaee, S., Royer, C., Cronin, D.S., 2023. Prediction of bonded asymmetric metallic cross-tension and single lap shear joints using finite element model with material-level adhesive properties and cohesive zone method. Int. J. Adhes. Adhes. 120, 103298.

Jäckel, M., Grimm, T., Falk, T., 2017. Process development for mechanical joining of 7xxx series aluminum alloys. In: European Aluminum Congress 2017. p. Paper 1, 17 pp.

Karachalios, E.F., Adams, R.D., da Silva, L.F.M., 2013a. Single lap joints loaded in tension with ductile steel adherends. Int. J. Adhes. Adhes. 43, 96–108.

Karachalios, E.F., Adams, R.D., da Silva, L.F.M., 2013b. Single lap joints loaded in tension with high strength steel adherends. Int. J. Adhes. Adhes. 43, 81–95.

Kaufmann, M., Flaig, F., Müller, M., Fricke, H., Vallée, T., 2023. International Journal of Adhesion and Adhesives How adhesives flow during joining. Int. J. Adhes. Adhes. 122, 103315.

Khanna, S.K., Long, X., Krishnamoorthy, S., Agrawal, H.N., 2006. Fatigue properties and failure characterisation of self-piercing riveted 6111 aluminium sheet joints. Sci. Technol. Weld. Join. 11, 544–549.

Khayer Dastjerdi, A., Tan, E., Barthelat, F., 2013. Direct Measurement of the Cohesive Law of Adhesives Using a Rigid Double Cantilever Beam Technique. Exp. Mech. 53, 1763–1772.

Kinloch, A.J., 1984. Adhesives in Engineering 211, 307–335.

Kinloch, A.J., 2003. Toughening epoxy adhesives to meet today’s challenges. MRS Bull. 28, 445–448.

Kinloch, A.J., Shaw, S.J., 1981. The Fracture Resistance of a Toughened Epoxy Adhesive. J. Adhes. 12, 59–77.

Kleinbaum, S., Jiang, C., Logan, S., 2019. Enabling sustainable transportation through joining of dissimilar lightweight materials. MRS Bull. 44, 608–612.

Koganti, R., Weishaar, J., 2009. Aluminum vehicle body construction and enabling manufacturing technologies. SAE Int. J. Mater. Manuf. 1, 491–502.

Kozbial, A., Li, Z., Conaway, C., McGinley, R., Dhingra, S., Vahdat, V., Zhou, F., Durso, B., Liu, H., Li, L., 2014. Study on the surface energy of graphene by contact angle measurements. Langmuir 30, 8598–8606.

Kubiak, K.J., Wilson, M.C.T., Mathia, T.G., Carval, P., 2011. Wettability versus roughness of engineering surfaces. Wear 271, 523–528.

Lanzerath, H., Pasligh, N., 2014. Benefit of Structural Adhesives in Full Car Crash Applications. SAE Tech. Pap. 2014-01–08.

LECONTE, N., BOUREL, B., LAURO, F., BADULESCU, C., MARKIEWICZ, E., 2020. Strength and failure of an aluminum/PA66 self-piercing riveted assembly at low and moderate loading rates: Experiments and modeling. Int. J. Impact Eng. 142, 103587.

Lee, C.J., Lee, J.M., Lee, K.H., Kim, D.H., Ryu, H.Y., Kim, B.M., 2014. Development of hybrid clinched structure by using multi-cohesive zone models. Int. J. Precis. Eng. Manuf. 15, 1015–1022.

Lee, M.H., Kim, H.Y., Oh, S.I., 2006. Crushing test of double hat-shaped members of dissimilar materials with adhesively bonded and self-piercing riveted joining methods. Thin-Walled Struct. 44, 381–386.

Leena, K., Athira, K.K., Bhuvaneswari, S., Suraj, S., Rao, V.L., 2016. Effect of surface pre-treatment on surface characteristics and adhesive bond strength of aluminium alloy. Int. J. Adhes. Adhes. 70, 265–270.

Lei, L., He, X., Zhao, D., Zhang, Y., Gu, F., Ball, A., 2018. Clinch-bonded hybrid joining for similar and dissimilar copper alloy, aluminium alloy and galvanised steel sheets. Thin-Walled Struct. 131, 393–403.

Li, B., Fatemi, A., 2006. An experimental investigation of deformation and fatigue behavior of coach peel riveted joints. Int. J. Fatigue 28, 9–18.

Li, D., Chrysanthou, A., Patel, I., Williams, G., 2017. Self-piercing riveting-a review. Int. J. Adv. Manuf. Technol. 92, 1777–1824.

Li, S., Bai, J., Wang, X., Song, L., Luo, K., Zuo, W., 2020. Equivalent substitution criteria of aluminum for steel and its application in automobile structures. Adv. Mech. Eng. 12, 1–17.

Liao, C.H., Watson, B., Worswick, M.J., Cronin, D.S., 2018. Mode I rigid double cantilever beam test and analysis applied to structural adhesives. Conf. Proc. Soc. Exp. Mech. Ser. 1, 73–81.

Licari, J.J., Swanson, D.W., 2005. 6 - Reliability. In: Licari, J.J., Swanson, D.W. (Eds.), Adhesives Technology for Electronic Applications, Materials and Processes for Electronic Applications. William Andrew Publishing, Norwich, NY, pp. 347–391.

Liu, M., Dawood, M., 2017. Reliability analysis of adhesively bonded CFRP-to-steel double lap shear joint with thin outer adherends. Constr. Build. Mater. 141, 52–63.

Liu, Y.B., 2019. Application of a Rate Dependent Cohesive Zone Model to Predict Impact Response in Adhesively Bonded Ultra-High Strength Steel Tubes.

Lorenz, D., Haufe, A., 2008. Recent Advances and New Developments in Hot Forming Simulation with LS-DYNA 21–30.

Luk, J.M., Kim, H.C., De Kleine, R.D., Wallington, T.J., MacLean, H.L., 2018. Greenhouse gas emission benefits of vehicle lightweighting: Monte Carlo probabalistic analysis of the multi material lightweight vehicle glider. Transp. Res. Part D Transp. Environ. 62, 1–10.

Mallick, P.K., 2020. Optimization of Structural Adhesive Joints. Struct. Adhes. Joints Des. Anal. Test. 79–96.

Marzi, S., Ramon-Villalonga, L., Poklitar, M., Kleiner, F., 2008. Usage of cohesive elements in crash analysis of large, bonded vehicle structures. Experimental tests and simulation. Ger. LS-Dyna Forum.

May, M., Hesebeck, O., Marzi, S., Böhme, W., Lienhard, J., Kilchert, S., Brede, M., Hiermaier, S., 2015. Rate dependent behavior of crash-optimized adhesives - Experimental characterization, model development, and simulation. Eng. Fract. Mech. 133, 112–137.

McMurray, H.N., Holder, A., Williams, G., Scamans, G.M., Coleman, A.J., 2010. The kinetics and mechanisms of filiform corrosion on aluminium alloy AA6111. Electrochim. Acta 55, 7843–7852.

Meschut, G., Hahn, O., Janzen, V., Olfermann, T., 2014a. Innovative joining technologies for multi-material structures. Weld. World 58, 65–75.

Meschut, G., Janzen, V., Olfermann, T., 2014b. Innovative and highly productive joining technologies for multi-material lightweight car body structures. J. Mater. Eng. Perform. 23, 1515–1523.

Meschut, Gerson, Matzke, M., Hoerhold, R., Olfermann, T., 2014. Hybrid technologies for joining ultra-high-strength boron steels with aluminum alloys for lightweight car body structures. In: Procedia CIRP. pp. 19–23.

Michalos, G., Makris, S., Papakostas, N., Mourtzis, D., Chryssolouris, G., 2010. Automotive assembly technologies review: challenges and outlook for a flexible and adaptive approach. CIRP J. Manuf. Sci. Technol. 2, 81–91.

Miturska-Barańska, I., Rudawska, A., Doluk, E., 2021. The influence of sandblasting process parameters of aerospace aluminium alloy sheets on adhesive joints strength. Materials (Basel). 14.

Modi, S., Vadhavkar, A., 2019. Technology Roadmap : Materials and Manufacturing. Cent. Automot. Res. Ann Arbor, MI 16.

Mori, K., Abe, Y., Kato, T., 2012. Mechanism of superiority of fatigue strength for aluminium alloy sheets joined by mechanical clinching and self-pierce riveting. J. Mater. Process. Technol. 212, 1900–1905.

Mori, K. ichiro, Abe, Y., 2018. A review on mechanical joining of aluminium and high strength steel sheets by plastic deformation. Int. J. Light. Mater. Manuf. 1, 1–11.

Morin, D., Bourel, B., Bennani, B., Lauro, F., Lesueur, D., 2013. A new cohesive element for structural bonding modelling under dynamic loading. Int. J. Impact Eng. 53, 94–105.

Mortimer, J., 2006. Jaguar uses castings, extrusions to reduce parts count in new sports car. Assem. Autom. 26, 115–120.

Nguyen, N.T., Kim, D.Y., Kim, H.Y., 2011. Assessment of the failure load for an AA6061-T6 friction stir spot welding joint. Proc. Inst. Mech. Eng. Part B J. Eng. Manuf. 225, 1746–1756.

O’Keeffe, C., 2018. “Experimental determination and computational prediction of load-bearing behavior of spot-welded components made of sheet steel connections under crash loading with the help of engineering concepts”. FAT / AVIF A172, February 2004. Thesis. University of Waterloo.

Pagerit, S., Sharer, P., Rousseau, A., 2006. Fuel economy sensitivity to vehicle mass for advanced vehicle powertrains. SAE Tech. Pap.

Park, K., Paulino, G.H., 2011. Cohesive zone models: A critical review of traction-separation relationships across fracture surfaces. Appl. Mech. Rev. 64.

Pasligh, N., Schilling, R., Bulla, M., 2017. Modeling of Rivets Using a Cohesive Approach for Crash Simulation of Vehicles in RADIOSS. SAE Int. J. Transp. Saf. 5, 208–216.

Pearson, R.A., Yee, A.F., 1986. Toughening mechanisms in elastomer-modified epoxies - Part 2 Microscopy studies. J. Mater. Sci. 21, 2475–2488.

Pereira, A.M., Ferreira, J.A.M., Antunes, F. V., Bártolo, P.J., 2014. Assessment of the fatigue life of aluminium spot-welded and weld-bonded joints. J. Adhes. Sci. Technol. 28, 1432–1450.

Pinlung, S.B., 2015. 7xxx Aluminum Sheets for Automotive Applications. Masters Appl. Sci. Thesis. University of Windsor.

Pirondi, A., Moroni, F., 2009. Clinch-bonded and rivet-bonded hybrid joints: Application of damage models for simulation of forming and failure. J. Adhes. Sci. Technol. 23, 1547–1574.

Piwowarczyk, T., Korzeniowski, M., 2018. Quality analysis of hybrid adhesive-spot welded joints. J. Adhes. Sci. Technol. 32, 656–672.

Poorna Chander, K., Vashista, M., Sabiruddin, K., Paul, S., Bandyopadhyay, P.P., 2009. Effects of grit blasting on surface properties of steel substrates. Mater. Des. 30, 2895–2902.

Porcaro, R., Hanssen, A.G., Aalberg, A., Langseth, M., 2004. Joining of aluminium using self-piercing riveting: Testing, modelling and analysis. Int. J. Crashworthiness 9, 141–154.

Porcaro, R., Hanssen, A.G., Langseth, M., Aalberg, A., 2006. The behaviour of a self-piercing riveted connection under quasi-static loading conditions. Int. J. Solids Struct. 43, 5110–5131.

Prillhofer, R., Rank, G., Berneder, J., Antrekowitsch, H., Uggowitzer, P.J., Pogatscher, S., 2014. Property criteria for automotive Al-Mg-Si sheet alloys. Materials (Basel). 7, 5047–5068.

Reil, M., Morin, D., Langseth, M., Knoll, O., 2021. A novel tests set-up for validation of connector models subjected to static and impact loadings. Int. J. Impact Eng. 158, 103978.

Reis, P.N.B., Ferreira, J.A.M., Antunes, F., 2011. Effect of adherends rigidity on the shear strength of single lap adhesive joints. Int. J. Adhes. Adhes. 31, 193–201.

Ripling, E.J., Mostovoy, S., C orten, H.T., 1971. Fracture Mechanics: A Tool for Evaluating Structural Adhesives †. J. Adhes. 3, 107–123.

Ritter, G.W., 1999. Rapid adhesive bonding: Kinetics or process? Plast. Eng. 55, 65–68.

Romanov, V.S., Heidari-Rarani, M., Lessard, L., 2021. A parametric study on static behavior and load sharing of multi-bolt hybrid bonded/bolted composite joints. Compos. Part B Eng. 217, 108897.

Rudawska, A., Wahab, M.A., 2019. The effect of cataphoretic and powder coatings on the strength and failure modes of EN AW-5754 aluminium alloy adhesive joints. Int. J. Adhes. Adhes. 89, 40–50.

Sadowski, T., Golewski, P., Zarzeka-Raczkowska, E., 2011. Damage and failure processes of hybrid joints: Adhesive bonded aluminium plates reinforced by rivets. Comput. Mater. Sci. 50, 1256–1262.

Saleema, N., Gallant, D., 2013. Atmospheric pressure plasma oxidation of AA6061-T6 aluminum alloy surface for strong and durable adhesive bonding applications. Appl. Surf. Sci. 282, 98–104.

Saleema, N., Sarkar, D.K., Paynter, R.W., Gallant, D., Eskandarian, M., 2012. A simple surface treatment and characterization of AA 6061 aluminum alloy surface for adhesive bonding applications. Appl. Surf. Sci. 261, 742–748.

Sarda, C., 2017. Review: Self Piercing Riveting in Automotive Industry. Int. J. Res. Appl. Sci. Eng. Technol. V, 1749–1755.

Sauvage, J.B., Aufray, M., Jeandrau, J.P., Chalandon, P., Poquillon, D., Nardin, M., 2017. Using the 3-point bending method to study failure initiation in epoxide-aluminum joints. Int. J. Adhes. Adhes. 75, 181–189.

Schmidt, R.G., Bell, J.P., 1986. Epoxy Adhesion To Metals. Adv. Polym. Sci. 75, 33–71.

Sommer, S., Maier, J., 2011. Failure Modeling of a Self Piercing Riveted Joint Using Ls-Dyna. Dynalook.Com.

Sønstabø, J.K., Morin, D., Langseth, M., 2016. Macroscopic modelling of flow-drill screw connections in thin-walled aluminium structures. Thin-Walled Struct. 105, 185–206.

Spaggiari, A., Castagnetti, D., Dragoni, E., 2019. A design oriented multiaxial stress-based criterion for the strength assessment of adhesive layers. Compos. Part B Eng. 157, 66–75.

Staley, J.T., Lege, D.J., 1993. Advances in aluminum alloy products for structural applications in transportation. J. Phys. 3, 179–190.

Sun, G., Tian, J., Liu, T., Yan, X., Huang, X., 2018. Crashworthiness optimization of automotive parts with tailor rolled blank. Eng. Struct. 169, 201–215.

Sun, X., Khaleel, M.A., 2005. Performance optimization of self-piercing rivets through analytical rivet strength estimation. J. Manuf. Process. 7, 83–93.

Szewczak, A., Łagód, G., 2022. Adhesion of Modified Epoxy Resin to a Concrete Surface. Materials (Basel). 15.

Szymańska, J., Bakar, M., Białkowska, A., Kostrzewa, M., 2018. Study on the adhesive properties of reactive liquid rubber toughened epoxy-clay hybrid nanocomposites. J. Polym. Eng. 38, 231–238.

Tang, L.C., Wang, X., Wan, Y.J., Wu, L. Bin, Jiang, J.X., Lai, G.Q., 2013. Mechanical properties and fracture behaviors of epoxy composites with multi-scale rubber particles. Mater. Chem. Phys. 141, 333–342.

Tardif, N., Kyriakides, S., 2012. Determination of anisotropy and material hardening for aluminum sheet metal. Int. J. Solids Struct. 49, 3496–3506.

The Aluminium Association, 2015. International Alloy Designations and Chemical Composition Limits for Wrought Aluminum and Wrought Aluminum Alloys With Support for On-line Access From: Aluminum Extruders Council Use of the Information. Alum. Assoc. Arlington, Virginia 31.

Tisza, M., Czinege, I., 2018. Comparative study of the application of steels and aluminium in lightweight production of automotive parts. Int. J. Light. Mater. Manuf. 1, 229–238.

Tolton, C.J., 2020. Characterization of Spot Weld Failure within Weld Groups under Predominantly Shear Loading, Master's thesis. University of Waterloo.

Toyota Canada Inc., n.d. 2014 Lexus IS 250/350 Product Information [WWW Document]. URL http://media.lexus.ca/2014-lexus-is-driving-dynamics-244452 (accessed 1.29.23).

Trimiño, L.F., Cronin, D.S., 2016. Evaluation of Numerical Methods to Model Structural Adhesive Response and Failure in Tension and Shear Loading. J. Dyn. Behav. Mater. 2, 122–137.

Turon, A., Dávila, C.G., Camanho, P.P., Costa, J., 2007. An engineering solution for mesh size effects in the simulation of delamination using cohesive zone models. Eng. Fract. Mech. 74, 1665–1682.

Tvergaard, V., Hutchinson, J.W., 1992. The relation between crack growth resistance and fracture process parameters in elastic-plastic solids. J. Mech. Phys. Solids 40, 1377–1397.

Ufferman, B., Abke, T., Barker, M., Vivek, A., Daehn, G.S., 2018. Mechanical properties of joints in 5052 aluminum made with adhesive bonding and mechanical fasteners. Int. J. Adhes. Adhes. 83, 96–102.

Venables, J.D., McNamara, D.K., Chen, J.M., Sun, T.S., Hopping, R.L., 1979. Oxide morphologies on aluminum prepared for adhesive bonding. Appl. Surf. Sci. 3, 88–98.

Watson, B., Liao, C.H., Worswick, M.J., Cronin, D.S., 2018. Mode I traction-separation measured using rigid double cantilever beam applied to structural adhesive. J. Adhes. 96, 717–737.

Watson, B., Nandwani, Y., Worswick, M.J., Cronin, D.S., 2019. Metallic multi-material adhesive joint testing and modeling for vehicle lightweighting. Int. J. Adhes. Adhes. 95, 102421.

Watson, B., Worswick, M.J., Cronin, D.S., 2020. Quantification of mixed mode loading and bond line thickness on adhesive joint strength using novel test specimen geometry. Int. J. Adhes. Adhes. 102, 102682.

Weiland, J., Debruyne, S., Vandepitte, D., Pulm, M., Schiebahn, A., Reisgen, U., 2019. Stiffness and strength analysis of hybrid adhesive bonded–resistance spot welded sandwich samples by means of virtual FE testing. J. Adhes.

Wenzel, R.N., 1936. Resistance of solid surfaces to wetting by water. Ind. Eng. Chem. 28, 988–994.

Wong, W.A., 1984. Monotonic and cyclic fatigue properties of automotive aluminum alloys. SAE Tech. Pap.

Wu, G., Li, D., Shi, Y., Avery, K., Huang, L., Huang, S., Su, X., Peng, Y., 2018. Stress Analysis on the Single-Lap SPR-Adhesive Hybrid Joint. In: SAE Technical Papers. pp. 1–5.

Xu, Y., Li, H., Shen, Y., Liu, S., Wang, W., Tao, J., 2016. Improvement of adhesion performance between aluminum alloy sheet and epoxy based on anodizing technique. Int. J. Adhes. Adhes. 70, 74–80.

Yamashita, M., Kenmotsu, H., Hattori, T., 2013. Dynamic crush behavior of adhesive-bonded aluminum tubular structure - Experiment and numerical simulation. Thin-Walled Struct. 69, 45–53.

Yang, X., Xia, Y., Zhou, Q., Wang, P.C., Wang, K., 2012. Modeling of high strength steel joints bonded with toughened adhesive for vehicle crash simulations. Int. J. Adhes. Adhes. 39, 21–32.

Yao, L., Feng, Q., Wan, D., Wu, L., Yang, K., Hou, J., Liu, B., Wan, Q., 2017. Experiment and finite element simulation of high strength steel adhesive joint reinforced by rivet for automotive applications. J. Adhes. Sci. Technol. 31, 1617–1625.

Young, R.J., 1986. Relationship Between Structure and Mechanical Properties in Polydiacetylenes. Polym. Mater. Sci. Eng. Proc. ACS Div. Polym. Mater. 54, 656–660.

Zaeri, A.R., Saeidi Googarchin, H., 2019. Experimental investigation on environmental degradation of automotive mixed-adhesive joints. Int. J. Adhes. Adhes. 89, 19–29.

Zhang, F., Yang, X., Xia, Y., Zhou, Q., Wang, H.P., Yu, T.X., 2015. Experimental study of strain rate effects on the strength of adhesively bonded joints after hygrothermal exposure. Int. J. Adhes. Adhes. 56, 3–12.

Zhang, J. sheng, Zhao, X. hui, Zuo, Y., Xiong, J. ping, 2008. The bonding strength and corrosion resistance of aluminum alloy by anodizing treatment in a phosphoric acid modified boric acid/sulfuric acid bath. Surf. Coatings Technol. 202, 3149–3156.

Zhang, J., Wang, J., Yuan, Z., Jia, H., 2018. Effect of the cohesive law shape on the modelling of adhesive joints bonded with brittle and ductile adhesives. Int. J. Adhes. Adhes. 85, 37–43.

Zhang, J., Yang, S., 2015. Self-piercing riveting of aluminum alloy and thermoplastic composites. J. Compos. Mater. 49, 1493–1502.

Zhang, X., He, X., Xing, B., Zhao, L., Lu, Y., Gu, F., Ball, A., 2016. Influence of heat treatment on fatigue performances for self-piercing riveting similar and dissimilar titanium, aluminium and copper alloys. Mater. Des. 97, 108–117.

Zhang, Y., Dong, P., Pei, X., 2022. Fracture Mechanics Modeling of Fatigue Behaviors of Adhesive-Bonded Aluminum Alloy Components. Metals (Basel). 12.

Zhao, L., He, X., Xing, B., Lu, Y., Gu, F., Ball, A., 2015. Influence of sheet thickness on fatigue behavior and fretting of self-piercing riveted joints in aluminum alloy 5052. Mater. Des. 87, 1010–1017.

Zheng, R., Lin, J., Wang, P.C., Zhu, C., Wu, Y., 2015. Effect of adhesive characteristics on static strength of adhesive-bonded aluminum alloys. Int. J. Adhes. Adhes. 57, 85–94.

Appendix A

A.1 The Parameters of the SPR Constraint Model Required for FE Model Implementation

The parameters calibrated for each SPR rivet according to the joint sheet thickness are presented. The parameters tangential parameters were calibrated to the SLJ test, and the normal parameters were calibrated to the H-specimen test.

Table 42. *Constrained_SPR2 keyword card used in this study for SPR joints with 1 mm sheet thickness.

Variable	**mid**	**sid**	**nsid**	**thick**	**d**	**fn**	**ft**	**dn**
Value	3	1	6	2	9.0	1841	2952	2.0
Variable	**dt**	**xin**	**xit**	**alpha1**	**alpha2**	**alpha3**	**dens**	**intp**
Value	5.5	0.95	0.85	0.15	0.65	1.7	7.8e-9	0.0

Table 43. *Constrained_SPR2 keyword card used in this study for SPR joints with 2 mm sheet thickness.

Variable	**mid**	**sid**	**nsid**	**thick**	**d**	**fn**	**ft**	**dn**
Value	3	1	6	4	9.0	4530	7359	4.0
Variable	**dt**	**xin**	**xit**	**alpha1**	**alpha2**	**alpha3**	**dens**	**intp**
Value	6.0	0.85	0.5	0.55	0.8	1.0	7.8e-9	0.0

Table 44. *Constrained_SPR2 keyword card used in this study for SPR joints with 3 mm sheet thickness.

Variable	**mid**	**sid**	**nsid**	**thick**	**d**	**fn**	**ft**	**dn**
Value	3	1	6	6.36	9.0	6860	10250	1.5
Variable	**dt**	**xin**	**xit**	**alpha1**	**alpha2**	**alpha3**	**dens**	**intp**
Value	7.0	0.85	0.33	0.45	0.5	0.7	7.8e-9	0.0

A.2 Script Required to Adjust the Cohesive Element Orientation using Nodal Renumbering

```
namespace eval orientElems {

###swap the comment to create vectors instead of plotels.
    variable type element ;
#   variable type "vector"

    variable xScale 0.4 ; # scale factor for x relative to element size
    variable yScale 0.7 ; # scale for y in relation to x
    variable zScale 0.4 ; # scale for z in relation to x

#============================
#Warranty and Disclaimer
#============================
#Custom macros are is not part of the official HyperWorks installation.
#These tools do not pass any automated QA process.
#These tools are provided without warranty - the Altair Software License
Agreement (in particular 6) applies.
#The update of the tools to upcoming versions of HyperWorks is not mandatory.
#The support and maintenance of these tools is not obligatory.
    variable orientationType
    variable tabname "OrientElements"
    variable main
    variable orientationElement
    if {[info exist orientationElement]==0} {
      set orientationElement 0
    }

    if {[info exist orientationType]==0} {
      set orientationType ""
    }

    namespace eval math {
      proc ADD {x y} {
        if {[llength $y] == 1} {
          foreach X $x {
            lappend res [expr {$X + $y} ]
          }
        } else {
          foreach X $x Y $y {
            lappend res [expr {$X + $Y} ]
```

```
    }
  }
  return $res
}

proc SUB {x y} {
  if {[llength $y] == 1} {
    foreach X $x {
      lappend res [expr {$X - $y} ]
    }
  } else {
    foreach X $x Y $y {
      lappend res [expr {$X - $Y} ]
    }
  }
  return $res
}

proc DOT {x y} {
 set sum 0
  foreach X $x Y $y {
    set sum [expr {$sum + 1.0 * $X * $Y}]
  }
  return $sum
}

proc NORM {x {unit "dummy"}} {
# 2. Param = Einheitsvekor, Return=Laenge
upvar $unit res
   set n [expr {sqrt([DOT $x $x])}]
   if {$n == 0} {
     set res $x
   } else {
     set res [DIV $x $n]
   }
   return $n
}

proc DIV {x y } {
  foreach X $x {
    lappend res [expr {1.0 * $X / $y} ]
  }
  return $res
}
```

```
    proc MUL {x y} {
      foreach X $x {
        lappend res [expr {1.0 * $X * $y }]
      }
      return $res
    }


    proc CROSS {x y} {
     foreach {ax ay az} $x {}
     foreach {bx by bz} $y {}
     return [list  [expr {$ay * $bz - $az * $by}] \
                   [expr {$az * $bx - $ax * $bz}] \
                   [expr {$ax * $by - $ay * $bx}] ]
    }
  }


proc createSystems {{what ""} {tempType "none"}} {
  variable orientationElement
  variable reverseText
  variable type
  variable xScale
  variable yScale
  variable zScale
  if {$what ==""} {
    set orientationType ""
    *createmarkpanel elements 1 "Select elements"
    foreach e [hm_getmark elements 1] {
      set cfg [hm_getentityvalue elements $e config 0]
      if {$cfg == 208 || $cfg == 220} {
        set orientationType "Solid"
        break
      } elseif {$cfg == 104 || $cfg == 108} {
        set orientationType "Shell"
        break
      }
    }
    if {$orientationType==""} {
      return
    }
  } else {
    if {$tempType == "none"} {
```

```
        variable orientationType
      } else {
        set orientationType $tempType
      }
      if {$what =="one" || $what== "attached" || $what == ""} {
        if {$orientationElement==0 || $what == ""} {
          *createmarkpanel elements 1 "Select elements"
        } else {
          *createmark elements 1 $orientationElement
        }
        if {$what=="attached"} {
          *appendmark elements 1 "by attached"
        }
      } else {
        upvar $what eList
        eval *createmark elements 1 $eList
      }
    }
    if {$orientationType =="Shell"} {
      *createmark elements 2 "by config" 104 108
    } else {
      *createmark elements 2 "by config" 208 220
    }
    *markintersection elements 1 elements 2
    set allE [hm_getmark elements 1]
    if {[hm_marklength elements 1]==0} {
      return
    }
#    set vecSize [expr $xScale * [hm_getentityvalue elements [lindex $allE 0] shortestside 0]]
    lappend header "*filetype(ASCII)" "*version(10.0build60)"
    foreach e $allE {
      lappend header "*node(${e}0,[join [set centerArr($e) [hm_entityinfo centroid elements $e]] ","],0,0,0,0,0)"
    }
    *findmark elements 1 1 0 nodes 0 1
    foreach n [hm_getmark nodes 1] {
      set coordArr($n) [lindex [hm_nodevalue $n] 0]
    }
    if {$type == "vector"} {
      *createmark vectorcols 1 "^X" "^Y" "^Z"
      if {[hm_marklength vectorcols 1]>0} {
        *deletemark vectorcols 1
      }
```

```
      set VX [list "*vectorcollector(1,\"^X\",[hm_getdisplaycolor 18])"]
      set VY [list "*vectorcollector(2,\"^Y\",[hm_getdisplaycolor 19])"]
      set VZ [list "*vectorcollector(3,\"^Z\",[hm_getdisplaycolor 20])"]
    } else {
      *createmark comps 1 "^X" "^Y" "^Z"
      if {[hm_marklength comps 1]>0} {
        *deletemark comps 1
      }
      set VX [list "*component(1,\"^X\",0,[hm_getdisplaycolor 18],0)"]
      set VY [list "*component(2,\"^Y\",0,[hm_getdisplaycolor 19],0)"]
      set VZ [list "*component(3,\"^Z\",0,[hm_getdisplaycolor 20],0)"]
    }


    foreach e $allE {
      set vecSize [expr $xScale * [hm_getentityvalue elements $e shortestside 0]]
      set YSize [expr $vecSize * $yScale]
      set ZSize [expr $vecSize * $zScale]
      if {$orientationType =="Shell"} {
        foreach {n1 n2 n3 n4} [hm_nodelist $e] break
        math::NORM [math::SUB $coordArr($n3) $coordArr($n1)] w1
        math::NORM [math::SUB $coordArr($n2) $coordArr($n4)] w2
        math::NORM [math::ADD $w1 $w2] X
        math::NORM [math::CROSS $w1 $w2] Z
        math::NORM [math::CROSS $Z $X] Y
      } else {
        foreach {n1 n2 n3 n4 n5 n6 n7 n8} [hm_nodelist $e] break
        set e67 [math::ADD $coordArr($n6) $coordArr($n7)]
        set e58 [math::ADD $coordArr($n5) $coordArr($n8)]
        set e23 [math::ADD $coordArr($n2) $coordArr($n3)]
        set e14 [math::ADD $coordArr($n1) $coordArr($n4)]
        set dz [math::SUB [math::ADD $e58 $e67] [math::ADD $e14 $e23]]
        set dx [math::SUB [math::ADD $e23 $e67] [math::ADD $e14 $e58]]
        math::NORM [math::CROSS $dz $dx] Y
        math::NORM [math::CROSS $Y $dz] X
        math::NORM $dz Z
      }
      if {$type=="vector"} {
        lappend VX "*vectorentity(${e}1,0,${e}0,0,[join $X ","],$vecSize)"
        lappend VY "*vectorentity(${e}2,0,${e}0,0,[join $Y ","],$YSize)"
        lappend VZ "*vectorentity(${e}3,0,${e}0,0,[join $Z ","],$ZSize)"
      } else {
        lappend header "*node(${e}1,[join [math::ADD $centerArr($e) [math::MUL $X
$vecSize]] ","],0,0,0,0,0)"
```

```
        lappend header "*node(${e}2,[join [math::ADD $centerArr($e) [math::MUL $Y
$YSize]] ","],0,0,0,0,0)"
        lappend header "*node(${e}3,[join [math::ADD $centerArr($e) [math::MUL $Z
$ZSize]] ","],0,0,0,0,0)"
        lappend VX "*plotel(${e}1,1,${e}0,${e}1)"
        lappend VY "*plotel(${e}2,1,${e}0,${e}2)"
        lappend VZ "*plotel(${e}3,1,${e}0,${e}3)"
      }
    }
    set oF [open "_vec.hmasc" w]
    puts $oF [join $header \n]
    puts $oF [join $VX \n]
    puts $oF [join $VY \n]
    puts $oF [join $VZ \n]
    close $oF
    *saveviewmask "_orient" 1
    hm_blockmessages 1
    hm_blockredraw 1
    *createstringarray 0
    *feinputwithdata2 "#hmascii\\hmascii" "_vec.hmasc" 0 0 0 0 0 1 0 1 0
    hm_blockmessages 0
    hm_blockredraw 0
    *clearmark nodes 1
    *clearmark elements 1
    *clearmark elements 2
    *vectorlabel 0
    file delete _vec.hmasc
    *restoreviewmask "_orient" 1
    *setdisplayattributes 0 0
  }

   proc setOriElem {} {
    variable orientationElement
    variable orientationType
    variable reverseText
    *createentitypanel elements 1 "Select orientation element"
    set selElem [hm_info lastselectedentity elements]
    if {$selElem==0} {
      set orientationType ""
      return
    }
    set cfg [hm_getentityvalue elements $selElem config 0]
    switch $cfg {
      108 - 104 {
```

```
        set orientationElement $selElem
        set orientationType "Shell"
        set reverseText "Reverse normal"
        createSystems one
      }
      220 - 208 {
        set orientationElement $selElem
        set orientationType "Solid"
        set reverseText "Turn downwards (z->x)"
        createSystems one
      }
    }
    return
  }

  proc turnOriElem {{what "left"}} {
    variable orientationElement
    variable orientationType

    if {$orientationType==""} {
      return
    }
    if {$orientationType=="Shell"} {
      switch $what {
        "left" {
           *element2Dshiftnodes $orientationElement  1 3 0 0 0
        }
        "right" {
           *element2Dshiftnodes $orientationElement  1 1 0 0 0
        }
        "normal" {
          *createmark elements 1 $orientationElement
          #foreach {n3 n2 n1} [lrange [hm_nodelist $orientationElement] 1 3]
break
           eval *element2Dshiftnodes $orientationElement 4 0 [hm_getentityvalue
elements $orientationElement node4.id 0] 0 0
        }
      }
    } else {
      switch $what {
        "left" {
           *element3Dshiftnodes $orientationElement  1 1 0 0 0 0
        }
        "right" {
```

```
         *element3Dshiftnodes $orientationElement  1 3 0 0 0 0
      }
      "normal" {
         *element3Dshiftnodes $orientationElement  1 52 0 0 0 0
      }
    }
  }
  createSystems one
}

proc clearSystems {} {
  variable type
  if {$type== "vector"} {
    *createmark vectorcols 1 "^X" "^Y" "^Z"
    if {[hm_marklength vectorcols 1]>0} {
      *deletemark vectorcols 1
    }
  } else {
    *createmark comps 1 "^X" "^Y" "^Z"
    if {[hm_marklength comps 1]>0} {
      *deletemark comps 1
    }
  }
}

proc DestroyPanel {} {
    variable tabname
    variable main
    hm_framework removetab $tabname
    destroy $main
    clearSystems
}

proc orientMesh {{what ""}} {
  variable orientationElement
  variable orientationType
  if {$orientationType==""} {
    return
  }
  if {$what =="attached"} {
    *createmark elements 1 $orientationElement
    *appendmark elements 1 "by attached"
  } else {
    *createmarkpanel elements 1 "Select Elements to orientate"
```

```
    if {[hm_marklength elements 1]==0} {
      return
    }
  }
  if {$orientationType == "Shell"} {
    *createmark elements 2 "by config" 104 108
  } else {
    *createmark elements 2 "by config" 208 220
  }
  *markintersection elements 1 elements 2
   set oElems [hm_getmark elements 1]
   if {[llength $oElems]>0} {
     *createmark elements 2 $orientationElement
     if {$orientationType == "Shell"} {
       *element2Dalign 1 2 1
     } else {
       *element3Dalign 1 2 1
     }
     createSystems oElems
   }
}

proc CreatePanel {} {
    variable tabname
    variable main
    variable debug
    variable reverseText
    variable orientationElement
    variable orientationType
    set pady 3
    set ns "[namespace current]::"
    set tablist [ hm_framework getalltabs ]
    if { [ lsearch $tablist $tabname ] > -1 } {
      DestroyPanel
    }
    if {[winfo exist .orientQuad]} {
      destroy .orientQuad
    }

    set main [ frame .orientQuad ]
    hm_framework addtab $tabname $main

    label $main.spaceHead
    pack $main.spaceHead
```

```
      set oElem [hwt::LabeledFrame $main.oElem   " Arrange orientation element"
topPad 2\
                                 -side    top \
                                 -anchor  nw \
                                 -padx    1 \
                                 -pady    $pady \
                                 -justify left \
                                 -expand  0]

      set nButton  [button $oElem.nButton \
             -bg yellow \
             -activebackground yellow \
             -command "${ns}setOriElem" \
             -text "Define orientation Element" \
             -font [hwt::AppFont]]
      set cwButton  [button $oElem.cwButton \
             -command "${ns}turnOriElem right" \
             -text "Turn clockwise" \
             -font [hwt::AppFont]]
      set acwButton  [button $oElem.acwButton \
             -command "${ns}turnOriElem left" \
             -text "Turn anti-clockwise" \
             -font [hwt::AppFont]]

      if {$orientationType == "" || $orientationType == "Shell"} {
        set reverseText "Reverse normal"
      } else {
        set reverseText "Turn downwards (z->x)"
      }
      set nrmButton  [button $oElem.nrmbutton \
             -command "${ns}turnOriElem normal" \
             -textvariable ${ns}reverseText \
             -font [hwt::AppFont]]

      set aButton  [button $oElem.abutton \
             -command "${ns}orientMesh attached" \
             -text "Orient attached mesh" \
             -font [hwt::AppFont]]
      set oButton  [button $oElem.obutton \
             -command "${ns}orientMesh" \
             -text "Orient Selection" \
             -font [hwt::AppFont]]
      set sButton  [button $oElem.sbutton \
```

```
             -command "${ns}createSystems" \
             -text "Show Systems" \
             -font [hwt::AppFont]]
      set cButton  [button $oElem.cbutton \
             -command "${ns}clearSystems" \
             -text "Delete Systems" \
             -font [hwt::AppFont]]
      set tLabel [label $oElem.tLabel -textvariable [namespace
current]::orientationElement -font [hwt::AppFont]]
      set tType  [label $oElem.tType  -textvariable [namespace
current]::orientationType -font [hwt::AppFont]]


      grid columnconfigure $oElem 0 -weight 1 -uniform A
      grid columnconfigure $oElem 1 -weight 1 -uniform A
      grid columnconfigure $oElem 2 -weight 1 -uniform A
      grid columnconfigure $oElem 3 -weight 1 -uniform A
      grid $nButton    -row 0 -column 0 -padx 4 -pady 5 -sticky we -columnspan 2
      grid $tLabel     -row 0 -column 3 -padx 4 -pady 2 -sticky w
      grid $tType      -row 0 -column 2 -padx 4 -pady 2 -sticky e

      grid $aButton    -row 3 -column 2 -padx 4 -pady 2 -sticky we -columnspan 2
      grid $oButton    -row 4 -column 2 -padx 4 -pady 2 -sticky we -columnspan 2

      grid $cwButton   -row 3 -column 0 -padx 4 -pady 2 -sticky we -columnspan 2
      grid $acwButton  -row 4 -column 0 -padx 4 -pady 2 -sticky we -columnspan 2
      grid $nrmButton  -row 5 -column 0 -padx 4 -pady 2 -sticky we -columnspan 2

      grid $sButton    -row 6 -column 0 -padx 4 -pady 2 -sticky we -columnspan 2
      grid $cButton    -row 6 -column 2 -padx 4 -pady 5 -sticky we -columnspan 2

      if {0==1} {
        set shButton  [button $main.shbutton \
             -command "${ns}shuffleShellElements" \
             -text "Shuffle Shells" \
             -font [hwt::AppFont]]
        pack $shButton -side top
        set shSButton  [button $main.shSbutton \
             -command "${ns}shuffleSolidElements" \
             -text "Shuffle Solids" \
             -font [hwt::AppFont]]
        pack $shSButton -side top
      }
  }
```

```
  proc shuffleShellElements {} {
    *createmark elements 1 "by config" 104  108
    set eL [hm_getmark elements 1]
    foreach e $eL {
      set shift [expr $e % 4]
      if {$shift} {
        *element2Dshiftnodes $e 1 $shift 0 0 0
      }
      if {[expr {$e & 8}]} {
        lappend reverse $e
      }
    }
    if {[info exist reverse]} {
      eval *createmark elements 1 reverse
      *normalsreverse elements 1 0
      *normalsoff
    }
    *createmark elements 1 "by config" 104 108
    createSystems eL Shell
  }
  proc shuffleSolidElements {} {
    *createmark elements 1 "by config" 208 220
    set eL [hm_getmark elements 1]
    foreach e $eL {
      set shift [expr $e % 4]
      set face [expr ($e / 4) % 6 -1]
      if {$face + $shift > 2} {
        *element3Dshiftnodes $e 1 ${face}$shift 0 0 0 0
      }
    }
    *createmark elements 1 "by config" 208  220
    createSystems eL Solid
  }

}

orientElems::CreatePanel
```

A.3 Mesh Refinement

The H-specimen models required refining the element size from 2 mm to 1 mm to capture the smooth curve of the bend radius and reduce nodal penetration; however, further refinement was trivial and did not improve the accuracy of the predicted response (Figure 236).

(a) H-specimen U-section Mesh Refinement

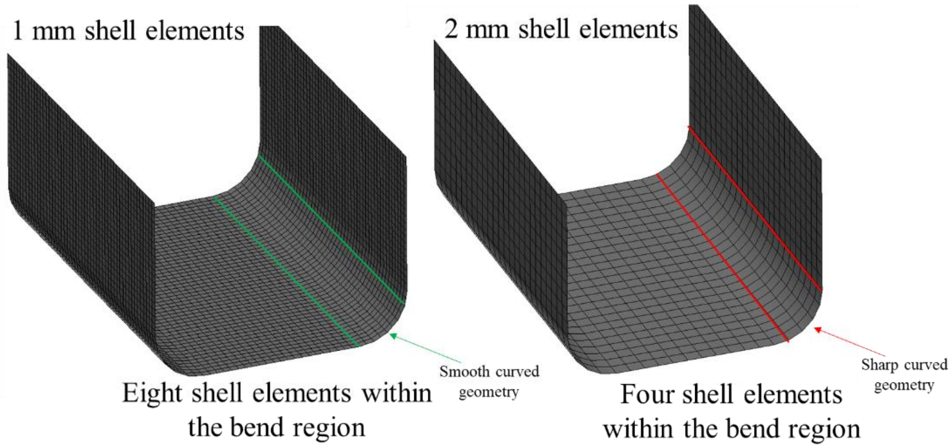

(b) Further Mesh Refinement from 1 mm to 0.5 mm was not needed

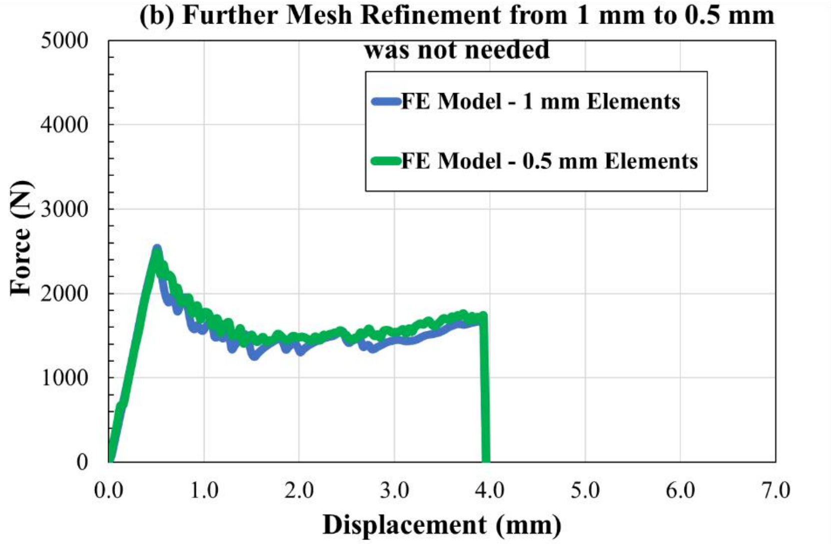

Figure 236: H-specimens models used a 1 mm element size to ensure a sufficient number of elements and achieve a smooth curved geometry within the bend region (a); however, further mesh refinement was not required (b).

A.4 Matlab Script to Fit the Experimental Data to a Power Law Curve and Output the Hardening Curve Using 100 Data Points with Positive Slope For FE Implementation

```
% Uses fitnlm() to fit a non-linear model (a power law curve) through noisy
data.
% Requires the Statistics and Machine Learning Toolbox, which is where
fitnlm() is contained.
% Initialization steps.
clc;    % Clear the command window.
close all;  % Close all figures (except those of imtool.)
clear;  % Erase all existing variables. Or clearvars if you want.
workspace;  % Make sure the workspace panel is showing.
format long g;
format compact;
fontSize = 20;
%% Import data from spreadsheet
% Script for importing data from the following spreadsheet:
%
%    Workbook: E:\OneDrive - University of Waterloo\Material
Characterization\AA6061\Summary.xlsx
%    Worksheet: Fitting
%
% Auto-generated by MATLAB on 25-Apr-2022 02:48:26

%% Set up the Import Options and import the data
opts = spreadsheetImportOptions("NumVariables", 6);

% Specify sheet and range
opts.Sheet = "Fitting";
opts.DataRange = "A3:F567";

% Specify column names and types
opts.VariableNames = ["STRESS_1", "STRAIN_1", "STRESS_2", "STRAIN_2",
"STRESS_3", "STRAIN_3"];
opts.VariableTypes = ["double", "double", "double", "double", "double",
"double"];

% Import the data
Summary = read ("C:\Users\ahamibra\OneDrive - University of Waterloo\Material
Characterization\AA6061\Summary.xlsx", opts, "UseExcel", false);


%% Clear temporary variables
clear opts

% Define data.
STRESS = Summary.STRESS_3;
STRAIN = Summary.STRAIN_3;
strain_at_failure = 0.1 %%plastic strain at failure
STRESS(any(isnan(STRESS), 2), :) = [];
STRAIN(any(isnan(STRAIN), 2), :) = [];
```

```
Slope = gradient(STRESS(:)) ./ gradient(STRAIN(:));

STRAIN(Slope<=50) = [];
STRESS(Slope<=50) = [];
p = polyfit(STRAIN(end-2:end),STRESS(end-2:end),1);
strain_interval =  linspace(STRAIN(end),strain_at_failure,(strain_at_failure-
STRAIN(end))/0.005);
stress_interval = polyval(p,strain_interval);
STRESS = [STRESS; transpose(stress_interval)];
STRAIN = [STRAIN; transpose(strain_interval)];
Slope = gradient(STRESS(:)) ./ gradient(STRAIN(:));

% Create the X and Y coordinates: only from second point onwards.
X = STRAIN(1:end);
Y = STRESS(1:end);

% send to fitnlm().
plot(X, Y, 'b*', 'LineWidth', 2, 'MarkerSize', 1);
grid on;
hold on;
beta0 = [150,0,0.1]; % Guess values to start with.  .


% Convert X and Y into a table, which is the form fitnlm() likes the input
data to be in.
tbl = table(X(:), Y(:));
% Define the model as Stress = A+B*(Plastic_Strain)^n
modelfun = @(b,x) (b(1)+b(2)*x(:, 1).^b(3))
mdl = fitnlm(tbl, modelfun, beta0);

% Extract the coefficient values from the the model object.
coefficients = mdl.Coefficients{:, 'Estimate'}

% Create smoothed/regressed data using the model:
yFitted = coefficients(1) + (coefficients(2) * X.^ coefficients(3));
% Do another fit but with the number of points needed for LS-DYNA.
X1000 = linspace(X(1), X(end), 100);
yFitted1000 = coefficients(1) + (coefficients(2) * X1000.^ coefficients(3));
% Now we're done and we can plot the smooth model as a red line going through
the noisy blue markers.
hold on;
% Plot red diamonds fitted values at the training X values.
plot(X, yFitted, 'rd', 'LineWidth', 2, 'MarkerSize', 1);
% Plot fitted values at all the 1000 X values with a red line.
plot(X1000, yFitted1000, 'r-', 'LineWidth', 2);
grid on;
title('Power Law Regression with fitnlm()', 'FontSize', fontSize);
xlabel('Equivalent Plastic Strain', 'FontSize', fontSize);
ylabel(Stress', 'FontSize', fontSize);
legendHandle = legend('Original Stress-Strain Data', 'Fitted Data',
'Location', 'southeast');
legendHandle.FontSize = 25;
```

```
message = sprintf('Coefficients for Y = C * (B + X) .^ n:\n  C = %8.5e\n  B = 
%8.5f\n  n = %8.5f',...
coefficients(1), coefficients(2), coefficients(3));
text(410, 0.25, message, 'FontSize', 23, 'Color', 'r', 'FontWeight', 'bold', 
'Interpreter', 'none');

%Tabulated data to copy to LS-DYNA
Strain_to_dyna = transpose(X1000)
Stress_todyna = transpose(yFitted1000)
```

Appendix B: Caiman Hat Section Drawings